Dissertation
submitted to the
Combined Faculties for the Natural Sciences and for Mathematics
of the Ruperto Carola University of Heidelberg, Germany
for the degree of
Doctor of Natural Sciences

presented by

Master of Arts - Physics:	André Butz
born in:	Coburg

Oral examination: 5 July 2006

Case Studies of
Stratospheric Nitrogen, Chlorine and Iodine Photochemistry
Based on Balloon Borne
UV/visible and IR Absorption Spectroscopy

Referees: Prof. Dr. Klaus Pfeilsticker

Prof. Dr. Frank Arnold

THESE DE DOCTORAT DE L'UNIVERSITE PARIS 6

Spécialité

PHYSIQUE MOLECULAIRE ET APPLICATIONS

Présentée par

André BUTZ

Pour obtenir le grade de

DOCTEUR DE L'UNIVERSITE PARIS 6

Sujet de la thèse:

CASE STUDIES OF STRATOSPHERIC NITROGEN, CHLORINE AND IODINE PHOTOCHEMISTRY BASED ON BALLOON BORNE UV/VISIBLE AND IR ABSORPTION SPECTROSCOPY

soutenue le 5 juillet 2006 devant le jury composé de:

M. Claude Camy-Peyret	Directeur de thèse
M. Klaus Pfeilsticker	Directeur de thèse
M. Michel Pirre	Rapporteur
M. Frank Arnold	Rapporteur
M. Claude Fabre	Examinateur
M. Iring Bender	Examinateur

Fallstudien zur Fotochemie stratosphärischen Stickstoffs, Chlors und Iods basierend auf ballongestützter Absorptionsspektroskopie im UV/sichtbaren and infraroten Spektralbereich

Stickstoff- und Halogenverbindungen spielen eine tragende Rolle beim katalytischen Abbau von stratosphärischem Ozon. Ballongestützte, spektroskopische Beobachtungen der Höhenprofile wichtiger Stickstoff-, Chlor- und Iodverbindungen erlauben, die Qualität modernster Messgeräte und Auswertealgorithmen abzuschätzen und neue Einsichten in die stratosphärische Fotochemie zu gewinnen.
Ein Vergleich zwischen Messungen von O_3 und NO_2 im UV/sichtbaren und infraroten Spektralbereich durch die DOAS und LPMA Ballon-Instrumente und das SCIAMACHY Satelliten-Instrument liefert vernünftige Übereinstimmung. Die Vielzahl an chemischen Spezies, die von den LPMA/DOAS Geräten gemessen werden, ermöglicht eine Untersuchung des Budgets und der Aufteilung stratosphärischen Stickstoffs und Chlors für verschiedene geophysikalische Bedingungen. Vergleiche mit 3-D Simulationen des Chemie-und-Transport Models (CTM) SLIMCAT weisen darauf hin, dass das Verhältnis von kurz- zu langlebigen Stickstoffspezies vom Modell überschätzt wird. Für einen Fall im polaren Winter, kann das 1-D model für stratosphärische Chemie LABMOS mittels der Beobachtungen getrimmt werden, um kürzlich veröffentlichte Neuerungen in Bezug auf die katalytischen ClO-ClO and ClO-BrO Zyklen zu testen und Ozonverlustraten zu modellieren. Die vorgeschlagenen kinetischen Neuerungen führen zu 20% bis 25% erhöhtem Ozonverlust. Messungen von Obergrenzen für IO and OIO bestätigen frühere Beobachtungen in hohen und mittleren Breiten und erweitern den Datensatz auf tropische Breiten. Ausgehend von den gemessenen Obergrenzen für IO and OIO zeigen Modellsimulationen, dass Iodverbindungen in der unteren tropischen Stratosphäre weniger als (0.32 ± 0.11) ppt oder (0.38 ± 0.10) ppt ausmachen je nachdem ob OIO photolysiert oder nicht.

Etudes de la photochimie stratosphérique de composés azotés, chlorés et iodés basées sur la spectroscopie d'absorption dans les domaines UV/visible et infrarouge effectuée sous ballon

Les espèces chimiques azotées et halogénées jouent un rôle important dans la destruction catalytique de l'ozone stratosphérique. Des mesures spectroscopiques de profils verticaux d'espèces azotées, chlorées et iodées sont utilisées pour améliorer la connaissance de la photochimie stratosphérique ainsi que pour évaluer la qualité des données fournies par les instruments embarqués.
La comparaison entre les concentrations d'O_3 et de NO_2 pour les domaines spectraux UV/visible et infrarouge déterminées par les instruments DOAS et LPMA embarqués sous ballon et par l'instrument satellitaire SCIAMACHY montre un accord raisonnable. L'ensemble des espèces mesurées par LPMA/DOAS sous ballon donne la possibilité d'étudier la répartition des espèces azotées et chlorées pour différentes conditions géophysiques. La comparaison des observations avec des simulations du modèle de chimie-transport (CTM) SLIMCAT, montre que le modèle surestime le rapport entre les espèces radicalaires et les espèces réservoir. Pour un cas hivernal dans les régions polaires, le modèle de chimie stratosphérique LABMOS peut être contraint par les mesures pour tester de nouvelles constantes cinétiques recommendées récemment pour les réactions chimiques des cycles catalytiques de ClO-ClO et de ClO-BrO ainsi que pour calculer le taux de destruction de l'ozone. Employant ces nouvelles données cinétiques, la destruction de l'ozone est plus grande de 20% à 25% par rapport au cas où on utilise les données standard. Les mesures des limites supérieures pour IO et OIO sont en accord avec les observations précédentes pour les hautes et moyennes latitudes et élargissent les observations aux latitudes tropicales. Basé sur ces limites supérieures de concentration de IO et OIO, un modèle photochimique montre que la limite supérieure de la quantité totale d'iode dans la basse stratosphère tropicale est de (0.32 ± 0.11) ppt, si OIO est photolysé, et de (0.38 ± 0.10) ppt, si OIO n'est pas photolysé.

Case Studies of Stratospheric Nitrogen, Chlorine and Iodine Photochemistry Based on Balloon Borne UV/visible and IR Absorption Spectroscopy

Nitrogen and halogen bearing compounds play an important role in catalytic loss of stratospheric ozone. Balloon borne spectroscopic measurements of the vertical distribution of the most important nitrogen, chlorine and iodine containing species are used to estimate the quality of state-of-the-art instruments and retrieval algorithms and to gain new insights into stratospheric photochemistry.

A comparison study between observations of O_3 and NO_2 in the UV/visible and infrared spectral ranges involving the DOAS and LPMA balloon borne instruments and the satellite borne SCIAMACHY instrument yields reasonable agreement. The variety of trace gases measured by the LPMA/DOAS balloon payload allows for investigation of the budget and partitioning of stratospheric nitrogen and chlorine under several geophysical conditions. Comparison of the observations with the 3-D chemical transport model (CTM) SLIMCAT indicates that the ratio between short- and long-lived nitrogen containing species is overestimated by the model. For a high-latitude winter scenario the 1-D stratospheric chemistry model LABMOS is constrained by the observations in order to test recently published updates of the reaction kinetics of the ClO-ClO and ClO-BrO catalytic cycles with respect to model-measurement agreement and ozone loss rates. The latter are enhanced by 20% to 25% when using the kinetic updates. The determination of upper limits for IO and OIO corroborate earlier findings of the budget of stratospheric iodine in high- and mid-latitudes and extend the data base to tropical latitudes. Given the measured IO and OIO upper limits, model calculations show that total gaseous iodine in the lower tropical stratosphere is less abundant than (0.32 ± 0.11) ppt or (0.38 ± 0.10) ppt depending on whether OIO photolysis occurs or does not.

Contents

Introduction

Ozone plays an ambiguous and manifold role in the Earth's atmosphere. Close to the Earth's surface it acts as an air pollutant and may cause health problems when inhaled by men. On the other hand ozone shields life on Earth from being harmed by solar UV radiation which is effectively absorbed by the stratospheric ozone layer. Besides absorbing solar UV, ozone emits radiation in the infrared spectral range and, thus, contributes to the global radiation budget which controls temperatures on Earth. Hence, knowing the distribution of ozone in space and time and understanding its transport, formation and loss processes as well as its link to the Earth's climate, is one of the most important and vital challenges of atmospheric physics and chemistry.
Figure 1 shows the vertical distribution of stratospheric ozone for several geophysical conditions. Evidently, the so-called ozone layer cannot be regarded as a uniform, spherical and stationary layer surrounding the Earth. Even the notion 'layer' may be questioned in the view of highly filamented structures observed in the lower Arctic winter stratosphere. Ozone concentrations are subject to a variety of dynamic and photochemical effects which comprise three-dimensional transport of air and photolytic as well as gas-phase and condensed-phase chemical reactions. Atmospheric research has accumulated evidence that anthropogenic influence is able to alter the natural equilibrium between formation and loss of ozone on a global scale. The most prominent example is the ozone hole which is annually observed in the Antarctic and to a lesser degree in the Arctic lower stratosphere during spring. Ozone hole events reveal an almost complete temporary loss of ozone (not shown in figure 1) triggered by man-made halogen bearing trace gases which are transported to the upper atmosphere. Dedicated research has led to a basic understanding of the involved physical and chemical processes and has paved the way for international protocols which prohibit the production and emission of most of the hazardous species. In general, the interplay between naturally occurring processes and anthropogenic perturbations results in a distribution of stratospheric ozone which is highly variable in time and space and which is not yet completely understood. Although the fundamental concepts of stratospheric dynamics and photochemistry are well-known, significant inconsistencies remain when it comes to comparing model simulations of the atmosphere with observations on a quantitative level or when predicting the future evolution of the ozone layer. The overall goal of the presented study is to contribute to an improved perception of some of the processes involved in transport, production and loss of stratospheric ozone and to facilitate modeling of the Earth's atmosphere in past and future.

The presented experimental approach relies on spectroscopic measurements of absorption signatures of atmospheric trace gases in the transmitted solar spectrum. The observations are performed by two DOAS (Differential Optical Absorption Spectroscopy) grating spectrometers sensitive to the UV and visible spectral ranges and by the LPMA (Limb Profile Monitor of the Atmosphere) Fourier

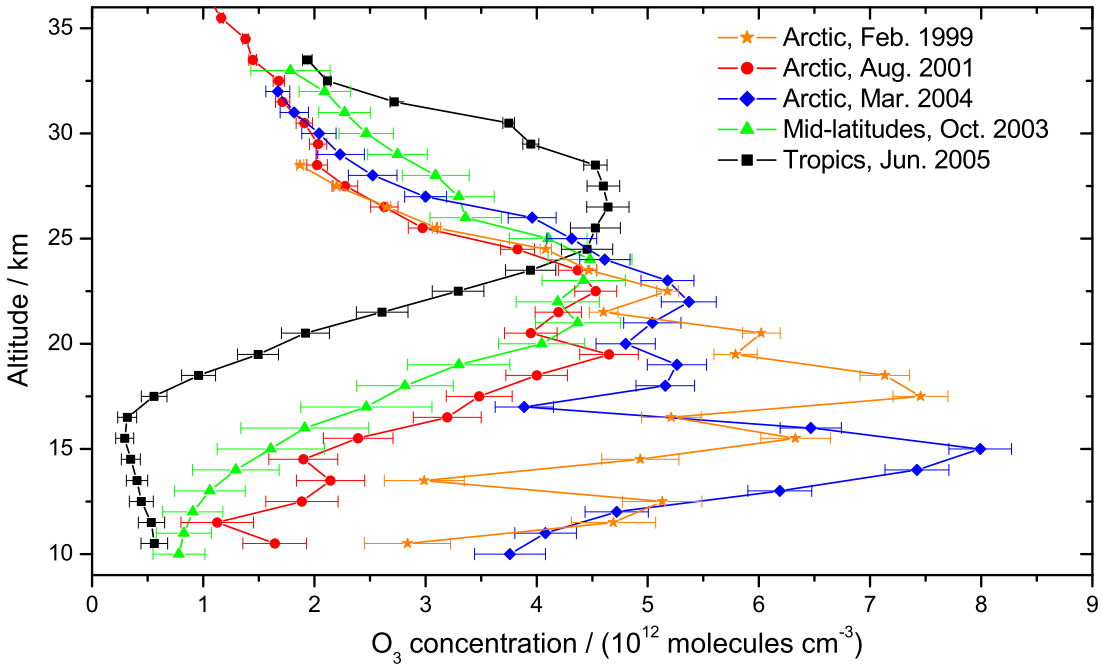

Figure 1: Ozone concentration versus altitude measured by the LPMA/DOAS balloon payload under various geophysical conditions.

Transform spectrometer which is sensitive to the infrared spectral range. A stratospheric balloon carries the instruments into the stratosphere up to 30 to 40 km altitude. In principle, the comprehensive setup of the LPMA/DOAS payload provides a platform from which almost all important processes for stratospheric photochemistry can be investigated. Former studies comprise observations of the oxygen (Pfeilsticker et al., 2001; Bösch, 2002), nitrogen (Payan et al., 1999; Bösch et al., 2001; Bösch, 2002; Dufour et al., 2005), chlorine (Payan et al., 1998), bromine (Harder et al., 1998; Ferlemann et al., 1998; Harder et al., 2000; Fitzenberger et al., 2000; Pfeilsticker et al., 2000; WMO, 2003; Dorf et al., 2005) and iodine (Bösch et al., 2003) involving chemical cycles, as well as measurements of the extra-terrestrial solar irradiance (Gurlit et al., 2005) and stratospheric aerosol abundances (Hirsekorn, 2003). Although balloon-borne measurements are inherently restricted to snapshot-like observations, dedicated case studies can serve as test cases for photochemical or physical processes which are typical of the large-scale stratospheric environment.

This study in particular aims at providing new insight into stratospheric and upper tropospheric nitrogen, chlorine and iodine driven ozone-related photochemistry based on LPMA/DOAS balloon borne observations and model calculations using the chemical transport model SLIMCAT and the stratospheric chemistry model LABMOS.
Since stratospheric photochemistry is understood to a large extent, new insights require high-quality measurements of the involved chemical species. Hence, the LPMA and DOAS observations performed in the infrared and UV/visible spectral ranges are inspected for internal consistency by comparing the simultaneously retrieved abundances of ozone (O_3) and nitrogen dioxide (NO_2). Further comparison

to satellite borne observations conducted by the SCanning Imaging Absorption spectroMeter for Atmospheric CHartographY (SCIAMACHY) yields an estimate of the agreement between different state-of-the-art instruments and retrieval techniques.
Based on the quality assessment for O_3 and NO_2, a detailed investigation of the nitrogen budget and partitioning under different geophysical conditions is performed using simultaneous LPMA/DOAS measurements of the most important long- and short-lived nitrogen containing species. The partitioning between long- and short-lived nitrogen compounds is crucial for ozone chemistry since the short-lived species, such as NO_2, on the one hand govern ozone loss in the middle stratosphere and on the other hand buffer ozone loss by deactivation of halogen bearing radicals. Under ozone-hole conditions in polar winter, conversion of the short-lived nitrogen oxides to their long-lived reservoirs and irreversible removal of nitrogen compounds from the stratosphere lead to prolonged ozone-loss periods. The proper representation of nitrogen chemistry in models of the stratosphere is tried by model-measurement comparisons.
LPMA/DOAS observations also allow for investigation of the chlorine budget and partitioning for dedicated cases. The stratospheric chlorine budget is largely influenced by anthropogenic emissions of chlorofluorocarbons (CFCs) which are transported to the stratosphere. There, CFCs are decomposed by UV radiation to yield inorganic chlorine compounds which can be converted to short-lived, ozone-destroying chlorine species by reactions on the surface of particles. Such short-lived chlorine species, together with their bromine bearing analogs, are responsible for the polar ozone hole events and also contribute to the observed decrease of ozone abundances in mid-latitudes. The comprehensive dataset provided by LPMA/DOAS allows for constraining model simulations and for testing alternative model formulations of chlorine and bromine induced ozone loss.
Given the important role of chlorine and bromine in ozone-related photochemistry, it is tempting to speculate on a similar, albeit less dominant role of stratospheric iodine bearing compounds. So far, iodine could not be detected in significant amounts in the mid- and high-latitudinal stratosphere where upper limits are currently on the threshold of relevance for ozone loss. Here, further observations supplement earlier findings for high- and mid-latitudes and extend the database to the tropical upper troposphere and lower stratosphere. Since transport of air from the troposphere to the stratosphere occurs primarily at low-latitudes, tropical observations are well suited to investigate the stratospheric iodine budget by observing the amount of iodine actually transported into the stratosphere.

The organization of the present manuscript follows the outline given above. Chapter 1 recapitulates the most important processes of atmospheric dynamics and photochemistry. Chapter 2 highlights the basics of radiative transfer and molecular absorption in the Earth's atmosphere and, hence, provides the theoretical background for chapter 3 where the instrumental setup and the methods used for the retrieval of trace gas abundances are discussed in detail. Chapter 4 evaluates the agreement of O_3 and NO_2 abundances simultaneously retrieved by LPMA and DOAS. Chapter 5 extends the O_3 and NO_2 comparison to the satellite borne dataset provided by the SCIAMACHY instrument and illustrates an approach how to compare observations which do not coincide in time and space. Chapter 6 addresses the budget and partitioning of stratospheric nitrogen and chlorine. It includes in-depth model-measurement comparisons as well as the deduction of ozone loss rates for polar winter. Measurements of IO and OIO at high-, mid- and low-latitudes and implications for the stratospheric iodine budget are presented in chapter 7.

Chapter 1

Atmospheric dynamics and photochemistry

The abundances of trace gases in the atmosphere are governed by dynamic and photochemical processes. In the following the basics of atmospheric dynamics and photochemistry are discussed in order to provide the framework for detailed investigations and case studies in the subsequent chapters. Since the present work focuses on processes in the lower and middle stratosphere emphasis is put on these specific layers of the Earth's atmosphere.

1.1 Basics of atmospheric dynamics

The lowermost layer of the Earth's atmosphere, the troposphere, is characterized by a temperature decrease between the ground and its upper boundary, the tropopause. Absorption of the incoming solar radiation by the Earth's surface, net radiative cooling in the middle and upper troposphere and release of latent heat by condensation of water vapor make convection the predominant mechanism of vertical transport. The influence of the Earth's surface on tropospheric air mass transport through frictional forces is important for small as well as large scale circulation patterns and renders the atmosphere sensitive to surface topography. As a consequence of these stirring processes, the troposphere is well mixed on the timescale of a few months, albeit interhemispheric mixing is slightly less rapid.
Above the tropopause temperature increases with altitude and creates an atmospheric layer, the stratosphere, where convective transport is not important. The energy balance of the stratosphere is dominated by radiative processes, e. g. absorption of solar UV radiation by ozone and molecular oxygen and emission of thermal radiation by carbon dioxide, water vapor and other trace gases. Radiative equilibrium is perturbed by so-called planetary waves which are generated in the troposphere and propagate partly into the stratosphere where they deposit energy and momentum and contribute substantially to stratospheric transport patterns. The timescale of meridional, hemispheric mixing in the stratosphere is on the order of four to six years. The upper boundary of the stratosphere, the stratopause, marks the lower boundary of the mesosphere where temperature again decreases.

When discussing dynamic aspects of the Earth's atmosphere it is convenient to introduce the con-

cept of potential temperature Θ which is defined by

$$\Theta = T \left(\frac{p_0}{p} \right)^{\frac{\kappa-1}{\kappa}}, \tag{1.1}$$

where T is temperature, p pressure, p_0 a reference pressure (commonly 1000 mbar) and $\kappa = \frac{c_p}{c_V}$ with the specific heat of air at constant pressure c_p and constant volume c_V. Hence, potential temperature is the temperature that an air parcel would attain if brought adiabatically, i. e. without heat exchange, to the reference pressure. Potential temperature is conserved as long as diabatic processes, e. g. release of latent heat or absorption of radiation, do not occur. This implies that without diabatic heating or cooling air parcels are constrained to move on surfaces of constant potential temperature, the isentropes.
A similar concept which is useful for horizontal transport problems is that of the potential vorticity Z defined through

$$Z = \frac{f + \zeta}{\rho} \frac{d\Theta}{dz} \tag{1.2}$$

where z is the vertical coordinate, ρ the density of air, ζ the relative vorticity and $f = 2\,\Omega \sin\phi$ the Coriolis parameter with the latitude ϕ and the absolute value of the angular velocity of the Earth Ω. Potential vorticity is expressed in units of $10^{-6}\,\mathrm{K\,m^2\,kg^{-1}\,s^{-1}} = 1\,\mathrm{PVU}$ (Potential Vorticity Unit). The relative vorticity ζ in horizontal cartesian coordinates is given by

$$\zeta = \frac{\partial v_y}{\partial x} - \frac{\partial v_x}{\partial y}, \tag{1.3}$$

with the horizontal components of wind speed v_x and v_y. Potential vorticity is conserved for adiabatic and frictionless flow. For many applications the timescales of adiabatic or dissipative processes are larger than the timescales of interest, so potential vorticity is a good tracer for air mass transport. If potential vorticity is conserved, air masses are constrained to move on surfaces of constant potential vorticity which are often aligned to latitude bands. This implies that meridional air mass transport is often only possible through dissipative processes, e. g. turbulences induced by planetary waves.

1.1.1 The general circulation of the stratosphere

The most important aspects of stratospheric dynamics are illustrated in figure 1.1 which represents a meridional cross section of the Earth's atmosphere.
In zonal direction strong winds are observed that originate from thermal gradients between the tropics and high-latitudes. In the lower stratosphere the coldest temperatures occur in the tropics while the summer polar stratosphere is heated by absorption of solar radiation and hence is relatively warm. The thermal gradient from the summer pole to the equator causes strong thermal easterlies, winds in East-West direction. In winter the polar stratosphere is colder than its tropical counterpart due to the lack of insolation which results in strong westerlies surrounding the winter pole, the polar vortex. The change from winter westerlies to summer easterlies in general occurs after the equinoxes. The polar vortex largely isolates polar from mid-latitudinal air and prevents meridional mixing of air masses due to the potential vorticity barrier which is a prerequisite for the occurrence of photochemical processes that lead to the formation of the ozone hole. While in the southern hemisphere the polar vortex generally evolves unperturbed, the northern polar vortex is subject to frequent perturbations by tropospheric waves propagating into the stratosphere. Their dissipation causes meridional transport of air and dynamic warming of the winter

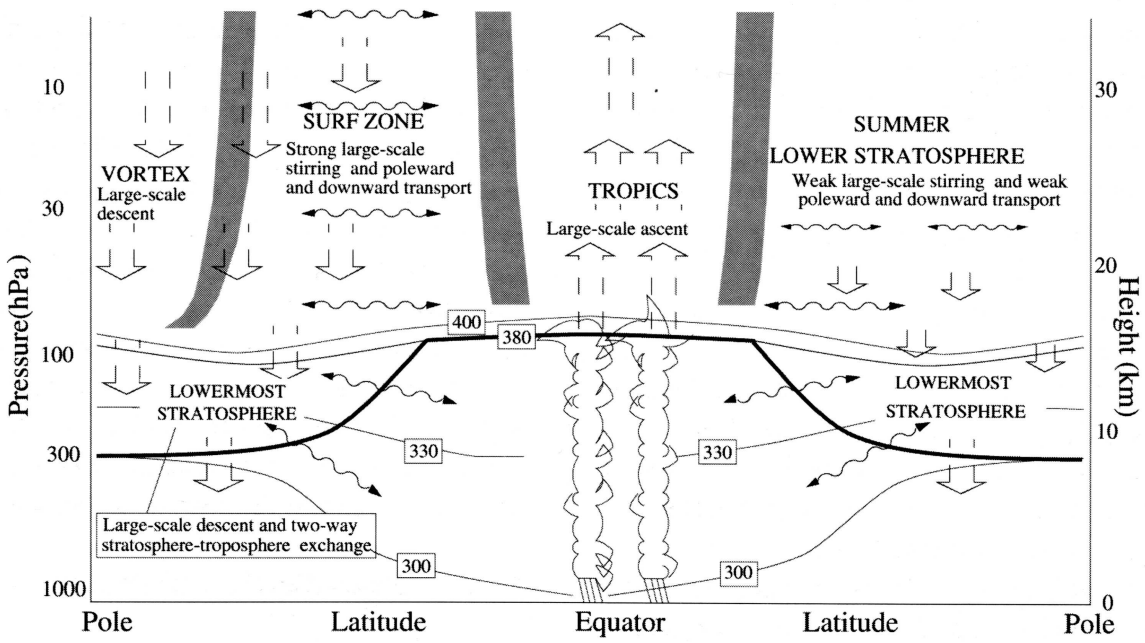

Figure 1.1: General circulation patterns in the atmosphere. For details see text. Adopted from WMO (1998).

polar regions.

Meridional transport in the stratosphere is governed by a large scale diabatic circulation which is historically referred to as the Brewer-Dobson circulation. It is characterized by rising motion in the tropics, poleward flow at mid-latitudes and sinking motion in the polar regions as depicted in figure 1.1. The meridional flow is driven predominantly by dissipation of tropospheric waves propagating into the stratosphere. In general waves are large scale disturbances of air flow from the zonal direction which are initiated for example by mountain ridges. Due to the decrease in air density the amplitude of such waves increases exponentially with altitude when propagating from the troposphere into the stratosphere. Eventually, the wave becomes unstable and its energy and momentum can be dissipated by the ambient atmosphere e. g. if the vertical potential temperature gradient becomes negative locally, dissipation of energy and momentum can occur through local turbulences. Dissipation of atmospheric waves together with the Coriolis force results in a net poleward motion. This mechanism is often referred to as the extratropical pump (Holton et al., 1995) since wave activity occurs mainly in mid-latitudes. Figure 1.1 calls the respective region “surf zone” which implies that the internal transport is rather fast. Since tropospheric waves can only propagate effectively into the winter stratosphere, which is dominated by westerlies (Roedel, 2000), the meridional circulation exhibits a strong seasonal cycle where meridional transport and polar subsidence are most effective in winter and less effective in summer. Since for topographic reasons waves are more frequent and intense in the northern than in the southern hemisphere, meridional flow in the northern hemisphere is more pronounced than in its southern counterpart. Important barriers for meridional transport are indicated as black shaded regions in figure 1.1. The polar transport barrier is represented by the edge of the winterly polar vortex where conservation of potential vorticity prevents meridional exchange of air masses. The subtropical transport barrier, located between

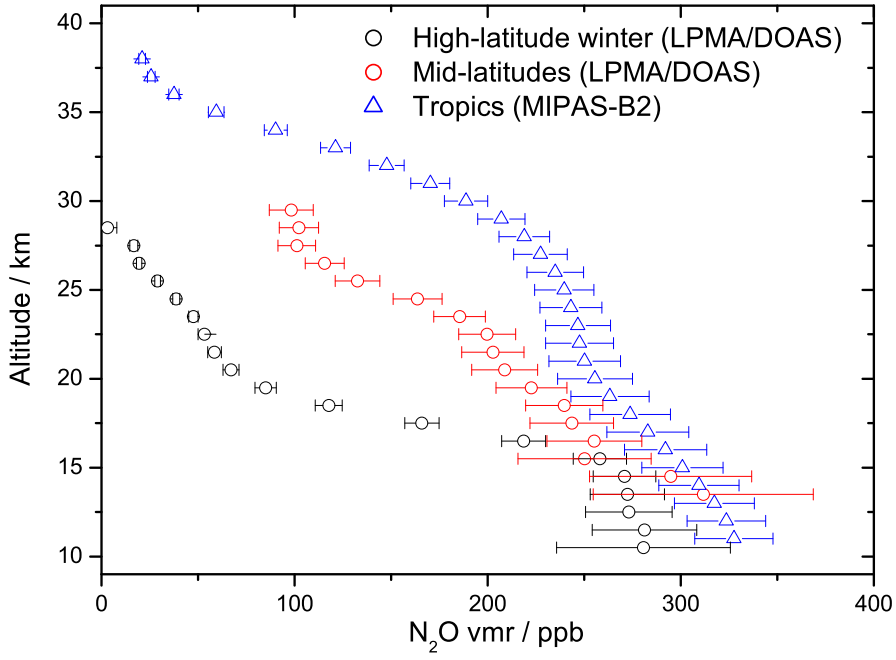

Figure 1.2: N_2O volume mixing ratio as a function of altitude as measured by the LPMA/DOAS and MIPAS-B2 balloon payloads at the mid-latitudinal station Leon (42.6°N, 5.7°W) in November 1996 (red circles), at the high-latitudinal station Kiruna (67.9°N, 21.1°E) in February 1999 (black boxes) and at the tropical station Teresina (5.4°S, 42.4°W) in June 2005 (blue triangles). The MIPAS-B2 data are by courtesy of G. Wetzel.

20°N/S and 30°N/S latitude, separates the horizontally well mixed surf zone from the tropical region where air is transported predominantly in vertical direction which is often referred to as “tropical pipe” (Plumb, 1996). The timescales of meridional transport and its division in three relatively well separated regions can be illustrated by vertical profiles of photochemically long-lived trace gases such as N_2O. Figure 1.2 shows N_2O vertical profiles measured by the LPMA/DOAS and MIPAS-B2 balloon payloads at high-, mid- and low-latitudes. In tropical regions, N_2O is transported from the troposphere into the stratosphere by uplift through the tropical pipe. Meridional transport and simultaneous sinking motion to mid- and high-latitudes causes aging of air masses and leads to a characteristic evolution of the N_2O vertical profile from equator to pole.

1.1.2 Stratosphere-troposphere exchange

The boundary between the stratosphere and the troposphere is the tropopause. Evidently, air that travels from the troposphere to the stratosphere or vice versa has to cross the tropopause. According to the World Meteorological Organization (WMO) the tropopause is defined as the lowest altitude where the temperature lapse rate decreases to $2\,\mathrm{K\,km^{-1}}$ or less and the lapse rate between this level and any level within the next higher 2 km does not exceed $2\,\mathrm{K\,km^{-1}}$. Alternatively, the extratropical tropopause is sometimes defined as the 2 PVU potential vorticity surface. In the tropics the 380 K isentrope is often considered as tropopause. For a better understanding of stratosphere-troposphere exchange the stratosphere can be di-

vided in a stratospheric overworld above the 380 K isentrope and an extratropical lowermost stratosphere which is the region between the extratropical tropopause ($\Theta < 380$K) and the 380 K isentrope (figure 1.1). The large scale stratosphere-troposphere exchange is controlled by the global circulation driven by the extratropical pump, implying that the bulk of air transport from the troposphere to the stratosphere occurs in the tropics (Holton et al., 1995). Accordingly, stratospheric air re-enters the troposphere predominantly in mid- and high-latitudes. In the lowermost stratosphere, stratosphere-troposphere exchange can occur through isentropic transport since the isentropes cross the tropopause. There, tropopause folds and stratospheric intrusions contribute to stratosphere-troposphere exchange, but the detailed mechanisms of exchange between the lowermost stratosphere and the troposphere are very complex (figure 3 in Stohl et al. (2003)) and far from being completely understood. Recent studies indicate that single events of deep convection to high altitudes could contribute to mass transport into the stratosphere (Dessler, 2002). Deep convection events can be triggered and enhanced by fires on the ground as observed by Damoah et al. (2006) who report on such pyro-convection in mid-latitudes penetrating up to 3 km above the tropopause. However, it remains unclear to what extent deep convection and pyro-convection contribute to the global budget of stratosphere-troposphere exchange.

1.2 Photochemistry of ozone in the stratosphere

Beside the dynamic aspects, stratospheric trace gas abundances are controlled by photochemical processes. The adjective 'photochemical' implies that solar radiation is the driving force for chemical activity in the stratosphere. Ozone is the most interesting chemical species as pointed out in the introduction. Formation and destruction of stratospheric ozone is controlled by reaction cycles involving oxygen, hydrogen, nitrogen and halogen containing species which are subject to solar radiation and may be processed in the gas phase or on the surface or in the bulk of liquid or particulate matter. The understanding of the complicated interplay between the different species is conceptually facilitated by considering the different timescales on which chemical reactions occur (Brasseur and Solomon, 1986). Typically, it is possible to define an artificial species which is the sum of all rapidly interchanging compounds of one chemical family, e. g. the odd oxygen species $O_x = O_3 + O$ or the sum of the short-lived nitrogen species $NO_x = NO_2 + NO$. In a mathematical sense the sum refers to the concentrations or the volume mixing ratios of the respective species. Although the components of such artificial species rapidly interchange, the artificial species themselves are subject to much slower chemical processes linking the short-lived entities with their long-lived reservoirs, e. g. O_2 or HNO_3. While the short-lived species are responsible for the actual ozone formation or destruction mechanisms, the rate of their removal to or supply from the long-lived reservoirs determines the efficiency of the respective reaction cycles. Often it proves useful to further distinguish the short- and long-lived species from their source gases which, in general, are transported from the troposphere to the stratosphere. There, the source gases are photolytically processed to supply the pool of species relevant for ozone chemistry. An attempt to sketch the interplay between the various species important for stratospheric chemistry is shown in figure 8.1 in the appendix.

1.2.1 Stratospheric odd oxygen photochemistry

The formation of the stratospheric ozone layer can be understood from the Chapman cycle (Chapman, 1930), a small number of reactions which involve oxygen species, only,

$$\mathrm{O_2} + h\nu \longrightarrow 2\,\mathrm{O} \tag{R1.1}$$
$$\mathrm{O} + \mathrm{O_2} + \mathrm{M} \longrightarrow \mathrm{O_3} + \mathrm{M} \tag{R1.2}$$

$$\mathrm{O_3} + h\nu \longrightarrow \mathrm{O_2} + \mathrm{O} \tag{R1.3}$$
$$\mathrm{O_3} + h\nu \longrightarrow \mathrm{O_2} + \mathrm{O}(^1\mathrm{D}) \tag{R1.4}$$
$$\mathrm{O}(^1\mathrm{D}) + \mathrm{M} \longrightarrow \mathrm{O} + \mathrm{M} \tag{R1.5}$$
$$\mathrm{O} + \mathrm{O} + \mathrm{M} \longrightarrow \mathrm{O_2} + \mathrm{M} \tag{R1.6}$$
$$\mathrm{O} + \mathrm{O_3} \longrightarrow 2\,\mathrm{O_2}. \tag{R1.7}$$

While reactions (R1.1) and (R1.2) produce ozone, reactions (R1.3) through (R1.7) represent loss processes of odd oxygen. Photodissociation of molecular oxygen according to reaction (R1.1) occurs at wavelengths smaller than 242 nm through absorption of UV radiation in the spectral ranges of the Herzberg continuum, the Schumann-Runge bands and the Schumann-Runge continuum. It generates ground-state O(^{3}P) as well as oxygen atoms in the excited O(^{1}D) state. Due to the strong attenuation of solar UV radiation, photolysis of molecular oxygen and thus O_3 production occurs mainly in the upper stratosphere. Photodissociation of O_3 (R1.3) to ground state fragments is possible at wavelengths $\leq$1080 nm. At wavelengths shorter than about 360 nm, one or even both of the products of O_3 photolysis are in electronically excited states (R1.4) and can be collisionally quenched (R1.5). On the timescale of minutes the photolysis of O_3 is not a net loss process since nearly all of the oxygen atoms produced reform ozone through reaction (R1.2). Over longer timescales, a small fraction of oxygen atoms produced from O_3 photolysis reacts with O_3 (R1.7) resulting in a net loss of odd oxygen O_x to the long-lived O_2 reservoir. Accordingly, the photochemical lifetimes of O_3 ($\tau \approx 30$ min at 30 km), O(^{1}D) ($\tau \approx 10^{-8}$ s) and O(^{3}P) ($\tau \approx 0.04$ s) are much shorter than the photochemical lifetime of their sum O_x ($\tau \approx$ weeks). Since the photochemical lifetime of odd oxygen is on the order of the transport timescales in the middle and lower stratosphere (section 1.1), the global distribution of ozone depends on latitude and season. Although production occurs predominantly at low-latitudes where photolysis of O_2 is most effective, the largest concentrations of O_3 are found at high-latitudes during spring (as long as the atmosphere is not perturbed by anthropogenic influence).

The Chapman cycle predicts formation of an ozone layer at somewhat higher altitudes and with concentrations larger than observed by modern scientific instruments. Hence, Chapman's chemistry must be complemented by missing reactions. Bates and Nicolet (1950) first suggested that ozone destruction can occur via catalytic cycles involving only two reactions,

$$\mathrm{X} + \mathrm{O_3} \longrightarrow \mathrm{XO} + \mathrm{O_2} \tag{R1.8}$$
$$\mathrm{O} + \mathrm{XO} \longrightarrow \mathrm{X} + \mathrm{O_2} \tag{R1.9}$$
$$\text{net}: \ \mathrm{O} + \mathrm{O_3} \longrightarrow 2\,\mathrm{O_2}\,. \tag{R1.10}$$

The catalyst X is recycled converting odd oxygen to its reservoir. Possible catalysts X are the radicals OH (Bates and Nicolet, 1950), NO (Crutzen, 1970; Johnston, 1971), Cl (Molina and Rowland, 1974), Br

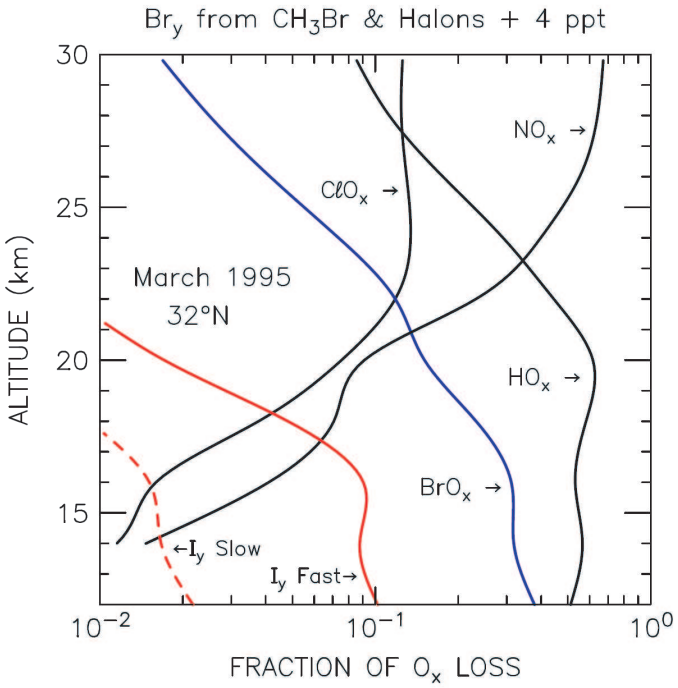

Figure 1.3: Calculated fractional contribution to odd oxygen (O_x) loss by catalytic cycles involving nitrogen (NO_x), hydrogen (HO_x), chlorine (ClO_x), bromine (BrO_x), and iodine (IO_x) for March 1995, 32ºN, using JPL-2002 kinetics (Sander et al., 2003) and recent updates. The ClO_x curve represents loss from the ClO+O and ClO+HO_2 cycles, plus other minor cycles that involve ClO, but not BrO or IO. The BrO_x curve represents loss from the BrO+ClO and BrO+HO_2 cycles, plus other minor cycles that involve BrO, but not IO. Figure by courtesy of R. Salawitch (JPL, Pasadena).

(Wofsy et al., 1975) and possibly I (Solomon et al., 1994) which all react faster with ozone than atomic oxygen. The relative importance of the proposed catalytic cycles with respect to O_3 destruction depends on the number of cycles completed before the catalyst X is lost in some chain termination reaction. This and further details of the photochemistry of the catalysts are described in dedicated sections below. Interestingly, fluorine is found not to participate in catalytic O_3 destruction as might have been expected. Since F rapidly reacts with H_2O and CH_4 to form HF which is photochemically stable, fluorine atoms are rapidly scavenged and, hence, are poor catalysts for O_3 destruction.
Further catalytic odd oxygen loss cycles involving the $HO_x = H + OH + HO_2$ catalyst are given by

$$\begin{aligned} \mathrm{OH + O} &\longrightarrow \mathrm{O_2 + H} && \text{(R1.11)}\\ \mathrm{H + O_2 + M} &\longrightarrow \mathrm{HO_2 + M} && \text{(R1.12)}\\ \mathrm{HO_2 + O} &\longrightarrow \mathrm{OH + O_2} && \text{(R1.13)}\\ \text{net :}\quad \mathrm{2\,O} &\longrightarrow \mathrm{O_2}\,. && \text{(R1.14)} \end{aligned}$$

$$\begin{aligned} \mathrm{OH + O_3} &\longrightarrow \mathrm{HO_2 + O_2} && \text{(R1.15)}\\ \mathrm{HO_2 + O_3} &\longrightarrow \mathrm{OH + 2\,O_2} && \text{(R1.16)}\\ \text{net :}\quad \mathrm{2\,O_3} &\longrightarrow \mathrm{3\,O_2}\,. && \text{(R1.17)} \end{aligned}$$

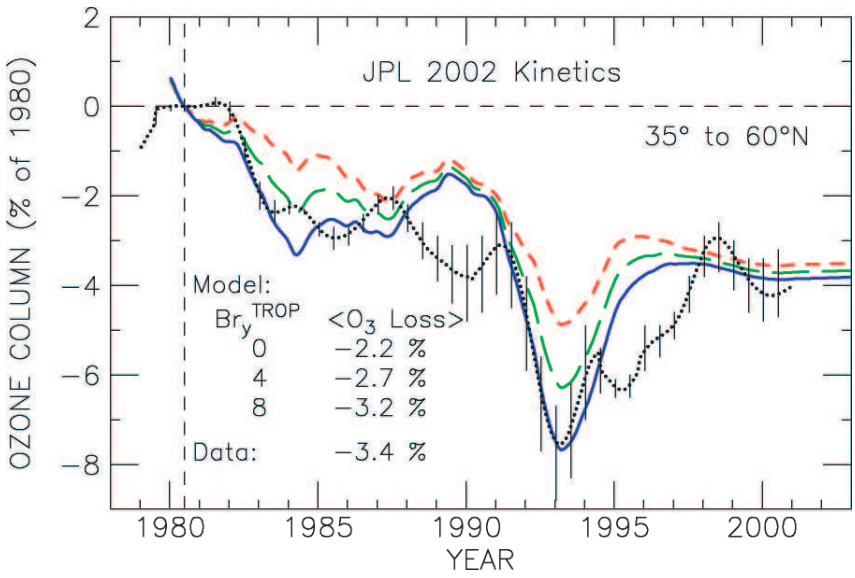

Figure 1.4: Change in column ozone relative to 1980 levels modeled by the AER 2-D model for tropopause reactive bromine of 0 (red), 4 (green) and 8 (blue) ppt for 35 - 60°N compared to observed trends in total ozone (black dotted line). The numerical values for the average of the modeled and measured ozone depletion refers to the period between beginning of 1980 to the end of 2000. Adopted from (Salawitch et al., 2005).

Since atomic oxygen is involved in reaction (R1.12), the respective catalytic cycle is important in the upper stratosphere and less important in the lower stratosphere where the reactions (R1.15) and (R1.16) dominate. O_3 destruction may also occur through catalytic cycles which couple different families of catalysts,

$$\mathrm{X} + \mathrm{O_3} \longrightarrow \mathrm{XO} + \mathrm{O_2} \tag{R1.18}$$

$$\mathrm{Y} + \mathrm{O_3} \longrightarrow \mathrm{YO} + \mathrm{O_2} \tag{R1.19}$$

$$\mathrm{XO} + \mathrm{YO} \longrightarrow \mathrm{X} + \mathrm{Y} + \mathrm{O_2} \tag{R1.20}$$

$$\text{net}: \quad 2\,\mathrm{O_3} \longrightarrow 3\,\mathrm{O_2}\,, \tag{R1.21}$$

where X = OH and Y = Cl, X = OH and Y = Br, X = Br and Y = Cl. The relative contributions of the various catalytic cycles to odd oxygen loss are illustrated in figure 1.3 as modeled for a mid-latitudinal station (32°N) in March 1995. In the lower stratosphere the HO_x and BrO_x catalytic cycles are most important while between 25 km and 40 km O_3 destruction is dominated by NO_x. Above about 40 km (not shown), the ClO_x catalytic cycle constitutes the major contribution. The overwhelming role of BrO_x compared to ClO_x in the lower stratosphere is somewhat misleading since O_3 loss due to the coupled ClO-BrO cycle is completely assigned to BrO_x. A more thorough discussion of figure 1.3 is given in section 7 emphasizing the role of iodine involving catalytic cycles.

The quoted fractional contributions to odd oxygen loss only hold true under non-ozone hole conditions. The severe depletion of O_3 during polar spring in the lower stratosphere observed since the mid-1980's is predominantly due to the ClO_x and BrO_x catalytic cycles and is discussed in detail in section 1.2.5. Besides the famous ozone holes over Antarctica and to a lesser degree over the Arctic, a global decrease of O_3 abundances is observed. When comparing the 1997-2001 average of total column ozone with the pre-1980 average, the effect amounts to a decrease by 3% and 6% in the northern and southern

hemisphere, respectively (WMO, 2003). However, the observed trend depends on season, latitude and the 11-year solar cycle. Moreover, it might be influenced by transport of ozone-poor air from polar regions to mid-latitudes. Figure 1.4 shows the evolution of total column O_3 between 1980 and 2001 for northern mid-latitudes. A clear trend is inferable from the observations (WMO, 2003) as well as model calculations (Salawitch et al., 2005) but discrepancies between the modeled and observed data evidently remain.

1.2.2 Stratospheric hydrogen photochemistry

The source of the HO_x catalyst in the stratosphere is the oxidation of H_2O, CH_4 and H_2. Since oxidation of CH_4 and H_2 ultimately leads to the formation of water vapor the discussion is often focused on total water i. e. $H_2O + 2\,CH_4 + H_2$. Satellite and balloon borne observations indicate that total water in the stratosphere increases by 1%/year which is twice as much as expected from the observed trend in tropospheric methane (WMO, 2003). A trend of pure water vapor in the stratosphere could originate from an increase of the average temperature of the tropical tropopause which is, however, not observed. Besides the pathway through formation of water vapor by oxidation of methane, HO_x can be directly produced from its sources through reaction with oxygen,

$$\begin{aligned} O(^1D) + H_2O &\longrightarrow 2\,OH && \text{(R1.22)}\\ O(^1D) + CH_4 &\longrightarrow OH + CH_3 && \text{(R1.23)}\\ &\longrightarrow CH_3O + H && \text{(R1.24)}\\ &\longrightarrow CH_2O + H_2 && \text{(R1.25)}\\ O(^1D) + H_2 &\longrightarrow OH + H. && \text{(R1.26)} \end{aligned}$$

Photodissociation of H_2O occurs at wavelengths shorter than 200 nm and thus is only important above 70 km (Zellner, 1999). HO_x catalyzes odd oxygen loss via reactions quoted in section 1.2.1. H_2O albeit being the dominant source represents also the primary sink species of HO_x. In the middle and upper stratosphere the main loss process is the direct reaction of OH with HO_2 while in the lower stratosphere, where the hydroperoxyl radical is more abundant than the peroxyl radical, the reaction cycle via the H_2O_2 catalyst is important,

$$\begin{aligned} OH + HO_2 &\longrightarrow H_2O + O_2 && \text{(R1.27)} \end{aligned}$$

$$\begin{aligned} HO_2 + HO_2 &\longrightarrow H_2O_2 + O_2 && \text{(R1.28)}\\ OH + H_2O_2 &\longrightarrow H_2O + HO_2 && \text{(R1.29)}\\ \text{net}: \quad OH + HO_2 &\longrightarrow H_2O + O_2\,. && \text{(R1.30)} \end{aligned}$$

Due to the photolytic instability of hydrogen peroxide reaction (R1.28) can be followed by photodissociation of H_2O_2 yielding a Null cycle for HO_x. Reactions of HO_x with NO_2 yield the reservoirs HNO_3 and HO_2NO_2,

$$\begin{aligned} OH + NO_2 + M &\longrightarrow HNO_3 + M && \text{(R1.31)}\\ HO_2 + NO_2 + M &\longrightarrow HO_2NO_2 + M. && \text{(R1.32)} \end{aligned}$$

Similar reactions of HO_x involving NO, Cl, ClO, Br and BrO forming HONO, HCl, HOCl, HBr and HOBr occur but are not explicitly discussed here. Nitric and pernitric acid can be photolyzed to reproduce HO_x,

$$\mathrm{HNO_3} + h\nu \longrightarrow \mathrm{OH} + \mathrm{NO_2} \quad \text{(R1.33)}$$

$$\mathrm{HO_2NO_2} + h\nu \longrightarrow \mathrm{OH} + \mathrm{NO_3} \quad \text{(R1.34)}$$

$$\longrightarrow \mathrm{HO_2} + \mathrm{NO_2} \quad \text{(R1.35)}$$

The photodissociation of HO_2NO_2 is subject of ongoing investigation since a photolytic pathway for wavelengths longer than 760 nm is found to be important (Roehl et al., 2002). This implies that the lifetime of HO_2NO_2 in the lower stratosphere is significantly reduced compared to previous estimates. Model studies showed that considering near IR photolysis of HO_2NO_2 yields significantly improved agreement between measured and modeled HO_x (Salawitch et al., 2002; Evans et al., 2003). In particular in the lower stratosphere, the total HO_x sink is governed by the reactions of nitric and to a lesser extent pernitric acid with OH,

$$\mathrm{HNO_3} + \mathrm{OH} \longrightarrow \mathrm{H_2O} + \mathrm{NO_3} \quad \text{(R1.36)}$$

$$\mathrm{HO_2NO_2} + \mathrm{OH} \longrightarrow \mathrm{H_2O} + \mathrm{NO_2} + \mathrm{O_2}. \quad \text{(R1.37)}$$

It is evident from the role of HNO_3 and HO_2NO_2 as temporary reservoirs and important intermediate products for sink processes of reactive hydrogen that stratospheric HO_x photochemistry is closely linked to reactive nitrogen. A similar link to the halogen catalytic cycles exists through the formation of HCl, HOCl, HBr and others.

The observed trend of total water mentioned above could be responsible for an increase of HO_x concentrations and hence could modify the importance of the chemical scheme outlined in this section with respect to ozone loss. In addition, an increase in total water can affect stratospheric O_3 through enhanced formation of ice containing particles providing surfaces for heterogeneous reactions. The radiative effect of enhanced water vapor concentrations suggests a possible cooling of the stratosphere by 0.5 K/decade (WMO, 2003) at 70°S and 70°N which in turn impacts temperature dependent chemical reactions. Some studies indicate that the trend in stratospheric water may have contributed up to 1 percentage point to the observed decrease of total column ozone (see e. g. figure 1.4) (WMO, 2003).

1.2.3 Stratospheric nitrogen photochemistry

The dominant source of the NO_x = NO + NO_2 catalyst is the greenhouse gas N_2O. Concentrations of N_2O increase by 0.8 ppt/year which amounts to about 0.3%/year of the tropospheric abundance of 320 ppb in 2005. The atmospheric life-time of N_2O is 120 years as estimated by IPCC (Houghton et al., 2001). In the stratosphere, N_2O is destroyed through photolysis and reaction with atomic oxygen,

$$\mathrm{N_2O} + h\nu \longrightarrow \mathrm{N_2} + \mathrm{O}(^1\mathrm{D}) \quad \text{(R1.38)}$$

$$\mathrm{N_2O} + \mathrm{O}(^1\mathrm{D}) \longrightarrow 2\,\mathrm{NO} \quad \text{(R1.39)}$$

$$\longrightarrow \mathrm{N_2} + \mathrm{O_2}\,. \quad \text{(R1.40)}$$

Reaction (R1.38), which does not produce any reactive nitrogen, occurs for wavelengths shorter than 397 nm and accounts for about 90% of N_2O loss. Since the branching ratio of reactions (R1.39) and (R1.40) is 0.58 in favor of the formation of NO, total reactive nitrogen NO_y

(NO_y = NO + NO_2 + NO_3 + 2 N_2O_5 + HNO_3 + HO_2NO_2 + $ClONO_2$ + $BrONO_2$) in the lower stratosphere amounts to roughly 6% of N_2O. This linear correlation between NO_y and N_2O is only true if there are no other sources of NO_y and if reactive nitrogen is not removed from the atmosphere. In the mesosphere and thermosphere a further source of NO_y is the reaction of molecular oxygen with atomic nitrogen which is produced by galactic cosmic rays, solar protons or energetic electron precipitation hitting the upper atmosphere (e.g. Rozanov et al., 2005). Reactive nitrogen formed in the upper atmosphere can descend into the stratosphere during winter and spring when there is large scale subsidence of air masses at mid- and high-latitudes. Such mesospheric intrusions have been observed to cause enhancements of stratospheric NO_y and NO_x on a fairly regular basis (e.g. Engel et al., 2006). Removal of reactive nitrogen occurs effectively in the middle to upper stratosphere through the reaction,

$$\mathrm{NO + N \longrightarrow N_2 + O\,,} \tag{R1.41}$$

which is negligible in the lower stratosphere due to the lack of available nitrogen atoms.
According to reactions (R1.8) and (R1.9) odd oxygen loss via the NO_x catalyst goes along with interconversion of NO and NO_2,

$$\mathrm{NO + O_3 \longrightarrow NO_2 + O_2} \tag{R1.42}$$
$$\mathrm{NO_2 + O \longrightarrow NO + O_2\,.} \tag{R1.43}$$

However, odd oxygen is re-produced through the photolysis ($\lambda < 405$ nm) of NO_2 which balances O_x loss due to reaction sequence (R1.42) and (R1.43) below 30 km,

$$\mathrm{NO_2} + h\nu \longrightarrow \mathrm{NO + O\,.} \tag{R1.44}$$

Conversion of NO to NO_2 by oxidants other than O_3 and subsequent photolysis of NO_2 even represent net formation processes of odd oxygen,

$$\mathrm{NO + HO_2 \longrightarrow NO_2 + OH} \tag{R1.45}$$
$$\mathrm{NO + RO_2 \longrightarrow NO_2 + RO} \tag{R1.46}$$
$$\mathrm{NO + ClO \longrightarrow NO_2 + Cl} \tag{R1.47}$$
$$\mathrm{NO + BrO \longrightarrow NO_2 + Br\,,} \tag{R1.48}$$

where RO_2 is an organo peroxy radical. From the above reactions, it is found that the Leighton ratio NO/NO_2 is almost constant and equal to one for altitudes below 40 km during daytime. Above 40 km the abundance of NO becomes rapidly larger than the abundance of NO_2 due to the increasing number of oxygen atoms available for reaction (R1.43).
During dusk photolysis of NO_2 fades out and NO is rapidly converted to NO_2 which forms NO_3 through the reaction with O_3,

$$\mathrm{NO_2 + O_3 \longrightarrow NO_3 + O_2\,.} \tag{R1.49}$$

During daytime NO_3 abundances are negligible since it is instantaneously destroyed by photolysis yielding NO_2 or NO. In the dark, NO_3 reacts with NO_2 to form the nighttime reservoir species N_2O_5,

$$\mathrm{NO_2 + NO_3 + M \longrightarrow N_2O_5 + M\,.} \tag{R1.50}$$

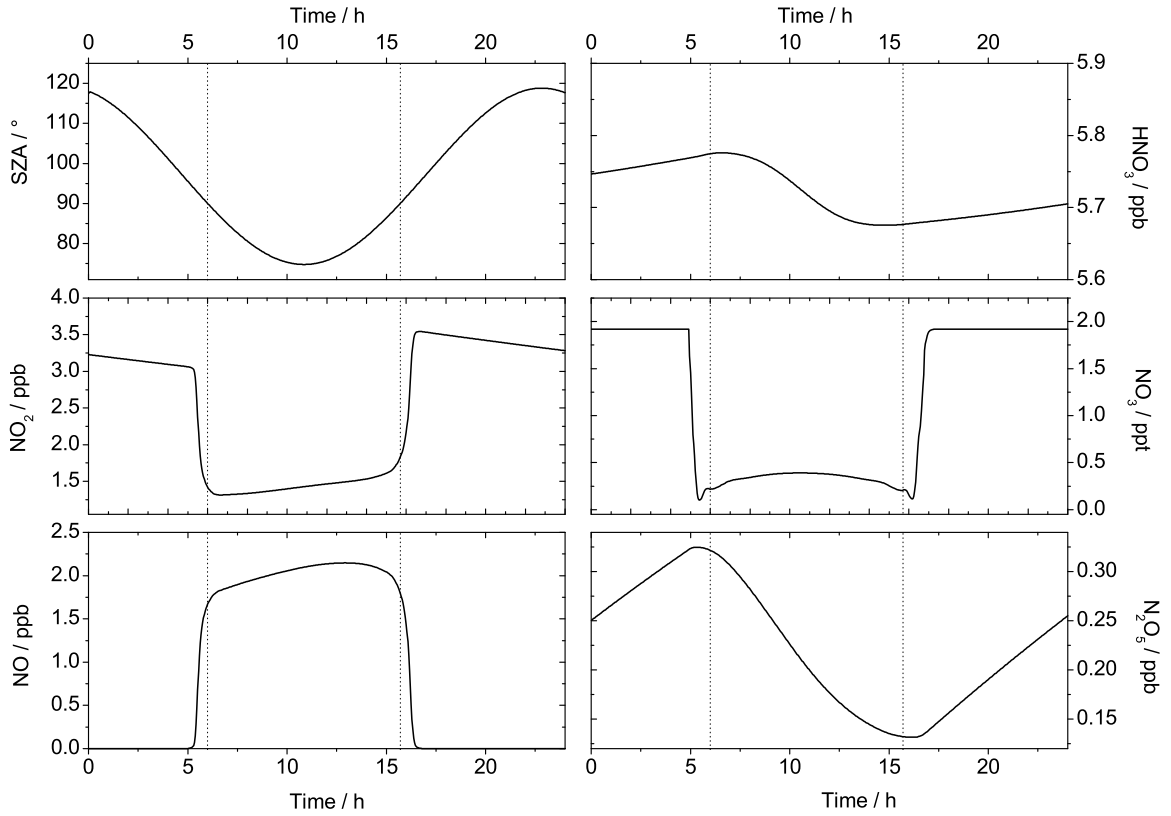

Figure 1.5: Temporal evolution of SZA (upper left panel), NO_2 (middle left panel), NO (lower left panel), HNO_3 (upper right panel), NO_3 (middle right panel) and N_2O_5 (lower right panel). The data are taken from a run of the LABMOS model of stratospheric chemistry on the 615 K potential temperature surface ($\approx$ 25 km). SZA = 90° is indicated by dotted vertical lines.

Reaction (R1.50) can be reversed to yield NO_2 and NO_3 from collisional decomposition of N_2O_5 which is, however, a slow process in the stratosphere. During the day, N_2O_5 is photolyzed at moderate rate reforming the educts of its formation reaction,

$$\mathrm{N_2O_5} + h\nu \quad \longrightarrow \quad \mathrm{NO_2} + \mathrm{NO_3}\,. \tag{R1.51}$$

The typical diurnal variation of some nitrogen species is depicted in figure 1.5. During night all NO_x resides in NO_2 and N_2O_5 is built up from NO_2 and NO_3. At dawn the concentration of NO_2 rapidly drops due to photolysis and NO is generated resulting in a fast equilibrium according to the Leighton ratio. The photolysis of N_2O_5 is rather slow causing a continuous decrease of N_2O_5 and a corresponding formation of NO_x during the day. At dusk, photolysis ceases resulting in a fast built-up of NO_2 and NO_3 and a steady formation of N_2O_5.
The relative diurnal variation of HNO_3 in figure 1.5 is small compared to the variation of the NO_x species indicating that HNO_3 is a long-lived species which serves as reservoir of reactive nitrogen and hydrogen as pointed out in the previous section. $ClONO_2$ and $BrONO_2$ are additional nitrogen reservoir species

which simultaneously act as reservoirs for ClO_x and BrO_x radicals and thus buffer catalytic O_3 loss

$$\begin{aligned} NO_2 + OH + M &\longrightarrow HNO_3 + M && \text{(R1.52)} \\ &\longrightarrow HOONO + M && \text{(R1.53)} \\ NO_2 + ClO + M &\longrightarrow ClONO_2 + M && \text{(R1.54)} \\ NO_2 + BrO + M &\longrightarrow BrONO_2 + M\,, && \text{(R1.55)} \end{aligned}$$

where pernitrous acid, HOONO, is rapidly dissociated to NO_2 and OH by collisions with other molecules or photolysis. Reaction (R1.53) is not included in the current Jet Propulsion Laboratory (JPL) recommendation on Chemical Kinetics and Photochemical Data for Use in Atmospheric Studies (Sander et al., 2003) but Golden and Smith (2000) and Nizkorodov and Wennberg (2002) suggested that formation of the nitric acid isomer HOONO might be important in the atmosphere. Prasad (2003) showed that the use of reaction pathway (R1.53) in modeling studies results in a better agreement between modeled and measured NO_x/NO_y and NO_x/HNO_3 since only 70% to 80% of the OH + NO_2 reaction yields the reservoir species HNO_3. In addition to reactions (R1.52) through (R1.55), HNO_3 can be produced from the nighttime reservoir N_2O_5 via hydrolysis on the surface of stratospheric aerosols

$$N_2O_5(g) + H_2O(s) \longrightarrow 2\,HNO_3(s)\,, \qquad \text{(R1.56)}$$

where (g) and (s) indicate gas and condensed phase, respectively. Release of the catalysts from the reservoirs can occur through photolysis

$$\begin{aligned} HNO_3 + h\nu &\longrightarrow OH + NO_2 && \text{(R1.57)} \\ ClONO_2 + h\nu &\longrightarrow ClO + NO_2 && \text{(R1.58)} \\ BrONO_2 + h\nu &\longrightarrow BrO + NO_2\,, && \text{(R1.59)} \end{aligned}$$

or in the case of HNO_3 via reaction with OH (R1.36). Through its ambiguous role as catalyst for O_3 loss and as a scavenger for ozone depleting radicals such as HO_x, ClO_x and BrO_x, odd nitrogen NO_x plays a crucial role in stratospheric ozone chemistry and in particular during ozone hole events as discussed in section 1.2.5.

1.2.4 Stratospheric halogen photochemistry

Halogen catalysts are known to play an important role in stratospheric ozone destruction, in particular under ozone hole conditions. Since a considerable fraction of halogen source gases transported to the stratosphere are man-made, the released halogen catalysts disturb the natural equilibrium between formation and destruction of ozone. The relative importance of the ClO_x (= Cl + ClO + 2 Cl_2O_2), BrO_x (= Br + BrO) and IO_x (= I + IO) catalysts for ozone loss depends on the lifetimes and the distribution of their source gases and on the efficiency of the respective catalytic cycles (see figure 1.3). Although chlorine being much more abundant than bromine, the latter is important when it comes to ozone depletion since each BrO_x radical cycles about 45-68 times more often through the respective ozone loss reactions than its ClO_x counterpart. IO_x radicals are even more effective but have not been detected in the stratosphere, so far. The relative, integrated efficiency of each halogen source species is quantified on the basis of its Ozone Depletion Potential (ODP) and is tabulated for example in WMO (2003).

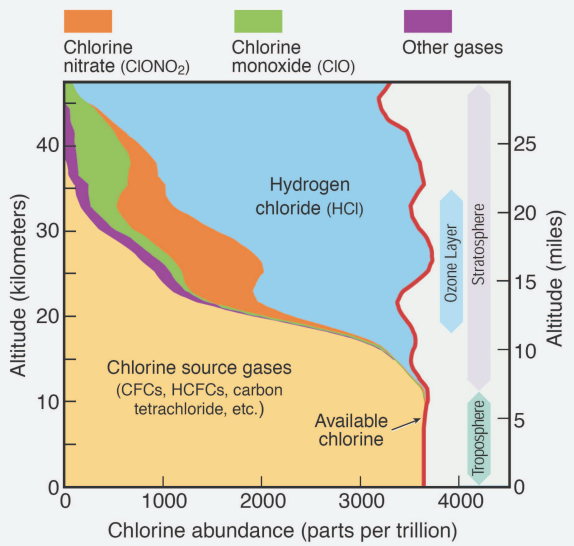

Figure 1.6: Budget of organic and inorganic chlorine containing gases. The organic source gases are long-lived in the troposphere and effectively transported into the stratosphere. There, they are converted to reactive, inorganic chlorine species, predominantly HCl, $ClONO_2$ and ClO. The sum of inorganic and organic chlorine containing gases is nearly constant with altitude up to 47 km. Adopted from (WMO, 2003).

Chlorine

Stratospheric ClO_x is released from halogenated organics by photolysis or reaction with OH and $O(^1D)$. The only natural source of stratospheric chlorine is methyl chloride (CH_3Cl) which contributes about 16% to the total budget (WMO, 2003). The most prominent anthropogenic source are the chlorofluorocarbons (CFCs) which are chemically inert, photostable and hardly soluble in water. Hence, the lifetime of CFCs in the troposphere is on the order of years to centuries resulting in an almost uniform distribution in the troposphere and effective transport to the stratosphere. Further, anthropogenic chlorine source gases exhibiting lifetimes on the order of years are carbon tetrachloride (CCl_4) and methyl chloroform (CH_3CCl_3). The Montreal Protocol (1987) and its amendments (London (1990), Copenhagen (1992), Vienna (1995), Montreal (1997), Bejing (1999)) limit the production of CFCs. The CFCs were partly replaced by hydrochlorofluorocarbons (HCFCs) which are less stable and thus have a shorter lifetime. The production and use of HCFCs is to be phased out by the year 2020. As a consequence, the total organic chlorine burden (CCl_y) in the troposphere reached its peak in 1992-1994 at (3.7 ± 0.1) ppb and since then declined by about 0.6% per year. The total inorganic chlorine burden (Cl_y) in the stratosphere stopped increasing in 1997-1998 and remained fairly constant since (WMO, 2003). A slow decline of stratospheric Cl_y is predicted to reach 12-14% in 2010 relative to the maximum chlorine loading in the late 1990s (Rinsland et al., 2003). A schematic view of the total chlorine budget in the troposphere and stratosphere is shown in figure 1.6.

Recent findings on the stratospheric bromine budget (see below) stimulated a discussion about a possible contribution of very short-lived (VSL) substances to the stratospheric halogen budget. VSL species exhibit atmospheric lifetimes of less than 0.5 years. Despite their rather short lifetime, VSLs can be transported to the stratosphere by deep convection to the upper troposphere and subsequent transport into the lower stratosphere. Evidently, such transport process are most likely in the tropics. The sum

of VSL chlorine species such as dichloroethane (C_2H_4Cl), chloroform ($CHCl_3$) or phosgene ($COCl_2$) is estimated to 1 - 50 ppt in the free troposphere (WMO, 2003). If transported to the stratosphere, these estimates correspond to less than 5% of the total stratospheric chlorine loading. Hence, the effect of VSL chlorine species on the stratospheric chlorine budget is considered small (WMO, 2003).
Once the ClO_x catalyst is released from the halocarbons, it undergoes rapid cyclic transformations between its constituents according to

$$\mathrm{Cl} + \mathrm{O_3} \longrightarrow \mathrm{ClO} + \mathrm{O_2} \quad \text{(R1.60)}$$
$$\mathrm{ClO} + \mathrm{O} \longrightarrow \mathrm{Cl} + \mathrm{O_2}\,, \quad \text{(R1.61)}$$

resulting in loss of odd oxygen. ClO_x cycling also occurs via

$$\mathrm{ClO} + \mathrm{NO} \longrightarrow \mathrm{Cl} + \mathrm{NO_2} \quad \text{(R1.62)}$$
$$\mathrm{ClO} + \mathrm{OH} \longrightarrow \mathrm{Cl} + \mathrm{HO_2}\,, \quad \text{(R1.63)}$$

which represent loss of odd oxygen if NO_2 and HO_2 subsequently react with atomic oxygen. ClO may also be photolyzed

$$\mathrm{ClO} + h\nu \longrightarrow \mathrm{Cl} + \mathrm{O_2}\,. \quad \text{(R1.64)}$$

The temporary reservoir species of the ClO_x catalyst are formed through reactions with NO_2, HO_2 and methane

$$\mathrm{ClO} + \mathrm{NO_2} + \mathrm{M} \longrightarrow \mathrm{ClONO_2} + \mathrm{M} \quad \text{(R1.65)}$$
$$\mathrm{ClO} + \mathrm{HO_2} \longrightarrow \mathrm{HOCl} + \mathrm{O_2} \quad \text{(R1.66)}$$
$$\mathrm{Cl} + \mathrm{HO_2} \longrightarrow \mathrm{HCl} + \mathrm{O_2} \quad \text{(R1.67)}$$
$$\mathrm{Cl} + \mathrm{CH_4} \longrightarrow \mathrm{HCl} + \mathrm{CH_3}\,. \quad \text{(R1.68)}$$

Chlorine nitrate and hypochloric acid can be photolyzed regenerating the active species

$$\mathrm{ClONO_2} + h\nu \longrightarrow \mathrm{Cl} + \mathrm{NO_3} \quad \text{(R1.69)}$$
$$\longrightarrow \mathrm{ClO} + \mathrm{NO_2} \quad \text{(R1.70)}$$
$$\mathrm{HOCl} + h\nu \longrightarrow \mathrm{OH} + \mathrm{Cl}\,. \quad \text{(R1.71)}$$

Since photolysis of HCl occurs at wavelengths shorter than 205 nm only, it is extremely inefficient and recovery of ClO_x from HCl is dominated by

$$\mathrm{HCl} + \mathrm{OH} \longrightarrow \mathrm{H_2O} + \mathrm{Cl}\,. \quad \text{(R1.72)}$$

Except for reaction (R1.71) the release of ClO_x from its reservoirs is very slow and the bulk of stratospheric chlorine resides in HCl and $ClONO_2$ (see figure 1.6). A significant activation of ClO_x occurs only between 30 km and 45 km (Solomon, 1999). Albeit recovery of ClO_x from its reservoirs being rather ineffective in the gas phase, heterogeneous reactions can lead to efficient activation and subsequent ozone loss.

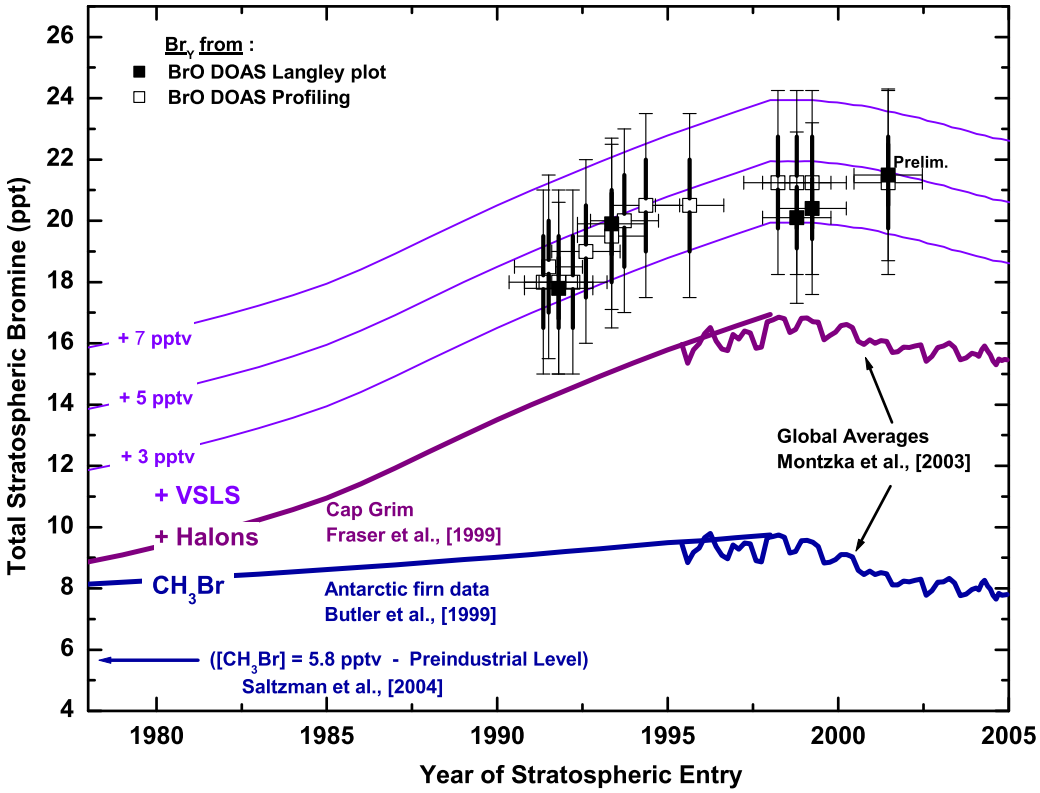

Figure 1.7: Trends for bromine in the near surface troposphere (lines) and stratosphere (points). The dark blue line shows global tropospheric bromine from methyl bromide as measured in ambient air and firn air. The purple line shows global tropospheric bromine from the sum of methyl bromide plus halons as measured in ambient air, archived air and firn air. The light blue lines show bromine from CH_3Br and halons plus bromine from very short-lived organic bromine compounds assuming total contributions of 3, 5, or 7 ppt. The points illustrate total inorganic bromine derived from stratospheric measurements of BrO by the DOAS balloon borne instrument. For stratospheric data, the date corresponds to the time when that air was last in the troposphere, i.e. sampling date minus mean time in the stratosphere. Adopted from Dorf (2005).

Bromine

The major source (more than 50%) of the BrO_x catalyst is methyl bromide (CH_3Br) which is of natural (60% - 80%) and anthropogenic origin. The man-made halons, halogenated hydrocarbons, contribute about 30% - 40% to the global bromine budget. Although controlled by the Montreal Protocol, the global abundance of halons is still increasing by 0.1 ppt/year due to the ongoing use of halon stocks and halon production in third world countries (Montzka et al., 2003). The tropospheric bromine loading from halons and methyl bromide peaked around 1998 at 16 - 17 ppt and started to decline afterwards by a mean annual rate of (0.25 ± 0.09) ppt/year (Montzka et al., 2003). Recent balloon borne measurements of BrO by Dorf (2005) indicate a total inorganic bromine burden of (21 ± 3) ppt in stratospheric air that was injected from the troposphere into the stratosphere in 1999. Consistent with the tropospheric trend, the increase of stratospheric total bromine is slowing down or leveling off. Figure 1.7 illustrates the

trend of the tropospheric and stratospheric bromine throughout the past 20 years. The apparent discrepancy between total stratospheric bromine and the sum of its long-lived tropospheric organic precursors is believed to be due to very short-lived brominated source gases or direct upward transport of inorganic bromine across the tropopause (WMO, 2003; Salawitch et al., 2005; Dorf, 2005).
Due to their rather short lifetime, the tropospheric concentrations of VSL bromocarbons show high spatial and temporal variability but tend to be highest near coastal areas in the tropics and subtropics. Oceanic emissions account for 90% to 95% of brominated and iodinated VSL species to the atmosphere with bromoform ($CHBr_3$) being the most important troposperic VSL bromine species. Amongst others, further contributions come from CH_2Br_2, $CHBr_2Cl$ and $CHBrCl_2$. Anthropogenic emissions of most VSL substances contribute only little to the global budget although being locally significant. To date it is subject of ongoing research what fraction of bromine released as VSL species enters the stratosphere as organic source gas (SG) or inorganic product gas (PG) produced from the decomposition of VSL SG. Bobrowski et al. (2003) suggested that volcanic emissions might contribute to the tropospheric inorganic bromine loading as well. An in-depth discussion on VSL brominated species and the inorganic bromine budget can be found in Dorf (2005).
Similar to the release of reactive chlorine from its organic precursors, brominated organics are decomposed in the stratosphere by photolysis or reactions with OH and O(^{1}D) yielding reactive inorganic bromine species. The BrO_x constituents undergo rapid interconversion according to

$$\mathrm{Br} + \mathrm{O_3} \longrightarrow \mathrm{BrO} + \mathrm{O_2} \tag{R1.73}$$
$$\mathrm{BrO} + \mathrm{O} \longrightarrow \mathrm{Br} + \mathrm{O_2}\,, \tag{R1.74}$$

and

$$\mathrm{BrO} + h\nu \longrightarrow \mathrm{Br} + \mathrm{O} \tag{R1.75}$$
$$\mathrm{BrO} + \mathrm{NO} \longrightarrow \mathrm{Br} + \mathrm{NO_2} \tag{R1.76}$$
$$\mathrm{BrO} + \mathrm{ClO} \longrightarrow \mathrm{Br} + \mathrm{OClO} \quad 59\% \tag{R1.77}$$
$$\longrightarrow \mathrm{Br} + \mathrm{ClO_2} \quad 34\% \tag{R1.78}$$
$$\longrightarrow \mathrm{BrCl} + \mathrm{O_2} \quad 7\%\,. \tag{R1.79}$$

The branching ratios of reactions (R1.77) through (R1.79) are indicated for T = 195 K according to Sander et al. (2003) although recent studies by Canty et al. (2005) indicate that an increase of the fractional yield of BrCl from 7% to 11% produces better agreement between modeled and observed data. Subsequent photolysis of BrCl to Br and Cl and collisional decomposition of ClOO to Cl and O_2 result in catalytic loss of odd oxygen. OClO is rapidly photolyzed to ClO and atomic oxygen which prevents the built-up of large OClO concentrations during daytime. Since reaction (R1.77) is the virtually only production pathway of OClO, this species can be used as a tracer for the efficiency of the coupled ClO-BrO catalytic ozone loss cycle. BrO_x radicals are scavenged by NO_2, HO_2, and CH_2O forming the main reservoir species

$$\mathrm{BrO} + \mathrm{NO_2} + \mathrm{M} \longrightarrow \mathrm{BrONO_2} + \mathrm{M} \tag{R1.80}$$
$$\mathrm{BrO} + \mathrm{HO_2} \longrightarrow \mathrm{HOBr} + \mathrm{O_2} \tag{R1.81}$$
$$\mathrm{Br} + \mathrm{HO_2} \longrightarrow \mathrm{HBr} + \mathrm{O_2} \tag{R1.82}$$
$$\mathrm{Br} + \mathrm{CH_2O} \longrightarrow \mathrm{HBr} + \mathrm{CHO}\,. \tag{R1.83}$$

Release of BrO_x from the reservoirs occurs through photolysis and in the case of HBr through reaction with OH

$$\begin{aligned} \mathrm{BrONO_2} + h\nu &\longrightarrow \mathrm{Br} + \mathrm{NO_3} && \text{(R1.84)} \\ &\longrightarrow \mathrm{BrO} + \mathrm{NO_2} && \text{(R1.85)} \\ \mathrm{HOBr} + h\nu &\longrightarrow \mathrm{OH} + \mathrm{Br} && \text{(R1.86)} \\ \mathrm{HBr} + \mathrm{OH} &\longrightarrow \mathrm{Br} + \mathrm{H_2O}\,. && \text{(R1.87)} \end{aligned}$$

Since photolysis and decomposition of the bromine reservoirs are very efficient, the partitioning between BrO_x and its reservoirs is shifted toward the active forms in comparison with chlorine. Hence, BrO_x is more efficient in destroying ozone than ClO_x. In the absence of light, heterogeneous processes can lead to bromine activation as observed in the presence of polar stratospheric clouds (section 1.2.5).

Iodine

All source gases of the IO_x catalyst with significant emissions are VSL halogenated compounds of predominantly natural origin. Oceanic emissions largely (90% to 95%) dominate other sources such as emissions from rice paddies. The most important source gas from a stratospheric point of view is methyl iodide (CH_3I) which has been measured in the marine boundary layer with abundances as high as 1830 ppt emitted primarily from macroalgae (Peters et al., 2005). Other halogenated organic compounds, e. g. CH_2I_2, CH_2ClI, CH_2BrI, C_2H_5I and iodopropane, seem to be much less abundant. Atmospheric lifetimes are generally very short, ranging from hours to days. CF_3I has been proposed as replacement for the greenhouse gas SF_6 and for halons used in aircraft fire extinguishers. Although being rapidly photolyzed, emission of CF_3I by aircraft at high altitudes could provide a pathway to inject iodine into the stratosphere. Observations of CH_3I above the boundary layer yielded abundances of 0.0 ppt to 0.2 ppt in the upper troposphere and lower stratosphere (WMO, 2003). Besides VSL organic compounds, inorganic iodine species have also been detected in the marine boundary layer (e.g. Schwärzle, 2005; Peters et al., 2005) and in the polar troposphere (e.g. Frieß et al., 2001). However, due to their short photochemical lifetimes direct transport to the stratosphere seems negligible. Several studies (Wennberg et al., 1997; Pundt et al., 1998; Bösch et al., 2003) indicate that abundances of inorganic iodine species in the stratosphere are very low and below the respective detection limits. Currently the best upper limit for gaseous inorganic iodine in the mid- and high-latitudinal stratosphere is (0.10 ± 0.02) ppt as inferred by Bösch et al. (2003) from measured upper limits of IO and OIO. These observations suggest that either much less iodine enters the stratosphere than expected from ground-level CH_3I abundances or that stratospheric iodine resides in other gaseous species besides IO and OIO or in particulate form. Somewhat in contradiction to the aforementioned studies, Wittrock et al. (2000) concluded on (0.65 - 0.8 ($\pm$ 0.2)) ppt stratospheric IO from their ground based measurements of zenith-scattered skylight. Murphy et al. (1997) and Murphy and Thompson (2000) reported on some iodine tied to aerosols in the upper troposphere and lower stratosphere. Formation of higher oxides and subsequent uptake into the aerosol phase could explain the lack of gaseous iodine species in the lower stratosphere. Clearly, high precision measurements in the tropical upper troposphere and lower stratosphere, where troposphere-to-stratosphere transport predominantly occurs, are necessary to further constrain the budget of iodine species.
As suggested by Solomon et al. (1994) and Bösch et al. (2003), the IO_x catalyst could significantly

contribute to lower stratospheric ozone loss through inter-halogen cycles.

$$\mathrm{I} + \mathrm{O_3} \longrightarrow \mathrm{IO} + \mathrm{O_2} \quad \text{(R1.88)}$$

$$\mathrm{IO} + \mathrm{ClO} \longrightarrow \mathrm{ICl} + \mathrm{O_2} \quad 20\% \quad \text{(R1.89)}$$
$$\longrightarrow \mathrm{Cl} + \mathrm{I} + \mathrm{O_2} \quad 25\% \quad \text{(R1.90)}$$
$$\longrightarrow \mathrm{I} + \mathrm{OClO} \quad 55\% \quad \text{(R1.91)}$$

$$\mathrm{IO} + \mathrm{BrO} \longrightarrow \mathrm{Br} + \mathrm{I} + \mathrm{O_2} \quad 20\% \quad \text{(R1.92)}$$
$$\longrightarrow \mathrm{Br} + \mathrm{OIO} \quad 80\% \quad \text{(R1.93)}$$

$$\mathrm{IO} + \mathrm{IO} \longrightarrow \mathrm{I_2} + \mathrm{O_2} \quad 5\% \quad \text{(R1.94)}$$
$$\longrightarrow \mathrm{I} + \mathrm{OIO} \quad 40\% \quad \text{(R1.95)}$$
$$\longrightarrow 2\mathrm{I} + \mathrm{O_2} \quad ? \quad \text{(R1.96)}$$
$$\longrightarrow \mathrm{I_2O_2} \quad 55\%\,. \quad \text{(R1.97)}$$

The I_2O_2 product of reaction (R1.97) is unstable and rapidly decomposes to OIO, implying that the effective OIO yield from the IO self reaction is high. The efficiency of the interhalogen cycles with respect to ozone loss is reduced if the halogen oxides formed in reactions (R1.91), (R1.93) and (R1.95) are photolyzed in a way that atomic oxygen is produced. Cycling between the IO_x constituents can also occur through photolysis of IO and reactions with radicals other than halogen oxides

$$\mathrm{IO} + h\nu \longrightarrow \mathrm{I} + \mathrm{O} \quad \text{(R1.98)}$$
$$\mathrm{IO} + \mathrm{NO} \longrightarrow \mathrm{I} + \mathrm{NO_2} \quad \text{(R1.99)}$$
$$\mathrm{IO} + \mathrm{OH} \longrightarrow \mathrm{I} + \mathrm{HO_2}\,. \quad \text{(R1.100)}$$

Removal of IO_x into its reservoirs occurs according to

$$\mathrm{IO} + \mathrm{HO_2} \longrightarrow \mathrm{HOI} + \mathrm{O_2} \quad \text{(R1.101)}$$
$$\mathrm{IO} + \mathrm{NO_2} + \mathrm{M} \longrightarrow \mathrm{IONO_2} + \mathrm{M} \quad \text{(R1.102)}$$
$$\mathrm{I} + \mathrm{HO_2} \longrightarrow \mathrm{HI} + \mathrm{O_2} \quad \text{(R1.103)}$$
$$\mathrm{I} + \mathrm{NO} + \mathrm{M} \longrightarrow \mathrm{INO} + \mathrm{M} \quad \text{(R1.104)}$$
$$\mathrm{I} + \mathrm{NO_2} + \mathrm{M} \longrightarrow \mathrm{INO_2} + \mathrm{M}\,. \quad \text{(R1.105)}$$

The reservoir species are destroyed through photolysis

$$\mathrm{INO} + h\nu \longrightarrow \mathrm{I} + \mathrm{NO} \quad \text{(R1.106)}$$
$$\mathrm{INO_2} + h\nu \longrightarrow \mathrm{I} + \mathrm{NO_2} \quad \text{(R1.107)}$$
$$\mathrm{HI} + h\nu \longrightarrow \mathrm{I} + \mathrm{H} \quad \text{(R1.108)}$$
$$\mathrm{HOI} + h\nu \longrightarrow \mathrm{I} + \mathrm{OH} \quad \text{(R1.109)}$$
$$\mathrm{IONO_2} + h\nu \longrightarrow \mathrm{IO} + \mathrm{NO_2} \quad > 95\% \quad \text{(R1.110)}$$
$$\longrightarrow \mathrm{I} + \mathrm{NO_3} \quad < 5\%\,. \quad \text{(R1.111)}$$

While INO, INO_2, HOI and $IONO_2$ are rapidly photolyzed, oxidation of HI by OH is more effective than its photolysis in the lower stratosphere

$$HI + OH \longrightarrow I + H_2O\,. \tag{R1.112}$$

The reservoir species OIO which is produced by the inter-halogen cycles is outstanding when compared to its analogs OClO and OBrO since it has been observed during daytime in the marine boundary layer (e.g Allan et al., 2001; Peters et al., 2005). These findings indicate that the photolysis of OIO is less effective than the photolysis of OClO and OBrO, which cannot be detected in significant amounts under sunlit conditions. Laboratory and field measurements show that OIO has a series of diffuse absorption bands between 470 nm and 610 nm, but recent studies suggest that absorption of radiation at 562 nm rather leads to excitation and subsequent collisional quenching than to dissociation of the OIO molecule (Joseph et al., 2005). The quantum yield for photolysis between 560 nm and 580 nm is estimated to less than 10% (Joseph et al., 2005; Tucceri et al., 2006).

$$OIO + h\nu \longrightarrow OIO^* \tag{R1.113}$$
$$OIO^* + M \longrightarrow OIO + M \tag{R1.114}$$

$$OIO + h\nu \longrightarrow I + O_2 \tag{R1.115}$$
$$OIO + h\nu \longrightarrow IO + O\,. \tag{R1.116}$$

While photolysis according to reaction (R1.115) would enhance O_x loss, reaction (R1.116) results in a Null cycle. Ingham et al. (2000) estimated upper limits of the yield for I + O_2 to 0.15 and for IO + O to 0.007. Besides photolysis, reactions with the NO and OH radicals cause loss of OIO

$$OIO + NO \longrightarrow IO + NO_2 \tag{R1.117}$$
$$OIO + OH \longrightarrow HOI + O_2\,. \tag{R1.118}$$

Hoffmann et al. (2001) suggested that OIO might initiate the formation of higher iodine oxides (e. g. I_2O_3) and polymeric structures. Jimenez et al. (2003) and O'Dowd and Hoffmann (2005) reported on the formation of iodine containing aerosols in the marine boundary layer, involving polymerization of OIO. Such aerosols remove iodine species from the gas phase and, hence, might provide a possible explanation for the undetectable low amounts of IO in the lower stratosphere.

1.2.5 Heterogeneous chemistry and the ozone hole

Besides gas-phase reactions discussed in the preceding sections, heterogeneous reactions on the surface of particles play an important role in stratospheric chemistry. The ubiquitous stratospheric sulfate aerosol consists mainly of H_2SO_4/H_2O droplets and is produced from oxidation of SO_2 which is transported to the stratosphere through its precursors such as naturally formed long-lived sulfur compounds, e. g. OCS. Further, volcanic eruptions may directly inject sulfur compounds into the stratosphere. Hence, stratospheric aerosol abundances are temporally greatly enhanced after large volcanic eruptions (Arnold et al., 1990). Typical aerosol surface area densities range between 1 and 10 $\mu m^2 cm^{-3}$ during volcanically

quiescent periods in the lower stratosphere.
Besides the ubiquitous sulfate aerosol, particles referred to as polar stratospheric clouds (PSCs) may form in the lower stratosphere under very cold conditions as encountered in the polar vortices during winter. Two types of PSCs were identified. Type 1 was found to form some degrees above and type 2 below the freezing point of water ($T_{ICE} \approx 188$ K) (Poole and McCormick, 1988). Crutzen and Arnold (1986) and Toon et al. (1986) suggested that type 1 particles consist of nitric acid hydrates with nitric acid trihydrate ($HNO_3 \cdot 3\,H_2O$, NAT) being the most likely to form under stratospheric conditions. Indeed, laboratory studies by Hansen and Mauersberger (1988) showed that the NAT crystal is stable under such conditions ($T_{NAT} \approx 196$ K). Type 2 PSCs were found to consist of water ice. Initially, sulfate aerosols were supposed to provide condensation nuclei for NAT and water but recent studies indicated that the PSC formation process is rather involved and remains a subject of ongoing research (WMO, 2003). A simplified picture is summarized by Zellner (1999): Stratospheric liquid sulfate aerosol droplets tend not to freeze above T_{ICE} but remain liquid and form supercooled ternary $H_2SO_4/HNO_3/H_2O$ solutions (STS) by HNO_3 uptake. These liquid particle PSCs are commonly referred to as type 1b. Upon warming of a few degrees, STS evaporate HNO_3 and crystallize to solid sulfate aerosol particles which then serve as condensation nuclei for NAT (type 1a) and water (type 2). If STS are further cooled, take-up of HNO_3 continues and freezing above T_{ICE} is possible.
Due to the stable and persistent polar vortex, temperatures in the winter Antarctic stratosphere are often low enough for the formation of type 1 and type 2 PSCs which are indeed regularly observed. Since the Arctic polar vortex is subject to frequent dynamic perturbations, temperatures are usually higher than in the southern hemisphere and the formation of PSCs is less frequent and persistent. Locally, PSCs can be formed in air masses which are adiabatically cooled below the PSC formation threshold by topographically induced vertical motion as observed in the lee of mountain ridges (lee-wave PSCs).

Heterogeneous chemistry

All stratospheric aerosol particles contain H_2O either in the liquid or solid phase. The halogen reservoir gases HCl or HBr may be dissolved in liquid droplets or adsorbed on aerosol surfaces. Thus, a number of key species are available for heterogeneous reactions. The importance of heterogeneous chemistry comes from the fact, that heterogeneous reactions typically require much lower activation energy and proceed much faster than gas phase reactions between the same species. Heterogeneous reactions involving chlorine and bromine species convert reservoirs to more reactive species,

$$\mathrm{ClONO_2}\,(g) + \mathrm{HCl}\,(s) \longrightarrow \mathrm{Cl_2}\,(g) + \mathrm{HNO_3}\,(s) \quad \text{(R1.119)}$$
$$\mathrm{ClONO_2}\,(g) + \mathrm{H_2O}\,(s) \longrightarrow \mathrm{HOCl}\,(g) + \mathrm{HNO_3}\,(s) \quad \text{(R1.120)}$$
$$\mathrm{HOCl}\,(g) + \mathrm{HCl}\,(s) \longrightarrow \mathrm{Cl_2}\,(g) + \mathrm{H_2O}\,(s) \quad \text{(R1.121)}$$

$$\mathrm{BrONO_2}\,(g) + \mathrm{HCl}\,(s) \longrightarrow \mathrm{BrCl}\,(g) + \mathrm{HNO_3}\,(s) \quad \text{(R1.122)}$$
$$\mathrm{BrONO_2}\,(g) + \mathrm{H_2O}\,(s) \longrightarrow \mathrm{HOBr}\,(g) + \mathrm{HNO_3}\,(s) \quad \text{(R1.123)}$$
$$\mathrm{HOBr}\,(g) + \mathrm{HCl}\,(s) \longrightarrow \mathrm{BrCl}\,(g) + \mathrm{H_2O}\,(s)\,, \quad \text{(R1.124)}$$

where (g) and (s) indicate gas phase and condensed phase, respectively. These reactions convert relatively long-lived halogen species from the gas phase and condensed phase to shorter-lived halogen

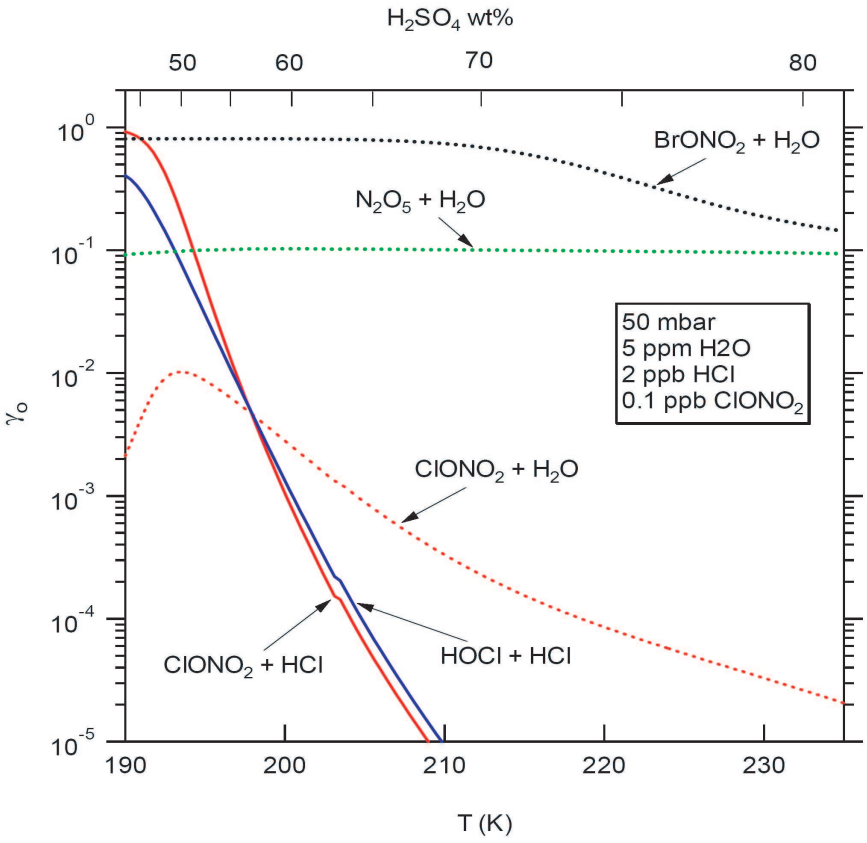

Figure 1.8: Calculated reactive uptake coefficients as a function of temperature for key heterogeneous processes on stratospheric sulfate aerosol. The uptake coefficient γ_o can be regarded as a measure of the reaction probability. Calculations are performed for typical conditions on the 50 mbar pressure level as indicated in the legend. Adopted from Sander et al. (2003).

species in the gas phase, but leave the NO_x or HO_x components in the condensed phase. Since the halogen bearing products are less stable with respect to photodissociation than their educts, the above reactions are often referred to as chlorine and bromine activation. A further important heterogeneous reaction removes the nighttime NO_x reservoir N_2O_5 from the gas phase,

$$\mathrm{N_2O_5(g) + H_2O\,(s) \;\longrightarrow\; 2\,HNO_3(s)\,.} \qquad \text{(R1.125)}$$

The reaction probability of the various heterogeneous reactions depends on temperature, composition and phase of the aerosol. As an example, figure 1.8 illustrates the reaction probability of some heterogeneous reactions on stratospheric sulfate aerosol. Hydrolysis of N_2O_5 and $BrONO_2$ are the most important reactions under typical conditions in the stratosphere. Their impact on stratospheric ozone could readily be seen after the volcanic eruption of Mount Pinatubo in 1991 where ozone abundances were found to decrease under the influence of enhanced sulfate aerosol (see also figure 1.4) (Solomon et al., 1998).

The ozone hole

The strong depletion of ozone over Antarctica in Austral spring occurring annually since the beginning of the 1980s (Farman et al., 1985) is commonly known as the ozone hole. It is driven by the interplay of dynamic isolation of the winter polar stratosphere, halogen activation and nitrogen de-activation by heterogeneous reactions, lacking insolation during polar night and perturbation of the natural halogen budget through large scale anthropogenic release of halogen containing species to the stratosphere. Ozone hole events are also observed in the Arctic stratosphere but less severe and persistent than in Antarctica due to the higher dynamic activity in the northern hemisphere.
The dynamic prerequisite for an ozone hole event is the isolation of the winterly polar stratosphere from the somewhat warmer mid-latitudinal stratosphere in order to provide temperatures low enough for the formation of polar stratospheric clouds (PSCs). The formation of type 1a and type 2 PSCs typically occurs on the timescales of 10^5 s and 10^3 s - 10^4 s, respectively. During polar night, when stratospheric temperatures are lowest, halogen reservoir species are heterogeneously converted on the surface of PSCs to more active forms, according to reactions (R1.119) through (R1.124). In contrast, reactive nitrogen species are converted to their long-lived reservoir HNO_3. The almost complete conversion of NO and NO_2 to HNO_3 through the pathway of N_2O_5 hydrolysis is most effective during polar night and is called denoxification. As a consequence, nearly all NO_y resides in HNO_3 which can be taken up by PSCs. If sedimentation of PSC particles occurs, HNO_3 and thus NO_y is permanently removed from the stratosphere, a process which is called denitrification. With the return of sunlight the photochemically unstable products of reactions (R1.119) through (R1.124), i. e. HOCl, Cl_2, HOBr, and BrCl are photolyzed yielding ClO_x, BrO_x and HO_x catalysts while NO_x is not available for scavenging. Loss of ozone occurs primarily by two halogen involving catalytic cycles, the ClO-ClO cycle (Molina and Molina, 1987) and the ClO-BrO cycle (McElroy et al., 1986)

$$\begin{aligned}
\mathrm{ClO} + \mathrm{ClO} + \mathrm{M} &\leftrightarrow \mathrm{Cl_2O_2} + \mathrm{M} && \text{(R1.126)}\\
\mathrm{Cl_2O_2} + h\nu &\longrightarrow \mathrm{Cl} + \mathrm{ClO_2} && \text{(R1.127)}\\
\mathrm{ClO_2} + \mathrm{M} &\longrightarrow \mathrm{Cl} + \mathrm{O_2} && \text{(R1.128)}\\
2 \times (\,\mathrm{Cl} + \mathrm{O_3} &\longrightarrow \mathrm{ClO} + \mathrm{O_2}\,) && \text{(R1.129)}\\
\text{net}: \quad 2\,\mathrm{O_3} &\longrightarrow 3\,\mathrm{O_2}\,, && \text{(R1.130)}
\end{aligned}$$

$$\begin{aligned}
\mathrm{ClO} + \mathrm{BrO} &\longrightarrow \mathrm{ClO_2} + \mathrm{Br} && \text{(R1.131)}\\
&\longrightarrow \mathrm{BrCl} + \mathrm{O_2} && \text{(R1.132)}\\
\mathrm{ClO_2} + \mathrm{M} &\longrightarrow \mathrm{Cl} + \mathrm{O_2} + \mathrm{M} && \text{(R1.133)}\\
\mathrm{BrCl} + h\nu &\longrightarrow \mathrm{Br} + \mathrm{Cl} && \text{(R1.134)}\\
\mathrm{Cl} + \mathrm{O_3} &\longrightarrow \mathrm{ClO} + \mathrm{O_2} && \text{(R1.135)}\\
\mathrm{Br} + \mathrm{O_3} &\longrightarrow \mathrm{BrO} + \mathrm{O_2} && \text{(R1.136)}\\
\text{net}: \quad 2\,\mathrm{O_3} &\longrightarrow 3\,\mathrm{O_2}\,. && \text{(R1.137)}
\end{aligned}$$

Since the ClO-ClO cycle involves the temperature dependent formation of the ClO dimer and further depends on sunlight, it is most effective at cold temperatures under sunlit conditions. The ClO-BrO cycle does not rely on formation of a dimer and thus is only weakly temperature dependent. Moreover,

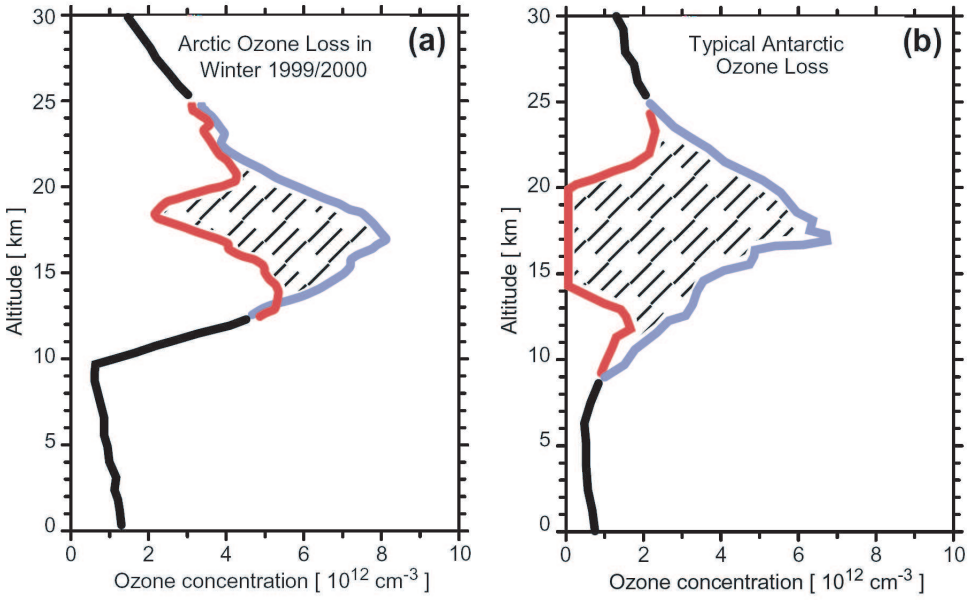

Figure 1.9: Concentration of O_3 as a function of altitude in early (blue) and late winter (red) in the Arctic (panel a)) and Antarctic (panel b)) stratosphere. Panel a): Ozone data are averaged from ozone sonde observations. The early winter concentration profile was corrected for subsidence using model estimates of air mass descend in winter 1999/2000. Panel b): Ozone data are taken from measurements at the Neumayer station (71°S) on July 15, 1997, (blue) and October 13, 1997, (red). Transport effects are not considered. Adopted from WMO (2003).

it can proceed in darkness. The abundance of BrO is not strongly affected by heterogeneous processes on PSCs, since the partitioning of stratospheric bromine is shifted towards the active BrO_x species and, hence, relatively small amounts of bromine reside in the reservoirs such as $BrONO_2$ or HBr. This implies that the ClO-BrO cycle is most important in the Arctic stratosphere where PSC formation is less frequent and chlorine activation is less complete than in the southern polar stratosphere (WMO, 2003).

Catalytic ozone destruction is terminated in spring when the polar stratosphere heats up and sublimation of PSCs releases HNO_3 into the gas phase. Photolysis of HNO_3 yields NO_x which scavenges the ClO_x and BrO_x radicals. If HNO_3 is permanently removed from the stratosphere by denitrification, catalytic ozone loss can be significantly prolonged since NO_x has to be supplied from mid-latitudes (Rex et al., 1997).

Figure 1.9 illustrates the magnitude and vertical distribution of ozone loss during a cold winter in the Arctic and a typical ozone hole event over Antarctica. Ozone loss is most severe in the lower stratosphere between 15 and 20 km altitude where ozone depletion is nearly complete in the southern hemisphere and can amount to more than 50% for selected altitude levels in the northern hemisphere. Rex et al. (2004) showed that ozone loss in the Arctic spring is highly variable and might also depend on climate change. They concluded that about 15 DU (Dobson Unit)[1] additional total column ozone loss can be expected per Kelvin cooling of the lower Arctic stratosphere.

[1]The Dobson unit is defined as a 0.01 mm thick layer of pure ozone at standard pressure and temperature. The total atmospheric ozone column amounts to 200 DU - 500 DU depending on latitude and season, i. e. if all the ozone above a certain area was brought to standard pressure and temperature it would form a 2 mm - 5 mm thick layer.

1.3 Photochemical models of the atmosphere

In order to test the understanding of atmospheric dynamics and photochemistry, the chemical reactions and dynamic processes described in the previous sections have to be appropriately translated into a mathematical model, which can be used for comparison with and interpretation of measurements. Ideally, the mutual interplay between observations and model results should refine both, model formulations and observation techniques, and lead to a comprehensive understanding of the Earth's atmosphere, allowing for trustable predictions of future scenarios.
The dynamics of air flow can be described in the framework of fluid dynamics by the continuity equations of mass, momentum, angular momentum and energy. Radiative transfer and transport across the boundaries of the atmosphere such as the ocean-atmosphere and land-atmosphere interface have to be considered (e.g. Brasseur and Solomon, 1986). Photochemical reactions can be described in terms of their rate coefficients which determine how fast the reactions proceed. The rate of a reaction is defined as the change of an involved species with time. Reactions involving two educts and two products such as

$$\mathrm{A} + \mathrm{B} \quad \longrightarrow \quad \mathrm{C} + \mathrm{D} \tag{R1.138}$$

are called bimolecular reactions. The corresponding rate coefficient k_{A+B} can be defined through

$$-\frac{d[A]}{dt} = -\frac{d[B]}{dt} = \frac{d[C]}{dt} = \frac{d[D]}{dt} = k_{A+B}\,[A]\,[B], \tag{1.4}$$

where parentheses represent concentrations of the respective species. Assuming [B] constant over the considered time scale, the temporal evolution of the concentration of species A is given by

$$[A](t) = [A]_0\, e^{-k_{A+B}\,[B]\,t}, \tag{1.5}$$

where $[A]_0$ is the initial concentration of species A. The temperature dependence of the bimolecular rate coefficients can be considered by Arrhenius' law

$$k(T) \;=\; A(T)\,\exp\frac{-E_A}{k_b\,T}, \tag{1.6}$$

where T is the temperature, k_b is Boltzmann's constant, $A(T)$ is the pre-exponential factor and E_A is the activation energy. Rate coefficients and the corresponding $A(T)$ and E_A are tabulated for various chemical reactions, for example by the IUPAC and JPL recommendations on reaction kinetics (Atkinson et al., 2006; Sander et al., 2003). While bimolecular reactions are not pressure dependent, reactions requiring a third body to carry off excess energy strongly depend on pressure since the third body is typically an ambient N_2 or O_2 molecule. The effective rate coefficient of termolecular reactions can be calculated from tabulated low and high pressure limits and correction terms for temperature dependencies.
The rate coefficients for reactions involving absorption of electromagnetic radiation such as

$$\mathrm{A} + h\nu \quad \longrightarrow \quad \mathrm{B} + \mathrm{C} \tag{R1.139}$$

are described in terms of the photolysis frequency J

$$-\frac{d[A]}{dt} = \frac{d[B]}{dt} = \frac{d[C]}{dt} = J_A\,[A] \qquad \text{with} \qquad J_A = \int q(\lambda)\,\sigma(\lambda)\,F(\lambda)\,d\lambda. \tag{1.7}$$

The integral extends over all wavelengths λ where the product of the actinic flux $F(\lambda)$, the absorption cross section $\sigma(\lambda)$ (both defined in chapter 2), and the quantum yield $q(\lambda)$ is non-zero. The quantum yield $q(\lambda)$ is a dimensionless number between 0 and 1 indicating the fraction of absorption processes that eventually lead to the formation of the products B and C.
Heterogeneous reactions between gaseous and condensed materials imply adsorption of the gaseous species on the surface of liquid or solid particles or absorption into the liquid phase. For reactions like

$$\mathrm{A}(g) + \mathrm{B}(s) \quad \longrightarrow \quad \mathrm{C}(g) + \mathrm{D}(s) \tag{R1.140}$$

it is possible to define a rate coefficient k_{het} in analogy to gas phase reactions which embodies the effects of adsorption and absorption,

$$-\frac{d[A]}{dt} = \frac{d[C]}{dt} = k_{het}\,[A]. \tag{1.8}$$

The rate coefficient k_{het} is proportional to the mean thermal velocity of the reactants, the uptake coefficient γ and the aerosol surface area density. The uptake coefficient γ is the fraction of surface collisions that lead to an irreversible chemical change of the gaseous educt (e.g. Zellner, 1999).
A more intuitive quantity than the rate coefficient of a chemical reaction is the lifetime of a reactant with respect to the considered reaction. The lifetime τ_{life} is defined as the time during which the concentration of reactant A decreases to $\frac{[A]}{e}$. For bimolecular reactions such as reaction (R1.138), the lifetime according to equation (1.5) is given by

$$\tau_{life} = \frac{1}{k_{A+B}\,[B]}. \tag{1.9}$$

Lifetimes with respect to termolecular, heterogeneous and photolysis reactions are defined analogously. An important conceptual approximation in atmospheric photochemistry is the assumption of photochemical steady state meaning that the concentration of reactant A is considered constant over time

$$\frac{d[A]}{dt} = 0. \tag{1.10}$$

The photochemical steady state approximation is applicable if the lifetime of species A is short compared to transport timescales and if the quantities contributing to production and loss of A are also constant over the considered timescales. Under the assumption of photochemical steady state, a set of coupled differential equations characterizing a set of chemical reactions collapses to a set of ordinary equations which allow for an *ad hoc* estimate of reactant concentrations (e.g. Brasseur and Solomon, 1986).

In the course of the present work, the 3-dimensional chemical transport model (CTM) SLIMCAT (Chipperfield, 1992, 1999) and the chemical box model LABMOS are used to interpret the observations and to test model formulations. SLIMCAT is a model which includes all relevant photochemical and dynamic processes in three dimensions according to the principles given above and in the previous sections. LABMOS is designed for dedicated studies of stratospheric photochemistry and comprises a comprehensive set of gas phase and heterogeneous reactions but no dynamic processes. Typically, LABMOS is initialized by SLIMCAT output and run in a Langrangian way, i. e. photochemistry is modeled along pre-calculated air mass trajectories.
The dynamic processes of SLIMCAT are forced by meteorological data from analyses of the European Center of Medium-Range Weather Forecast (ECMWF) (Uppala et al., 2004). In the vertical,

SLIMCAT extends from the ground to about 55 km altitude on 24 potential temperature levels. In horizontal direction SLIMCAT uses a $7.5° \times 7.5°$ latitude$\times$longitude grid. The chemical schemes of SLIMCAT and LABMOS correspond to recommendations given by the JPL-2002 report on Chemical Kinetics and Photochemical Data (Sander et al., 2003). SLIMCAT output is downloadable at http://www.env.leeds.ac.uk/$\sim$martyn/chelosba.html. The 1-D chemistry model LABMOS is an updated version of the model used in Bösch et al. (2003). Stratospheric photochemistry is modeled on 19 potential temperature levels typically between $\Theta = 336\,\mathrm{K}$ ($\simeq$11 km) and $\Theta = 1900\,\mathrm{K}$ ($\simeq$47 km). Photolysis rates are interpolated with respect to pressure, temperature, overhead ozone and solar zenith angle from a lookup table where the actinic fluxes are calculated as recommended by Lary and Pyle (1991) and validated for J_{NO_2} by Bösch et al. (2001).

Chapter 2

Physics of radiation and molecular absorption

The Earth's atmosphere is subject to electromagnetic radiation coming from the Sun and from the Earth's surface. Absorption and scattering of solar and terrestrial radiation and emission by the atmosphere itself control atmospheric temperatures and, thus, atmospheric chemistry and dynamics. Hence, radiative transfer in the Earth's atmosphere is of primary interest by itself but also yields information on atmospheric composition e. g. by deducing trace gas abundances from molecular absorption features in the electromagnetic spectrum. In this chapter the basics of radiation and radiative transfer in the Earth's atmosphere as well as the principles of molecular physics are discussed. As in the course of this work solar absorption spectroscopy is used to infer atmospheric trace gas concentrations, emphasis is put on the absorption of electromagnetic radiation by molecules.

2.1 Radiative transfer in the Earth's atmosphere

Radiative transfer in the Earth's Atmosphere is driven by solar short wave and terrestrial long wave radiation. Solar radiation reaching the top of the atmosphere (TOA) can be approximated as a black body spectrum. Most of the radiative energy originates from the photosphere, a thin layer of the Sun's atmosphere at about $7 \cdot 10^8$ m distance from the center. The temperature of the photosphere decreases from 7000 K at the inner to 4000 K at the outer boundary, resulting in an effective emission temperature of 5770 K. According to Planck's law, emission peaks at about 503 nm in the visible wavelength range. The black body spectrum is superimposed by absorption lines (Fraunhofer lines) since radiation emitted from the inner layers of the photosphere is absorbed in the outer ones. The solar intensity observed on Earth decreases when going from the center to the edge of the solar disk. This center-to-limb darkening effect is due to the fact that the effective emission temperature is higher for radiation coming from the center of the solar disk than from the edge. At the edge the path through the solar atmosphere is longer and hence attenuation of radiation is more important.

Terrestrial radiation is emitted by the Earth's surface at a mean temperature of 288 K. Correspondingly, emission peaks at about 10 μm in the infrared wavelength range. When studying atmospheric radiation

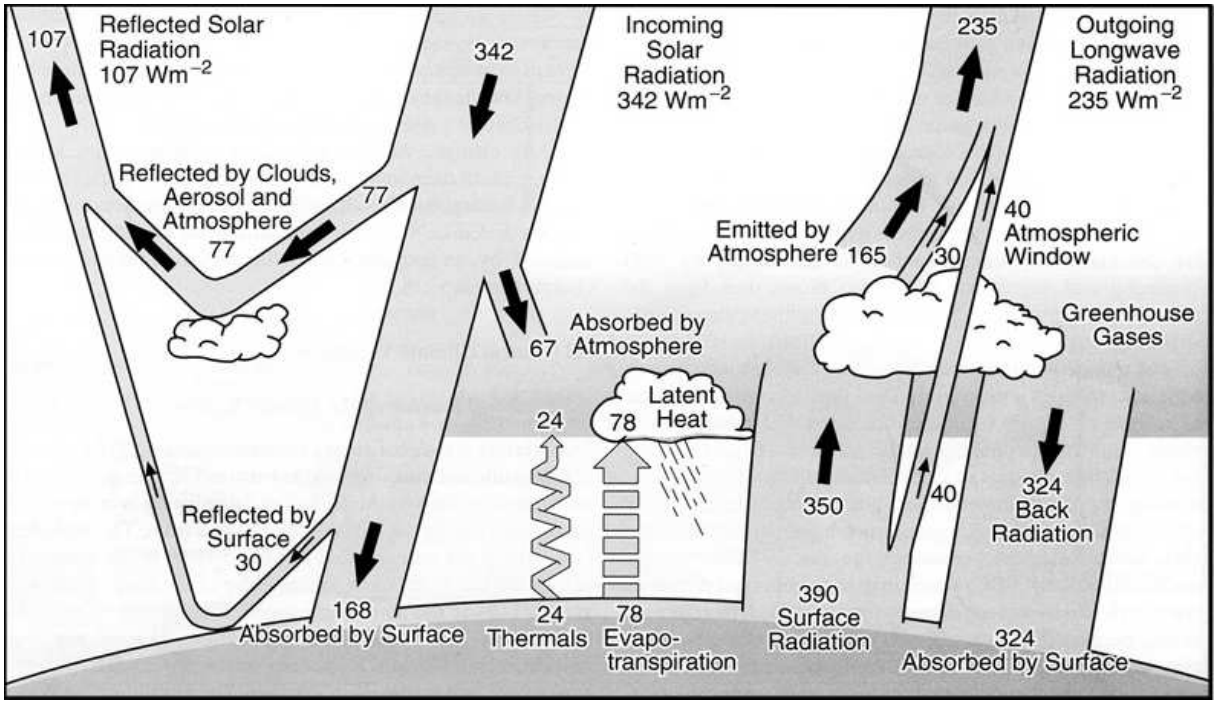

Figure 2.1: The Earth's annual and global mean energy balance. Roughly one third of the incoming solar radiation is reflected by the atmosphere and the Earth's surface. About 50% is absorbed by the Earth's surface which returns the absorbed energy to the atmosphere as sensible heat, latent heat and thermal infrared radiation. The atmosphere absorbs solar short wave and terrestrial long wave radiation and in turn re-emits radiation both up and down. The absorption of terrestrial infrared radiation and subsequent back radiation by the atmosphere causes the greenhouse effect. Adapted from Houghton et al. (2001).

it is often convenient to distinguish between the short wave spectral region (wavelengths smaller than $4\,\mu$m) where solar radiation dominates and the long wave spectral region (wavelengths longer than $4\,\mu$m) where terrestrial and atmospheric radiation are predominant. Figure 2.1 schematically illustrates the Earth's energy balance and the corresponding atmospheric energy fluxes.

2.1.1 Basic radiometric quantities

The radiance L_λ, sometimes simply called the intensity, is the amount of radiant energy dR_λ in a wavelength range $(\lambda, \lambda + d\lambda)$ transported across an element of area dA in directions confined to a solid angle $d\Omega$ during a time dt,

$$dR_\lambda = L_\lambda \cos\theta \, d\lambda \, dA \, d\Omega \, dt, \tag{2.1}$$

where θ is the angle between the considered direction and the normal to dA. The amount of radiant energy within a cone of solid angle Ω incident on or coming from an element of area dA per unit time and unit wavelength interval is called irradiance and given by

$$E_\lambda = \int_\Omega L_\lambda \cos\theta \, d\Omega. \tag{2.2}$$

The energy density u_λ is the amount of radiant energy in the wavelength interval $(\lambda, \lambda + d\lambda)$ per unit volume,

$$u_\lambda = \frac{1}{c} \int_{4\pi} L_\lambda \, d\Omega, \tag{2.3}$$

where the integral extends over all solid angles. A quantity important for photochemistry is the actinic flux F_λ which represent the radiant energy available for photolytic reactions,

$$F_\lambda = \int_{4\pi} L_\lambda \, d\Omega = c \cdot u_\lambda. \tag{2.4}$$

In this work the Sun is used as light source for atmospheric absorption spectroscopy. For our purposes sunlight can be regarded as a parallel beam of radiation coming from the Sun's disk, subtending a solid angle Ω_S. The corresponding irradiance can be approximated by

$$E_{\lambda,S} = \int_{\Omega_S} L_\lambda \, \cos\theta \, d\Omega \simeq \overline{L}_\lambda \, \Omega_S \, \cos\theta, \tag{2.5}$$

where $\overline{L}_S$ is the solar radiance averaged over the Sun's disk and θ is the angle between the viewing direction and the incident sunlight. When looking directly to the Sun the solar irradiance I_λ is given by

$$I_\lambda = \overline{L}_\lambda \, \Omega_S. \tag{2.6}$$

The index λ indicates that all quantities depend on wavelength and are considered per wavelength interval. Integrated quantities can be inferred easily by integration over all wavelengths.

Interaction of radiation with matter either leads to an increase or a decrease in intensity. The underlying processes are classified as emission and extinction, respectively. Assuming a beam of radiation incident on a small cylindrical volume of cross section dA and length ds, which is oriented parallel to the incident beam, the change of intensity dL_λ along ds is the sum of all extinction and emission processes,

$$dL_\lambda = dL_\lambda(\text{extinction}) + dL_\lambda(\text{emission}). \tag{2.7}$$

In the following, scattering, absorption and emission of radiation are identified as processes contributing to equation (2.7). A detailed treatment of radiative transfer can be found in Chandrasekhar (1960).

2.1.2 Scattering

Scattering of radiation by matter can be described in the framework of classical electrodynamics. Mie (Mie, 1908) provided a comprehensive theoretical treatment for a plane electromagnetic wave incident on a spherical dielectric particle. Later, Mie's theory was extended to non-spherical particles (Van de Hulst, 1981). The incident electromagnetic wave causes an oscillating polarization of the particle, i. e. the barycenters of the positive and negative charges on the particle oscillate spatially under the influence of the incident electromagnetic field. According to the laws of electrodynamics, the accelerated charge re-radiates electromagnetic radiation, which is called the scattered electromagnetic wave. When considering the properties of the scattered wave in one particular direction, the scattering angle ϑ is the angle between this specific direction and the incident radiation. In atmospheric physics the scattering processes are distinguished according to the size of the scattering particle. Scattering on particles which are small

compared to the wavelength of the incident radiation is called Rayleigh scattering. This holds applicable for air molecules and small aerosol particles ($< 0.1\,\mu$m). Scattering on larger particles is referred to as Mie scattering.

Rayleigh scattering

Since Rayleigh scattering is the limit of Mie's theory for small particles the scattered radiation can be approximated as dipole radiation. Assuming the incident electromagnetic radiation is passing through a small volume of length ds, where the number density of scatterers is n, the incident radiation is attenuated by dL_{λ,R_-},

$$dL_{\lambda,R_-} \;=\; -\,n\,\sigma_{\lambda,R}\,L_\lambda\,ds \;=\; -\,k_{\lambda,R}\,L_\lambda\,ds, \tag{2.8}$$

where $\sigma_{\lambda,R}$ is the Rayleigh scattering cross section and $k_{\lambda,R} \;=\; n\,\sigma_{\lambda,R}$ is the Rayleigh scattering coefficient. The Rayleigh scattering cross section for spherical particles is given by

$$\sigma_{\lambda,R} \;=\; \frac{8\,\pi^3\,\alpha^2}{3\,\epsilon_o^2\,\lambda^4}, \tag{2.9}$$

where α is the polarizability of the scatterer. For non-spherical particles the anisotropy of the molecules has to be considered. An empirical formula for atmospheric conditions is given by Chance and Spurr (1997),

$$\sigma_{\lambda,R} \;=\; \frac{3.9993\cdot 10^{-56}\,\mathrm{m}^6\,\lambda^{-4}}{1\;-\;1.069\cdot 10^{-14}\,\mathrm{m}^2\,\lambda^{-2}\;-\;6.681\cdot 10^{-29}\,\mathrm{m}^4\,\lambda^{-4}} \quad . \tag{2.10}$$

The angular distribution $p_R(\vartheta)$ of the scattered radiation peaks in forward and backward direction with respect to the direction of the incident wave,

$$p_R(\vartheta) \;=\; \frac{3}{4}\,(\,1\;+\;\cos^2\vartheta\,). \tag{2.11}$$

Under atmospheric conditions, taking into account the anisotropy of the most important atmospheric constituents (Goody and Yung, 1989) equation (2.11) reads

$$p_R(\vartheta) \;=\; 0.7629\,(\,1\;+\;0.932\,\cos^2\vartheta\,). \tag{2.12}$$

On the one hand the incident radiation is attenuated by scattering radiant energy out of the propagation direction according to equation (2.8), on the other hand radiation coming from an arbitrary direction can be scattered into the propagation direction. The increase of radiation in propagation direction dL_{λ,R_+} is given through

$$dL_{\lambda,R_+} \;=\; k_{\lambda,R}\,\frac{1}{4\pi}\int_o^{2\pi}\int_o^{\pi} p_R(\vartheta,\varphi,\vartheta',\varphi')\,L_\lambda(\vartheta',\varphi')\sin\vartheta'\,d\vartheta'\,d\varphi'\;\;ds, \tag{2.13}$$

where the radiation $L_\lambda(\vartheta',\varphi')$ coming from an arbitrary direction (ϑ', φ') is weighted by its probability $p_R(\vartheta,\varphi,\vartheta',\varphi')$ to be scattered in propagation direction (ϑ, φ) of the incident wave and integrated over all directions.

So far, we only considered elastic scattering where the incoming and the scattered radiation have the same wavelength. When the scattering molecule changes its quantum-mechanical state during the

scattering process the wavelength of the scattered radiation is shifted with respect to the incident wave. This process is called Raman scattering. The molecule may change its rotational and vibrational state leading to an increase or decrease of the scattered wavelength by the corresponding amount of emitted or absorbed energy. Hence, the spectrum of scattered radiation originating from a monochromatic incident wave consists of several distinct wavelengths corresponding to the elastically scattered Rayleigh line and several vibrational Raman lines each consisting of several rotational Raman lines. The Raman scattering cross section represents only a few percent of the Rayleigh scattering cross section. For details see Haug (1996). When measuring scattered sunlight Raman scattering can be observed as 'filling in' of solar Fraunhofer lines. This effect is referred to as the Ring effect (Grainger and Ring, 1962; Bussemer, 1993).

Mie scattering

The electromagnetic dipole approximation fails when the dimension of the scatterer is not small compared to the wavelength of the incident radiation. Rather, a large number of elementary radiation sources on the scattering particle has to be considered. Interference of the scattered elementary waves yields the scattering cross section $\sigma_{\lambda,M}(\eta)$ which cannot be calculated analytically for arbitrary shaped particles. Numerical calculations of the scattering cross section yield an oscillating function of the size parameter $\eta = 2\,\pi\,\frac{r}{\lambda}$, with the particle radius r. The macroscopic scattering coefficient $k_{\lambda,M}$ of a composite aerosol containing N particles with different radii is defined by

$$k_{\lambda,M} = \int_0^\infty \sigma_{\lambda,M}(\eta)\, n(\hat{r})\, d\hat{r} \tag{2.14}$$

with $n(\hat{r}) = \frac{dN}{d\hat{r}}$ the particle size distribution with respect to a normalized radius $\hat{r}$. Atmospheric aerosols commonly exhibit particle size distributions of the type $n(\hat{r}) \sim \hat{r}^{-m}$ with $4 \leq m \leq 4.5$, implying only weakly wavelength dependent scattering coefficients $k_{\lambda,M} \sim \lambda^{3-m}$.
The angular distribution $p_M(\vartheta)$ of Mie-scattered radiation reveals a strong predominance of the forward direction which increases with particle radius. Several approximations to $p_M(\vartheta)$ exist, e. g. the Henyey-Greenstein (Henyey and Greenstein, 1941) and double Henyey-Greenstein phase functions. A thorough discussion on the theoretical background of Mie theory, numerical calculations of the angular distribution of Mie-scattered radiation and applications in atmospheric physics can be found in Shangavi (2003).
The incident electromagnetic radiation is altered by Mie-scattering in a similar way as in the case of Rayleigh scattering. Let dL_{λ,M_-} represent the radiance scattered out of the incident beam and dL_{λ,M_+} the radiance scattered into the direction of propagation. Both contributions can readily be obtained in analogy to equation (2.8) and (2.13) by replacing the quantities specific to Rayleigh scattering through their analogs for Mie scattering.

As in the case of Rayleigh scattering, inelastic scattering on particles occurs. Absorption of incident radiation by the scattering particle can be quantified elegantly by introducing the complex refractive index where the imaginary part represents the absorption characteristics of the particle. The single scattering albedo ϖ_λ is commonly used to classify absorption and scattering properties of aerosols,

$$\varpi_\lambda = \frac{k_{\lambda,M}}{k_{\lambda,M} + k_{\lambda,A}}, \tag{2.15}$$

where $k_{\lambda,A}$ is the absorption coefficient of the particle.

2.1.3 Absorption and emission

Apart from scattering electromagnetic radiation, air molecules interact with radiation through absorption, stimulated emission and spontaneous emission of radiation. Absorption and emission of radiation induce transitions among the quantum mechanical energy levels of the interacting molecule. Quantum electrodynamics allows to calculate the absorption and emission probabilities by treating the incident electromagnetic wave as a small, time-dependent perturbation to the unperturbed atomic or molecular Hamiltonian. First-order perturbation theory yields the transition rates between an upper energy level j and a lower energy level i in terms of the Einstein coefficients for absorption B_{ij} and stimulated emission B_{ji}, where the incident electromagnetic wave is treated in dipole approximation (e.g. Bransden and Joachain, 2003). The transition rate due to spontaneous emission is given in terms of the Einstein coefficient A_{ji}. The change of the number of molecules in the lower state dn_i depends on the population densities n_i and n_j and the energy density u_λ of the radiation field,

$$\frac{dn_i}{dt} \;=\; -\,n_i\,u_\lambda\,B_{ij} \;+\; n_j\,u_\lambda\,B_{ji} \;+\; n_j\,A_{ji}. \tag{2.16}$$

Each radiative transition yields a change of the energy of the radiation field by $\frac{h\,c}{\lambda}$ with the wavelength λ of the transition, the speed of light c and Planck's constant h. The corresponding change in intensity of radiation passing through a small volume of length ds with $n \;=\; n_i \;+\; n_j$ molecules (per volume) is given by

$$dL_{Abs} \;+\; dL_{StE} \;+\; dL_{SpE} \;=\; -\,n_i\,\frac{B_{ij}\,h}{\lambda}\,L_\lambda\,ds \;+\; n_j\,\frac{B_{ji}\,h}{\lambda}\,L_\lambda\,ds \;+\; n_j\,\frac{A_{ji}\,h\,c}{4\,\pi\,\lambda}\,ds, \tag{2.17}$$

where the factor $\frac{1}{4\,\pi}$ indicates that spontaneous emission is isotropic whereas stimulated emission only occurs in propagation direction. In local thermodynamic equilibrium, which is a good approximation for altitudes below 80 km in the Earth's atmosphere, the energy levels are populated according to Boltzmann's law and the energy density of the radiation is given by Planck's distribution. The corresponding relations between n_i and n_j and the Einstein coefficients read

$$\frac{n_j}{n_i} \;=\; \frac{g_j}{g_i}\,e^{\frac{-\,\Delta\,E}{k_B\,T}}, \qquad g_j\,B_{ji} \;=\; g_i\,B_{ij}, \qquad A_{ji} \;=\; \frac{8\,\pi\,h\,c}{\lambda^5}\,B_{ji} \tag{2.18}$$

with the Boltzmann constant k_B, the temperature T, the degeneracies of the upper and lower energy level g_j and g_i, and the energy difference between the two levels ΔE (Goody and Yung, 1989; Bransden and Joachain, 2003). Inserting relations (2.18) into equation (2.17) yields

$$\begin{aligned}
&dL_{Abs} \;+\; dL_{StE} \;+\; dL_{SpE} \;=\\
&=\; -\,n_i\,\tfrac{B_{ij}\,h}{\lambda}\,L_\lambda\,ds \;+\; n_i\,\tfrac{B_{ij}\,h}{\lambda}\,L_\lambda\,e^{\frac{-\,\Delta\,E}{k_B\,T}}\,ds \;+\; n_i\,\tfrac{B_{ij}\,h}{\lambda}\,\tfrac{8\,\pi\,h\,c^2}{4\,\pi\,\lambda^5}\,e^{\frac{-\,\Delta\,E}{k_B\,T}}\,ds \;=\\
&=\; -\,n_i\,\sigma_{\lambda,A}\,\left(1 \;-\; e^{\frac{-\,\Delta\,E}{k_B\,T}}\right)\,\left[L_\lambda \;-\; \tfrac{2\,h\,c^2}{\lambda^5}\,\tfrac{1}{e^{\frac{\Delta\,E}{k_B\,T}}-1}\right]\,ds \;=\\
&=\; -\,k_{\lambda,A}\,\left[\,L_\lambda \;-\; P_\lambda\,\right]\,ds,
\end{aligned} \tag{2.19}$$

where $\sigma_{\lambda,A} = \frac{B_{ij}\,h}{\lambda}$ is the absorption cross section, $k_{\lambda,A} = n_i\,\sigma_{\lambda,A}\left(1 - e^{\frac{-\Delta E}{k_B T}}\right)$ is the the absorption coefficient and P_λ is Planck's distribution of thermal radiation in units of intensity per wavelength interval. For temperatures encountered in the troposphere and stratosphere the population of the lower energy level n_i is much larger than n_j and can be approximated by the number density of molecules available in the considered volume $n \simeq n_i$. For the same reason the radiant energy emitted by stimulated emission is much smaller than the absorbed energy, although the cross section is identical for both processes. Therefore, the exponential term in the expression of the absorption coefficient $k_{\lambda,A}$ can often be neglected in the UV/visible and infrared.

2.1.4 Equation of radiative transfer

In the previous sections scattering, absorption and emission of radiation are identified as extinction and emission processes which contribute to the radiative transfer in the Earth's atmosphere according to equation (2.7). Contributions from Rayleigh and Mie-scattering (equations (2.8) and (2.13)) and from absorption and emission processes (equation (2.19)) sum up to the equation of radiative transfer

$$\begin{aligned} dL_\lambda &= dL_{\lambda,R-} + dL_{\lambda,R+} + dL_{\lambda,M-} + dL_{\lambda,M+} + dL_{Abs} + dL_{StE} + dL_{SpE} = \\ &= \left[-\left(k_{\lambda,S} + k_{\lambda,A}\right) L_\lambda + k_{\lambda,A}\,P_\lambda + \tfrac{k_{\lambda,S}}{4\pi} \int p_S(\vartheta',\varphi')\,L_\lambda(\vartheta',\varphi')\sin\vartheta'\,d\vartheta'\,d\varphi' \right] ds, \end{aligned} \tag{2.20}$$

where the Rayleigh and Mie scattering coefficients and phase functions are combined to $k_{\lambda,S} = k_{\lambda,R} + k_{\lambda,M}$ and $p_S = p_R + p_M$. dL_λ represents the change in intensity of a beam of radiation after passing through a small atmospheric volume of length ds. When observing light coming directly from the Sun and its close vicinity, terrestrial long wave radiation and radiation scattered into the viewing direction can be neglected. Equation (2.20) reduces to Beer-Lambert's law,

$$dL_\lambda = -\left(k_{\lambda,S} + k_{\lambda,A}\right) L_\lambda\,ds = -\,e_\lambda\,L_\lambda\,ds, \tag{2.21}$$

with the extinction coefficient e_λ. The solution to equation (2.21) is obtained via integration

$$L_\lambda(s) = L_\lambda(s_o)\,e^{-\int_{s_o}^{s} e_\lambda(s')ds'} = L_\lambda(s_o)\,e^{-\tau_\lambda(s_o,s)} \tag{2.22}$$

where $\tau_\lambda(s_o,s) = \ln\frac{L_\lambda(s_o)}{L_\lambda(s)} = \int_{s_o}^{s} e_\lambda(s')ds'$ is the optical density between s_o and s, and $L_\lambda(s_o)$ is the incident radiance.

2.2 Principles of molecular physics

As described in section 2.1.3 the interaction of radiation with molecules induces transitions between the molecular energy levels through absorption and emission of radiation. In general, molecules consist of several nuclei and electrons which interact with each other through attraction and repulsion. The corresponding Schrödinger equation of the many-body system comprises the kinetic energies of the particles and the interaction potentials given by Coulomb's law. The general problem can be solved numerically, only. However, several approximations exist which allow to analytically deduce energy

eigenstates and eigenfunctions for small molecules. A detailed treatment of molecular physics is found in Herzberg (1950).

The motion of a molecule can be subdivided in translational motion of the whole system, motion of the electrons and motion of the nuclei. The translational motion can be separated by changing the coordinate system to the center-of-mass system. In the absence of external forces the center-of-mass moves as a free particle and its motion is not discussed further. In general, electronic and nuclear motion are coupled, i. e. changes of the nuclear motion induce changes of the electronic wave functions and vice versa. Due to their lower mass, electrons move much faster than the nuclei and the electronic wavefunctions adjust almost instantaneously to motions of the nuclei. Based on this approximation the coupling between electronic and nuclear motion can be neglected and the Schrödinger equation can be separated in an electronic and in a nuclear part which can be solved independently (Born-Oppenheimer approximation). The total energy E and the total wave function ψ of the molecule can be separated in an electronic and in a nuclear part, E_e and E_N and ψ_e and ψ_N,

$$E = E_e + E_N \qquad \psi = \psi_e \cdot \psi_N. \tag{2.23}$$

2.2.1 Electronic motion

The Hamiltonian of the electronic Schrödinger equation comprises the kinetic energy of the electrons and the Coulomb interactions between the charged particles, including the repulsive interaction between the nuclei. The latter is only a constant as the position of the nuclei is assumed fixed according to the Born-Oppenheimer approximation. Hence, the energy eigenstates $E_e(R)$ of the electronic motion depend parametrically on the internuclear distance R. Since the nuclei are hold together by the electrons it is intuitive that $E_e(R)$ acts as potential energy for the motion of the nuclei. The large panel in figure 2.2 schematically illustrates typical electronic energy levels $E_e(R)$ of a diatomic molecule. At short internuclear separation, $R \rightarrow 0$, the electronic energy $E_e(R)$ increases strongly due to the increasing repulsive force between the nuclei. At large separations, $R \rightarrow \infty$, the electronic energy converges towards the separated atom limit. In between the two limits, stable molecular states exhibit a minimum of the electronic energy. In general, the ground state (figure 2.2 a)) and the excited electronic states (figure 2.2 b) and c)) can form stable molecules. The internuclear distance where the electronic energy is minimal is referred to as the equilibrium distance R_e of the nuclei and can differ for ground and for excited states. In figure 2.2 a) the equilibrium distance of the ground state is indicated as R_0. The dissociation energy D_e necessary to separate a stable molecule into two atoms is given through $D_e = E_e(\infty) - E_e(R_e)$. Electronic energy levels which decrease monotonically with R (figure 2.2 d)) correspond to unstable molecular states leading to the dissociation of the molecule.

Bound molecular states can be obtained when the negative charge density between the nuclei is larger than what is expected when placing two non-interacting nuclei at the equilibrium distance. The charge density in between the nuclei depends on the electronic wave functions. Commonly, single electron wave functions of the molecule are constructed as linear combination of the known atomic wavefunctions centered on each nucleus (LCAO: Linear Combination of Atomic Orbitals). The total molecular electronic wave function ψ_e is then built from the single electron wave functions (Hund-Mulliken approach). In general, the combination of two atomic orbitals (spatial wavefunctions)

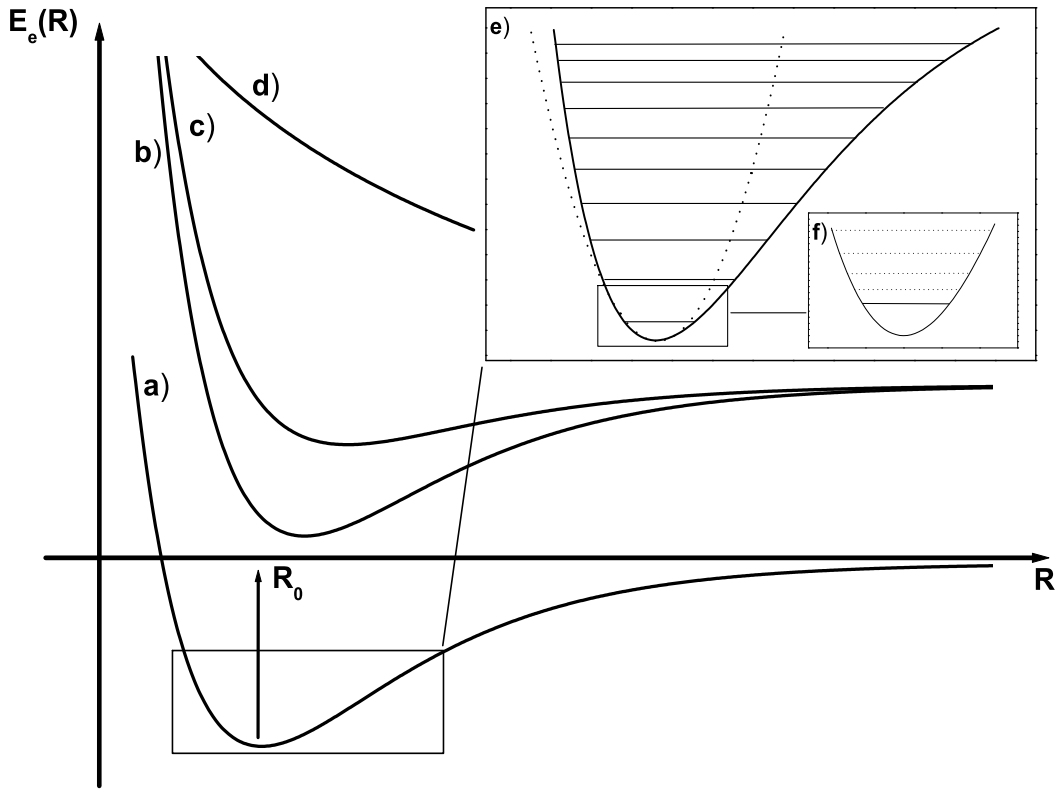

Figure 2.2: Large Panel: Electronic energy levels $E_e(R)$ as a function of the internuclear distance R. Curve a) represents the ground state of the molecule exhibiting minimum electronic energy at the equilibrium distance R_0. Curve b) and c) are excited electronic energy levels forming a stable molecular state. Curve d) shows an excited electronic state which has no minimum and hence, leads to dissociation of the molecule. Inset e): Zoom of the lowest electronic state. The dotted line indicates the potential energy of a harmonic oscillator about the equilibrium position R_0. The horizontal lines illustrate vibrational energy levels. Inset f): Zoom of the lowest vibrational state. The dotted horizontal lines schematically show the corresponding rotational energy levels.

yields two molecular single electron orbitals, where one orbital corresponds to an elevated and the other to a decreased charge density between the nuclei. Accordingly, the two molecular orbitals are called bonding and anti-bonding. Each of the single electron orbitals is twofold degenerate in the electronic spin according to the Pauli principle. A stable molecule is formed when the number of electrons in bonding states is in excess of the number of electrons in anti-bonding states.

2.2.2 Nuclear motion

The motion of the nuclei can be classified as vibrational and rotational motion. In principle, both classes are coupled, i. e. the vibration about the equilibrium position and the vibrational equilibrium position itself depend on the rotation of the molecule and vice versa. It is convenient to describe the motion of the nuclei in terms of the reduced mass μ which in the case of a diatomic molecule with nuclear masses m_A and m_B is given by $\mu = \frac{m_A m_B}{m_A + m_B}$. The Hamiltonian of the nuclear motion consists of the kinetic

energies of the nuclei and the electronic energy $E_e(R)$ which includes the Coulomb repulsion of the nuclei and acts as potential energy. Neglecting the dependency of the rotation of the molecule on the internuclear distance R, the vibrational and the rotational motion uncouple and E_N is given by

$$E_N = E_V + E_R \qquad \psi_N = \psi_V \cdot \psi_R \tag{2.24}$$

with the vibrational and the rotational energy E_V and E_R and the vibrational and rotational wave functions ψ_V and ψ_R.

In the vicinity of the equilibrium position $R \approx R_e$ the potential energy $E_e(R)$ can be approximated by the potential of a harmonic oscillator (see inset e) in figure 2.2). It is evident that at large distances of the nuclei, $R \to \infty$, the attractive force between the nuclei is zero and the harmonic oscillator approximation fails. The empirically derived Morse potential reconciles the experimental observations and yields the harmonic approximation in the limit $R \to R_e$,

$$E_e(R) = D_e \left[1 - e^{-\beta(R-R_e)}\right]^2 \overset{R \to R_e}{\approx} D_e \beta^2 (R - R_e)^2, \tag{2.25}$$

where D_e is the dissociation energy and β is a constant specific to the considered molecule. Still, the Morse potential fails to model the large repulsive interaction when the nuclei come close together (Herzberg, 1950). The corresponding vibrational energy levels E_N are given by

$$E_V = \hbar\omega_o (v + \frac{1}{2}) - \frac{\hbar^2}{4 D_e} \omega_o^2 (v + \frac{1}{2})^2, \tag{2.26}$$

where $v = 0, 1, 2, \ldots$ is the vibrational quantum number and $\hbar\omega_o = \frac{hc}{\lambda_o} = \hbar\sqrt{\frac{2D_e}{\mu}}\,\beta$ is the spacing of the vibrational energy levels of the harmonic oscillator. Inset e) in figure 2.2 illustrates the vibrational energy levels corresponding to the quantum numbers $v = 0, 1 \ldots 9$. Equation (2.26) shows that the vibrational energy levels are not equidistant like those of the harmonic oscillator. Their separation decreases with increasing quantum number v. Putting $v = 0$ yields a finite value for the zero-point energy $E_{V,0}$ of the vibrational motion indicating that there is vibration of the molecule even in absence of any external energy deposition. The vibrational eigenfunctions ψ_V are very similar to the eigenfunctions of the harmonic oscillator, however, they are not totally symmetric about the equilibrium position R_e. Since the potential $E_e(R)$ (inset e) in figure 2.2) is steeper for $R < R_e$ than for $R > R_e$, occurrence of the latter distances is more probable and thus the corresponding eigenfunctions exhibit larger absolute values on the shallower side of the potential.

As long as the rotation of the nuclei is assumed to have no effect on the internuclear distance R (rigid rotator approximation), the rotation of the molecule is a free motion whose energy depends on the moment of inertia $I = \mu R_e^2$ of the molecule. In a true rotating molecule the centrifugal force associated with the rotation of the nuclei causes a stretch of the molecule and thus influences the equilibrium position R_e and the moment of inertia I. The influence of centrifugal distortion depends on the shape of the potential energy in the neighborhood of the equilibrium distance. A flat potential curve corresponding to small β in equation (2.25) allows for a greater impact of the centrifugal force on the equilibrium distance of the molecule. Thus, the rotational energy of the molecule depends on the potential energy $E_e(R)$ and is given through

$$E_R = \frac{\hbar^2}{2I} J(J+1) - \frac{\hbar^4}{2 I^3 \omega_o^2} J^2 (J+1)^2 \tag{2.27}$$

where $\hbar^2\, J\,(\,J\,+\,1\,)$ are the eigenvalues of the angular momentum operator J^2 with the rotational quantum numbers $J\,=\,0,\,1,\,2,\,\ldots$. Inset f) in figure 2.2 illustrates rotational energy levels corresponding to the quantum numbers $J\,=\,0,\,1,\,2,\,3$. Neglecting centrifugal distortion, the corresponding eigenfunctions ψ_R are the eigenfunctions of the J^2 operator and given in terms of the associated Legendre polynomials (e.g. Bransden and Joachain, 2003).

So far, vibrational and rotational motion have been assumed to be uncoupled. The actual coupling of vibrational and rotational motion comes into play when considering the change of the internuclear distance R due to vibration during the rotation of the molecule. Since the rotation of a molecule is much slower than its vibration the moment of inertia can be calculated with respect to a mean distance between the nuclei. Due to the anharmonicity and the corresponding asymmetry of the vibrational wave functions the mean vibrational distance of the nuclei is larger than R_e and increases with larger vibrational quantum numbers. In second order approximation the total nuclear energy E_N is given by adding a term to equations (2.26) and (2.27) which is due to ro-vibrational coupling,

$$\begin{aligned} E_N \;&=\; \hbar\omega_o\,(\,v\,+\,\tfrac{1}{2}\,)\,+\,\tfrac{\hbar^2}{2I}\,J\,(\,J\,+\,1\,)\,-\,\tfrac{\hbar^2}{4D_e}\,\omega_o^2\,(\,v\,+\,\tfrac{1}{2}\,)^2\,- \\ &-\;\; \tfrac{\hbar^4}{2\,I^3\,\omega_o^2}\,J^2\,(\,J\,+\,1\,)^2\,-\,\beta_1\,(v\,+\,\tfrac{1}{2}\,)\,J\,(\,J\,+\,1\,), \end{aligned} \tag{2.28}$$

where β_1 is a coupling constant specific to the considered molecule.

2.3 Molecular absorption spectra

Sections 2.1 and 2.2 discuss the basics of interaction between radiation and molecules and the principles of molecular structure. In this section emphasis is put on how molecular absorption spectra can be understood based on the presented theoretical setup. Implications for spectra originating from spontaneous and stimulated emission are in most cases equivalent in a sense that radiation is not absorbed but emitted.

2.3.1 Radiative transitions between molecular energy levels

Incident radiation on a molecule with energy $\hbar\,\omega$ can be absorbed by the molecule if there is an upper molecular energy level E_j and a lower level E_i with

$$\hbar\,\omega\;=\;E_j(e_j,v_j,J_j)\;-\;E_i(e_i,v_i,J_i) \tag{2.29}$$

and if the transition probability between the two levels does not vanish. According to section 2.2 the energy levels in equation (2.29) are labeled by their vibrational and rotational quantum numbers v and J and a representative electronic quantum number e which identifies the electronic energy level. As mentioned above, time dependent perturbation theory yields the transition probabilities between molecular energy levels, given the molecular wave functions. According to the symmetry properties of the wavefunctions, selection rules of the quantum numbers identify transitions with non-zero probability. Depending on the degree of coupling between electronic, vibrational and rotational motion which is necessary to describe observed absorption spectra a variety of selection rules exist which can be found in Herzberg (1950).

In general each transition of the electronic state $(e_j, v_j, J_j) \leftarrow (e_i, v_i, J_i)$ goes along with changes of the vibrational and rotational states. Thus spectra orginating from electronic transitions consist of several bands which can be associated to vibrational transitions which in turn consist of bands of rotational transitions. The energy of electronic transitions corresponds to wavelengths in the ultraviolet (UV) and visible part of the electromagnetic spectrum. When studying electronic spectra in the UV/visible, the spectral resolution of the observing instrument is often not sufficient to resolve the underlying ro-vibrational structure.

Transitions between the vibrational energy levels of a single electronic state $(e, v_j, J_j) \leftarrow (e, v_i, J_i)$ correspond to absorption spectra in the infrared (IR) spectral range. Each vibrational transition consists of a band of rotational transitions. Here, the selection rule $\Delta J = J_j - J_i = \pm 1$ applies yielding the P ($\Delta J = +1$) and the R ($\Delta J = -1$) rotational branch corresponding to a single vibrational transition. For polyatomic molecules and degenerate states also a Q-branch ($\Delta J = 0$) can be observed. For homonuclear diatomic molecules the probability for transitions between the vibrational energy levels of a single electronic level vanishes due to symmetry properties. Accordingly, the molecules N_2 and O_2, which are the most abundant in the Earth's atmosphere, cannot absorb terrestrial IR radiation and hence cannot contribute to the green house effect.

Molecular absorption spectra in the far infrared ($> 10\mu$ m) and microwave spectral range correspond to transitions between rotational energy levels of a single vibrational state $(e, v, J_j) \leftarrow (e, v, J_i)$. Microwave spectroscopy of rotational transitions among atmospheric trace molecules has played a major role in identifying and quantifying contributions to ozone loss above Antarctica in the late 1980's (de Zafra et al., 1987).

If the upper energy level E_j of the radiative transition lies above the dissociation energy D_e of the molecular state or is by itself a dissociative molecular state (e. g. figure 2.2 d)), the absorbed energy is partly converted to translational energy of the dissociating molecule. Since the translational energy can attain arbitrary values, there is no need for the absorbed energy to be quantized and the corresponding absorption spectra are continuous.

2.3.2 Strength of absorption lines

Equation (2.16) gives the transition probability between two energy levels due to absorption of radiation in terms of the Einstein coefficient B_{ij}. The absorption cross section $\sigma_{\lambda,A}$ and the absorption coefficient $k_{\lambda,A}$ are defined as a function of B_{ij} assuming a population distribution of the upper and lower energy level according to thermodynamic equilibrium. The integrated absorption coefficient S_N of a single absorption line is given by

$$S_N = \int_{\lambda_o - \Delta\lambda}^{\lambda_o + \Delta\lambda} k_{\lambda,A}\, d\lambda, \tag{2.30}$$

where $\lambda_o = \frac{2\pi c}{\omega_o}$ is the center wavelength of the transition and $\Delta\lambda$ is a suitable wavelength interval. According to equation (2.19) S_N depends on the number of molecules in the lower energy state n_i along

the absorbing path ds. Therefore, the line strength S is defined as

$$S = \frac{S_N}{\int n_i \, ds}. \tag{2.31}$$

Spectral databases commonly tabulate S for a variety of possible molecular transitions at a reference temperature (HITRAN[1]: $T_{ref} = 296\,K$) and give correction terms for the temperature dependence.

2.3.3 Spectral line shapes

Besides the line strength the shape of an absorption line is an important feature which has to be taken into account when performing absorption spectroscopy. The line shape factor $f(\lambda - \lambda_o)$ describes the profiles of absorption lines and is normalized according to

$$\int_0^\infty f(\lambda - \lambda_o)\, d\lambda = 1. \tag{2.32}$$

Since the integral over the line shape factor is normalized to one, the absorption coefficient $k_{\lambda,A}$ of an absorption line can be written as

$$k_{\lambda,A} = S_N \, f(\lambda - \lambda_o) = S \, f(\lambda - \lambda_o) \int n_i \, ds \tag{2.33}$$

where S_N and S are defined by equations (2.30) and (2.31). If stimulated emission of radiation can be neglected, equation (2.33) can be written in terms of the absorption cross section

$$\sigma_{\lambda,A} = S \, f(\lambda - \lambda_o). \tag{2.34}$$

In general, the shape of atmospheric absorption lines is dominated by Doppler and collisional broadening. Natural line broadening which originates from the finite width of the molecular energy levels is negligible for atmospheric absorption in the infrared and UV/visible wavelength range.

Doppler broadening

Due to thermal motion there may be a non-zero relative velocity u between the detector and the absorbing molecule. In thermal equilibrium, the probability to find a molecule moving with relative velocity u is given by Maxwell's distribution. The wavelength of an absorption line of a moving molecule is shifted with respect to the molecule at rest according to the Doppler shift

$$\lambda = \lambda_o \, (\, 1 \pm \frac{u}{c} \,), \tag{2.35}$$

where $\frac{u}{c} << 1$ and c is the speed of light. For an ensemble of molecules the shape of an absorption line is derived from the Maxwell's distribution of molecular velocities and is given by the Doppler profile

$$f_D(\lambda - \lambda_o) = \sqrt{\frac{\ln 2}{\pi}} \frac{1}{\gamma_D} \, e^{-\ln 2 \left(\frac{\lambda - \lambda_o}{\gamma_D} \right)^2}, \tag{2.36}$$

where $u_p = \sqrt{\frac{2\,k_b\,T}{m}}$ is the most probable velocity at a temperature T in a gas with molecular mass m. The half width at half maximum (HWHM) γ_D of the doppler profile is given by

$$\gamma_D = \sqrt{\ln 2} \, \frac{u_p \, \lambda_o}{c}. \tag{2.37}$$

[1](Rothman et al., 2005)

Collisional broadening

So far, the interaction between individual molecules has been neglected. However, when two molecules approach each other the collisional interaction Hamiltonian may cause distorsion of the molecular energy levels illustrated in figure 2.2. Based on van-der-Waals theory, in a first approximation the interaction Hamiltonian can be assumed proportional to R^{-6} with the internuclear distance R. In an ensemble of molecules the difference between two molecular energy levels and accordingly the wavelength of the corresponding absorption line are statistically scattered about a mean energy difference and a mean wavelength λ_o. Under the assumption that the time in close interaction is much shorter than the time between two collisions, the line shape of the respective absorption line is given by the Lorentz profile,

$$f_P(\lambda - \lambda_o) = \frac{1}{\pi} \frac{\gamma_P}{(\lambda - \lambda_o)^2 + \gamma_P^2}. \tag{2.38}$$

The half width at half maximum γ_P is proportional to the pressure and depends on the temperature of the respective gas. When investigating finer details of collisionally broadened absorption lines, inelastic collisions between the molecules causing additional spectral broadening have to be considered. Further, when the interaction Hamiltonian is large and the time spent in close interaction is not short compared to the time between collisions, the colliding molecules may form meta-stable or even truly bound dimers. Such species owe absorption lines significantly different from the isolated monomer case (Camy-Peyret and Vigasin, 2003; Pfeilsticker et al., 2001).

Voigt profile

In the Earth's atmosphere Doppler broadening dominates over collisional broadening at low pressure ($p < 1\,\text{mbar}$) in the upper atmosphere while collisional broadening predominates in the lower atmosphere ($p > 100\,\text{mbar}$). In general the line shape of an atmospheric absorption line is a composite of both effects accounted for by the Voigt profile f_V, which is a convolution of a Gaussian and Lorentzian line shape,

$$f_V(\lambda - \lambda_o) = \int_{-\infty}^{\infty} f_D(x)\, f_P(\lambda - \lambda_o - x)\, dx = \sqrt{\frac{\ln 2}{\pi^3}} \frac{\gamma_P}{\gamma_D} \int_{-\infty}^{\infty} \frac{e^{-\ln 2 \left(\frac{x}{\gamma_D}\right)^2}}{(\lambda - \lambda_o - x)^2 + \gamma_P^2}\, dx. \tag{2.39}$$

The line shape of an atmospheric absorption line can be calculated from equation (2.39) given ambient temperature and pressure and the temperature dependence of γ_P which is tabulated in spectral databases for a variety of absorption lines. Finer effects arising from molecular collisions mentioned above and from Dicke narrowing (Dicke, 1953) can be neglected for our purposes.

Chapter 3

The LPMA/DOAS experiment

The LPMA/DOAS experiment is designed to investigate atmospheric photochemistry in the upper troposphere and stratosphere by remote sensing of trace gas abundances. A balloon gondola carries the LPMA Fourier Transform InfraRed (FT-IR) Interferometer and the DOAS UV/visible grating spectrometer up to 30 km to 40 km altitude while both instruments measure the direct solar irradiance attenuated by extinction in the Earth's atmosphere. Absorption spectra are measured in virtually the entire spectral range from the UV to the mid-infrared (IR). Based on the principles of radiative transfer and molecular absorption discussed in section 2 the vertical distribution of many trace gases important for atmospheric photochemistry (see section 1.2) can be inferred.
This section gives a brief overview of the technical setup of the instruments and discusses the algorithms used for the retrieval of trace gas abundances. The trace gas retrievals rely on a two-step approach. In the first step the number of absorbing molecules integrated along the line-of-sight (or slant column density) is inferred for each measured spectrum . In the second step an ensemble of column measurements is inverted into vertical trace gas profiles considering the viewing geometry of each line-of-sight. In the following, the first step is referred to as spectral retrieval, the second step is called profile retrieval. The spectral retrieval is inherently different for spectra in the UV/visible and IR spectral range, while the profile retrieval is independent of the spectral range of the measurements.

3.1 Instrumentation and observational setup

The gondola which carries the scientific instruments is connected to the actual balloon through the flight train which consists of the landing parachutes and auxiliary equipment necessary to control and monitor the balloon flight. The large volume of the balloon (100 000 m^3 to 400 000 m^3) filled with helium allows to lift payloads as heavy as several hundred kilograms up to 30 km to 40 km altitude. Balloon launch preparation, the launch itself and flight control are managed by the balloon division of the French space agency CNES (Centre Nationale d'Etudes Spatiales).
Table 3.1 provides a summary of the most important characteristics of the DOAS and LPMA instruments which are discussed in more detail in sections 3.1.2 and 3.1.3.

Table 3.1: Summary of the most important characteristics of the DOAS and LPMA instruments.

	DOAS	LPMA
Type:	Grating Spectrometer	Fourier Transform Interferometer
Covered Spectral range:	316.5 nm - 653.0 nm	mid-IR, near-IR
Spectral resolution:	0.45 nm (UV), 1.48 nm (vis)	$0.02\,cm^{-1}$
Field-of-view:	10° (UV), 16° (vis)	0.2°
Signal-to-noise:	$\sim 10^4$	$\sim 10^2$
Sampling rate:	1 spectrum per $<$1 s to 30 s	1 interferogram per 50 s
Target species:	O_3, NO_2, H_2O, O_4, IO, OIO, NO_3, BrO, OClO, HCHO, HONO	O_3, NO_2, NO, HNO_3, N_2O_5, N_2O, CH_4, $ClONO_2$, HCl, H_2O, CO, CO_2, COF_2, HF, CF_2Cl_2, C_2H_6

3.1.1 The balloon gondola

The LPMA/DOAS balloon gondola has been developed in collaboration with the Observatoire de Genève (Camy-Peyret et al., 1995) (see figure 3.1). It consists of a rigid yet deformable aluminum structure which protects the scientific payload from damage due to rough landing. Since the whole gondola can be rotated and stabilized in azimuthal direction, it is possible to align the payload in the direction of the Sun to within several degree accuracy. The sun-tracker developed by Hawat et al. (1995) provides fine pointing to the center of the solar disk to within 60 arcsec and collects a parallel beam of sunlight. The inner core of the solar beam is directed into the LPMA FT-IR while two small telescopes mounted into the beam's edge feed sunlight into the DOAS spectrometer via two glass fiber bundles. This optical setup guarantees that the LPMA and DOAS spectrometers analyze direct sunlight which traversed almost the same atmospheric air masses. Ancillary scientific equipment involves GPS (Global Positioning System) receivers and antennas, pressure and temperature sensors as well as an *in situ* ozone sonde.

3.1.2 The DOAS instrument

The DOAS instrument has been designed for balloon borne applications requiring low weight, low power consumption and insignificant drift of the optical setup with changing ambient temperature and pressure (Ferlemann, 1998; Harder, 1999; Ferlemann et al., 2000). The instrument consists of two spectrographs which are mounted into the same housing and are sensitive to the UV and visible spectral ranges. Typically, the setup allows to record single spectra with high signal-to-noise ($\sim 10^4$), moderate spectral resolution and integration times less than 1 s. For large SZA during sunset, integration times are somewhat longer since the incoming intensity is weaker. A variety of atmospheric trace gases can be retrieved from the covered wavelength ranges, e. g. O_3, NO_2, H_2O, O_4, IO, OIO, NO_3 in the visible spectral range and O_3, BrO, OClO, NO_2, O_4, HCHO, HONO in the UV.

Figure 3.2 shows a schematic drawing of the DOAS instrument. The direct sunlight is collected by two entrance telescopes mounted into the edge of the solar beam provided by the sun-tracker. The telescope optics is designed to homogenize the incoming light and to limit and optimize the spectral transmission to the range actually analyzed by the spectrographs. The field of view (10° in the UV, 16°

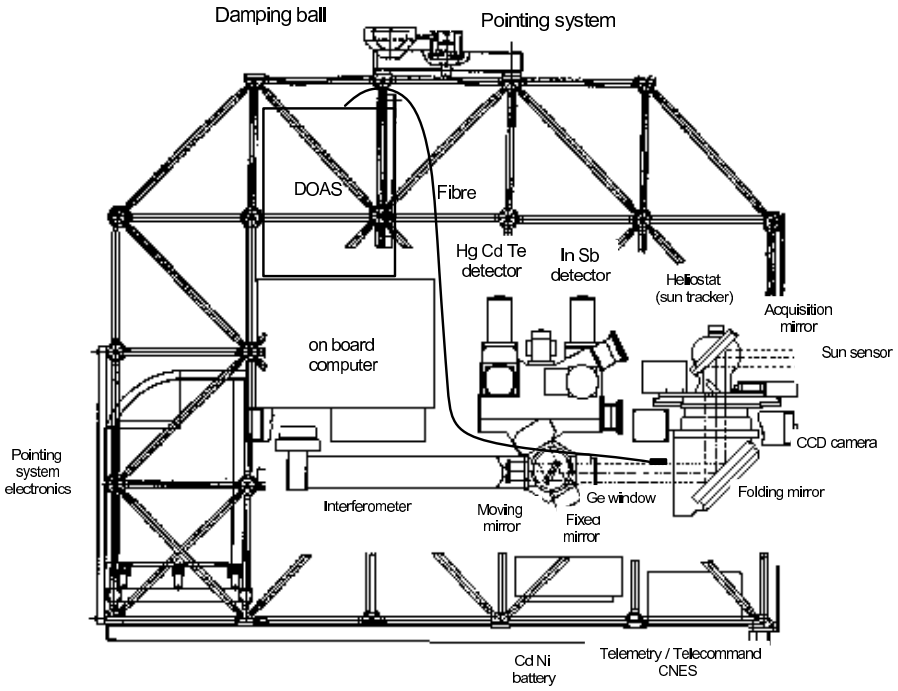

Figure 3.1: The LPMA/DOAS balloon gondola adapted from Jeseck (1996). Sunlight is collected by the automated sun-tracker and directed into the Fourier transform interferometer. Two glass fiber bundles feed the sunlight into the DOAS spectrometer.

in the visible) is chosen larger than the apparent size of the solar disk (0.53°) making light detection insensitive to possible misalignments of the sun-tracker optics and the entrance telescopes. Two glass fiber bundles forming a rectangular slit on the spectrograph side guide the light from the telescopes into the spectrograph housing where holographic gratings disperse solar light of the respective wavelength range (UV: 316.5 nm–417.3 nm, visible: 399.9 nm–653.0 nm) onto the detector of either spectrograph. The spectral imaging is designed to match the requirements for proper line sampling given by Roscoe et al. (1996). Accordingly, the spectral resolution amounts to about five photo diode pixels equivalent to the full width at half maximum (FWHM), i. e. 0.45 nm and 1.48 nm for the UV and visible spectrograph, respectively. The photo diode array detectors can be cooled and temperature stabilized by on-chip integrated Peltier elements. The heat generated at the warm sides of the Peltier elements is removed by cycling a refrigerant through a cooling system that consists of a reservoir containing about 10 kg of a liquid-water-ice mixture. Since the reservoir is filled into a vessel surrounding the spectrograph housing, the liquid-water-ice mixture additionally serves as heat bath for the whole instrument stabilizing the spectrographs' temperature at $(0.0 \pm 0.2)^{\circ}$C for the duration of a balloon flight. The spectrograph housing is vacuum sealed to prevent condensation of water vapor onto the cooled photo diode array detectors and changes in the optical imaging due to changing ambient pressure. Instrumental straylight is minimized by spectral filtering of the incoming light and suppressing unused diffraction orders by light traps. A detailed characterization of the DOAS instrument can be found in Bauer (1997). Minor modifications of the optical and mechanical setup effective by end of 2005 are summarized by Dorf (2005).

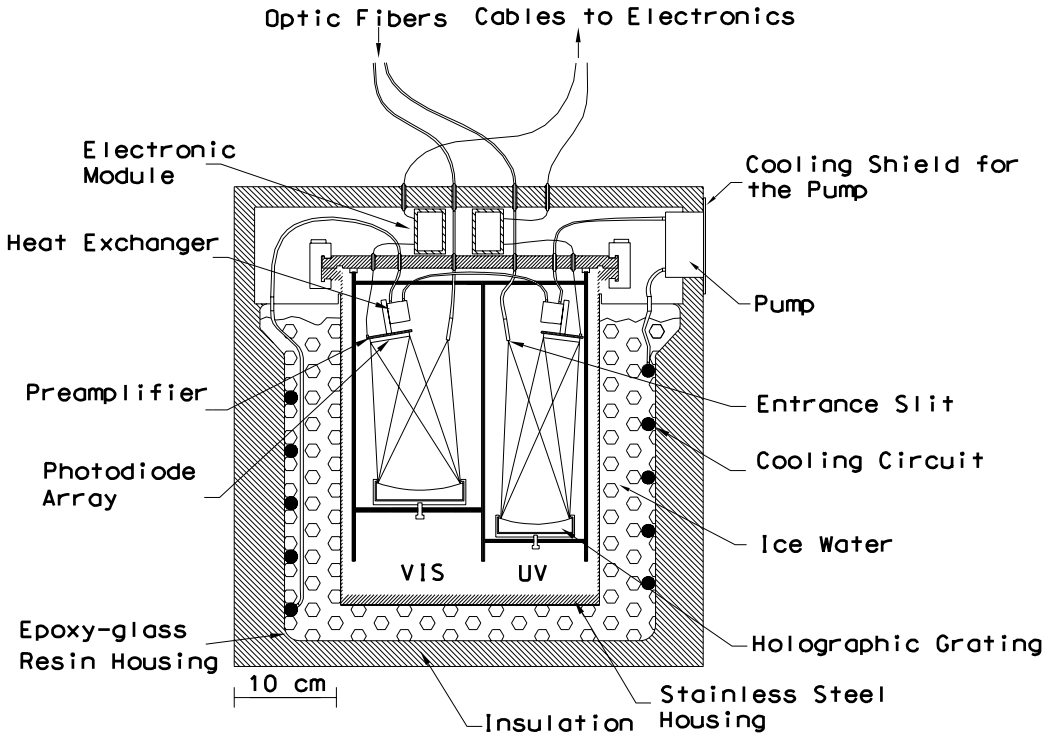

Figure 3.2: Schematic drawing of the DOAS instrument adapted from Ferlemann et al. (2000). The instrument consists of two spectrographs sensitive to the UV and visible spectral ranges. Two holographic gratings, two photodiode array detectors with on-chip Peltier cooling and the read out electronics including pre-amplifiers are placed in a vacuum-sealed aluminum container. Light input via the two glass fiber bundles as well as data output to the instrument control electronics is handled through vacuum connectors on the top of the housing. The whole container is thermally stabilized by a surrounding liquid-water-ice reservoir which also serves as heat sink for the internal cooling circuit.

The read-out and data acquisition electronics as well as the corresponding instrument control software have been extensively described in Ferlemann (1998); Harder (1999); Ferlemann et al. (2000). Since some electronic parts were subject to significant degradation and stable performance was no longer warranted the electronics has been partially rebuilt by Hoffmann Meßtechnik[1] in accordance with the original plans.

The incoming signal is detected by the 1024-channel photo diode array detectors (Hamamatsu S5931-N) and subsequently amplified by the pre-amplifiers situated inside the instrument housing. Both components are left unchanged with respect to their original implementation by Ferlemann (1998) since no significant degradation could be identified and all changes of the optical and electronic characteristics prior to digitalization of the signal would directly affect the comparability of the recorded spectra to previously obtained data. The adaptors on the top of the instrument which connect the pre-amplifiers with the analog-to-digital converters outside the spectrograph housing have been rebuilt in order to thermally decouple the jacks and connectors form the 0°C cold housing and to avoid short circuits caused by condensation of water. The adaptors have been elongated, enlarged in diameter and placed on the existing connector drillings, a measure which has proven of value during the tropical measurement

[1]Hoffmann Messtechnik GmbH, Schloßstraße 32, 69231 Rauenberg, Germany, http://www.hmm.de

campaigns in the highly humid environment of northern Brazil. All electronic components down-signal of the instrument flange have been replaced. The signal coming from the pre-amplifiers is integrated and digitized in the analog-to-digital converter box (previously two separated small boxes for the UV and visible spectrograph) spatially close to the instrument to avoid possible perturbations of the analog signal due to electromagnetic interferences. The digitized signal is then transferred to two single board CPUs (Motorala MC 68332, short 68k-CPU) which handle the basic data acquisition (e. g. co-adding of spectra) and instrument control functions (e. g. automatic calculation of exposure time). In addition, the single board CPUs possess 12-bit stand-alone analog-to-digital converters where ancillary data (e. g. temperature and pressure sensors) can be processed. All the measurement and communication processes are controlled by a Cool RoadRunner II PC board[2], which is driven by a National Geode 300 MHz processor exhibiting low power consumption ($\sim$ 6W) and a large operational temperature range (-45°C to +85°C). An additional 16-bit analog-to-digital converter card (Diamond-MM-32-AT) and a module (Lippert PC/104-COM8) with eight serial interfaces is connected to the master PC through the PC/104 bus. The master PC coordinates the communication with the ground station, with the slave CPUs of the two spectrographs and with a GPS receiver (Rockwell Jupiter) via serial interfaces. Data storage is handled by the lab-built instrument control and data handling software (Harder, 1999) via telemetry transfer to the ground station and simultaneously on a local compact flash disk (Sandisk 128 MB). In addition, data transfer to storage devices via USB has been implemented. The software has been updated from the previous version to meet the hardware requirements of the new electronic components. A detailed wiring scheme, pin assignments and data sheets including register maps and address assignments of the electronic components can be found in our internal documentation.
Hirsekorn (2003) reported on some serious deficits of the firmware of the 68k-CPUs which hindered the accurate retrieval of stratospheric aerosol extinction coefficients. In the course of our programming work on the new electronics, remaining errors have been identified which caused erroneous exposure times of single spectra. After correcting these errors, it is possible to record absolutely calibrated solar irradiance spectra with high accuracy (Gurlit et al., 2005; Lindner, 2005). In the future, a re-assessment of our previous work on stratospheric aerosol extinction coefficients will be facilitated.

3.1.3 The LPMA instrument

The LPMA instrument is a Fourier transform interferometer based on a commercial spectrometer BOMEM DA2.01 and optimized for balloon borne applications by Jeseck (1996). The setup allows to record single interferograms every 50 s with moderate signal-to-noise ($\sim 10^2$) and high spectral resolution (0.02 cm^{-1}) in the infrared wavelength range. A huge number of trace gases absorb in the infrared and could in principle be measured by the LPMA instrument depending on the spectral filters, beamsplitters and detectors used. A subset of species most important for atmospheric photochemistry comprises O_3, NO_2, NO, HNO_3, N_2O_5, N_2O, CH_4, $ClONO_2$, HCl, H_2O, CO, CO_2, COF_2, HF, CF_2Cl_2, C_2H_6.

The LPMA Fourier Transform Interferometer is a Michelson type interferometer with a fixed and a moving plane mirror and a beamsplitter that splits the incoming solar beam directing one part onto the moving and the other part onto the fixed mirror. The light reflected by the two mirrors recombines at

[2]Lippert Automationstechnik GmbH, Hans-Thoma-Straße 11, 68163 Mannheim, Germany, http://www.lippert-at.com

Table 3.2: Instrumental configurations of the LPMA Fourier Transform Interferometer and the corresponding spectral ranges and most important target species. Adapted from Dufour (2005).

Configuration	Detector	Beamsplitter	Covered spectral range / cm^{-1}	Target species
Long Wave Infrared	HgCdTe	KCl	650–1300; 1750–2000	$ClONO_2$, HNO_3, CH_4, N_2O, NO,
(LWIR)	InSb		2750–3150; 4100–4150	NO_2, HCl, HF, O_3, CO_2, H_2O
Short Wave Infrared	InSb	CaF_2	2050–2220; 4220–4440	as LWIR, but no $ClONO_2$
(SWIR)	InSb		2700–3150; 4770–5320	and no HNO_3, in addition CO
Near Infrared	Si	Quartz	10300–11000	oxygen A band
(NIR)	Si		12700–13400	

the beamsplitter and forms an interferogram which can be recorded as a function of the position of the moving mirror. The maximum displacement of the moving mirror is 25 cm corresponding to a maximum optical path difference of the interfering light beams of 50 cm. Accordingly, the spectral resolution is given by $0.02\,cm^{-1}$. Interferograms are recorded when the moving mirror moves away from as well as towards its initial position (forward, reverse). The beam of a HeNe-Laser ($\nu = 15798\,cm^{-1}$) is injected into the center of the solar beam to detect possible misalignments of the moving and the fixed mirror caused for example by thermal drifts of the mechanical components. The laser drives a feedback loop which dynamically compensates the detected misalignment by adjusting the orientation of the fixed mirror. In addition, the laser provides the timing for the sampling of the interferograms according to Nyquist's theorem[3]. The type of beamsplitter (KCl, CaF_2, Quartz) can be chosen depending on the desired spectral range to be measured. The commercial detector optics has been replaced by a lab-built optical setup that limits the field of view to about 0.2° and allows for the simultaneous use of two detectors covering different spectral ranges. The detectors (HgCdTe, InSb, Si) are placed in Dewars and cooled by liquid nitrogen. Table 3.2 provides an overview of the used instrumental configurations and corresponding wavelength ranges. For our purposes, the LWIR and SWIR configurations, which both comprise four distinct spectral regions covered by the HgCdTe and InSb detectors, are important. The whole instrument can be evacuated to minimize mechanical drift of the optical components due to changing ambient pressure. The interferometer is controlled by a PC-type Pentium 60 MHz processor that also handles the communication by telemetry with the ground station and onboard data storage. More details on the LPMA instrument can be found in Jeseck (1996), Camy-Peyret et al. (1995) and Dufour (2005).

3.1.4 Observation geometry

During a balloon flight the LPMA and DOAS instruments measure direct Sun light collected by the sun-tracker. A balloon flight can be subdivided in three phases as illustrated in figure 3.3. In the first phase following balloon launch the balloon ascends from the ground to maximum altitude. During balloon ascent the solar zenith angle (SZA) is smaller than 90° and variations of the detected trace gas abundances can mainly be attributed to the crossed height segments. After attaining maximum altitude the balloon floats at rather constant altitude. Typically, spectra recorded during the second phase, i.

[3]For a detailed treatment on the basics of Fourier Transform Spectroscopy see e. g. Griffiths and de Haseth (1986).

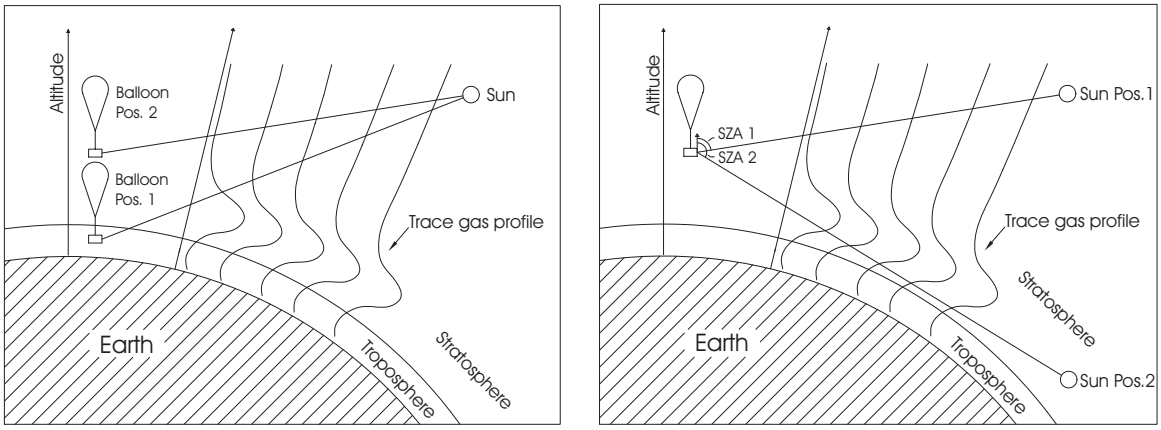

Figure 3.3: Observation geometry of the LPMA/DOAS balloon payload. Direct sunlight is measured during balloon ascent (left panel), during balloon float and solar occultation (right panel).

e. balloon float at maximum altitude and SZA $< 90°$, exhibit minimal atmospheric extinction since the number of molecules integrated along the line-of-sight is minimal. The third phase, solar occultation, starts when the SZA becomes larger than $90°$. The balloon remains approximately at float altitude but the line-of-sight is plunging downward into the atmosphere. Light going from the Sun to the balloon borne instruments passes atmospheric layers below the balloon twice while atmospheric layers above are passed only once. The point where the distance of the light path to the Earth's surface is smallest and the local SZA is $90°$, is called tangent point. During sunset the SZA increases with time and the line-of-sight penetrates deeper into the atmosphere scanning through the trace gas profiles to be retrieved.
Due to the deployed GPS instrumentation the position of balloon is known very accurately. The same is true for the position of the Sun which is tabulated as a function of time and date. Pressure and temperature sensors monitor the ambient atmospheric conditions. Considering their impact on the refractive index, the lines-of-sight of our direct Sun measurements can be calculated with high accuracy from purely (except for the pressure and temperature dependence of the refractive index) geometrical considerations. This is in contrast to experiments which measure scattered skylight where the actual, often uncertain atmospheric conditions, e. g. aerosols, clouds, heavily impact radiative transfer calculations. An intrinsic drawback of our remote sensing measurements is the considerable averaging in horizontal direction. In deep solar occultation (float altitude ~ 30 km, SZA $\sim 94°$) the distance from the balloon to the tangent point is several hundred kilometers (~ 500 km). The assumption of horizontally homogeneous trace gas distributions on such large spatial scales is no longer valid, in particular under dynamically active atmospheric conditions close to the polar vortex. Averaging also occurs with respect to the photochemical conditions along the line-of-sight. In principle, every point on the line-of-sight exhibits different illumination and consequently different photochemical conditions which contribute to a composite observed by the balloon borne instruments. The effect is negligible for trace gases which are photochemically stable on timescales of a balloon flight, e. g. O_3, HNO_3, N_2O, CH_4, but important for trace gases whose concentration strongly depends on illumination, e. g. NO_2, NO. Section 5.3 describes how to partly overcome this constraint.

3.2 Spectral retrieval of trace gas abundances

The balloon borne instruments measure spectra of direct sunlight penetrating the Earth's atmosphere. As pointed out in chapter 2 emission of radiation by the Earth's atmosphere and radiation scattered into viewing direction can be neglected for our purposes. The solar irradiance incident on the balloon can be described in analogy to equation (2.6) and (2.22) by Beer-Lambert's law,

$$I(\lambda) \;=\; I_0(\lambda)\, e^{-\tau(\lambda)} \tag{3.1}$$

with the optical density $\tau(\lambda)$ between the top of the atmosphere (TOA) and the balloon borne detector and the solar irradiance $I_0(\lambda)$ at TOA. Assuming N types of absorbing molecules labeled by the index i, the optical density can be written in terms of the absorption and scattering coefficients, $k_A(\lambda)$ and $k_S(\lambda)$, and the molecular absorption cross sections $\sigma_i(\lambda)$[4] defined in section 2.1,

$$\tau(\lambda) \;=\; \ln \frac{I_0(\lambda)}{I(\lambda)} \;=\; \int_L k_A(\lambda) \;+\; k_S(\lambda)\, ds \;=\; \int_L \sum_{i=1}^{N} \sigma_i(\lambda)\, n_i \;+\; k_S(\lambda)\, ds, \tag{3.2}$$

where n_i represents the number density of absorbers of type i and the integral is meant along the line-of-sight L. The transmission T is defined through

$$T(\lambda) \;=\; \frac{I(\lambda)}{I_0(\lambda)} \;=\; e^{-\tau(\lambda)} \;=\; \exp\left(- \int_L \sum_{i=1}^{N} \sigma_i(\lambda)\, n_i \;+\; k_S(\lambda)\, ds \right). \tag{3.3}$$

The goal of the spectral retrievals is to infer the number density of absorbing molecules integrated along the line-of-sight which is referred to as Slant Column Density (SCD),

$$SCD_i \;=\; \int_L n_i\, ds. \tag{3.4}$$

The analyzing spectrographs modify the incoming solar spectrum, given by equation (3.1), corresponding to their instrumental characteristics. Accordingly, the measured spectrum $I^*(\lambda)$ is given as a convolution of the incoming signal $I(\lambda)$ with the normalized instrumental line shape function $g(\lambda)$,

$$I^*(\lambda) \;=\; \int_{-\infty}^{\infty} I(\lambda')\, g(\lambda \;-\; \lambda')\, d\lambda' \;=\; I(\lambda) \;\otimes\; g(\lambda). \tag{3.5}$$

Upon registration by the detectors the incoming continuous signal is mapped on a discrete grid with a finite number of pixels. It is appropriate to write the measured spectrum as a function of the pixel number $n(\lambda)$,

$$I^*(\lambda) \rightarrow I^*(n). \tag{3.6}$$

The general approach for the spectral retrieval is to define a state vector $\mathbf{x}$, which comprises the parameters to be retrieved e. g. the SCDs, and a model function $\mathbf{F}$ which is supposed to model the measurement vector $\mathbf{y}$. The measurement vector $\mathbf{y}$ consists of the points (or a simple function of the points) of the observed spectrum $I^*(n)$ in a chosen wavelength range. The equation to solve is given by

$$\mathbf{y} \;=\; \mathbf{F}(\mathbf{x}, \mathbf{b}) \;+\; \boldsymbol{\epsilon}, \tag{3.7}$$

[4] In contrast to section 2.1 we drop the index A in the symbol of the absorption cross section for simplicity. Further, the wavelength dependence of all quantities is not indicated by the index λ but explicitly given.

where $\boldsymbol{\epsilon}$ is the measurement error and $\mathbf{b}$ is a vector comprising all auxiliary parameters, e. g. absorption cross sections. Given the measurements $\mathbf{y}$ and the auxiliary parameters $\mathbf{b}$ an inverse problem has to be solved to retrieve the state vector $\mathbf{x}$ (Rodgers, 2000). The methods applicable to spectra measured in the UV/visible and IR spectral range are inherently different and will be described in detail in sections 3.2.1 through 3.2.4.

3.2.1 Differential Optical Absorption Spectroscopy (DOAS) in the UV/visible

Our goal is to find a model function $\mathbf{F}$ that models the measured spectrum (or a simple function of the measured spectrum) as accurately as possible. In principle the exact knowledge of the TOA solar irradiance I_0 and all extinction processes along the line-of-sight corresponding to equation (3.2) as well as the instrumental line shape function are necessary to retrieve the SCD of a certain absorber. In the UV/visible, approximations to equation (3.1) through (3.6) allow for the construction of a model function $\mathbf{F}$ based on quantities measured by our spectrograph. Subsequently, the inverse problem, equation (3.7), can be solved for the absorber SCDs.
In the UV/visible, the spectra are recorded by photo diode array detectors which show a temperature dependent dark signal caused by the thermal discharge of the photo diodes. In addition, prior to digitalization an offset signal is added to the spectra to avoid negative values. Provided that the temperature of the photo diode array is constant, dark and offset signal are constant with time. Hence, they can be measured in the laboratory and subtracted from the measured spectra (Lindner, 2005). In the following, we assume that the correction of the dark and offset signal has been applied to the measured spectra.

Assumptions and approximations

According to the Differential Optical Absorption Spectroscopy (DOAS) technique (Platt et al., 1979; Platt, 1994; Platt and Stutz, 2005, in press), the extinction processes are divided into those which vary strongly and those which vary only weakly with wavelength. Rayleigh and Mie scattering clearly belong to the latter. In the UV/visible, the molecular absorption cross sections[5] can be split into a low and a high frequency component $\sigma_{i,b}$ and $\sigma_{i,d}$, respectively

$$\sigma_i \;=\; \sigma_{i,b} \;+\; \sigma_{i,d}. \tag{3.8}$$

The indices 'b' and 'd' symbolize 'broadband' and 'differential'. Accordingly, equation (3.2) reads

$$\tau(\lambda) \;=\; \int_L \sum_{i=1}^{N} \sigma_{i,b}(\lambda)\, n_i \;+\; k_S(\lambda)\, ds \;+\; \int_L \sum_{i=1}^{N} \sigma_{i,d}(\lambda)\, n_i\, ds \;=\; \tau_b(\lambda) \;+\; \tau_d(\lambda) \tag{3.9}$$

with $\tau_b(\lambda)$ the broadband optical density and $\tau_d(\lambda)$ the differential optical density. Further, the molecular absorption cross sections are assumed to be independent of temperature and pressure. Hence, $\sigma_{i,d}$ can be

[5] In the UV/visible spectral range the observed absorption bands correspond to electronic or dissociating molecular transitions as emphasized in section 2.3. The underlying ro-vibrational structure is often not resolved by DOAS spectrographs as is true for our instrument. Hence, the molecular absorption cross sections are commonly directly given and not as function of line strength and line shape as expressed by equation (2.34).

assumed to be independent of the line-of-sight and the differential optical density is given by

$$\tau_d(\lambda) \simeq \sum_{i=1}^{N} \sigma_{i,d}(\lambda) \int_L n_i \, ds = \sum_{i=1}^{N} \sigma_{i,d}(\lambda) \, SCD_i. \tag{3.10}$$

From equation (3.10) it becomes clear that the exact knowledge of the light path through the Earth's atmosphere is not required under the approximation of temperature and pressure independent absorption cross sections. Considering the definitions above, Beer-Lambert's law can be written

$$I(\lambda) = I_0(\lambda) \, e^{-(\tau_b(\lambda) + \tau_d(\lambda))} = I_{0,b}(\lambda) \, e^{-\tau_d(\lambda)}, \tag{3.11}$$

where $I_{0,b}(\lambda)$ comprises the TOA spectrum and all broadband extinction processes,

$$I_{0,b}(\lambda) = I_0(\lambda) \, e^{-\tau_b(\lambda)}. \tag{3.12}$$

Taking into account the finite spectral resolution of the spectrograph according to equation (3.5), the logarithm of the measured spectrum is given by

$$\ln I^*(\lambda) = \ln \left[\left(I_{0,b}(\lambda) \, e^{-\tau_d(\lambda)} \right) \otimes g(\lambda) \right]. \tag{3.13}$$

Assuming that the differential optical density is small ($\tau_d(\lambda) << 1$) and $I_{0,b}$ only varies negligibly with wavelength ($I_{0,b}(\lambda) = const$), equation (3.13) can be linearized,

$$\ln I^*(\lambda) \simeq \ln \left[I_{0,b}(\lambda) \otimes g(\lambda) \right] - \tau_d(\lambda) \otimes g(\lambda). \tag{3.14}$$

From equation (3.14) it is possible to construct an appropriate model function $\mathbf{F}$. However, the approximations in the derivation of equation (3.14) have to be considered as possible sources of systematic errors. The differential optical densities encountered in our spectra are usually small (10^{-3} to 10^{-1}) and the approximation $\tau_d(\lambda) << 1$ is justified. The assumption of temperature and pressure independent molecular absorption cross sections is more critical and is discussed in section 3.2.2. Further, the TOA solar spectrum I_0 and accordingly $I_{0,b}$ is by no means independent of wavelength as has been assumed when linearizing Beer-Lambert's law. However, Huppert (2000) showed for the example of a BrO DOAS retrieval that the systematic errors caused by the approximation of constant $I_{0,b}$ are small. Johnston (1996) suggested a possible correction of this effect. Section 3.2.2 discusses these systematic errors and possible corrections in detail.

The DOAS model function

The model function $\mathbf{F}$ used for the spectral retrieval in the UV/visible is given by

$$F(\lambda) = \ln \left[I_0^*(\lambda, d_{0,0}, d_{1,0}, \ldots) \right] + P(\lambda, p_0, \ldots, p_m) - \sum_{i=1}^{N} a_i \, \sigma_{i,d}(\lambda, d_{0,i}, d_{1,i}, \ldots). \tag{3.15}$$

$I_0^*(\lambda, d_{0,0}, d_{1,0}, \ldots)$ is a pseudo-TOA solar spectrum measured by the DOAS spectrograph during balloon float at high Sun when absorption by atmospheric constituents is minimal. The use of a solar spectrum actually measured by the DOAS spectrograph guarantees the correct representation of the solar Fraunhofer lines in the model function. $P(\lambda, p_0, \ldots, p_M)$ is a polynomial of degree M approximating

the broadband extinction processes. Molecular absorption is described in terms of the scaled molecular absorption cross sections $a_i\,\sigma_{i,d}(\lambda, d_{0,i}, d_{1,i}, \ldots)$. The absorption cross sections are either taken from high resolution measurements, which are *a priori* convolved by the instrumental line shape function[6], or from measurements by the DOAS spectrograph in the laboratory (Dorf, 2005). Differential absorption cross sections can be obtained by appropriate high-pass filtering of the absolute cross sections. While polynomial and pseudo-TOA spectrum are meant to represent the first term in equation (3.14), the scaled molecular absorption cross sections obviously correspond to the second term. Since the DOAS retrieval includes quantities measured during the balloon flight, e. g. the spectra and the pseudo-TOA solar spectrum, and quantities determined by pre-flight measurements in the laboratory, e. g. the instrumental line shape function, the temporal stability of the optical imaging and the detectors is most important. Small changes of the instrumental line shape cause systematic deficiencies of the model function and render the retrieval of low abundant trace gases impossible.
The state vector $\mathbf{x}$ of parameters to be retrieved consists of the scaling factors a_i ($i = 1, \ldots, N$) which correspond to the SCD_i of the absorbers, the polynomial coefficients p_m ($m = 0, \ldots, M$) and the parameters $d_{j,i}$. The latter are spectral alignment parameters which describe a possible shift and squeeze of the wavelength-pixel mapping between the measured spectra, the pseudo-TOA spectrum ($i = 0$) and the absorption cross sections ($i > 0$). The parameter $d_{0,i}$ represents a shift of the respective wavelength-pixel mapping by $d_{0,i}$ pixels. The parameter $d_{1,i}$ describes an additional squeeze/stretch of the wavelength-pixel mapping, i. e. pixel n is shifted by $d_{1,i}(n - n_c)$ pixels with n_c the center pixel of the considered wavelength range. Higher order squeezing/stretching is described analogously by $d_{j,i}$ with $j > 1$. Possible changes in the wavelength-pixel mapping arise from small changes in the mechanical setup e. g. due to changes in ambient pressure and temperature. The auxiliary parameter vector $\mathbf{b}$ consists of the pseudo-TOA spectrum and the molecular absorption cross-sections. The measurement vector $\mathbf{y}$ is given by the logarithm of the measured spectra $\ln I^*(\lambda)$.

Solution of the inverse problem

Remembering the discretization of the measured spectrum, the inverse problem of equation (3.7) is solved for the state vector $\mathbf{x}$ by a least squares fitting method, i. e. the components of the state vector are derived in a sense that

$$\chi^2 = \frac{1}{W - V - 1} \sum_{n=1}^{W} \left(\frac{y_n - F_n(\mathbf{x})}{\epsilon_n} \right)^2 = \frac{1}{W - V - 1} \sum_{n=1}^{W} \left(\frac{\ln I^*(n) - F(n)}{\epsilon_n} \right)^2 \tag{3.16}$$

is minimized, where W is the number of pixels considered for the spectral retrieval and V the number of parameters to be retrieved, i. e. the dimension of $\mathbf{x}$. Minimizing equation (3.16) yields the maximum likelihood solution for the fitting parameters if the measurement error $\boldsymbol{\epsilon}$ obeys a Gaussian distribution with expectation value 0[7]. The minimization process yields values $\chi^2 \simeq 1$ if χ^2 is defined as above. If $\chi^2 > 1$, the model function is insufficient. If $\chi^2 < 1$, the measurement error is overestimated.

[6]The instrumental line shape function of the DOAS spectrograph can be obtained by measuring the spectra of low pressure emission lamps (Hg, Cd) which exhibit emission lines much narrower than the spectral resolution of the spectrograph.

[7]The measurement error of the DOAS instrument is governed by counting statistics of the detectors and hence obeys a Poisson distribution. Nonetheless, χ^2-minimization is used to retrieve the desired parameters since in the limit of many counting events the expectation value of the measurement obeys a Gaussian distribution (central limit theorem) and standard routines (Press et al., 1988) can be used.

The statistical significance of deviations from 1 can be calculated from the confidence limits of a χ^2-distribution with $W - V - 1$ degrees of freedom. Often, the measurement error is set to a fixed value $\epsilon_n = \epsilon$ and equation (3.16) is used to estimate the actual measurement error.

The DOAS model function is a linear function of the fitting parameters $\mathbf{x}$ except for the spectral alignment parameters $d_{j,i}$. In a first step equation (3.16) is solved for the linear parameters with fixed $d_{j,i}$. In the second step, the linear parameters are set to the value retrieved in the first step and the problem is solved for the non-linear parameters $d_{j,i}$ by a Levenberg-Marquardt fitting algorithm. The obtained values are used as initial values for another call of the linear fit, which subsequently calls the non-linear fit with the updated linear parameters as initial conditions. The iteration stops when changes in χ^2 are smaller than a stopping criterion which is chosen depending on the required precision of the fit. The least-squares solution of the linear fit can be found analytically while the Levenberg-Marquardt algorithm is an iterative, numerical procedure which combines the steepest gradient and an expansion method to find the minimum of χ^2. Since the fitting routines and their implementation have been extensively described in the literature (Bevington, 1969; Press et al., 1988; Rodgers, 2000) and our own publications (Payan, 1996; Bösch, 2002; Dufour, 2005), no detailed discussion is given here. The spectral retrieval is performed by the WinDOAS software package (Fayt and van Roozendael, 2001).

Error treatment

According to equation (3.7) errors of the retrieval parameters $\mathbf{x}$ come from retrieval noise due to measurement error, errors of the auxiliary parameters, errors due to correlations of the retrieval parameters and errors of the model function (Rodgers, 2000). The latter and possible corrections are discussed in section 3.2.2.

Retrieval noise due to measurement error

As pointed out by Ferlemann et al. (2000), the measurement error of the DOAS spectrographs is governed by the photo-electron shot noise ϵ_{ph} of the detectors as long as the integration times of individual spectra are sufficiently short. The statistics of the number of electrons generated by the photons illuminating a detector pixel is described by a Poisson distribution. Accordingly, the photo-electron shot noise ϵ_{ph} is given by $\sqrt{N_{ph}}$ with N_{ph} the number of photo-electrons. For large integration times the noise of the dark signal $\epsilon_{dc} \propto t$ becomes important (Lindner, 2005). It strongly depends on the temperature of the detector, but is negligible for our direct Sun measurements since integration times are sufficiently short ($<$1 s to 30 s) and the detector temperature is sufficiently low and stable (-10.00°C $\pm$ 0.05°C). However, when performing pre-flight radiometric calibration with calibration lamps on the ground (Gurlit et al., 2005), typical integration times range between 5 min and 30 min and the noise of the dark signal becomes the dominant noise contribution. Also, for on ground calibration purposes, the non-linear dependence of the dark signal on pixel saturation needs to be considered (Stutz, 1996). Further contributions to instrumental noise originate from the readout, amplification and digitalization electronics ϵ_{el}. The measurement error $\boldsymbol{\epsilon}$ can be calculated from ϵ_{ph}, ϵ_{dc} and ϵ_{el} via Gaussian error propagation[8].

[8]For a single spectrum recorded with 1 s integration time and 80% saturation of the detector pixels the total noise is approximately given by $1.2 \cdot 10^4$ electrons which corresponds to 6 binary units (BU) of the detected signal. The corresponding total

The retrieval noise due to the measurement error $\boldsymbol{\epsilon}$ is represented by the errors given by the fitting routines. Both, the linear and the Levenberg-Marquardt fitting routine, provide the standard deviations of the retrieval parameters as output, i. e. the true value of parameter x_l lies with 68.3% probability within the boundaries of the given error. However, the influence of the errors of the non-linear parameters on the linear parameters is not automatically accounted for. It can be estimated by performing the linear fit once with the original set of non-linear parameters and once with a set of non-linear parameters which are changed by their errors. The difference of the retrieved linear parameters between the two fitting runs can be used to estimate the impact of the error of the non-linear parameters on the linear parameters. Assuming independence of both error contributions, the total error of the linear parameters is given by Gaussian error propagation.

The retrieval noise is appropriately represented by the fitting errors only if the residual spectrum $R(n) = \ln I^*(n) - F(n)$ consists of pure noise. This is not completely true for the UV/visible spectra since the residual structures show groups of interdependent neighboring pixels. Stutz and Platt (1996) showed that the impact of interdependent residual structures on the fitting results can be estimated by a numerical procedure. A synthetic pure noise spectrum is smoothed by a running mean over n_{rm} pixels in a way that the smoothed spectrum exhibits systematic features with similar widths as the interdependencies observed in the measured spectrum. The impact of these systematic structures on the retrieval of trace gases which are characterized by absorption structures of width n_σ can be estimated by Monte-Carlo simulations. Influences on the fitting parameters are found negligible but the fitting errors have to be corrected by a factor which is given as function of n_{rm} and n_σ by Stutz and Platt (1996).

Auxiliary parameter error

The auxiliary parameters $\mathbf{b}$ consist of the molecular absorption cross sections and the pseudo-TOA spectrum. The principal errors of the molecular absorption cross sections originate from uncertainties of their absolute magnitude and their temperature dependence which are commonly given by the authors of the measurements. The O_3 and NO_2 absorption cross section from Anderson and Mauersberger (1992) and Harder et al. (1997) have stated accuracies of 1% and 4%, respectively. The convolution of high resolution cross sections with the instrument function can introduce further errors which are estimated by using different instrument functions and comparing the retrieval results. When using instrument functions obtained in January 2003 and August 2004 for the convolution of a high resolution cross section from Harder et al. (1997), the deviations found are smaller than 1%. The errors of the molecular absorption cross sections are added to the fitting errors through Gaussian error propagation.

The pseudo-TOA spectrum is not a true TOA spectrum since it contains small but detectable absorption of some absorbers. The residual absorber SCD corresponding to the absorption observed in the pseudo-TOA spectrum can be determined based on Langley's extrapolation to zero air mass which is discussed below in section 3.3.4. The inferred SCD offset has to be added to the SCDs retrieved by the DOAS retrieval. The associated error is considered via Gaussian error propagation.

Errors due to correlations of the retrieval parameters

Bösch (2002) investigated the correlations between the retrieval parameters of the NO_2, O_3, IO and OIO

number of photo-electrons is given by $N_{ph} \approx 1.04 \cdot 10^8$ corresponding to $5.2 \cdot 10^4$ BU which results in a signal-to-noise-ratio of $\sim 10^4$. The individual error contributions are $\epsilon_{ph} = \sqrt{N_{ph}} \approx 1\,10^4$ electrons ≈ 5 BU, $\epsilon_{dc} \approx 91$ electrons ≈ 0.05 BU and $\epsilon_{el} \approx 4\,10^3$ electrons ≈ 2 BU.

retrieval by calculating the correlation coefficients r_{kl} for the retrieval parameters x_k and x_l defined by

$$r_{kl} = \frac{S_{kl}}{\sqrt{S_{kk}\, S_{ll}}}, \tag{3.17}$$

where $\mathbf{S}$ is the covariance matrix of the retrieval parameter vector $\mathbf{x}$ and its elements are defined through

$$S_{kl} = \langle (x_k - \bar{x}_k)\,(x_l - \bar{x}_l) \rangle \tag{3.18}$$

with $\bar{x}_k$ the mean of the retrieval parameter x_k over the retrieval range. Correlation coefficients with absolute values close to 1 indicate strong correlations while values around 0 represent weak correlations. The impact of correlations between the retrieval parameters is hard to quantify[9]. In practice the correlation coefficients are used to minimize observed correlations by e. g. decreasing the degree of the polynomial or changing the spectral retrieval range. Commonly, the detected correlations between the absorber SCDs and the remaining retrieval parameters are small. Hence, the correlation error is not considered in the DOAS error budget.

3.2.2 Corrections and shortcomings of the DOAS model function

In the following some effects which are not considered by the DOAS model function, equation (3.15), are discussed below and if possible a correction is implemented in the spectral retrieval.

Solar I_0 effect

In general the approximations which allow for the linearization of Beer-Lambert's law, i. e. constant TOA spectrum $I_{0,b}$ and small optical densities ($\tau_d << 1$) in equation (3.13) are not satisfied. As mentioned above, the latter assumption holds true for our purposes. The former, however, is not justified, as the TOA solar spectrum I_0 exhibits many Fraunhofer absorption lines which cause a highly structured spectral pattern. Since the DOAS model function is constructed from the linearized version of Beer-Lambert's law (equation (3.14)) it cannot perfectly model the measured spectrum. This systematic deficiency is referred to as solar I_0 effect. Its impact on the retrieved parameters becomes important when several species absorb in the same wavelength range and the strong absorbers have to be removed in order to detect underlying weakly absorbing species. The solar I_0 effect can be corrected by attributing the systematic residual structures originating from non-constant I_0 to the molecular absorption cross sections $\sigma_{i,d}$ (Huppert, 2000). Assuming a single absorber with slant column density SCD_i, the corresponding I_0-corrected molecular absorption cross section $\sigma_{i,d,corr}(\lambda)$ is given by

$$\sigma_{i,d,corr}(\lambda) = \frac{1}{SCD_i} \ln \frac{\left(I_0(\lambda)\, e^{-\sigma_{i,d}(\lambda)\, SCD_i}\right) \otimes g(\lambda)}{I_0(\lambda) \otimes g(\lambda)}. \tag{3.19}$$

Absorption cross sections can be measured in the laboratory by putting a flow tube between a light source and the DOAS spectrograph (Dorf, 2005). If the Sun is used as light source the numerator of equation (3.19) corresponds to the spectrum measured when the flow tube is filled with a known amount of absorber i. The denominator corresponds to a spectrum which is measured with empty flow tube. The

[9] In principle an averaging kernel approach as presented for the trace gas profile retrieval, section 3.3, is possible but not yet implemented in our software.

SCD_i can be calculated from the dimensions of the flow tube and the amount of absorber filled in.
If the absorption cross sections are not measured by the DOAS spectrograph but taken from high resolution measurements, $\sigma_{i,d,corr}(\lambda)$ can be calculated according to equation (3.19) by assuming a representative value of SCD_i and identifying $\sigma_{i,d}(\lambda)$ with the high resolution absorption cross section, $I_0(\lambda)$ with a high resolution solar spectrum, e. g. Kurucz et al. (1984), and $g(\lambda)$ with the instrument function of the DOAS spectrograph. Unfortunately, convolution of high resolution data by the instrument function introduces new systematic errors and yields absorption cross section with inferior quality compared to spectra measured with the DOAS spectrograph itself.
In our studies, absorption cross sections are used which have been measured in the laboratory by the DOAS spectrograph using halogen lamps as light source. Halogen lamps in contrast to the Sun exhibit only little spectral structures. The I_0 effect is considered by calculating $\sigma_{i,d}(\lambda)$ and $\sigma_{i,d,corr}(\lambda)$ from high resolution measurements. The lab-measured absorption cross sections are then multiplied by the ratio $\frac{\sigma_{i,d,corr}(\lambda)}{\sigma_{i,d}(\lambda)}$.

Instrumental straylight

Instrumental straylight originates from unused diffraction orders of the incoming light dispersed by the holographic gratings and from reflections on the walls of the spectrographs. Spectral filters in the UV entrance telescope which cut off the visible and infrared spectral ranges and absorbing light traps inside the spectrograph are intended to minimize instrumental straylight (Lindner, 2005). Straylight can affect the DOAS retrieval only if its contribution to the pseudo-TOA spectrum and the spectrum to be analyzed is different. The change in straylight contribution can be corrected for by introducing a polynomial $O(n)$ of up to 2nd order in the fitting process as follows

$$\chi^2 = \frac{1}{W-V-1} \sum_{n=1}^{W} \left(\frac{\ln\left[I^*(n) - O(n)\right] - F(n)}{\epsilon_n} \right)^2 . \tag{3.20}$$

The polynomial coefficients are additional non-linear parameters which are determined by the Levenberg-Marquardt fitting algorithm.

Center-to-limb darkening effect

Section 2.1 pointed out that the observed solar intensity is non-uniform across the solar disk due to the center-to-limb darkening effect (e.g. Unsöld and Baschek, 1999). The DOAS retrieval relies on the assumption that the structures of the solar Fraunhofer spectrum are properly accounted for by the pseudo-TOA solar spectrum. Since the solar Fraunhofer lines exhibit optical densities 100–1000 times larger than terrestrial absorption structures, small deficiencies in their representation can render the retrieval of atmospheric trace gas abundances difficult. During sunset and sunrise, light coming from the upper edge of the Sun traversed significantly less air mass than light coming from the lower edge. Accordingly, extinction in the Earth's atmosphere attenuates light from the lower edge stronger than light from the upper edge. The contribution of the upper parts of the solar disk to the measured spectrum becomes larger than the contribution of the lower parts. This effect is increasingly important for increasing air masses along the line-of-sight, i. e. increasing SZAs. Since, for a terrestrial observer, the intensity of the Sun and the optical densities of the Fraunhofer lines vary across the solar disk, the change in the

composition of the observed spectrum goes along with a change of the optical densities of the observed Fraunhofer lines. The relative change of the solar lines is non-uniform which makes an exact treatment difficult.
Bösch (2002) developed an empirical approach how to correct for the center-to-limb darkening (CLD) effect. High resolution solar spectra taken from the center of the solar disk $I_C(\lambda)$ and averaged over the whole solar disk $I_D(\lambda)$ (Brault and Neckel, 1987) are used to define the CLD correction term

$$a_{cld}\,\sigma_{cld} \;=\; a_{cld}\,\frac{I_D(\lambda)\otimes\, g(\lambda) - I_C(\lambda)\otimes\, g(\lambda)}{I_C(\lambda)\otimes\, g(\lambda)}, \tag{3.21}$$

which is included in the DOAS model function as pseudo absorber. The parameter a_{cld} is an additional parameter of the state vector which has to be retrieved by the fitting routine. The CLD correction is important for the retrieval of NO_2 and IO abundances in the visible spectral range (400 nm to 500 nm) and for the OClO retrieval in the UV (360 nm to 400 nm).

Ring effect

Besides elastic scattering processes, inelastic Raman scattering occurs in the Earth's atmosphere (section 2.1.2), which can be observed in the spectra of scattered skylight as filling in of Fraunhofer lines, the so-called Ring effect. In direct Sun spectra, the contribution from inelastically scattered light is negligible (Bauer, 1997; Pundt et al., 1998). Therefore, a correction of the Ring effect is used only for sensitivity tests. The correction term can be obtained by model calculations (Bussemer, 1993; Funk, 2000) and is commonly included in the DOAS model function as additional pseudo-absorber.

Instrumental shortcomings

The wavelength-pixel mapping of the DOAS spectrograph critically depends on the mechanical and optical setup of the instrument, which is influenced by ambient parameters e. g. temperature and pressure. Possible changes in the wavelength-pixel mapping between the spectra to be analyzed, the TOA solar spectrum and the molecular absorption cross sections are considered by the non-linear shift and squeeze parameters $d_{j,i}$ in the DOAS model function. Since the spectra and absorption cross sections are given as a function of pixel number n, non-zero shift and squeeze goes along with interpolation of the respective data. Interpolation errors decrease with increasing sampling ratio, i. e. number of pixels per FWHM of the instrument function. As pointed out above, the spectral resolution of the DOAS spectrographs is about 5 pixels and hence, undersampling effects due to interpolation errors are small (Roscoe et al., 1996).
Likewise, the instrument function $g(\lambda)$ is sensitive to changes of the optical and mechanical setup. Since some absorption cross sections measured in the laboratory by the DOAS spectrograph are supposed to be used for several balloon flights, the instrument function is required to be stable over several years. Hence, the replacement of optical components, e. g. glass fibers, has to be avoided and care must be taken to reproduce stable ambient conditions for the measurements. Therefore, the whole DOAS instrument is stabilized with respect to temperature and pressure.
The use of high resolution absorption cross sections can introduce errors when the convolution with the instrument function is carried out. The instrument function used for convolution is obtained from spectra

of an atomic (HgCd) emission lamp. Consequently, $g(\lambda)$ is not given over the entire spectral range but at some wavelengths, only. Often the wavelength dependence of the instrument function is neglected which causes a systematic deficiency of the model function, but which can be avoided by using absorption cross section measured in the laboratory by the DOAS instrument.
Further instrumental effects such as the memory effect of the detectors and the etalon effect due to multiple reflections on optical components have been investigated by Bauer (1997) and Ferlemann (1998). They are found to be small for the DOAS instrument.

Temperature and pressure dependence of the absorption cross sections

The molecular absorption cross sections in the UV/visible show a significant temperature dependence. Since DOAS spectrographs typically do not resolve the ro-vibrational structure of the absorption bands, the temperature and pressure dependence is investigated empirically by measuring the respective absorption bands at different ambient conditions and different spectral resolution. Generally, the shape as well as the absolute value of the absorption cross sections depend on temperature and pressure. Most important for our study are the absorption cross sections of NO_2, O_3, O_4, H_2O, OClO, IO and OIO. An excellent overview of the available O_3 and NO_2 absorption cross sections and their temperature and pressure dependence is given by Orphal (2003).
The shape of the NO_2 absorption cross section between 300 nm and 790 nm is a Gaussian-like continuum superimposed by a lot of differential structures which are caused by the high density of rovibronic energy states close to the dissociation limit at about 400 nm. There are numerous studies which investigate the temperature dependence of the NO_2 absorption cross section in the UV/visible, e. g. Davidson et al. (1988); Harwood and Jones (1994); Harder et al. (1997); Vandaele et al. (1998); Burrows et al. (1998); Pfeilsticker et al. (1999); Voigt et al. (2002); Vandaele et al. (2003); Nizkorodov et al. (2004). The general observation with decreasing temperature is a tilt of the baseline and a large increase of the differential cross section depending on the spectral resolution of the used instrument. The maxima of the differential cross section become larger while the minima become smaller. For a spectral resolution of 0.54 nm the differential cross section at 448 nm increases almost linearly by 40% when temperature decreases from 298 K to 200 K (Pfeilsticker et al., 1999). Below 400 nm the relative changes of the differential cross section with temperature become smaller. The integrated cross section seems to increase slightly with temperature. Observations of the pressure dependence of the NO_2 absorption cross section are fewer in number, e. g. Harder et al. (1997); Vandaele et al. (1998); Pfeilsticker et al. (1999); Voigt et al. (2002); Vandaele et al. (2003). At very high spectral resolution (0.00006 nm) the observed changes with total pressures between 7 mbar and 870 mbar are as high as 40%, but negligible ($< 0.05\%$) at coarser spectral resolution (0.2 nm) (Harder et al., 1997; Pfeilsticker et al., 1999).
The O_3 absorption cross section in the 240 nm to 790 nm spectral range consists of the Hartley band (200 nm to 320 nm), the Huggins bands (300 nm to 390 nm), the Chappuis band (380 nm to 800 nm), and the Wulf bands (700 nm to $>$800 nm). Since in our study absorption of O_3 in the Chappuis band is of primary importance, we will restrict the discussion to that spectral range. A number of studies by Bass and Paur (1985); Brion et al. (1998); Burkholder and Talukdar (1994); Burrows et al. (1999); Voigt et al. (2001) show very small ($< 1\%$) or no change of the peak cross sections between 550 nm and 650 nm for temperatures between 200 K and 300 K. The differential structure slightly increases with decreasing temperature. Beyond the center region, i. e. below 550 nm and above 650 nm, the

temperature dependence is strong but there is no quantitative agreement between the available data sets (Orphal, 2003). Besides an increase of the differential cross section, a shift towards shorter wavelength is observed for the blue tail of the Chappuis band when temperature decreases. A pressure dependence is not observed.
Osterkamp (1997) and Pfeilsticker et al. (2001) investigated the pressure and temperature dependence of the O_4 collisional pair absorption cross section. The shape has been found independent of temperature and pressure while the magnitude increased by 11% when decreasing temperature by 50 K. The H_2O absorption cross section can be calculated for different pressures and temperatures from spectral parameters tabulated in Rothman et al. (2005). At high spectral resolution the temperature and pressure dependence is strong, but decreases with decreasing resolution. As for our measurements H_2O absorption plays a minor role, the dependence of the absorption cross section on ambient parameters is of minor importance. The cross section of OClO exhibits several absorption bands with an underlying broad continuum. The continuum decreases with decreasing temperature, while the differential part becomes larger and the peak cross section increases (Wahner et al., 1987; Kromminga et al., 2003). The IO absorption cross section consists of a broad continuum and a superimposed band structure as studied by Laszlo et al. (1995), Harwood et al. (1997), Hoelscher and Zellner (2000), Hönninger (1999), Gomez Martin et al. (2005), Spietz et al. (2005) and Dillon et al. (2005). Some studies found that the differential absorption cross section is independant of temperature which is in contrast to Bloss et al. (2001) who found a detectable temperature dependence. The OIO absorption cross section has been studied by Himmelmann et al. (1996); Cox et al. (1999); Ingham et al. (2000); Allan et al. (2001); Spietz et al. (2005); Gomez Martin et al. (2005). But no assessment on the temperature and pressure dependence is available.

Molecular absorption detected in each spectrum is a composite of absorption in several atmospheric layers with different temperatures and pressures. Since the pressure dependence of the cross sections of all relevant species is found negligible at our spectral resolution, only temperature dependences are considered here. The temperature dependence of the absorption cross sections can be accounted for in the model function by using several cross sections of the same species recorded at different temperatures. In order to reduce the inter-dependence between the cross sections of the same species, it proves worthwhile to orthogonalize them with respect to each other (Fayt and van Roozendael, 2001). However, this approach is only useful if the absorption of the considered species has to be removed from the spectrum in order to detect underlying absorbing species.
The retrieval of the actual SCDs of an absorber with temperature dependent cross section is more difficult. In our studies, a correction for the temperature dependence of the absorption cross section is only necessary for NO_2. The O_3 retrieval is performed in the center of the Chappuis band where negligible temperature dependence of the O_3 cross section is observed. The retrievals of IO and OIO aim at estimating an upper limit of the abundances or at a possible detection close to the detection limit and hence temperature and pressure dependences are not critical factors. Orphal (2003) suggests several methods to account for the temperature dependence of the NO_2 absorption cross section by interpolation to the actual temperature of the measurement. Our approach is similar.
Assuming a layered atmosphere with L layers k each with constant temperature T_k and constant NO_2

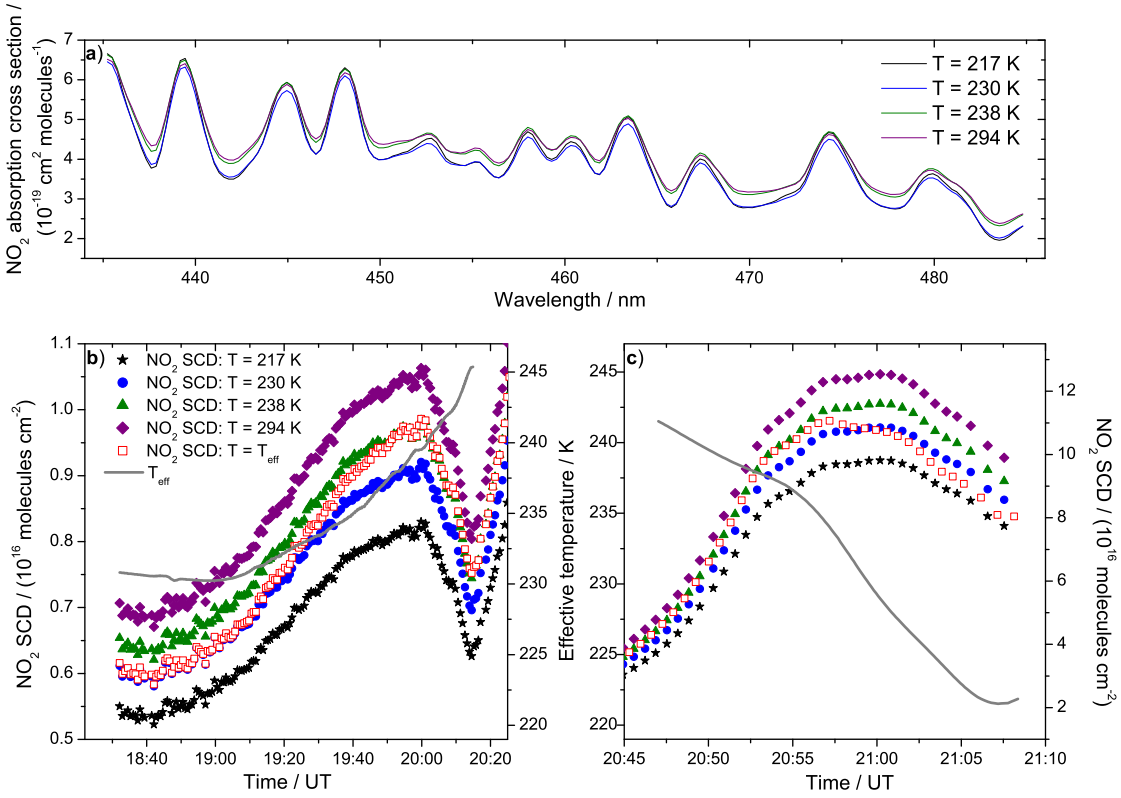

Figure 3.4: Panel a): NO_2 absorption cross section in the NO_2 retrieval range between 435 nm and 485 nm for T=217 K (black), T=230 K (blue), T=238 K (green) and T=294 K (purple). The absorption cross sections were measured in the laboratory by the DOAS spectrograph and scaled to convolved cross sections taken from Harder et al. (1997). Panel b): NO_2 SCDs as a function of time inferred from measurements during balloon ascent at Teresina in June 2005 using the absorption cross sections shown in panel a). The SCDs corresponding to T=217 K (black stars), T=230 K (blue circles), T=238 K (green triangles) and T=294 K (purple diamonds) are the basis for the interpolation to the effective temperature (gray line). The temperature corrected NO_2 SCDs are shown as open red boxes. For better visibility only every fifth measurement is shown. Panel c): Same as panel b) but for solar occultation measurements.

concentration n_k, each spectrum can be characterized by an effective temperature T_{eff} defined through

$$T_{eff} = \frac{\sum_{k=1}^{L} K_k T_k n_k}{\sum_{k=1}^{L} K_k n_k}. \tag{3.22}$$

K_k is the air mass factor in layer k corresponding to the line-of-sight of the considered spectrum, i. e. the ratio of the slant path through layer k to the thickness of layer k. T_{eff} is the mean absorber concentration weighted temperature along the line-of-sight. Temperature as a function of altitude is taken from the meteorological support data of the balloon flight or from meteorological model data. The NO_2 concentration profile can be taken from a first evaluation of the measured spectra where the temperature dependence of the cross section is neglected. Given the effective absorber temperature T_{eff} for each spectrum, the spectral retrieval is performed several times with cross sections recorded at different temperatures. The temperature corrected SCDs of NO_2 can be retrieved by linear interpolation to the effective temperature T_{eff}. If necessary the procedure can be employed iteratively by replacing n_k

by the NO_2 profile retrieved in the previous step of temperature correction. Figure 3.4 shows an example of the temperature correction for the NO_2 SCDs retrieved from measurements at Teresina in June 2005. The absorption cross sections used for the spectral retrieval have been measured in the laboratory by the DOAS spectrograph and are scaled to convolved cross sections taken from Harder et al. (1997). (The corresponding temperatures are T = 217 K, T = 230 K, T = 238 K and T = 294 K.)

3.2.3 Forward modeling of absorption spectra in the IR (LPMA)

Again, the goal is to find a model function **F** corresponding to equation (3.7) that models the observed spectra in the infrared wavelength range as accurately as possible and to retrieve the SCDs of the absorbing species. In the IR spectral range approximations which allow for the linearization of Beer-Lambert's law are not applicable since the optical densities of many absorption lines are large ($\tau > 1$). Further, the correct representation of the temperature and pressure dependence of line strength, line shape and consequently the molecular absorption cross sections (equation (2.34)) is essential.
The LPMA FT-IR measures interferograms, i. e. the intensity of two interfering light beams as a function of the path difference. Spectra, i. e. intensity as a function of wavelength or wavenumber, can be obtained by Fourier transformation of the interferograms (Griffiths and de Haseth, 1986; Jeseck, 1996). In our discussion below, we assume that the Fourier transformation has been carried out and that intensity is given as a function of wavenumber. Wavenumber $\nu = \frac{1}{\lambda}$ is commonly used in IR retrievals since the sampling of spectra measured by a Fourier transform interferometer occurs naturally at equidistant wavenumbers.

The LPMA model function

The general approach is to construct a model function **F** which corresponds directly to the observed spectrum (equation (3.5)). According to equations (3.1) through (3.5), this approach requires to model the light path, the optical density along the light path $\tau(\nu)$, the TOA solar irradiance $I_0(\nu)$ and the instrument function $g(\nu)$ (Payan, 1996; Dufour, 2005).

Tracing the light path

Following the explanations in section 3.1.4, each spectrum measured during a balloon flight corresponds to a unique line-of-sight from the detector to the Sun. While the position of the balloon is known accurately from the onboard GPS sensors, the position of the Sun is tabulated by ephemerides. The refractive index is calculated from temperature and pressure data measured by the sensors aboard the LPMA/DOAS gondola or by radiosondes launched temporally and spatially close to the balloon launch. For high altitudes atmospheric model data (ECMWF, MSIS-90) are used. The raytracing software considers refraction and the spherical geometry of the atmosphere. The atmosphere between ground-level and 120 km altitude is divided into 56 layers each with constant temperature and pressure. The actual light path is calculated iteratively with the 'un-refracted' light path as initial guess.

Optical density along the light path

The optical density along the line-of-sight is given by equation (3.2). Since in the IR spectral range Rayleigh and Mie scattering are very weak and exhibit very broad spectral structures, extinction due to

scattering is neglected when calculating the optical density along the line-of-sight. Possible residual extinction due to scattering is accounted for by adjusting the modeled TOA solar irradiance. The line-of-sight is divided into a finite number of discrete elements according to the layered model of the atmosphere described above. Assuming that the atmosphere consists of L concentric layers k each with constant pressure and constant temperature, equation (3.2) reads

$$\tau(\nu) \;=\; \sum_{i=1}^{N} \sum_{k=1}^{L} \sigma_i(\nu, T_k, p_k) \int_{s_k}^{s_{k+1}} n_i \, ds, \tag{3.23}$$

where T_k and p_k are effective temperature and effective pressure in layer k defined through

$$x_k \;=\; \frac{\int_{s_k}^{s_{k+1}} x(s)\, n_{air}(s)\, ds}{\int_{s_k}^{s_{k+1}} n_{air}(s)\, ds}, \tag{3.24}$$

with $x = T, p$. The number density of air molecules n_{air} is calculated from the ambient temperature and pressure data. The molecular absorption cross sections are calculated via equation (2.34) corresponding to the calculated effective temperature and pressure. Data on line strength, line shape and their temperature and pressure dependence are taken from the HITRAN database (Rothman et al., 2005). From equation (3.23) the slant column density of absorber type i in layer k can be defined through

$$SCD_{i,k} \;=\; \int_{s_k}^{s_{k+1}} n_i \, ds. \tag{3.25}$$

The total slant column density of absorber i is given by

$$SCD_i \;=\; \sum_{k=1}^{L} SCD_{i,k} \tag{3.26}$$

and the optical density can be written

$$\tau(\nu) \;=\; \sum_{i=1}^{N} \sum_{k=1}^{L} \sigma_i(\nu, T_k, p_k)\, SCD_{i,k}. \tag{3.27}$$

The TOA solar irradiance

In a small spectral range the TOA solar irradiance I_0 can be modeled by a polynomial $P(\nu, p_0, \ldots, p_M)$ of degree M ($M < 4$). Solar Fraunhofer lines play a minor role in the IR, since most of the micro-windows used for the spectral retrieval are free of solar absorption lines. If there are any Fraunhofer lines present, they are identified, modeled individually and included as auxiliary parameters in the model function. The TOA solar irradiance as actually measured by the LPMA instrument is not constant during a balloon flight, since the gain of the detector electronics and the optical alignment of the sun-tracker are adjusted several times to yield a maximum of the detected signal[10]. In addition, broadband extinction

[10] Adjustments of the sun-tracker optics affect also the spectra measured in the UV/visible. However, the field-of-view of the DOAS spectrographs is much larger than the apparent size of the solar disk and small changes of the sun-tracker alignment should only shift the position of the Sun within the field-of-view of the DOAS instruments. Indeed, it is found that the spectra in the visible recorded by the DOAS spectrograph are not affected. Spectra in the UV show small changes of the instrument's response which are attributable to re-alignments of the sun-tracker optics (Dorf, 2005).

due to scattering, which has been neglected in the calculation of the optical density but might occur to a detectable degree in the lower atmosphere, can be accounted for by choosing the polynomial appropriately.

Instrumental line shape

The instrument function $g(\nu)$ cannot be obtained by measuring atomic emission lines, since the width of the emission lines is comparable to the width of $g(\nu)$. During a balloon flight, the instrument function might even be subject to small changes. Therefore, $g(\nu)$ is described by a composite of two functions,

$$g(\nu) \;=\; \frac{g_1(\nu) \,+\, g_2(\nu - d_1)}{\int \left[g_1(\nu) \,+\, g_2(\nu - d_1)\right] \, d\nu} \tag{3.28}$$

where g_1 is a sine cardinal, shortly sinc, with an overlaid exponential decay and g_2 is the weighted sum of a Lorentzian and a Gaussian displaced by d_1 wavenumbers with respect to the sinc function,

$$g_1(\nu) \;=\; b_1 \, \frac{\sin(2\,\pi\,\nu\,\Delta)}{2\,\pi\,\nu\,\Delta} \, \exp\left[- \, m_1 \left(|\nu| - \frac{1}{2\,\Delta} \right) \right], \tag{3.29}$$

$$g_2(\nu) \;=\; b_2 \left[m_2 \, \exp\left(- \left(\frac{\nu}{r_2} \right)^2 \ln 2 \right) \,+\, \frac{1 \,-\, m_2}{1 \,+\, \left(\frac{\nu}{r_2} \right)^2} \right]. \tag{3.30}$$

The parameters b_1 and b_2 represent the relative amplitudes of $g_1(\nu)$ and $g_2(\nu)$, Δ is the maximum path difference of the interfering light beams[11], m_1 represents the attenuation coefficient which is set to zero for $|\nu| \leq \frac{1}{2\,\Delta}$, m_2 represents the relative weight of the Lorentzian and the Gaussian in $g_2(\nu)$ and r_2 is the corresponding HWHM. Accordingly, the model of the instrument function is given as an explicit function of the parameters listed above, $g(\nu, b_1, b_2, \Delta, m_1, m_2, r_2, d_1)$. The sinc function $g_1(\nu)$ models the instrumental line shape of a perfect FT-IR with finite optical path difference where no apodization is applied to the measured spectra. The function $g_2(\nu)$ accounts for small misalignments of the optics which e. g. render the instrumental line shape asymmetric (Griffiths and de Haseth, 1986; Jeseck, 1996).

The model function

According to the definitions above, the model function $\mathbf{F}$ used for the spectral retrieval is given by

$$F(\nu) = \int_{-\infty}^{\infty} P(\nu', p_0, \ldots, p_M) \, \exp\left(- \sum_{i=1}^{N} a_i \sum_{k=1}^{L} \sigma_i(\nu', T_k, p_k) \, SCD_{i,k} \right) g(\nu' - d_2 - \nu) \, d\nu'. \tag{3.31}$$

The state vector $\mathbf{x}$ of parameters to be retrieved consists of the polynomial coefficients p_m ($m = 0, \ldots, M$), the parameters of the instrument function, the scaling factors a_i ($i = 1, \ldots, N$), and a spectral shift parameter d_2, that accounts for spectral misalignments due to small variations of the wavenumber of the alignment laser. In contrast to the DOAS retrieval the a_i do not correspond to the SCD_i themselves but are scaling factors for an *a priori* guess of the $SCD_{i,k}$[12]. The auxiliary parameters $\mathbf{b}$ comprise the molecular absorption cross sections dependent on temperature and pressure and, if necessary, a spectrum of solar Fraunhofer lines. The measurement vector $\mathbf{y}$ is the measured spectrum itself.

[11] In our retrieval software Δ is replaced by the FWHM of the sinc function given by $\frac{1.207}{2\,\Delta}$.

[12] In our retrieval software the *a priori* guess of $SCD_{i,k}$ is constructed from an *a priori* guess of the volume mixing ratio profile of absorber i. The scaling factor a_i scales the entire volume mixing ratio profile. For details on the *a priori* calculation of $SCD_{i,k}$ see Dufour (2005).

Solution of the inverse problem

As in the case of the DOAS retrieval a least squares fitting method is used to solve the inverse problem of equation (3.7). Remembering the discretization of the spectrum, the state vector $\mathbf{x}$ is obtained by choosing its components such that

$$\chi^2 = \frac{1}{W-V-1}\sum_{n=1}^{W}\left(\frac{y_n - F_n(\mathbf{x})}{\epsilon_n}\right)^2 = \frac{1}{W-V-1}\sum_{n=1}^{W}\left(\frac{I^*(n) - F(n)}{\epsilon_n}\right)^2 \tag{3.32}$$

is minimized, where W is the number of spectral elements used for the retrieval and V the number of retrieved parameters, i. e. the dimension of $\mathbf{x}$.

Since the LPMA model function is non-linear in the fitting parameters a Levenberg-Marquardt algorithm is used to solve the inverse problem, equation (3.32). The algorithm combines the steepest gradient and a 2nd order expansion method. The Levenberg-Marquardt method is modified to include an additional constraint on the retrieval by *a priori* knowledge of the parameters, i.e. the retrieval does not search to minimize χ^2 but

$$\chi^2 + \sum_{l=1}^{V}\left(\frac{x_l - x_{a,l}}{\epsilon_{a,l}}\right)^2, \tag{3.33}$$

where $x_{a,l}$ is the *a priori* knowledge of parameter x_l and $\epsilon_{a,l}$ is the error estimate of the *a priori*. The additional constraint prevents the fitting algorithm from finding solutions corresponding to a local minimum of χ^2 which have no physical meaning. The relative weight of the *a priori* with respect to the measurements is governed by the relative magnitude of the measurement error and the *a priori* error. The dependence of the retrieved fitting parameters on the *a priori* is checked by calling another iteration of the fit with the retrieved parameters as *a priori*. If there is a significant dependence, the iteration can be repeated until the change of the retrieved parameters with changing *a priori* is negligible. But typically, the dependence on the *a priori* is small and a single iteration is sufficient. The fitting algorithm has been implemented by Payan (1996) and is extensively described there and in Dufour (2005).

Error treatment

Retrieval theory (Rodgers, 2000) states four sources of error associated with equation (3.7). The retrieved parameters are affected by retrieval noise due to measurement error, errors of the auxiliary parameters, errors due to correlations of the retrieval parameters and errors of the model function (Rodgers, 2000). The latter contribution and possible corrections are discussed in a separate section (section 3.2.4).

Retrieval noise due to measurement error

The contributions to measurement error of the FT-IR are manifold. Besides the detector noise, which depends on the sensitivity and the area of the detector, noise generated from the optical and mechanical setup, e. g. by non-constant speed of the moving mirror, and noise originating from the read-out and digitalization electronics are important. The use of optical and numerical filters, which limit the recorded spectral range, reduces noise by cutting contributions from unused spectral regions. Jeseck (1996) experimentally investigated the signal-to-noise ratio in LPMA spectra recorded during three of the first

balloon flights of the LPMA instrument. Typically, the signal-to-noise ratio of the spectral regions covered by the HgCdTe detector (see Table 3.2) is of the order of several 10^2 for spectra recorded during balloon float and close to 10^2 for spectra recorded in solar occultation where the overall signal is weaker. The signal-to-noise ratios of the spectral regions covered by the InSb detector (see Table 3.2) show similar values but sometimes exceed 10^3 for spectra measured during balloon float.
Similar to the DOAS retrieval the measurement error is represented by the standard deviations of the retrieved parameters given by the fitting routine. Since the IR spectra originate from the Fourier transform of the recorded interferograms, there are no spectral elements which are *per se* inter-dependent.

Auxiliary parameter error

The errors of the absorption line parameters and their pressure and temperature dependence contribute to the auxiliary parameter error. The line parameters, i. e. line strength and shape according to ambient pressure and temperature, are taken from the HITRAN 2004 spectroscopic database (Rothman et al., 2005) where also the associated errors are tabulated. For $ClONO_2$ the absorption cross section and the corresponding error is taken from (Wagner and Birk, 2003).
The impact of errors of the ambient temperature and pressure data is estimated by sensitivity runs. The stated errors of the onboard temperature and pressure sensors are 0.2 K and 0.5 mbar, respectively (Dorf, 2005). When the entire pressure and temperature profile is changed according to these uncertainties, the sensitivity of all absorber SCDs is smaller than 1%. However, the actual impact depends strongly on the species and the line-of-sight of the considered spectrum. Horizontal variations of the meteorological data are not considered. Hence the actual error due to uncertainties of these parameters might be larger.
The geographical position of the balloon and the Sun are known very accurately. The relative position of the Sun with respect to a terrestrial observer is tabulated as a function of time, latitude and longitude in the ephemerides. The accuracy of the GPS instrumentation is typically ± 25 m in horizontal and ± 78 m in vertical direction. The combination of several GPS signals and altitude data calculated from pressure and temperature improves the accuracy of the knowledge on the position of the balloon. The timing of the measurements is precise to within some seconds. However, there is an offset between GPS time and universal time of about -13 s (in 2005) which has to be considered. In addition, it is not obvious which measurement time has to be assigned to the LPMA interferograms since a single mirror scan takes 50 s. Here, the time of zero path difference ± 25 s is attributed to the corresponding forward and reverse spectra.

Error due to correlations of the retrieval parameters

Correlations between the retrieval parameters are investigated by (Dufour, 2005) in analogy to what is done for the DOAS retrieval. Initially, sizeable correlations have been found between the scaling factors of the absorber SCDs and the parameters of the instrument function. These correlations could be largely removed by introducing the multifit retrieval which performs the LPMA retrieval simultaneously in several microwindows. The multifit retrieval is discussed in detail in section 3.2.4. Using the new retrieval, essentially no correlations occur between the retrieval parameters which directly translates into a significantly improved agreement between LPMA and DOAS data. Hence, the correlation error is neglected.

3.2.4 Corrections and shortcomings of the LPMA model function

As in the case of the DOAS retrieval some effects are not considered by the LPMA model function (equation (3.31)). Since such deficiencies cause systematic errors of the retrieval, they are discussed below with respect to their impact on the retrieved parameters and possible corrections.

Correction to the line-of-sight

When tracing the ray of the light from the Sun to the balloon, the LPMA retrieval assumes that the sun-tracker adjusts the pointing of the instrument to the center of the Sun. In solar occultation the light path in the Earth's atmosphere becomes very long and due to refraction the image of the Sun used by the sun-tracker to control the pointing becomes elliptic. In addition, extinction for light coming from the upper edge of the Sun is smaller than for light from the lower edge and the barycenter of the solar intensity shifts upward on the solar disk as already mentioned in the discussion of the impact of the center-to-limb darkening effect on the DOAS retrieval. As a consequence the light path calculated from the balloon to the center of the solar disk is longer than the intensity weighted average light path through the atmosphere. Accordingly, the inferred absorber SCDs are too small. Especially for absorbers that exhibit large abundances at low altitudes, e. g. CH_4 and N_2O, it is important to correct the line-of-sight in order to avoid a significant underestimation of their concentration profile (Dufour, 2005).
The lines-of-sight can be corrected by choosing an absorber whose atmospheric abundance is known and by subsequently adjusting the line-of-sight in a way that the retrieval yields the *a priori* known absorber SCD. CO_2 has a well known mixing ratio throughout the atmosphere. From the known vertical profile an *a priori* CO_2 SCD is calculated for each spectrum according to the initially determined lines-of-sight. Then, the spectral retrieval is performed for all spectra measured during the balloon flight and the scaling factors a_{CO_2} are retrieved according to equation (3.31). If the lines-of-sight are correct, the a_{CO_2} are constant and approximately equal to 1 for all spectra. The scaling factors retrieved from spectra measured during sunset or sunrise are commonly smaller than those retrieved from balloon ascent or float measurements indicating slightly erroneous lines-of-sight in solar occultation. Hence, the lines-of-sight are recalculated by shifting the light path upward on the solar disk. A new set of scaling factors a_{CO_2} is retrieved corresponding to the new lines-of-sight. This procedure is iterated until the retrieved scaling factors are constant for all spectra measured during a balloon flight and the calculated lines-of-sight correspond to the true observation geometry.

Etalon structure

Jeseck (1996) identified a sinusoidal pattern on top of the baseline of LPMA spectra. The observed feature occurs for both detectors and its magnitude depends on the spectral region. Its origin are multiple etalon-like reflections in the optics which guide the radiation into the detector. For our purposes, the long-wave region of the HgCdTe detector (see table 3.2) is affected which hinders the retrieval of HNO_3 and $ClONO_2$. The observed wavenumber of the sinusoidal pattern is about $1.4\,cm^{-1}$ and its amplitude is about 2% of the baseline. An example is shown in panel a) of figure 3.5.
Since the etalon-structures are approximately constant in spectral position and magnitude for all spectra during a balloon flight, they can be corrected by adding a mean sinusoidal pattern to the modeled TOA

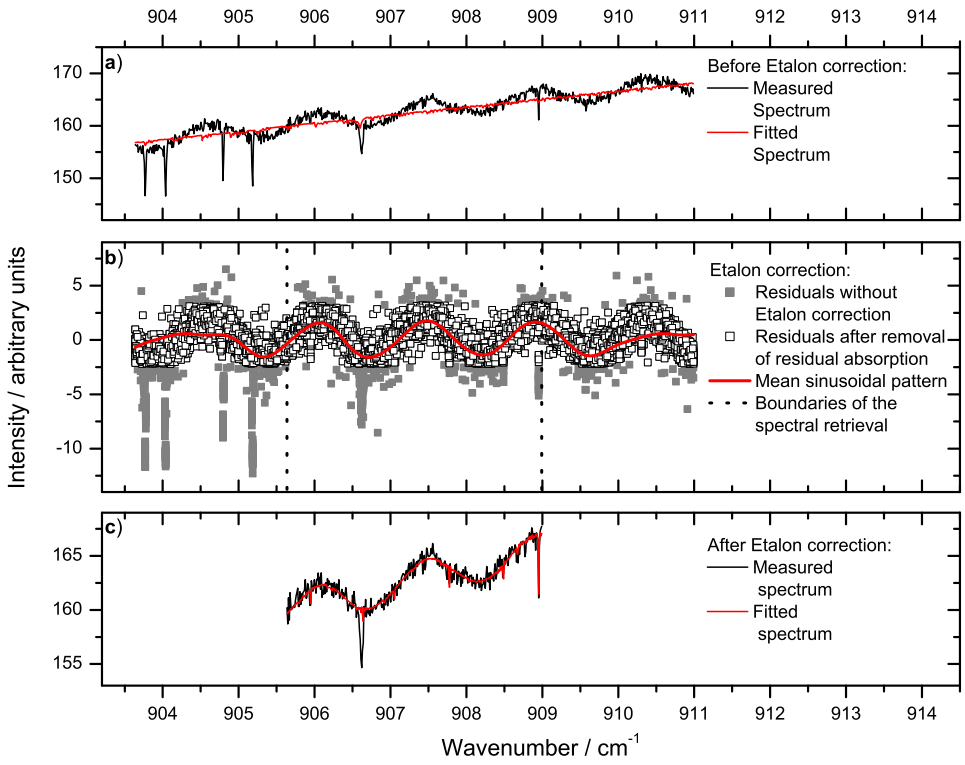

Figure 3.5: Panel a): Measured (black) and modeled (red) spectrum without etalon correction in the spectral range of the HNO_3 retrieval. The spectrum is recorded at 18:13 UT on Aug. 21, 2001, during balloon float above Kiruna. Panel b): Residual structures (gray boxes) inferred from a spectral retrieval without etalon correction of the float spectra measured at Kiruna on Aug. 21, 2001. The open black boxes are the residuals used for the fit of the Fourier polynomial, which is shown as solid red line. The vertical dotted lines represent the boundaries of the HNO_3 retrieval window. Panel c): The same measured (black) spectrum as in panel a). The modeled spectrum (red) is retrieved with etalon correction. The absorption feature at about 906.6 cm^{-1} is a solar Fraunhofer line.

I_0 polynomial. The mean pattern is determined separately for all spectral windows subject to correction. First the spectral retrieval is performed on an ensemble of float spectra without applying the etalon correction. The obtained residual structures are governed by the sinusoidal pattern. If there are any absorption structures left in the residual they are removed by hand. The ensemble of residuals is then used to determine the coefficients of a Fourier expansion by a linear least squares fit, i. e. the residuals $R(n) = I^*(n) - F(n)$ are fitted by a Fourier polynomial P_F which yields the mean sinusoidal pattern,

$$P_F(n, s_1, \ldots, s_{10}, c_1, \ldots, c_{10}) \;=\; \sum_{m=1}^{10} \left[s_m \, \sin(m\, n) \;+\; c_m \, \cos(m\, n) \right]. \tag{3.34}$$

When determining $P_F(n, s_1, \ldots, s_{10}, c_1, \ldots, c_{10})$, it is important to choose a spectral range which is larger than the retrieval range to avoid border effects impacting the retrieval (see figure 3.5 panel b)). The choice of the order of the Fourier expansion depends on the retrieval range and is based on a trade-off between accurate representation of the sinusoidal pattern and smoothing over high frequency noise, but is somewhat arbitrary set to 10 in our case. The etalon correction is illustrated in panel b) of figure 3.5. The mean sinusoidal pattern $P_F(n, s_1, \ldots, s_{10}, c_1, \ldots, c_{10})$ is then added to the TOA I_0 polynomial

$P(n, p_0, \ldots, p_M)$ in the spectral range considered for correction. Subsequently, the spectral retrieval can be performed for all spectra with etalon-corrected baseline as shown for an example in panel c) of figure 3.5.

Instrumental line shape

The instrumental line shape of the LPMA FT-IR is modeled according to equation (3.28) and (3.29). Commonly, the parameters of the modeled instrumental line shape are retrieved in various test runs from spectra recorded during balloon float. Then they are kept fixed for the whole balloon flight. Float spectra are used to determine the parameters, since the broadening of atmospheric absorption lines is very small at low pressure and the absorption lines are well separated. The instrumental line shape parameters are determined separately for the four spectral regions covered by the two detectors (see table 3.2). The retrieval of $ClONO_2$ is performed close to the longwave border of the spectral region which is covered by the HgCdTe detector at about $780\,cm^{-1}$ where the attenuating effect of the optical filter is clearly observable. Therefore, the instrumental line shape is determined separately for the $ClONO_2$ microwindow. During some of the more recent measurement campaigns, the instrumental line shape is tested before the actual balloon flight by on ground measurements of absorption due to OCS which has been filled into a gas cell. If the instrumental line shape is found to be distorted, optical components can be readjusted.
The instrumental line shape can change during a balloon flight because of changes in the optical setup that can be induced by mechanical deformations due to changing ambient pressure and temperature[13]. In principle, it is possible to determine the instrumental line shape separately for each spectrum. In practice, however, the retrieval of the parameters is difficult if absorption lines overlap and their optical densities are large. Various test runs show that it is most appropriate to determine the instrumental line shape from spectra with little absorption and to keep it fixed for the whole balloon flight. A possible change of the instrumental line shape with wavenumber within the different ranges covered by the detectors is neglected.
It has to be pointed out that the determination of instrumental line shape is crucial for the retrieval since the parameters can correlate with the scaling factors of the SCDs and errors impact all retrieved parameters. Accordingly, much effort is put on the determination of the corresponding parameters which is difficult if the instrumental line shape is heavily distorted form a pure sinc function.

Multifit retrieval

Some absorbers show absorption features in several microwindows. When retrieving all microwindows separately, Dufour (2005) found that the retrieved scaling factors of a single species show significant differences depending on the underlying spectral ranges. The discrepancies are attributed to deficiencies of the modeled instrument function. If a species exhibits weak absorption within the wing of a strong absorption line of a different species small errors in the representation of the line wings can cause large errors of the secondary absorbing species, i. e. the scaling factor of the secondary absorber correlates with

[13]Due to the relatively simple optical and compact mechanical setup of the DOAS instrument, it is possible to shield the DOAS instrument from mechanical deformations by keeping it vacuum sealed and temperature stabilized. The LPMA instrument is vacuum sealed but not isolated from atmospheric temperature changes.

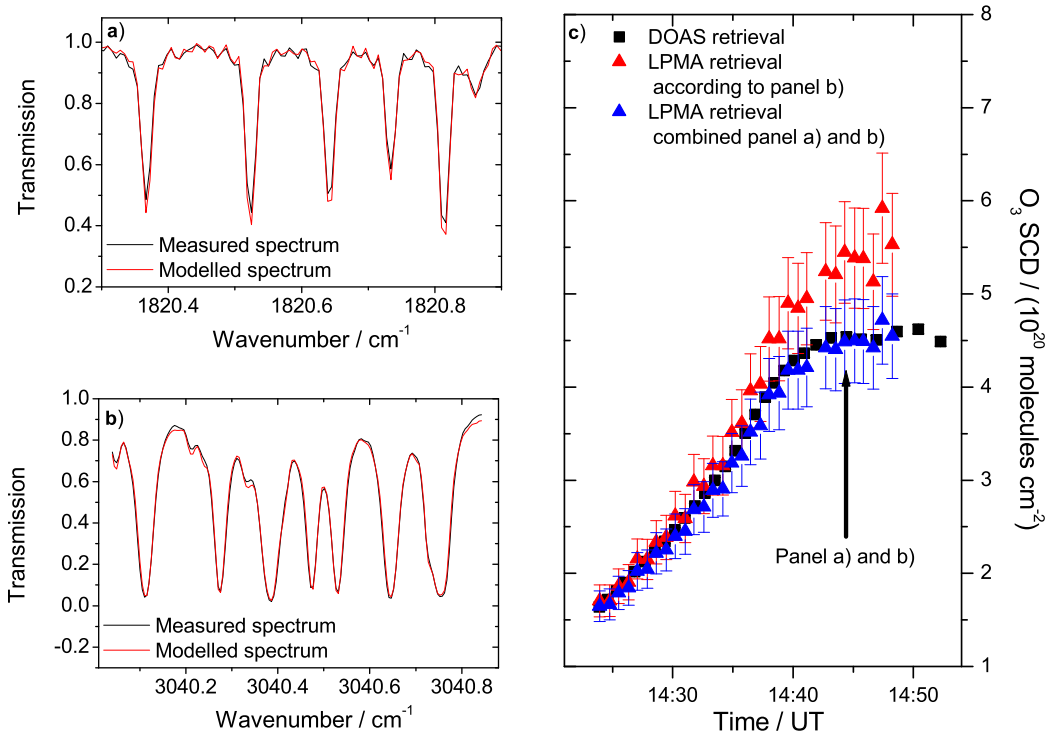

Figure 3.6: Panel a): Measured (black) and modeled (red) spectrum in the 1820 cm^{-1} range where the O_3 absorption lines are relatively weak. The spectrum is recorded at Kiruna on Feb. 10, 1999, at a tangent height of about 16 km. Panel b): Measured (black) and modeled (red) spectrum in the standard O_3 retrieval range around 3040 cm^{-1} where the O_3 absorption lines become optically thick in solar occultation. The spectrum shown is the same as in panel a). Panel c): O_3 SCDs as a function of time retrieved from DOAS measurements (black boxes), from LPMA measurements in the 3040 cm^{-1} range (red triangles) and from LPMA measurements simultaneously in the 1820 cm^{-1} and 3040 cm^{-1} range (blue triangles). The arrow indicates the spectrum shown in panels a) and b). For better visibility only every fifth DOAS measurement is shown.

the parameters of the instrument function. This shortcoming can be overcome by performing the spectral retrieval simultaneously in all microwindows which is referred to as multifit (Dufour, 2005). Correlations between the retrieval parameters are minimized since species which are secondary absorbers in a microwindow show strong absorption in another microwindow. Hence, the secondary absorption can be fitted well only if the strong absorption and the instrument functions in the different spectral ranges are represented appropriately.

A further advantage of the multifit comes into play for solar occultation measurements where the light path through the atmosphere is long and some of the absorption lines used for the spectral retrieval become optically thick ($\tau >> 1$ at the line center), i. e. a change in the number of absorbing molecules along the line-of-sight results in almost no change of the optical density at the center of the line. The relative importance of the line wings increases and the sensitivity of the retrieval of slant column abundances of the respective absorber decreases. Since the multifit allows to fit several microwindows simul-

taneously, the sensitivity of the retrieval can be increased by including a microwindow with optically less thick absorption lines of the considered species. Figure 3.6 shows the effect for the example of an ozone retrieval. The comparison with the independent DOAS measurements shows that the inclusion of a microwindow with weak ozone absorption improves the agreement between the two measurements significantly.

3.3 Retrieval of vertical trace gas profiles

The previous section discussed the retrieval of slant column densities from the measured spectra. SCDs however depend on the observation geometry of the measurement and hence cannot be compared to measurements conducted by satellite or ground based instruments. A more general representation of the measured data are trace gas concentration profiles, i. e. trace gas concentration as a function of altitude. In analogy to equation (3.7) a model can be setup which links the measurements $\mathbf{y}$ and the retrieval parameters $\mathbf{x}$

$$\mathbf{y} = \mathbf{F}(\mathbf{x}, \mathbf{b}) + \boldsymbol{\epsilon}. \tag{3.35}$$

In contrast to section 3.2, the measurement vector $\mathbf{y}$ represents an ensemble of SCDs and the retrieval vector $\mathbf{x}$ is the concentration of the considered trace gas on the chosen altitude levels. The measurement ensemble comprises all SCDs measured during balloon ascent or during solar occultation. Accordingly, its dimension is the number of considered SCDs $\dim(\mathbf{y}) = m$. The number of retrieval parameters is equivalent to the number of altitude levels $\dim(\mathbf{x}) = n$. The model function $\mathbf{F}$ models the observation geometry, i. e. it describes the path of the light through the atmosphere for each spectrum. The auxiliary parameters $\mathbf{b}$ are parameters which are not retrieved but necessary to model the light path. In our case $\mathbf{b}$ is given by pressure and temperature profiles which allow for the calculation of the refractive index, time and location of the measurements and the location of the Sun. For direct Sun observations the light path does not depend on the trace gas profile to be retrieved but is given by purely geometrical considerations. Equation (3.35) can be written in linear form

$$\mathbf{y} = \mathbf{K}(\mathbf{b})\,\mathbf{x} + \boldsymbol{\epsilon}. \tag{3.36}$$

The weighting function matrix $\mathbf{K}(\mathbf{b})$ is an $m \times n$ matrix. Its coefficient K_{ij} is the ratio of the slant light path through altitude layer j to the height of the altitude layer for the observation geometry of spectrum i. $\mathbf{K}(\mathbf{b})$ is often called the air mass factor matrix and its coefficients K_{ij} the box air mass factors.

The light path from the Sun to the balloon is calculated by the ray-tracing software DAMF (Schulte, 1996) which takes into account the spherical geometry of the atmosphere and pressure and temperature dependent refraction[14]. The atmosphere is divided in n spherical layers j with constant pressure, temperature and trace gas concentration where the layering can be chosen arbitrarily within reasonable limits. The size of the solar disk can be taken into account by calculating the weighting function matrix

[14]The calculation of the light-path through the atmosphere is also performed by the LPMA spectral retrieval software (section 3.2.3). DAMF is a different software package developed at the Institut für Umweltphysik of the University of Heidelberg. The two programs are designed to accept the output either of the LPMA or of the DOAS spectral retrievals as input. Since DAMF was developed as a stand-alone software it was found easier to adopt it to the formats of both retrievals. The lines-of-sight calculated by both programs agree very well as has been tested when generating absolutely calibrated TOA solar irradiance spectra (Gurlit et al., 2005; Lindner, 2005).

for eight rays starting from different positions on the solar disk. The rays represent equal areas of the Sun and the effective weighting function matrix is obtained by averaging over the eight individual matrices.

In principle equations (3.35) and (3.36) pose the same problem as in section 3.2. Given the measurements $\mathbf{y}$ and the model function $\mathbf{F}$ which relies on the auxiliary parameters $\mathbf{b}$, the state vector $\mathbf{x}$ has to be found. Typically, the number of measurements is larger than the number of retrieval parameters which implies that either some measurements are not independent or that the measurements are inconsistent and no exact solution exists. If the measurements were linearly related, the set of linear equations (3.36) could be reduced to an $n \times n$ problem and simple matrix inversion would give $\mathbf{x}_r = \mathbf{K}_r^{-1}\mathbf{y}_r$ where r indicates the reduced linearly independent set. In the presence of measurement error, however, the common case is inconsistency of the measurements. Rodgers (2000) lists a variety of methods how to retrieve the trace gas concentration profile when the measurements are inconsistent due to measurement error, i. a. the least-squares fitting methods employed in section 3.2. Sections 3.3.1 and 3.3.2 discuss two alternate methods, truncated Singular Vector Decomposition and the *Maximum a posteriori* approach.

Averaging kernels

Before discussing the actual retrieval algorithms the concept of averaging kernels is introduced (Rodgers, 2000). In general, the trace gas concentration profile is retrieved by operating with an inverse method $\mathbf{R}$ on the measurements

$$\hat{\mathbf{x}} = \mathbf{R}(\mathbf{y}, \mathbf{x_a}), \tag{3.37}$$

where $\hat{\mathbf{x}}$ is the retrieved trace gas profile which is explicitly distinguished from the true trace gas profile $\mathbf{x}$. The vector $\mathbf{x_a}$ represents any *a priori* estimate of $\mathbf{x}$ that is used by the retrieval method. The inverse method can be expanded to first order about $\mathbf{y} = \mathbf{F}(\mathbf{x_a}) = \mathbf{K}\,\mathbf{x_a}$

$$\hat{\mathbf{x}} = \mathbf{R}(\mathbf{K}\,\mathbf{x_a}, \mathbf{x_a}) + \frac{\partial \mathbf{R}}{\partial \mathbf{y}}(\mathbf{y} - \mathbf{K}\mathbf{x_a}) = \mathbf{R}(\mathbf{K}\,\mathbf{x_a}, \mathbf{x_a}) + \mathbf{G}_y\mathbf{K}(\mathbf{x} - \mathbf{x_a}) + \mathbf{G}_y\boldsymbol{\epsilon}, \tag{3.38}$$

where $\mathbf{G}_y = \frac{\partial \mathbf{R}}{\partial \mathbf{y}}$ is the contribution function matrix which characterizes the sensitivity of the retrieval method to the measurement and the measurement error. The term $\mathbf{R}(\mathbf{K}\,\mathbf{x_a}, \mathbf{x_a})$ evidently is equal to the *a priori* $\mathbf{x_a}$ since it represents the inverse of the measurements corresponding to the *a priori* profile. The averaging kernel matrix $\mathbf{A}$ is defined as the sensitivity of the retrieval to the true state

$$\mathbf{A} = \frac{\partial \hat{\mathbf{x}}}{\partial \mathbf{x}} = \mathbf{G_y}\,\mathbf{K}. \tag{3.39}$$

Accordingly, the relation between the true and retrieved state, equation (3.38), reads

$$\hat{\mathbf{x}} = \mathbf{x_a} + \mathbf{A}(\mathbf{x} - \mathbf{x_a}) + \mathbf{G_y}\,\boldsymbol{\epsilon}. \tag{3.40}$$

A single row of the averaging kernel matrix is called the averaging kernel of the corresponding retrieval altitude. The averaging kernels can be used as diagnostics of the quality of the profile retrieval since they quantify the contributions of all altitude levels of the true trace gas profile to the retrieved trace gas concentration of the considered altitude levels. Evidently, in a perfect retrieval the averaging kernel matrix

is the unit matrix since the retrieved profile is equivalent to the true profile. In a realistic retrieval, an averaging kernel is a peaked function the widths of which is a measure of altitude resolution. Commonly, the FWHM of an averaging kernel is considered as the altitude resolution of the retrieval at the respective altitude level. It is important to distinguish between altitude resolution and the spacing of the retrieval grid, since altitude resolution can be worse than the sampling step for a fine retrieval grid. Further for a reasonable retrieval, the sum of the elements of the averaging kernel should be close to unity and can be regarded as a measure of the fractional contribution of the measurement and the *a priori* to the retrieved profile point.

Error treatment

As pointed out in section 3.2, the errors attributable to the retrieved parameters originate from retrieval noise due to measurement error, errors of the auxiliary parameters, errors of the model function and correlations between the retrieved parameters. Since we are concerned with the retrieval of trace gas profiles, the latter is intuitively called smoothing error. For our purposes, only retrieval noise and smoothing error are important. They can be illustrated by looking at the difference between the retrieved state $\hat{\mathbf{x}}$ and the true state $\mathbf{x}$ according to equation (3.40),

$$\hat{\mathbf{x}} - \mathbf{x} = (\mathbf{A} - \mathbf{1})(\mathbf{x} - \mathbf{x_a}) + \mathbf{G_y}\boldsymbol{\epsilon}. \tag{3.41}$$

The first term on the right side represents the smoothing error. In analogy to equation (3.18), it can be quantified by the smoothing error covariance matrix $\mathbf{S_s} = (\mathbf{A} - \mathbf{1})\ \mathbf{S_a}\ (\mathbf{A} - \mathbf{1})^T$. $\mathbf{S_a}$ is the *a priori* covariance matrix which, in our case, is chosen diagonal such that the elements are the variances of the *a priori* trace gas concentrations. The second term in equation (3.41) is due to measurement error and can be represented by the retrieval noise covariance $\mathbf{S_m} = \mathbf{G_y}\ \mathbf{S}_\epsilon\ \mathbf{G_y}^T$, where $\mathbf{S}_\epsilon$ is the measurement error covariance. Assuming that the measurements are independent, $\mathbf{S}_\epsilon$ is a diagonal matrix with the squares of the SCD errors as elements. The total covariance of the retrieved profile $\hat{\mathbf{S}}$ is the sum of $\mathbf{S_s}$ and $\mathbf{S_m}$. The explicit representation of the covariance matrices is discussed together with the retrieval algorithms. Auxiliary parameter and model error are neglected, since both of them are considered small or hardly quantifiable. The auxiliary parameters which represent the position and time of the balloon borne measurements and the relative position of the Sun are known very accurately from GPS instrumentation and tabulated ephemerides, respectively (see section 3.2.3). Pressure and temperature data for the calculation of the refractive index are taken from measurements by sensors aboard the LPMA/DOAS gondola (accuracy of ± 0.5 mbar and ± 0.2 K) and from model data for high altitudes. Errors of the lines-of-sight due to the errors of the temperature and pressure data are negligible. A systematic shortcoming is the assumption that the intensity maximum of the Sun always coincides with the center of the solar disk which is not true for solar occultation measurements (see sections 3.2.2 and 3.2.4). Further, a possible contribution of scattered light is not considered by the model function. Both shortcomings might be sources of errors in deep solar occultation and result in an altitude offset of the retrieved trace gas profile which, however, is directed in opposite direction for both effects. A correction of these deficiencies must be subject of a future update of the retrieval software. It has to be emphasized that the model function for the direct Sun measurements presented here does not rely on atmospheric parameters except for temperature and pressure but results from purely geometrical considerations.

3.3.1 Truncated Singular Vector Decomposition

According to the theory of Singular Vector Decomposition (SVD) (Press et al., 1988; Rodgers, 2000), an arbitrary non square matrix $\mathbf{K}$ ($m \times n$) can be written as the product of an orthogonal[15] $m \times n$ matrix $\mathbf{U}$, an diagonal $n \times n$ matrix $\mathbf{\Lambda}$ and an orthogonal $n \times n$ matrix $\mathbf{V}^T$,

$$\mathbf{K} = \mathbf{U}\,\mathbf{\Lambda}\,\mathbf{V}^T. \tag{3.42}$$

The matrices $\mathbf{U}$ and $\mathbf{V}^T$ are constructed from the singular vectors of $\mathbf{K}$ while $\mathbf{\Lambda}$ is the diagonal matrix of the corresponding singular values λ_i. Since $(\mathbf{V}\mathbf{\Lambda}^{-1}\mathbf{U}^T)\,(\mathbf{U}\mathbf{\Lambda}\mathbf{V}^T) = \mathbf{1}$, $\mathbf{K}^* = \mathbf{V}\mathbf{\Lambda}^{-1}\mathbf{U}^T$ can be considered as the pseudo-inverse of $\mathbf{K}$ and equation (3.36) can be solved by the retrieval

$$\hat{\mathbf{x}} = \mathbf{K}_\mathbf{t}^*\,\mathbf{y} = \mathbf{V_t}\mathbf{\Lambda_t}^{-1}\mathbf{U_t}^T\,\mathbf{y}. \tag{3.43}$$

The subscript $\mathbf{t}$ indicates truncation, i. e. only the largest singular values and corresponding singular vectors are retained. The inverses of singular values which are equal to zero or smaller than a threshold are discarded. Commonly, the threshold is chosen in terms of a maximum condition number which is the ratio of the largest to the smallest non-zero singular value. Rewriting equation (3.43),

$$\hat{\mathbf{x}} = \mathbf{V_t}\mathbf{\Lambda_t}^{-1}\mathbf{U_t}^T\,(\mathbf{K}\,\mathbf{x} + \boldsymbol{\epsilon}) = \mathbf{V_t}\,\mathbf{V_t}^T\,\mathbf{x} + \mathbf{V_t}\mathbf{\Lambda_t}^{-1}\mathbf{U_t}^T\,\boldsymbol{\epsilon}, \tag{3.44}$$

illustrates that small singular values produce large contributions to the retrieved state from measurement error and render the retrieved profile unrealistic. Hence, as a rule-of-thumb for truncation, the inverse of those singular values should be set to zero which contribute more to the error than to the actual profile (Rodgers, 2000). As can be shown (Press et al., 1988), truncated singular vector decomposition always yields the best solution of the problem in a least squares sense[16]. It is interesting to note that the averaging kernel matrix of the truncated SVD retrieval is given by $\mathbf{A} = \mathbf{V_t}\mathbf{V_t}^T$, which is not the unit matrix after truncation. In other words, truncation is a trade-off between dropping contributions from measurement error and adjusting the altitude resolution of the retrieval to the resolution of the actual observation.

The error associated with the retrieved profile comes from smoothing and measurement error since model error and model parameter error are explicitly neglected. In our software the smoothing error of the truncated SVD retrieval is not considered since smoothing error can be minimized by choosing the truncation and the altitude levels of the retrieval in a way that $\mathbf{A} \simeq \mathbf{1}$. Hence, according to equation (3.41) and (3.44), the error covariance of the retrieved profile is equal to the contribution from retrieval noise, which is given by

$$\hat{\mathbf{S}} = \mathbf{S_m} = (\mathbf{V_t}\mathbf{\Lambda_t}^{-1}\mathbf{U_t}^T)\,\mathbf{S}_\epsilon\,(\mathbf{V_t}\mathbf{\Lambda_t}^{-1}\mathbf{U_t}^T)^T. \tag{3.45}$$

Equation (3.45) corresponds to Gaussian error propagation of the SCD errors into the retrieved profile. The actual error bars attributed to the retrieved profile are the square roots of the variances of $\hat{\mathbf{S}}$, i. e. $\sqrt{\hat{S}_{kk}}$.

[15] If $\mathbf{W}$ is orthogonal, then $\mathbf{W}^T\,\mathbf{W} = \mathbf{1}$.

[16] In section 3.2.1 the DOAS retrieval has been described as a combination of a linear and a non-linear least squares fitting method. The algorithm actually implemented to find the linear solutions is a singular value decomposition method.

Truncated SVD is predominantly used for comparison with the standard retrieval, the *Maximum a posteriori* algorithm. Since truncated SVD does not use an explicit *a priori* profile it can be used to check the influence of potential *a priori* information used by other techniques. The somewhat arbitrary choice of the truncation threshold, however, has to be considered as kind of *a priori* information impacting also the truncated SVD retrieval. In addition, the lack of *a priori* information can induce unrealistic oscillations of the retrieved trace gas profile in altitudes where only a few measurements contribute and where *a priori* knowledge would help to keep the retrieved profile realistic.

3.3.2 *Maximum a posteriori* solution

The *Maximum a posteriori* solution (MAP) to equation (3.35) is based on the Bayesian approach which relies on the probability density functions of the involved quantities $\mathbf{y}$, $\mathbf{x}$ and $\mathbf{x_a}$. Assuming that all the probability density functions are Gaussian, the expectation value $\hat{\mathbf{x}}$ of the retrieved profile is given by

$$\hat{\mathbf{x}} = (\mathbf{K}^T \mathbf{S}_\epsilon{}^{-1} \mathbf{K} + \mathbf{S_a}{}^{-1})^{-1}(\mathbf{K}^T \mathbf{S}_\epsilon{}^{-1} \mathbf{y} + \mathbf{S_a}{}^{-1} \mathbf{x_a}). \tag{3.46}$$

The associated covariance $\hat{\mathbf{S}}$ reads

$$\hat{\mathbf{S}} = (\mathbf{K}^T \mathbf{S}_\epsilon{}^{-1} \mathbf{K} + \mathbf{S_a}{}^{-1})^{-1} \tag{3.47}$$

and the averaging kernel matrix $\mathbf{A}$ is given by

$$\mathbf{A} = \hat{\mathbf{S}} \mathbf{K}^T \mathbf{S}_\epsilon{}^{-1} \mathbf{K}. \tag{3.48}$$

A detailed derivation of equations (3.46) through (3.48) can be found in Rodgers (1976, 2000).
The MAP solution according to equation (3.46) represents a weighted average between the measured SCDs and the *a priori* knowledge of the trace gas profile. The weight of the measurements is characterized by the observation geometry $\mathbf{K}$ and the measurement error covariance $\mathbf{S}_\epsilon$ while the weight of the *a priori* information is determined by its covariance $\mathbf{S_a}$. If the latter is large, the *a priori* will have only little impact on the retrieved profile. As pointed out above, in our retrieval $\mathbf{S_a}$ is assumed diagonal. The absolute value of the variances of $\mathbf{S_a}$ can be taken from climatologies of the trace gas profile under investigation. Often truly statistical climatologies which are not impacted by systematic effects, e. g. uncorrected temporal or latitudinal dependences, are not available. Therefore, in our retrievals, the elements of $\mathbf{S_a}$ are chosen to be large such that the retrieved profile is unaffected by the *a priori* in the core altitude range between the lowest tangent heights covered and balloon float altitude. At the boundaries of this range where only very few measurements contribute or where the weighting functions are unfavorable for retrieving profile information, the *a priori* has significant impact on the retrieved profile. The *a priori* profile $\mathbf{x_a}$ itself is either taken from climatologies or from output of a 3-D chemical transport model (Chipperfield, 1999).

The error of the retrieved profile, equation (3.47), comprises the smoothing error and the measurement error. As for the retrieved profile itself, the total covariance $\hat{\mathbf{S}}$ tends toward the *a priori* covariance where the weighting functions are unfavorable for profile retrieval or where only few measurements contribute. The error bars attributed to the retrieved profile are given by the square roots of the diagonal elements of $\hat{\mathbf{S}}$.

3.3.3 Comparison of different instruments

When comparing trace gas profiles retrieved by different instruments and retrieval algorithms, care has to be taken to compare the same quantities. Since every retrieval is characterized by its own averaging kernel matrix which in turn depends on the weighting functions and the involved measurement and *a priori* covariances, trace gas profiles inferred from different instruments will differ in the degree of smoothing and the attributed error bars. The differing degree of smoothing can be accounted for by degrading the altitude resolution of the high-resolution measurement to the lower resolution of the comparison data set (Connor et al., 1994; Rodgers and Connor, 2003; Hendrick et al., 2004). Assuming that $\hat{\mathbf{x}}_\mathbf{h}$ is the high-resolution retrieval performed on the same low-resolution altitude grid as the low-resolution retrieval $\hat{\mathbf{x}}_\mathbf{l}$, the latter can be considered as a smoothed state of the former if the high-resolution retrieval exhibits an averaging kernel matrix which is approximately equal to the unit matrix. In analogy to equation (3.40) a smoothed state $\hat{\mathbf{x}}_{\mathbf{s,h}}$ of the high-resolution retrieval is given by

$$\hat{\mathbf{x}}_{\mathbf{s,h}} = \mathbf{x_a} + \mathbf{A_l}\,(\hat{\mathbf{x}}_\mathbf{h} - \mathbf{x_a}), \tag{3.49}$$

where $\mathbf{A_l}$ is the averaging kernel matrix of the low-resolution retrieval and $\mathbf{x_a}$ is the *a priori* simultaneously used for both retrievals. The smoothed state $\hat{\mathbf{x}}_{\mathbf{s,h}}$ is the trace gas profile which the low-resolution retrieval should give if the high-resolution retrieval was the true state and the only source of error was smoothing error. Whenever smoothed profiles are shown in this study they are generated according to equation (3.49).

The degree of smoothing can be quantified by a covariance matrix $\mathbf{S_R}$ which gives an estimate of the error due to comparing retrievals from different instruments,

$$\mathbf{S_R} = (\mathbf{A_h} - \mathbf{A_l})\,\mathbf{S_a}\,(\mathbf{A_h} - \mathbf{A_l})^T, \tag{3.50}$$

where $\mathbf{A_h}$ is the averaging kernel matrix of the high-resolution retrieval on the low-resolution altitude grid (Rodgers, 2000). Further on, the square roots of the variances of $\mathbf{S_R}$ will be called altitude resolution error.

3.3.4 Langley's method

The DOAS spectral retrieval (section 3.2.1) uses a pseudo-TOA solar I_0 spectrum which is recorded by the DOAS spectrograph at high altitude and relatively high Sun, typically during the beginning of balloon float. This pseudo-TOA spectrum contains residual absorption by trace gases in the overhead air mass. Accordingly, the absolute SCDs $\mathbf{y}$ can be written as the sum of SCDs $\mathbf{y}'$ retrieved with respect to the pseudo-TOA spectrum and the residual absorber SCD of the pseudo-TOA spectrum y_0,

$$\mathbf{y} = \mathbf{y}' + y_0. \tag{3.51}$$

Before profile retrieval can be performed the SCDs $\mathbf{y}'$ given by the spectral retrieval have to be converted to absolute SCDs $\mathbf{y}$. The so-called Fraunhofer offset y_0 can be obtained by extrapolation to zero air mass according to Langley's method (Langley, 1904).

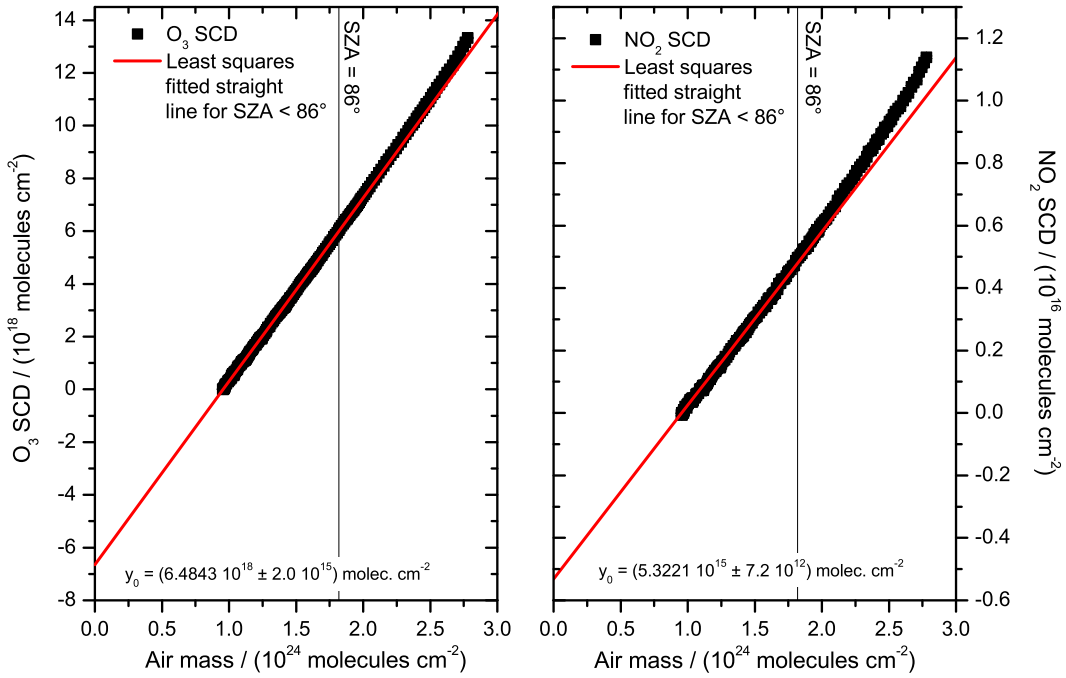

Figure 3.7: Langley plot for O_3 (left panel) and NO_2 (right panel) measurements conducted during balloon float at Aire sur l'Adour in October 2003. The data points are shown as black boxes. The red line represents a straight line fit to all data points for which SZA<86°. The Fraunhofer offset y_0 is inferred from the straight line fit where the stated errors correspond to the statistical errors of the fit. The horizontal black line indicates SZA=86°. For large air masses the impact of photochemistry on the NO_2 Langley plot is clearly visible as curvature.

In the following we consider only spectra recorded during balloon float. Since the weighting functions are zero below balloon float altitude, the lowest considered altitude layer $j = 1$ corresponds to balloon altitude. The air mass $\mathbf{y_{air}}$ for such an ensemble of spectra is given by

$$\mathbf{y_{air}} = \mathbf{K}\,\mathbf{x_{air}}, \tag{3.52}$$

where $\mathbf{x_{air}}$ is the concentration of air in the considered altitude layers which is known from the meteorological support data set. The SCDs obtained from the spectral retrieval are given by

$$\mathbf{y'} = \mathbf{K}\,\mathbf{x} - y_0 \tag{3.53}$$

Equations (3.52) and (3.53) can be written omitting matrix notation

$$y_{i,air} = \sum_{j=1}^{n} K_{ij}\, x_{air,j} \tag{3.54}$$

and

$$y'_i = \sum_{j=1}^{n} K_{ij}\, x_j - y_0. \tag{3.55}$$

Assuming that the weighting functions are independent of altitude for all considered layers, equations (3.54) and (3.55) can be simplified

$$y_{i,air} = K_{ij} \sum_{j=1}^{n} x_{air,j}, \qquad y'_i = K_{ij} \sum_{j=1}^{n} x_j - y_0 \tag{3.56}$$

and the absorber SCD can be written as a function of the overhead air mass

$$y'_i = \frac{\sum_{j=1}^{n} x_j}{\sum_{j=1}^{n} x_{air,j}} y_{i,air} - y_0. \tag{3.57}$$

Under the assumption that the absorber as well as the air concentration do not change for all considered spectra e. g. due to photochemistry or horizontal inhomogeneities, equation (3.57) can be used to infer y_0 by plotting the retrieved SCDs y'_i against the corresponding air masses $y_{air,i}$. A straight line fit yields the Fraunhofer offset y_0 at zero air mass. Figure 3.7 illustrates the Langley plot for O_3 and NO_2 for DOAS measurements during balloon float at Aire sur l'Adour in October 2003.

The assumptions in the derivation of equation (3.57) are possible sources of systematic errors. Lindner (2005) showed that for our balloon borne observations at about 30 km altitude the approximation of altitude independent weighting function is applicable for SZA$<86^\circ$ on a 10% error level. The assumption of constant absorber concentration is critical for absorbers which are photochemically active and show large variations during sunset and sunrise. The impact of photochemistry can be seen from a curvature of the Langley plot. Since NO_2, one of our target species, is photochemically active, we estimate the error due to photochemical change by performing several Langley plots where the range of SZAs contributing to the straight line fit is varied.

Chapter 4

LPMA/DOAS inter-comparison of O_3 and NO_2 abundances

The instrumental setup of the LPMA/DOAS experiment allows for measuring solar absorption spectra simultaneously over virtually the entire spectral range from the UV to the mid-IR. The instrumentation and retrieval algorithms are inherently different but the lines-of-sight are the same for the LPMA and the DOAS spectrometers. Thus, the setup provides a stringent test scenario for instrumentation, retrieval techniques, spectroscopic and ambient parameters by comparing simultaneously retrieved parameters. Here, the abundances of O_3 and NO_2 are chosen as basis for the comparison. An overview of the spectral retrievals in the various wavelength ranges is given and the inferred slant column densities of O_3 and NO_2 are compared and discussed with respect to precision and accuracy of the instruments. Finally, the corresponding vertical profiles are analyzed regarding altitude resolution and implications for comparison studies with other instruments.

4.1 Spectral retrieval and comparison of slant column densities of O_3 and NO_2

The algorithms for the spectral retrieval of SCDs from absorption spectra measured by the DOAS and the LPMA instruments are described in sections 3.2.1 and 3.2.3. Here, details of the retrieval of O_3 and NO_2 are given. Subsequently, the corresponding SCDs inferred from DOAS and LPMA measurements are compared.

4.1.1 DOAS retrieval

The spectral retrieval of O_3 and NO_2 from DOAS spectra follows the recommendations given by Bösch (2002). The standard retrieval ranges are covered by the DOAS spectrograph which is sensitive to the visible wavelength range. In principle O_3 and NO_2 absorb also in the wavelength range of the DOAS spectrograph which is sensitive to the UV. However, the spectral retrieval of O_3 in the UV is cumbersome due to the strong temperature dependence of the O_3 absorption cross section in the Huggins

Table 4.1: Characteristics of the DOAS retrieval of O_3 and NO_2.

Species:	O_3	NO_2
Instrument:	vis	vis
Wavelength range:	545 nm to 615 nm	435 nm to 485 nm
Cross section:	Anderson and Mauersberger (1992)	Harder et al. (1997)
Interfering species:	NO_2 at T = 223 K (Voigt et al., 2002) NO_2 at T = 246 K (Voigt et al., 2002) O_4 (Hermans et al., 1999) H_2O (Rothman et al., 2003)	O_3 at T = 223 K (Voigt et al., 2001) O_3 at T = 246 K (Voigt et al., 2001) O_4 (Hermans et al., 1999) (H_2O (Rothman et al., 2003))
Broadband polynomial:	3rd order	4th order
Straylight correction:	1st order	1st order
Temperature correction:	no	Interpolation based on T = 217 K, T = 230 K, T = 238 K, T = 294 K

bands which results in a spectral shift of the absorption features with changing temperature. For NO_2, test retrievals are performed in the 362 nm to 390 nm wavelength range exploiting the same absorption band as in the visible range. Typically, the precision of the retrieved SCDs is inferior compared to the precision of those inferred from the visible wavelength range. Since no additional information is gained on the accuracy of the spectroscopic parameters and retrieval algorithms and due to the considerable effort for data analysis, only O_3 and NO_2 SCDs inferred from the visible spectral range are presented. A summary of the involved parameters is presented in table 4.1.

The O_3 spectral retrieval is performed in the Chappuis band (545 nm to 615 nm). The absorption cross section is taken from the measurements of Anderson and Mauersberger (1992) which are performed with a spectral resolution comparable to that of the DOAS spectrograph. Interfering absorption from NO_2 is handled by simultaneously fitting two absorption cross sections corresponding to T = 223 K and T = 246 K which were measured in the laboratory and subsequently scaled and wavelength aligned with respect to convolved cross sections from Voigt et al. (2002). The two NO_2 cross sections are orthogonalized with respect to each other. Absorption of the oxygen dimer O_4 is considered through the reference set of Hermans et al. (1999). Line parameters of H_2O are taken from Rothman et al. (2003) at T = 230 K and p = 200 mbar and are convolved by the DOAS instrument function. A 3rd and a 1st order polynomial account for the broadband extinction processes and instrumental straylight, respectively. The relative wavelength alignment between the absorption cross sections and the pseudo-TOA spectrum is found in various test runs which allow for a 1st order stretch of the wavelength pixel mapping. In the final evaluation a first order stretch of the measured spectrum is allowed, only. An example of an O_3 evaluation is shown in figure 4.1.
The errors attributed to the retrieved O_3 SCDs are represented by the statistical 1-σ errors given by the fitting routine multiplied by 3 in order to account for systematic residual features according to Stutz and Platt (1996). The impact of the non-linear shift and stretch parameters on the inferred SCDs is estimated to 0.3%. A systematic contribution comes from the accuracy of the absorption cross section which is stated to 1% (Anderson and Mauersberger, 1992). Errors caused by convolution with the DOAS instrument functions do not apply since no convolution is performed. The impact of the

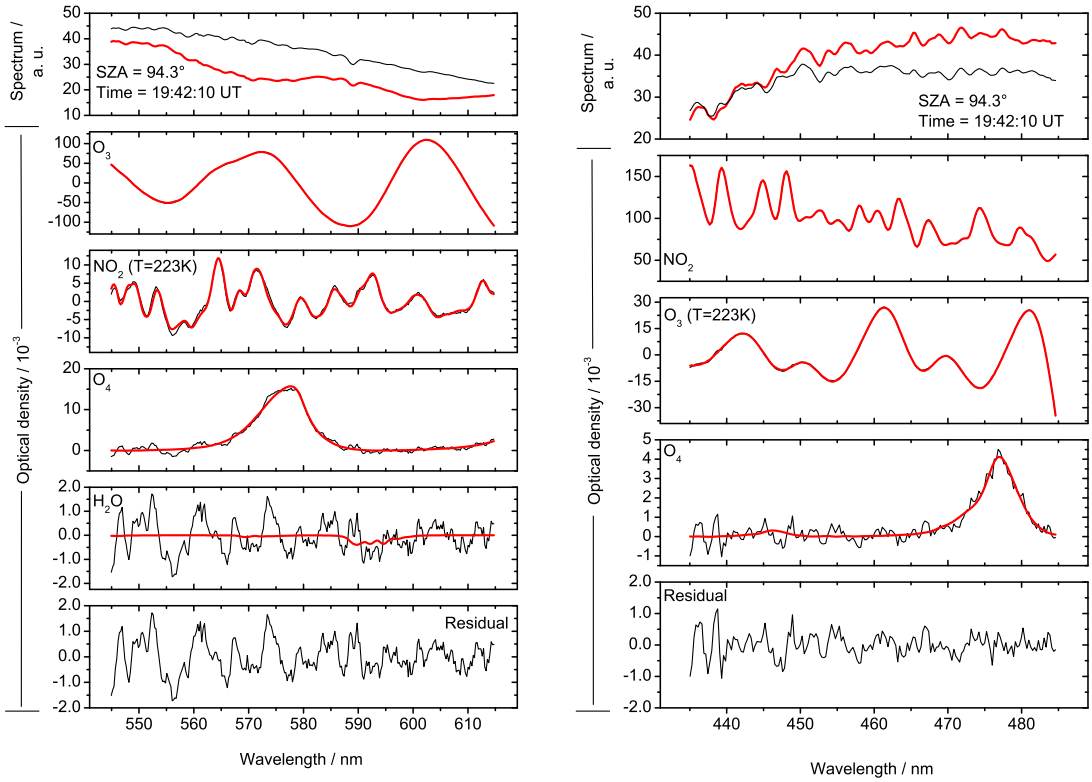

Figure 4.1: O_3 (left panel) and NO_2 (right panel) evaluation in the visible spectral range for a spectrum measured at Kiruna on Aug. 21, 2001, during solar occultation at 19:42:10 UT (SZA = 94.3°). The upper panels show the pseudo-TOA spectrum (black line) and the measured spectrum (red line). In the panels below, the retrieved trace gas absorptions of O_3, NO_2 (T = 223 K), O_4, and H_2O (left panel) and NO_2 (T = 230 K), O_3 (T = 223 K) and O_4 (right panel) are shown. The lowest panels illustrate the remaining residuals of the fitting procedure. The red lines indicate the spectral absorption and the black lines the sum of the spectral absorption and the residual.

temperature dependence of the O_3 absorption cross section on the retrieved SCDs is found smaller than 1%. Correlations between the retrieval parameters and the O_3 SCDs are small as long as the order of the broadband extinction polynomial is chosen smaller than 4 (Bösch, 2002). A further error contribution originates from the error of the Fraunhofer offset which is listed in table 8.1 of the appendix for all flights analyzed within this work and which is added to the SCD error through Gaussian error propagation.

The NO_2 SCDs are retrieved from absorption in the 435 nm to 485 nm spectral range. The NO_2 absorption cross section was measured in the laboratory for temperatures ranging between 200 K and 280 K (Dorf, 2005). Subsequently, the lab-measured absorption cross sections are scaled and wavelength aligned to the data of Harder et al. (1997) given for T = 217 K, T = 230 K, T = 238 K and T = 294 K which are *a priori* convolved by the respective instrument function. The temperature correction is performed as described in section 3.2.2 by interpolation to the effective NO_2 concentration weighted temperature based on four sets of SCDs corresponding to the four temperatures of the absorption cross sections. All NO_2 absorption cross sections are corrected for the solar I_0 effect. The relative wavelength alignment of the absorption cross sections and the pseudo-TOA spectrum is determined the same as for the O_3

retrieval.
In the 435 nm to 485 nm range interfering absorption comes from O_3. This is accounted for by simultaneously fitting two O_3 absorption cross sections recorded in the laboratory and aligned to the convolved reference set of Voigt et al. (2001) at T = 223 K and T = 246 K. The two O_3 absorption cross sections are orthogonalized with respect to each other. The collisional pair absorption cross section of O_4 is taken from Hermans et al. (1999). For the balloon flight at Teresina in June 2005 an H_2O absorption cross section constructed from line parameters of Rothman et al. (2003) at T = 230 K and p = 200 mbar is included in the fitting procedure. Due to the high tropopause at 16.5 km a significant amount of the recorded spectra probed tropospheric air masses and water absorption is detectable. Broadband extinction and instrumental straylight is considered via a 4th and a 1st order polynomial. A correction term for the center-to-limb darkening effect is neglected since the retrieval range omits the prominent CLD structures at 434 nm and 486 nm.
The errors given by the fitting routine are multiplied by 2 accounting for systematic structures of the residuals (Stutz and Platt, 1996). The impact of the error of the non-linear shift and stretch parameters on the retrieved NO_2 SCDs is smaller than 0.2%. The accuracy of the absorption cross section is 4% (Harder et al., 1997). Additionally, 1% error due to convolution with the instrument functions is estimated from sensitivity studies. The error coming from unaccounted features of the temperature dependence of the NO_2 absorption cross section is estimated to 2%. The error of the Fraunhofer offset is tabulated in table 8.2. All error contributions are added according to Gaussian error propagation.

The Fraunhofer offset can be determined by Langley's method as desribed in section 3.3.4. However, for many balloon flights the flight trajectory does not provide ideal conditions to perform a Langley plot, since balloon float is reached late when SZAs are large and the assumptions made in the derivation of equation (3.57) are not fulfilled. Fortunately, the DOAS instrument has proven to be stable with respect to its instrument function over several years. Hence, DOAS evaluations can be performed with respect to a pseudo-TOA spectra recorded during a previous or a later balloon flight which satisfies the requirements for a Langley plot. Here, Langley plots are performed for the balloon flights from Gap in June 1997, from Aire sur l'Adour in October 2003 and from Teresina in June 2005. It is necessary to use three different flights, since repairs and readjustments of the optical setup in 2002 and 2004 caused changes of the instrument function. The remaining 10 balloon flights are analyzed twice, once with respect to the pseudo-TOA spectrum of the considered balloon flight and once with respect to a pseudo-TOA spectrum of one of the three flights mentioned above for which a Langley plot can be performed. The difference between the two runs together with the offset derived from Langley's method yields the total Fraunhofer offset.
The error of the retrieved Fraunhofer offset consists of the statistical error of the Langley plot and, if applicable, the statistical error coming from the two analyses with different pseudo-TOA spectra. The systematic error contribution is estimated by performing Langley plots over several ranges of SZAs. Additionally, the error of the air mass is conservatively estimated to 5% (Lindner, 2005) since its determination relies on meteorological model data above balloon float altitude. Figure (3.7) illustrates the Langley plot performed for the flight from Aire sur l'Adour in October 2003 and tables 8.1 and 8.2 in the appendix provide the Fraunhofer offsets and associated errors of all balloon flights discussed here.

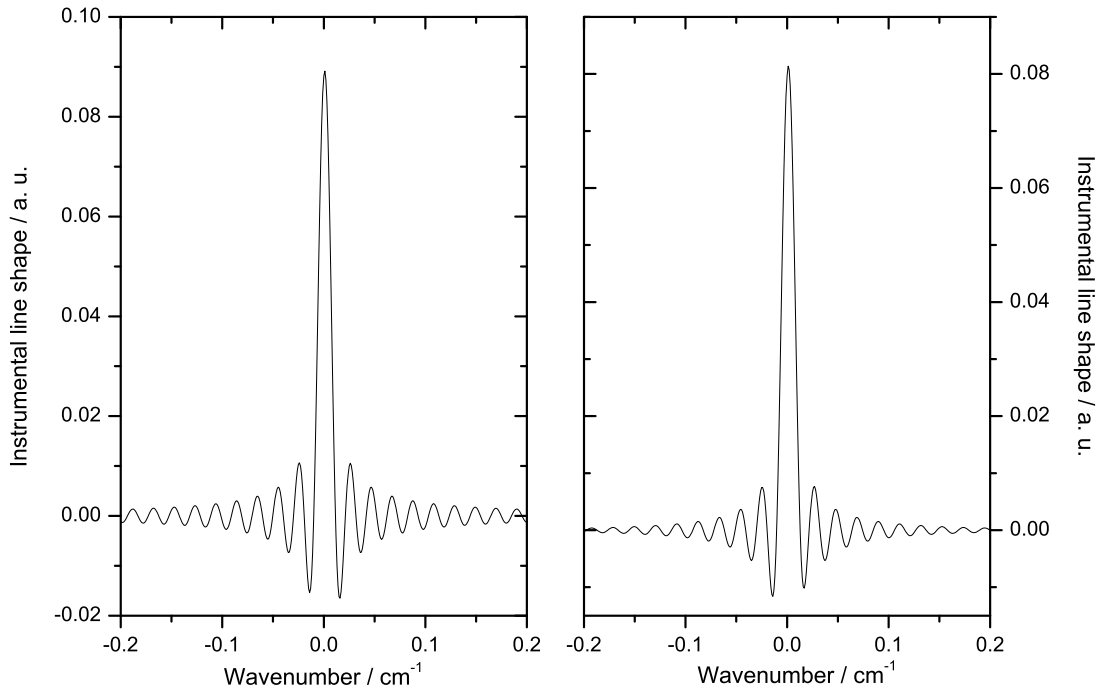

Figure 4.2: Instrumental line shape of the 1750 cm^{-1} to 2000 cm^{-1} (left panel) and 2750 cm^{-1} to 3150 cm^{-1} (right panel) spectral ranges which are covered by the HgCdTe and InSb detectors, respectively.

4.1.2 LPMA retrieval

The LPMA O_3 retrieval is performed simultaneously in two target micro-windows, 1818.10 cm^{-1} to 1820.97 cm^{-1} and 3040.04 cm^{-1} to 3040.84 cm^{-1}. For some flights the former window is not available due to the use of filters which are not covering the corresponding spectral region. As pointed out in section 3.2.4, the use of two retrieval windows for the O_3 retrieval improves the sensitivity to the slant column in solar occultation where some of the O_3 absorption lines in the window at around 3040 cm^{-1} get optically thick. Interfering absorption in the retrieval window around 1820 cm^{-1} comes from NO, CO_2 and H_2O and from solar Fraunhofer lines. In the 3040 cm^{-1} window weak absorption can be attributed to CH_4 and H_2O. Additional information on O_3 SCDs comes from secondary absorption in the micro-windows dedicated to NO_2 (2914.36 cm^{-1} to 2915.16 cm^{-1}) and CO_2 (1933.89 cm^{-1} to 1940.00 cm^{-1}). All line parameters are taken from HITRAN 2004 (Rothman et al., 2005). The TOA spectrum is represented by a 1st order polynomial in both spectral ranges of the O_3 retrieval. The inferred instrument functions, shown in figure 4.2, are slightly asymmetric for both spectral ranges but stable for each considered balloon flight.

The statistical errors given by the fitting routine are complemented by the errors of the line parameters given by the HITRAN 2004 (Rothman et al., 2005) database, which is 5% in the case of O_3. Further errors arising from uncertainties of pressure and temperature and their impact on the line parameters are estimated from sensitivity runs as described in section 3.2.3. The error going along with the

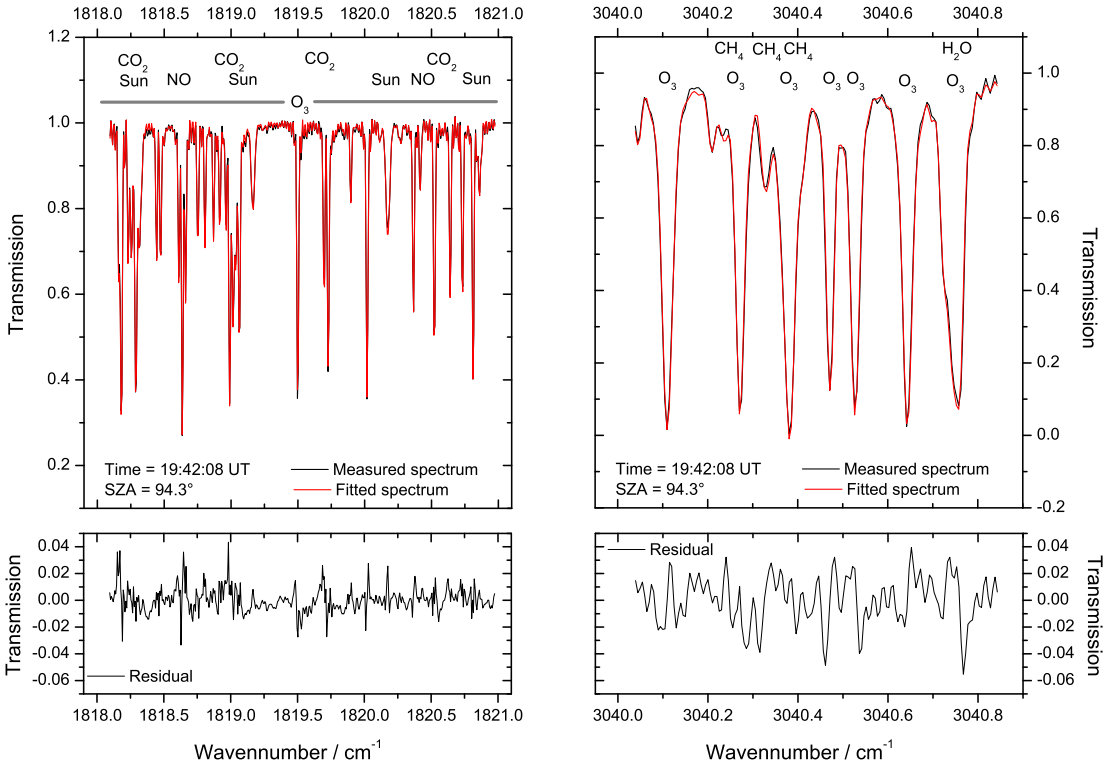

Figure 4.3: Example of the O_3 SCD retrieval from LPMA spectra in the 1818.10 cm^{-1} to 1820.97 cm^{-1} (left panel) and 3040.04 cm^{-1} to 3040.84 cm^{-1} (right panel) spectral range. The spectrum is recorded at 19:42:08 UT (SZA = 94.3°) above Kiruna on August 21, 2001. Black and red lines represent the measured and the fitted spectrum, respectively. The lower panels show the residuals. The approximate positions of the O_3 absorption lines and interfering species are indicated by their chemical symbols. In the window around 1820 cm^{-1} solar Fraunhofer lines, indicated by 'Sun', have to be considered in the spectral retrieval.

determination of the instrumental line shape is hard to quantify and depends on the optical alignment and stability during the balloon flight. In total 10% systematic contribution is added to the fitting error by Gaussian error propagation.

An example O_3 evaluation is shown in figure 4.3 for the balloon flight from Kiruna in August 2001. The spectrum shown is recorded at about 38 km altitude at SZA = 94.3° which corresponds to a tangent height of about 20 km and a distance from the balloon to the tangent point of about 500 km. Both microwindows used for the O_3 SCD retrieval are shown. The transmission at the centers of the O_3 absorption lines in the 3040 cm^{-1} window tends to zero, whereas in the 1820 cm^{-1} window O_3 absorption is weaker.

The target window for the NO_2 SCD retrieval ranges from 2914.36 cm^{-1} to 2915.16 cm^{-1}. The range centered at 1620 cm^{-1}, which is often used for IR retrievals of NO_2, is cut by spectral filters. Interfering absorption comes from H_2O, O_3 and CH_4. The latter is very prominent in the considered spectral range. Additional weak absorption of NO_2 can be detected in the HCl retrieval window (2925.77 cm^{-1} to 2926.01 cm^{-1}). All line parameters are taken from HITRAN 2004 (Rothman

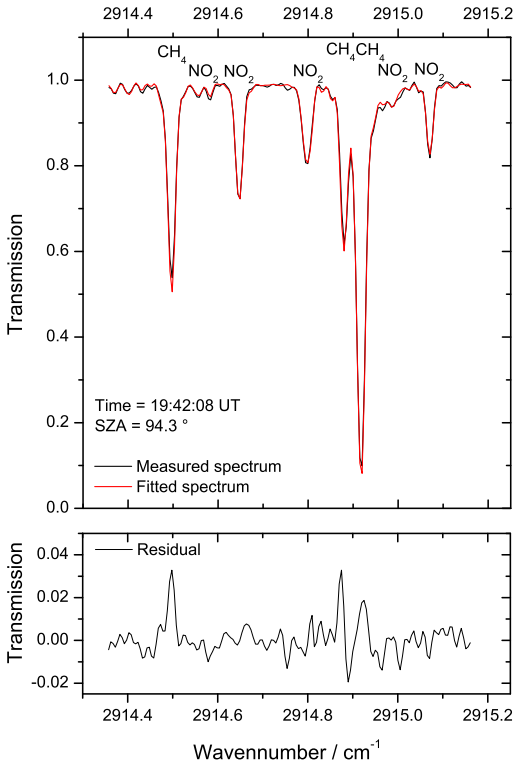

Figure 4.4: Example of the NO_2 SCD retrieval from LPMA spectra in the 2914.36 cm^{-1} to 2915.16 cm^{-1} spectral range. The spectrum is recorded at 19:42:08 UT (SZA = 94.3°) above Kiruna on August 21, 2001. Black and red lines represent the measured and the fitted spectrum, respectively. The lower panel shows the residual. The approximate position of the NO_2 absorption lines and interfering absorption by CH_4 are indicated by their chemical symbols.

et al., 2005). The TOA spectrum is represented by a 2nd order polynomial. The instrument function corresponds to that of the O_3 retrieval in the 3040 cm^{-1} range and is shown in the right panel of figure 4.2. A sample NO_2 evaluation is shown in figure 4.4. Since the CH_4 absorption lines are very prominent, care has to be taken that the NO_2 absorption lines are correctly represented within the line wings of CH_4. The multifit-retrieval has essentially solved this problem (Dufour, 2005) by constraining the retrieval of CH_4 with the help of several micro-windows. The errors attributed to the retrieved SCDs are given by the fitting errors and as for O_3 a 10% systematic contribution due to uncertainties of the line parameters and of the instrumental line shape.

4.1.3 Comparison of slant column densities

All DOAS balloon flights conducted so far between 1996 and 2005 are reanalyzed with respect to O_3 and NO_2 SCDs. Due to the considerable effort for data evaluation, only five LPMA flights are reprocessed using the multifit-retrieval implemented by Dufour (2005). A further flight suitable for the LPMA/DOAS comparison has been reprocessed by Sébastien Payan and Gaëlle Dufour who are gratefully acknowledged. In total six flights are presented where the corresponding geophysical

Table 4.2: Compendium of joint LPMA/DOAS balloon flights chosen for reanalysis and comparison. BA, BD, SS and SR indicate balloon ascent, balloon descent, sunset and sunrise, respectively. (The balloon flight from Kiruna in March 2003 has been processed by Sébastien Payan and Gaëlle Dufour.)

Balloon flight, date, time/UT	Location	Geophysical condition	Data sets
Nov 23, 1996, 14:56 - 16:54	Leon, 42.6^o N, 5.7^o	mid-lat. fall, SZA: 74.0^o - 92.7	BA,SS
Feb 14, 1997, 12.29 - 14:53	Kiruna, 67.9^o N, 21.1^o E	high-lat. winter, SZA: 82.7^o - 94.4^o,	BA,SS
Feb 10, 1999, 11:40 - 14:52	Kiruna, 67.9^o N, 21.1^o E	high-lat. winter, SZA: 82.8^o - 94.6^o	BA,SS
Jun 25, 1999, 04:32 - 07:46	Gap, 44.2^o N, 4.6^o E	mid-lat. summer, SZA: 86.7^o - 54.7^o	BD
Aug 21/22, 2001, 16:04 - 02:30	Kiruna, 67.9^o N, 21.1^o E	high-lat. summer, SZA: 75.6^o - 95.8^o, 95.4^o - 90.0^o	BA,SS,SR
Mar 23, 2003, 14:47 - 17:28	Kiruna, 67.9^o N, 21.1^o E	high-lat. spring, SZA: 77.9^o - 94.7^o	BA,SS

conditions range from high-latitude winter and summer to mid-latitude fall comprising measurements inside as well as outside the northern polar vortex. Table 4.2 summarizes the selected balloon flights and the respective geophysical conditions. Figure 4.5, 4.6, 4.8 and 4.9 show all O_3 and NO_2 SCDs retrieved for the comparison study. Statistical analyses of the deviations between the SCDs inferred from DOAS and LPMA measurements are shown in figures 4.7 and 4.10.

The O_3 comparison is shown in detail in figures 4.5 and 4.6 where the SCDs inferred from DOAS and LPMA measurements as well as the relative deviations and errors are plotted as a function of time. The relative deviations between the two datasets are calculated by interpolating the DOAS data, which are much more numerous, to the measurement instances of LPMA. The error bars associated with the DOAS data are typically smaller than 3% and governed by the error of the Fraunhofer offset. LPMA errors are dominated by the 10% systematic contribution from uncertainties of the intrumental line shape and absorption line parameters. The general agreement of the two data sets is on the order of 10%, i. e. most of the data points lie within the combined error bars. However, in some cases the relative deviations exceed the stated errors and are as large as 30%.
This is true for the balloon ascent and descent measurements at Gap in 1999 (figure 4.6 a)) and at Kiruna in 2001 (figure 4.6 b)) where the DOAS data are almost constantly offset with respect to the LPMA data. The observed offset (about $0.2{\cdot}10^{19}$ molecules cm^{-2}) suggests a problem when inferring the Fraunhofer offset of the DOAS SCDs. In both cases the DOAS Fraunhofer offset is determined by a fit with respect to the TOA solar spectrum measured at Gap in 1997. The quality of the fit is investigated in detail but no systematic error can be identified, that could explain the observed discrepancy amounting to about 20% of the actual Fraunhofer offset. An error of the Fraunhofer offset inferred by Langley's method from the measurements at Gap in 1997 is unlikely, since the same Fraunhofer offset is used for the observations at Leon in 1996 (figure 4.5 a)) at Kiruna in 1997 (figure 4.5 c)) and at Kiruna in 1999 (figure 4.5 e)) where the agreement is better.
Deviations up to 20% are observed for sunset measurements at Leon in 1996 (figure 4.5 b)) where the DOAS SCDs are systematically higher than the LPMA data. The opposite is true for sunset at Kiruna in 1997 (figure 4.5 d)) where LPMA is consistently higher than DOAS. In both cases, the O_3 retrieval window at 1820 cm^{-1} is not available since the spectral region is not covered by the filters used for the particular flights. Further, the LPMA instrument function for the flight from Leon is found strongly

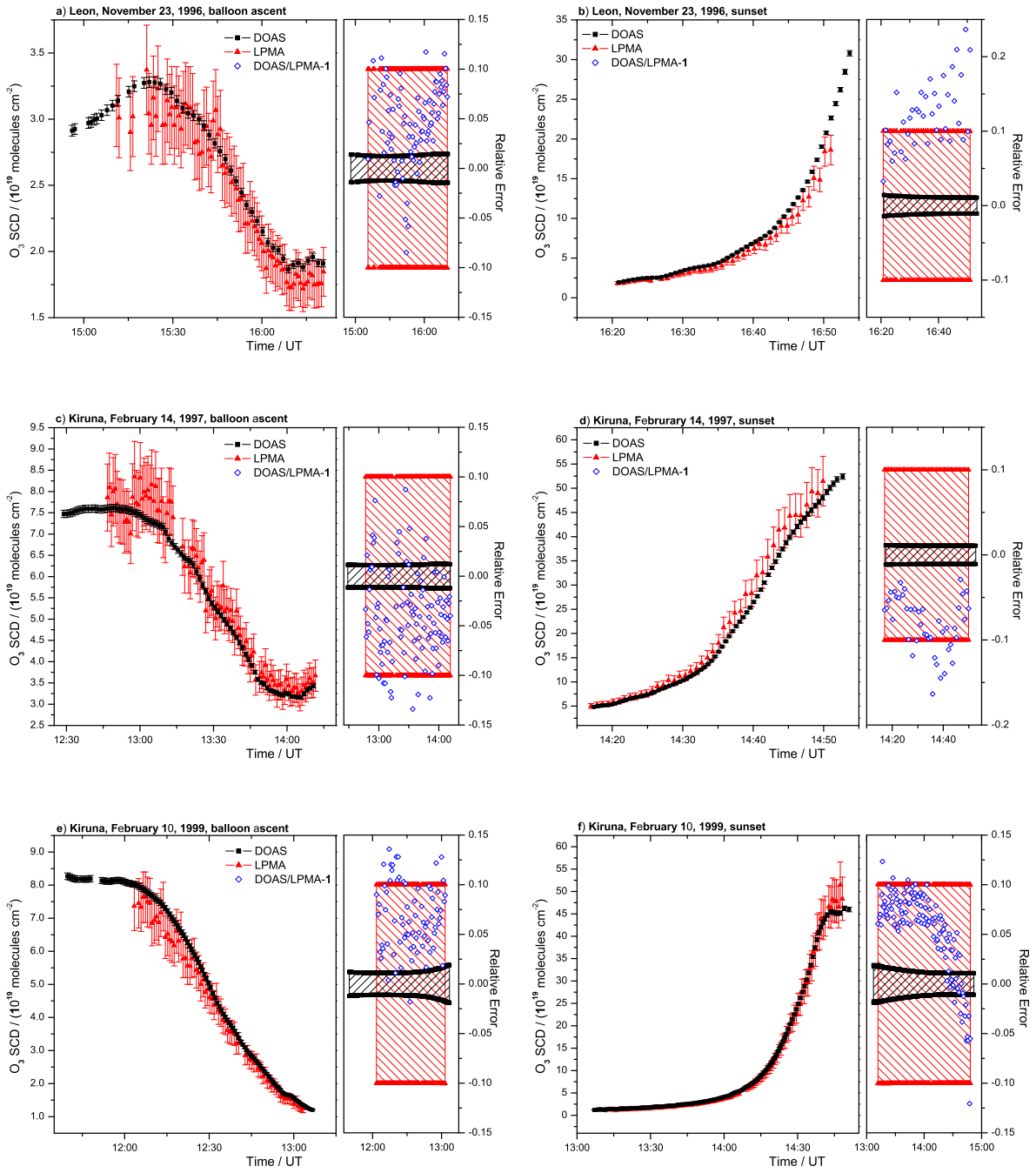

Figure 4.5: Slant column densities of O_3 retrieved from LPMA (red triangles) and DOAS (black boxes) measurements at Leon on November 23, 1996, during balloon ascent (panel a)) and sunset (panel b)), at Kiruna on February 14, 1997, during balloon ascent (panel c)) and sunset (panel d)) and at Kiruna on February 10, 1999, during ballon ascent (panel e)) and sunset (panel f)). Each panel consists of two sub-panels showing the measured SCDs on the left and the corresponding relative errors and deviations (blue open diamonds), i.e. SCD(DOAS) / SCD(LPMA) - 1, on the right. For clarity not all DOAS data points are shown.

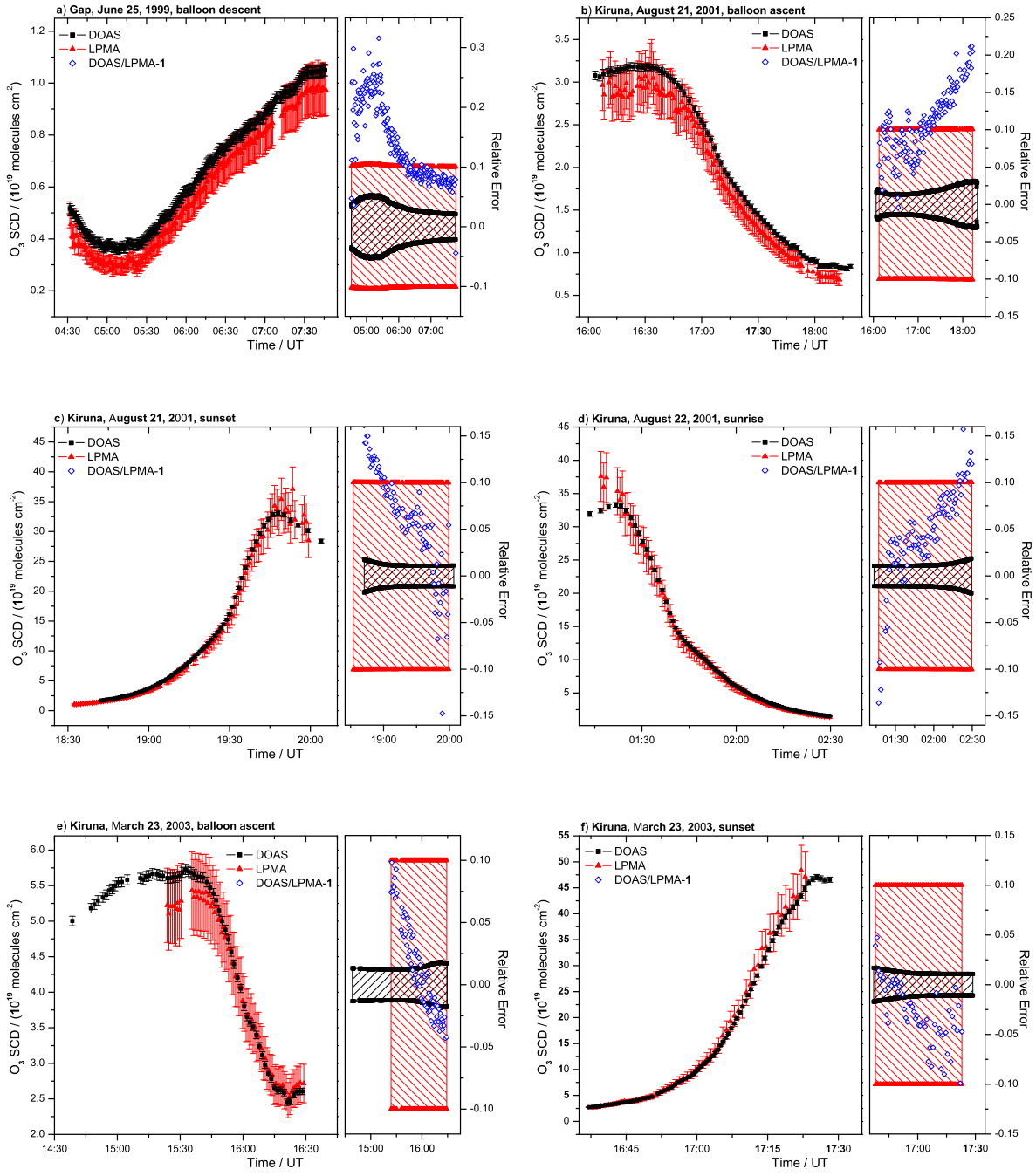

Figure 4.6: Slant column densities of O_3 retrieved from LPMA (red triangles) and DOAS (black boxes) measurements at Gap on June 25, 1999, during balloon descent (panel a)), at Kiruna on August 21 and 22, 2001 during balloon ascent (panel b)), sunset (panel c)) and sunrise (panel d)) and at Kiruna on March 23, 2003, during balloon ascent (panel e)) and sunset (panel f)). Each panel consists of two sub-panels showing the measured SCDs on the left and the corresponding relative errors and deviations (blue open diamonds), i.e. SCD(DOAS) / SCD(LPMA) - 1, on the right. For clarity not all DOAS data points are shown.

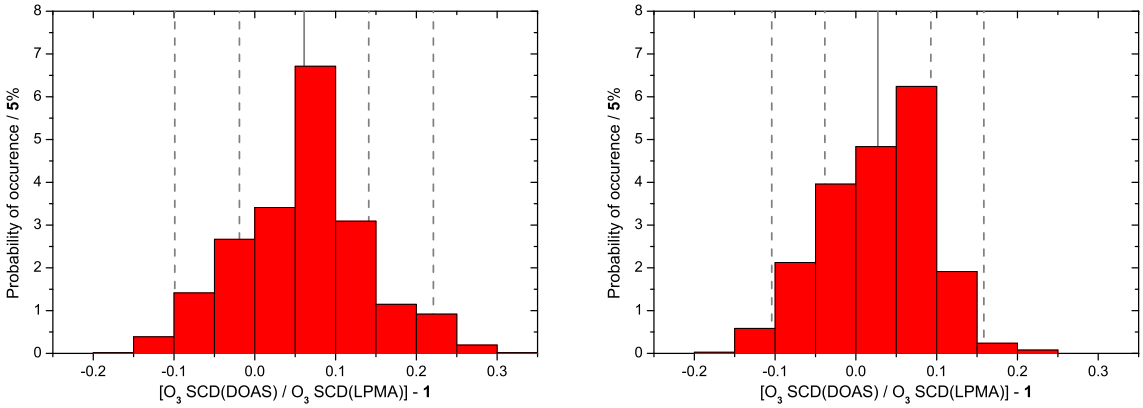

Figure 4.7: Histograms of the relative deviations between O_3 SCDs retrieved by DOAS and LPMA, i.e. SCD(DOAS) / SCD(LPMA) - 1. The data points are grouped and counted for occurrence in bins of 5% relative deviation. The left panel shows the statistical analysis for all 1132 datapoints (mean: 6.1%, standard deviation: 8.0%), in the right panel the measurements at Gap in 1999 and during balloon ascent at Kiruna in 2001 are suppressed resulting in 753 datapoints (mean: 2.7%, standard deviation: 6.6%). The mean values are shown as gray solid lines, gray dashed lines correspond to 1-σ and 2-σ.

asymmetric which makes a misrepresentation of the line wings likely.
The statistical analysis (figure 4.7) of all deviations between the retrieved O_3 SCDs confirms that in general DOAS data are higher than LPMA data. The mean deviation is 6.1% and the standard deviation of the distribution is 8.0%. The measurements at Gap in 1999 and during balloon ascent at Kiruna in 2001 show a systematic offset between the LPMA and DOAS data which is not observed for the remaining comparisons. Therefore, another statistical analysis is performed where the corresponding two datasets are suppressed. Then, the mean deviation is smaller, namely 2.7%, and the standard deviation amounts to 6.6%. As the suppression of a subset of datapoints shows, the statistical analysis is of limited value since the deviations are not independently scattered about the inferred mean values. Rather, a grouping according to the individual balloon flights is observed. For the observations at Leon (figures 4.5 a) and b)), at Kiruna in 1999 (figures 4.5 e) and f)), at Gap (figure 4.6 a)), and at Kiruna in 2001 (figures 4.6 b), c) and d)) DOAS SCDs are consistently larger than LPMA SCDs causing the overall mean deviation of +6.1% (+2.7%). On the other hand, for Kiruna in 1997 (figures 4.5 c) and d)) and for sunset at Kiruna in 2003 (figure 4.5 f)) LPMA tends to be higher than DOAS. Hence, the observed mean deviation cannot be unambiguously attributed to parameters which are independent of the actual balloon flight such as spectroscopic parameters. Rather, instrumental or retrieval related shortcomings are responsible for the observed disagreement. Since the combined error bars of the DOAS and LPMA O_3 SCDs as well as the spread of the observed deviations are larger than the bias, the discrepancy can be regarded as part of the error budget which can hopefully by reduced by upcoming improvements of the instrument or the retrieval algorithms.

Figures 4.8 and 4.9 show the comparison study for NO_2 SCDs. The relative deviations between DOAS and LPMA data are calculated by interpolating the DOAS data to the measurement instances of LPMA. The error bars of the NO_2 SCDs retrieved from DOAS spectra is dominated by the error of the

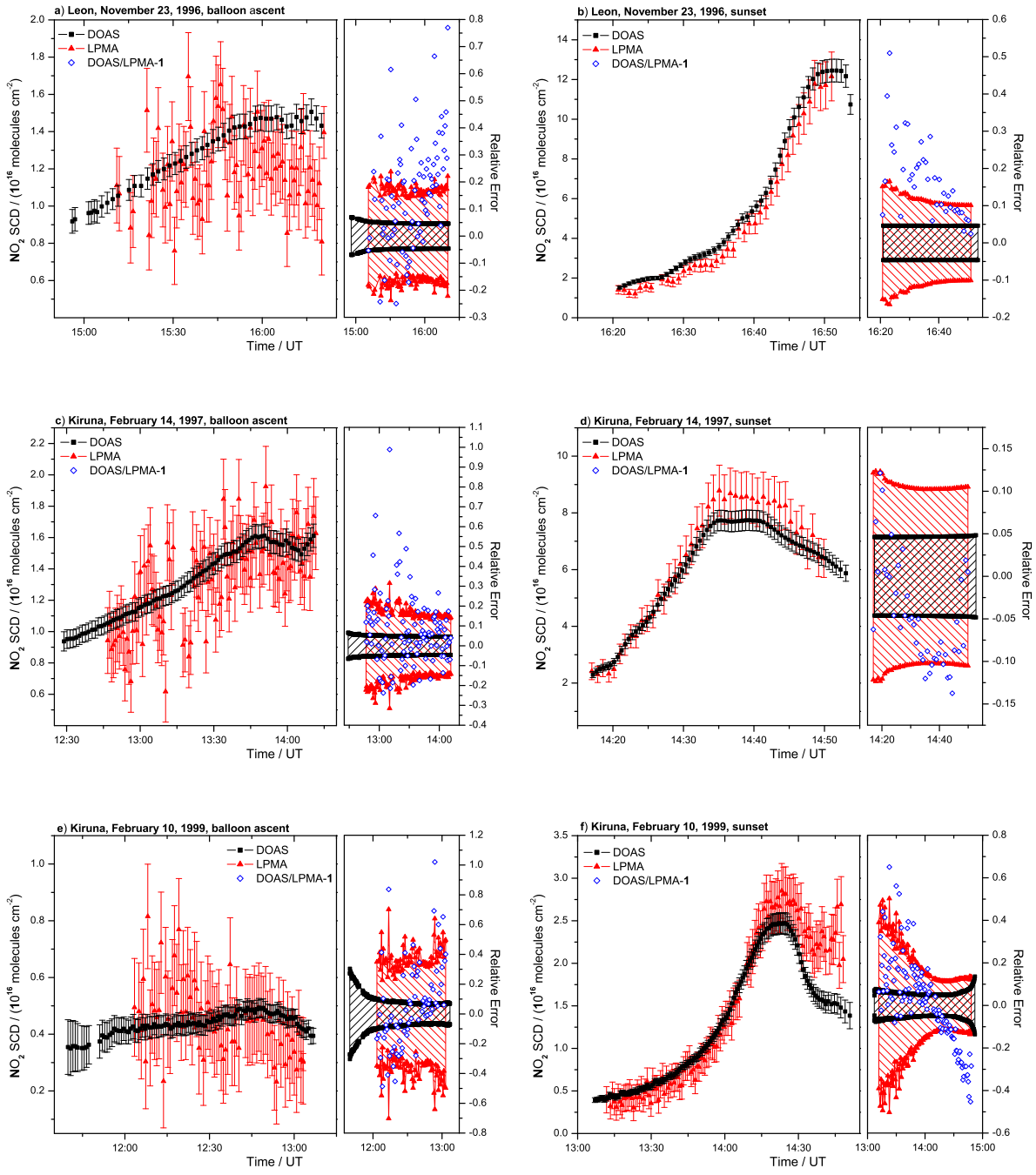

Figure 4.8: Slant column densities of NO_2 retrieved from LPMA (red triangles) and DOAS (black boxes) measurements at Leon on November 23, 1996, during balloon ascent (panel a)) and sunset (panel b)), at Kiruna on February 14, 1997, during balloon ascent (panel c)) and sunset (panel d)) and at Kiruna on February 10, 1999, during ballon ascent (panel e)) and sunset (panel f)). Each panel consists of two sub-panels showing the measured SCDs on the left and the corresponding relative errors and deviations (blue open diamonds), i.e. SCD(DOAS) / SCD(LPMA) - 1, on the right. For clarity not all DOAS data points are shown.

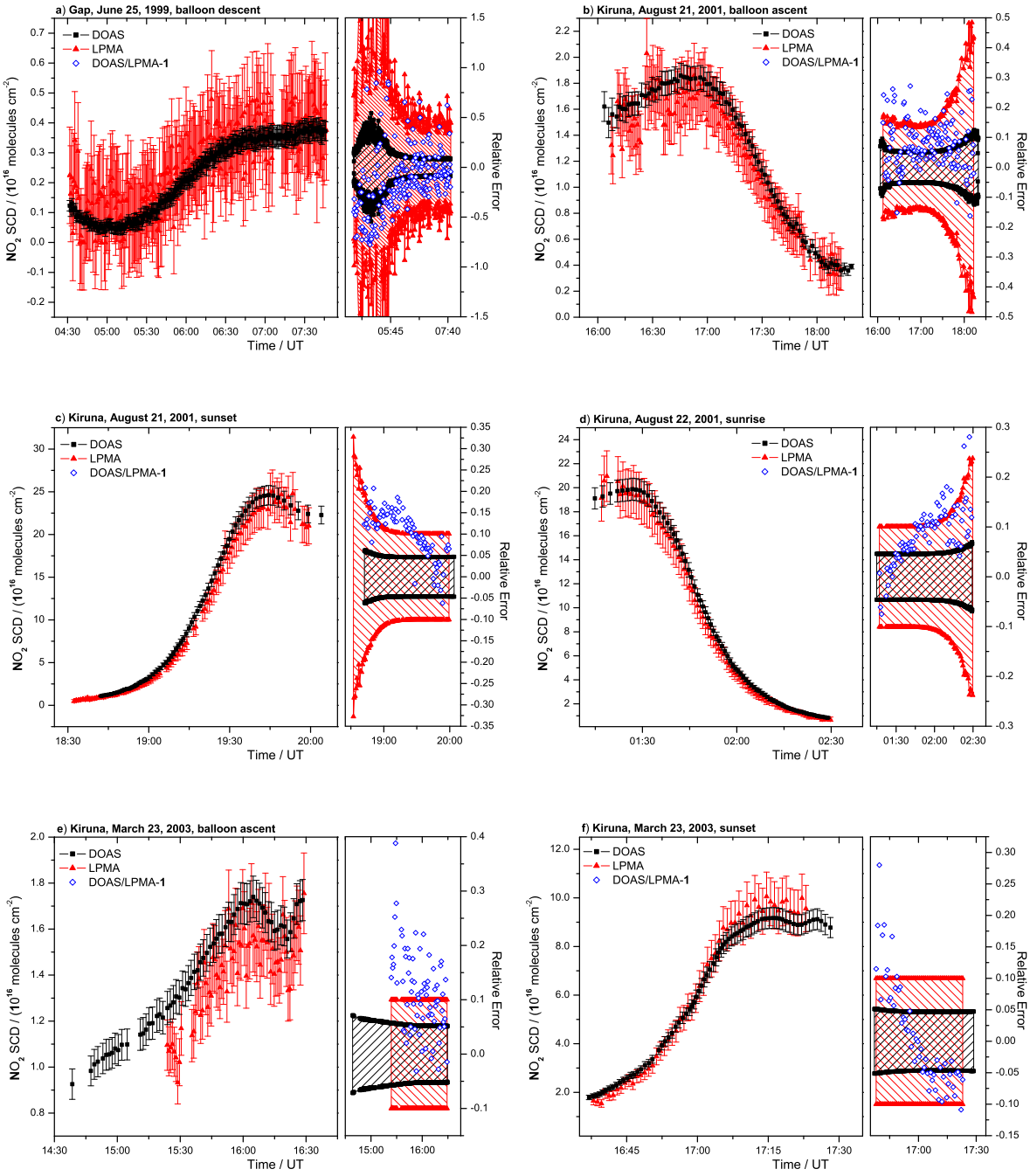

Figure 4.9: Slant column densities of NO_2 retrieved from LPMA (red triangles) and DOAS (black boxes) measurements at Gap on June 25, 1999, during balloon descent (panel a)), at Kiruna on August 21 and 22, 2001 during balloon ascent (panel b)), sunset (panel c)) and sunrise (panel d)) and at Kiruna on March 23, 2003, during balloon ascent (panel e)) and sunset (panel f)). Each panel consists of two sub-panels showing the measured SCDs on the left and the corresponding relative errors and deviations (blue open diamonds), i.e. SCD(DOAS) / SCD(LPMA) - 1, on the right. For clarity not all DOAS data points are shown.

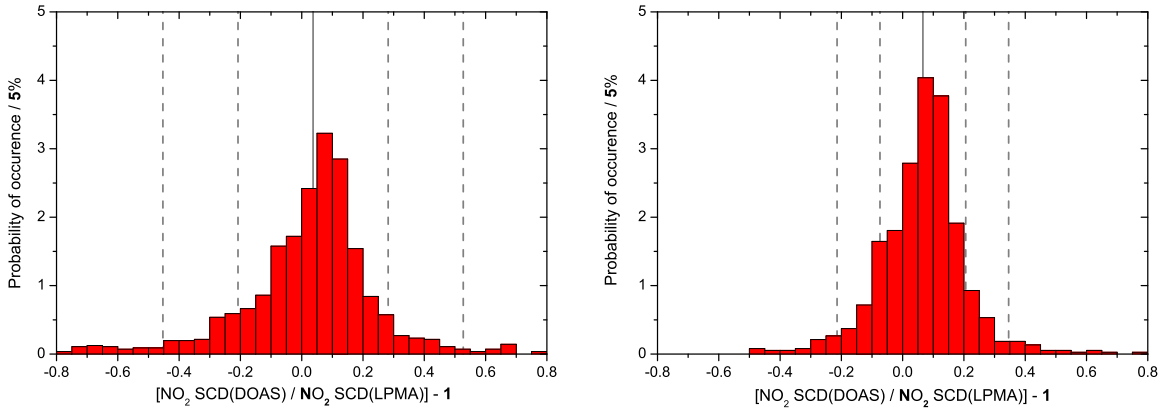

Figure 4.10: Histograms of the relative deviations between NO_2 SCDs retrieved by DOAS and LPMA, i.e. SCD(DOAS) / SCD(LPMA) - 1. The data points are grouped and counted for occurrence in bins of 5% relative deviation. The left panel shows the statistical analysis for all 1116 datapoints (mean: 3.7%, standard deviation: 24.5%), in the right panel all data with error bars larger than 25% are suppressed resulting in 753 datapoints (mean: 6.6%, standard deviation: 14.0%). The mean values are shown as gray solid lines, gray dashed lines correspond to 1-σ and 2-σ.

Fraunhofer offset and in cases where the NO_2 abundances are low by the fitting error (e. g. figure 4.8 f)). DOAS errors typically range between 5% and 10%. Fitting errors are also important for the LPMA retrieval which operates sometimes close to its detection limit (e. g. figure 4.9 a)). Typical error bars of NO_2 SCDs inferred from LPMA measurements range between 10% and 25%.

The NO_2 comparison study is difficult to assess since LPMA SCDs inferred from balloon ascent or descent measurements before 2001 (figures 4.8 a), c), e) and figure 4.8 a)) are very noisy. This is not true for balloon ascent measurements in 2001 and 2003 (figures 4.8 c) and e)), although the abundances of NO_2 along the lines-of-sight are similar as for some of the earlier flights. This is a clear hint, that the pre-flight optical alignment and in-flight stability of the LPMA instrument improved during the suite of balloon flights. Apart from the aforementioned noisy data, the general agreement is on the order of 20%. For the solar occultation measurements at Leon in 1996 (figure 4.8 b)), at Kiruna in 1997 (figure 4.8 d)), at Kiruna in 2001 (figures 4.9 c) and d)), and at Kiruna in 2003 (figure 4.9 f)) the LPMA/DOAS agreement is reasonable, since both measurements mostly lie within the combined error bars. Maximum deviations up to 50% are observed for the solar occultation measurements at Kiruna in 1999 (figure 4.8 f)). In the latter case, the NO_2 abundances are the lowest observed in solar occultation for the ensemble of considered balloon flights and are almost one order of magnitude smaller than those measured during sunset at Kiruna in 2001 (figure 4.9 c)). In addition stratospheric temperatures at Kiruna in 1999 were below 217 K implying an extrapolation of the DOAS SCDs for temperature correction, since the lowest temperature of the absorption cross sections given by Harder et al. (1997) is 217 K. The extrapolation might not reproduce the true atmospheric state.

The statistical analysis of all data (figure 4.10) confirms the large scatter of deviations. The mean deviation is found to 3.7% and the standard deviation of the distribution is 24.5%. Since some of the LPMA NO_2 SCDs are noisy or close to the detection limit, another statistical analysis is performed where all SCDs with errors larger than 25% are removed. Then, the inferred mean deviation is 6.6% and

the spread is 14.0%. Although a grouping of the observed deviations is not as obvious as in the case of O_3, the deduced bias cannot be attributed to parameters independent of the two retrievals. Observations, where DOAS is consistently higher than LPMA (e. g. figures 4.9 b), c), d) and e)) are contrasted by observations where DOAS is lower than LPMA (figure 4.8 d)) and observations, where the deviations change from positive to negative (e. g. figures 4.8 f) and 4.9 f)). Hence, the observed bias depends on the dataset chosen for the statistical analysis and further lies within the typical error bars of the individual measurements. Therefore, as in the case of O_3, a conclusion on deficiencies of spectroscopic parameters is not possible.

4.2 Profile retrieval and comparison of O_3 and NO_2 vertical profiles

The previous section discussed the level of the LPMA/DOAS agreement by comparing the inferred slant column densities of O_3 and NO_2. According to section 3.3 vertical profiles of the respective gases can be retrieved. The concept of averaging kernels gives useful insight into the altitude resolution of the LPMA and the DOAS experiment and their suitability for external comparison studies such as satellite validation. Hence, first the LPMA and the DOAS retrieval of vertical profiles are characterized regarding altitude resolution. Then, the actual vertical profiles of O_3 and NO_2 are directly compared.

4.2.1 Characterization of the LPMA and DOAS profile retrievals

The retrieval of vertical profiles from slant column densities depends on the observation geometry characterized by the weighting function matrix $\mathbf{K}$, on the measurements $\mathbf{y}$ and their errors characterized by the measurement error covariance matrix $\mathbf{S}_\epsilon$ and on the *a priori* profile $\mathbf{x_a}$ and its covariance $\mathbf{S_a}$. In particular, the number of measurements and their errors are different for the LPMA and the DOAS profile retrieval. The averaging kernel matrix $\mathbf{A}$ defined through equation (3.40) and in the case of the MAP retrieval through equation (3.48) provides a means to characterize the impact of these differences on the retrieved trace gas profiles.
Figures 4.11 and 4.12 show O_3 and NO_2 profiles and the corresponding averaging kernels, i. e. the rows of $\mathbf{A}$, for balloon ascent and sunset measurements at Kiruna in August 2001 using the *Maximum a posteriori* retrieval. Balloon ascent and solar occultation measurements represent two different observation geometries since the respective weighting functions are different (section 3.1.4). For comparison trace gas profiles are presented which are retrieved on a 1-km altitude grid and on a 3-km altitude grid. The retrieval with 3-km grid spacing is iterated three times on altitude grids displaced by one kilometer in order to obtain profile points each kilometer. The *a priori* profiles are taken from SLIMCAT model output. The associated *a priori* variances correspond to 30% error.

The retrieval of O_3 vertical profiles from DOAS measurements on the 1-km altitude grid shows well-shaped averaging kernels peaking close to one for altitudes between 15 km and balloon float for both, balloon ascent and sunset observations (figures 4.11 b) and d)). Below 15 km, the averaging kernels get smaller and broader since less and less measurements contribute and since in the case of solar occultation the solar disk produces a larger vertical average. However, profile retrieval is feasible down to 10 km altitude for both observation geometries. The averaging kernels of the LPMA retrieval on the

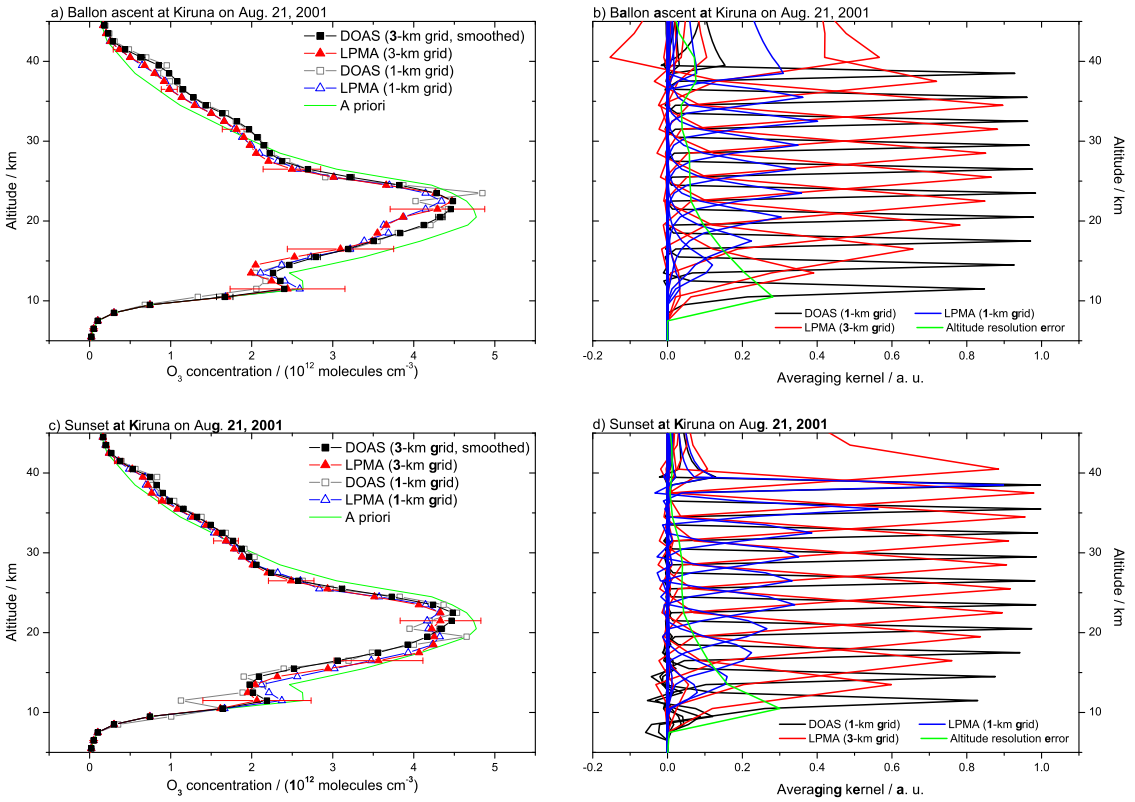

Figure 4.11: O_3 vertical profiles (panels a) and c)) and corresponding averaging kernels (panels b) and d)) for balloon ascent (panels a) and b)) and solar occultation (panels c) and d)) measurements at Kiruna in August 2001. Panels a) and c): The gray open boxes and blue open triangles correspond to trace gas profiles inferred from DOAS and LPMA measurements on a 1-km altitude grid, respectively. Red filled triangles and black filled boxes are LPMA and DOAS profiles retrieved on a 3-km altitude grid where the latter are smoothed by the LPMA averaging kernels. The green line is the *a priori* profile taken from SLIMCAT model output on the day of measurement. For clarity, only selected error bars are shown. Panels b) and d): Selected DOAS averaging kernels corresponding to a 1-km altitude retrieval grid are shown as black lines. Selected LPMA averaging kernels for a 1-km and 3-km altitude grid are shown as blue and red lines, respectively. The green lines illustrates the altitude resolution error.

1-km altitude grid are smaller than 0.4 and much wider than the grid spacing except for altitudes close to balloon float in solar occultation. Below 15 km, there is almost no independent altitude information. On the 3-km grid, the LPMA averaging kernels are well-shaped and reasonably close to one which makes profile retrieval possible between about 12 km and balloon float altitude. For comparison, the DOAS profiles are retrieved on the 3-km altitude grid and smoothed by the LPMA averaging kernels according to equation (3.49). Obviously, filamented structures observed by the high-resolution DOAS profile between 10 km and 25 km cannot be resolved by the LPMA and the smoothed DOAS profiles. The degree of smoothing applied to the DOAS profile is presented in terms of the altitude resolution error, defined in equation (3.50). As expected from the LPMA and DOAS averaging kernels, smoothing is most important in the range between 10 km and 20 km and less important above.

In the case of the NO_2 retrieval, the averaging kernels corresponding to the 1-km DOAS retrieval (figures 4.12 b) and d)) are well shaped in the altitude range between 20 km and balloon float at 38 km

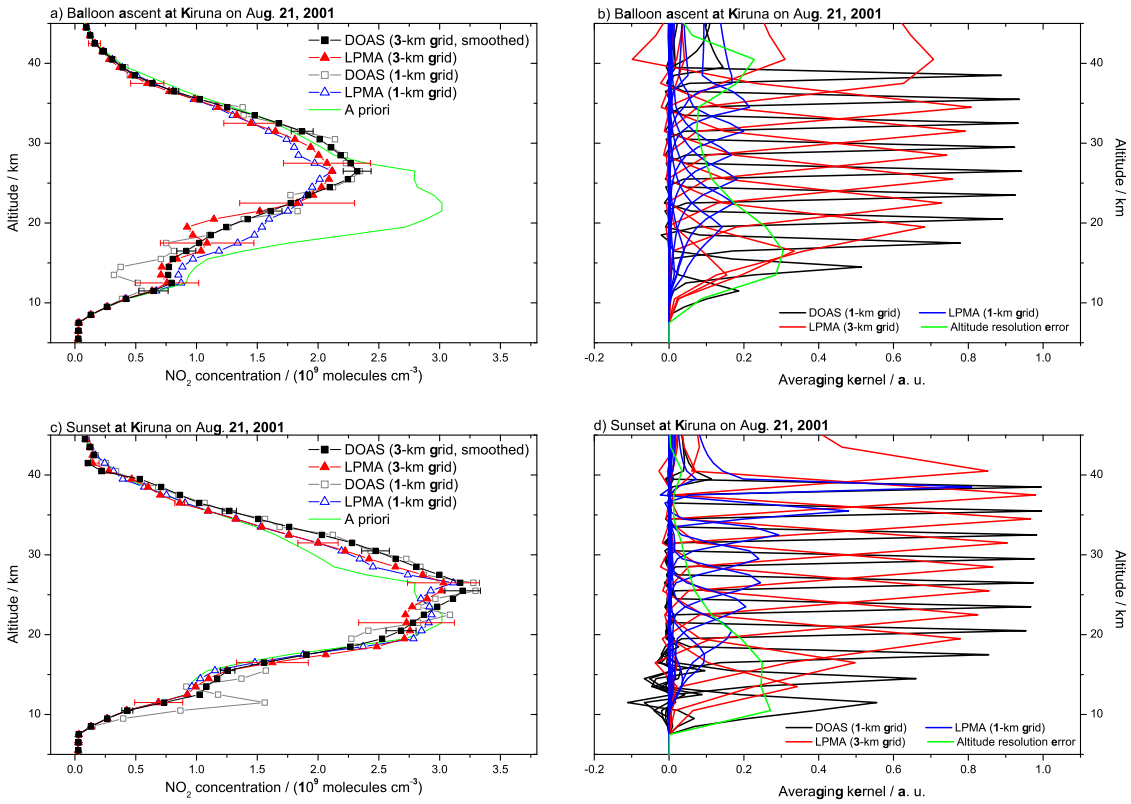

Figure 4.12: NO_2 vertical profiles (panels a) and c)) and corresponding averaging kernels (panels b)and d)) for balloon ascent (panels a) and b)) and solar occultation (panels c) and d)) measurements at Kiruna in August 2001. Panels a) and c): The gray open boxes and blue open triangles correspond to trace gas profiles inferred from DOAS and LPMA measurements on a 1-km altitude grid, respectively. Red filled triangles and black filled boxes are LPMA and DOAS profiles retrieved on a 3-km altitude grid where the latter are smoothed by the LPMA averaging kernels. The green line is the *a priori* profile taken from SLIMCAT model output on the day of measurement. For clarity, only selected error bars are shown. Panels b)and d): Selected DOAS averaging kernels corresponding to a 1-km altitude retrieval grid are shown as black lines. Selected LPMA averaging kernels for a 1-km and 3-km altitude grid are shown as blue and red lines, respectively. The green line illustrates the altitude resolution error.

for both observations geometries. Below 20 km, the averaging kernels get smaller and broader for the same reasons as for the O_3 profile retrieval. The LPMA retrieval on the 1-km altitude grid, however, exhibits averaging kernels significantly smaller than one and wider than the grid spacing. This indicates that the retrieved profile points are not independent. Below 20 km, there is only very little independent altitude information from LPMA measurements and the retrieved profiles are pushed toward the *a priori* as can be seen in figures 4.12 a) and c). The better choice for the LPMA retrieval is the 3-km grid, since there the averaging kernels are closer to one and their width is only slightly larger than the grid spacing in the range between 20 km and balloon float altitude. Between 15 km and 20 km the averaging kernels indicate that altitude information is better exploited than on the 1-km grid which results in profile points less influenced by the *a priori*. In addition, the DOAS profile is retrieved on the 3-km altitude grid and smoothed by the LPMA averaging kernel matrix. The effect of smoothing is most obvious for the balloon ascent measurements (figure 4.12 a)) between 10 km and 20 km altitude where the high resolution DOAS profile is pushed towards the LPMA and *a priori* profile. The latter finding is

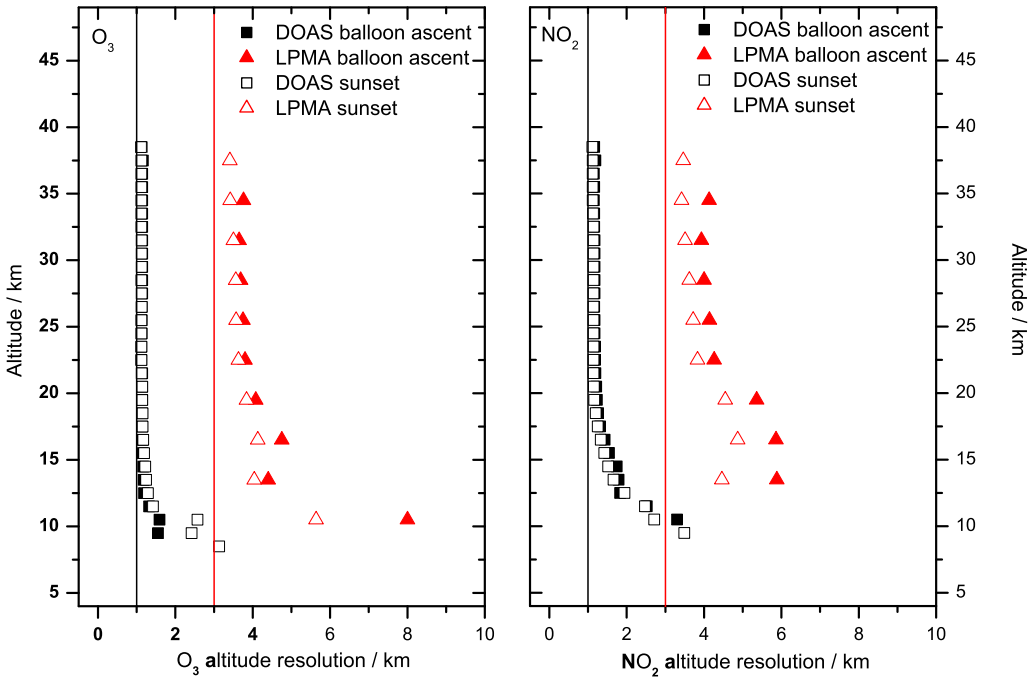

Figure 4.13: Altitude resolution of the O_3 (left panel) and NO_2 (right panel) profile retrieval for measurements at Kiruna in August 2001. Altitude resolution inferred from DOAS averaging kernels on a 1-km retrieval grid are shown as black filled and black open boxes for balloon ascent and solar occultation, respectively. Red filled and open triangles correspond to LPMA profiles on a 3-km grid inferred from balloon ascent and solar occultation measurements, respectively. The black and red lines at 1 km and 3 km indicate the spacings of the retrieval grids. In cases where the averaging kernels are strongly asymmetric and determination of the FWHM is ambiguous, data points are suppressed.

supported by the altitude resolution error which is largest in the altitude range below 20 km.

Following the detailed findings above, profile retrieval from DOAS and LPMA measurements can be performed from balloon float altitude down to 10 km to 15 km. Above balloon float altitude the weighting functions are not suitable for profile retrieval. As pointed out in section 3.3, the width (FWHM) of the averaging kernels is a measure for the altitude resolution of the retrieved profiles. Figure 4.13 illustrates the corresponding altitude resolution for the DOAS and LPMA O_3 and NO_2 profile retrievals.
Typically, the DOAS retrieval exhibits an altitude resolution of about 1 km or better between balloon float altitude and 20 km. Evidently, resolutions better than 1 km cannot be obtained when using a 1-km retrieval grid. Below 20 km altitude resolution decreases to 3 km and 4 km at 10 km altitude. The decrease in altitude resolution at low altitudes is due to the smaller number of contributing measurements, the larger measurement errors and in the case of solar occultation increasing vertical averaging due to the finite effective field-of-view. For NO_2, altitude resolution is slightly worse than for O_3 since NO_2 SCDs exhibit larger error bars. LPMA O_3 and NO_2 profiles retrieved on a 3-km grid have

3 km to 4 km altitude resolution between balloon float altitude and 20 km for both gases. Below, altitude resolution decreases for the same reasons as for the DOAS retrieval. Typically, LPMA solar occultation measurements have a slightly better altitude resolution than measurements during balloon ascent, mainly since the weighting functions in solar occultation are sharply peaked and hence better suited for profile retrieval. Due to smaller measurement errors, O_3 profiles can be retrieved with better altitude resolution than NO_2 profiles. Comparing the LPMA and DOAS profile retrieval, the latter exhibits superior altitude resolution due to the larger number of measurements contributing to profile retrieval and the smaller measurement errors. In solar occultation, the smaller field-of-view of the LPMA instrument partly compensates these deficiencies compared to DOAS measurements.

It has to be pointed out that the details of the above findings are true for the chosen example, only. The general approach, however, can be applied to each balloon flight. During the balloon flight from Kiruna in 2001, considered here, the balloon ascended to about 38 km altitude. Sensitivity of solar occultation measurements to the lower stratosphere is better for balloon flights with lower float altitude, since the effective field-of-view produces an average over a smaller altitude range. In addition, measurement errors are specific to each balloon flight and altitude resolution can vary accordingly. An example of the above analysis for a flight to about 30 km float altitude can be found in Butz et al. (2006) and section 5.4.

4.2.2 Comparison of vertical profiles

The O_3 and NO_2 SCDs presented in figures 4.5 through 4.9 are inverted to vertical profiles using the MAP approach. Trace gas concentrations as well as volume mixing ratios are shown as a function of altitude in figures 4.14 through 4.17. The retrieved profiles are presented in the altitude range where the corresponding averaging kernels are suitable for profile retrieval as described in detail in the previous section. The *a priori* profiles are taken from SLIMCAT model output or climatological data as used by Payan (1996) and Dufour (2005). The associated *a priori* covariance matrix is chosen diagonal with variances corresponding to 30% error of the *a priori*. While LPMA profiles are retrieved on a 3-km altitude grid, DOAS profiles are retrieved on both, a 1-km and a 3-km altitude grid. The DOAS profiles on the coarser grid are smoothed to match the altitude resolution of the LPMA measurements. For comparison, O_3 mixing ratios are shown which are measured by an *in situ* ozone-sonde deployed aboard the gondola or launched shortly after the LPMA/DOAS payload from the respective ground station.

Obviously, the inferred O_3 vertical profiles reproduce the general agreement of the LPMA and DOAS O_3 SCDs presented above. In most cases the LPMA and the smoothed DOAS profiles lie within the combined error bars and roughly agree within 10%. The offsets between LPMA and DOAS O_3 SCDs observed for balloon ascent at Kiruna in 2001 and for balloon descent at Gap in 1999 are mapped into discrepancies amounting up to 30% in the upper most part of the vertical profiles (figures 4.15 a), b), c) and d)). The lower part of the corresponding profiles is almost unaffected since the offset between the SCDs is mainly attributed to altitudes above balloon float. Systematic discrepancies affecting the entire profile occur where the underlying SCDs do not differ by a constant offset, but show an increasing or decreasing deviation with time, e. g. during sunset at Leon in 1996 and at Kiruna in 1997. There, a bias of up to 25% can be detected between the LPMA and DOAS O_3 profiles. Smoothing the DOAS profiles

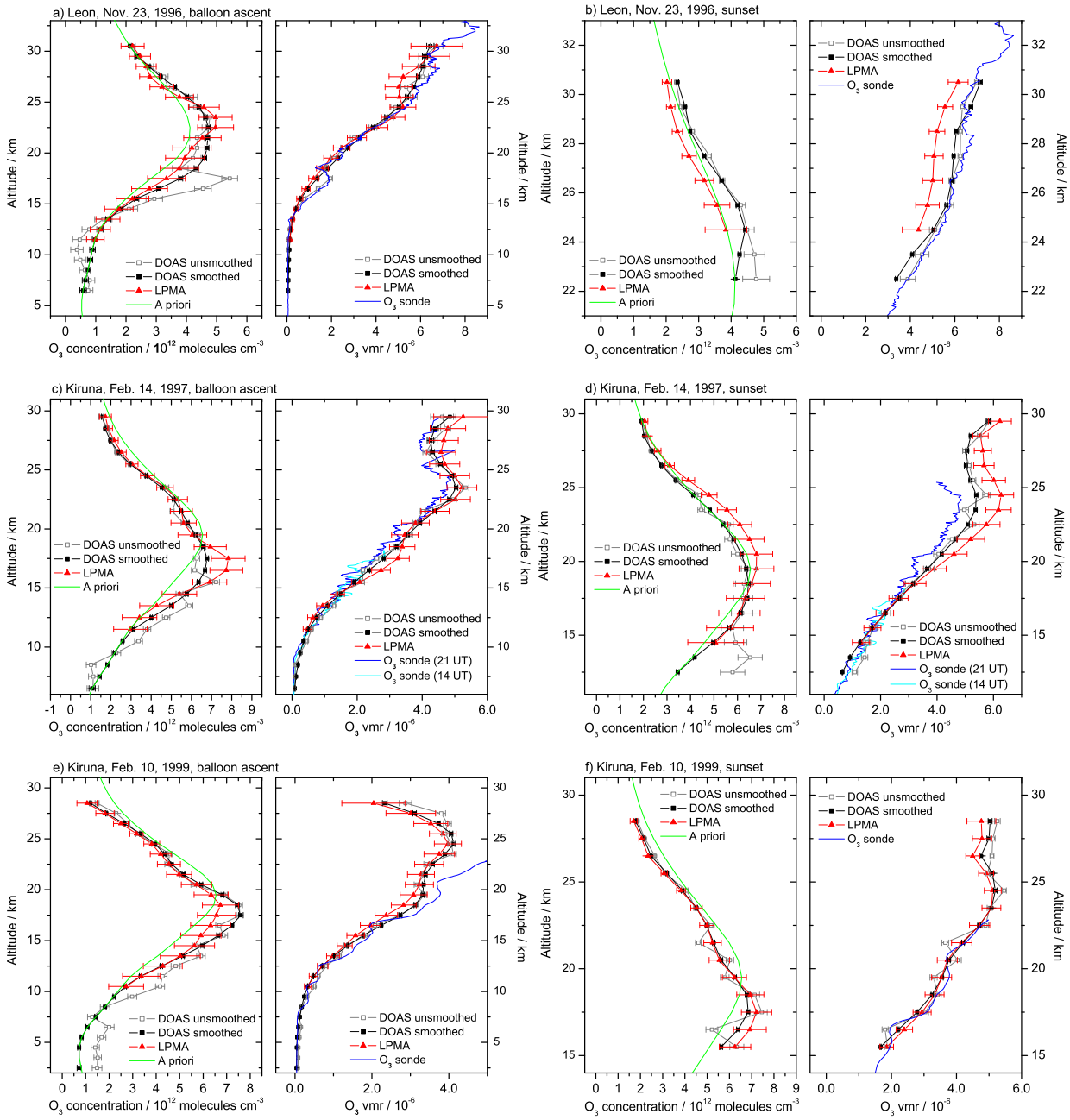

Figure 4.14: Vertical profiles of O_3 retrieved from LPMA (red triangles) and DOAS (black filled boxes and gray open boxes) measurements at Leon on November 23, 1996, during balloon ascent (panel a)) and sunset (panel b)), at Kiruna on February 14, 1997, during balloon ascent (panel c)) and sunset (panel d)) and at Kiruna on February 10, 1999, during ballon ascent (panel e)) and sunset (panel f)). Each panel consists of two sub-panels showing the O_3 concentration and the O_3 volume mixing ratio on the left and on the right, respectively. The gray open boxes correspond to DOAS data retrieved on a 1-km altitude grid while the black filled boxes are DOAS data retrieved on a 3-km grid and smoothed to match the coarser altitude resolution of the LPMA measurements. The green line indicates the *a priori*. The blue line represents the O_3 profiles *in situ* measured by an electrochemical concentration cell (ECC) ozone sonde deployed onboard the LPMA/DOAS gondola or launched shortly after.

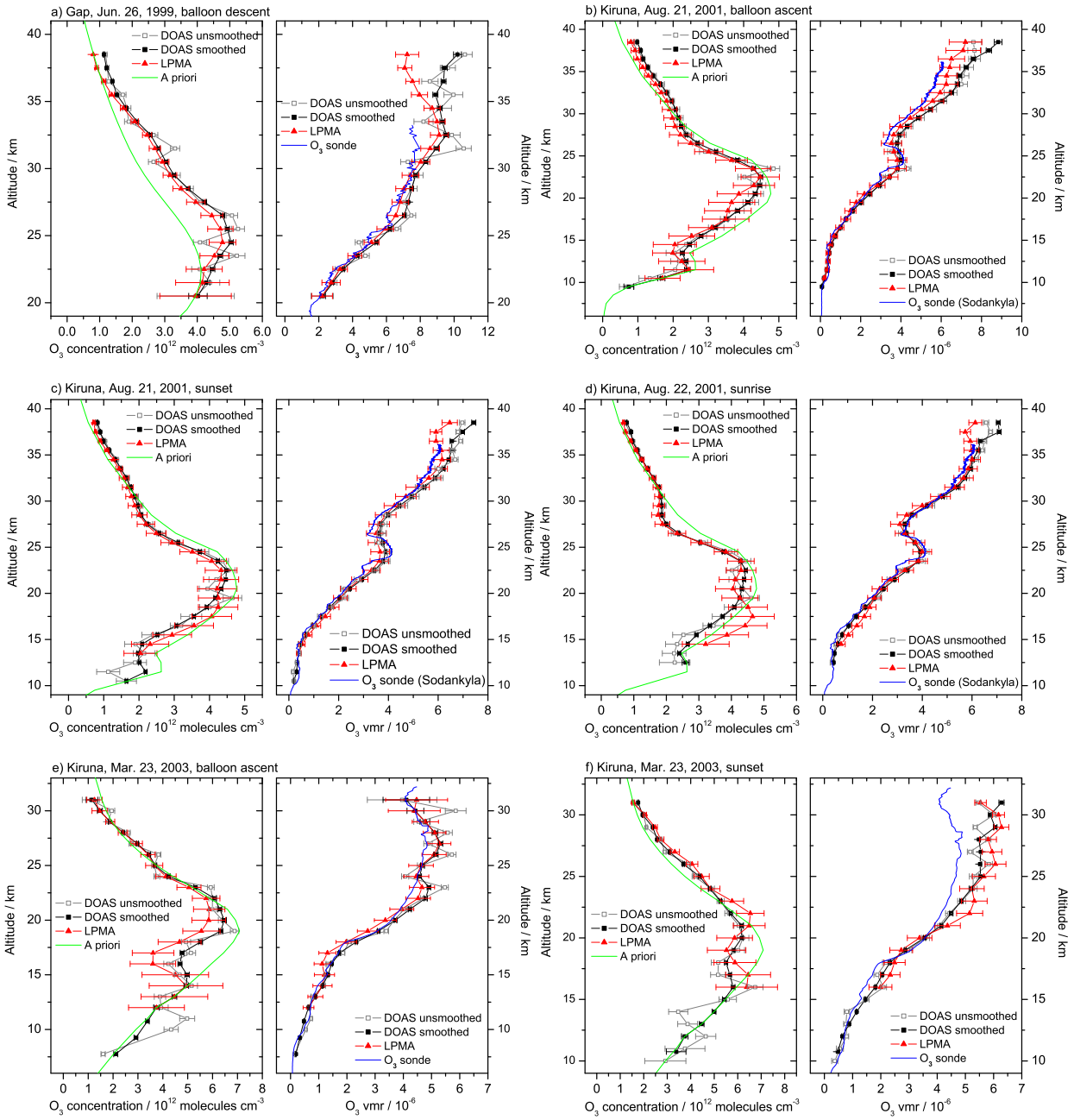

Figure 4.15: Vertical profiles of O_3 retrieved from LPMA (red triangles) and DOAS (black filled boxes and gray open boxes) measurements at Gap on June 25, 1999, during balloon descent (panel a)), at Kiruna on August 21 and 22, 2001 during balloon ascent (panel b)), sunset (panel c)) and sunrise (panel d)) and at Kiruna on March 23, 2003, during balloon ascent (panel e)) and sunset (panel f)). Each panel consists of two sub-panels showing the O_3 concentration and the O_3 volume mixing ratio on the left and on the right, respectively. The gray open boxes correspond to DOAS data retrieved on a 1-km altitude grid while the black filled boxes are DOAS data retrieved on a 3-km grid and smoothed to match the coarser altitude resolution of the LPMA measurements. The green line indicates the *a priori*. The blue line represents the O_3 profiles *in situ* measured by an electrochemical concentration cell (ECC) ozone sonde deployed onboard the LPMA/DOAS gondola or launched shortly after. For the flight from Kiruna in 2001, panels b) through d), the O_3 sonde is launched at Sodankyla, Finland.

to account for the differing altitude resolution of LPMA is clearly important and improves the agreement between the two data sets. In contrast to the DOAS retrieval, LPMA is not able to detect filamented structures of the O_3 profile in the lower stratosphere (e. g. figures 4.14 a), c) and e)). Smoothing the DOAS retrieval simulates the coarser sensitivity of the LPMA retrieval and improves the agreement. These filaments in the lower stratosphere are real since they are simultaneously observed by the *in situ* O_3 sonde. This can be seen for balloon ascent at Leon in 1996 (figure 4.14 a)) where the filament at about 17 km altitude is present in both, the *in situ* O_3 sonde and DOAS high-resolution mixing ratio profile.
However, a caveat is in order when comparing the *in situ* O_3 sonde and remote sensing LPMA/DOAS data, since the sampled air masses are not identical. In particular, close to the polar vortex the gradient of the O_3 concentration can be large on small spatial scales and the horizontal average from the balloon to the Sun observed by the LPMA/DOAS instruments can differ significantly from the *in situ* probed O_3 concentration close to the balloon. In most cases, the LPMA/DOAS agreement with the O_3 sonde data is good but no conclusion can be drawn on whether the DOAS or the LPMA data agree better with the *in situ* measured profiles. Above 20 km, there is a tendency of the sonde data to underestimate the LPMA/DOAS profiles (e. g. figures 4.14 c), d) and figure 4.15 c)). A quantitative conclusion, however, is not possible remembering the unaccounted impact of horizontal inhomogeneities. In contrast to the tentative underestimation of the LPMA/DOAS measurements by the *in situ* sondes observed here, Johnson et al. (2002) detected a 10% - 15% overestimation of the O_3 concentration at 30 km when using the standard 1% potassium iodide solution for the *in situ* measurements.
The impact of horizontally inhomogeneous air masses can also be seen when comparing O_3 profiles inferred from balloon ascent and solar occultation measurements of the same flight. Since the photochemical variation of O_3 on a diurnal timescale is weak profiles measured within a single balloon flight should be identical. This is not true e. g. for the balloon flights from Kiruna in 1999 and 2003 (figures 4.14 e) and f) and figures 4.15 e) and f)), where the O_3 profiles inferred from sunset measurements are significantly larger than those inferred from balloon ascent.

The NO_2 vertical profiles inferred from LPMA and DOAS measurements mostly agree within 20% or better. Large differences can be found for the flight from Kiruna in 1999 (figure 4.16 e) and f)) where the NO_2 abundances are the lowest among the ensemble of balloon flights presented here. The LPMA profile retrieved from balloon ascent measurements (figure 4.16 e)) is unreasonable and is heavily impacted by the noise of the underlying SCDs (figure 4.8 e)) which is reflected by the large error bars. The considerable effect resulting from the smoothing of the DOAS profile by the LPMA averaging kernels is an indication, that the averaging kernels of the LPMA retrieval are hardly suitable for profile retrieval and allow for a large influence of the *a priori*. In solar occultation (figure 4.16 f)) the retrieved LPMA profile is of reasonable shape and agreement with the DOAS profile is on the order of 50% below 20 km and better above. Systematic discrepancies follow the observations discussed in section 4.1.3. LPMA underestimates the DOAS profiles in solar occultation during the flights from Kiruna in 2001 (figures 4.17 c) and d)), and Leon in 1996 (figure 4.16 b)) while it overestimates the DOAS retrieval in solar occultation at Kiruna in 1997, 1999 and 2003 (figures 4.16 d) and e) and figure 4.17 e)). No clear trend is inferable.
As for the O_3 retrieval, LPMA is not able to detect trace gas filaments in the lower stratosphere and hence adjusting the DOAS profiles to the altitude resolution of LPMA is important for comparison purposes. The filaments observed by the DOAS measurements at Gap in 1999 (figure 4.17 a)), and at

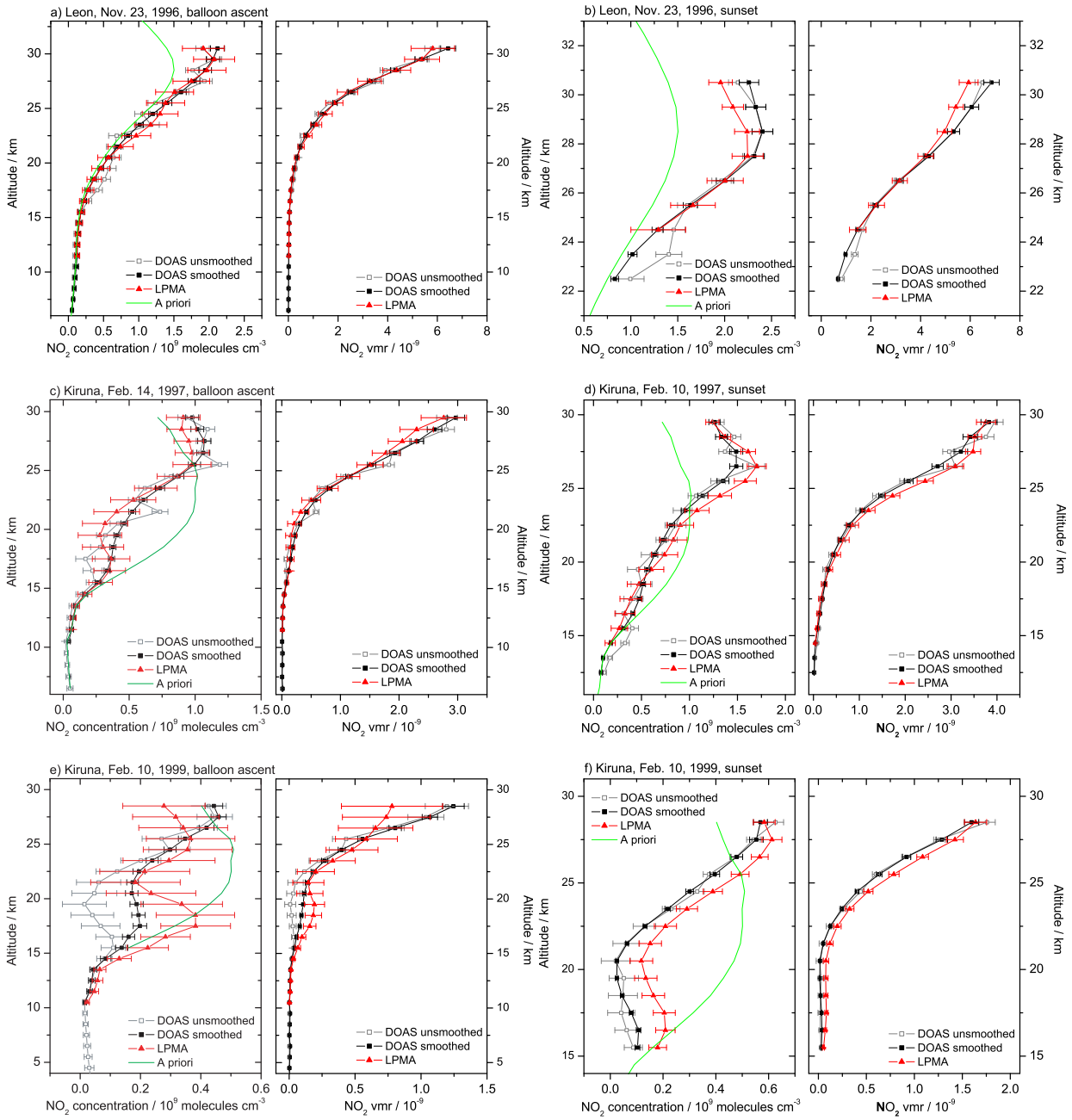

Figure 4.16: Vertical profiles of NO_2 retrieved from LPMA (red triangles) and DOAS (black filled boxes and gray open boxes) measurements at Leon on November 23, 1996, during balloon ascent (panel a)) and sunset (panel b)), at Kiruna on February 14, 1997, during balloon ascent (panel c)) and sunset (panel d)) and at Kiruna on February 10, 1999, during ballon ascent (panel e)) and sunset (panel f)). Each panel consists of two sub-panels showing the O_3 concentration and the O_3 volume mixing ratio on the left and on the right, respectively. The gray open boxes correspond to DOAS data retrieved on a 1-km altitude grid while the black filled boxes are DOAS data retrieved on a 3-km grid and smoothed to match the coarser altitude resolution of the LPMA measurements.

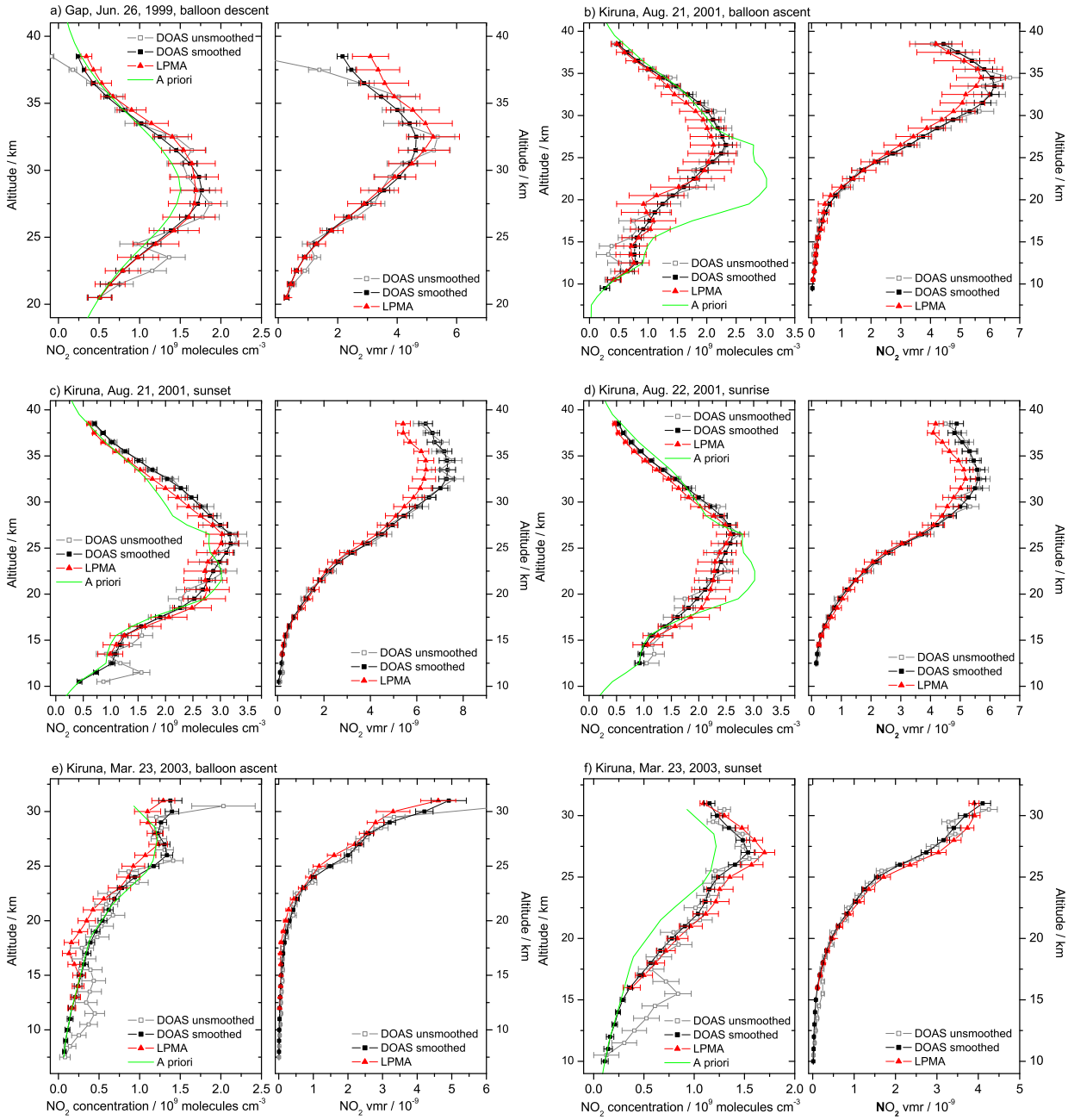

Figure 4.17: Vertical profiles of NO_2 retrieved from LPMA (red triangles) and DOAS (black filled boxes and gray open boxes) measurements at Gap on June 25, 1999, during balloon descent (panel a)), at Kiruna on August 21 and 22, 2001 during balloon ascent (panel b)), sunset (panel c)) and sunrise (panel d)) and at Kiruna on March 23, 2003, during balloon ascent (panel e)) and sunset (panel f)). Each panel consists of two sub-panels showing the O_3 concentration and the O_3 volume mixing ratio on the left and on the right, respectively. The gray open boxes correspond to DOAS data retrieved on a 1-km altitude grid while the black filled boxes are DOAS data retrieved on a 3-km grid and smoothed to match the coarser altitude resolution of the LPMA measurements. The green line indicates the *a priori*.

Kiruna in 2003 (figures 4.16 e) and f)), are not present in the LPMA profiles. Accordingly, the smoothed DOAS profiles are pushed towards the *a priori* and the LPMA data.

4.3 Conclusion on the LPMA/DOAS comparison

Sections 4.1.3 and 4.2.2 presented O_3 and NO_2 abundances inferred from LPMA/DOAS measurements in the IR and visible spectral ranges. The datasets agree roughly within $\pm 10\%$ for O_3 and $\pm 20\%$ for NO_2. This finding represents a major improvement compared to previous comparison studies such as in Bösch (2002). The progress is mainly due to the newly implemented LPMA multifit-retrieval (Dufour, 2005), that minimizes the correlations between the retrieved trace gases and the parameters of the instrument function and hence significantly improves the LPMA/DOAS agreement. The DOAS retrieval is complemented by an empirical correction term for the temperature dependence of the NO_2 absorption cross section which adjusts the measured SCDs to the observed atmospheric conditions. Finally, when comparing the retrieved trace gas profiles it is found important to account for the different altitude resolution of the instruments in order to compare like with like.

Still, sizeable discrepancies remain which can be due to instrumental and retrieval related shortcomings of either technique. In general, the retrieval of trace gas SCDs from DOAS measurements yields smaller errors than the spectral retrieval from LPMA observations. In the visible spectral range where the Sun's intensity peaks, typical integration times for individual spectra are less than 1 s, whereas in the IR it takes about 50 s to record a single interferogram. Hence, the DOAS instruments sample the atmosphere with a much higher rate than the LPMA FT-IR. Taking into account the errors of the considered trace gas retrievals, it is evident that altitude resolution is significantly better for the DOAS observations. In solar occultation geometry, the smaller field-of-view of the FT-IR (FOV $\simeq 0.2^\circ$) partly compensates deficiencies of the LPMA experiment concerning altitude sampling compared to the DOAS measurements (effective FOV $\simeq 0.53^\circ$). On the other hand, the small field-of-view of the FT-IR renders the intensity of the measured interferograms very sensitive to small pointing errors of the sun-tracker as the solar irradiance is not uniform across the solar disk (Bösch, 2002). According to figures 4.7 and 4.10 LPMA O_3 and NO_2 SCDs tend to be low biased with respect to the corresponding DOAS SCDs. For both trace gases the typical errors of individual measurements are larger than the bias. Errors of the absorption cross sections with respect to magnitude or pressure and temperature dependencies would directly cause a bias. The DOAS retrieval of NO_2 might exhibit shortcomings when accounting for the temperature dependence of the NO_2 absorption cross section, since the interpolation is performed linearly using four reference temperatures, only. In the IR spectral range, errors in the spectroscopic parameters and the ambient temperature and pressure data propagate into the shape of the absorption lines causing systematic errors of the retrieved trace gas SCDs. Correlations between the various fitting parameters considered for the spectral retrieval are minimized but, still, might cause small unaccounted systematic errors in both data sets.

Summing up the arguments, the O_3 and NO_2 stratospheric profiles inferred from DOAS measurements appear to be more accurate and better suited for comparison studies with other instruments than the LPMA data. In particular, this is true for satellite validation since the DOAS profiles exhibit smaller error bars and better altitude resolution than the LPMA profiles. Nonetheless, stratospheric FT-IR measurements are indispensable since the majority of trace gases important for a comprehensive understanding of stratospheric photochemistry do not absorb in the UV/visible.

Chapter 5

Validation of SCIAMACHY O_3 and NO_2 profiles

The previous chapter discussed the agreement between the balloon borne measurements of O_3 and NO_2 of the LPMA and DOAS instruments and the implications for external comparison studies. This chapter compares the balloon borne profiles to observations of the SCanning Imaging Absorption spectroMeter for Atmospheric CHartographY (SCIAMACHY) instrument aboard the Envisat satellite operated by the European Space Agency (ESA). A comparison scheme is developed which accounts for the spatial and temporal mismatch between the balloon and satellite borne measurements by identifying coincident air masses through an air mass trajectory model. The differing photochemical conditions are considered by a photochemical model of the stratosphere which is run along the temporal history of the air masses actually observed. Finally, the properly inferred vertical profiles are compared and discussed with respect to accuracy and shortcomings of the satellite retrievals. Figure 5.1 shows a schematic drawing of the validation strategy.

5.1 The SCIAMACHY instrument

In March 2002, Envisat was launched into a Sun synchronous orbit with an equator crossing time at 10:00 LT. Together with MIPAS and GOMOS, SCIAMACHY is one of its three atmospheric chemistry instruments. A detailed description of the instrument can be found in Burrows et al. (1995) and Bovensmann (1999). Here, O_3 and NO_2 stratospheric profiles are presented which are inferred using algorithms developed at the Institute for Environmental Physics of the Universities of Bremen (IUP-Bremen) and Heidelberg (IUP-Heidelberg) and at the Harvard-Smithsonian Center for Astrophysics (Harvard). No official ESA products are available for the data considered here.

SCIAMACHY measures the absorption, reflection and scattering characteristics of the atmosphere by monitoring the extraterrestrial solar irradiance and the upwelling radiance observed in different viewing geometries, depicted in figure 5.2. In solar occultation measurement mode, SCIAMACHY measures the direct solar irradiance during sunrise similar to the balloon borne LPMA/DOAS observations. In addition, the moon can be used as light source to perform lunar occultation measurements. In nadir

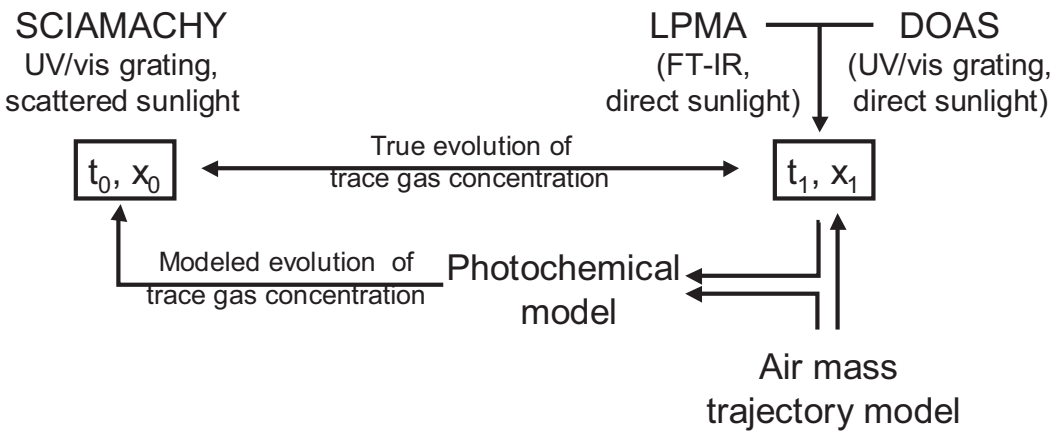

Figure 5.1: Schematic drawing of the presented comparison and validation strategy. SCIAMACHY observations are conducted at time t_0 and location x_0. Prior to the balloon flight dedicated to SCIAMACHY validation, the air mass trajectory model is used to optimize the time t_1 and location x_1 of the LPMA/DOAS balloon borne observations, e. g. by optimizing the launch time of the balloon. After the balloon flight, the trajectory model calculates the air mass history in order to identify satellite measurements which actually sampled the same air masses as the balloon borne instruments. In a Lagrangian approach the illumination history of the coincident air masses is fed into a photochemical model to reproduce the evolution of the considered trace gases between satellite and balloon borne observations as realistically as possible. The modeled evolution of the trace gas history is used to appropriately scale the balloon borne data to the photochemical conditions of the satellite measurements.

viewing geometry, SCIAMACHY observes sunlight scattered by the Earth's atmosphere or surface beneath the satellite. A scanning mirror in the nadir entrance optics provides a typical spatial resolution of 30 km along the track of the satellite and 240 km across the track. Here, data are presented which are inferred from measurements in the limb viewing geometry, where the instrument observes scattered sunlight tangentially to the Earth's surface in flight direction of the satellite. The limb entrance optics scans the Earth's atmosphere vertically in steps of approximately 3.3 km from the ground to about 100 km tangent height. Horizontal scanning covers about 960 km at each tangent point. While the nadir measurements provide mainly total columns of the observed trace gases, the limb measurements allow for the derivation of vertical trace gas profiles. The measurement sequence is designed to observe the same air column subsequently in limb and in nadir viewing geoemtry. In principle, this allows to discriminate between the total atmospheric trace gas column inferred from nadir measurements and the total stratospheric column obtained from integrated stratospheric profiles and yields the tropospheric column amounts of the considered trace gases (Bovensmann, 1999; Sioris et al., 2004).

SCIAMACHY is a dispersive spectrometer which covers the entire spectral range from 220 nm to 2380 nm in eight spectral channels. The spectral resolution of the spectrometer varies between 0.24 nm and 1.48 nm depending on channel number. The spectral imaging is designed to be stable regarding spectral shifts to within 1/50 of a detector pixel, which requires a temperature stability of the spectrometer of better than 250 mK over one orbit. The covered spectral ranges allow for the retrieval of the atmospheric abundances of various trace gases, e. g. O_3, NO_2, NO_3, BrO, OClO, O_4, SO_2, H_2CO, CO, CO_2, N_2O and CH_4. In addition, the measured spectra are radiometrically calibrated to high accuracy (2% to 4%) by on-ground and in-flight radiometric calibration procedures. Contributions of the LPMA/DOAS instruments to the validation of the solar irradiance measured by SCIAMACHY are

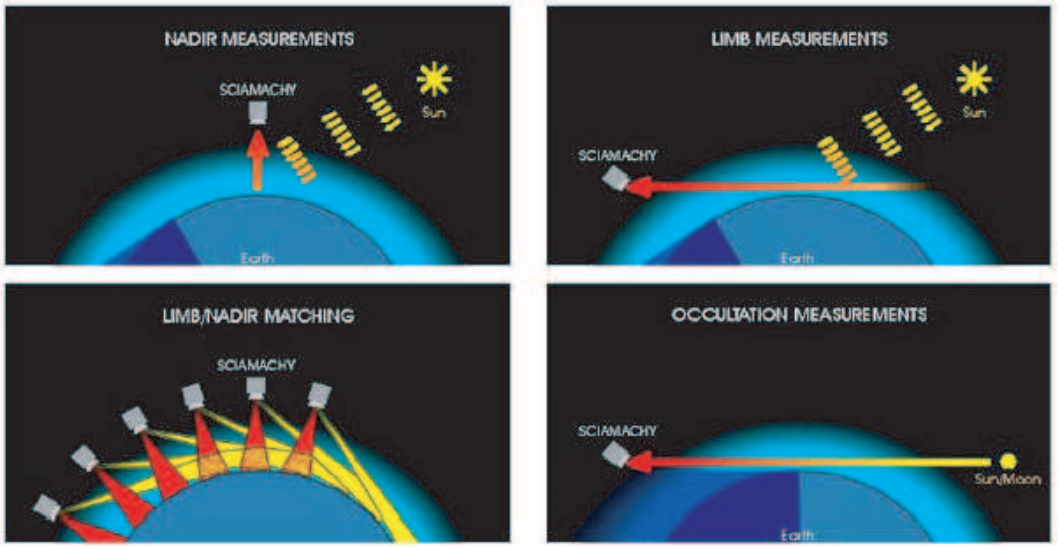

Figure 5.2: Viewing geometries of SCIAMACHY adopted from Beirle (2005). SCIAMACHY is able to measure scattered or direct sun- or moonlight in nadir (upper left panel), limb (upper right panel) and solar/lunar occultation (lower right panel) viewing geometry. The measurement sequence is designed to allow for limb/nadir matching (lower left panel), i. e. the same air column can be observed subsequently in limb and nadir mode.

reported elsewhere (Gurlit et al., 2005; Lindner, 2005).
O_3 and NO_2 trace gas retrievals applied to SCIAMACHY limb spectra of scattered sunlight are by courtesy of Christian von Savigny (IUP-Bremen), Alexei Rozanov (IUP-Bremen), Christopher Sioris (Harvard), Sven Kühl (IUP-Heidelberg) and Janis Pukite (IUP-Heidelberg). A short description of the relevant retrieval characteristics can be found in Butz et al. (2006).

5.2 Air mass trajectory modeling

Balloon borne measurements exhibit several inherent constraints with respect to time and location of the balloon launch. Balloon launches are possible at a few sites around the world, only. The launching possibility depends on the local surface weather conditions and the balloon's trajectory is determined by the tropospheric and stratospheric wind fields. Furthermore, the LPMA/DOAS payload is supposed to be launched at a time close to local sunset or sunrise as LPMA/DOAS performs measurements during solar occultation. In practice, these constraints make it difficult to get a direct temporal and spatial coincidence with individual satellite measurements such as SCIAMACHY limb observations. In part, the use of air mass trajectory models can help to overcome the shortcomings in balloon borne satellite validation (Bacmeister et al., 1999; Lu et al., 2000; Danilin et al., 2002b,a).
Within the framework of the Envisat/SCIAMACHY validation, an air mass trajectory model is operated by Katja Grunow at FU Berlin which uses operational ECMWF analyses and forecasts given every 6 h on a $2.5° \times 2.5°$ latitude/longitude grid (Langematz et al., 1987). Forward and backward trajectories are calculated on isentropic levels from the surface up to 1600 K potential temperature with interpolation between the levels. The internal time step is 10 minutes and the diabatic and climatological heating rates are based on Newtonian cooling. The results (trajectory points) are stored for each hour.

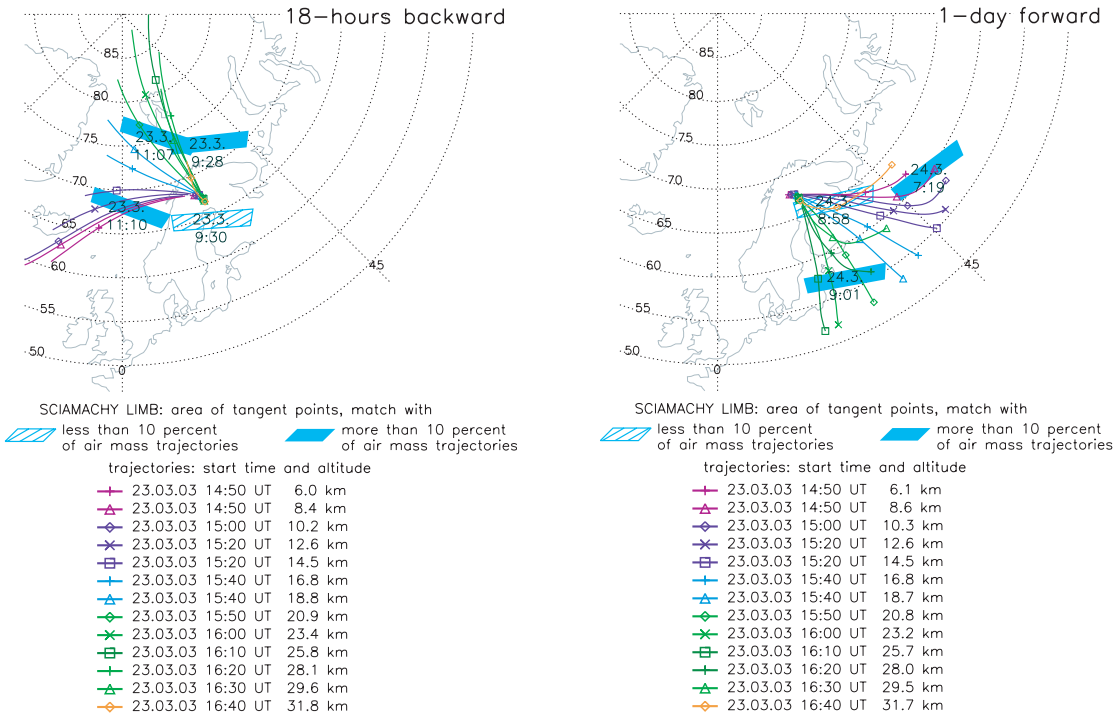

Figure 5.3: Air mass trajectories modeled 18 hours backward (left panel) and 24 hours forward (right panel) in time for the balloon ascent measurements of the LPMA/DOAS payload at Kiruna on March 23, 2003. The trajectories are color-coded according to their starting altitude as indicated in the legend. A symbol is plotted every 12 hour interval. The areas covered by the tangent points of SCIAMACHY limb observations is projected onto the Earth's surface and illustrated as blue rectangles. Filled rectangles correspond to SCIAMACHY limb observations for which more than 10% of the calculated air masses are coincident with the LPMA/DOAS measurements. The shaded rectangles represent SCIAMACHY limb observations for which less than 10% of the calculated air masses are coincident with the LPMA/DOAS measurements. The time and date of the satellite measurements is given next to the rectangles. Figure by courtesy of Katja Grunow (FU Berlin).

The modeled air mass trajectories are used for pre-flight planning of the actual date and time of the balloon launch as well as for post-flight analysis of the air mass history concerning the spatial and temporal mismatch between the air masses sampled by SCIAMACHY and the LPMA/DOAS instruments. For that purposes, backward and forward trajectories are started at the balloon measurement locations which are represented by the position of the balloon for balloon ascent and by the tangent points for solar occultation. For post-flight analysis air mass trajectories are calculated for up to 10 days forward and backward in time, but for balloon flight planning purposes the time range is limited by the available ECMWF forecasts: the latest analysis is from 12:00 UT the day before, forecasts are available every 6 h and up to 72 h into the future.

The actual geolocations of Envisat/SCIAMACHY observations are provided by the SCIAMACHY Operational Support Team (SOST) through its website (http://atmos.af.op.dlr.de/projects/scops/). For each Envisat orbit, overpass time, geolocation and detailed measurement specifications (e.g. swath, measurement duration, ground pixel size) can be downloaded. For the air mass trajectory based matching technique only the area covered by the tangent points of SCIAMACHY limb observations is considered.

This information is used to find satellite measurement points along the individual air mass trajectories for which the spatial and temporal mismatch is as small as possible with respect to the air masses probed by LPMA/DOAS. The match criteria are chosen based on the experience of the ozone Match experiment (von der Gathen et al., 1995). The maximum mismatch in time between the satellite observation and the air mass trajectories started at the balloon observation is one hour and the maximum mismatch in space is 500 km with respect to the center of the SCIAMACHY limb ground pixel. In cases where no Envisat/SCIAMACHY observations satisfy these limits, the distance criterion is weakened to a maximum spatial mismatch of 1000 km.
Figure 5.3 illustrates the modeled air mass trajectories and the corresponding SCIAMACHY observations coincident with the LPMA/DOAS measurements for the balloon flight at Kiruna in March 2003. For the backward calculations a grouping of the trajectories is observed. Below 15 km, coincidences between air masses probed simultaneously by SCIAMACHY and LPMA/DOAS are found for the limb scan on March 23, 2003, at 11:10 UT. Above 20 km, the most favorable limb scan for validation took place on the same day at 11:07 UT. The forward calculations indicate that the SCIAMACHY limb scan on March 24, 2003, at 9:01 UT is most suitable for validation. Since the sensitivity of the SCIAMACHY limb measurements to altitudes below 20 km is limited, those limb scans are typically chosen for validation which exhibit many coincidences in the altitude range between 20 km and 30 km.

5.3 Photochemical modeling

The previous section discusses how to identify air masses which are sampled by both, the satellite and balloon borne instruments. The example in figure 5.3 shows that for a balloon flight conducted in the evening close to sunset typical satellite coincidences are found in the morning before and after the balloon launch. That means, even if identical air masses are sampled, they are not probed at the same time and hence photochemical processing can occur between the satellite and the balloon borne measurements. For species which are photochemical inert on timescales of one day photochemical processing is negligible as can be seen from the upper left panel of figure 5.4 where the diurnal variation of the O_3 concentration is shown as a function of altitude. The concentration of O_3 is essentially constant over one day and hence no photochemical correction is necessary when SCIAMACHY performs its measurements several hours before or after the LPMA/DOAS balloon flight. The diurnal variation of NO_2 however is strong due to the photolysis of N_2O_5 during the day and its built-up from NO_2 during the night as illustrated in the lower left panel of figure 5.4. Hence, air masses sampled in the morning before the balloon launch undergo significant photochemical processing until they are probed by the LPMA/DOAS instruments in the evening and a photochemical correction is necessary when validating photochemically active species like NO_2 (Bracher et al., 2005).
A further impact of photochemistry on remote-sensing atmospheric measurements is illustrated in the upper right and lower right panel of figure 5.4 for O_3 and NO_2, respectively. In principle, each point on the line-of-sight from the remote-sensing instrument to the Sun can be identified with a unique local solar zenith angle and hence unique insolation and local photochemical conditions. The observed spectrum is a composite of all photochemical conditions along the line-of-sight. The lines-of-sight of a balloon borne solar occultation measurement, shown in the right panels of figure 5.4, cross the altitude layers below the balloon twice and above the balloon once. By definition the tangent point corresponds to a local SZA of 90°, points on the line-of-sight which are closer to the balloon than the

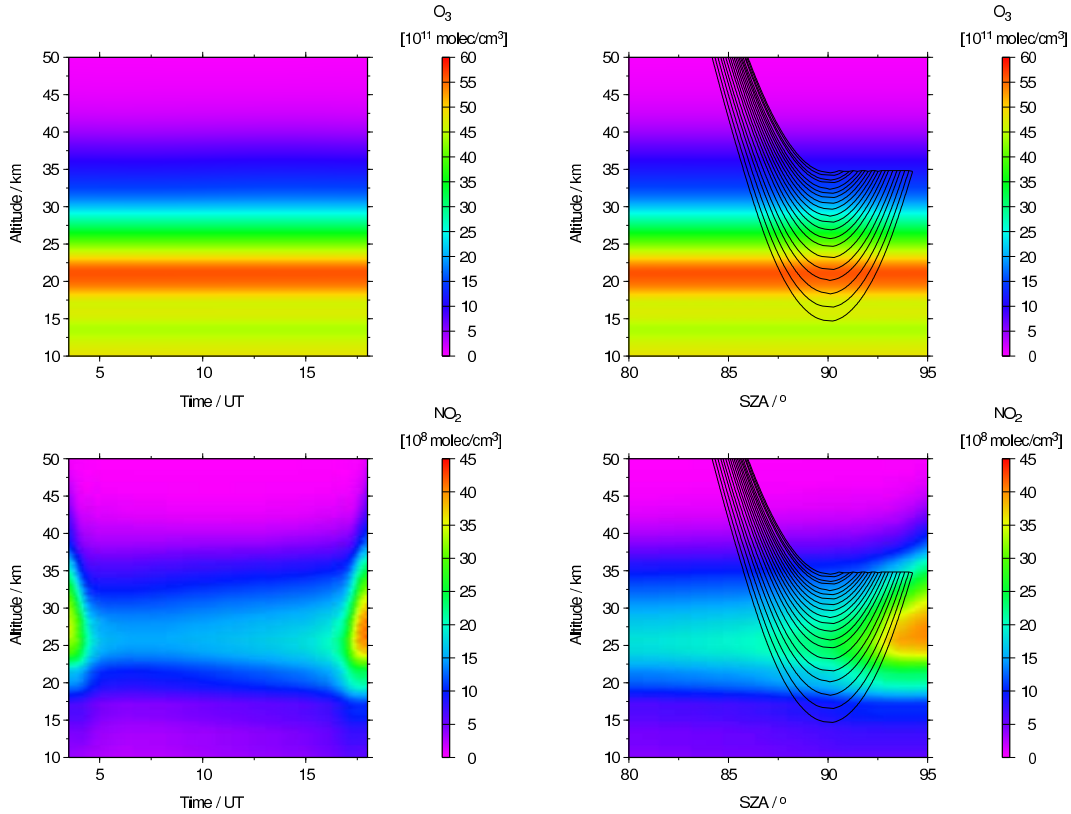

Figure 5.4: Concentration of O_3 (upper row) and NO_2 (lower row) as a function of time and altitude (left column) and as a function of SZA (pm) and altitude (right column). The color-code indicates the concentrations of the respective gases as modeled by the SLIMCAT 3-D chemical transport model (Chipperfield, 1999) for Kiruna on March 23, 2003. Typically, SCIAMACHY measurements take place in the morning while LPMA/DOAS balloon flights are conducted over a 2 to 3 hour period close to sunset in the evening. The lines-of-sight of the LPMA/DOAS solar occultation measurements are shown as black lines in the upper right and lower right panel. For better visiblilty, the lines-of-sight for measurements during balloon ascent are suppressed.

tangent point exhibit SZA $> 90°$, points on the line-of-sight which are closer to the Sun than the tangent point exhibit SZA $< 90°$. For chemical species which are inert on timescales of the balloon flight, like O_3, profile retrieval is unambiguous since the concentration in each altitude layer does not depend on the local SZA. Profile retrieval of photochemically active species, like NO_2, is problematic since the concentration profile changes during the course of the measurements and spectra recorded at the beginning of the balloon flight sample a different concentration profile than at the end. In particular, this effect is important for solar occultation measurements of NO_2 since its variation during sunset is strong due to the decrease in NO_2 photolysis (Kerr et al., 1977; Roscoe and Pyle, 1987).

Following the above discussion, a photochemical model is required to correctly validate the SCIAMACHY limb measurements of NO_2 by the LPMA/DOAS balloon borne observations. A combination of the 3-D chemical transport model (CTM) SLIMCAT and the 1-D chemistry model LABMOS is

employed as described in section 1.3. SLIMCAT output from the multi-annual run (# 323) is saved every two days at 0:00 UT interpolated to the launch sites of the balloon flights and used to initialize the 1-D chemistry model LABMOS. Here, LABMOS models stratospheric photochemistry on 19 potential temperature levels between $\Theta = 336\,\mathrm{K}$ ($\simeq$11 km) and $\Theta = 1520\,\mathrm{K}$ ($\simeq$42 km). As recommended by Dufour et al. (2005), aerosol surface area densities are taken from balloon borne *in situ* measurements of the aerosol size distribution at Laramie (41°N), Wyoming, conducted by Deshler et al. (2003) in 2003. The stratospheric abundance of aerosols is currently at background levels corresponding to a volcanically quiescent period and assumed constant for all validation flights between 2003 and 2005. The 1-D model is initialized at 0:00 UT with SLIMCAT output of the day of the balloon flight at the launch site. If output is not available on the actual day of the balloon flight, we decide whether to take output from the day before or after by comparing the measured O_3, NO_2 and if available CH_4 and N_2O profiles to the modeled ones and choosing the output which produces the best agreement with the measurements. While the model is run with fixed pressure and temperature for each Θ level taken from the meteorological support data of the balloon flight, the SZA timeline is taken from the air mass trajectory calculations to guarantee that the photochemical evolution of the modeled air mass corresponds to the true evolution between initialization of the model, satellite measurement and balloon borne observation. For simplicity, a single SZA timeline for all Θ levels is chosen which is representative for the altitude range where the air masses coincide. As recommended by Bracher et al. (2005), the concentrations of O_3, NO_2, NO and N_2O_5 are scaled upon initialization in a way that the model can reproduce the O_3 and NO_2 profiles measured in the evening. All other SLIMCAT output parameters are left unchanged for initialization of the 1-D model.

All satellite measurements of NO_2 profiles presented here are conducted far from sunset or sunrise and completed within minutes. Hence, a fixed SZA is assumed for the SCIAMACHY observations. The photochemical variation between the satellite and balloon borne measurements and during the course of the balloon flight is corrected by introducing the photochemical weighting factors κ_{kj}. Given the photochemical model data along the SZA timeline of an air mass trajectory, κ_{kj} is defined through

$$\kappa_{kj} = \frac{a_{kj}}{b_j}, \tag{5.1}$$

where b_j is the modeled NO_2 concentration in altitude layer *j* and at the SZA of the SCIAMACHY measurement and a_{kj} is the modeled NO_2 concentration in altitude layer *j* and at SZA *k*. When tracing the light path through the atmosphere from the Sun to the balloon borne detector, each point on the line-of-sight can be identified through its altitude and its local SZA. The slant path through layer *j* at local SZA *k* is multiplied by κ_{kj}. Hence, a photochemically corrected weighting function matrix $\tilde{\mathbf{K}}$ is obtained. Replacing $\mathbf{K}$ by $\tilde{\mathbf{K}}$ in equation (3.36) and solving the inverse problem as described in section 3.3 yields the balloon borne trace gas profile scaled to the photochemical conditions of the satellite measurement. It has to be emphasized that the transformation of $\mathbf{K}$ to $\tilde{\mathbf{K}}$ is not a simple matrix multiplication since the lines-of-sight of solar occultation measurements cross altitude layers below the balloon twice.

Following a similar approach as in Bracher et al. (2005) the modeling error is estimated by sensitivity studies. For the flight at Kiruna on March 24, 2004, several model runs are performed along a representative air mass trajectory varying model parameters important for the photochemical variation of

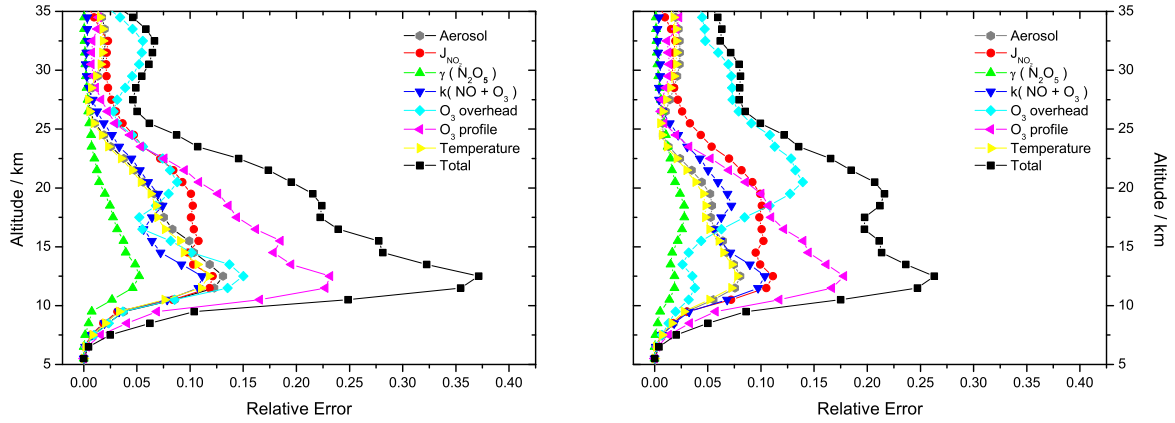

Figure 5.5: Modeling error of the backward (left panel) and forward (right panel) calculations. The different contributions inferred from sensitivity runs are indicated in the legend. An altitude smoothing filter of 3 km width is applied in order to remove small scale features.

NO_2. The output of each model run is used to produce scaled balloon borne NO_2 profiles corresponding to a backward and a forward satellite match in the morning before and after the balloon flight. The root mean square of the differences between the sensitivity runs and the standard run represents our estimate of the modeling error which is inferred separately for forward and backward calculations. This is a very conservative estimate since the modeling error is not estimated from the differences between the photochemical weighting factors κ_{kj} (Dorf, 2005) but from the differences between the modeled NO_2 profiles. The tested parameters include the O_3 profile (-33%,+50%), which is varied in a range beyond the actual measurement errors of the O_3 profile in order to account for possible spatial gradients which are not captured by the air mass matching technique. NO_2 abundances are influenced by the O_3 profile mainly through its reaction with NO, equation (R1.42). The column abundance of overhead ozone ($\pm$74%) modifies the incoming actinic flux and hence the photolysis rates. The temperature for each Θ-level ($\pm$7K) is varied by its typical variation along a 24-h air mass trajectory between 20 km and 30 km altitude. The rate constants of reaction (R1.42) and (R1.44) ($\pm$20%), which directly impact NO_2 concentrations, are varied by the error estimates given in Sander et al. (2003). The same is true for the γ-coefficient for N_2O_5 uptake on liquid aerosol (-50%,+100%). Aerosol surface area densities ($\pm$40%) are varied by the precision estimates of Deshler et al. (2003).

The resulting modeling error and its contributions are shown in figure 5.5 as a function of altitude. The total modeling error increases from below 10% at 30 km alitude to about 20% at 20 km. Below 20 km it increases up to about 40% for the backward calculations and up to 30% for the forward calculations. For both scenarios, it is dominated by the sensitivity to the O_3 profile and the amount of overhead O_3. The parameters influencing heteorogeneous reactions, i. e. the γ coefficient for N_2O_5 uptake on liquid aerosol and the aerosol surface density, in total contribute less than 8% in the range between 30 km and 20 km and at most 15% below 15 km. The sensitivity to the reaction of O_3 with NO and to the variation of temperature amounts to about 10% in the lower stratosphere and is smaller above. The error due to uncertainties of the photolysis rate of NO_2 increases from less than 5% at 30 km to

Table 5.1: Compendium of joint LPMA and DOAS O_3 and NO_2 profile measurements and Envisat/SCIAMACHY overpasses. BA and SO indicate balloon ascent and solar occultation measurements.

Balloon flight date, time/UT	Location	Geophysical condition	Available datasets	Satellite coincidence orbit,date,time/UT	Altitude range/km	Time delay/h	Spatial distance/km
Mar 04, 03	Kiruna	high-lat. spring	SO: LPMA	5273, Mar 4, 11:05	20-30	-5.1	369-496
13:20 - 16:17	67.9^o N, 21.1^o E	SZA: 71.1^o - 94.1^o		5285, Mar 5, 7:17	23-24	+15.3	498-499
Mar 23, 03	Kiruna	high-lat. spring	BA: LPMA, DOAS	5545, Mar 23, 11:07	18-28	-5.2	268-496
14:47 - 17:28	67.9^o N, 21.1^o E	SZA: 78.9^o - 94.7^o		5558,Mar 24, 9:01	19-29	+17.4	10-495
			SO: LPMA, DOAS	5545, Mar 23, 11:07	20-30	-6.2	63-458
				5558, Mar 24, 9:01	17-30	+16.0	256-453
Oct 9, 03	Aire sur l'Adour	mid-lat. fall	BA: DOAS	8407, Oct 9, 9:51	17-31	-6.5	738-988
15:39 - 17:09	43.7^{o}N, 0.3^o W	SZA: 72.0^o - 87.8^o		8421, Oct 10, 9:20	25-33	+17.2	547-977
Mar 24, 04	Kiruna	high-lat. spring	BA: DOAS	10798, Mar 24, 10:35	12-33	-5.4	371-499
14:04 - 17:31	67.9^o N, 21.1^o E	SZA: 74.5^o - 95.3^o		10812, Mar 25, 10:04	6-16	+19.9	32-485
			SO: DOAS	10798, Mar 24, 10:35	10-33	-6.9	191-436
				10812, Mar 25, 10:04	10-20	+16.7	301-475
Jun 17, 05	Teresina	tropics	BA: DOAS	17240, Jun 17, 11:53	25-30	-8.1	382-491
18:32 - 21:13	5.1^o S, 42.9^o W	SZA: 60.6^o - 95.8^o		17255, Jun 18, 13:02	5-33	+18.4	6-490
			SO: DOAS	17240, Jun 17, 11:53	23-32	-9.1	519-971
				17255, Jun 18, 13:02	8-33	+16.2	12-496

more than 10% below 20 km. The total modeling error is added to the error bars of the photochemically corrected NO_2 profiles by Gaussian error propagation.

5.4 Comparison of vertical profiles of O_3 and NO_2

5.4.1 Observations

The validation study reports on five LPMA/DOAS balloon flights conducted since 2003: Three from ESRANGE, Kiruna, in northern Sweden, one from Aire sur l'Adour in southern France and one from Teresina in northern Brazil close the equator. For each balloon flight a satellite coincident measurement is identified in the morning before and after the balloon flight using the trajectory matching technique described in section 5.2. In the following these coincidences are referred to as backward and forward coincidences. If trace gas profiles inferred from balloon ascent and solar occultation are available the satellite coincidences are identified separately. For each balloon flight table 5.1 provides information on the measurement site, the geophysical condition, the SZA range covered by the balloon borne observations, the available data sets and some details on the selected SCIAMACHY limb scans. Besides orbit number, time and date of the satellite measurement, the matching altitude, the distance with respect to the air masses probed by the balloon borne instruments and the time delay between satellite overpass and balloon flight are given. Albeit the limited number of balloon flights, the validation dataset represents a wide range of geophysical conditions comprising high-latitude winter, mid-latitude and tropical scenarios.

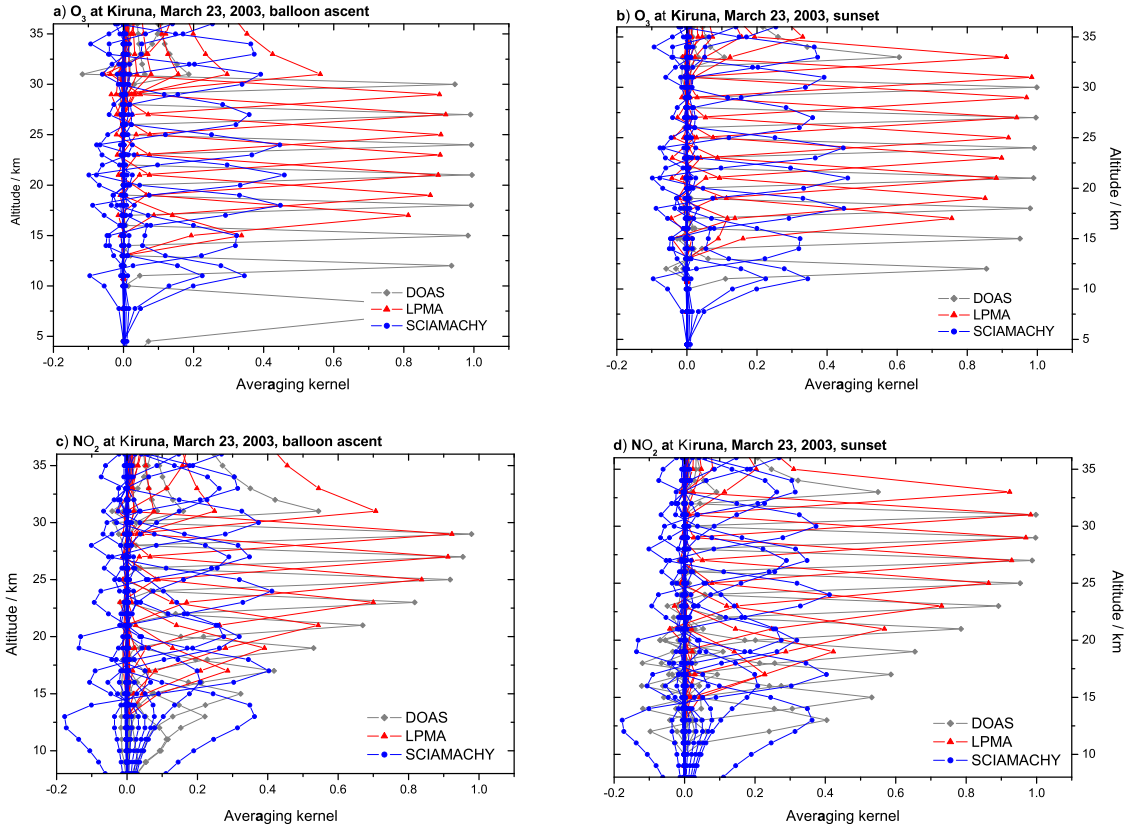

Figure 5.6: Averaging kernels of the DOAS (gray diamonds), LPMA (red triangles) and SCIAMACHY (blue circles) trace gas retrievals for measurements at Kiruna on March 23, 2003. Averaging kernels are shown for O_3 (panels a) and b)) and NO_2 (panels c) and d)) for balloon ascent (panels a) and c)) and solar occulation (panels b) and d)) viewing geometry. The DOAS and SCIAMACHY data are retrieved on the same altitude grid which corresponds to a 1-km grid spacing above 10 km altitude and is coarser below. The LPMA data are retrieved on a 2-km grid.

In general, we succeed in identifying satellite coincidences in the altitude range from about 20 km to 30 km. In some cases the characteristics of the coincidences are not perfect for validation purposes, e. g. for the flight from Kiruna in 2004 where the forward coincident altitude range is below 20 km and for the flight from Kiruna on March 4, 2003, where the forward coincidence is restricted to a small altitude range. Nevertheless, remembering that coincidence criteria are somewhat artifical the balloon and satellite borne trace gas profiles are compared in the whole retrieved altitude range. For the flight from Aire sur l'Adour on Oct. 9, 2003, the match criterion is weakened to a maximum spatial mismatch of 1000 km, as no coincidence is found applying the 500 km criterion. Furthermore, assuming the weakened match criterion, the satellite overpass in the morning of Oct. 9 coincides directly with the balloon measurement locations. Hence, the backward model calculations for this flight are not performed along the SZA timeline given by air mass trajectory calculations, but are carried out along the SZA timeline corresponding to air masses stationary at Aire sur l'Adour. LPMA data are processed for the two flights at Kiruna in 2003, only. DOAS data are lacking for March 4, 2003, due to instrumental

malfunction.
Figure 5.6 compares the averaging kernels of the SCIAMACHY O_3 and NO_2 retrieval with the LPMA and DOAS averaging kernels for balloon ascent and solar occultation measurements at Kiruna on March 23, 2003. SCIAMACHY exhibits an altitude resolution of 3 km to 5 km for both gases which is evidently coarser than for DOAS but on the order of the LPMA altitude resolution (see also section 4.2.1). Accordingly, DOAS O_3 and NO_2 profiles are retrieved on the same altitude grid as the satellite profiles and smoothed to match the satellite's coarser altitude resolution except for NO_2 measured during balloon ascent below 20 km where no smoothing is applied. LPMA trace gas profiles are generated on a 2-km altitude grid without smoothing. In all cases, the a piori profiles are taken from the satellite retrievals performed at the IUP-Bremen.

Before the actual trace gas profiles are compared a quality check of our combined meteorological and photochemical modeling approach can be performed by comparing photochemically corrected balloon borne profiles inferred from the balloon ascent and solar occultation measurements of the same balloon flight. As listed in table 5.1 for the balloon flights from Kiruna in 2003, from Kiruna in 2004 and from Teresina in 2005 the air mass trajectory model identified air mass coincidences with the same SCIAMACHY scans for balloon ascent and solar occultation observations. Using the photochemical model to scale the balloon borne NO_2 profiles to the same satellite observation should yield identical profiles for both viewing geometries. If any discrepancies are observed, either the trajectory model or the photochemical model is insufficient or the profiles retrieved from balloon ascent and solar occultation are inconsistent. Figure 5.7 illustrates the comparison for the three considered balloon flights. The left column of panels shows the O_3 profiles inferred from balloon ascent and solar occultation measurements while the two columns on the right display the retrieved and photochemically corrected NO_2 profiles.
The O_3 profiles can be used as tracer for the inhomogeneity of the sampled air masses. Since ozone is not subject to considerable photochemical variation on a timescale of hours, all discrepancies observed between the balloon ascent and sunset observations can be attributed to spatial inhomogeneities of the O_3 concentration or to inconsistencies of the measurements. The latter can be considered small, since the estimated accuracy of the DOAS O_3 retrieval is better than 5% (section 4.1.1). From figure 5.7 it is apparent that the LPMA/DOAS instruments sampled slightly inhomogeneous air masses below 20 km for the high-latitude flights from Kiruna in March 2003 and 2004, which have been conducted close to the polar vortex. For the tropical balloon flight no considerable impact of horizontal trace gas variations is detected.
The comparison of NO_2 concentrations which are inferred from balloon ascent and sunset measurements and photochemically scaled to the same SCIAMACHY observation is convincing for Kiruna in 2003 and in particular for Kiruna in 2004 (figure 5.7 a) and b)). Although the applied scaling is quite substantial in particular for the sunset data, only small discrepancies are observed for the former flight around 20 km which might be due to unaccounted inhomogeneities of air masses, since deviations are also seen in the comparison of the respective O_3 profiles. For the tropical flight from Teresina in 2005, the photochemically corrected profiles inferred from sunset are consistently lower than those inferred from balloon ascent measurements. Sampling of horizontally inhomogeneous air masses seems unlikely, since the dynamics of the tropical stratosphere does not allow for large gradients of trace gas abundances on small spatial scales as observed close to the polar vortex. In addition to that, the corresponding O_3 profiles show good agreement. A possible source of error originates from the actual measurements. The optical densities of NO_2 encountered during balloon ascent at tropical latitudes are very small since the

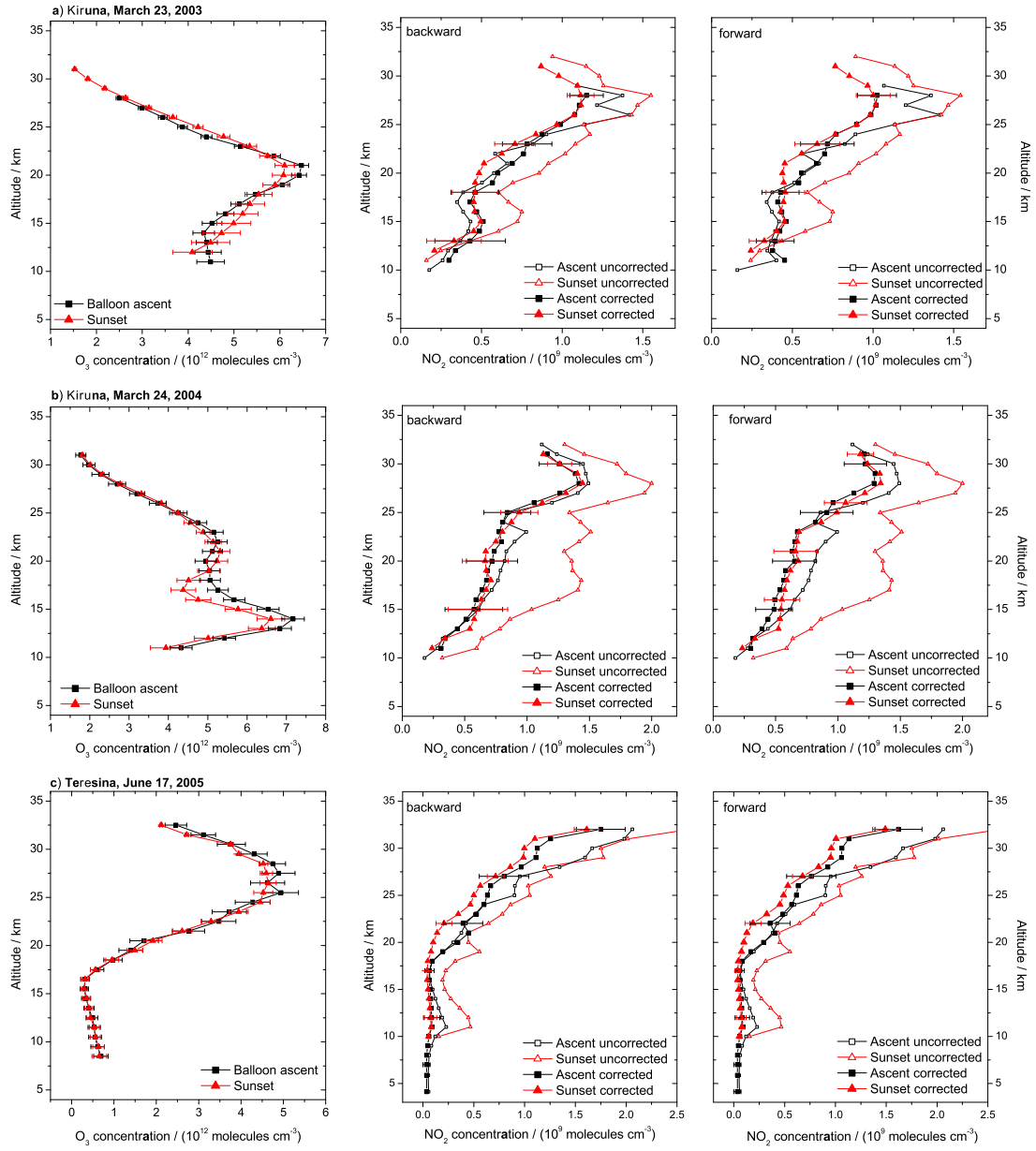

Figure 5.7: DOAS O_3 (left column) and NO_2 profiles (right columns) measured at Kiruna in 2003 (row a)), at Kiruna in 2004 (row b)) and at Teresina in 2005 (row c)). The profiles inferred from balloon ascent (black boxes) and solar occultation measurements (red triangles) are scaled to the photochemical conditions of the coincident SCIAMACHY measurements listed in table 5.1. For each balloon flight the identified coincidences are identical for balloon ascent and solar occultation measurements. Photochemical corrected NO_2 profiles corresponding to backward and forward coincidences are shown.

low SZAs allow for small air mass factors, only. Further, the determination of the Fraunhofer offset of the DOAS NO_2 SCDs is particularly difficult for the flight from Teresina in 2005, because balloon float is reached very late at SZA $> 83°$ and because the NO_2 concentration maximum is found above ballon

float altitude. A systematic overestimation of the DOAS Fraunhofer offset would impact the balloon ascent SCDs more seriously than the SCDs measured in solar occultation since the former are one order of magnitude smaller than the latter. Therefore, the Fraunhofer offset is calculated independently from the SCIAMACHY NO_2 profile above balloon float altitude and from the weighting functions for the pseudo-TOA spectrum used for the DOAS retrieval. It is found that the difference between the inferred Fraunhofer offsets cannot account for the observed discrepancy[1]. The photochemical model has proven to yield valuable results for the mid- and high-latitudinal balloon flights. Since all parameters depending on latitude are adjusted to the tropical conditions, at the moment the reason for the observed discrepancy remains unclear. However, in all cases the error bars comprising the measurement errors, the retrieval errors and the modeling errors represent well the actual accuracy of our approach.

5.4.2 Discussion

The retrieved vertical trace gas profiles for O_3 and NO_2 are shown in figures 5.8, 5.10 and 5.11. Satellite observations in the morning before and after the balloon flight are compared to balloon borne trace gas profiles. Smoothed (and in the case of NO_2 photochemically corrected) balloon borne profiles are presented. For reference, vertical profiles without photochemical correction at full altitude resolution are plotted. In the case of O_3, *in situ* sonde data are included if available. The O_3 sonde data are taken from an electrochemical cell either deployed on the gondola or launched from the ground station shortly after balloon launch. The relative deviations between the satellite and balloon borne measurements are assessed in figure 5.9 for O_3 and figure 5.12 for NO_2.

O_3 validation study

The internal consistency of the validation data set has been discussed in depth in sections 4.1.3 and 4.2.2 where a general agreement on the order of 10% is observed. In all cases the agreement between *in situ* sonde and remote sensing balloon borne O_3 data is good. Sometimes even highly filamented structures (e. g. figure 5.8 e)) can be observed simultaneously in the high resolution balloon borne and the *in situ* observations.

In most cases SCIAMACHY limb O_3 profiles agree to within $\pm$ 20% with the validation data set in the 20 km to 30 km altitude range. The agreement ranges from close to perfect as for the observations at Kiruna on March 4, 2003 (figure 5.8 a)) to fair as in the case of figure 5.8 d), where the agreement in the considered altitude range is on the order of 30%, only, and the profile shape is rather different for satellite and balloon borne data. The relative deviations (figure 5.9) show a systematic underestimation of the balloon borne by the satellite borne profiles at 24 km to 28 km altitude. The underestimation decreases and sometimes changes to overestimation when going up to 31 km and down to 20 km. This finding is similar to conclusions of Brinksma et al. (2006), where a zigzag shape of the deviations between a validation data set (lidar, SAGE II) and the IUP-Bremen O_3 retrieval is observed, indicating that O_3 concentrations at 27 km inferred from SCIAMACHY limb are low. Although different corrections for tangent height errors are already included in the SCIAMACHY retrievals there might be a remaining small tangent height error causing the observed deviations. The combined error bars of the balloon and satellite borne

[1]The Fraunhofer offset inferred from the NO_2 Langley plot is $(8.31\,10^{15} \pm 4.9\,10^{14})$ molecules cm^{-2} while the value inferred from the SCIAMACHY profile is $8.16\,10^{15}$ molecules cm^{-2}.

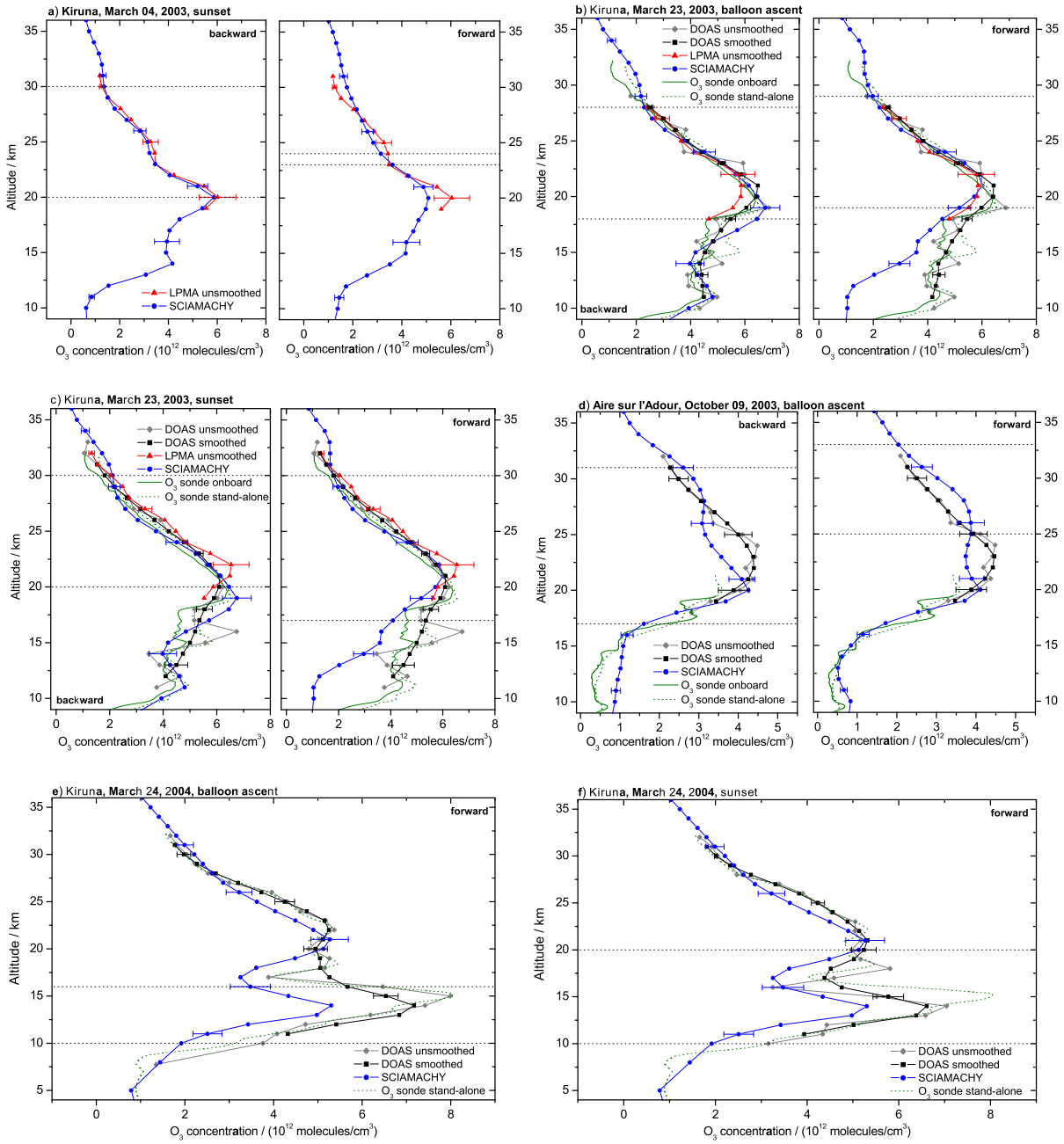

Figure 5.8: Comparison of O_3 profiles inferred from SCIAMACHY limb observations with correlative balloon borne measurements. Panels a) to f) correspond to observations at a) Kiruna on March 4, 2003, at Kiruna on March 23, 2003, during b) balloon ascent and c) sunset, at d) Aire sur l'Adour on October 9, 2003 and at Kiruna on March 24, 2004, during e) balloon ascent and f) sunset. The left and right sub-panels correspond to backward and forward coincidences. Satellite data are shown as blue circles. Smoothed DOAS data are plotted as black boxes, LPMA data as red triangles. The gray diamonds represent DOAS O_3 profiles at full altitude resolution without smoothing. If available, O_3 profiles measured during balloon ascent by an electrochemical cell aboard the gondola are shown as green line. The dashed green lines correspond to O_3 profiles inferred from stand-alone *in situ* sondes launched from the ground station shortly after balloon launch. The altitude range between the horizontal dotted lines represents the range where coincident air masses are identified. Unfortunately, for the backward coincidence at Kiruna on March 24, 2004, and for the flight from Teresina on June 17, 2005, no SCIAMACHY O_3 data are available. For better visibility, only selected error bars are shown.

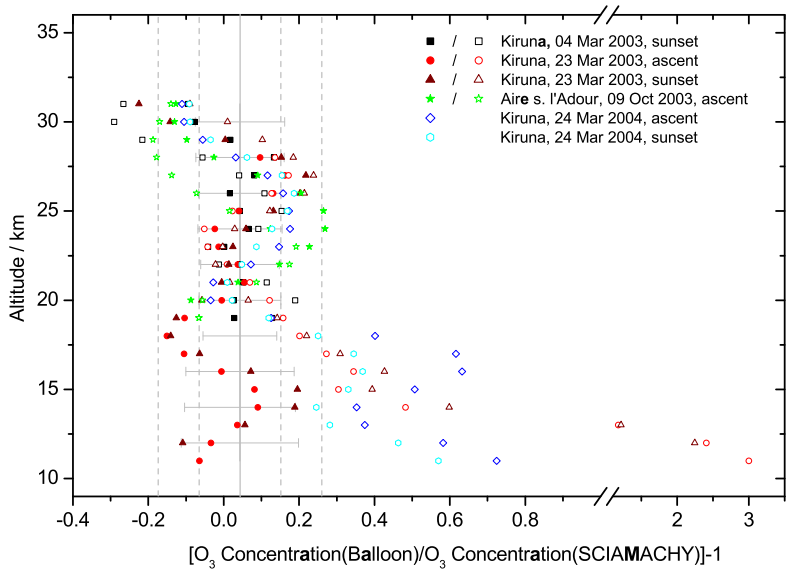

Figure 5.9: Relative deviations between satellite and balloon borne measurements of O_3 profiles. Filled and open symbols correspond to backward and forward coincidences, respectively. Observation sites and conditions are indicated in the legend. The mean deviation of all coincident data in the 20 km – 31 km altitude range is 4.3% with 10.8% standard deviation. The gray lines indicate the mean at +0.043 and the one and two times standard deviation boundaries with respect to the 20 km – 31 km altitude range. The error bars represent the combined errors of the satellite and balloon borne observations. Note the broken abscissa.

observations are on the order of the observed standard deviation of all coincident measurements in the 20 to 30 km altitude range. However, a number of data points differ by more than the combined error bars which might point to a systematic error as suggested above.

Below 20 km, SCIAMACHY O_3 profiles underestimate the balloon borne data in most cases and cannot reproduce the frequently highly filamented O_3 profiles observed at high-latitudes during winter (e. g. figures 5.8 e) and f)). The balloon flights from Kiruna on March 23, 2003, and on March 24, 2004, were conducted close to the polar vortex edge where the gradients in O_3 concentration are large on small spatial scales. When identifying coincident balloon and satellite measurements, the air mass trajectory calculations allow for a sizeable mismatch in space and time. A spatial mismatch of up to 500 km is possible and, hence, the influence of horizontally inhomogeneous air masses can be important close to the polar vortex edge. Further, SCIAMACHY measurements represent an average over a 960 km wide horizontal area, whereas the LPMA/DOAS measurements average the horizontal trace gas distribution along the line-of-sight from the balloon to the Sun. Deviations as in figures 5.8 e) and 5.8 f) might originate from the difference in horizontal averaging. Unfortunately, there are no DOAS or LPMA data available for the observations below 19 km at the mid-latitudinal station Aire sur l'Adour, but SCIAMACHY limb profiles and the corresponding profiles inferred from *in situ* O_3 sondes agree well (figure 5.8 d)). Figure 5.9 reveals that the combined error bars cannot explain the observed discrepancies below 20 km altitude.

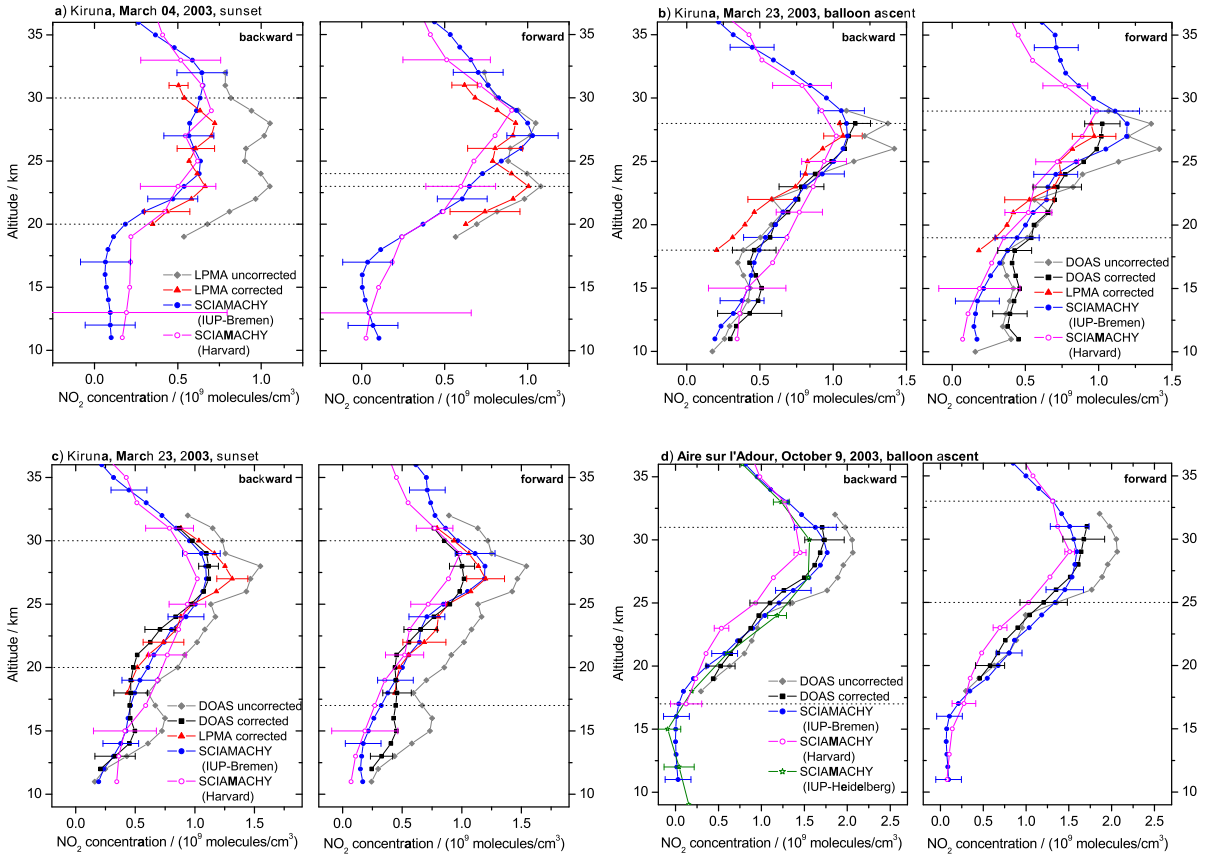

Figure 5.10: Comparison of NO_2 profiles inferred from SCIAMACHY limb observations with correlative balloon borne measurements. Panels a) to d) correspond to observations at a) Kiruna on March 4, 2003, at Kiruna on March 23, 2003, during b) balloon ascent and c) sunset, and at d) Aire sur l'Adour on October 9, 2003, during balloon ascent. The left and right sub-panels correspond to backward and forward coincidences. Satellite data inferred by IUP-Bremen are shown as blue full circles, by Harvard as open magenta circles, by IUP-Heidelberg as green open stars. Photochemically corrected and smoothed DOAS data are plotted as black boxes, photochemically corrected LPMA data as red triangles. The gray diamonds represent balloon borne profiles at full altitude resolution without photochemical correction which are taken from the DOAS data except for the flight from Kiruna on March 4, 2003, where LPMA data are used. The altitude range between the horizontal, dotted lines represents the range where coincident air masses are identified. For better visibility, only selected error bars are shown.

NO_2 validation study

The internal agreement of the balloon borne NO_2 measurements is assessed in sections 4.1.3 and 4.2.2 and was found to be about 20%. Accordingly, the LPMA/DOAS observations in figures 5.10 b) and 5.10 c) mostly lie within the combined error bars. Nonetheless, for the flight from Kiruna on March 23, 2003, LPMA underestimates the DOAS profile for balloon ascent and overestimates it for sunset.

The comparison between NO_2 profiles inferred from the SCIAMACHY limb measurements and the validation data set is presented in figures 5.10, 5.11 and 5.12. The internal agreement of the satellite retrievals is variable. NO_2 profiles inferred by IUP-Bremen and IUP-Heidelberg show good agreement.

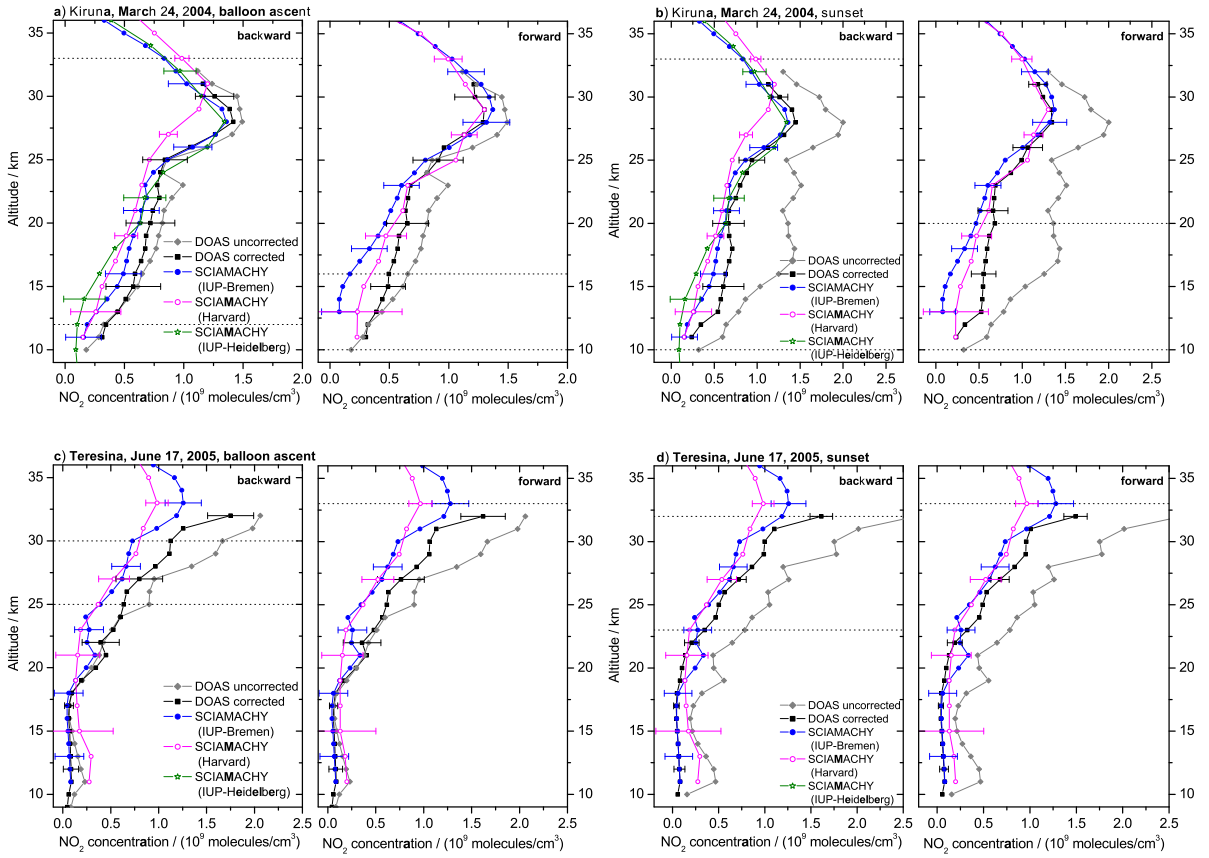

Figure 5.11: Comparison of NO_2 profiles inferred from SCIAMACHY limb observations with correlative balloon borne measurements. Panels a) to d) correspond to observations at Kiruna on March 24, 2004, during a) balloon ascent and b) sunset, and at Teresina on June 17, 2005, during c) balloon ascent and d) sunset. The left and right sub-panels correspond to backward and forward coincidences. Satellite data inferred by IUP-Bremen are shown as blue full circles, by Harvard as open magenta circles, by IUP-Heidelberg as green open stars. Photochemically corrected and smoothed DOAS data are plotted as black boxes, photochemically corrected LPMA data as red triangles. The gray diamonds represent DOAS profiles at full altitude resolution without photochemical correction. The altitude range between the horizontal, dotted lines represents the range where coincident air masses are identified. For better visibility, only selected error bars are shown.

Deviations are observed for October 9, 2003, (figure 5.10 d)) at 30 km altitude and for March 24, 2004, (figure 5.11 a)) below 20 km. In some cases (e. g. figures 5.10 d), 5.11 c) an d)) the Harvard NO_2 retrieval yields smaller trace gas concentrations than the IUP-Bremen algorithm around the NO_2 concentration maximum. In one case, the backward coincidence in figure 5.11 a) and 5.11 b), where SCIAMACHY was operating in a non-nominal measurement mode and pointing could not be verified, the Harvard profiles are offset by +2 km to +3 km with respect to the other satellite data. Agreement is good for the corresponding forward coincidence at Kiruna in 2004. In the following, the discussion is based on the IUP-Bremen records as the latter agree best with the balloon borne data. Implications for the Harvard and IUP-Heidelberg retrievals can be inferred analogously.

For the high- and mid-latitude stratosphere between 20 km to 30 km altitude the agreement between the

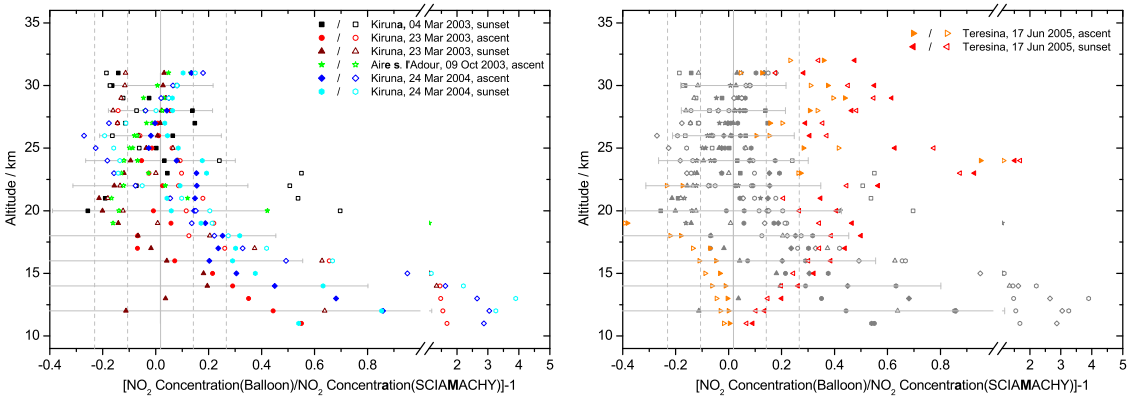

Figure 5.12: Left panel: Relative deviations between satellite (IUP-Bremen) and balloon borne measurements of NO_2 profiles. Filled and open symbols correspond to backward and forward coincidences, respectively. Observation sites and conditions are indicated in the legend. SCIAMACHY data corresponding to the backward coincidence on March 4, 2003, at Kiruna are shifted by -2 km. Data from Teresina in 2005 are suppressed. The mean deviation of all coincident data in the 20 km – 31 km altitude range is 1.8% with 12.4% standard deviation. The gray lines indicate the mean at 0.018 and the one and two times standard deviation boundaries with respect to the 20 km – 31 km altitude range. Right panel: Same as left panel but data from Teresina in 2005 are overlaid and highlighted. Note the broken abscissa. The error bars represent the combined errors of the satellite and balloon borne observations.

balloon borne NO_2 profiles and the satellite observations is on the order of 20% and most often well represented by the combined error bars. The latter amount to about 1.5 to 3 times the observed standard deviation between the two data sets for all coincident datapoints in the considered altitude range. No general trend can be observed. The backward observations at Kiruna on March 4, 2003, (figure 5.10 a)) reveal an altitude offset of +2 km to +3 km of the SCIAMACHY with respect to the LPMA data. A systematic underestimation is found between SCIAMACHY data and balloon borne measurements at Teresina in June 2005 (figures 5.11 c) and d)) which is particularly obvious when looking at the relative deviations (figure 5.12). As described in the previous section, there might be an inconsistency within the balloon borne data set which contributes to the observed discrepancy. The inferred deviations between balloon and satellite borne data for tropical latitudes in the core altitude range between 20 km and 30 km are unprecedented among the presented validation study.

Below 20 km the level of agreement among the entire data set is variable. Further, as can be seen in figure 5.11 a), the SCIAMACHY limb profiles retrieved by the IUP-Bremen, IUP-Heidelberg and Harvard algorithms exhibit sizeable discrepancies below 20 km. This indicates that for low altitudes the SCIAMACHY retrieval might depend on the auxiliary parameters used in the retrieval such as *a priori* information. The combined relative errors shown in figure 5.12 increase dramatically with decreasing altitude. This can be explained because the absolute abundances of NO_2 are very low in the corresponding altitude region. The relative errors of SCIAMACHY NO_2 measurements below 15 km are typically larger than 50%. Adding the rather large modeling error and the error of the balloon borne measurements, the combined error bars are often on the order of the observed deviation. Despite the large combined error bars, a systematic underestimation of the balloon by the satellite borne data is obvious.

5.5 Conclusion on SCIAMACHY validation

This chapter presents a validation study for O_3 and NO_2 stratospheric profiles inferred from SCIAMACHY skylight limb observations based on balloon borne LPMA/DOAS direct Sun measurements. An air mass trajectory model is used to identify coincident balloon and satellite borne measurements and to model the meteorological history of the coincident air masses. A 1-D model of stratospheric chemistry is run along the inferred air mass trajectories in order to account for photochemical processing between the satellite and balloon borne observations and during the course of the balloon flight. The modeled photochemical weighting factors κ_{kj} (equation (5.1)) are employed to scale the balloon borne NO_2 profiles to the photochemical conditions of the satellite measurements.

The validation study covers five balloon flights at different geophysical conditions. For both considered gases, typical deviations between SCIAMACHY observations and balloon borne profiles amount to 20% in the 20 km to 30 km altitude range except for the tropical data set, where deviations are larger. In the case of O_3, our observations support findings of a previous study (Brinksma et al., 2006) indicating that the IUP-Bremen O_3 retrievals are systematically low between 24 km and 28 km altitude. Below 20 km the agreement worsens for both gases due to the lower sensitivity of the satellite retrieval, unaccounted horizontal variations of the trace gases and in the case of NO_2, modeling uncertainty.

Under tropical conditions, no SCIAMACHY O_3 data suitable for the validation study are available to date. SCIAMACHY NO_2 profiles underestimate the balloon borne observations in the entire retrieved altitude range. Parts of the observed discrepancy might be due to deficiencies of the combined meteorological and photochemical modeling approach or due to a systematic error of the balloon borne profiles. The present study provides a data set which can contribute to the improvement and the validation of future official ESA algorithms which are currently under development.

Chapter 6

Case studies on stratospheric nitrogen and chlorine

The quality of the LPMA/DOAS measurements is assessed in the previous chapters by comparing the simultaneously retrieved abundances of O_3 and NO_2 from the LPMA and DOAS instruments. The dataset provided by the space borne SCIAMACHY instrument is validated. Beyond O_3 and NO_2, there is a variety of trace gases which can be retrieved from LPMA/DOAS measurements and which allow for developing a comprehensive picture of stratospheric photochemical processes.
Four LPMA/DOAS balloon flights are chosen to study the photochemistry of stratospheric nitrogen and chlorine and its representation in the chemical transport model SLIMCAT and the chemical box model LABMOS. First, some details of the spectral retrieval of the target species are given. Then a meteorological and dynamic analysis of the air masses sampled by the LPMA/DOAS instruments is presented. Case studies are chosen to represent different geophysical conditions ranging from mid-latitude fall to high-latitude summer and winter. The budget and partitioning of stratospheric nitrogen is discussed with respect to latitudinal and seasonal effects and the agreement with model calculations. The chlorine budget and partitioning is investigated and interpreted regarding ozone loss with the help of model studies constrained by the LPMA/DOAS observations.

6.1 Spectral retrieval of target species

The spectral retrieval of O_3 and NO_2 from DOAS and LPMA spectra is described in sections 4.1.1 and 4.1.2 and is not revisited here. LPMA spectra allow for the spectral retrieval of various trace gases besides O_3 and NO_2, i. e. HNO_3, NO, $ClONO_2$, HCl, N_2O, CH_4, H_2O, CO_2. A summary of the retrieved species and corresponding retrieval characteristics is given in table 6.1. 11 microwindows are identified which are simultaneously used by the multifit retrieval (section 3.2.4). The listed microwindows represent the maximum number of retrieval windows employed in the course of the present study. Depending on the choice of spectral filters, microwindows 1, 5, 6 and 7 are not available for some of the LPMA/DOAS balloon flights. Microwindows 1 to 4, which are covered by the HgCdTe detector, require correction of the sinusoidal artifact according to equation (3.34) and section 3.2.4. The ILS is determined separetely

Table 6.1: Microwindows, absorbing species, systematic retrieval errors and corresponding figures. For each microwindow, the target species is indicated by bold face letters.

Micro-window	Spectral range / cm^{-1}	Absorbing species (**target species**)	Systematic error of target species / %	Illustration
1	779.960–780.593	**$ClONO_2$**, O_3, CO_2	20	figure 6.1
2	905.637–908.585	**HNO_3**, H_2O, CO_2	15	figure 6.1
3	1240.387–1243.626	**CH_4, N_2O**, H_2O, CO_2	10	figure 6.1
4	1257.005–1258.833	**N_2O, CH_4**, H_2O, CO_2	10	figure 6.1
5	1818.095–1820.969	**O_3**, NO, H_2O, CO_2	10	figure 4.3
6	1901.000–1904.978	**NO**, H_2O, CO_2	10	figure 6.1
7	1933.898–1939.982	**CO_2**, O_3, H_2O, NO, COF_2	10	figure 6.1
8	2914.358–2915.156	**NO_2**, CH_4, O_3, H_2O	10	figure 4.4
9	2925.768–2926.014	**HCl**, CH_4, NO_2	7	figure 6.1
10	2944.716–2945.103	**HCl**, CH_4	7	figure 6.1
11	3040.039–3040.843	**O_3**, CH_4, H_2O	10	figure 4.3

for microwindow 1, microwindows 2 to 4, microwindows 5 to 7 and microwindows 8 to 11. Since the target window of $ClONO_2$ (microwindow 1) is situated at the low-wavenumber end of the filter bandpass, the corresponding ILS has to be determined independently. Examples of typical ILS are shown in figure 4.2. Absorption line parameters are taken from Rothman et al. (2005) except for $ClONO_2$ where the data set of Wagner and Birk (2003) is used. The errors of the retrieved SCDs are calculated by adding the statistical errors given by the fitting routine and the systematic retrieval errors listed in table 6.1. The latter are estimated from the errors of the absorption line parameters given by Rothman et al. (2005), uncertainties of the ambient pressure and temperature data, and errors due to incorrect knowledge of the ILS as described in section 4.1.2 for the O_3 and NO_2 retrieval. While the spectral retrievals of O_3 and NO_2 in microwindows 5, 8 and 11 are illustrated in figures 4.3 and 4.4, the retrieval of the remaining target species is depicted in figure 6.1 for a spectrum recorded during the balloon flight at Kiruna on Feb. 10, 1999, at about 20 km tangent height.

In addition to the trace gases retrieved from LPMA spectra and from spectra recorded by the 'visible' DOAS spectrograph, measurements of the 'UV' DOAS spectrograph are used to infer abundances of BrO and OClO. The spectral retrieval of the latter gases is performed according to the specifications given in Dorf (2005) and following the same principles as for gases measured by the 'visible' DOAS spectrograph[1].

Vertical profiles of the respective gases are generated according to section 3.3.2 applying the MAP retrieval (equation (3.46)). Errors of the vertical profiles are calculated from the errors of the SCDs and the smoothing error through equation (3.47). Inspection of the corresponding averaging kernels implies that a 3-km altitude grid is best suited for profile retrieval from LPMA SCDs. In order to get profile points each kilometer the retrieval is performed three times on altitude grids displaced by one kilometer. Commonly, vertical trace gas profiles from DOAS data are inferred on a 1-km altitude grid. Altitude resolution depends on the species but the analysis presented in section 4.2.1 can be considered representative for the LPMA and DOAS retrieval, i. e. altitude resolution of DOAS vertical profiles is in

[1] BrO and OClO retrievals are performed by Marcel Dorf who is gratefully acknowledged.

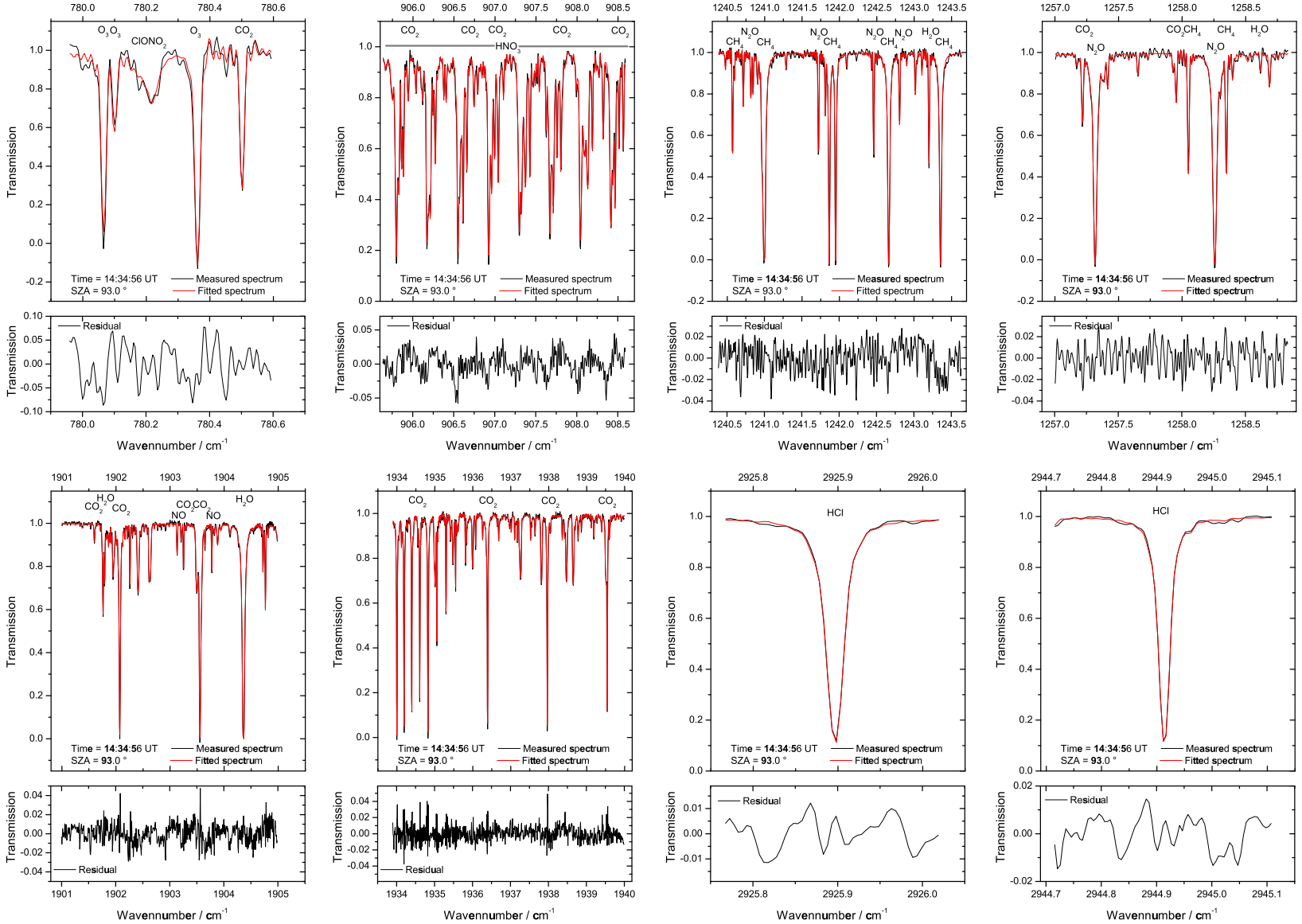

Figure 6.1: Spectral retrieval of $ClONO_2$ (upper row, first panel), HNO_3 (upper row, second panel), CH_4 (upper row, third and forth panel), N_2O (upper row, third and forth panel), NO (lower row, first panel), CO_2 (lower row, second panel) and HCl (lower row, third and forth panel) for an LPMA spectrum recorded in solar occultation during the balloon flight from Kiruna on February 10, 1999, at 20 km tangent height. The large sub-panels illustrate the measured (black line) and modeled transmission (red line). The small sub-panels show the residual.

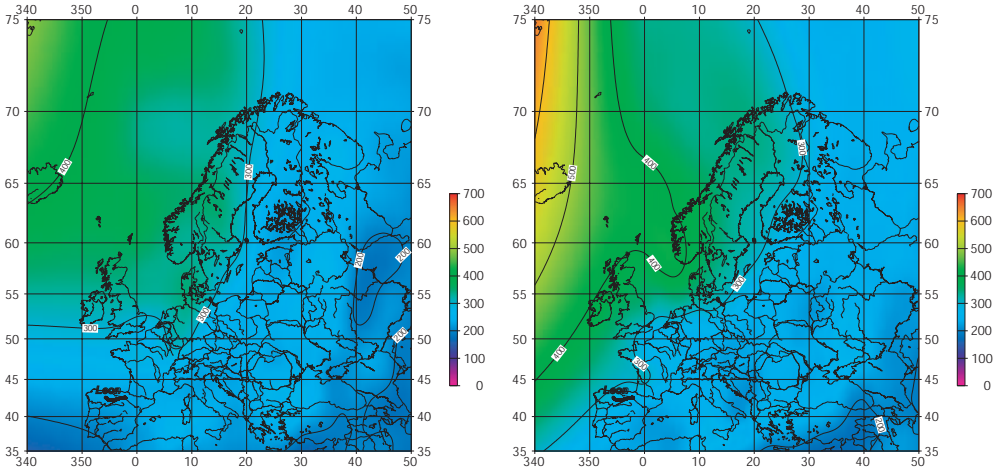

Figure 6.2: Map of potential vorticity on the 475 K potential temperature level over Europe as given by ECMWF analyses at 12 UT on Nov. 23 (left panel) and Nov. 24 (right panel), 1996. Potential vorticity is color-coded according to the scales in units of 10^{-7} K m^2 kg^{-1} s^{-1} = 0.1 PVU. Longitude and latitude are given in degree East and degree North, respectively. The trajectory of the LPMA/DOAS balloon launched from Leon (42.6°N, 5.7°W) at 14:45 UT on Nov. 23, 1996, is shown as thick solid line.

general on the order of 1 km above 20 km, decreasing to 3 - 4 km at lower altitudes while LPMA profiles generally exhibit 3 km altitude resolution above 20 km and 4 - 6 km below.

6.2 Meteorological and dynamic analysis

The LPMA/DOAS balloon flights chosen for further analysis were conducted at Leon (42.6°N, 5.7°W) on Nov. 23, 1996, and at Kiruna (67.9°N, 21.1°E) on Feb. 14, 1997, on Feb. 10, 1999 and on Aug. 21/22, 2001. The dataset is meant to represent typical case studies of the mid-latitude stratosphere in fall and of the high-latitude stratosphere in winter and summer. However, the meteorological conditions are specific for each balloon flight and determine to what extent the results inferred from the presented case studies are suited for general applicability. Hence, the meteorological and dynamic situation is shortly discussed in the following section.

6.2.1 Mid-latitude fall 1996 at Leon

The balloon flight from Leon (42.6°N, 5.7°W) in northern Spain was launched on Nov. 23, 1996, at 14:45 UT (SZA $\approx$ 73°) and terminated at 16:53 UT (SZA $\approx$ 93°) during early solar occultation. The meteorological analysis provided by FU Berlin shows that the Arctic polar vortex developed strongly in October 1996, but was split in early November due to a warming event. A fragment above Greenland intensified and moved eastward toward northern Spain causing an increase of potential vorticity and a decrease of temperature over Leon. After Nov. 11 the center of the polar vortex moved further eastward and extra-vortex conditions re-established over northern Spain. Figure 6.2 illustrates the potential vorticity at the 475 K potential temperature level over Europe on Nov. 23 and 24 at 12 UT. The trajectory of the balloon follows the westerly wind pattern starting from Leon in northern Spain.

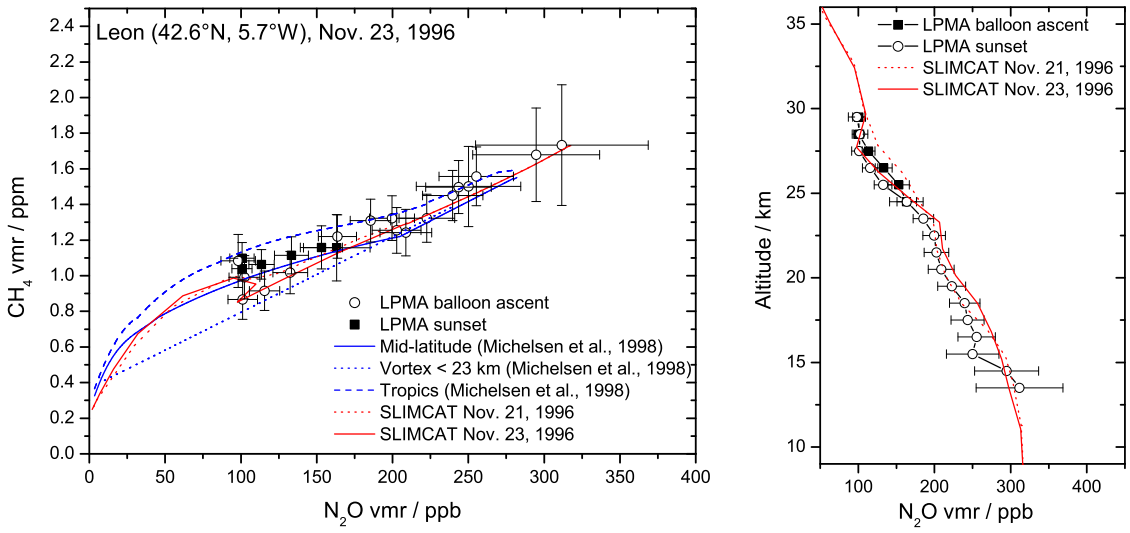

Figure 6.3: CH_4-N_2O correlation (left panel) and N_2O vertical profile (right panel) inferred from measurements of the LPMA/DOAS payload conducted during balloon ascent (open black circles) and solar occultation (filled black boxes) at Leon on Nov. 23, 1996. SLIMCAT model output interpolated to Leon for Nov. 21 (dotted red line) and Nov. 23 (solid red line) is shown for comparison. Further, the standard CH_4-N_2O correlations given by Michelsen et al. (1998b) for the tropics (blued dashed line), for mid-latitudes (solid blue line) and for the polar vortex (blue dotted line) are plotted. Note that the Michelsen et al. (1998b) study was conducted between 1992 and 1994 and that the trend in stratospheric N_2O (0.8 ppt/year according to Houghton et al. (2001)) and CH_4 (7.0 ppt/year according to Houghton et al. (2001)) is not considered.

Clearly, the LPMA/DOAS payload probed air masses outside the polar vortex which should be typical of mid-latitudes in the fall/winter hemisphere.

A concept often used to identify the dynamic origin of air masses is the inspection of tracer profiles or tracer-tracer correlations (Plumb and Ko, 1992). Suitable tracers are species such as N_2O and CH_4 which have no significant source in the stratosphere and whose photochemical lifetimes are longer than or on the order of the timescales for horizontal transport. Concentrations of these species should decrease monotonically with altitude and are specific to the respective transport regime. Inside the polar vortex for example subsidence of air masses is stronger than at mid-latitudes. Consequently, the tracer profiles of intra-vortex air are “shifted downward” compared to mid-latitude tracer profiles (see e. g. figure 1.2). Correlations between two tracers should be compact varying only with altitude. If at a certain altitude level air masses of different transport regimes undergo mixing processes, tracer profiles appear distorted, e. g. by showing filamented structures. Since the photochemical lifetimes of N_2O and CH_4 are controlled by inherently different photochemical processes, the correlations between the two species are specific to the large scale environment. Michelsen et al. (1998b) derived CH_4-N_2O correlations from ATMOS measurements aboard the space shuttle for a variety of geophysical conditions and inferred compact correlations for the tropics, mid-latitudes and polar vortex conditions. The correlations for the polar vortices result from mixing between extra- and intra-vortex air masses which experienced different degrees of subsidence.

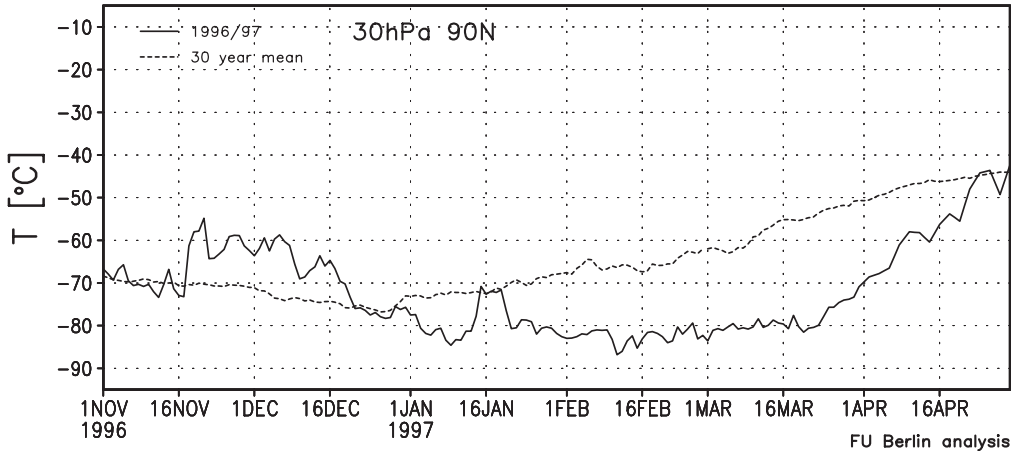

Figure 6.4: Temporal evolution of temperature at the 30 hPa pressure level above the North pole. Data for the winter 1996/97 are shown as black solid line while the dashed line corresponds to the 30 year mean. Adopted from Naujokat et al. (1997).

In figure 6.3 the standard correlations are shown together with the corresponding correlation inferred from the LPMA/DOAS balloon flight. The LPMA/DOAS data scatter around the mid-latitude correlation of Michelsen et al. (1998b) but error bars are rather large and do not allow for a clear distinction between the three dynamic regimes. The inferred N_2O vertical profile (right panel of figure 6.3) reveals no intrusion of intra-vortex air. For comparison, SLIMCAT model data are also plotted for Nov. 21 and Nov. 23, 1996, interpolated to Leon. The agreement with the measurements is good for both days suggesting that the dynamic situation is modeled correctly.

6.2.2 High latitude winter 1996/97 at Kiruna

The LPMA/DOAS payload was launched from Kiruna at 12:15 UT (SZA $\approx 82°$) on Feb. 14, 1997. Balloon float at 30 km altitude was reached about two hours later and measurements in solar occultation could be conducted down to 13 km tangent height (SZA $\approx 95°$). During the Arctic winter 1996/97, the polar vortex formed very late due to a warming event in late November, but quickly intensified and persisted into April 1997 (Coy et al., 1997). Since the vortex remained isolated from January through the end of March, temperatures were well below the threshold for PSC type 1 formation. Figure 6.4 shows the temperature as a function of time on the 30 hPa pressure level above the North pole. There, temperatures were well below the 30-year mean from January throughout mid-April.
Unfortunately, the LPMA/DOAS balloon flight was conducted close to the polar vortex edge as can be seen from the potential vorticity plotted in figure 6.5. The core of the polar vortex on the 475 K potential temperature level was situated in the north of Scandinavia and the strongest gradients occurred between 70° and 62° latitude. That means that the LPMA/DOAS measurements during balloon ascent and solar occultation may have probed air masses of different dynamic regimes. Even within a single measurement extra-vortex as well as intra-vortex air masses may have been sampled which can readily be seen in a folding of the dynamic tracer profiles and the tracer-tracer correlations. The CH_4-N_2O cor-

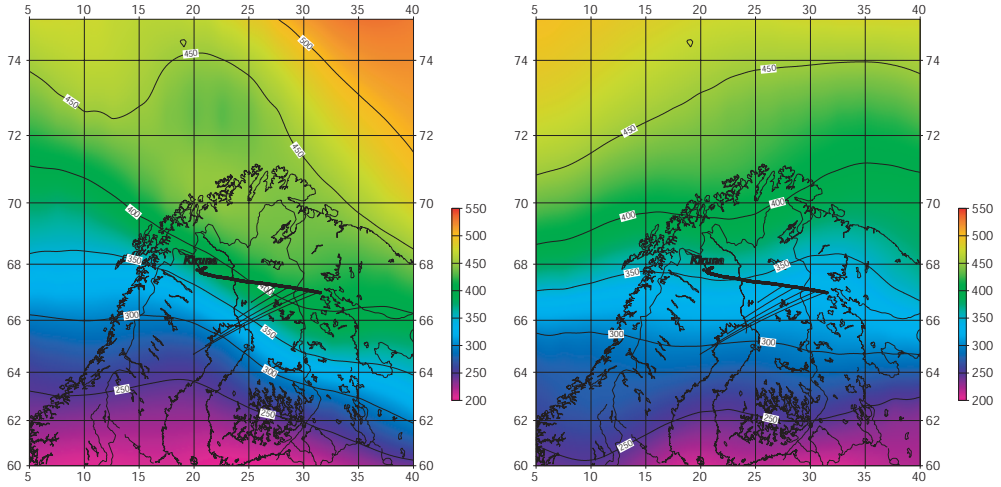

Figure 6.5: Map of potential vorticity on the 475 K potential temperature level over Europe as given by ECMWF analyses at 12 UT on Feb. 14 (left panel) and Feb. 15 (right panel), 1997. Potential vorticity is color-coded according to the scales in units of $10^{-7}\,\mathrm{K\,m^2\,kg^{-1}\,s^{-1}} = 0.1\,\mathrm{PVU}$. Longitude and latitude are given in degree East and degree North, respectively. The trajectory of the LPMA/DOAS balloon launched from Kiruna (67.9°N, 21.7°E) at 12:15 UT on Feb. 14, 1997, is shown as thick solid line. Selected lines-of-sight during solar occultation are represented by thin black lines.

relations shown in the left panel of figure 6.6 imply that the balloon ascent measurements predominantly sampled intra-vortex air while the solar occultation measurements probed extra-vortex air masses of mid-latitudinal character although the scatter of the data points is rather large. The N_2O vertical profile plotted in the right panel of figure 6.6 shows indeed that different dynamic regimes were sampled during balloon ascent and during solar occultation. The folding between 21 km and 26 km altitude corresponds to air masses which experienced less subsidence than those contributing to the profile points below 21 km. SLIMCAT model output on Feb. 13 corresponds to the intra-vortex CH_4-N_2O correlation while model output on Feb. 15 follows the mid-latitudinal correlation. The agreement with the LPMA/DOAS measurements is moderate, remembering that altitude dependent horizontal inhomogeneities as observed by the remote sensing measurements cannot be reproduced by the model.

6.2.3 High latitude winter 1998/99 at Kiruna

The LPMA/DOAS balloon flight was conducted on Feb. 10, 1999, between 11:35 UT (SZA $\approx 82.5°$) and 14:55 UT (SZA $\approx 94.9°$). After two hours of balloon ascent to 28.5 km float altitude solar occultation measurements were performed down to tangent heights of about 14 km. The 1998/99 winter was among the warmest observed in the Arctic in the 1990s (EORCU, 1999). Although a strong polar vortex was well established in November with temperatures low enough for formation of PSCs, a strong warming event in mid-December caused a displacement of the polar vortex toward mid-latitudes. During January, temperatures in the lower and middle stratosphere decreased but circulation patterns remained disturbed until the end of January, when a cold vortex re-established over the polar region. In the beginning of February, at the time of the LPMA/DOAS balloon flight, temperatures around the threshold for PSC type 1 formation were observed. A further warming event in mid-February caused the polar vortex to split

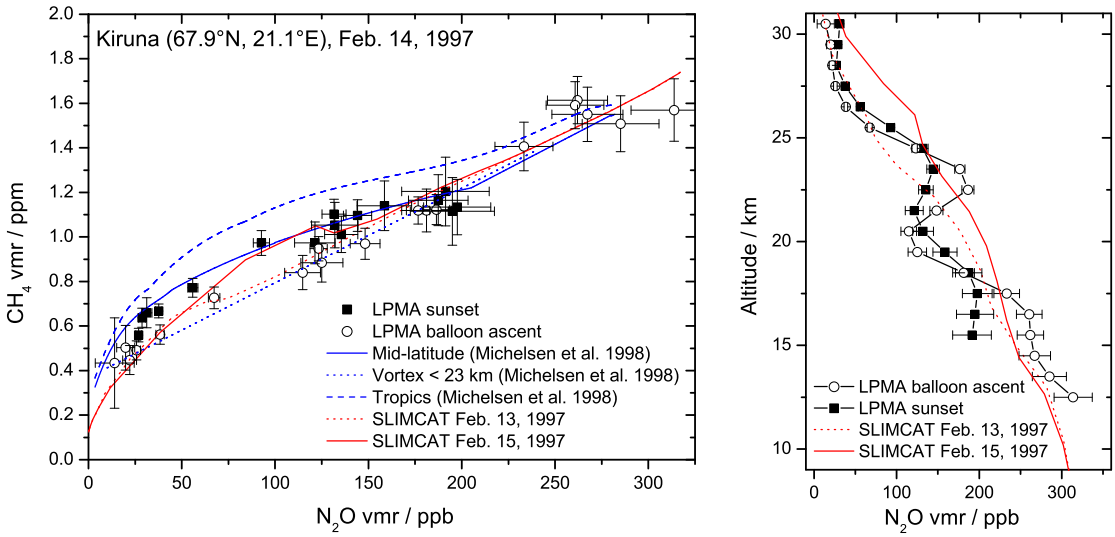

Figure 6.6: CH_4-N_2O correlation (left panel) and N_2O vertical profile (right panel) inferred from measurements of the LPMA/DOAS payload conducted during balloon ascent (open black circles) and solar occultation (filled black boxes) at Kiruna on Feb. 14, 1997. SLIMCAT model output interpolated to Kiruna for Feb. 13 (dotted red line) and Feb. 15 (solid red line) is shown for comparison. Further, the standard CH_4-N_2O correlations given by Michelsen et al. (1998b) for the tropics (blued dashed line), for mid-latitudes (solid blue line) and for the polar vortex (blue dotted line) are plotted. Please note that the Michelsen et al. (1998b) study was conducted between 1992 and 1994 and that the trend in stratospheric N_2O (0.8 ppt/year according to Houghton et al. (2001)) and CH_4 (7.0 ppt/year according to Houghton et al. (2001)) is not considered.

and finally led to an early springtime warming by the end of February. The general evolution of polar temperatures is shown in figure 6.7. Two distinct warming events in December and February can clearly be seen. In the beginning of December, PSCs could be observed over Scandinavian stations, but not for the cold period in February albeit temperatures were occasionally below 195 K. However, observations were very sparse in February 1999.

Since the LPMA/DOAS balloon flight from Kiruna in 1999 is studied extensively in the following sections, a more detailed meteorological and dynamic analysis is given than for the other flights. Figure 6.8 shows air mass trajectories calculated 10 days backward starting at Kiruna at 12 UT on Feb. 10, 1999. The trajectories are shown on the 400 K (15.5 km), 475 K (19.8 km) and 550 K (22.9 km) potential temperature levels. Air masses at all altitudes traveled from northern Canada across Greenland to northern Scandinavia. While at lower altitudes the trajectories made their way from Canada to Kiruna between 60°N and 70°N latitude, at higher altitudes air masses crossed polar regions some days before reaching northern Scandinavia. For the 550 K level, ECMWF analyses indicate temperatures low enough for the formation of PSCs. At that time of the year, the terminator of the polar night was at about 75° northern latitude which implies that air masses on the 475 K and 550 K levels experienced dark conditions over 4 to 6 days between Feb. 2 and Feb. 8. However, all air masses encountered sunlight about 48 h before arriving at Kiruna. Figure 6.9 shows the distribution of potential vorticity over northern Europe for the 400 K, 475 K and 550 K potential temperature levels on Feb. 10 and 11, 1999, at 12 UT. The filamented

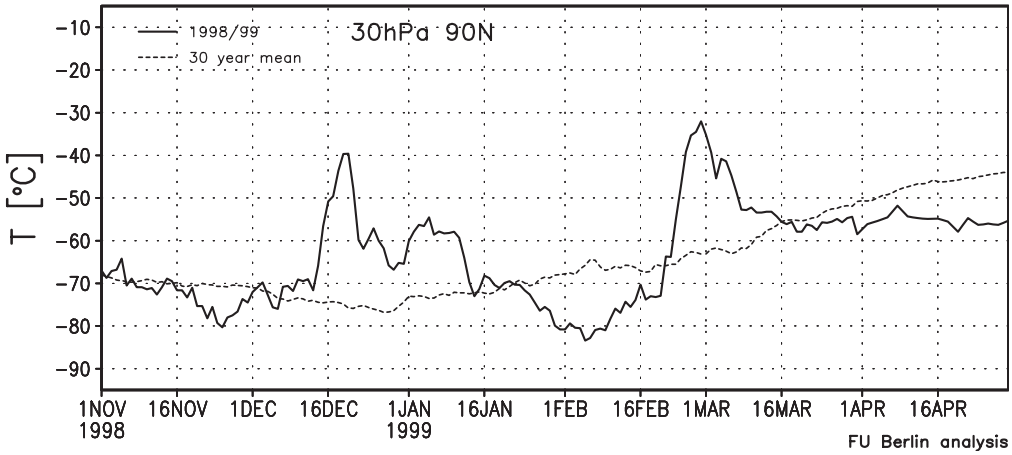

Figure 6.7: Temporal evolution of temperature at the 30 hPa pressure level above the North pole. Data for the winter 1998/99 are shown as black solid line while the dashed line corresponds to the 30 year mean. Adopted from Naujokat et al. (1999).

structure of the vortex is clearly visible. At 400 K an elongated part of the vortex was situated in the west of the LPMA/DOAS measurements and moved in south-eastern direction. Given the potential vorticity fields for 12 UT on Feb. 10 and 11 and that the flight was conducted over several hours after 12 UT on Feb. 10, it is well possible that some lines-of-sight of the balloon borne instruments crossed the vortex filament. At 475 K a pronounced vortex filament occurred close to the LPMA/DOAS measurements. In particular, for solar occultation measurements the lines-of-sight seem to point into the core of the vortex while balloon ascent was conducted at the vortex edge. A region of high potential vorticity is found in the north-west of the balloon borne observations on Feb. 10 at the 550 K level. Since the filament moved towards Kiruna, it seems likely that the remote sensing instruments sampled air masses at the boundary of the vortex.

The CH_4-N_2O correlation (left panel of figure 6.10) supports the findings of the meteorological analysis. Air masses of different dynamic regimes were sampled during the balloon flight from Kiruna in 1999. Air masses with N_2O larger than 100 ppb show mid-latitudinal tracer characteristics or even slightly larger CH_4 mixing ratios than expected from the mid-latitudinal standard correlation. However, error bars are rather large. Air masses with N_2O mixing ratios in the range of 100 ppb to 50 ppb fall in between the vortex and the mid-latitudinal correlation which is a hint that indeed some intra-vortex air was probed by the lines-of-sight.

Given the coarse horizontal resolution, the SLIMCAT model has difficulties to reproduce the complicated dynamic situation of the considered LPMA/DOAS balloon flight. The CH_4-N_2O correlations taken from model output on Feb. 9 and Feb. 11 show vortex characteristics for $[N_2O] > 120$ ppb and tend toward the mid-latitudinal correlation for $[N_2O] < 120$ ppb. The altitude profile of N_2O (right panel of figure 6.10) reveals a rather unperturbed shape for the balloon ascent measurements which is slightly offset in altitude with respect to the solar occultation profile. In this latter case, similar to the observations at Kiruna in 1997, larger than expected mixing ratio values between 22 km and 26 km altitude are observed.

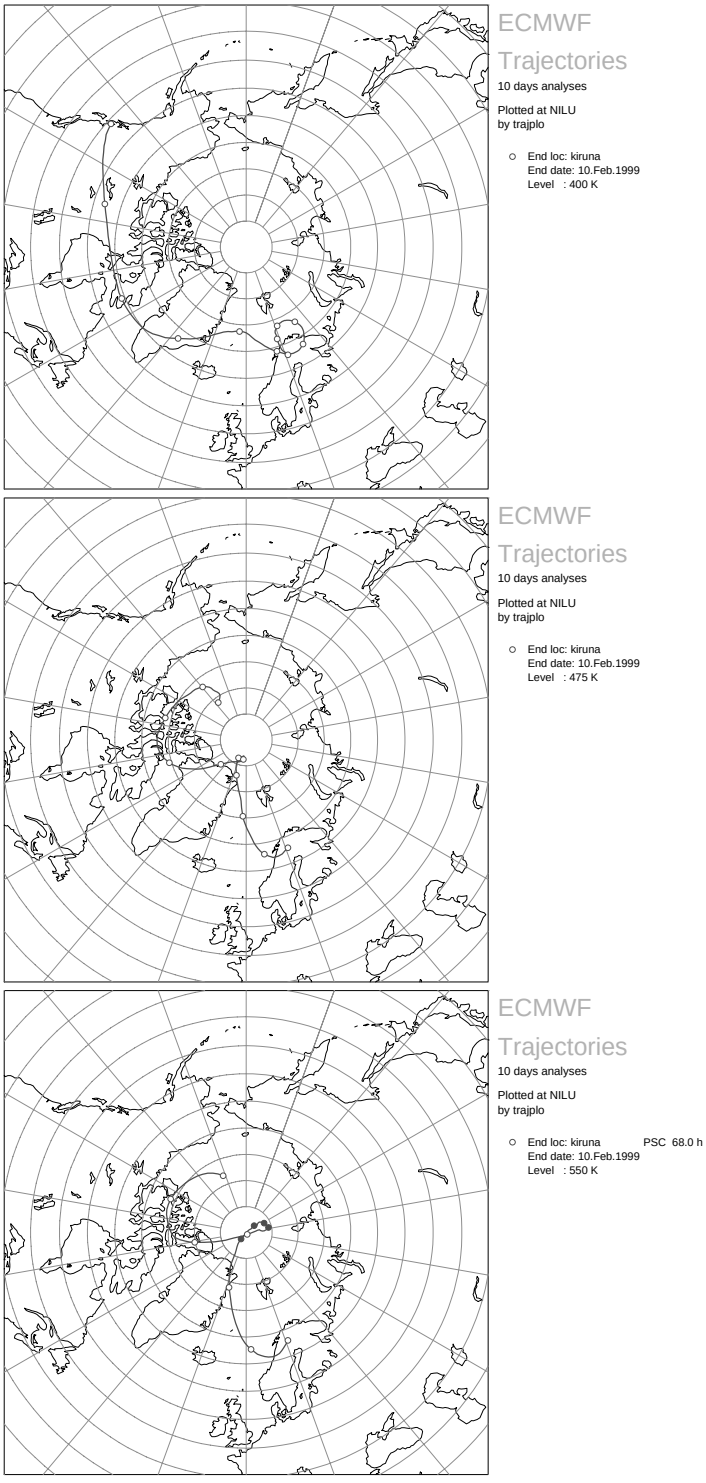

Figure 6.8: 10-day backward trajectories on the 400 K (upper panel), 475 K (middle panel) and 550 K (lower panel) potential temperature level starting over Kiruna at 12 UT on Feb. 10, 1999. Circles on the trajectories are plotted each 24 h. Filled circles correspond to intervals where temperatures low enough for PSC type 1 formation occurred. The calculations were performed using ECMWF analyses and software tools provided by NILU.

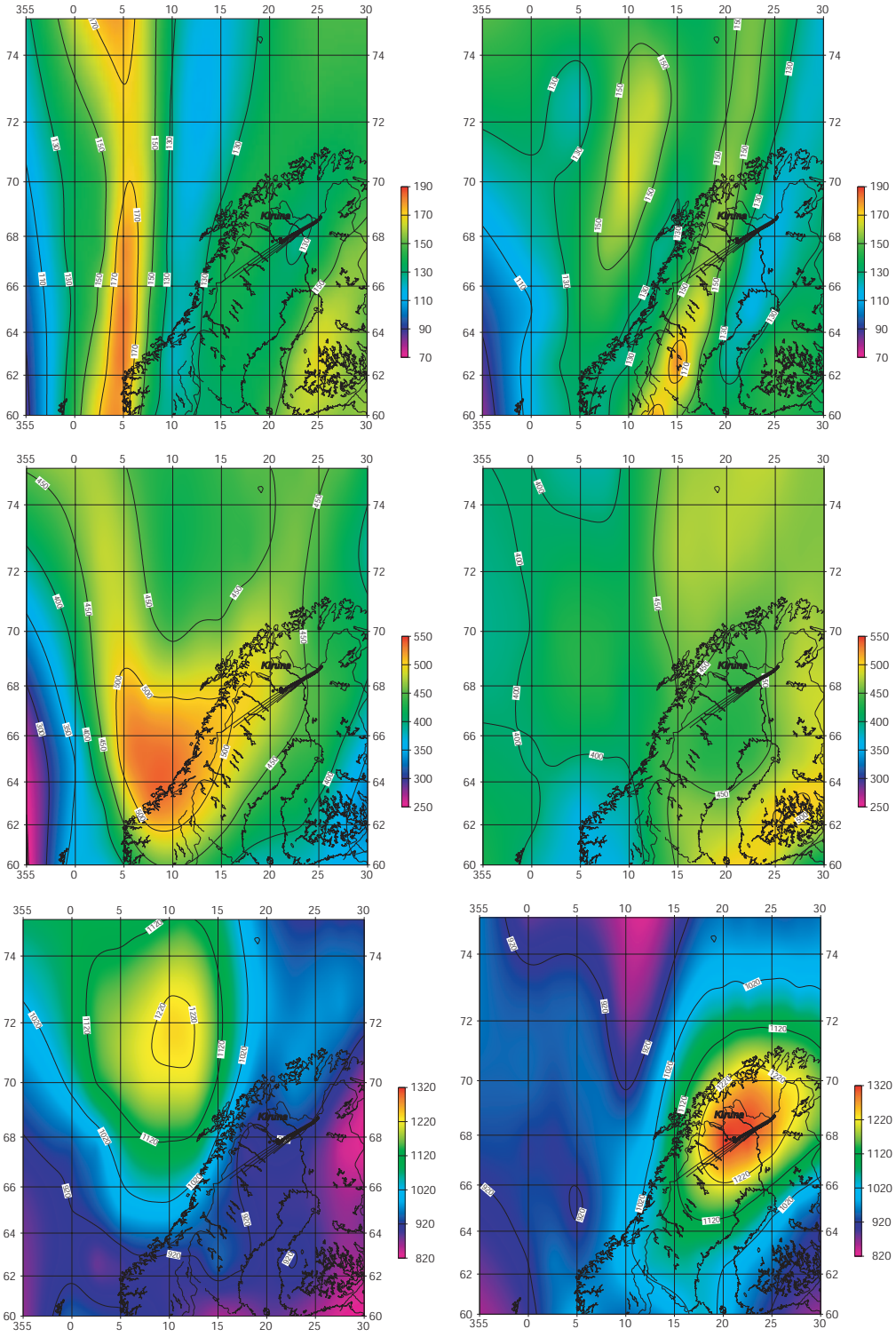

Figure 6.9: Map of potential vorticity on the 400 K (upper row) (15.5 km), 475 K (middle row) (19.8 km) and 550 K (lower row) (22.9 km) potential temperature level over Europe as given by ECMWF analyses at 12 UT on Feb. 10 (left panels) and Feb. 11 (right panels), 1999. Potential vorticity is color-coded according to the scales in units of $10^{-7}\,\mathrm{K\,m^2\,kg^{-1}\,s^{-1}} = 0.1\,\mathrm{PVU}$. Longitude and latitude are given in degree East and degree North, respectively. The trajectory of the LPMA/DOAS balloon launched from Kiruna (67.9°N, 21.7°E) at 11:35 UT on Feb. 10, 1999, is shown as thick solid line. Selected lines-of-sight during solar occultation are represented by thin black lines.

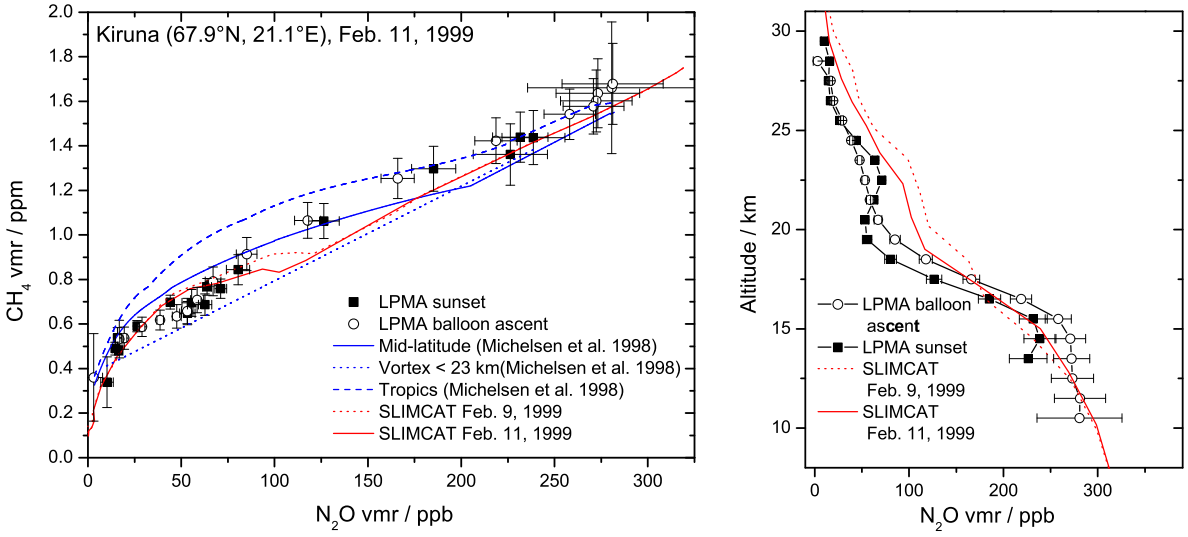

Figure 6.10: CH_4-N_2O correlation (left panel) and N_2O vertical profile (right panel) inferred from measurements of the LPMA/DOAS payload conducted during balloon ascent (open black circles) and solar occultation (filled black boxes) at Kiruna on Feb. 10, 1999. SLIMCAT model output interpolated to Kiruna for Feb. 9 (dotted red line) and Feb. 11 (solid red line) is shown for comparison. Further, the standard CH_4-N_2O correlations given by Michelsen et al. (1998b) for the tropics (blued dashed line), for mid-latitudes (solid blue line) and for the polar vortex (blue dotted line) are plotted. Please note that the Michelsen et al. (1998b) study was conducted between 1992 and 1994 and that the trend in stratospheric N_2O (0.8 ppt/year according to Houghton et al. (2001)) and CH_4 (7.0 ppt/year according to Houghton et al. (2001)) is not considered.

Hence, air masses of mid-latitudinal origin dominated the N_2O solar occultation profile in the altitude range between 22.0 km and 26 km while intra-vortex air dominated below. As already indicated by the tracer-tracer correlations, SLIMCAT model output shows less subsidence above 18 km altitude.

6.2.4 High latitude summer 2001 at Kiruna

In 2001, a LPMA/DOAS balloon flight was conducted between 15:35 UT on Aug. 21 and 2:50 UT on Aug. 22 allowing for measurements during balloon ascent (SZA $\approx 77°$pm to SZA $\approx 88°$pm), sunset (SZA $\approx 90.0°$pm to SZA $\approx 94.5°$pm) and sunrise (SZA $\approx 95.1°$am to SZA $\approx 90.0°$am). Balloon float was reached at 38.5 km altitude. The dynamic conditions in the high-latitude summer stratosphere resemble those at mid-latitudes as illustrated schematically in figure 1.1. The flight was conducted at the time when the stratospheric circulation patterns changed from summertime easterlies to wintertime westerlies and winds were accordingly weak. The balloon drifted slowly to the east but remained close to Kiruna which allowed for a long duration flight and sunrise measurements in the morning after balloon launch.

The trajectory of the balloon and selected lines-of-sight for sunset and sunrise measurements are depicted in figure 6.11. A plot of potential vorticity is omitted here since no major gradients are encountered on the spatial scales pertaining to the balloon flight. Lines-of-sight which exhibit a western component cor-

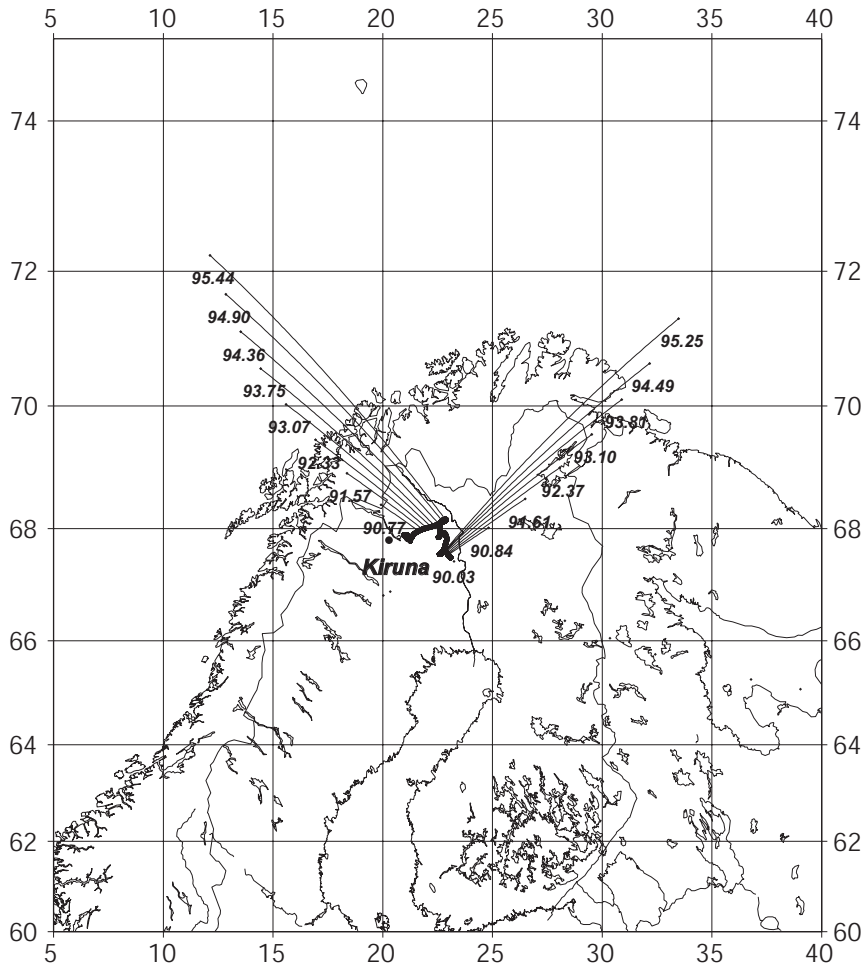

Figure 6.11: Map of northern Scandinavia showing the trajectory of the LPMA/DOAS balloon launched at Kiruna on Aug. 21, 2001 (black thick line). The lines-of-sight for solar occultation measurements are plotted as thin black lines and terminated at the tangent point. The numbers attached to the tangent points are the corresponding solar zenith angles in degree. The branch of lines-of-sight directed to the west corresponds to measurements during sunset, the branch directed to the east corresponds to measurements during sunrise on Aug. 22, 2001. Longitude and latitude are given in degree East and degree North.

respond to sunset measurements while those with an eastern component illustrate sunrise measurements. The CH_4-N_2O correlation (left panel of figure 6.12) has no direct analog among the set of standard correlations provided by Michelsen et al. (1998b). The measured CH_4-N_2O correlation corresponds well to mid-latitudes for $[N_2O] > 125$ ppb and tends to lower CH_4 values for $[N_2O] < 125$ ppb. This might be a indication that polar air masses experienced more aging than mid-latitudinal ones.

SLIMCAT model output on Aug. 21, 2001, agrees well with the observations except for low N_2O where some discrepancies are observed. The N_2O altitude profile (right panel in figure 6.12) supports the finding that air masses are of mid-latitudinal character. The discrepancies observed between balloon ascent and solar occultation profiles below 20 km are hardly understandable from dynamic considerations. In the summer polar stratosphere, horizontal gradients of trace gases due to dynamic reasons, such as observed in polar winter, are not important. Discrepancies as the ones encountered here could arise if the

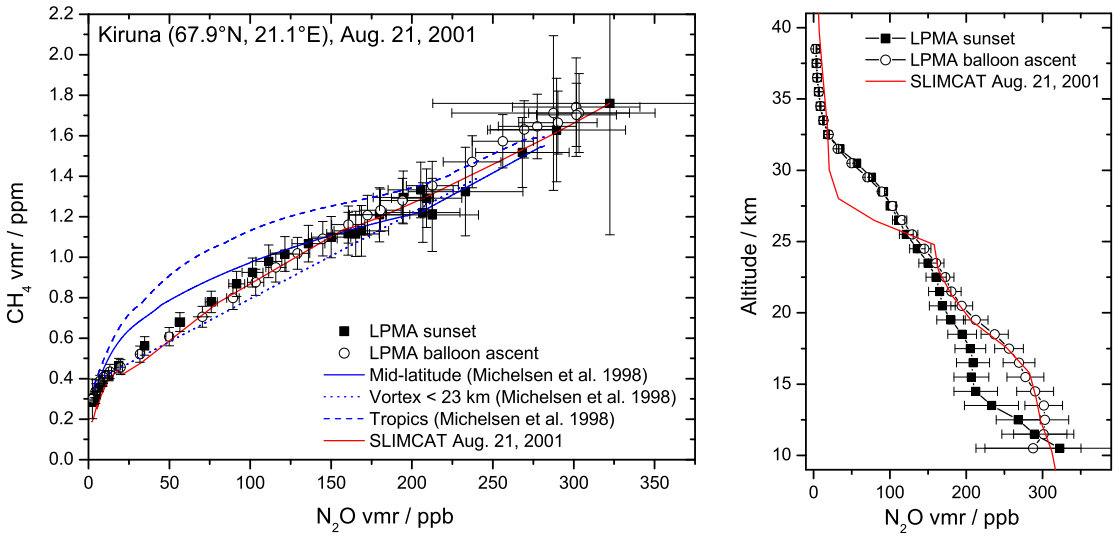

Figure 6.12: CH_4-N_2O correlation (left panel) and N_2O vertical profile (right panel) inferred from measurements of the LPMA/DOAS payload conducted during balloon ascent (open black circles) and solar occultation (filled black boxes) at Kiruna on Aug. 21, 2001. SLIMCAT model output interpolated to Kiruna for Aug. 21 (solid red line) is shown for comparison. Further, the standard CH_4-N_2O correlations given by Michelsen et al. (1998b) for the tropics (blued dashed line), for mid-latitudes (solid blue line) and for the polar vortex (blue dotted line) are plotted. Please note that the Michelsen et al. (1998b) study was conducted between 1992 and 1994 and that the trend in stratospheric N_2O (0.8 ppt/year according to Houghton et al. (2001)) and CH_4 (7.0 ppt/year according to Houghton et al. (2001)) is not considered.

pointing of the LPMA instrument to the Sun was not correctly described by the retrieval algorithm as discussed in section 3.2.4. Although the lines-of-sight are corrected for pointing errors, a remaining small error can cause an erroneous N_2O profile at low altitudes. The impact of such a pointing error is largest for those species which exhibit their concentration maximum in the troposphere and a sharp concentration decrease in the stratosphere, like N_2O (Dufour, 2005). The agreement between observations during balloon ascent and SLIMCAT model data is good up to 25 km. Above 25 km SLIMCAT underestimates the measured N_2O mixing ratio.

6.3 NO_y budget and partitioning

The budget of reactive nitrogen NO_y and the partitioning of its constituents is of major importance for stratospheric photochemistry (e.g. Crutzen, 1970; Portmann et al., 1999). On the one hand, short-lived NO and NO_2 species act as ozone loss catalysts which dominate ozone destruction between 25 km and 40 km altitude, on the other hand NO_x plays an important role as scavenger of the HO_x, ClO_x and BrO_x catalysts and thus hinders ozone loss due to the respective catalytic cycles (section 1.2.3). The partitioning between the short- and long-lived species is of particular importance since it is the ratio NO_x/NO_y which determines the amount of nitrogen compounds available for catalytic ozone destruction or scavenging of other catalysts. In the Arctic and Antarctic winter stratosphere the budget and partitioning of NO_y is difficult to assess since mixing processes of intra- and extra-vortex air, intra-vortex subsidence and denitrification may lead to misinterpretation when not correctly accounted for. Ultimately, the correct representation of the NO_y budget and partitioning under various geophysical conditions in chemistry transport models of the stratosphere is a prerequisite for modeling the past and future evolution of stratospheric ozone correctly.
Here, we present model-measurement comparisons for some case studies performed by the LPMA/DOAS balloon payload. In the following, the NO_y budget and the partitioning of its constituents are investigated for a high-latitude winter and high-latitude summer scenario. The discussion highlights the differences between the considered scenarios and the agreement with the SLIMCAT chemical transport model. Then, the partitioning between short- and long-lived NO_y species is assessed by comparing modeled and measured NO_2/HNO_3 under mid- and high-latitude winter and summer conditions. Finally, a case study of the Arctic winter NO_y budget is revisited and discussed with respect to transport, mixing processes and possible denitrification.

6.3.1 NO_y and its constituents

Numerous studies investigated the NO_y budget in the stratosphere under various geophysical conditions. Around 1999 it was found that the understanding of the partitioning between the NO_x catalyst and available nitrogen NO_y was incomplete (Morris et al., 1997; Sen et al., 1998; Danilin et al., 1999; Drdla et al., 1999; Gao et al., 1999; Osterman et al., 1999; Randeniya et al., 1999; Bösch, 2002). Atmospheric models substantially underestimated the NO_x/NO_y or alternatively the NO_2/HNO_3 ratios compared to observations by balloon and space borne instruments. These findings implied that either rate constants as recommended by the commonly used JPL-1997 compilation (DeMore et al., 1997) were incorrect or some chemical reactions were missing. Subsequent laboratory studies discovered that the rate constants of the OH + NO_2 association reaction (R1.31) and of the OH + HNO_3 reaction (R1.36) were indeed incorrect (Dransfield et al., 1999; Brown et al., 1999a,b; D'Ottone et al., 2001). Model-measurement comparisons (Gao et al., 1999; Payan et al., 1999; Salawitch et al., 2002; Prasad, 2003) confirmed the expected improvement when using the newly recommended rate constants later implemented in the updated JPL-2000 recommendation (Sander et al., 2000). As pointed out in section 1.2.3, Golden and Smith (2000) suggested the formation of pernitrous acid (HOONO) from reaction (R1.31). This second pathway would cause a decrease of the overall HNO_3 formation rate since the HOONO isomer is collisionally or photolytically decomposed into its educts. Since the findings on the importance of the HOONO formation are somewhat contradictory (Dransfield et al., 1999; Nizkorodov and Wennberg,

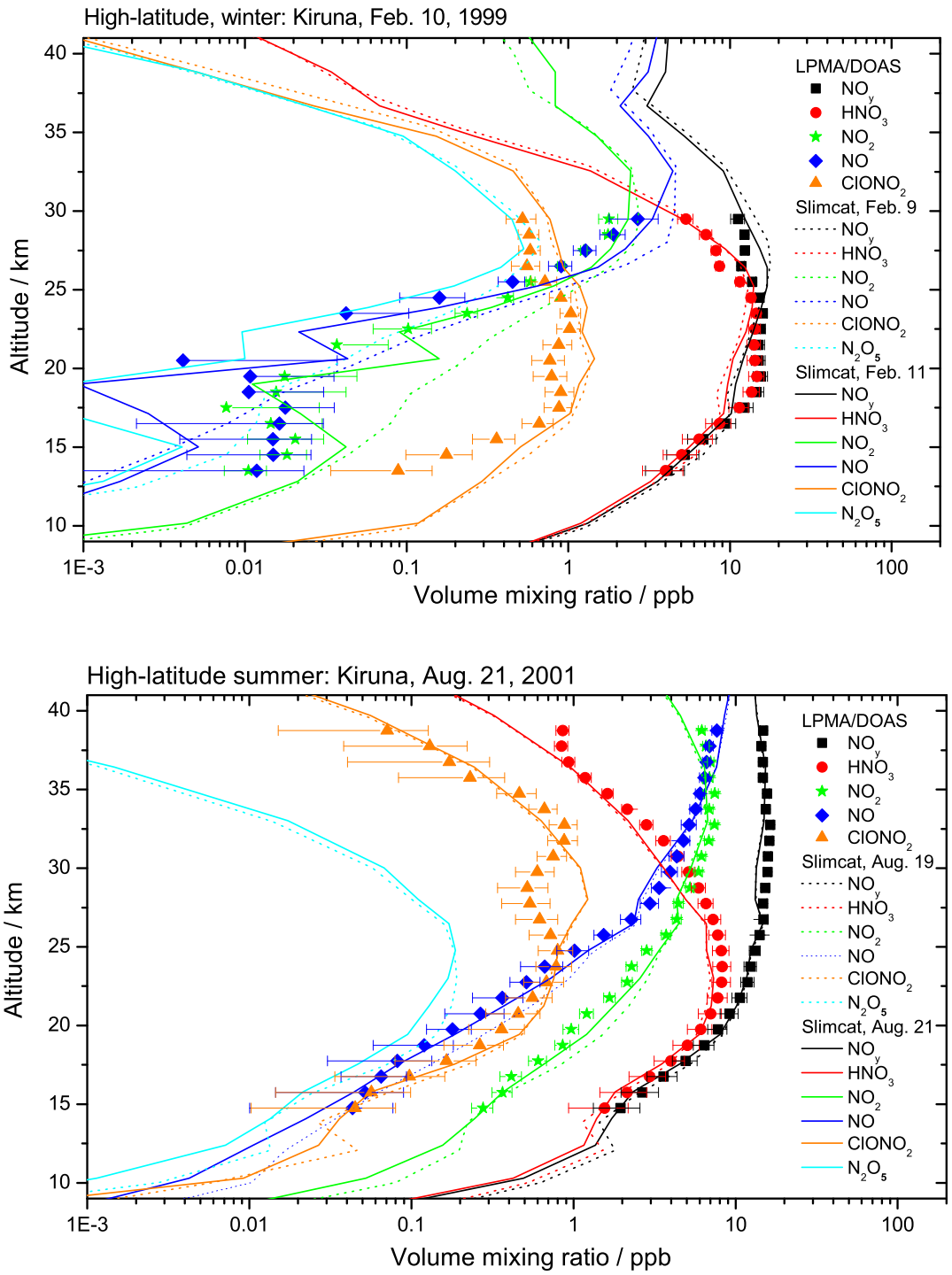

Figure 6.13: Measured (symbols) and modeled (lines) volume mixing ratios of NO_y (black boxes), HNO_3 (red circles), NO_2 (green stars), NO (blue diamonds), N_2O_5 (cyan, modeled only) and $ClONO_2$ (orange triangles) for sunset measurements conducted during the balloon flights from Kiruna on Feb. 11, 1999, (upper panel) and on Aug. 21, 2001 (lower panel). Model output is shown for Feb. 9 (dotted lines) and Feb. 11 (solid lines), 1999, and for Aug. 19 (dotted lines) and Aug. 21 (solid lines), 2001.

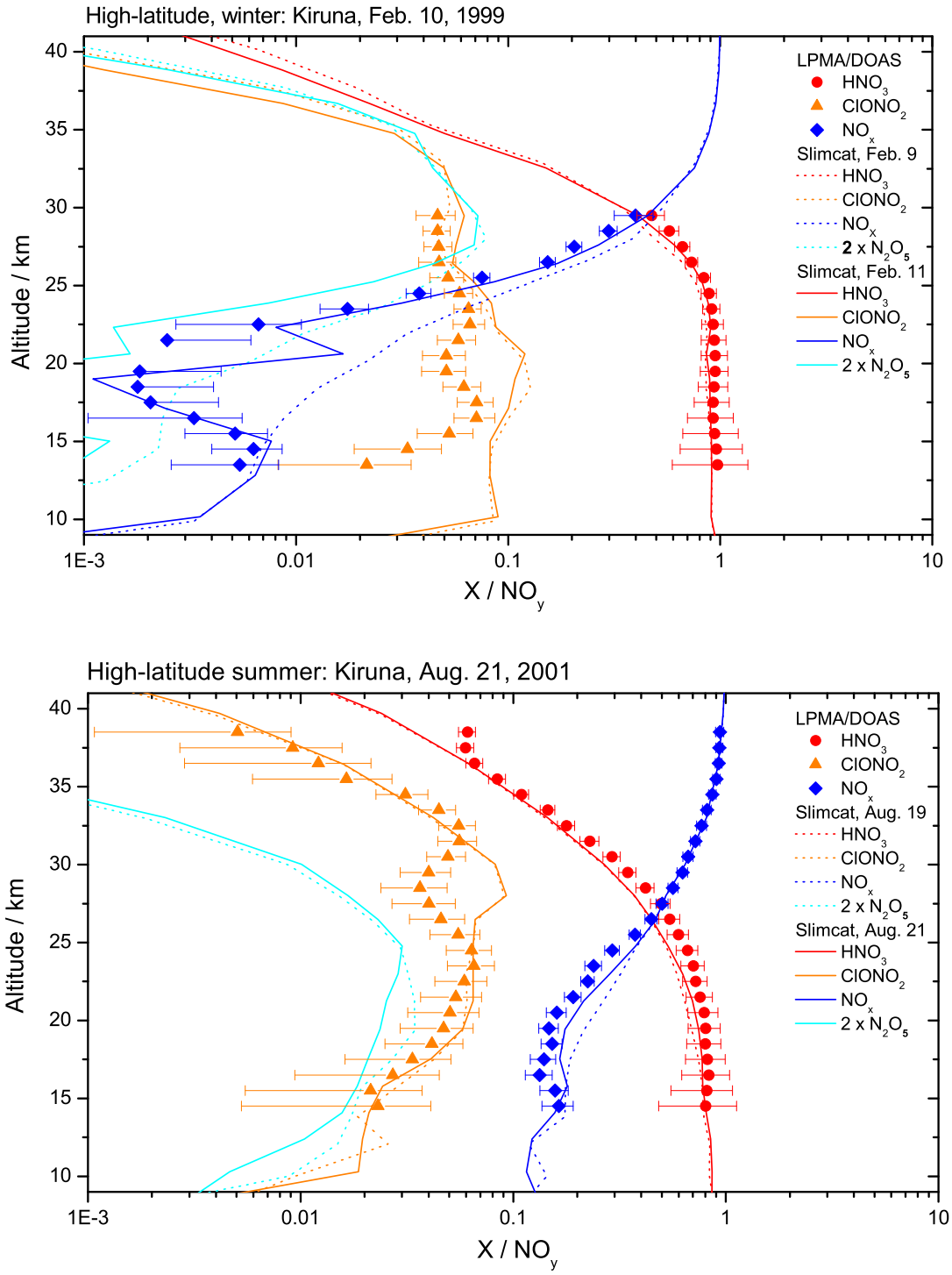

Figure 6.14: Measured (symbols) and modeled (lines) abundances of HNO_3 (red circles), NO_x (blue diamonds), N_2O_5 (cyan, modeled only) and $ClONO_2$ (orange triangles) with respect to NO_y for sunset measurements conducted during the balloon flights from Kiruna on Feb. 11, 1999, (upper panel) and on Aug. 21, 2001 (lower panel). Model output is shown for Feb. 9 (dotted lines) and Feb. 11 (solid lines), 1999, and for Aug. 19 (dotted lines) and Aug. 21 (solid lines), 2001.

2002), the latest JPL compendium on reaction constants, JPL-2002 (Sander et al., 2003), recommends to consider only HNO_3 formation from reaction (R1.31). JPL-2002 further includes some minor updates on the values of the respective rate constants. Recently, Wetzel et al. (2002) and Stowasser et al. (2002) compared their balloon borne measurements conducted in the Arctic winter stratosphere to output of the CTM KASIMA and found, that in particular under dynamically active conditions, the CTM still fails to reproduce the measured partitioning of reactive nitrogen. In the polar summer stratosphere, Dufour et al. (2005) found good agreement when comparing LPMA/DOAS measurements of NO_y constituents to output of the CTM REPROBUS.

Here, the dataset of Dufour et al. (2005) obtained at Kiruna in August 2001 is revisited and supplemented by the measurements conducted by the LPMA/DOAS payload in the winterly Arctic stratosphere at Kiruna in February 1999 during sunset. The latter scenario was analyzed by Bösch (2002) but before the multifit retrieval was implemented. The instrumental setup of both flights allows for the retrieval of the NO_y constituents NO, NO_2, HNO_3 and $ClONO_2$. Here, NO_y is calculated from $NO + NO_2 + HNO_3 + ClONO_2 + 2\,N_2O_5$ where N_2O_5 is taken from output of the SLIMCAT CTM since it is not directly measured. Minor abundant constituents, e. g. HO_2NO_2 and $BrONO_2$, are neglected. NO_x is given as the sum of NO and NO_2. Vertical profiles of the radical species NO and NO_2 are scaled to SZA = 90° using LABMOS model output according to the method described in section 5.3. The major difference between the retrieval used in Dufour et al. (2005) and here, is the spectral range of the HNO_3 retrieval window which was narrowed from a $25\,cm^{-1}$ wide range centered about $860\,cm^{-1}$ to the interval $[905.64\,cm^{-1}, 908.59\,cm^{-1}]$. Further, we use NO_2 and O_3 profiles measured by the DOAS instead of the LPMA instrument according to the findings in section 4. The observed trace gas profiles are compared to SLIMCAT model output interpolated to the launch site. SLIMCAT uses rate constants according to the latest JPL-2002 recommendation (Sander et al., 2003). Since SLIMCAT output is only available every two days, two sets of model output are shown for each balloon flight corresponding to different days.

Figures 6.13 and 6.14 show the measured and modeled trace gas profiles and their composites NO_y and NO_x retrieved from solar occultation measurements in the Arctic stratosphere under winter and summer conditions. The volume mixing ratios of the trace gases are plotted in figure 6.13 while their relative abundances with respect to NO_y are shown in figure 6.14.
In the lower stratosphere, NO_y increases due to its release from N_2O and peaks with about 15 ppb in the middle stratosphere. At higher altitudes the primary sink process for NO_y, i. e. the reaction of NO with atomic nitrogen forming atomic oxygen and molecular nitrogen, becomes important and NO_y decreases. In accordance with the general circulation patterns, which predict strong subsidence of air masses in the winter hemisphere, the NO_y profile appears downward shifted when comparing the winter with the summer observations. For the Arctic winter flight observed HNO_3 constitutes more than 95% and 85% of NO_y at 15 km and 25 km, respectively. The corresponding fractions for the summerly stratosphere are 80% at 15 km and 60% at 25 km. The measurement of the reservoir species $ClONO_2$ indicates a broad layer peaking with about 1.2 ppb between 15 km and 25 km altitude for the Kiruna 1999 flight. For Kiruna 2001, a somewhat broader layer between 15 km and 35 km peaking around 0.8 ppb is observed. NO_x is by one order of magnitude more abundant for the summer than for the winter observations in the lower stratosphere. While the fractional contribution of summerly NO_x to NO_y increases from about 15% at 20 km to 50% at 28 km, winterly NO_x contributes less than 1% to NO_y below 20 km and attains

50% contribution at 30 km. Above 30 km NO_x dominates NO_y for both scenarios. The low amounts of NO_x around and below 20 km observed for Kiruna 1999 point at denoxification, i. e. air masses in the considered altitude layer are strongly depleted in NO_x since most of NO_x is converted to N_2O_5 and subsequently to HNO_3. This finding is a very likely scenario since air masses at 19.8 km (475 K) experienced several days of darkness over the North Pole 48 h before reaching Kiruna as illustrated in figure 6.8.
SLIMCAT model output is shown for two days temporally close to the date of the balloon flight. While for Aug. 21, 2001, model output is available on the actual day of the measurement, model data for Kiruna 1999 correspond to one day before and one day after the balloon flight on Feb. 10, 1999. The large differences between model output on Feb. 9 and Feb. 11, 1999, reveal the difficulty when performing ad-hoc model-measurement comparisons under dynamically active conditions: Close to the polar vortex gradients of trace gas concentrations may be large on small spatial scales depending on the dynamic and photochemical history of the considered air masses. Concentration gradients may impact the agreement in model-measurement comparisons, since the LPMA/DOAS measurements represent horizontal averages of the trace gas profiles and model output is rather a model grid point snapshot. In the presented case, model output on Feb. 11 seems to simulate the dynamic and photochemical conditions encountered during the balloon flight better than model output on Feb. 9. This finding is supported by the comparison of the modeled and observed N_2O profiles (figure 6.10, right panel). Hence, the following discussion for Kiruna 1999 is based on model output for Feb. 11, 1999. For Kiruna 2001 differences between the two days of model output are small as expected from the rather unperturbed flow of polar air masses in summer.
In the Arctic winter stratosphere, SLIMCAT underestimates observed NO_y between 17 km and 24 km and overestimates it above. Underestimation in the lower stratosphere mainly comes from HNO_3 which is low compared to observations. Overestimation of NO_y above 24 km originates from higher than observed NO_2, NO and $ClONO_2$ concentrations. Below 24 km, the measured abundances of NO, NO_2 and $ClONO_2$ are modeled fairly well except for a layer around 21 km altitude where SLIMCAT output of the respective species is higher than the observed abundances.
Under summerly conditions, measured NO_y is captured very well by the SLIMCAT model in the entire retrieved altitude range. Small discrepancies can be observed between 25 km and 35 km altitude where the model underestimates measured HNO_3 and accordingly the composite NO_y. Similarly, observed $ClONO_2$ is reproduced well by the model except for an altitude layer around 29 km where a dip in the trace gas profile is not captured. However, SLIMCAT overestimates NO and NO_2 and consequently NO_x by up to 30% between 15 km and 28 km altitude.
Modeled abundances of N_2O_5 cannot be compared to measurements. However, from the model calculations it is evident that its abundances in the Arctic winter and summer stratosphere are quite different. For the winterly dataset Kiruna 1999, N_2O_5 concentrations below 20 km are very low indicating that most of the NO_x converted to the night-time reservoir N_2O_5 is further processed to HNO_3 causing strong denoxification of the lower stratosphere. Above 25 km, N_2O_5 abundances constitute up to 3% of NO_y. In the Arctic summer stratosphere, N_2O_5 accounts for less than 1% of NO_y exhibiting a wide layer between 15 km and 25 km altitude. This is consistent with the fact that during summer NO_x is effectively recovered from its night-time reservoir N_2O_5 since the sunlit fraction of the day is large.

In general, the LPMA/DOAS observations at Kiruna in winter 1998/99 and summer 2001 corroborate the picture that in winter the partitioning between NO_y constituents in the Arctic stratosphere

is shifted toward the reservoir species compared to summerly conditions. For the Arctic winter observations in 1998/99 strong denoxification was found in the lower stratosphere. SLIMCAT describes well the overall partitioning of NO_y including the denoxified layer observed for the Arctic winter case. However, the case studies indicate a tendency of the model to underestimate HNO_3 and to overestimate NO and NO_2. The latter finding is discussed in detail in the following section.

6.3.2 NO_2 / HNO_3 partitioning

Unfortunately, NO and $ClONO_2$ cannot be inferred from LPMA spectra for some flights due to the choice of spectral filters which cut the respective retrieval ranges. In addition, $ClONO_2$ can only be retrieved from solar occultation measurements, since the $ClONO_2$ signal is too small for a retrieval from balloon ascent measurements. Hence, retrieval of NO_x and NO_y is often not possible from LPMA/DOAS measurements. The ratio NO_2/HNO_3, however, can be used in model-measurement comparisons to estimate the agreement between modeled and measured NO_x/NO_y. The previous section indicated that SLIMCAT tends to underestimate HNO_3 and to overestimate NO and NO_2. Here, we present NO_2/HNO_3 measured during balloon ascent and solar occultation by the LPMA/DOAS payload at Leon in 1996, at Kiruna in 1997, 1999 and 2001. The observations are compared to SLIMCAT model data in figure 6.15. For the high-latitude summer observations, also output of the REPROBUS CTM (Lefèvre et al., 1994) is presented.

In general the NO_2/HNO_3 ratio increases with altitude since photolysis of the reservoir species becomes more effective at high altitudes. Typically, NO_2 and HNO_3 are equally abundant around 30 km altitude. The finding of the previous section that the NO_y partitioning is shifted toward the reservoir species during high-latitude winter is confirmed by figure 6.15. During high-latitude winter at Kiruna on Feb. 14, 1997, and Feb. 10, 1999, NO_2 concentrations are less than 1% of the HNO_3 concentrations in the lower stratosphere. For Kiruna 1999, a denoxified layer around 20 km altitude is discernible in the NO_2/HNO_3 ratio which is also identified in the NO_x/NO_y ratio in the previous section. In contrast, the high-latitude winter observations at Kiruna in 1997 show no signs of denoxification. Under polar summer conditions encountered for Kiruna 2001, NO_2 in the lower stratosphere amounts to about 10% of HNO_3. The mid-latitude observations at Leon on Nov. 23, 1996, are conducted close to winter solstice but still exhibit a larger NO_2/HNO_3 ratio than the polar winter measurements. Differences between balloon ascent, sunset and sunrise measurements are either due to sampling of air masses with different photochemical and dynamic character (section 6.2) or due to the diurnal variation of NO_2 described in section 1.2.3. From the latter, NO_2/HNO_3 is expected to be largest for sunset observations and slightly smaller for balloon ascent and sunrise.
SLIMCAT model output is shown for several SZAs on two days temporally close to the balloon flights. Balloon ascent measurements are typically conducted between SZA = 75° and SZA = 85° while solar occultation observations correspond to SZA = 90°. Due to the night-time build-up and day-time decomposition of the N_2O_5 reservoir it is important to distinguish between SZA = 90°am for sunrise and SZA = 90°pm for sunset. When comparing model output at different days it is evident that dynamic and photochemical variability is largest in the winter polar stratosphere rendering model-measurement comparisons somewhat delusive. For Kiruna 1997, SLIMCAT output on Feb. 15 agrees reasonably well with the measurements conducted the day before. SLIMCAT output on Feb. 13 shows a distinct

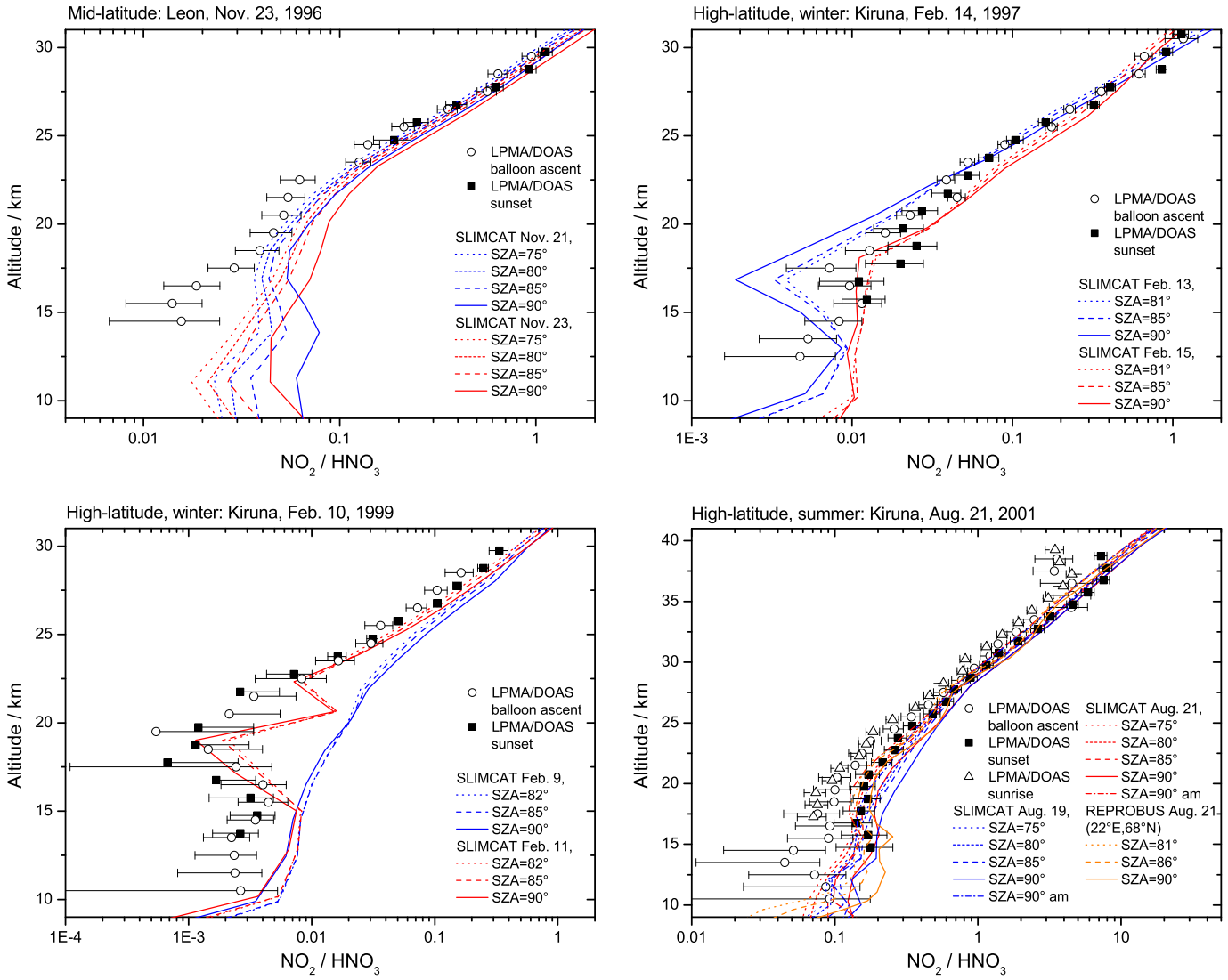

Figure 6.15: NO_2/HNO_3 for the balloon flights from Leon in 1996 (upper left panel), from Kiruna in 1997 (upper right panel), 1999 (lower left panel) and 2001 (lower right panel). Data inferred from balloon ascent, sunset and sunrise are shown as black open circles, black filled boxes and black open triangles respectively. SLIMCAT model output corresponds to the days and SZAs (pm if not stated otherwise) as indicated in the legend. If necessary for clarity, measured data are slightly offset in altitude.

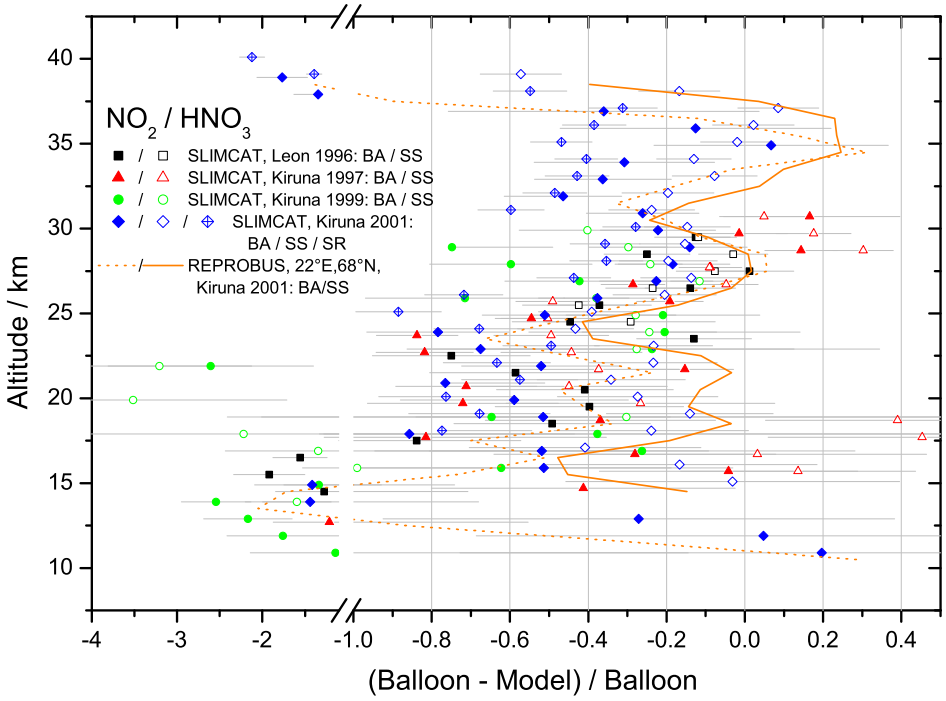

Figure 6.16: Relative deviations between SLIMCAT (and REPROBUS for Kiruna 2001) model output and balloon borne measurements of NO_2/HNO_3. The symbols are labeled according to their observations sites and conditions as given by the legend (BA: balloon ascent, SS: sunset, SR: sunrise). Error bars correspond to the relative errors of the measurements. Note the broken abscissa.

denoxified layer around 17 km which cannot be seen in the measured NO_2/HNO_3 profile. For Kiruna 1999 the agreement between model and measurement is best for output on Feb. 11, where the observed denoxified layer is reproduced by the model below 20 km. Above 20 km modeled NO_2/HNO_3 is larger than observed. Model simulations for Feb. 9 are consistently larger than observations. For the mid-latitude and high-latitude summer datasets spatial inhomogeneities of the trace gases are less important. There, the model is larger than LPMA/DOAS over the entire altitude range. Figure 6.15 also shows output of one grid point (22°E, 68°N) of the REPROBUS CTM for Kiruna 2001. The REPROBUS data are used and refined by a temporal and spatial interpolation scheme in the Dufour et al. (2005) study.

Figure 6.16 summarizes the deviations between modeled NO_2/HNO_3 and the corresponding LPMA/DOAS measurements. SLIMCAT output on Nov. 23, 1996, Feb. 15, 1997, Feb. 11, 1999, and Aug. 21, 2001, is chosen for comparison. The model data are interpolated to the altitude grid of the measured trace gas profiles and subsequently referenced to the balloon borne data. Although the scatter is large, a clear overestimation of the observations by the model is obvious. Above 25 km the bias is less pronounced than below where the mean difference amounts to about 50%. Interpretation of the differences between model and measurement with respect to photochemistry is difficult since dynamic effects might hinder the comparison in particular for the high-latitude winter data sets in the lower

stratosphere. However, nearly all data points independent of season and latitude reveal a high-bias of the model with respect to the balloon borne NO_2/HNO_3 observations which is larger than the measurement errors. A low-bias is only observed for single data points. The REPROBUS dataset for Kiruna 2001 seems to be less high-biased than the corresponding SLIMCAT data.
Somewhat in contradiction to these findings, Dufour et al. (2005) showed that the LPMA/DOAS Kiruna 2001 dataset is in good agreement with the REPROBUS CTM. The dataset presented by Dufour et al. (2005) for Kiruna 2001 is not directly comparable to the data shown here, since here NO_2 is taken from DOAS observations which are found to be more accurate than LPMA NO_2 measurements (section 4). The internal agreement of LPMA and DOAS NO_2 profiles for Kiruna 2001 is shown in figures 4.9 and 4.16 where LPMA is found to underestimate the DOAS data by about 10% - 30% above 25 km. Furthermore, at altitudes lower than 20 km *a priori* information impacts the LPMA retrieval more than the DOAS retrieval (figure 4.12). Hence, using NO_2 inferred from LPMA measurements would produce even larger differences between measured and modeled NO_2/HNO_3. However, Dufour et al. (2005) concluded on good model-measurement agreement after constraining REPROBUS to measured O_3 and NO_y and using aerosol surface area densities measured by Deshler et al. (2003). These constraints are not applied to the SLIMCAT model, here.

In the considered altitude range production and loss of HNO_3 is essentially governed by reactions (R1.31), (R1.57), (R1.36), (R1.56) and (R1.123), i. e. the production of HNO_3 through OH and NO_2, the loss of HNO_3 through photolysis and reaction with OH, and the heterogeneous conversion of N_2O_5 and $BrONO_2$ to HNO_3. Assuming photochemical steady state for HNO_3 and balancing the loss and production mechanisms yields

$$\frac{[NO_2]}{[HNO_3]} \approx \frac{J_{HNO_3} + k_{HNO_3+OH}\,[OH]}{k_{NO_2+OH}\,[OH] + 2\,k_{N_2O_5(g)+H_2O(s)}\,\frac{[N_2O_5]}{[NO_2]} + k_{BrONO_2(g)+H_2O(s)}\,\frac{[BrONO_2]}{[NO_2]}}. \quad (6.1)$$

When assuming photochemical steady state, a caveat applies since the considered trace gas concentrations and the photolysis frequency J_{HNO_3} exhibit diurnal variations. Equation (6.1), however, should be approximately valid for 24-h averaged quantities (Randeniya et al., 1999). Besides, equation (6.1) is not meant as an exact relation but rather serves as a starting point for an estimate of the relative importance of errors and uncertainties which might be responsible for the observed model-measurement discrepancy.
The terms of equation (6.1) are plotted in figure 6.17 as effective first order rate constants and relative contributions to numerator and denominator. The Kiruna 1999 and 2001 case studies representing high-latitude winter and summer are chosen for illustration. Concentrations are taken from SLIMCAT model output on Feb. 11, 1999, and Aug. 21, 2001, and averaged over 24 hours. The rate coefficients are calculated from the JPL-2002 (Sander et al., 2003) recommendation using ECMWF temperature and pressure profiles of the respective dates while the 24-h average of J_{HNO_3} is taken from the LABMOS calculation scheme for photolysis frequencies (section 1.3). Aerosol surface area densities originate from the SLIMCAT aerosol climatology based on SAGE II measurements.
Photolysis of HNO_3 is the dominant loss term during high-latitude summer and winter above about 25 km. In summer J_{HNO_3} governs HNO_3 loss also below 25 km while in winter the reaction of HNO_3 with OH becomes important. Similarly, production of HNO_3 through OH + NO_2 is most important above 25 km for both seasons but is exceeded by the heterogeneous processes below 25 km for the winter scenario. The overwhelming contribution of the $BrONO_2$ + H_2O(s) reaction below 20 km for

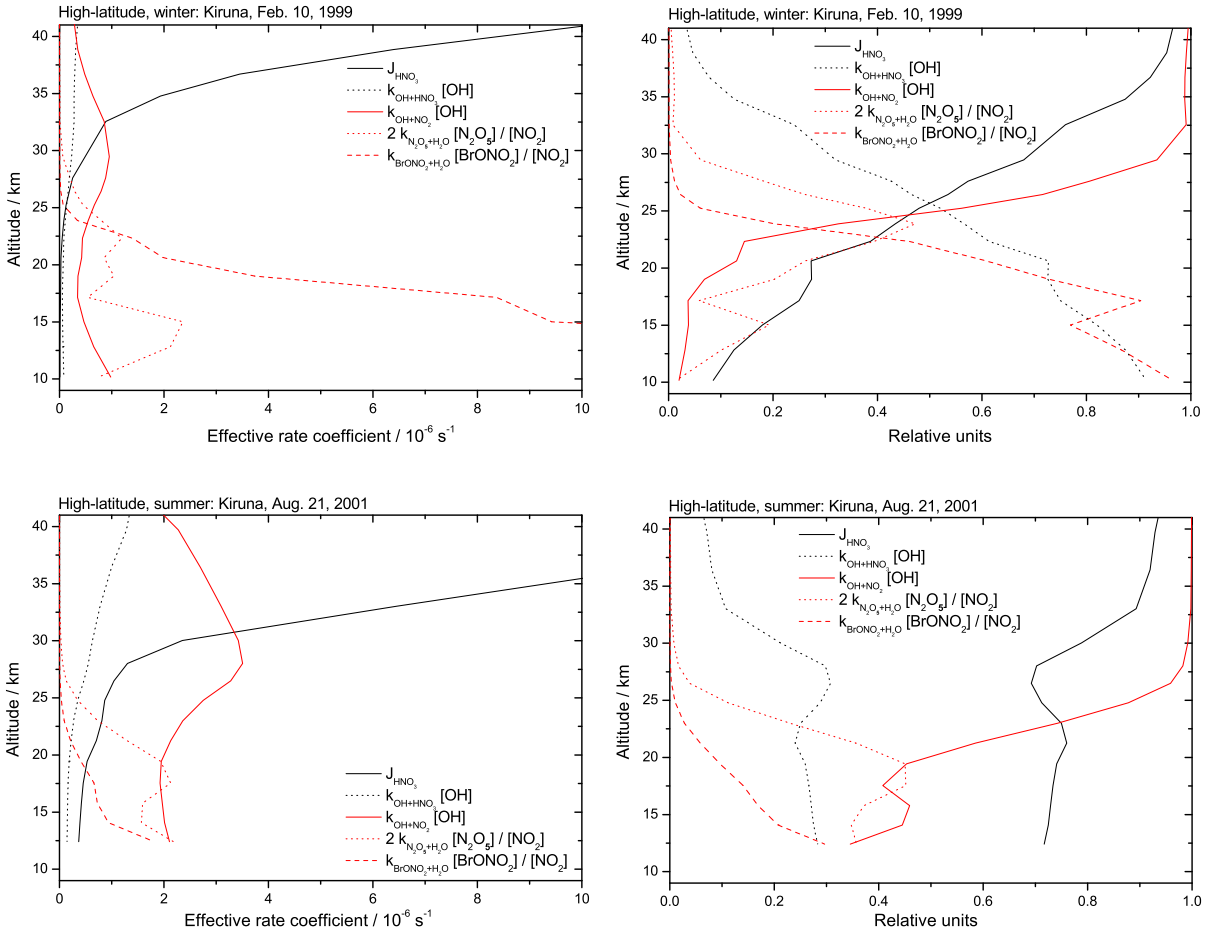

Figure 6.17: Effective first order rate coefficients (left column) and relative contributions to production and loss of HNO_3 (right column) for the high-latitude winter scenario Kiruna 1999 (upper row) and the high-latitude summer scenario Kiruna 2001 (lower row). All data shown are 24h-averaged quantities. Black lines correspond to loss terms of HNO_3 represented by the numerator of equation (6.1) while red lines correspond to production terms of HNO_3 in the denominator of equation (6.1). The relative contributions (right column) are calculated with respect to the numerator and the denominator of equation (6.1), i. e. the sum of all black/red lines is equal to one. Since at Kiruna in 2001 the tropopause was located around 12 km altitude, no data are shown below that altitude. See legend for further details.

high-latitude winter comes from denoxification in the respective altitude range (figure 6.13). There, NO_2 abundances are particularly small and hence, the term $\frac{[BrONO_2]}{[NO_2]}$ becomes large while $\frac{[N_2O_5]}{[NO_2]}$ plays a minor role since N_2O_5 concentrations are low, too. It has to be pointed out that the Kiruna 1999 case is neither typical of an intra-vortex nor an extra-vortex high-latitude winter scenario due to the complex dynamic and meteorological situation. Heterogeneous processes on PSCs are not considered for the steady-state estimate. The Kiruna 2001 scenario seems to be less ambiguous and typical of high-latitude summer conditions.

The photolysis frequency of HNO_3 is of major importance for the partitioning between NO_2 and HNO_3. The uncertainty factor of J_{HNO_3} is stated as 1.3 by Sander et al. (2003). Dividing J_{HNO_3} by 1.3

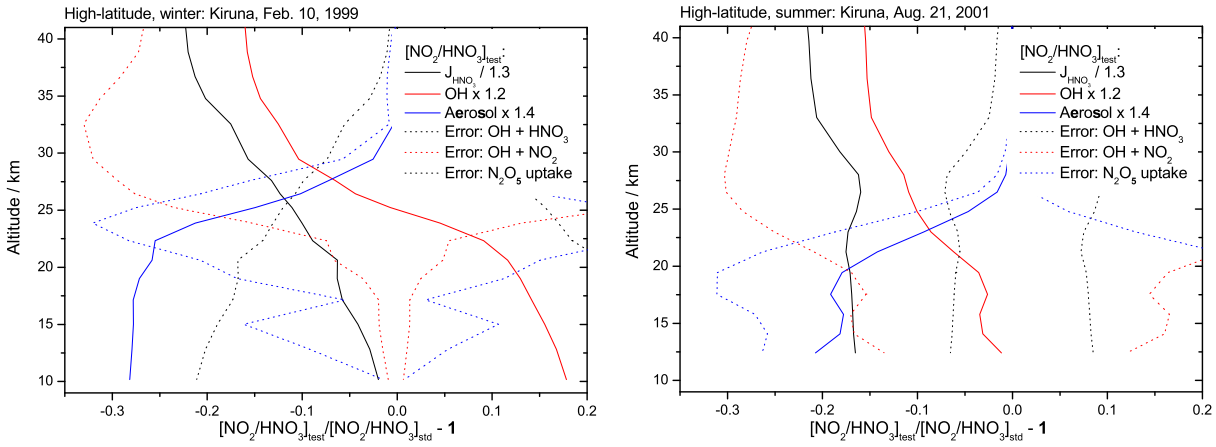

Figure 6.18: Relative sensitivity of calculated NO_2/HNO_3 to errors and uncertainties of several parameters for the Kiruna 1999 (left panel) and Kiruna 2001 (right panel) scenario. Various test-calculations where a single parameter is changed are referenced to the standard calculation described in the text. Negative sensitivities indicate that the modeled NO_2/HNO_3 ratio would be shifted toward the measured one. For details see legend and accompanying text.

shifts the NO_2/HNO_3 ratio toward HNO_3. Hence, if J_{HNO_3} was lowered by its uncertainty factor, the agreement between SLIMCAT and LPMA/DOAS measurements would improve. J_{HNO_3} is calculated according to equation (1.7) from the absorption cross section, the quantum yield and the actinic flux. The uncertainty factor refers to the product of the absorption cross section and the quantum yield. Additionally, erroneous calculation of the actinic flux, e. g. by erroneously modeled ozone abundances, could impact modeled J_{HNO_3}. Figure 6.18 shows the relative sensitivity of NO_2/HNO_3 calculated according to equation (6.1) to changes of several parameters i. a. J_{HNO_3}. Under summerly conditions where photolysis of HNO_3 is the major loss process a decrease of J_{HNO_3} by its uncertainty factor almost linearly maps into a decrease of calculated NO_2/HNO_3 by about 20%. For the high-latitude winter case the sensitivity to J_{HNO_3} decreases at lower altitudes where the reaction of OH with HNO_3 becomes the dominant loss process of nitric acid. The uncertainty factor of the latter loss process is 1.2 (Sander et al., 2003). Corresponding to its relative importance, the impact on NO_2/HNO_3 is largest for low altitudes during winter. In addition, this second loss term depends on the concentration of OH, which is also involved in the production of HNO_3 through the NO_2 + OH reaction. Increasing the concentration of OH by 20% causes a net decrease of NO_2/HNO_3 above 25 km for both seasons while below 25 km the decrease gets smaller for summer conditions and even becomes a net increase for the Kiruna 1999 scenario. The uncertainty factor of the OH + NO_2 reaction is 1.3 at room temperature and increases with decreasing temperature. Its impact on NO_2/HNO_3 is largest above 25 km where OH + NO_2 is the dominant production process of HNO_3.

The uncertainties of the heterogeneous processes are controlled by the uncertainties of the uptake coefficients of N_2O_5 and $BrONO_2$ and the aerosol surface area density. Sander et al. (2003) recommends $0.05 < \gamma_{N_2O_5} < 0.2$ with the most probable value $\gamma_{N_2O_5} = 0.1$. Increasing $\gamma_{N_2O_5}$ to its upper limit causes the NO_2/HNO_3 ratio to decrease by up to 30% in the altitude range where N_2O_5 hydrolysis is

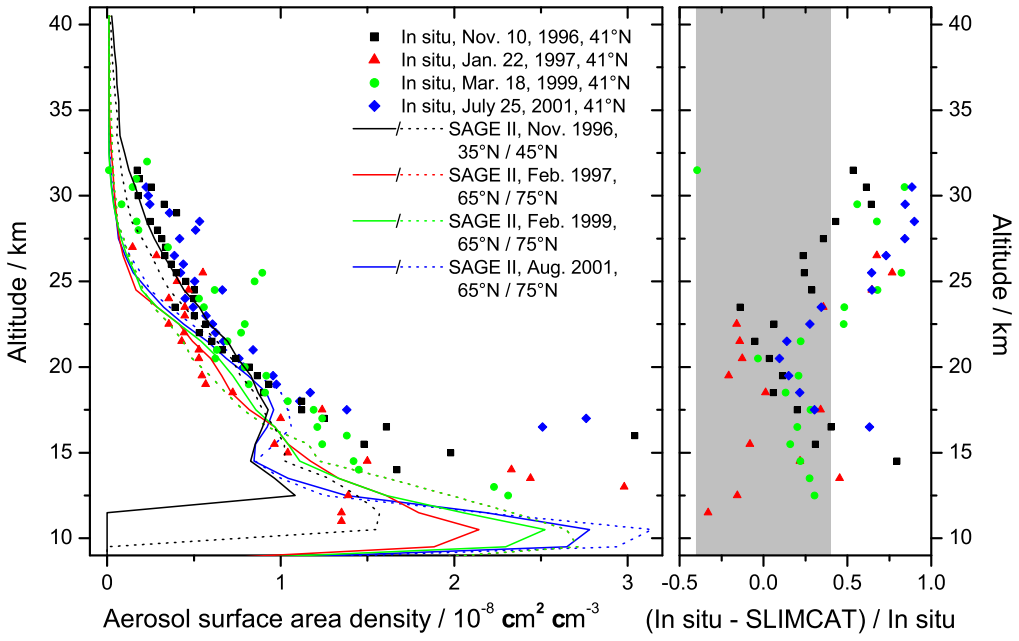

Figure 6.19: Aerosol surface area density taken from the SAGE II climatology used for SLIMCAT input (left panel) and relative differences (right panel) between the climatological and *in situ* data measured by Deshler et al. (2003) at Laramie, Wyoming (41°N). The shaded area in the right panel indicates the relative error of the *in situ* measurements (40%). The monthly zonal mean climatological data are presented for the two latitude bands closest to the considered LPMA/DOAS balloon flights. *in situ* data are selected as temporally close as possible to the LPMA/DOAS observations.

an important HNO_3 production process. For $BrONO_2$ the uptake coefficient depends on sulfuric acid concentrations and is set to its upper limit, here. Hence, true HNO_3 production through $BrONO_2$ + H_2O(s) is most likely smaller than indicated.

The aerosol surface area density (SAD) is a model input parameter which is usually not very well known since measurements are sparse and exhibit large error bars (Deshler et al., 2003). SLIMCAT uses a composite climatology of surface area densities of stratospheric sulfate aerosol based on the satellite borne instrument SAGE II (Russell and McCormick, 1989; Thomason et al., 1997) with contributions from SAGE I (Stratospheric Stratospheric Aerosol and Gas Experiment), SAM II (Stratospheric Aerosol Measurement, (McCormick et al., 1979)), and SME (Solar Mesosphere Explorer, (Eparvier et al., 1994)). The climatological zonal mean data are used as monthly SLIMCAT input and converted to H_2SO_4 volume mixing ratios from the zonal mean pressure, temperature and water abundance. Over the course of one month, H_2SO_4 is advected as inert species and SAD is re-calculated from H_2SO_4 at each model grid point and timestep using local pressure, temperature and H_2O. Deshler et al. (2003) showed that their balloon borne *in situ* measurements of aerosol SAD above Laramie, USA (41°), are on average 40% larger than SAGE II data under background aerosol conditions. Figure 6.19 shows a comparison between the SAGE II climatological data corresponding to the dates and locations of the LPMA/DOAS measurements and *in situ* measurements conducted by Deshler et al. (2003). The

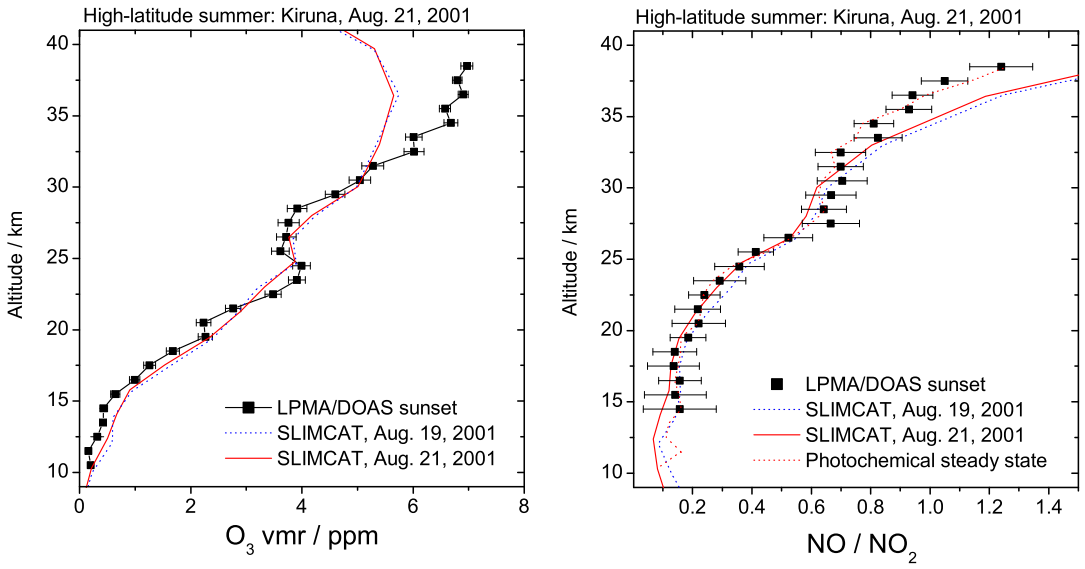

Figure 6.20: Measured (boxes) and modeled (lines) O_3 volume mixing ratios (left panel) and NO/NO_2 ratios (right panel) for sunset measurements conducted during the balloon flights from Kiruna on Aug. 21, 2001. Model output is shown for Aug. 19 (dotted blue line) and Aug. 21 (solid red line) and in the right panel for a photochemical steady state approximation (dotted red line) using the measured O_3 profile.

comparison can only be of illustrative nature, since the *in situ* data are measured at mid-latitudes and the LPMA/DOAS balloon flights are conducted at high-latitudes except for the flight at Leon in 1996. Moreover, during high-latitude winter formation of PSCs might alter the actually encountered and modeled SAD. However, figure 6.19 confirms the findings of Deshler et al. (2003) that the climatological data tend to underestimate the *in situ* data. If there was a low-bias of the aerosol SAD used by SLIMCAT, heterogeneous reactions would proceed less efficiently in the model than in the true atmosphere. The impact of a 40% error of aerosol SAD used by SLIMCAT on the modeled NO_2/HNO_3 ratio is estimated from equation (6.1) and illustrated in figure 6.18. Clearly, the impact is largest (20% to 30%) below 25 km and under winter conditions where heterogeneous processes play an important role. Above 25 km, the impact of erroneous aerosol abundances is small ($< 10\%$).

The above sensitivity estimates used 24h-averaged quantities. A quantity which is not included in equation (6.1) is the partitioning between NO_2 and NO which attains equilibrium on timescales of minutes in the sunlit atmosphere. The modeled NO_2/HNO_3 ratio could easily be wrong if the partitioning between NO and NO_2 was modeled incorrectly. Since photochemistry is rather straightforward in the high-latitude summer stratosphere, the Kiruna 2001 dataset is chosen to illustrate that point. During high-latitude summer the NO/NO_2 ratio is controlled by photolysis of NO_2 and reaction of NO with ozone according to (R1.42) and (R1.44). Hence, incorrectly modeled O_3 could be responsible for erroneous NO/NO_2. Figure 6.20 shows measured and modeled NO/NO_2 and O_3 for sunset measurements at Kiruna in 2001. SLIMCAT underestimates the O_3 profile above 32 km and overestimates it below 18 km. Measured NO/NO_2 is overestimated by the model above 33 km altitude, but is correctly reproduced below. Neglecting the $NO \leftrightarrow NO_2$ cycling reactions (R1.43) and (R1.45) through (R1.48)

and assuming photochemical steady state, NO/NO_2 is given as a function of O_3,

$$\frac{[NO]}{[NO_2]} \approx \frac{J_{NO_2}}{k_{NO+O_3}\,[O_3]}. \tag{6.2}$$

Again the assumption of photochemical steady state is questionable in particular for the LPMA/DOAS solar occultation measurements. The typical lifetimes of NO and NO_2 at SZA = 90° in the stratosphere is in the order of several minutes which in turn is not negligible with respect to the considered timescales. Remembering this drawback and the corresponding limited value of a photochemical steady state approximation, NO/NO_2 is calculated from the measured O_3 profile using equation (6.2) where J_{NO_2}/k_{NO+O} is calculated from the modeled NO/NO_2 ratio and the modeled O_3 concentration. The dotted red line in the left panel of figure 6.20 shows that the differences between modeled and measured O_3 could account for the observed discrepancy in NO/NO_2 above 33 km but changes in the lower stratosphere are small. Moreover, using the measured O_3 would shift the NO/NO_2 partitioning toward NO_2 which in turn would render the modeled NO_2/HNO_3 even larger and worsen the model-measurement comparison. Inspection of the modeled O_3 profiles for the remaining datasets gives no hint on the origin of the systematic model bias for NO_2/HNO_3.

Summing up the above findings on the sensitivity of the NO_2/HNO_3 ratio on various parameters, it is evident that the combined uncertainty of measurement errors, reaction kinetics, aerosol uptake coefficients, trace gas concentrations and aerosol abundances can account for the observed model-measurement discrepancies. As pointed out before, the rate coefficients of the OH + NO_2 and HNO_3 + OH reactions were subject of various studies including such that concluded on good model-measurement agreement. Hence, a major error in the reaction kinetics is unlikely although the recommended uncertainties are large. Photolysis of HNO_3 is an important loss process of HNO_3. Thus small errors in J_{HNO_3} could impact the modeled NO_2/HNO_3 ratio in particular at high altitudes. The systematic low-bias between SLIMCAT and LPMA/DOAS measurements for winter as well as summer is inconsistent with a large error of J_{HNO_3} which should be more significant under summer conditions. OH concentrations modeled by SLIMCAT are difficult to validate and hence the actual error of NO_2/HNO_3 due to erroneous OH is hard to quantify but might be limited due to the cancellation effect of the reactions OH + HNO_3 and OH + NO_2. Aerosol surface area densities and aerosol uptake coefficients are important sources of uncertainty in the lower stratosphere. Comparison of two aerosol data sets revealed that aerosols used by SLIMCAT are systematically low. The NO/NO_2 ratio seems to be modeled fairly well by SLIMCAT and cannot account for the observed high-bias of modeled NO_2/HNO_3.
From the magnitude and altitude dependence of the model-measurement discrepancies and the above sensitivity estimates it is evident that none of the investigated processes alone can account for the observed disagreement. In the lower stratosphere aerosol abundances might be underestimated by SLIMCAT and hence heterogeneous production of HNO_3 is underestimated.

6.3.3 Denitrification versus subsidence and isentropic mixing in the Arctic winter

Denitrification is a process occurring in the winterly polar vortex which permanently removes NO_y from the stratosphere by sedimentation of HNO_3 containing particles (section 1.2.5). As a consequence the abundance of NO_x generated from HNO_3 during spring is too low to effectively scavenge the ClO_x

and BrO_x catalysts which are activated from their reservoirs by heterogeneous reactions on PSCs. Hence, ozone loss periods can be enhanced significantly by denitrification. While denitrification is a common process in the Antarctic (e.g. Toon et al., 1989; Fahey et al., 1990), denitrification in the Arctic is only observed for very cold winters (e.g. Rex et al., 1997; Arnold et al., 1998; Wetzel et al., 2002; WMO, 2003; Davies et al., 2005). The degree of denitrification is commonly estimated through the comparison of the measured NO_y-N_2O correlation with a standard correlation that corresponds to unperturbed conditions. In the lower stratosphere, the standard NO_y-N_2O correlation, e. g. under mid-latitude conditions, shows an almost linear increase of NO_y with decreasing N_2O since the latter is the only source of NO_y and no sink processes exist. At higher altitudes loss of NO_y through the reaction of NO with atomic nitrogen forming atomic oxygen and molecular nitrogen becomes important and the NO_y-N_2O correlation is highly non-linear. Hence, apart from loss of NO_y through denitrification, the NO_y-N_2O correlation can also be altered by mixing of air masses which correspond to different points on the non-linear correlation curve e. g. since they experienced different degrees of subsidence. The lower panel of figure 6.21 shows the NO_y-N_2O correlation measured during sunset at Kiruna in February 1999 and the standard mid-latitude NO_y-N_2O correlations inferred by Michelsen et al. (1998a) and Sugita et al. (1998) from mid-latitude and extra-vortex ATMOS measurements aboard the space shuttle. In the following, NO_y given by the standard correlation is referred to as NO_y^*. Observed NO_y is slightly smaller than NO_y^* for $50\,\text{ppb} < [N_2O] < 100\,\text{ppb}$ and hence the sampled air masses must have undergone mixing or denitrification. Since the winter 1998/99 was an exceptionally warm winter and PSC formation occurred only occasionally, denitrification can be excluded (Stowasser et al., 2002). Albeit NO_y being systematically lower than NO_y^*, it has to be noted that the differences between measured NO_y and NO_y^* are hardly larger than the error bars and hence could also be due to instrumental and retrieval related shortcomings. Nonetheless, the NO_y-N_2O correlation is further analyzed for possible mixing processes.

The degree of mixing can be estimated by examining the CH_4-N_2O correlation. Since the correlation between these long-lived tracers cannot be changed by chemical or reversible transport processes, the intra-vortex CH_4-N_2O correlation should be identical to the extra-vortex correlation as long as no irreversible mixing of air masses occurred (Waugh et al., 1997; Rex et al., 1998). The upper panel of figure 6.21 shows that the measured CH_4-N_2O correlation lies below the mid-latitude standard correlation of Michelsen et al. (1998b) for $50\,\text{ppb} < [N_2O] < 100\,\text{ppb}$. Thus, mixing of air masses of different dynamic origin indeed must have happened. An upper limit of the impact of mixing on the NO_y-N_2O correlation can be inferred by assuming a single isentropic mixing event between intra- and extra-vortex air after subsidence occurred throughout the winter. This extreme case is exemplified for the measurement at the 495 K potential temperature level which corresponds to 20.5 km altitude (green point in figure 6.21) following an approach suggested by Michelsen et al. (1998a), Kondo et al. (1999) and Rex et al. (1998). If mixing occurred isentropically after subsidence of intra-vortex air, the 495 K measurement is a composite of extra-vortex and intra-vortex air on the 495 K level. The CH_4-N_2O characteristic of the extra-vortex air parcel is given by the standard CH_4-N_2O correlation at the 495 K level and corresponds, in our example, to $[N_2O] = 210\,\text{ppb}$. The intra-vortex mixing member can be identified by drawing a line through the extra-vortex mixing member and the observed CH_4-N_2O relation at 495 K. The intersection between the extrapolated mixing line and the extra-vortex standard correlation yields the intra-vortex mixing member which in our case corresponds to air masses with $[N_2O] = 17.3\,\text{ppb}$. The fractional contribution from intra- and extra-vortex air can be inferred from the relative position of the measurement along the mixing line. The N_2O values of the mixing members

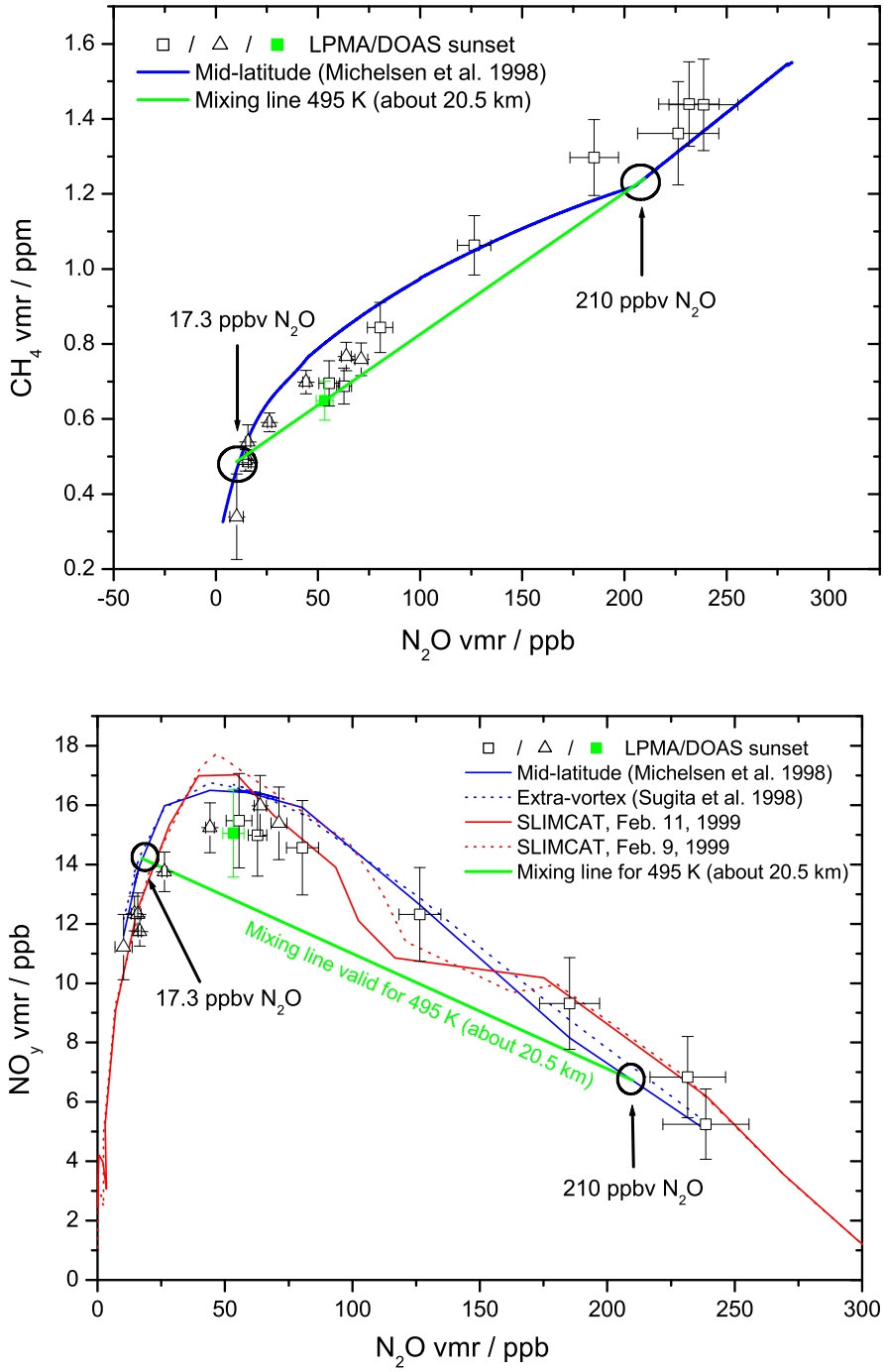

Figure 6.21: CH_4-N_2O (upper panel) and NO_y-N_2O correlation for solar occultation measurements of the LPMA/DOAS payload at Kiruna on Feb. 10, 1999. Measurements are shown as symbols: Boxes and triangles correspond to altitudes below 22 km and above 22 km, respectively. The green box is the data point on the 495 K potential temperature level (20.5 km altitude). Blue lines are standard mid-latitude and extra-vortex correlations given by Michelsen et al. (1998a,b) (solid blue line) and Sugita et al. (1998) (dotted blue line). The green line is the "mixing line" for the 495 K level as explained in the text. SLIMCAT output of NO_y-N_2O is given for Feb. 9 (dotted red line) and Feb. 11 (solid red line).

are transferred to the NO_y-N_2O correlation and connected by a further mixing line. Any air sample at the 495 K level which experienced a single event of isentropic mixing after intra-vortex subsidence should lie on the 495 K mixing line. If additionally denitrification occurred before the mixing event the measurement should lie below the mixing line. Obviously, the LPMA/DOAS measurement at 495 K lies above the mixing line which indicates that denitrification did not occurr and that the assumed model of the mixing process is not appropriate in our case. Plumb et al. (2000) showed that continuous mixing between intra- and extra-vortex air or several mixing events can alter the NO_y-N_2O correlation in a way that quantification of the degree of mixing is difficult. In our example, mixing events could have occurred in early winter 1998/99, most likely during the major warming event in December 1998 and January 1999 (figure 6.7).

Additional complications in the interpretation of the Arctic winter balloon flight from Kiruna in February 1999 arise from the complex meteorological conditions, e. g. illustrated by the N_2O vertical profile in figure 6.10. The balloon flight was conducted partially inside, and partially outside a vortex filament and lines-of-sight sampled extra- and intra-vortex air at the same time. Typically, several spectra and several lines-of-sight contribute to the retrieval of a single profile point which might be a composite of extra- and intra-vortex observations. Such an artificial mixing process could produce a distortion of the NO_y-N_2O correlation similar to the physical mixing process described above.
Figure 6.21 distinguishes between LPMA/DOAS measurements below 22 km (boxes) and above 22 km altitude (triangles) since the simultaneously measured N_2O profile suggests that intra-vortex air is sampled below 22 km and extra-vortex air above. However, the comparison of measured NO_y with NO_y^* remains inconclusive with respect to the question whether two different regimes of air masses were indeed observed.
For completeness SLIMCAT model output is also shown in figure 6.21. The agreement with the measurements is reasonable although the dip in modeled NO_y for $100\,\text{ppb} < [N_2O] < 200\,\text{ppb}$ is not observed. The dip corresponds to low HNO_3 and low NO_y in figure 6.13 between 17 km and 24 km altitude.

6.3.4 Conclusion on the budget and partitioning of NO_y

The LPMA/DOAS observations at high-latitudes in winter 1998/99 show that in the Arctic winterly stratosphere the reservoir species HNO_3 and $ClONO_2$ are the dominant NO_y constituents below 25 km. Strong denoxification is found in the lower stratosphere in winter 1998/99. Under summerly conditions probed in 2001, HNO_3 and NO_x are the most abundant species. Above 30 km most of NO_y resides in NO_x for both seasons. The general findings are corroborated by measurements of NO_2 and HNO_3 at mid- and high-latitudes during fall 1996 and winter 1996/97.
The observations during the polar winter of 1998/99 are analyzed with respect to denitrification and mixing processes between extra- and intra-vortex air masses. From the measurements and the temperature record it is clear that denitrification did not occur. The observed air masses must have experienced continuous mixing or several mixing events before the LPMA/DOAS balloon flight. Besides, large measurement errors and a rather complex meteorological and dynamic situation contribute to an ambiguous identification of air mass history.
The chemical transport model SLIMCAT reproduces the general characteristics of the observed budget of

NO_y fairly well. Further investigation of the agreement between the measured and modeled NO_2/HNO_3 ratio reveals that SLIMCAT NO_2/HNO_3 is high-biased with respect to LPMA/DOAS measurements. Since the observational data set is rather small and dynamic variability impacts the comparison, it is found difficult to draw firm conclusions on magnitude and origin of the observed bias which is observable in all presented datasets independent of season and latitude. The impact of several modeling parameters on modeled NO_2/HNO_3 is tested by photochemical steady state estimates and it is found that an error in the assumed aerosol abundances could be responsible for the observed discrepancies in the lower stratosphere.

6.4 Cl_y budget and partitioning

The budget of stratospheric inorganic chlorine[2] Cl_y is subject to considerable human influence. Long-lived organic chlorine compounds such as CFCs are transported to the stratosphere and subsequently photolyzed yielding inorganic chlorine containing species which participate in catalytic ozone destruction (section 1.2.4). The partitioning between long- and short-lived chlorine species determines the efficiency of chlorine involving catalytic ozone loss cycles and may be significantly altered through heterogeneous processes occurring on PSCs formed in the polar winter vortices. The understanding of winterly polar ozone destruction is still incomplete since stratospheric chemistry models tend to underestimate the observed loss (WMO, 2003; Rex et al., 2003). Recent studies indicate that the kinetics of some reactions involved in the ClO-ClO cycle and ClO-BrO cycle (section 1.2.5) might have to be revised (Stimpfle et al., 2004; Canty et al., 2005; von Hobe et al., 2005; Berthet et al., 2005).
Here, we present two case studies of the Cl_y budget and partitioning based on simultaneous measurements of HCl and $ClONO_2$ in the Arctic winter and summer stratosphere. The observations are compared with output of the chemical transport model SLIMCAT. For the Arctic winter observations the unique setup of the LPMA/DOAS payload combining IR and UV/visible spectroscopy provides a comprehensive set of trace gases which can be used to put tight constraints on the reaction kinetics of the BrO and ClO involving ozone loss cycle. The stratospheric chemistry model LABMOS is used to test recent suggestions on updates of the involved reaction kinetics and to infer implications for ozone loss.

6.4.1 Cl_y and its constituents

A series of studies indicates that the inorganic chlorine budget is in good agreement with estimates based on the decomposition of organic halocarbons transported to the stratosphere. Hence, organic chlorocarbons, CCl_y, are the dominant source of inorganic chlorine, Cl_y (Engel et al., 1997; Sen et al., 1999; Bonne et al., 2000; Rinsland et al., 2003; WMO, 2003). Earlier observations of measured Cl_y being on average about 40% lower than Cl_y inferred from CCl_y (Webster et al., 1994) are most probably due to systematic errors of HCl measurements (Bonne et al., 2000). Very short-lived substances (VSLS) are not a major source of stratospheric Cl_y (WMO, 2003).
The partitioning of Cl_y in the high- and mid-latitude stratosphere under non-ozone hole conditions is governed by HCl and $ClONO_2$. Some dedicated model studies report on very good to reasonable agreement between observations of HCl and/or $ClONO_2$ (Sen et al., 1999; Randeniya et al., 1999; Stimpfle et al., 1999) while sizeable model-measurement discrepancies are observed for some aircraft in situ measurements (Voss et al., 2001). The latter study concludes that measurements of the ratio $ClONO_2$/HCl are 55% to 60% lower than model data. A recent model-measurement comparison based on mid-latitude balloon borne *in situ* measurements of ClO indicates good model-measurement agreement (Vogel et al., 2005). In the winter polar stratosphere, chlorine activation through heterogeneous reactions on PSCs (section 1.2.5) converts reservoir species to more active species and ClO_x becomes an important constituent of Cl_y. The temporal evolution of the Cl_y partitioning during polar winter and early spring has been extensively studied in the Arctic and in the Antarctic stratosphere (Payan et al., 1998; Michelsen et al., 1999; WMO, 2003; Dufour et al., 2006). Models reproduce fairly well the timing and extent of chlorine activation in the southern winter hemisphere fairly well and can

[2] $Cl_y = HCl + ClONO_2 + HOCl + ClO + 2 \cdot Cl_2O_2 + Cl + OClO + BrCl + 2 \cdot Cl_2$

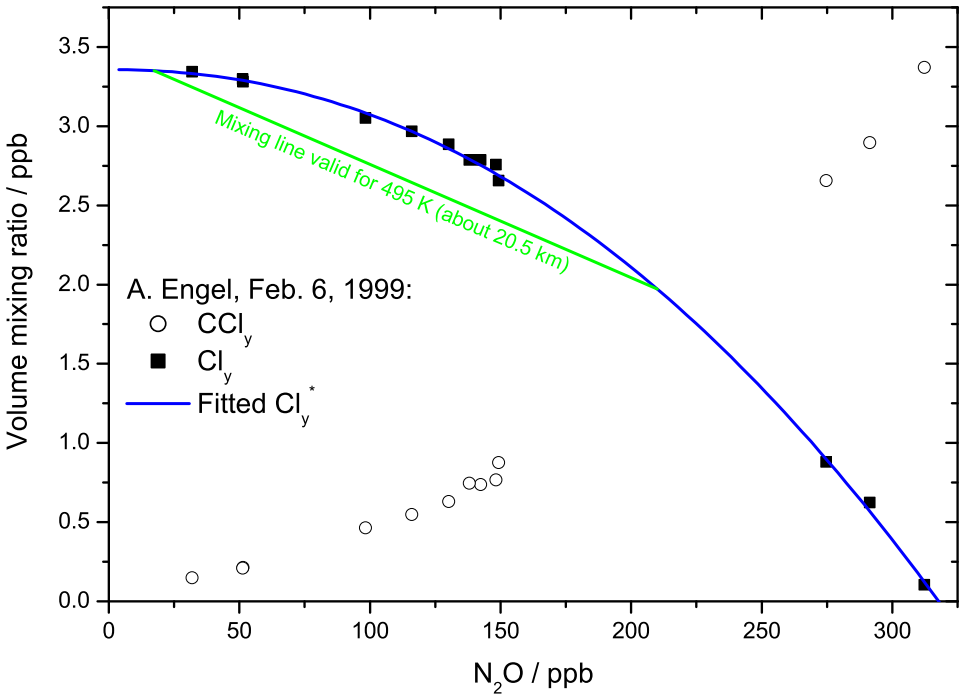

Figure 6.22: Cl_y (filled boxes) and CCl_y (open boxes) as a function of N_2O. The measurements are conducted by the cryogenic whole air sampler operated by the University of Frankfurt (A. Engel) on Feb. 6, 1999, during a stratospheric balloon flight from Kiruna. The solid blue line indicates the fitted standard correlation. The green mixing line is transferred from figure 6.21.

simulate Antarctic ozone loss in a quantitative manner (Solomon et al., 2000, 2002; WMO, 2003). In the Arctic, the year-to-year variability of polar vortex meteorology (and the corresponding chlorine activation and ozone loss) is considerably larger than in Antarctica (Wagner et al., 2001). Models have difficulties to account for the observed chlorine activation and ozone loss in warm (WMO, 2003) as well as cold Arctic winters (Rex et al., 2003). For winters where Arctic temperatures are close to the threshold for the formation of PSCs part of the discrepancies might be due to errors in the temperature records and nucleation schemes used in the models (WMO, 2003). Reactions involved in the ClO-ClO and ClO-BrO ozone loss cycles are also subject to considerable debate and are discussed in section 6.4.2.

Since the LPMA/DOAS payload measures $ClONO_2$ and HCl but not directly Cl_y or CCl_y, the amount of inorganic chlorine has to be determined with the help of *in situ* measurements of organic halocarbons conducted by a balloon borne cryogenic whole air sampler. The cryogenic whole air sampler is operated by the University of Frankfurt (Engel et al., 1997) and measures the most abundant chlorine containing source gases such as CF_2Cl_2, $CFCl_3$, $C_2F_3Cl_3$, CCl_4, CH_3Cl, CH_3CCl_3 and several tracer species (CH_4, CO_2, N_2O, SF_6). The sum of all organic source gases yields CCl_y. The total amount of organic and inorganic chlorine, i. e. CCl_y + Cl_y, can be calculated from the tropospheric chlorine burden taking into account the age of air at different altitudes of the stratosphere (Engel et al., 2002). The age of air can be inferred from trace gases such as CO_2 and SF_6 which exhibit a continuous increase in the troposphere but have no significant sources and sinks in the stratosphere. The concept relies on

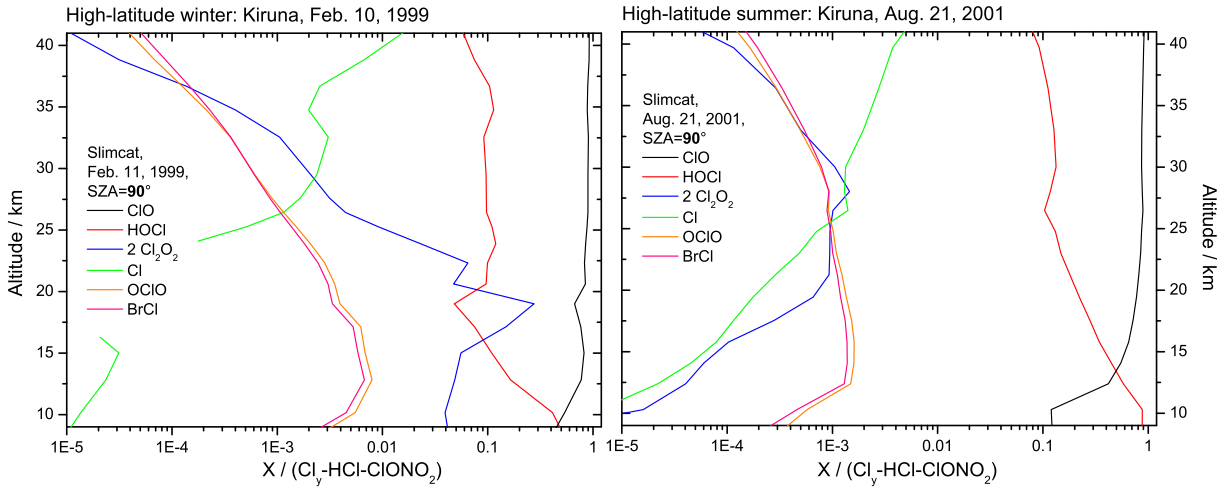

Figure 6.23: Partitioning of $ClO_x = Cl_y^*$ - HCl - $ClONO_2$ as modeled by the SLIMCAT CTM for two days during high-latitude winter (left panel) and high-latitude summer (right panel). See text for further details.

the fact that the CO_2 and SF_6 mixing ratios observed in the stratosphere can be related to mixing ratios that occurred some years earlier in the troposphere. From the tropospheric CO_2 and SF_6 record the year of stratospheric entry and hence the age of the air masses and their total chlorine content can be inferred. The actual derivation of the age of air is far more complicated since a stratospheric air mass is a composite of air parcels which experienced different transport pathways and timescales (Engel et al., 2002). Given the organic chlorine budget and the amount of total chlorine in the stratosphere, inorganic stratospheric chlorine, Cl_y, is given by the difference between the total chlorine and the organic chlorine burden. Figure 6.22 shows Cl_y and CCl_y inferred from cryogenic whole air sampler measurements at Kiruna on Feb. 6., 1999, during a stratospheric balloon flight. The decrease of CCl_y and simultaneous increase of Cl_y with increasing altitude, i. e. decreasing N_2O, is clearly visible. Fitting the inferred Cl_y data according to Engel et al. (1997), yields a standard correlation of Cl_y with N_2O,

$$Cl_y^*\,[\mathrm{ppt}] = -0.0151\,N_2O^{2.137}\,[\mathrm{ppb}] + 3357\,[\mathrm{ppt}], \tag{6.3}$$

where the asterisk indicates that the corresponding Cl_y value is calculated from a standard correlation and does not correspond to an actual measurement.

The standard correlation inferred from measurements conducted four days before the LPMA/DOAS balloon flight at Kiruna on Feb. 10, 1999, is used to estimate Cl_y for the LPMA/DOAS observations by inserting LPMA/DOAS measurements of N_2O into equation (6.3). Since the Cl_y-N_2O correlation is non-linear a similar caveat applies as in the case of the NO_y-N_2O correlation where mixing processes between air masses of different dynamic origin can cause distortion of the standard tracer-tracer correlation. Significant distortions would be expected if air masses inside the Arctic vortex experienced much more subsidence than extra-vortex air masses and mixing between these differently subsided air masses occurred. Section 6.3.3 showed that the NO_y-N_2O correlation is only slightly distorted for the LPMA/DOAS observations at Kiruna in 1999 compared to standard correlations and that mixing

of extra- and intra-vortex air masses must have occurred continuously or during several events. Since the Cl_y-N_2O correlation is "less non-linear" than the NO_y-N_2O correlation the effect of mixing on the Cl_y-N_2O correlation should be even smaller. For illustration, the 495 K mixing line calculated in section 6.3.3 from the CH_4-N_2O correlation is shown in figure 6.22. The hypothetical strong mixing event at 495 K potential temperature would have less significant impact on the Cl_y-N_2O correlation than on the NO_y-N_2O correlation (figure 6.21). The LPMA/DOAS measurements lie even significantly above the mixing line in the NO_y-N_2O plot and thus can be expected to lie in a similar manner above the mixing line in the Cl_y-N_2O plot, i. e. close to the standard correlation. Hence, the error associated with the calculation of Cl_y from a standard correlation is considered small and is neglected here. Due to lack of an updated dataset, equation (6.3) is also used to calculate Cl_y for the LPMA/DOAS observations at Kiruna on Aug. 21, 2001. The trend of the stratospheric chlorine burden between 1999 and 2001 is negligible.

Given Cl_y^* and the LPMA/DOAS measurements of the reservoirs HCl and $ClONO_2$, the abundance of the more active chlorine species can be estimated as $ClO_x = Cl_y^*$ - HCl - $ClONO_2$. In the following, the composite species ClO_x is used as defined here, which is different from the more accurate definition in section 1.2.4 where ClO_x is limited to the species actively participating in ozone loss cycles. The above more general definition additionally comprises species which are not directly involved in catalytic cycles and which can be regarded as temporary reservoir species. Among these, HOCl contributes indeed about 10% to ClO_x between 20 km and 40 km and becomes more important in the lower stratosphere somewhat depending on season as illustrated in figure 6.23. The largest contribution between 15 km and 40 km comes from ClO for polar winter and polar summer. In Arctic winter the ClO-dimer, Cl_2O_2, plays an important role around 20 km. For our purposes the definition of ClO_x is only a matter of convention as long as model-measurement comparisons compare like with like.
Vertical profiles of Cl_y^*, HCl, $ClONO_2$ and ClO_x inferred from LPMA/DOAS measurements during sunset at Kiruna on Feb. 10, 1999, and Aug. 21, 2001, are compared to SLIMCAT output. Figures 6.24 and 6.25 show the measured and modeled trace gas profiles of chlorine species. The volume mixing ratios of the trace gases are plotted in figure 6.24 while their relative abundances with respect to Cl_y are shown in figure 6.25. For clarity, figure 6.24 is split in separate panels for Kiruna 1999. The scales in each panel are the same in order to allow for inter-panel comparison. SLIMCAT data are plotted for two days temporally close to the respective balloon flight.

For the Arctic winter observations, Cl_y^* peaks with about 3.35 ppb around 20 km altitude. There, 0.15 ppb chlorine resides in CCl_y. The effect of transport on the vertical profile of Cl_y^* can readily be seen from the comparison with the Kiruna 2001 summer dataset where Cl_y^* attains its maximum at significantly higher altitudes, around 30 km. The small dip in Cl_y^* for Kiruna 1999 between 22 km and 26 km altitude is consistent with the observation of air with mid-latitudinal character indicated by the N_2O profile (figure 6.10), from which Cl_y^* is actually calculated. HCl is the most abundant inorganic chlorine species between 15 km and 40 km for the winter and the summer high-latitude scenarios. For Kiruna 2001 the fraction of inorganic chlorine residing in HCl ranges between 60% and 90%. Above 22 km the same is true for Kiruna 1999 but below 22 km the fractional contribution of HCl is as low as 40%. $ClONO_2$ peaks around 1.25 ppb for Kiruna 1999 and is less abundant for Kiruna 2001. The fractional contribution of $ClONO_2$ to Cl_y ranges from 20% to 30% in a broad altitude layer which is shifted to lower altitudes during the winterly observations. The composite ClO_x species representing the

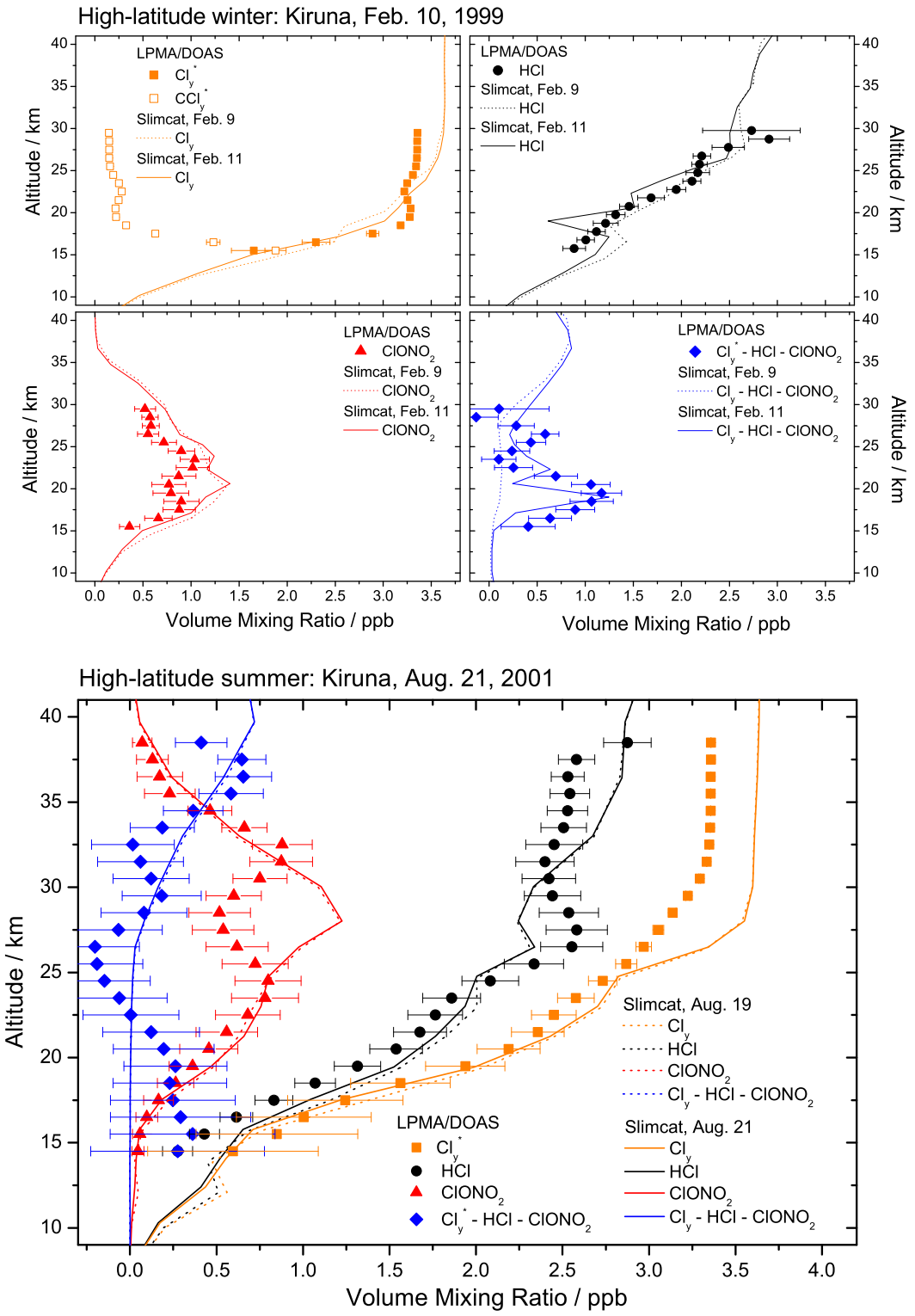

Figure 6.24: Measured (symbols) and modeled (lines) volume mixing ratios of Cl_y or Cl_y^* (orange boxes), HCl (black circles), $ClONO_2$ (red triangles) and $ClO_x = Cl_y$ - HCl - $ClONO_2$ (blue diamonds) for sunset measurements conducted during the balloon flights at Kiruna on Feb. 10, 1999, (upper four panels) and on Aug. 21, 2001 (lower panel). For Kiruna 1999, CCl_y^* derived from a similar relation as given by equation (6.3) is plotted as open orange boxes. Model output is shown for Feb. 9 (dotted lines) and Feb. 11 (solid lines), 1999, and for Aug. 19 (dotted lines) and Aug. 21 (solid lines), 2001.

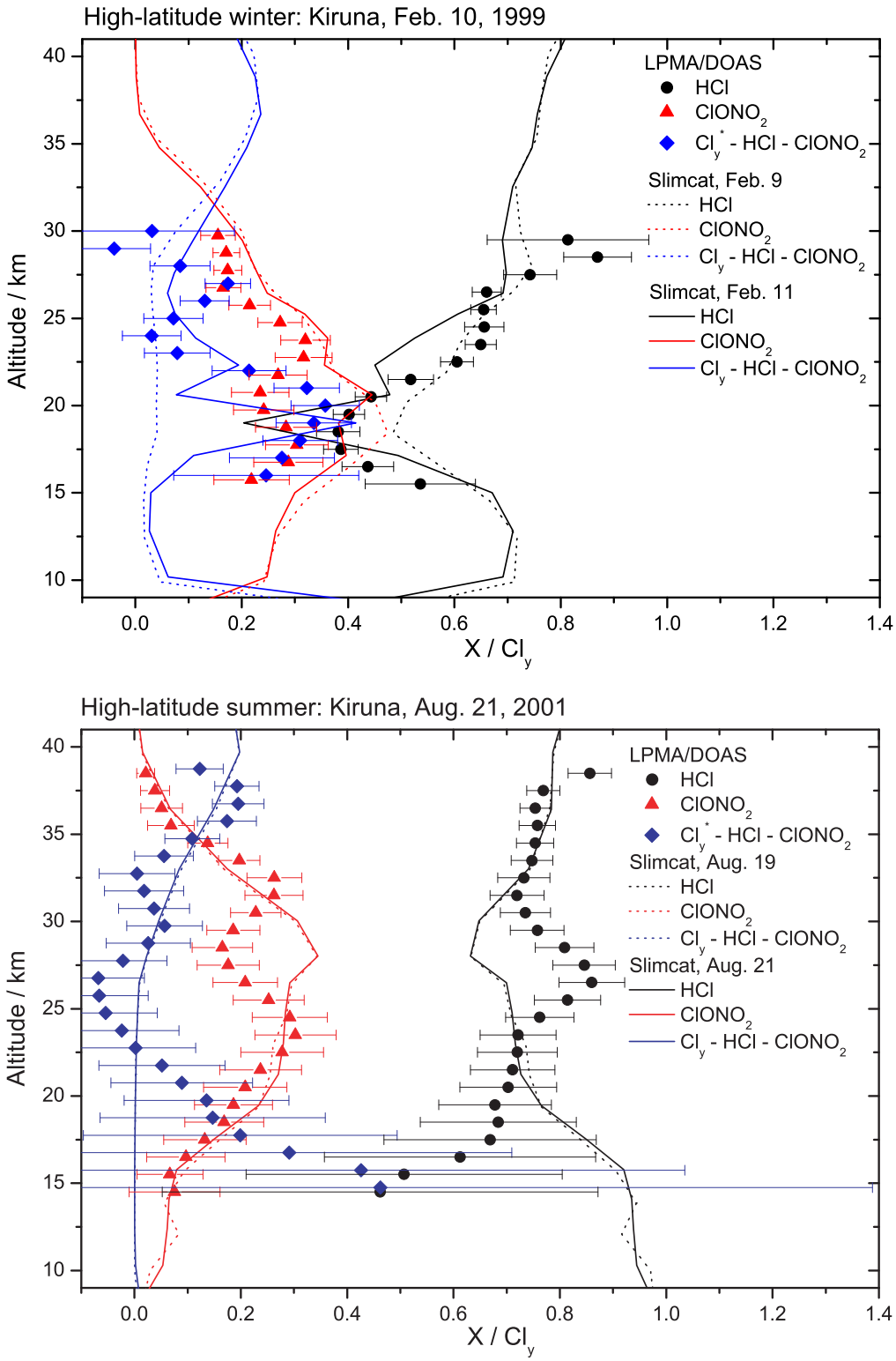

Figure 6.25: Measured (symbols) and modeled (lines) abundances HCl (black circles), $ClONO_2$ (red triangles) and $ClO_x = Cl_y - HCl - ClONO_2$ (blue diamonds) with respect to Cl_y or Cl_y^* for sunset measurements conducted during the balloon flights at Kiruna on Feb. 10, 1999, (upper panel) and on Aug. 21, 2001 (lower panel). Model output is shown for Feb. 9 (dotted lines) and Feb. 11 (solid lines), 1999, and for Aug. 19 (dotted lines) and Aug. 21 (solid lines), 2001.

chemically active chlorine speciesF show a very complicated pattern for Kiruna 1999: Between 15 km and 22 km a layer of high ClO_x peaking at 1.17 ppb contributes 20% to 40% to Cl_y. From figure 6.25 it is evident that the layer of enhanced ClO_x coincides with a layer of relatively low HCl. Between 22 km and 26 km a layer of low ClO_x coincides with high $ClONO_2$ and observation of mid-latitudinal air. Above 26 km an increase of ClO_x and simultaneous decrease of $ClONO_2$ suggests the continuation of the high ClO_x layer in the lower stratosphere. For Kiruna 2001 the findings are rather straight forward: Below 33 km ClO_x is zero within the error bars which become very large below 20 km and render the derivation of ClO_x from Cl_y^*, HCl and $ClONO_2$ very uncertain. Clearly, the fractional contribution of 0.5 to Cl_y by ClO_x around 15 km altitude in the summer high-latitude stratosphere is not realistic but has to be considered as an artifact of small absolute chlorine abundances. Above 33 km ClO_x increases to 0.65 ppb.
As discussed in section 6.3.1, SLIMCAT output reveals considerable day-to-day variability for the high-latitude winter observations while variability is low in summer. In general, SLIMCAT overestimates the peak amount of inorganic chlorine in the stratosphere compared to our derivation by roughly 300 ppt. For Kiruna 1999, HCl is reproduced quite well by both days of model output. On Feb. 11, SLIMCAT shows a very distinct layer of low HCl which is also observed by the observations, but not to the same extent. $ClONO_2$ is overestimated in both, absolute numbers and relative partitioning. The observed layer of high ClO_x between 15 km and 22 km altitude is reproduced reasonably well by SLIMCAT output on Feb. 11 but clearly underestimated on Feb. 9, where zero chlorine activation is modeled. Albeit missing the observed vertical extent of the ClO_x layer, the relative partitioning of ClO_x and HCl (figure 6.25) modeled for Feb. 11 shows nicely the simultaneous drop of HCl and rise of ClO_x. The modeled relative partitioning on Feb. 9 can be considered representative for the non-activated case. For Kiruna 2001, observed HCl is overestimated by the model above 33 km which can be attributed to an overestimation of Cl_y since the relative partitioning HCl/Cl_y (figure 6.25) is reproduced very well. The model underestimates HCl around 27 km altitude where $ClONO_2$ is overestimated. This layer of high $ClONO_2$ and low HCl coincides with a layer of low modeled N_2O in comparison to the observations (figure 6.12) and, thus, indicates a transport problem. Below and above that layer, $ClONO_2$ is modeled very well. The same is true for the observed increase of ClO_x above 33 km.

The above findings support the general conclusion that the LPMA/DOAS measurements at Kiruna in February 1999 sampled air masses which are characterized by high ClO_x and relatively low HCl between 16 km and 22 km altitude indicating that heterogeneous processing of the respective air masses has led to chlorine activation. This conclusion is corroborated by identification of a coinciding denoxified layer (section 6.3.1, figures 6.13 and 6.14) which could be produced by heterogeneous processing of N_2O_5 to HNO_3 and which prevents scavenging of ClO_x by NO_x. Above 22 km altitude, mid-latitudinal air dominates the probed air masses and correspondingly ClO_x is effectively scavenged by available NO_x to form $ClONO_2$. The LPMA/DOAS measurements from Kiruna in August 2001 seem to be rather typical of high-latitude summer conditions where most of inorganic chlorine resides in HCl and a smaller fraction in $ClONO_2$. Above 33 km altitude, photolysis of $ClONO_2$ and HCl produces significant levels of ClO_x.
SLIMCAT succeeds in modeling the general partitioning of Cl_y for the considered high-latitude winter and summer case while the peak amount of Cl_y is overestimated. For the winter scenario the observed layer of high ClO_x and low HCl in the lower stratosphere is qualitatively reproduced. Some discrepancies remain when quantitatively comparing modeled and measured trace gas abundances.

6.4.2 Constrained modeling of ClO_x and ozone loss in the Arctic winter

The previous section discussed the chlorine budget and partitioning for a high-latitude summer and winter scenario. For the latter, a layer of enhanced ClO_x abundances is identified in the lower stratosphere which could be responsible for catalytic ozone loss. For this high-latitude winter case simultaneous DOAS measurements of BrO and OClO are available and are used here to test the current understanding of polar ozone loss due to the dominating ClO-ClO and ClO-BrO catalytic cycles by means of constrained model simulations.

Recalling reactions (R1.126) through (R1.129), the ClO-ClO cycle is given by

$$\mathrm{ClO} + \mathrm{ClO} + \mathrm{M} \leftrightarrow \mathrm{Cl_2O_2} + \mathrm{M} \quad \text{(R6.1)}$$

$$\mathrm{Cl_2O_2} + h\nu \longrightarrow \mathrm{Cl} + \mathrm{ClO_2} \quad \text{(R6.2)}$$

$$\mathrm{ClO_2} + \mathrm{M} \longrightarrow \mathrm{Cl} + \mathrm{O_2} + \mathrm{M} \quad \text{(R6.3)}$$

$$2 \times (\mathrm{Cl} + \mathrm{O_3} \longrightarrow \mathrm{ClO} + \mathrm{O_2}) \quad \text{(R6.4)}$$

$$\text{net}: \quad 2\,\mathrm{O_3} \longrightarrow 3\,\mathrm{O_2}\,. \quad \text{(R6.5)}$$

Recently, there has been considerable debate on the formation rate $k_{ClO+ClO}$ of the ClO-dimer, its photolysis frequency $J_{Cl_2O_2}$ as well as its thermal decomposition rate $k_{Cl_2O_2+M}$ and the associated equilibrium constant $K_{eq} = \frac{k_{ClO+ClO}}{k_{Cl_2O_2+M}}$. Stimpfle et al. (2004) published the first simultaneous measurements of the ClO monomer and dimer conducted in the Arctic winter 2000 by *in situ* instrumentation deployed on the ER-2 NASA aircraft. The comparison of the observations with model simulations showed that the current recommendations of the JPL-2002 compendium (Sander et al., 2003) regarding $k_{ClO+ClO}$ and $J_{Cl_2O_2}$ are inconsistent with daytime measurements. Moreover, nighttime measurements indicated that the recommended K_{eq} was too high. The latter finding is corroborated by laboratory studies of Plenge et al. (2005) as well as atmospheric measurements by von Hobe et al. (2005) who showed that *in situ* measurements of ClO and Cl_2O_2 performed by the HALOX instrument aboard the Geophysica aircraft deployed from Kiruna in January 2003 cannot be reconciled with the JPL-2002 recommendations of K_{eq} at stratospheric temperatures. They suggested a modified temperature dependence of the equilibrium constant. A similar conclusion is found by Berthet et al. (2005) who used measurements of ClO by a microwave instrument on the Odin satellite to infer that K_{eq} most probably lies in-between the recent recommendation of von Hobe et al. (2005) and the earlier work of Cox and Hayman (1988), but definitely below the JPL-2002 value. Frieler et al. (2006) investigated the impact of the new kinetics on ozone loss in the polar winter stratosphere and concluded that considering the findings of Stimpfle et al. (2004) and von Hobe et al. (2005) significantly improves the agreement between measured and modeled ozone loss in polar winter which previously was significantly underestimated by model simulations using JPL-2002 (e.g. Rex et al., 2003). While the suggested changes of $k_{ClO+ClO}$ and $J_{Cl_2O_2}$ lead to increased ozone loss due to the ClO-ClO cycle, the proposed reduction of K_{eq} yields larger ClO mixing ratios under dark and twilight conditions and, therefore, enhances the importance of the ClO-BrO cycle which can proceed under sunlit and dark conditions.

Frieler et al. (2006) concluded on the best agreement between measured and modeled ozone loss when using the mentioned suggestions on reaction kinetics and BrO_x abundances constrained to BrO measurements of the DOAS instrument (Dorf, 2005). Employing DOAS measurements of stratospheric BrO further enhances the importance of the ClO-BrO cycle since those observations yield significantly higher

BrO than inferred from the abundances of the BrO_x-precursors CH_3Br and halons alone. The ClO-BrO cycle is given by reactions (R1.131) through (R1.136), revisited here,

$$\begin{aligned}
\mathrm{ClO} + \mathrm{BrO} &\longrightarrow \mathrm{BrCl} + \mathrm{O_2} && 7\% && \text{(R6.6)}\\
&\longrightarrow \mathrm{ClO_2} + \mathrm{Br} && 34\% && \text{(R6.7)}\\
&[\longrightarrow \mathrm{OClO} + \mathrm{Br} && 59\%] && \text{(R6.8)}\\
\mathrm{ClO_2} + \mathrm{M} &\longrightarrow \mathrm{Cl} + \mathrm{O_2} + \mathrm{M} && && \text{(R6.9)}\\
\mathrm{BrCl} + h\nu &\longrightarrow \mathrm{Br} + \mathrm{Cl} && && \text{(R6.10)}\\
\mathrm{Cl} + \mathrm{O_3} &\longrightarrow \mathrm{ClO} + \mathrm{O_2} && && \text{(R6.11)}\\
\mathrm{Br} + \mathrm{O_3} &\longrightarrow \mathrm{BrO} + \mathrm{O_2} && && \text{(R6.12)}\\
\text{net}: \quad 2\,\mathrm{O_3} &\longrightarrow 3\,\mathrm{O_2}\,. && && \text{(R6.13)}
\end{aligned}$$

Percentage yields are given for T = 195 K. Since reaction (R6.8) is followed by photolysis of OClO to ClO and O, it is not part of the catalytic ClO-BrO ozone loss cycle and is written in parentheses. OClO measurements can be used to test the efficiency of the involved catalytic cycle as reaction (R6.8) is virtually the only formation mechanism of OClO in the polar winter stratosphere. Canty et al. (2005) showed that balloon borne measurements of nighttime OClO by the SALOMON lunar occultation instrument are significantly smaller than model simulations. If the model is constrained with BrO_x inferred from DOAS BrO measurements and if the branching ratio of reaction (R6.6) is adjusted to 11% at the expense of the OClO yield, model and measurement agree well. Simultaneous observations of nightime NO_2 and OClO in the Arctic winter stratosphere by the SALOMON and AMON lunar and stellar occultation instruments indicated that modeled and measured NO_2 and OClO cannot be reconciled with standard photochemistry (Rivière et al., 2003). Rivière et al. (2004) suggested that model-measurement agreement could be significantly improved if scavenging of ClO and BrO by NO_2 was hindered by formation of the highly unstable species ClOONO and BrOONO instead of the longer-lived isomers $ClONO_2$ and $BrONO_2$. ClOONO and BrOONO would rapidly dissociate to reproduce ClO, BrO and NO_2. However, no laboratory studies confirmed the latter suggestion so far.
In contrast to the uncertainties of chlorine and bromine catalyzed ozone loss in the polar winter stratosphere, mid-latitudinal chemistry involving ClO seems to be well understood as shown by Vogel et al. (2005) by model-measurement comparisons using balloon-borne *in situ* ClO observations. A modeling study by Vogel et al. (2006) investigated the impact of ClO_x radical-molecule complexes such as $ClO{\cdot}O_2$, $ClO{\cdot}H_2O$, $OClO{\cdot}H_2O$ on polar stratospheric ozone loss. Such ClO_x complexes could enhance the formation of the ClO-dimer and, thus, could influence catalytic ozone loss cycles. Considering gas phase chemistry, only, the impact of ClO_x radical-molecule complexes on ozone loss was found to be small but could be enhanced if heterogeneous processes were important. Further, the formation of such complexes could possibly explain some of the discrepancies found between laboratory and field studies on the equilibrium constant K_{eq}.

The LPMA/DOAS solar occultation measurements on Feb. 10, 1999, provide abundances of HCl, $ClONO_2$, OClO and BrO and hence are well suited to investigate the suggested modifications of the reaction kinetics of the chlorine and bromine involving ozone loss cycles, in particular regarding the ClO-BrO cycle. HCl and $ClONO_2$ are inferred from LPMA spectra and are used to calculate $ClO_x = Cl_y^*$ - HCl - $ClONO_2$ from the standard correlation of Cl_y^* with N_2O (equation (6.3)) derived

from measurements four days before the LPMA/DOAS observations. OClO and BrO are retrieved from DOAS measurements probing the same air masses as the LPMA measurements. In addition to the halogen bearing compounds simultaneous measurements of O_3, HNO_3, NO_2 and NO are available. Similar to the approach presented in section 5.3 the photochemical model LABMOS is initialized in a way that it can reproduce the LPMA/DOAS observations. The model is run over a 1.5 day period on isentropes stationary above Kiruna. The modeled abundances of OClO are then compared to the measured ones.

Initialization of the model

The LABMOS chemistry model is initialized at 0:05 UT (SZA = 125°) on Feb. 10, 1999, with SLIMCAT output (run 336) from the following day since output on the actual day of measurement is not available. Upon initialization the initial volume mixing ratios of O_3, NO_2, HNO_3, $ClONO_2$, HCl, Cl_y and Br_y are scaled in a way that the model can reproduce the measurements of O_3, NO_2, NO, HNO_3, $ClONO_2$, HCl, BrO and ClO_x conducted 14 h to 15 h later between 14:00 UT and 14:50 UT nearby Kiruna. The initial volume mixing ratios of these species are determined in various test runs and listed in table 6.2. The volume mixing ratio of ClO_x is initialized as $ClO_x = Cl_y$ - HCl - $ClONO_2$ and the partitioning among its constituents ClO, Cl_2O_2, HOCl and OClO is taken from SLIMCAT. The same is true for the initial partitioning of the Br_y constituents. The remaining species are left unchanged with respect to SLIMCAT output.
The most important scaling parameter is the initial abundance of NO_2 (= NO_x at night) since it controls the amounts of BrO_x and ClO_x which are scavenged to $ClONO_2$ and $BrONO_2$. The total amount of inorganic chlorine is initialized as inferred from the Cl_y^*-N_2O standard correlation except for altitudes below 16 km where N_2O-profile information from the LPMA measurements is very limited (see figures 4.11 and 4.12) and calculating Cl_y^* involves large errors. There, Cl_y is initialized such that the agreement of measured and modeled NO_2 and $ClONO_2$ is optimal. The total amount of inorganic bromine is kept at Br_y = 19.5 ppt above 20 km as suggested by Dorf (2005). Below 20 km, Br_y is initialized such that modeled BrO agrees best with measured BrO when simultaneously scaling NO_2.

Figure 6.26 shows the measured and modeled abundances of all relevant species as a function of tangent height or altitude. For all species which are measured by the LPMA/DOAS payload, SCDs are plotted for model-measurement comparison. Modeled SCDs are calculated from LABMOS and SLIMCAT model output by integrating the modeled trace gas concentrations along the lines-of-sight. Figure 5.4 illustrates the LPMA/DOAS lines-of-sight during solar occultation and the corresponding trace gas concentrations for O_3 and NO_2. Lines-of-sight and trace gas concentrations are given in coordinates of altitude and SZA (or time). In analogy to figure 5.4, the LABMOS model yields concentrations of all relevant trace gases which can be integrated along the lines-of-sight in altitude-SZA-space resulting in modeled SCDs. In-between the modeled altitude layers the trace gas concentrations are interpolated linearly[3]. Comparing SCDs instead of vertical profiles has the advantage that further errors due to profile inversion are avoided, and that the photochemical variation of short-lived species such as NO_2, NO, BrO and OClO does not need to be corrected but is implicitly accounted for. Since Cl_y and ClO_x are not directly measured but inferred from trace gas profiles and a Cl_y^*-N_2O standard correlation, vertical

[3] Altitude interpolation is performed linearly in log-pressure coordinates.

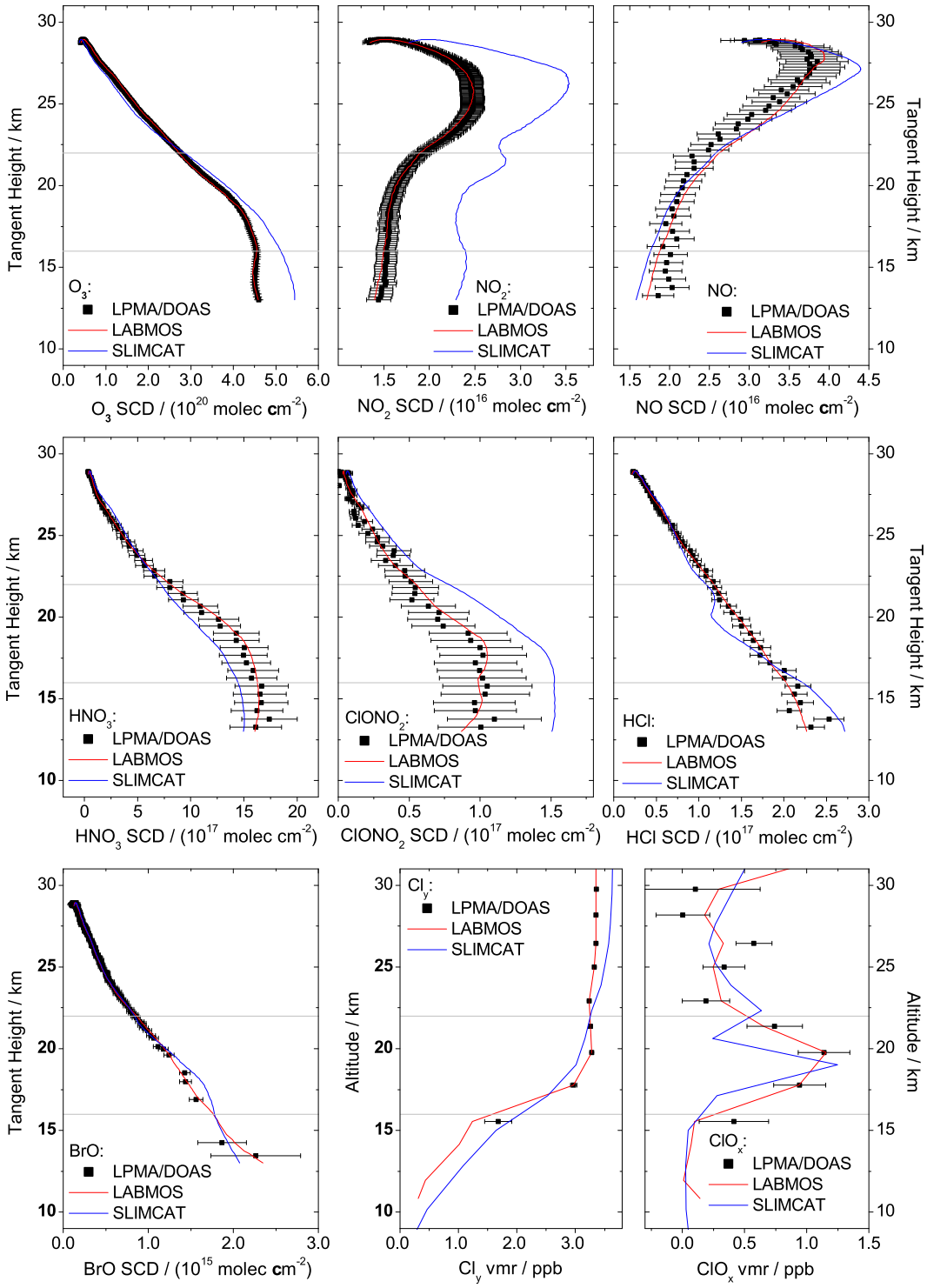

Figure 6.26: Measured (symbols) and modeled (lines) SCDs of O_3, NO_2, NO, HNO_3, $ClONO_2$, HCl and BrO as a function of tangent height and measured (symbols) and modeled (lines) volume mixing ratios of Cl_y and ClO_x as a function of altitude for solar occultation observations at Kiruna on Feb. 10, 1999. LABMOS model output is shown corresponding to LPMA/DOAS observations for a best guess of the initial trace gas concentrations to reproduce the measurements (table 6.2). The blue lines illustrate pure SLIMCAT model output. The altitude range between the horizontal gray lines represents the range of activated ClO_x.

Table 6.2: Volume mixing ratios used for initialization of the LABMOS model at 0:05 UT at Kiruna on Feb. 10, 1999.

Θ / K	alitude / km	O_3 / ppm	NO_2 / ppb	HNO_3 / ppb	$ClONO_2$ / ppb	HCl / ppb	Cl_y / ppb	Br_y / ppt
336	10.85	0.550	0.000	0.720	0.008	0.146	0.309	10.00
350	11.94	0.750	0.000	2.100	0.012	0.411	0.435	11.00
380	14.14	1.000	0.000	4.400	0.250	0.666	1.010	12.00
400	15.54	1.700	0.000	6.300	0.270	0.860	1.240	13.00
435	17.78	3.050	0.000	12.000	0.860	1.126	2.971	16.00
475	19.78	3.400	0.000	15.000	0.720	1.324	3.279	19.00
510	21.32	3.700	0.043	14.000	0.850	1.637	3.257	19.50
550	22.92	5.000	0.073	15.000	0.910	2.023	3.232	19.50
615	25.00	5.200	0.329	13.000	1.100	2.189	3.325	19.50
675	26.45	5.100	1.867	8.200	0.000	2.261	3.350	19.50
750	28.17	5.400	3.320	7.600	0.000	2.879	3.350	19.50
820	29.77	4.300	3.545	4.500	0.635	2.711	3.350	19.50

profiles are shown for comparison.
Figure 6.26 shows that the LABMOS model is able to reproduce the LPMA/DOAS measurements of all considered species mostly within the error bars if scaling upon initialization is carried out as described above. The inferred non-zero ClO_x abundances at about 26 km altitude cannot be reconciled with the LABMOS model calculations. At 26 km NO_2 mixing ratios are on the order of 1 ppb causing rapid scavenging of ClO_x to form $ClONO_2$. Given the constraints of measured NO_2, $ClONO_2$ and HCl and inferred Cl_y^* there is no way to reproduce sizeable amounts of ClO_x at that altitude. In contrast, the activated layer of ClO_x between 16 km and 22 km altitude is reproduced very well by the model, given the very low amounts of NO_2 in the respective altitude range. BrO, which controls the formation of OClO through reaction (R6.8), is also modeled very well by the scaled model run. Model-measurement agreement is worse for pure SLIMCAT output. Nonetheless, the layer of activated ClO_x in the lower stratosphere is reproduced qualitatively and BrO abundances are only slightly overestimated.

Stacked versus air mass trajectory based modeling

All LABMOS model calculations shown here are performed in a stacked manner, i. e. the modeled air masses are assumed stationary above Kiruna. Hence, the history of air masses between initialization of the model at 0:05 UT and the LPMA/DOAS measurements in the afternoon is parameterized by fixed temperatures and pressures and by the SZA-timeline for 67.9°N, 21.1°E. The Lagrangian-type approach, which was introduced in section 5.2, uses an air mass history which is explicitly calculated from a meteorological model run. Test runs are performed using the trajectories shown in figure 6.8 which are calculated for air masses arriving at Kiruna at 12 UT. Since the LPMA/DOAS measurements are conducted between 14 and 15 UT and lines-of-sight during solar occultation (figure 6.9) point somewhat in the south-west direction, those trajectories do not truly represent the short-term history of the observed air masses and moreover fall short by 2 h to 3 h hours. Unfortunately, a dedicated model run that uses the LPMA/DOAS measurements as starting/ending points for trajectory calculations is not available so far.

Model results applying the *ad hoc* trajectory calculations until 12 UT and a stacked time grid between 12 UT and 15 UT produce results indistinguishable from the overall stacked model run as can be seen in figure 6.28.
As far as the production and loss of OClO and BrO are concerned, Canty et al. (2005) showed that the air mass history is of particular importance if the minimum SZA during the 12 hours before the observations is larger than 92°. Due to the wavelength dependence of OClO and BrCl photolysis, OClO is photolyzed more effectively than BrCl for $92° \leq \text{SZA} \leq 95°$. Consequently, air masses that experienced a minimum SZA between 92° and 95° could have lost OClO through photolysis while only little formation of BrO after BrCl photolysis occurred. Production of OClO through BrO + ClO would be small and the air masses could be depleted in OClO, even after sunset. For $\text{SZA} > 95°$ neither OClO nor BrCl are photolyzed and OClO which built up during previous days is not removed. For $\text{SZA} < 92°$ both, OClO and BrCl, are readily photolyzed. Here, the minimum SZA observed during the last 12 hours before the LPMA/DOAS observations was 82° which is well below the critical range and which causes almost complete removal of OClO during the day (see also figure 6.28) and its build-up from ClO + BrO during sunset.
Moreover, the scaling of the initial trace gas abundances implicitly considers air mass history since small meteorological mis-representations can be balanced by modified initial parameters in the attempt to match the observations. Hence, the error due to an erroneous representation of air mass history is considered small and in the following only stacked model calculations are performed.

Model-measurement comparison for OClO

The LABMOS model is initialized as detailed above and run over 1.5 days. The modeled temporal evolution of OClO during sunset at Kiruna on Feb. 10, 1999, is used to calculate modeled SCDs which can be compared to the measured ones. Figure 6.27 shows the model-measurement comparison for OClO SCDs as a function of tangent height. The layer of high ClO_x between 16 km and 22 km altitude is highlighted although it has to be remembered that SCDs at each tangent height exhibit contributions from all altitude layers above and from some layers below the considered tangent heights. At 20 km tangent height the diameter of the solar disk at the tangent point is about 3 km for the LPMA/DOAS solar occultation viewing geometry. Below 15 km tangent height observations and some modeling constraints (Cl_y^*, $ClONO_2$ etc.) get uncertain as emphasized above. Thus, discussion should focus on tangent heights above 15 km. Comparison of SCDs is favored over comparison of vertical profiles since the rapid photochemical build-up of OClO during sunset does not allow for profile retrieval without considerable photochemical corrections.
The agreement of the measured OClO SCDs with the modeled ones inferred from the standard LABMOS run using JPL-2002 reaction kinetics is good in the entire range of considered tangent heights. Errors of the measurements are larger than the observed discrepancies. Despite the good model-measurement agreement, the model yields OClO SCDs which are roughly 5% smaller than the observations. SLIMCAT also relies on JPL-2002 reaction kinetics but underestimates OClO for the Kiruna 1999 observations which is mostly due to overestimation of NO_2 (figure 6.26). Starting from the LABMOS run using JPL-2002 kinetics, various kinetic parameters are modified according to recently published recommendations. Unless stated otherwise, for each model run it is ensured that model-measurement agreement for O_3, NO_2, NO, HNO_3, $ClONO_2$, HCl, BrO, Cl_y and ClO_x is

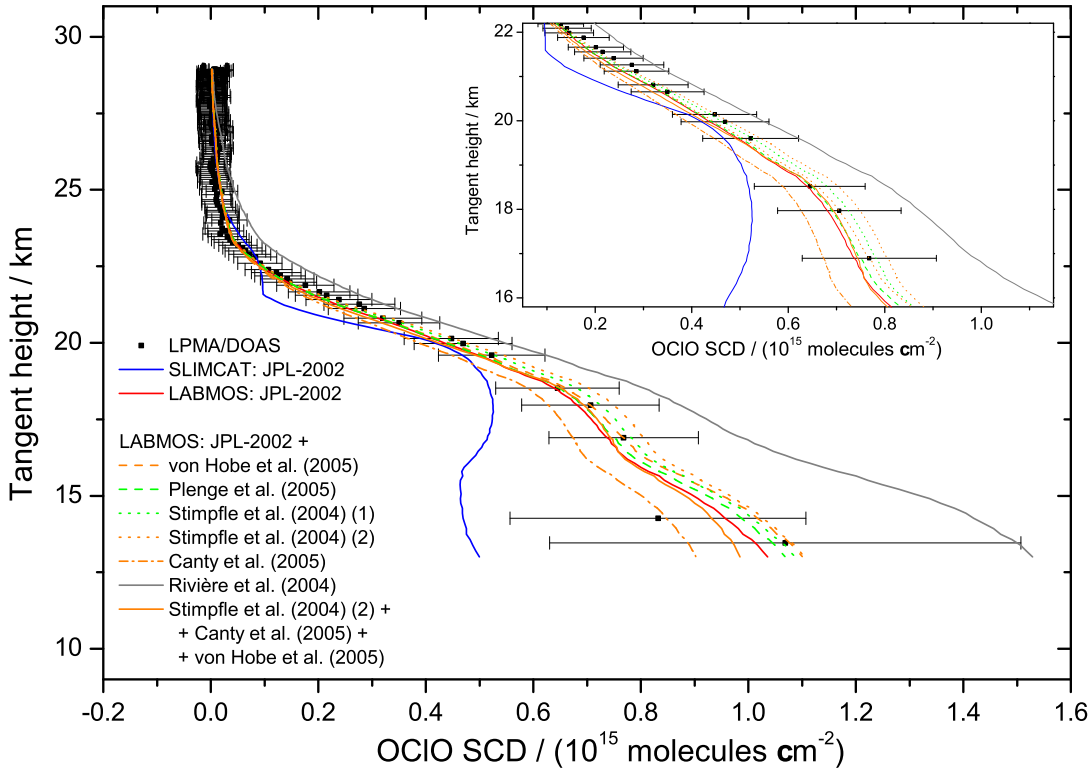

Figure 6.27: Measured (boxes) and modeled (lines) OClO SCDs as function of tangent height for solar occultation measurements at Kiruna on Feb. 10, 1999. The small inset highlights the altitude range of the ClO_x layer between 16 km and 22 km altitude. The various model runs indicated in the legend are discussed in detail in the text.

comparable to figure 6.26 by scaling the respective trace gas abundances upon initialization.

The model run denoted by von Hobe et al. (2005) uses the parameterization for the equilibrium constant K_{eq} given by the respective study: $K_{eq} = 5.47\,10^{-25}\,\mathrm{cm^3 molecules^{-1}}\,(T/300\,\mathrm{K})^{-2.29}\cdot\exp(6969\,\mathrm{K}/T)$. The inferred equilibrium constant is smaller than the JPL-2002 recommendation for stratospheric temperatures and hence, the equilibrium between Cl_2O_2 and ClO is shifted toward the monomer. Since more ClO is available for the formation of OClO through reaction (R6.8), modeled OClO SCDs are slightly larger than those using JPL-2002 recommendations. The effect is not as large as might be expected since the production of OClO is limited by the abundances of BrO. Around 20 km altitude, about 1.2 ppb ClO_x and 15 ppt BrO are available. Under such conditions, it has been shown that an increase of ClO_x abundances has only little effect on OClO (figure 2 in Canty et al. (2005)).

Plenge et al. (2005) found a Cl_2O_2/ClO equilibrium constant in-between the JPL-2002 and von Hobe et al. (2005) recommendations for temperatures between 190 K and 230 K. Accordingly, their equilibrium constant, $K_{eq} = 1.92\,10^{-27}\,\mathrm{cm^3\,molecules^{-1}}\,\exp(8430\,\mathrm{K}/T)$, produces OClO SCDs in-between the von Hobe et al. (2005) and JPL-2002 model run.

Besides an overestimation of K_{eq} by JPL-2002, Stimpfle et al. (2004) concluded that their measurements are in good agreement with a model run either if the rate coefficient of Cl_2O_2 production ($k_{ClO+ClO}$) is lowered or if the photolysis rate of Cl_2O_2 ($J_{Cl_2O_2}$) is increased with respect to JPL-2002. The former hy-

pothesis is tested by setting the low and high pressure limits of the ClO + ClO association reaction to the values recommended by JPL-2000, $k_{low,ClO+ClO} = 2.2\,10^{-32}\,\mathrm{cm^6\,molecules^{-2}\,s^{-1}}\,(T/300\,\mathrm{K})^{-3.1}$ and $k_{high,ClO+ClO} = 3.4\,10^{-12}\,\mathrm{cm^3\,molecules^{-1}\,s^{-1}}\,(T/300\,\mathrm{K})^{-1}$. Lowering the production rate of Cl_2O_2 shifts the equilibrium between dimer and monomer toward ClO and hence, has a similar effect as lowering K_{eq}. The inferred OClO SCDs, denoted by Stimpfle et al. (2004) (1), are larger than the model run using JPL-2002 kinetics and show an improved agreement with the measurements, although differences are small with respect to the observational errors. The alternative possibility proposed by Stimpfle et al. (2004) is an increase of $J_{Cl_2O_2}$ with respect to JPL-2002 recommendations by using the absorption cross section of Burkholder et al. (1990) and extrapolating it from 410 nm to 450 nm. Figures 2 b) and c) of the study by Stimpfle et al. (2004) illustrate ratios of $J_{Cl_2O_2}$ inferred from the Burkholder et al. (1990) data with respect to JPL-2002 as a function of SZA. Those ratios are used to scale the photolysis frequency of Cl_2O_2 implemented in LABMOS. The corresponding test run is denoted Stimpfle et al. (2004) (2). Increasing $J_{Cl_2O_2}$ renders the production of Cl atoms from the ClO-dimer more effective and, thus, enhances the cycling efficiency of the ClO-ClO catalytic cycle. OClO abundances are larger than the JPL-2002 run by about 10% in the altitude range of activated ClO_x. Accordingly, modeled OClO SCDs are slightly larger than the measured SCDs but fall well within the error bars of the measurements.

A study by Canty et al. (2005) found that a night-time observation of OClO can only be reconciled with modeled abundances if the branching ratio of the ClO + BrO reaction is altered such that 11% instead of the recommended 7% of the reaction processes yield BrCl and only 55% instead of 59% yield OClO (at 195 K). The respective rate constants are altered accordingly assuming that the altered branching ratio is applicable in the entire observed temperature range. Decreasing the yield for OClO production directly impacts the build-up of OClO during sunset and hence yields smaller modeled SCDs. In the altitude range of the activated ClO_x layer, modeled SCDs fall within the lower boundaries of the error bars, but model-measurement agreement is less good than for the JPL-2002 scenario.

Rivière et al. (2004) suggested to introduce highly unstable isomers of $ClONO_2$ and $BrONO_2$ to improve model agreement with their night-time measurements of NO_2 and OClO. They suggested a branching ratio of 1/3 for the formation of $ClONO_2$ and $BrONO_2$. Accordingly, 2/3 of the reactions ClO + NO_2 and BrO + NO_2 would yield unstable isomers and rapidly reproduce ClO, BrO and NO_2. This scenario is tested by reducing the rate coefficients k_{ClO+NO_2} and k_{BrO+NO_2} to 1/3 of their values recommended by JPL-2002. The explicit formation of the unstable isomers ClOONO and BrOONO with a finite lifetime is not considered. Rather it is assumed that both isomers are instantaneously photolyzed or collisionally decomposed to their educts. In contrast to all other presented test runs of the model, it is not possible to scale the initial trace gas abundances in a way that model-measurement agreement is similar to that shown in figure 6.26. Reducing the formation rate of $ClONO_2$ and $BrONO_2$ either yields NO_2 considerably larger than the observations or $ClONO_2$ considerably smaller than the observations depending on whether model-measurement agreement is optimized for NO_2 or $ClONO_2$. BrO is less impacted since $BrONO_2$ abundances during the day are small compared to BrO. Our finding is in contradiction to Rivière et al. (2004) who speculated on the formation of ClOONO and BrOONO since they could not reconcile simultaneous night-time measurements of NO_2 and OClO with JPL-2002 reaction kinetics. The modeled OClO SCDs plotted in figure 6.27 are calculated for a model run where NO_2 was scaled such that the measurements are reproduced while modeled $ClONO_2$ is lower than the measured abundances and even lower than the lower boundary of the error bars. Given the initialization constrained to observed NO_2, the Rivière et al. (2004) scenario produces larger OClO SCDs than all

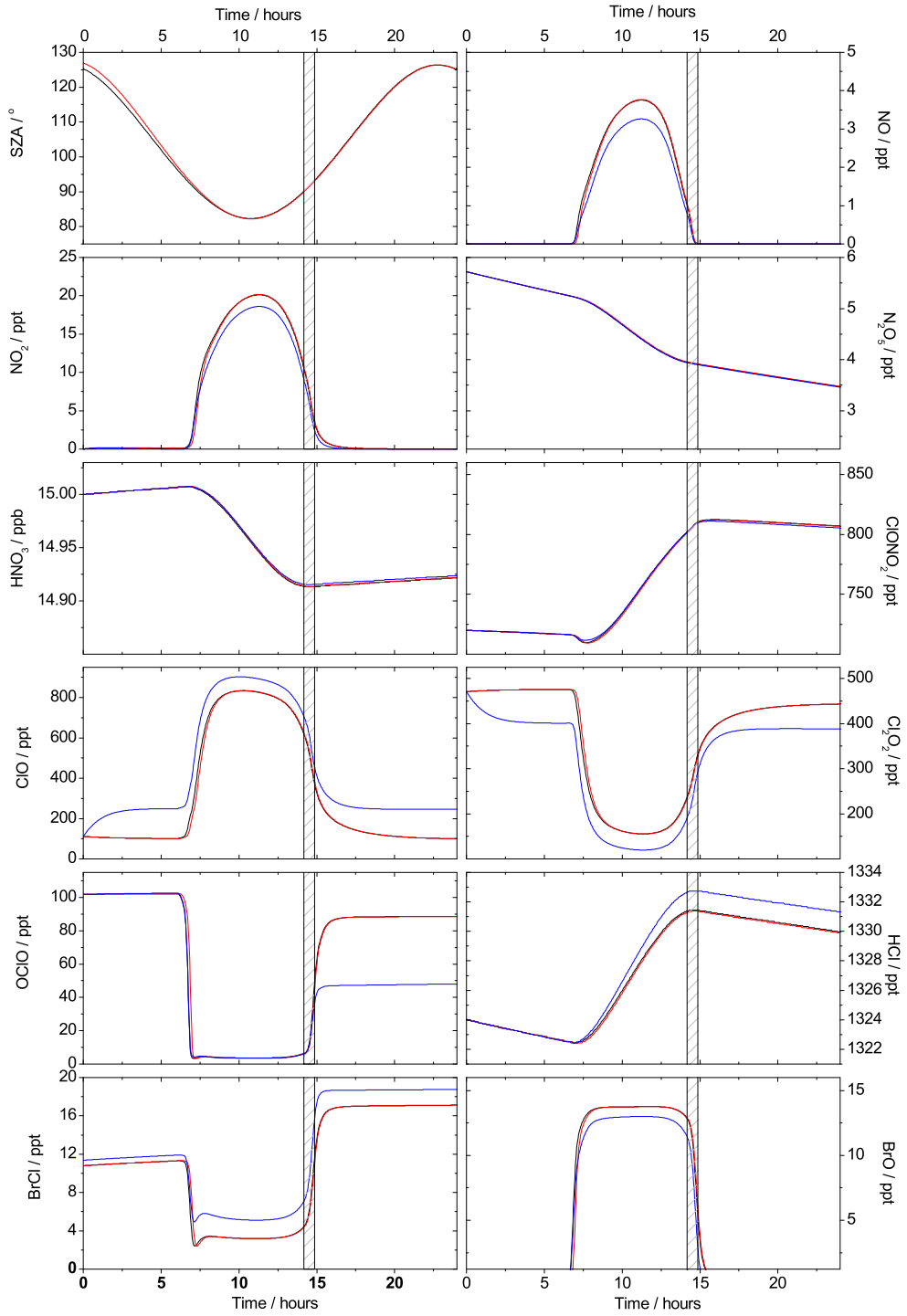

Figure 6.28: Temporal evolution of the most important nitrogen, chlorine and bromine species on the 475 km (19.78 km) potential temperature surface as modeled by LABMOS initialized at 0:05 UT on Feb. 10, 1999, at Kiruna. The black lines correspond to the standard model run on a stacked time grid. Red lines illustrate the same model run along an air mass trajectory arriving at Kiruna at 12 UT. After 12 UT the calculation is continued on a stacked time grid. Blue lines show a model run where JPL-2002 reaction kinetics are updated by the recommendations of Stimpfle et al. (2004) (2), von Hobe et al. (2005) and Canty et al. (2005) discussed in the text. The shaded area represents the time frame of the LPMA/DOAS solar occultation observations.

other scenarios.
A composite run using the recommendations of Stimpfle et al. (2004) (2), von Hobe et al. (2005) and Canty et al. (2005) for $J_{Cl_2O_2}$, K_{eq} and the ClO + BrO branching ratio yields modeled OClO SCDs similar to those inferred from JPL-2002 kinetics. The reduced fractional yield of OClO from the reaction ClO + BrO is canceled by more available ClO due to a more effective Cl_2O_2 photolysis and a shift of the ClO-monomer/dimer equilibrium to the monomer. Although the test run using the combined kinetic updates yields similar good agreement between measured and modeled OClO as when using the JPL-2002 recommendations, the implications for O_3 loss are somewhat different as discussed below.

Figure 6.28 shows the temporal evolution of selected species on the 475 K (19.78 km) potential temperature level which represents the altitude layer where the peak of ClO_x is observed. Besides the standard JPL-2002 model run, model runs are shown which are performed along air mass trajectories arriving at Kiruna at 12 UT and which use the aforementioned three recommended kinetic updates. The general pattern shows day-time formation of small amounts of NO_x from HNO_3 and to a small degree from N_2O_5. Most of NO_x is converted to $ClONO_2$ through the reaction with ClO which is generated from its dimer through photolysis upon sunrise. OClO is rapidly photolyzed during the day and reveals day-time abundances on the order of 5 ppt while at night mixing ratios are on the order of several ten ppt. BrO is the most abundant daytime bromine species but rapidly reacts to BrCl during sunset when photolysis fades out.
The trajectory based run yields results which are nearly indistinguishable from the standard run in the time frame of the LPMA/DOAS observations. When using the combined kinetic updates, the partitioning between ClO and Cl_2O_2 is shifted toward the monomer as explained above. The build-up of OClO during sunset is slower and consequently the night-time abundance of OClO is smaller than for the JPL-2002 scenario. In turn, production of BrCl is more effective if the ClO + BrO branching ratio is set to 11% BrCl yield and consequently night-time abundances of BrCl are larger than for the standard run.
Figure 6.28 also reveals the shortcomings of our approach: During the time when LPMA/DOAS observations are performed, the OClO abundances modeled by the standard run and by the run with updated kinetics are nearly indistinguishable while at night differences are large. Hence, night-time measurements would be better suited to test OClO reaction kinetics.

In summary, the presented approach which constrains all relevant nitrogen, chlorine and bromine species to their observed abundances during sunset succeeds in modeling the observed OClO abundances very well using JPL-2002 reaction kinetics. Recent recommendations on kinetic updates by Stimpfle et al. (2004), Plenge et al. (2005), von Hobe et al. (2005) and Canty et al. (2005) or combinations of them, concerning $J_{Cl_2O_2}$, $k_{ClO+ClO}$, K_{eq} and the ClO + BrO branching ratio, yield modeled OClO SCDs within the errors of the measurement and similarly good model-measurement agreement as observed for JPL-2002 kinetics. Given the observational error bars, the LPMA/DOAS solar occultation measurements do not allow for judging on whether the recommended updates or combinations of them ultimately lead to an improved description of the ClO-ClO and ClO-BrO ozone loss cycles. The formation of unstable isomers of $ClONO_2$ and $BrONO_2$ as proposed by Rivière et al. (2004) cannot be reconciled with the simultaneous LPMA/DOAS observations of the relevant nitrogen and chlorine species.

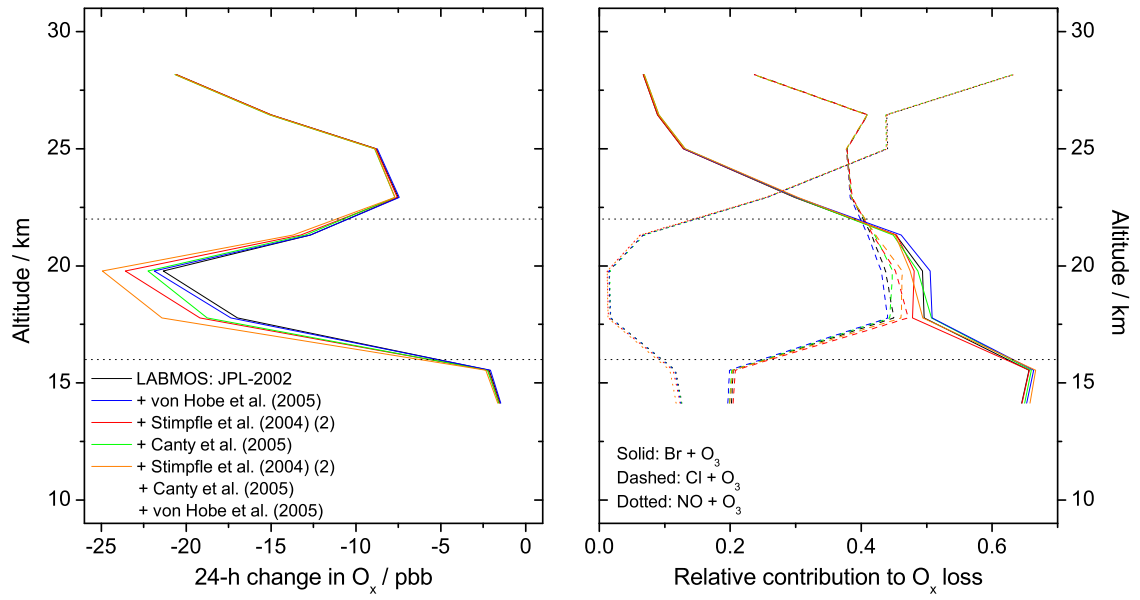

Figure 6.29: Loss of odd oxygen (left panel) and relative contributions (right panel) integrated over 24 hours between 10:50 UT (SZA = 82.3°) on Feb. 10 and Feb. 11, 1999. The modeled air masses experienced 8 h 50 min with SZA<95°. Loss of odd oxygen is inferred from various LABMOS model runs as indicated in the legend. The relative contributions from Br + O_3 (solid lines), Cl + O_3 (dashed lines) and NO + O_3 (dotted lines) illustrated in the right panel sum up to more than 90% of total odd oxygen loss in the entire altitude range displayed. The horizontal dotted lines confine the layer of activated ClO_x.

Ozone loss

Given the good model-measurement agreement for OClO discussed in the previous section, the LABMOS model which is constrained to the LPMA/DOAS observations of all relevant nitrogen, chlorine and bromine bearing species seems to reproduce well the photochemical processes occurring in the stratosphere in February 1999. Therefore, the model can be used to quantitatively infer odd oxygen loss and to test the impact of recently published kinetic updates. As pointed out above, the LABMOS model is initialized at 0:05 UT on Feb. 10 and run over 1.5 days in a way that the LPMA/DOAS measurements between 14 UT and 15 UT are reproduced. Odd oxygen loss is inferred by summing up the net instantaneous loss of atomic oxygen and ozone in each model time step between 10:50 UT on Feb. 10 and 10:50 UT on Feb. 11. Simultaneously, the relative contributions from all relevant O_x loss and production processes are logged. The starting and ending points of the integration period correspond to the instances where the modeled air masses experienced the minimum SZA (= 82.3°). The corresponding sunlit fraction of the day is 8 h 50 min. The integration period is chosen sufficiently far from initialization and sunrise, such that the partitioning of short-lived species and the loss of odd oxygen are not impacted by initialization effects (see also temporal evolution of the relevant species in figure 6.28).

Figure 6.29 shows the net odd oxygen loss and its primary contributions as a function of altitude. Odd

oxygen loss peaks with about 20 ppb to 25 ppb in the altitude range of the activated ClO_x layer between 16 km and 22 km. There, the dominating O_x loss processes are the reactions Br + O_3 and Cl + O_3 which are part of the ClO-ClO and ClO-BrO catalytic cycles. At altitudes above 22 km, the importance of the bromine involving reactions decreases and O_x loss due to NO + O_3 dominates. Thus, the secondary increase of net O_x loss above 25 km mostly originates from loss processes involving nitrogen species.
Various model runs are performed testing the aforementioned updates of the reaction kinetics. The model run using the Cl_2O_2/ClO equilibrium constant inferred by von Hobe et al. (2005) shifts the partitioning between monomer and dimer toward ClO and can be considered illustrative for the findings of Plenge et al. (2005) and Stimpfle et al. (2004) (1), which imply a similar conclusion. Lowering K_{eq} according to von Hobe et al. (2005) results in slightly larger O_x loss between 16 km and 22 km altitude than inferred from JPL-2002 kinetics. The efficiency of the ClO-BrO cycle is enhanced while the ClO-ClO cycle is less important. Due to these canceling effects the net impact on O_x loss is smaller than 5% or smaller than 1 ppb.
In contrast, increasing the photolysis rate of the ClO-dimer according to Stimpfle et al. (2004) (2) has a large effect on odd oxygen loss which can be as large as 15% or 3 ppb compared to JPL-2002 kinetics. Since an increase of $J_{Cl_2O_2}$ enhances the cycling efficiency of the ClO-ClO cycle, more Cl atoms are available for ozone destruction per unit time. Hence, the importance of O_x loss due to Cl + O_3 is enhanced compared to the standard run.
The findings of Canty et al. (2005) foster the importance of the ClO-BrO cycle since more BrCl is formed by ClO + BrO than recommended by JPL-2002. Accordingly O_x loss is larger by up to 10% or 2 ppb than modeled by the standard run.
If the combined recommendations of Stimpfle et al. (2004) (2), Canty et al. (2005) and von Hobe et al. (2005) are considered, odd oxygen loss in the activated altitude layer is significantly increased compared to the JPL-2002 model run. Peak O_x loss is larger by 20% to 25% or 4 ppb to 4.5 ppb. The main contribution comes from the enhanced efficiency of the Cl_2O_2 photolysis and thus from a larger importance of the ClO-ClO cycle. Above about 22 km altitude differences in O_x loss between the various model runs are small as can be expected from the dominating role of the NO_x catalyst.

The above findings on the impact of the new reaction kinetics on O_x loss are similar to those inferred by Frieler et al. (2006). They conclude on up to 20% increased maximum possible O_3 loss when using the recommendations of Stimpfle et al. (2004) (2), and von Hobe et al. (2005) in their modeling study for the Arctic winter 1999/2000. During the stratospheric winter 1998/1999, which is considered here, the polar vortex was very disturbed and the amount of chlorine activation and ozone loss inferred from the LPMA/DOAS observations cannot be regarded as typical of this Arctic winter. Several studies indicate that total ozone loss during the winter 1998/1999 was on the order of 5% and barely significant in the entire lower and middle stratosphere (WMO (2003), Rex, M. (personal communication)). Hence the inferred loss rate cannot be extrapolated to conclude on total O_3 loss during the winter but rather has to be considered as a snapshot of catalytic ozone destruction which was limited in space and time. Unfortunately, a comprehensive observational set of all relevent chlorine, nitrogen and bromine species, as for the Kiruna 1999 case, is not available for other winters such as 1999/2000 where ozone loss was more severe and persistent.

6.4.3 Conclusions on the budget and partitioning of Cl_y

LPMA/DOAS observations of HCl and $ClONO_2$ are used together with *in situ* measurements of organic chlorine species to infer total inorganic chlorine (Cl_y^*) and the sum of the shorter-lived species (ClO_x) for the Kiruna 1999 high-latitude winter scenario and the Kiruna 2001 high-latitude summer case. It was found that for high-latitude summer $ClONO_2$ and HCl are the major constituents of Cl_y throughout the lower and middle stratosphere. For the high-latitude winter 1998/1999 a layer of enhanced ClO_x and low HCl is observed between 16 km and 22 km altitude which coincides with a layer of strong denoxification and which points at heterogeneous activation of chlorine bearing catalysts.
The winter observations for Kiruna 1999 are further investigated by constraining the chemical model LABMOS to simultaneous observations of all important nitrogen (NO_2, NO, HNO_3), chlorine (HCl, $ClONO_2$, Cl_y^*) and bromine (BrO) species. After constraining the model, simultaneously observed OClO abundances during twilight are modeled very well using the standard JPL-2002 reaction kinetics. Test-runs show that recent suggestions on updates of the reaction kinetics fall within the observational error bars and that a composite scenario which simultaneously considers the most important updates yields similarly good model-measurement agreement as the JPL-2002 case. However, formation of highly unstable isomers of $ClONO_2$ and $BrONO_2$ cannot be reconciled with the LPMA/DOAS observations. Inferred 24 h odd-oxygen loss amounts to 20 ppb to 25 ppb in the altitude range of activated ClO_x between 16 km and 22 km. The various model runs reveal that the proposed kinetic updates imply substantially increased O_x loss due to the ClO-ClO and ClO-BrO cycles when compared to standard kinetics, albeit yielding comparable results for twilight OClO abundances.
The SLIMCAT chemical transport model is able to reproduce the abundances of HCl and $ClONO_2$ fairly well for the high-latitude summer and the high-latitude winter scenario. In the latter case, even the layer of activated ClO_x in the lower stratosphere is modeled qualitatively. OClO abundances are underestimated with respect to LPMA/DOAS measurements which mainly originates from NO_2 being overestimated as already observed in section 6.3.

Chapter 7

Iodine in the upper troposphere and stratosphere

Section 1.2 pointed out that the transport of very small amounts of iodine containing species to the stratosphere could have a significant impact on the stratospheric ozone layer. However, there are only a few studies investigating the stratospheric iodine budget, e. g. Wennberg et al. (1997), Pundt et al. (1998), Wittrock et al. (2000), Berthet et al. (2003), Bösch et al. (2003), where the latter one gives the currently best estimates on upper limits of stratospheric IO and OIO in high- and mid-latitudes. The ground-based measurements of Wittrock et al. (2000) are the only observations which report on concentrations of stratospheric IO above the detection limit. Our efforts extend the study of Bösch et al. (2003) to the years between 2001 and 2005 and, for the first time, investigate tropical latitudes, which are of particular importance due to their crucial role in transporting tropospheric air to the stratosphere.
An overview of the spectral retrieval of IO and OIO from DOAS spectra is given. Then, upper limits of stratospheric IO and OIO inferred from measurements in the extra-tropics are presented. Since the observations in tropical latitudes are somewhat ambiguous, a dedicated section discusses particularities and gives a conservative estimate of upper limits of IO and OIO in the tropical upper troposphere and stratosphere. Finally, some thoughts on the impact on stratospheric photochemistry are presented.

7.1 IO and OIO retrieval

The spectral retrieval of IO and OIO SCDs from DOAS spectra in the visible wavelength range relies on the correct removal of the strong absorbers O_3 and NO_2 in order to detect the underlying, weakly absorbing iodine species. Small deficiencies in the representation of the strong absorbers can generate systematic residual features which can mask the underlying weak absorbers or, even worse, induce fake detection. Therefore, it is of major importance to use O_3 and NO_2 absorption cross sections measured by the DOAS spectrograph in the laboratory (Dorf, 2005). Errors due to the wavelength dependence of the slit function or due to convolution of high resolution cross sections are avoided. Here, two sets of lab-measured cross sections are used which have been recorded in our laboratory in 1997 and 2002. Two sets of cross sections are necessary since the optical setup has been changed in 2002 (Dorf, 2005) resulting in a significant change of the instrument function. A minor instrumental upgrade in 2004 and

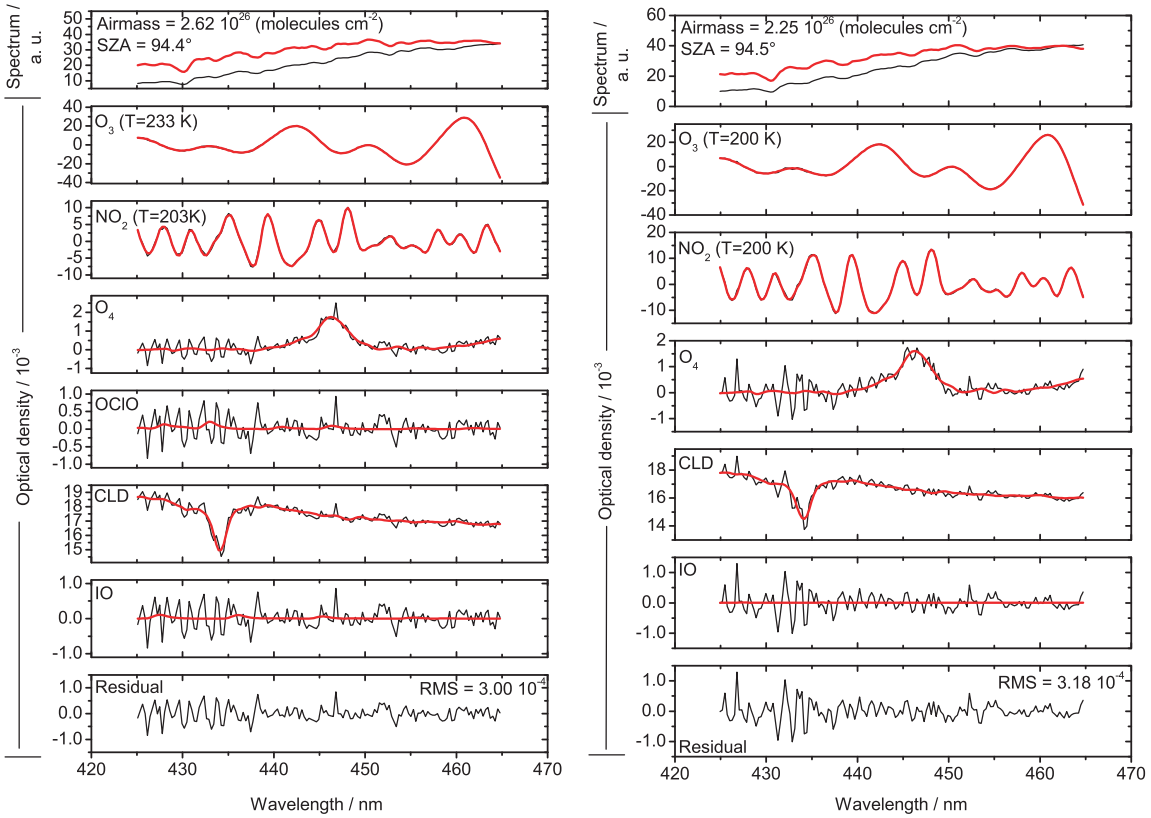

Figure 7.1: Spectral retrieval of IO in the visible spectral range for a spectrum measured at Kiruna on February 14, 1997, (left panel) and on March 23, 2003 (right panel). The upper most panels show the pseudo TOA spectrum (black line) and the measured spectrum (red line). The panels below illustrate the retrieved trace gas absorptions of O_3, NO_2, O_4, OClO (Kiruna 1997 only) and IO as well as the CLD correction. The lowest panels show the remaining residuals of the fitting procedure. The red lines indicate the spectral absorption and the black lines the sum of spectral absorption and residual.

its impact on the IO and OIO retrieval are discussed in section 7.3.1.

7.1.1 IO retrieval

The spectral retrieval of IO SCDs is performed in the wavelength range between 425 nm and 465 nm as recommended by Bösch et al. (2003). The IO absorption cross section measured by Hönninger (1999) is scaled to the IO spectrum of Bloss et al. (2001) and spectrally aligned to the NO_2 absorption cross section of Harder et al. (1997). Hönninger (1999) recorded the IO absorption cross section at a spectral resolution of 0.09 nm and found a peak cross section of $2.5\,10^{-17}$cm^2 of the 4←0 vibrational band of the $A^2\Pi \leftarrow X^2\Pi$ electronic transition at 427.2 nm. Recent studies at a comparable spectral resolution indicate that the IO absorption cross section at 427.2 nm is as large as $(3.5\pm0.3)\,10^{-17}$cm^2 (Gomez Martin et al., 2005; Spietz et al., 2005) or $(3.55\pm0.35)\,10^{-17}$cm^2 (Dillon et al., 2005). Accordingly, the SCDs and upper limits of IO retrieved using the Hönninger (1999) absorption cross section are somewhat larger than those inferred using the Gomez Martin et al. (2005), Spietz et al. (2005) or Dillon et al. (2005) data. In order to sustain continuity and internal consistency with the Bösch et al. (2003) study,

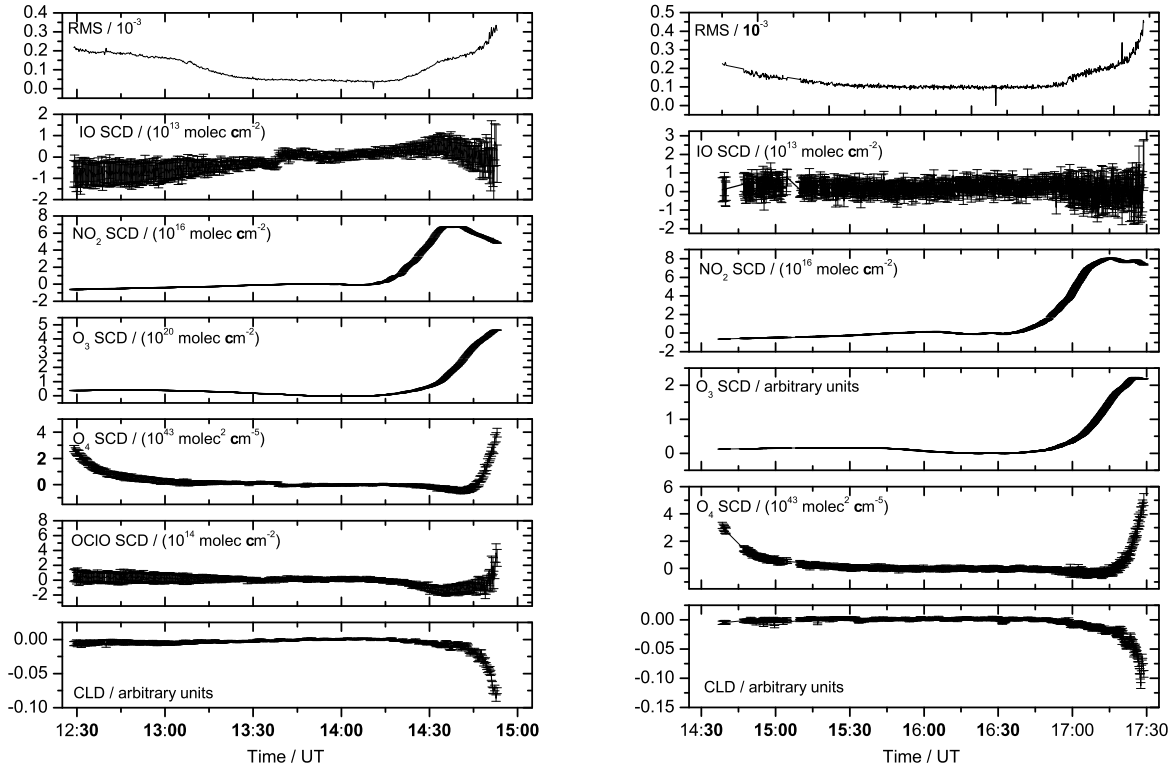

Figure 7.2: IO evaluation for all spectra measured at Kiruna on February 14, 1997, (left panel) and on March 23, 2003 (right panel). The upper most panels show the root mean square, i. e. $\sqrt{\chi^2 - 1}$. The panels below illustrate the retrieved SCDs of IO, NO_2, O_3, O_4, OClO (Kiruna 1997 only) and the CLD correction.

the IO absorption cross section of Hönninger (1999) is favored over the more recent measurements. O_3 and NO_2 are the strongest absorbers in the IO retrieval range. Two sets of absorption cross sections are used to account for the absorption of both gases. The analysis of all flights before 2002 is performed by simultaneously fitting absorption cross sections of O_3 at T = 233 K, O_3 at T = 253 K, NO_2 at T = 203 K and NO_2 at T = 228 K. After 2002, a set of O_3 at T = 200 K, O_3 at T = 220 K, NO_2 at T = 200 K and NO_2 at T = 238 K is used. All O_3 and NO_2 absorption cross sections are recorded by the DOAS spectrograph in the laboratory and are spectrally aligned to the NO_2 reference of Harder et al. (1997). In general, the absorption cross section corresponding to the higher temperature is numerically orthogonalized to the one at lower temperature. The collisional pair absorption cross section of O_4 is taken from Hermans et al. (1999). For the high-latitude winter flight at Kiruna in 1997 the absorption of OClO is accounted for by a lab-measured absorption cross section which is aligned to Wahner et al. (1987). Broadband extinction is considered through a 3rd order polynomial. Straylight is corrected according to equation (3.20) by a first order polynomial. The relative wavelength alignment between absorption cross sections and the pseudo-TOA reference spectra is determined in various test runs and kept fixed for the final evaluation, where only the measured spectrum is allowed to shift and stretch. As identified by Bösch et al. (2003), it is of major importance to include a center-to-limb-darkening correction in the model function used for spectral retrieval. Neglecting the CLD-effect generates systematic residual structures

which can be misinterpreted as absorption of IO.

The impact of the CLD effect on the measured spectra is clearly visible from figure 7.1 where the spectral retrieval of IO from two spectra recorded in deep solar occultation during the balloon flights from Kiruna in 1997 and 2003 is shown. The former balloon flight is re-analyzed although it has already been analyzed by Bösch et al. (2003) in order to demonstrate our capability to perform retrievals of similar quality as Bösch et al. (2003). While the CLD correction term is clearly detected, essentially no IO absorption is found in both spectra. The residual shows remaining systematic features in particular in the proximity of the solar Fraunhofer line at about 432 nm. This might be due to interpolation errors or errors of the relative wavelength alignment between pseudo-TOA and measured spectrum. The residuals observed for the flight from Kiruna in 2003 are slightly larger and more systematic than those observed for the flight in 1997 which is caused by the use of different sets of O_3 and NO_2 absorption cross sections. The theoretical noise levels of about $1.9\,10^{-4}$ and $2.5\,10^{-4}$ at 440 nm for the flights in 1997 and 2003, respectively, are only slightly smaller than the observed root-mean-square ($3.0\,10^{-4}$ for Kiruna 1997 and $3.18\,10^{-4}$ for Kiruna 2003) which indicates that the retrieval operates close to its theoretical limit. Figure 7.2 shows the fitting results of all spectra recorded during the two balloon flights. IO SCDs are in all cases below the detection limit, which is commonly defined as twice the SCD error (Stutz and Platt, 1996; Bösch et al., 2003). The definition of the detection limit is discussed in section 7.2. O_3 and NO_2 SCDs show the typical pattern of a trace gas with a concentration maximum in the stratosphere. While the O_4 concentration decreases rapidly with altitude, OClO builds up in the lower stratosphere during sunset and is only detectable during the flight from Kiruna in 1997. The CLD-correction is negligible for balloon ascent and float measurements where the shift of the brightness center of the Sun due to Rayleigh scattering is small, but becomes more important as the lines-of-sight penetrate deeper the Earth's atmosphere during sunset.
Further evidence for the importance of the CLD effect when performing direct Sun DOAS measurements can be found in Bösch (2002) where measurements during the solar eclipse on August 11, 1999, are analyzed. Reichl (2005) found that a CLD correction is also necessary for ground based direct Sun DOAS measurements where the Sun is partially obscured by thin clouds. A partial cloud cover shifts the brightness center of the Sun toward the less covered regions of the solar disk and, hence, induces changes of the optical density of the Fraunhofer lines.

7.1.2 OIO retrieval

OIO is retrieved in the 530 nm to 570 nm spectral range using the absorption cross section reported by Rowley et al. (2001) and Bloss et al. (2001) which has a value of $(1.29\pm0.22)\,10^{-17}\mathrm{cm}^2$ at 1.13 nm spectral resolution at the peak of the vibrational band at 548.6 nm. This is in good agreement with the data of Gomez Martin et al. (2005) and Spietz et al. (2005) where the OIO cross section at 548.6 nm is found to be $(1.3\pm0.3)\,10^{-17}\mathrm{cm}^2$ at a spectral resolution of 0.35 nm. Ingham et al. (2000) inferred values up to $3.5\,10^{-17}\mathrm{cm}^2$. Hence, the absolute scaling of the OIO absorption cross section is uncertain. The scaling used here is at the lower limit of the reported range implying that the presented SCDs and upper limits could be somewhat smaller if a different scaling of the OIO cross section had been used.
The absorptions of O_3 and NO_2 are fitted by the same reference sets as in the case of the IO retrieval. The respective cross sections, however, are spectrally aligned to the data of Voigt et al. (2001, 2002). Cross

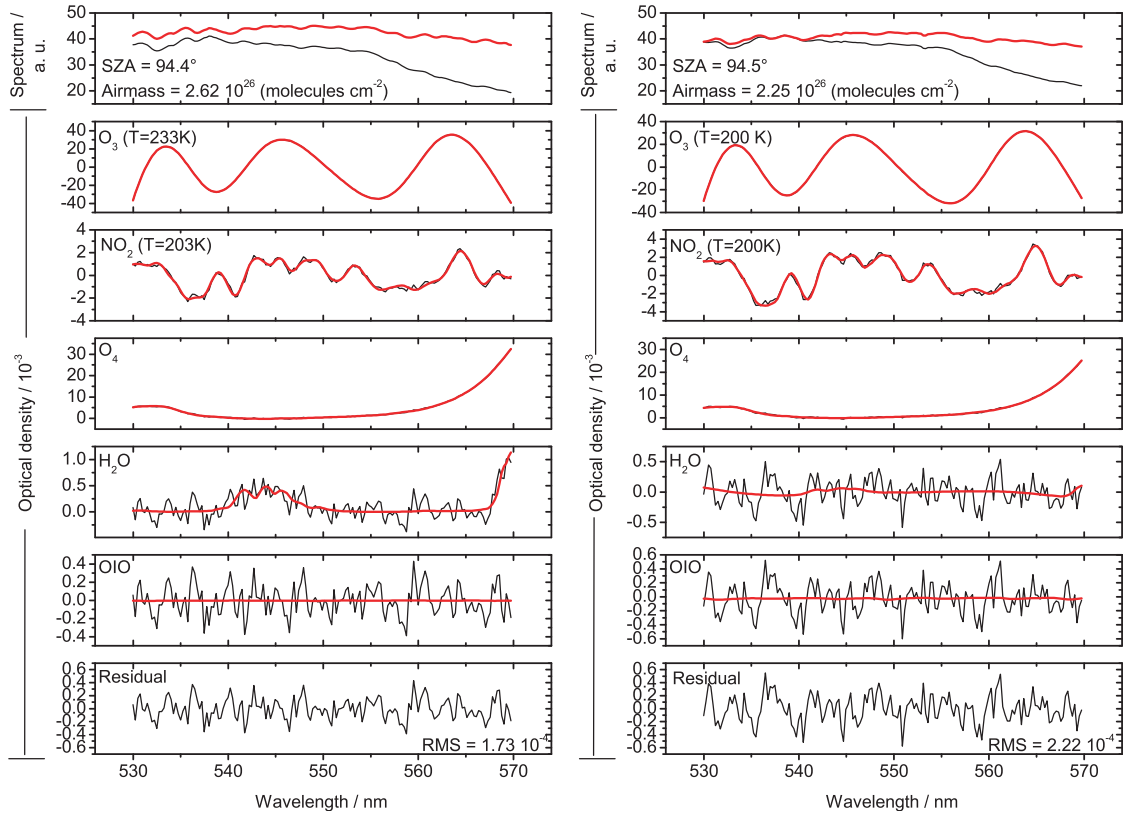

Figure 7.3: Spectral retrieval of OIO in the visible spectral range for a spectrum measured at Kiruna on February 14, 1997, (left panel) and on March 23, 2003 (right panel). The upper most panels show the pseudo TOA spectrum (black line) and the measured spectrum (red line). The panels below illustrate the retrieved trace gas absorptions of O_3, NO_2, O_4, H_2O and OIO. The lowest panels show the remaining residuals of the fitting procedure. The red lines indicate the spectral absorption and the black lines the sum of spectral absorption and residual.

sections at high temperatures are orthogonalized with respect to cross sections at low temperatures. As usual, O_4 absorption is considered through the reference set of Hermans et al. (1999) and H_2O is accounted for by convolving a H_2O absorption cross section generated from line parameters corresponding to T = 213 K and p = 80 mbar given by Rothman et al. (2005). The relative wavelength alignment between the package of absorption cross sections, the pseudo-TOA spectrum and the measured spectra is handled in the same way as for the IO retrieval. Broadband extinction and straylight correction are represented by 3rd and 1st order polynomials, respectively. The center-to-limb darkening effect is found negligible for the considered wavelength range.

A sample OIO retrieval for two spectra recorded at Kiruna in 1997 and 2003 is shown in figure 7.3. In both cases, OIO is not found by the fitting routine. The peak-to-peak residual structures are smaller than those for the IO retrieval illustrated in figure 7.1, since the OIO retrieval is performed at longer wavelengths where the signal decreases less strongly in solar occultation and the signal-to-noise is better than in the IO retrieval range. Systematic residual structures are not as prominent as for the IO retrieval but still exist most likely due to deficiencies of the absorption cross sections of O_3 and NO_2. The theoretical noise at 550 nm is $1.1\,10^{-4}$ and $1.7\,10^{-4}$ for the flights in 1997 and 2003, respectively. Again, the root-mean-square of the residual is in the range of the theoretical limit for both flights. Figure 7.4 illustrates

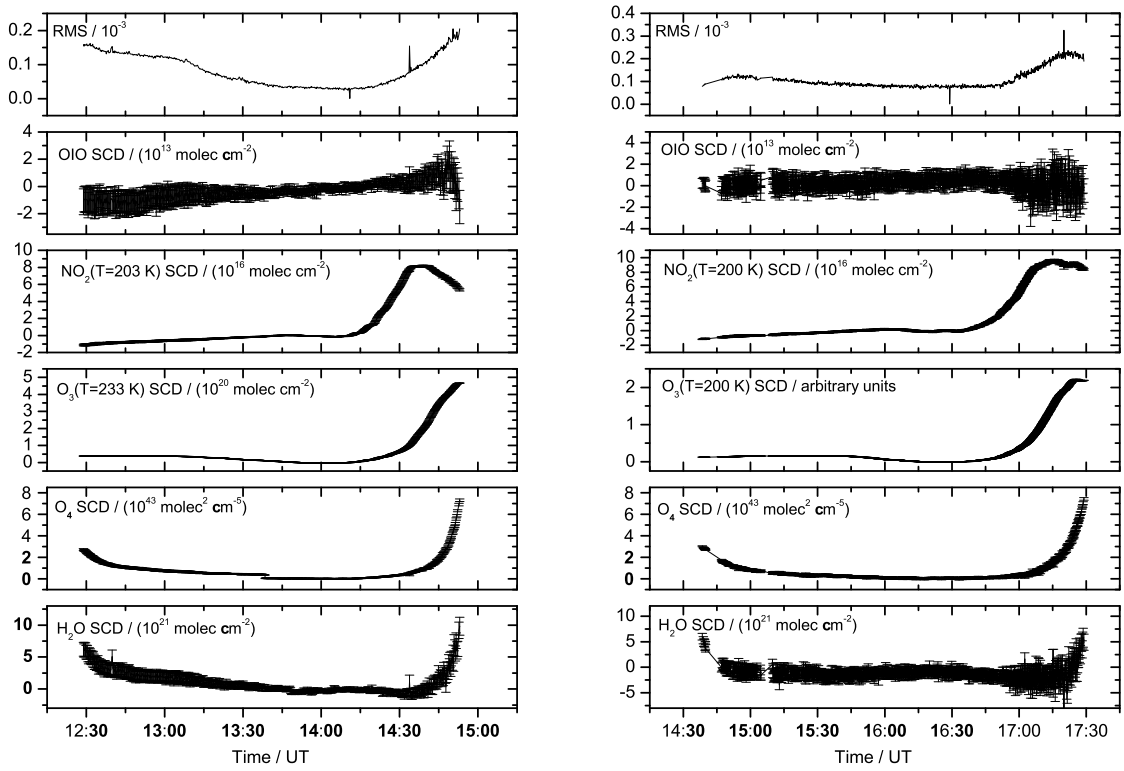

Figure 7.4: OIO evaluation for all spectra measured at Kiruna on February 14, 1997, (left panel) and on March 23, 2003 (right panel). The upper most panels show the root mean square, i. e. $\sqrt{\chi^2 - 1}$. The panels below illustrate the retrieved SCDs of OIO, NO_2, O_3, O_4 and H_2O.

.

the OIO retrieval for all spectra recorded during the two selected balloon flights. Clearly, OIO SCDs are below the detection limit.

7.2 Upper limits of IO and OIO in the extra-tropical stratosphere

Based on the details described in the previous section the spectral retrieval of IO and OIO is performed for the balloon flights from Kiruna in 1997, 2001, 2003 and 2004 and from Aire sur l'Adour in 2003. Since the meteorological situation corresponding to the different flights is described extensively by Bösch (2002), Dorf (2005) and section 6.2, a detailed investigation is omitted here. The flights from the high-latitudinal station Kiruna (67.9°, 21.1°E) probed the border of the northern polar vortex in February 1997, the winterly extra-vortex stratosphere in March 2003 and 2004 and the summerly stratosphere in August 2001. The balloon flight from Aire-sur-l'Adour (43.7°N, 0.25°W) in October 2003 investigated the mid-latitudinal stratosphere. In all cases neither IO nor OIO can be detected since the retrieved SCDs are below the detection limit.

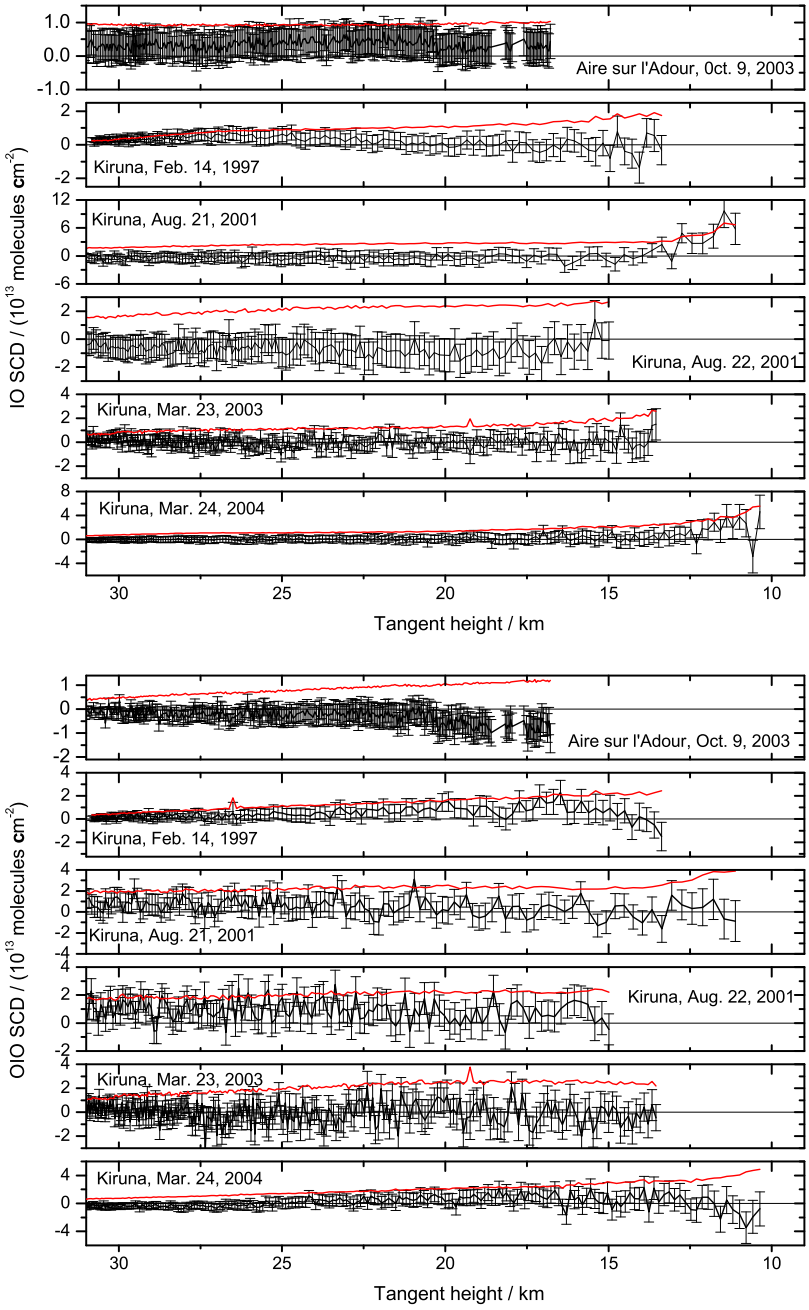

Figure 7.5: IO (upper panel) and OIO (lower panel) SCDs (black lines with error bars) and statistical detection limits (red line) as a function of tangent height. The data from Aire sur l'Adour in 2003 originate from balloon ascent measurements (tangent height equal to detector altitude) while solar occultation measurements are shown for the balloon flights from Kiruna. Observations at Kiruna on Aug. 21, 2001, are conducted during sunset, those on Aug. 22, 2001, during sunrise.

Detection limit

As mentioned above the detection limit applied here corresponds to twice the SCD retrieval error (Stutz and Platt, 1996; Bösch et al., 2003), i. e. SCDs are considered different from zero if their errors are less than 50%. The criterion is a good estimate of the actual detection limit as long as the errors attributed to the SCDs are reasonable. However, section 3.2.1 pointed out that this is only true if the residual consists of statistical noise. Corrections for the inter-dependencies of neighbouring pixels can be applied (Stutz and Platt, 1996), but the impact of systematic residual structures caused by deficiencies of the fitted absorption cross sections or by unaccounted absorbers cannot be estimated easily. In fact, a detailed treatment of the impact of systematic residuals on the retrieved SCDs would require the knowledge of the effects which cause the observed pattern. Systematic residual structures can be misinterpreted as trace gas absorption and generate absorber SCDs larger than the detection limit although the absorber is not present. An illustrative example is the effect of the CLD correction investigated by Bösch (2002) and Bösch et al. (2003). If the DOAS model function is insufficient in a way that it does not include a correction for the CLD effect, systematic residual structures remain which induce fake detection of IO with SCDs larger than twice the SCD error. Accounting for the CLD effect by a correction term based on the physical properties of the Sun removes these systematic features and yields IO SCDs clearly below the detection limit. Briefly, absorber SCDs which are even larger than twice the SCD error can be retrieval artifacts if the residual of the spectral retrieval does not consist of pure noise. Hence, the detection limit defined by twice the SCD error will further on be called statistical detection limit in order to emphasize the statistical nature of its derivation. Fortunately, for all flights presented in this section virtually all retrieved SCDs are smaller than the statistical detection limit. Hence, we are confident that the statistical detection limit is indeed a good estimate of the true detection limit.

Upper limits of IO and OIO

Figure 7.5 illustrates the retrieved SCDs and corresponding statistical detection limits of IO and OIO for all considered flights. If available, SCDs inferred from solar occultation measurements are shown since detection limits are commonly smaller for solar occultation than for balloon ascent. For Kiruna in 2001 and 2003, IO and OIO SCDs can be retrieved down to about 11 km. In 1997 and 2003, the pointing toward the Sun was lost early by the sun-tracker and the lowest tangent heights correspond to about 14 km. The balloon ascent measurements at Aire sur l'Adour in 2003 started late at about 17 km altitude due to problems with the stabilization of the gondola. Unfortunately, we missed the sunset in Aire sur l'Adour.

Virtually all inferred IO and OIO SCDs are below the detection limit and mostly consistent with a zero value within the error bars. The only IO SCD slightly above the detection limit is observed for the sunset measurements at Kiruna in 2001 at about 12 km tangent height. Given the somewhat controversy definition of the detection limit discussed above, this observation cannot be interpreted as detection of IO. Moreover no systematic increase spanning several spectra is observable. It has to be emphasized that none of the presented balloon flights sampled tropospheric air masses except for the flight from Kiruna in 2001 where the thermal tropopause corresponds to 12 km altitude. There, the observed increase of the retrieved IO SCDs for tangent heights below 15 km might be due to a contribution of light that sampled the upper troposphere and introduced systematic residual structures which are mis-interpreted

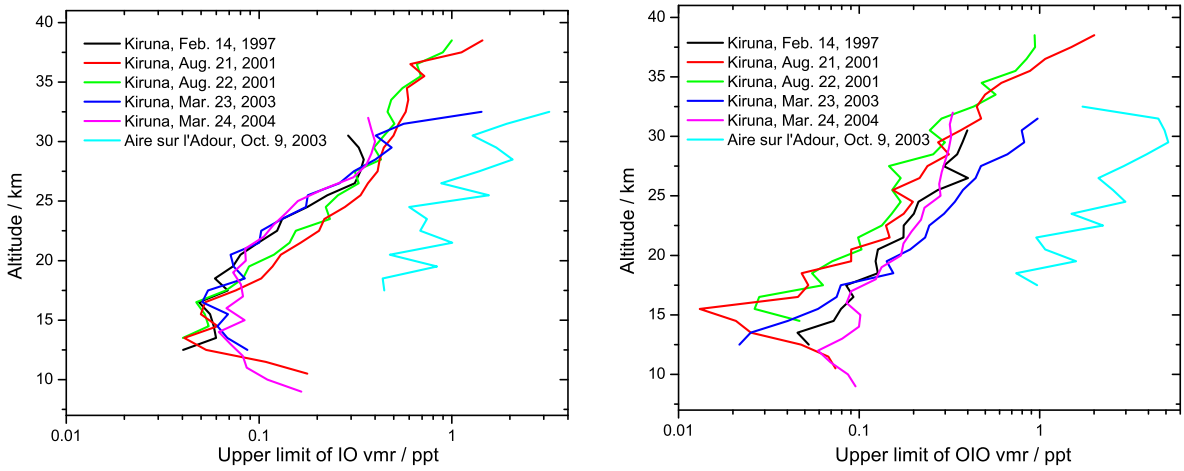

Figure 7.6: Upper limits of the IO (left panel) and OIO (right panel) vmr as a function of altitude. Data from Kiruna are inferred from solar occultation measurements while data from Aire sur l'Adour originate from balloon ascent. Observations at Kiruna on Aug. 21, 2001, are conducted during sunset, those on Aug. 22, 2001, during sunrise.

as IO absorption.

The inferred statistical detection limits for the IO and OIO SCDs are inverted to vertical profiles using the SVD profile retrieval algorithm described in section 3.3.1. Figure 7.6 shows the corresponding vertical profiles which can be regarded as upper limits of the IO and OIO mixing ratios as a function of altitude. Due to the shorter light path through the atmosphere, balloon ascent measurements, e. g. those from Aire sur l'Adour, yield upper limits which are up to 10 times larger than those inferred from solar occultation measurements and hence are omitted if solar occultation measurements are available. The upper limits of IO and OIO inferred from the statistical detection limits clearly fall into the same range as those reported by Bösch (2002) and Bösch et al. (2003). In the lower stratosphere, between 10 km and 20 km altitude the upper limits range between about 0.05 ppt and 0.11 ppt for IO and between 0.01 ppt and 0.11 ppt for OIO. For higher altitudes the upper limits increase mainly due to the decrease in air density. Inferred upper limits are somewhat larger for the mid-latitudinal station Aire sur l'Adour since solar occultation measurements are not available.

7.3 IO and OIO in the tropical upper troposphere and stratosphere

The LPMA/DOAS payload has been launched for the first time from a tropical site, close to the city of Teresina in northern Brazil (42.35°W, 5.38°S) on June 17, 2005. Due to clear sky conditions and a very smooth launch it was possible to record spectra from below 2 km up to balloon float altitude of about 33 km. Solar occultation measurements could be performed between SZA = 90.0° at 20:47 UT and SZA = 95.3° at about 21:10 UT. Due to the rapid sunset at low-latitudes, only 164 spectra could be recorded in solar occultation geometry. Temperature decreased from about 310 K at the ground to 194 K at 16.5 km altitude. The high tropopause altitude estimated from the temperature minimum at 16.5 km

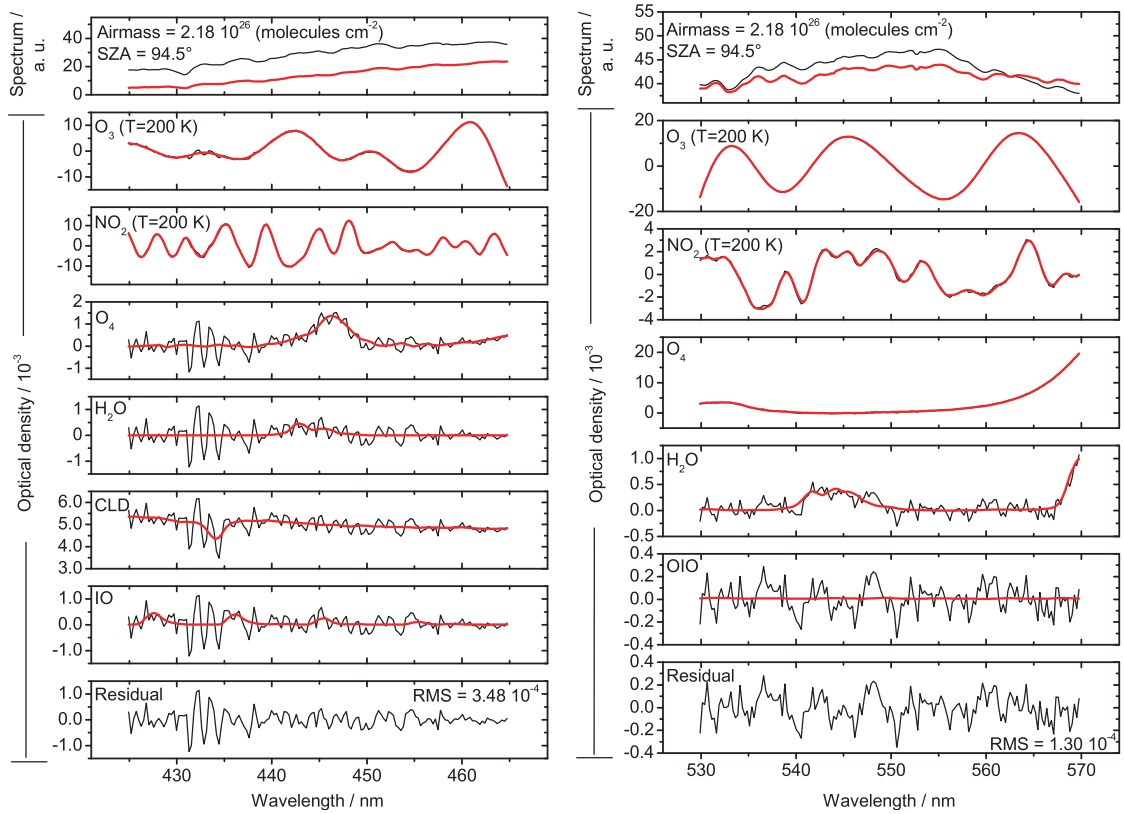

Figure 7.7: Spectral retrieval of IO (left panel) OIO (right panel) in the visible spectral range for a spectrum measured at Teresina on June 17, 2005. The upper most panels show the pseudo TOA spectrum (black line) and the measured spectrum (red line). The panels below illustrate the retrieved trace gas absorptions of O_3, NO_2, O_4, H_2O, CLD and IO (left panel) and O_3, NO_2, O_4, H_2O and OIO (right panel). The lowest panels show the remaining residuals of the fitting procedure. The red lines indicate the spectral absorption and the black lines the sum of the spectral absorption and the residual.

is typical of tropical latitudes and allows for probing tropospheric air masses even in solar occultation geometry with the lowest tangent height being 10.5 km. A more detailed meteorological discussion can be found in Dorf (2005).

7.3.1 Particularities of the IO and OIO retrieval in the tropics

The retrieval of IO and OIO from spectra recorded at Teresina in 2005 follows the same specifications as given in section 7.1. The IO retrieval is supplemented by an H_2O cross section corresponding to T = 213 K and p = 80 mbar taken from Rothman et al. (2003) since water absorption is clearly detectable for spectra sampling tropospheric air masses. For the OIO retrieval, it proves worthwhile to include a second H_2O absorption cross section corresponding to T = 253 K and p = 250 mbar which is orthogonalized to the standard water absorption cross section.

Figure 7.7 illustrates the spectral retrieval of IO and OIO. In comparison to previous flights, e. g. those shown in figure 7.1, the residual of the IO retrieval exhibits larger systematic residual structures. In particular, the IO retrieval is hindered by a strongly oscillating systematic feature between 430 nm and

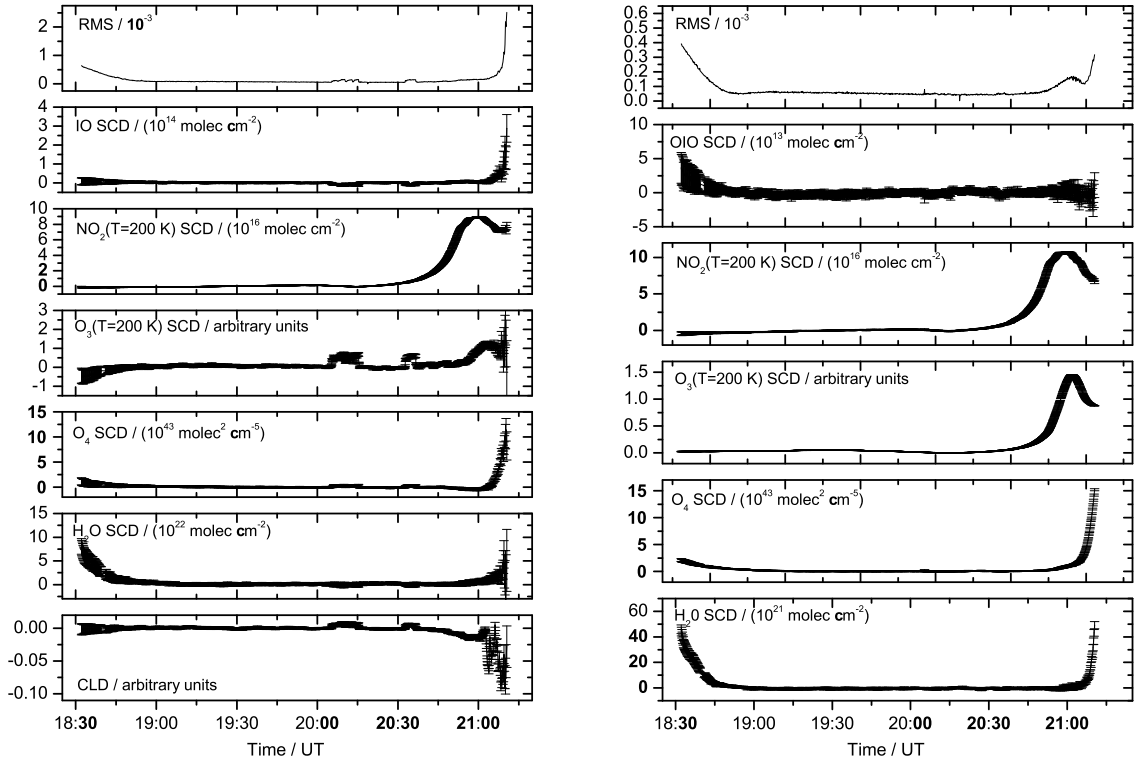

Figure 7.8: IO (left panel) and OIO (right panel) evaluation for all spectra measured at Teresina on June 17, 2005. The upper most panels show the root mean square, i. e. $\sqrt{\chi^2 - 1}$. The panels below illustrate the retrieved SCDs of IO, NO_2, O_3, O_4, H_2O and CLD (left row) and OIO, NO_2, O_3, O_4 and H_2O (right row).

435 nm which is also observable to a lesser degree for the flights at Kiruna in 2003 and 2004. As a consequence, the prominent CLD structure at about 434 nm is not fitted as clearly as for the previous flights. The retrieved IO absorption is non-zero although hardly perceivable by eye. The theoretical noise level at 440 nm is $2.0\,10^{-4}$, which is 57% of the observed root-mean-square ($3.48\,10^{-4}$). For the flight from Kiruna in 2003 (figure 7.1) the ratio of theoretical noise level at 440 nm to the root-mean-square of the IO retrieval was better (79%). The same is true for the OIO retrieval. The theoretical noise level at 550 nm for the spectrum shown in figure 7.7 is $0.8\,10^{-5}$ amounting to about 62% of the observed root-mean-square ($1.3\,10^{-4}$) while for Kiruna in 2003 the respective ratio is 77%. However, there is no obvious correlation between the residual structures and the retrieved parameters of the OIO retrieval.
The IO and OIO spectral retrieval from all spectra recorded during the balloon flight from Teresina on June 17, 2005, is illustrated in figure 7.8. As already observed in figure 7.7, the spectral retrieval yields non-zero amounts of IO for solar occultation measurements. The inferred IO SCDs are approximately one order of magnitude larger than those observed for the previous flights and for some of the spectra well above the statistical detection limit. Whether the non-zero IO absorption found by the spectral retrieval is real or an artifact of the systematic residual structures is discussed below. Simultaneously, the retrieved fitting parameters of the CLD correction term do not show a monotonic decreasing pattern with setting Sun as observed for the previous flights but reveal some oscillations. Between 20:00 UT and 20:45 UT, two periods can be identified where several parameters, most prominently the O_3 SCD

retrieved from the IO spectral range, exhibit discontinuities in their temporal evolution. Although hardly visible in figure 7.8, the observed discontinuities go along with an increase of the root-mean-square residual of the fitting procedure and can be attributed to an instrumental problem as discussed below. The OIO retrieval yields OIO SCDs which are consistent with zero within their error bars except for the very first spectra recorded during balloon ascent where the inferred OIO SCDs are slightly larger than the attributed error. However, all OIO SCDs retrieved from the tropical balloon flight are well below the statistical detection limit.

It is evident from the examination of figures 7.7 and 7.8 that the retrieval of IO from spectra recorded at Teresina in 2005 needs further investigation, in particular it is necessary to perform a careful analysis of instrumental performance and retrieval related issues which are specific to the tropical balloon flight and which could lead to fake detection of IO. In the following several arguments are discussed in order to facilitate a decision on whether IO is detected or not: (1) A shift of the wavelength-pixel mapping is observed due to the instrumental upgrade before the Teresina 2005 balloon flight. (2) The discontinuities in the temporal evolution of various fitting parameters can be ascribed to a hardware problem which might also impact the retrieval of IO. (3) There are some hints for an aerosol layer in the lower tropical stratosphere which could impact the CLD-correction and hence the IO retrieval by partly obscuring the Sun. (4) Sensitivity studies are performed in order to test the stability of the IO spectral retrieval. (5) Spectra which yield non-zero IO SCDs are inspected by eye.

Shift of wavelength-pixel mapping

Section 3.1.2 pointed out that prior to the tropical balloon campaign in 2005 the DOAS instrument was upgraded by new connectors on the top of the instrument housing in order to thermally decouple the jacks and connectors form the 0°C cold housing and to avoid condensation of water on the electronic adaptors. The instrument housing had to be removed to feed the cables through the housing. Although no change of the optical setup was carried out and care was taken to avoid any impact on the optical components, a shift of the wavelength-pixel mapping of the 'visible' DOAS spectrograph by (1.03 ± 0.05) pixel ($0.252\,\text{nm}\pm0.013\,\text{nm}$) is observed. The shift is illustrated in figure 7.9, where two emission lines of a mercury lamp in the IO and OIO retrieval ranges are shown. A comparison of the spectral position of the emission lines recorded before and after the instrumental upgrade shows that the shift is detectable in both retrieval ranges. An additional stretch is not observed. A shift of the wavelength-pixel mapping is considered as parameter in the DOAS spectral retrieval and does not directly impact the inferred SCDs. However, the lab-measured absorption cross sections of O_3 and NO_2 are recorded some years ago by an instrument function which is displaced with respect to the current one. Hence, the wavelength dependence of the instrument function or differing sensitivity of the detector pixels might introduce systematic deficiencies into the DOAS model function. Interpolation errors are of principle concern when shifts and stretches of the wavelength-pixel mapping are observed, since either the set of absorption cross sections or the spectra have to be interpolated. Here, interpolation errors should be negligible since the inferred shift corresponds almost exactly to one pixel. Interpolation errors would be largest for a shift of 0.5 pixel.

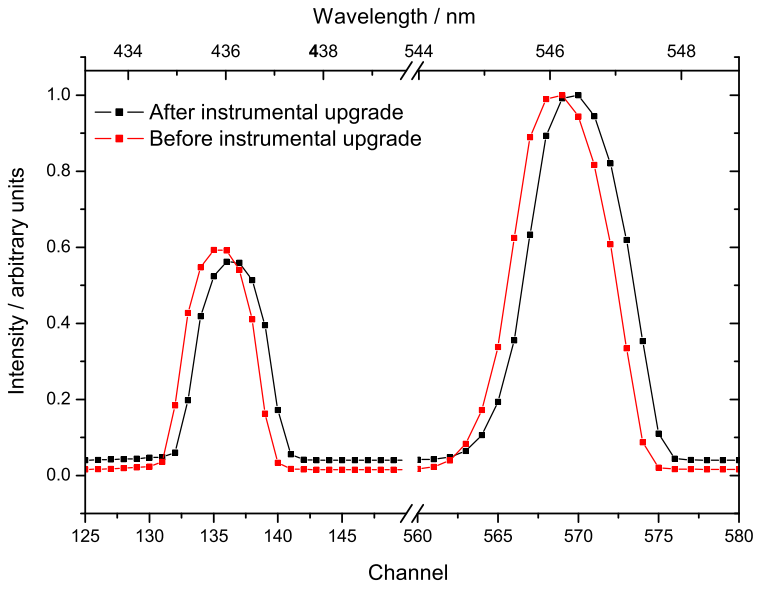

Figure 7.9: Emission lines of mercury recorded before (red) and after (black) the instrumental upgrade in 2004. The intensity is normalized to an arbitrary value and cannot be compared between the two data sets, since the emission lamp is not radiometrically stable with time. The wavelength scale (top) corresponds to the wavelength-pixel mapping observed before the instrumental upgrade.

Discontinuities in the temporal evolution of retrieval parameters

The spectral retrievals of IO and OIO (figure 7.8) reveal discontinuities in the temporal evolution of various retrieval parameters. The discontinuities cannot be attributed to real effects in the atmosphere but must be of instrumental origin. The upper panel of figure 7.10 shows the peak intensity as a function of recording time for all spectra measured by the 'visible' DOAS instrument during the considered balloon flight. The overall strong decrease after 20:30 UT is due to less incoming radiation during sunset. Discontinuities are observed at the same instances as for the retrieval parameters. The small variations between 20:20 UT and 20:30 UT can be attributed to test-runs of the sun-tracker where the primary mirror is defocused from the Sun's center in order to check the alignment of the sun-tracker optics. The drop in intensity observed between 20:05 UT and 20:15 UT and between 20:30 UT and 20:40 UT is of questionable origin. Erroneous integration times of the spectra as reported in previous studies (Hirsekorn, 2003) can be excluded since all programming errors were removed in the course of the absolute calibration of the instrument (Lindner, 2005; Gurlit et al., 2005). The features cannot be observed for spectra recorded by the spectrograph sensitive to the UV which points to a problem of the mechanical or optical setup of the 'visible' spectrograph. The lower panel of figure 7.10 illustrates two successively recorded spectra which are measured by the 'visible' DOAS spectrograph shortly before and during the sudden drop in intensity at about 20:05 UT. The spectra shown are composed of 13 co-added spectra and exhibit at total integration time of 4.000 s. The ratio of the two spectra shows that the intensity drop occurred while the spectrum was recorded and happened on the timescale of the read-out time of 10 pixels i. e. about 0.5 ms. This leads us to speculate that an optical component e. g. a dispersion plate inside the entrance

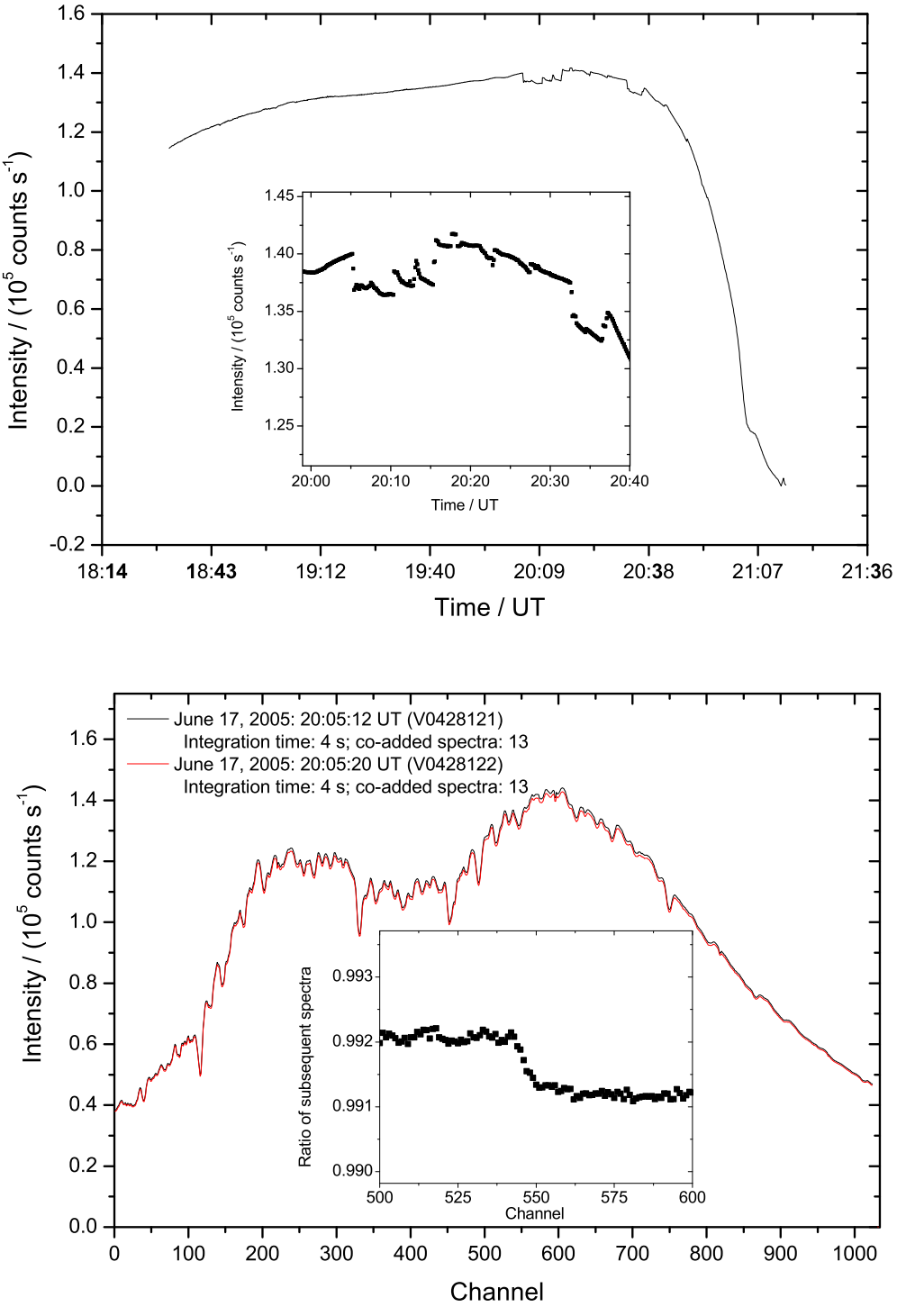

Figure 7.10: Upper panel: peak intensity in binary units as a function of recording time for all spectra measured by the 'visible' DOAS spectrograph during the balloon flight from Teresina in 2005. The inset highlights the interval between 20:00 UT and 20:40 UT where discontinuities in the measured intensity are observed. Lower panel: Subsequent spectra recorded shortly before and during the sudden drop in intensity at 20:05 UT. The inset shows the ratio of the two spectra.

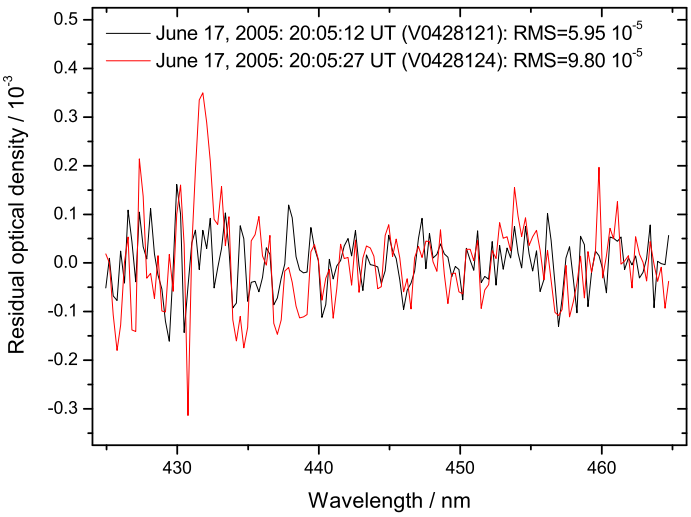

Figure 7.11: Residual optical density of the IO retrieval for two spectra recorded shortly before and shortly after the sudden intensity drop at about 20:05 UT.

telescope or a glass fiber partially broke or degraded. However, the process causing the intensity drop must be instable and even reversible since intensity is somewhat fluctuating and not continuously low. Further evidence for the above hypothesis comes from the residual of the IO spectral retrieval. Figure 7.11 depicts the residual optical density of the IO retrieval for two spectra recorded 25 s apart at the time of the first intensity drop. A change in the residual structure between 430 nm and 435 nm is obvious. After the intensity drop, the peak-to-peak residual is almost doubled and its pattern is highly systematic close to the solar Fraunhofer line at 432 nm. The spectral feature is observable during the two periods of low intensity identified above and cannot be detected for all other spectra. Dorf (2005) reported a similar pattern for spectra recorded by the 'UV' DOAS spectrograph during the test-runs of the sun-tracker where a change of the light path through the sun-tracker and telescope optics induces changes of the residual structures of the BrO retrieval. Clearly, optical components which have a transfer function that depends on the incidence angle or the spatial distribution of illumination could cause systematic residual structures if the light path through the instrument is altered by any effect. Post-flight examination of the optical components which are accessible without removing the instrument housing yielded no conclusive result on the origin of the observation. In order to avoid further changes of the instrument function and in the view of an upcoming measurement campaign, we decided not to open the instrument housing or to change any components moreover since the retrieval of the trace gases O_3 and NO_2 is not hindered. Nonetheless, as soon as the schedule of measurement campaigns allows for it, an in-depth investigation of the observed degradation and a subsequent re-characterization of the instrument which includes the measurement of O_3 and NO_2 absorption cross sections in the laboratory is necessary. Measurements during solar occultation, which are most important for the IO retrieval, show no obvious drop in intensity. However, a further period of low intensity could be masked by the overall decrease of incoming radiation during sunset. Inspection of the residual optical densities is inconclusive since the typical residuals of solar occultation retrievals are larger than the systematic pattern observed in figure 7.11.

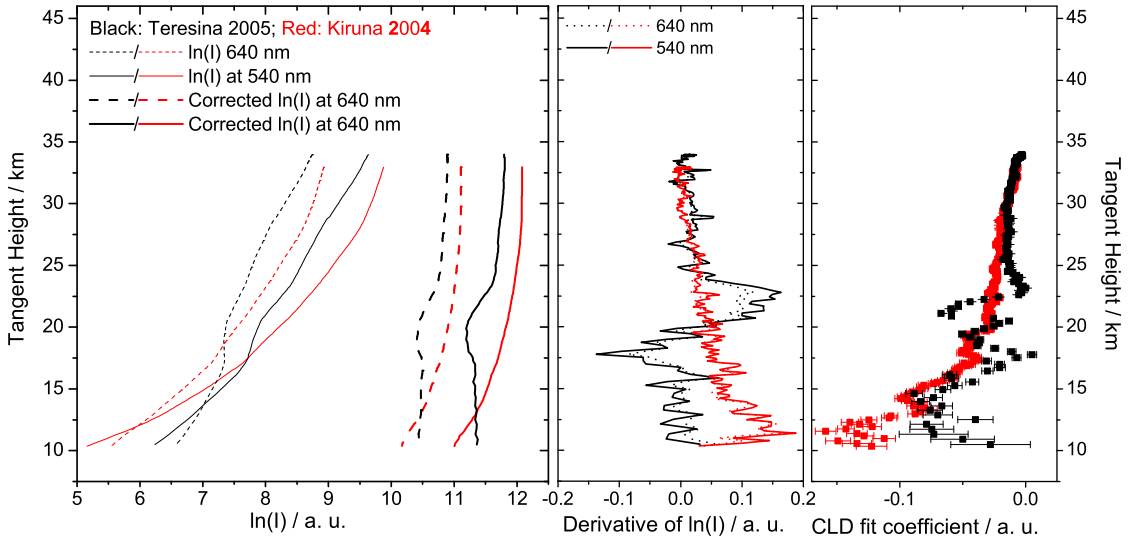

Figure 7.12: Left panel: Logarithm of the incoming intensity measured by the 'visible' DOAS spectrograph at 540 nm (solid lines) and 640 nm (dashed lines) inferred from observations at Kiruna in 2004 (red) and Teresina in 2005 (black). The thin lines show the logarithms of the measured intensity while the thick lines show the logarithmic intensity corrected for gaseous absorption of O_3, NO_2 and H_2O and for Rayleigh scattering. The data are slightly offset for clarity. Middle panel: Derivative of the corrected, logarithmic intensity with respect to tangent height at 540 nm (solid lines) and 640 nm (dashed lines) for Kiruna in 2004 (red) and Teresina in 2005 (black). Right panel: Fit coefficient of the CLD correction term inferred from measurements at Kiruna in 2004 (red) and Teresina in 2005 (black).

Possible aerosol layer in the lower stratosphere

Figure 7.10 (left panel) further reveals a knee-shaped pattern of the measured peak intensity between 21:02 UT and 21:07 UT which corresponds to tangent heights between 23.5 km and 16.5 km altitude and which cannot be attributed to the instrumental problem discussed above. The intensity dip is not only observable in the peak intensity but also in the average intensity measured by the 'visible' DOAS spectrograph and the intensity at single wavelengths, e. g. 440 nm, 540 nm and 640 nm. At small wavelengths, however, the overall intensity decrease due to Rayleigh scattering masks the pattern. The dip is not observable in spectra measured by the 'UV' DOAS spectrograph since the measured intensity at 350 nm is almost zero at 20 km tangent height.

In principle, the interplay of Rayleigh scattering and altitude dependent gaseous absorption could generate a pattern similar to that observed. However, there are some arguments that extinction by aerosols or cloud particles may contribute. Figure 7.12 investigates this hypothesis in detail. It displays the logarithm of the measured intensities at 540 nm and 640 nm as a function of tangent height. The pair of wavelengths is chosen since molecular absorption is small and intensity is sufficiently high throughout solar occultation. The measured intensities are corrected for the absorption of O_3, NO_2 and H_2O using the respective SCDs retrieved as described in section 4.1.1. Rayleigh scattering is corrected by calculating the optical density using the corresponding cross section according to equation (2.10) and

the air column along the lines-of-sight. From the left panel of figure 7.12 it is evident that the intensity dip around 20 km tangent height is present in the corrected and uncorrected data gathered during the tropical balloon flight, but not observable for the balloon flight from Kiruna in 2004 which is shown for reference. Since gaseous absorption and Rayleigh scattering is already considered, an additional extinction process such as extinction by particles must have occurred. The process must originate from a layered structure in the lower stratosphere. The latter conclusion is highlighted by the middle panel of figure 7.12 where the derivative of the corrected intensity with respect to tangent height is plotted. A similar approach using the color index method is employed by von Savigny et al. (2005) in order to identify polar stratospheric clouds from satellite skylight limb measurements. While for Kiruna in 2004 the derivative shows a continuous increase to lower altitudes where aerosols get more and more abundant (figure 6.19), the derivative increases sharply for Teresina in 2005 at about 23.5 km followed by on oscillation at lower altitudes. Further independent evidence that extinction by particles might have played a role for the tropical LPMA/DOAS measurements comes from the fit coefficient of the CLD correction term depicted in the right panel of figure 7.12. As anticipated by the model defining the CLD correction term (section 3.2.2), the CLD fit coefficient for the DOAS measurements during solar occultation should decrease continuously as the lines-of-sight penetrate deeper the atmosphere since the brightness center of the Sun shifts more and more upward on the solar disk. This is clearly true for the measurements at Kiruna in 2004 where an almost monotonic decrease is observed down to about 13 km tangent height. Below 13 km, only few measurements are available and the error bars increase due to the overall decrease of incoming radiation. For Teresina however, the CLD fit coefficient shows strong oscillations with tangent height starting below 25 km which coincides nicely with the low-intensity observations in the left and middle panel of figure 7.12. A layered structure of particles contributing to the extinction could cause the observed oscillations of the CLD fit coefficient since the brightness center of the Sun would be shifted upward or downward depending on how the lines-of-sight cross the respective altitude layers. Reichl (2005) showed by ground-based direct Sun measurements that a CLD correction is indispensable when the Sun is covered by thin clouds causing spatial fluctuations of the Sun's brightness center.

Stability of the spectral retrieval

In the discussion above, some instrumental deficits and some particularities of the ambient atmosphere are identified which are encountered during the balloon flight from Teresina in 2005 and which complicate the retrieval of IO SCDs. In order to test the stability of the retrieval, sensitivity studies are performed. Starting from the standard run which corresponds to the specifications given in section 7.1 several retrieval parameters which could influence the retrieved IO SCDs are varied within a reasonable range. Table 7.1 lists the tested parameters and the respective modifications with respect to the standard setup. Figure 7.13 shows the results. The gray lines indicate the results for the set of sensitivity runs. Above about 13 km tangent height the retrieval is stable, i. e. the retrieved IO SCDs typically fall within the error bars of the standard retrieval or are zero within their error bars. This is not true for two sensitivity runs which yield non-zero IO SCDs between 33 km and 20 km altitude. There, the inferred IO SCDs are significantly larger than the SCDs retrieved from the standard run. However, these sensitivity runs correspond to reduced retrieval ranges ([433 nm, 452 nm] and [433 nm, 465 nm]) where the

Table 7.1: Sensitivity studies of the IO retrieval for the balloon flight from Teresina in 2005.

Tested Parameter	Tested range/Difference w.r.t. the standard run
Spectral range	[415 nm, 452 nm]; [415 nm, 465 nm]; [425 nm, 452 nm]; [433 nm, 452 nm]; [433 nm, 465 nm]; [425 nm, 465 nm] with gap [430 nm, 435 nm]
Absorbing species	no NO_2 (T=238 K); no O_3(T=220 K); no H_2O; additional OClO; NO_2(T=217 K) and NO_2(T=230 K) from Harder et al. (1997); O_3(T=223 K) and O_3(T=246 K) from Voigt et al. (2001); simultaneously NO_2 from Harder et al. (1997) and O_3 from Voigt et al. (2001);
Retrieval corrections	no CLD correction; no straylight correction; additional Ring effect; CLD correction prescribed by fit coefficients retrieved from measurements at Kiruna in 2004;
Polynomial	degree 2; degree 4; degree 5;
Spectral alignment	O_3 shifted by $\pm$0.5 pixels; O_3 stretched by $\pm$0.002 pixels; NO_2 shifted by $\pm$0.1 pixels;
pseudo-TOA spectrum	replaced by V0428979 corresponding to 22 km tangent height

strongest IO absorption band (4←0) is not included in the fitting process and the corresponding error bars are large. Below 13 km, the sensitivity of the IO SCDs to the retrieval parameters is large and the errors increase rapidly. Remarkable stability is observed in the altitude range of the upper troposphere and lower stratosphere between 13 km and 20 km altitude. There all retrievals show non-zero IO SCDs which are in the order of twice the statistical detection limit. A sensitivity run of special importance is highlighted by blue triangles in figure 7.13. The fit coefficient of the CLD correction term is prescribed by the values inferred from the balloon flight at Kiruna in 2004. The fit coefficients are assigned to the individual spectra according to the air mass integrated along the respective lines-of-sight. Since Bösch et al. (2003) pointed out that the accurate representation of the CLD effect is crucial for the retrieval of IO SCDs and our retrieval for spectra recorded at Teresina in 2005 shows unexpected values of the CLD fit coefficient (figures 7.7 and 7.8), we consider this a stringent test for the inferred IO SCDs. However, as argued above the unexpected values of the CLD fit coefficient might be real and due to a layer of particles in the lower stratosphere. Unfortunately, the comparison between the standard and the test run remains inconclusive as there are sizeable discrepancies between 16 km and 18 km but agreement is within the error bars outside that altitude range. Also the sensitivity study where the CLD fit coefficients are prescribed yields IO SCDs clearly larger than the statistical detection limit in the upper troposphere and lower stratosphere.

Figure 7.13 further shows the ratio of the mean tropospheric to the mean stratospheric air mass factor which is a measure of the portion of the observed direct sunlight traveled through the troposphere. The presented data are calculated assuming tropopause altitude equal to 16.5 km and an effective field-of-view of 0.53° corresponding to the size of solar disk. All spectra with tangent heights below about 19 km have a contribution from tropospheric air. The increasing contribution from the troposphere coincides with the increase in IO SCDs although the latter seems to start at altitudes slightly above 19 km. This might either indicate that - if detected - IO resides in the troposphere or the transition layer between the troposphere and stratosphere or that - if IO is not detected - tropospheric absorbers deteriorate the retrieval quality and induce fake detection of IO. Sampling of tropospheric air masses indeed introduces systematic residual structures which originate from weak unaccounted absorbers or unknown absorption features of highly abundant tropospheric absorbers, e. g. H_2O. This is of particular importance if purely

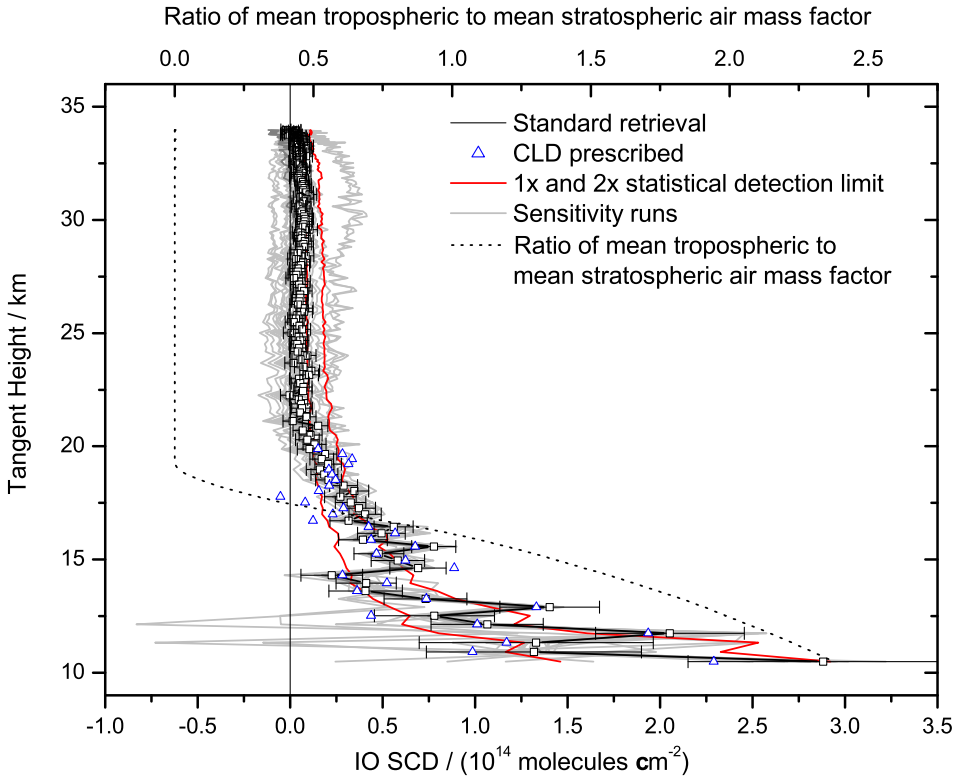

Figure 7.13: IO SCD as a function of tangent height retrieved from sensitivity runs. The standard run corresponds to open black boxes. A variety of sensitvity runs is shown as gray lines. The sensitvity run where the CLD correction is prescribed by values inferred from the balloon flight at Kiruna in 2004 is highlighted by blue triangles. The statistical detection limits (1x and 2x) are shown as red lines. In addition the dotted black line (top abscissa) shows the ratio of the mean tropospheric to the mean stratospheric air mass factor in order to illustrate that below 19 km tangent height tropospheric air masses contribute to the measured spectra.

stratospheric spectra are referenced to spectra with tropospheric contribution as in our case. Ground based measurements by Reichl (2005) using the DOAS spectrograph confirm this observation. There, the use of a pseudo-TOA spectrum recorded during a stratospheric balloon flight at high altitude results in residuals which are larger by as much as one order of magnitude.

Inspection by eye

Finally, inspection by eye might yield further insight on whether the inferred IO abundances are real or a retrieval artifact. Figure 7.14 depicts the detected IO optical density, the residual structures and the theoretical optical density of IO assuming 0.5 ppt IO between 0 km and 20 km altitude. Three spectra are chosen from solar occultation measurements of the tropical balloon flight at tangent heights of 20 km, 16.8 km and 13.8 km. Data inferred from the balloon flight at Kiruna in 1997 corresponding to 13.8 km tangent height are shown for comparison. The latter observation corresponds to figure 3 in Bösch et al. (2003). During the tropical balloon flight, the spectrum recorded at 20 km tangent height sampled purely stratospheric air masses while the spectrum recorded at 16.8 km tangent height sampled stratospheric and tropospheric air in the tropopause region and the spectrum recorded at 13.8 km tangent height sampled

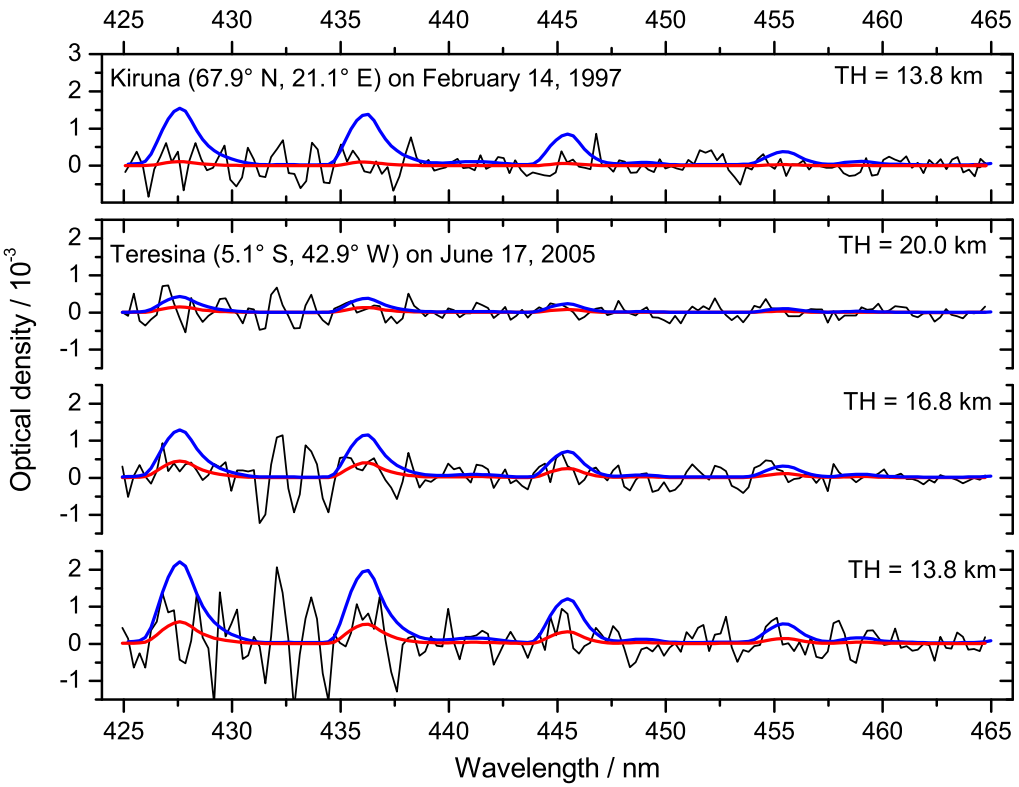

Figure 7.14: IO optical density (red line) inferred from solar occultation measurements at Kiruna on Feb. 14, 1997, at 13.8 km tangent height (upper panel) and at Teresina on June 17, 2005, at 20 km, 16.8 km and 13.8 km tangent height (TH) (three lower panels). IO absorption + residual is shown as black line. The blue line illustrates the theoretical optical density of IO assuming 0.5 ppt IO between 0 km and 20 km altitude.

mostly tropospheric air. Although recorded at the same tangent height as the latter tropical spectrum, the spectrum taken from the high-latitude observations at 13.8 km tangent height sampled purely stratospheric air due to the low tropopause in high-latitudes. The increase of the residual structures for lower tangent heights is obvious for the tropical dataset. Comparing the high- and low-latitudinal residuals at 13.8 km tangent height reveals that the high-latitudinal retrieval is superior to the low-latitudinal one by a factor of 3 when looking at the peak-to-peak residuals. As emphasized in the previous paragraph, sampling of tropospheric air during the tropical balloon flight might partially explain this finding. In all cases the optical density calculated from 0.5 ppt IO between 0 km and 20 km is clearly larger than the detected IO absorption. The inferred IO absorption at 16.8 km and 13.8 km tangent height corresponds roughly to 0.2 ppt IO and is about twice as large as the statistical detection limit. Stutz and Platt (1996) derived from Monte-Carlo simulations that detection of trace gas absorption which is not identifiable by eye is indeed possible using the DOAS retrieval provided that the residual structures consist of pure noise. Since in our case the residuals are highly systematic we doubt that IO is truely detected in figure 7.14.

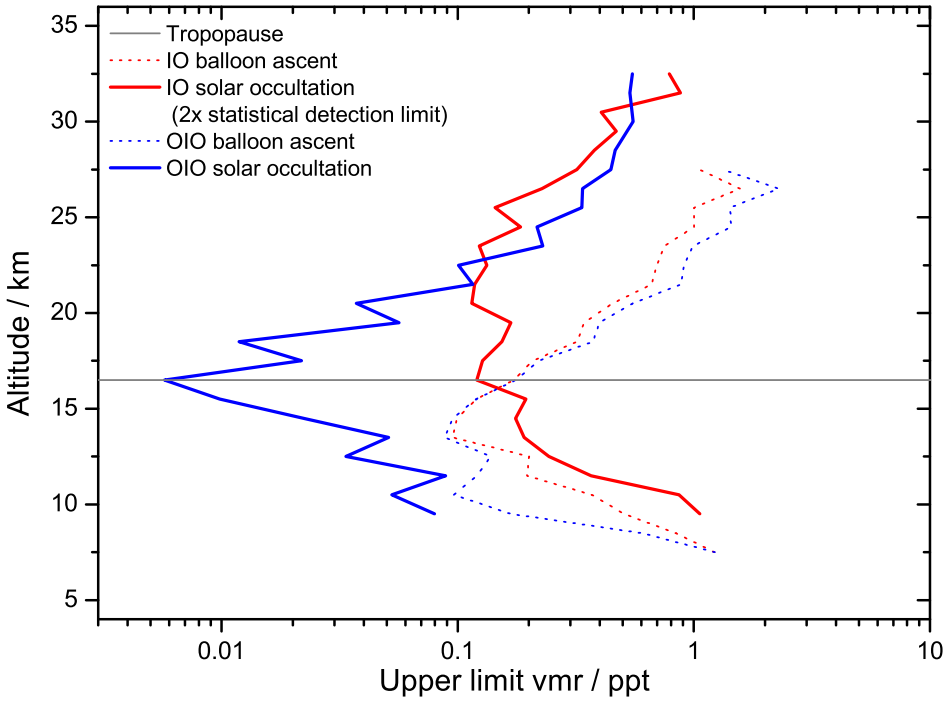

Figure 7.15: Upper limits of IO (red) and OIO (blue). Solid and dotted lines are upper limits inferred from solar occultation and balloon ascent measurements, respectively. For IO, upper limits retrieved from solar occultation correspond to twice the statistical detection limit of the underlying SCDs.

7.3.2 Upper limits of IO and OIO in the tropical upper troposphere and stratosphere

The retrieval of IO and OIO SCDs from spectra recorded at Teresina in 2005 is discussed in the previous section. For the first time, IO abundances above the statistical detection limit are inferred. However, due to instrumental and retrieval related problems the applicability of the statistical detection limit as criterion whether IO is truly detected or not is questioned. The previous section highlights the problems which could impact the retrieved IO SCDs or could be responsible for fake detection of IO. Despite our efforts to characterize the particularities of the tropical balloon flight, we cannot come to a firm conclusion whether IO abundances in the tropical lower stratosphere and upper troposphere are on the order of twice the statistical detection limit of the DOAS spectrograph or if fake detection of IO is caused by systematic residual structures. Hence, we restrict ourselves to give a conservative estimate of an upper limit of the tropical IO abundance which is in agreement with our measurements. Upper limits of OIO can be inferred from the statistical detection limits since the OIO retrieval is less impacted by the problems discussed above. An IO upper limit which is in accordance with the LPMA/DOAS measurements can be estimated from figure 7.13 to twice the statistical detection limit.

Vertical profiles of IO and OIO upper limits are inferred from the SCD detection limits using the SVD profile retrieval algorithm (figure 7.15). The upper limit of the IO volume mixing ratio correspond-

Table 7.2: Upper limits of IO and OIO inferred from LPMA/DOAS measurements. Adopted and complemented from Bösch et al. (2003).

Date	Location	IO upper limit / ppt			OIO upper limit / ppt			remarks
		20 km	15 km	12.5 km	20 km	15 km	12.5 km	
Nov. 23, 1996	Leon (42.6°N,5.7°W)	0.11	-	-	0.18	-	-	mid-lat. fall, sunset[a]
Feb. 14, 1997	Kiruna (67.9°N,21.1°E)	0.10	0.07	0.06	0.13	0.07	0.06	high-lat. winter, sunset[a,b]
Jun. 20, 1997	Gap (44.0°N,6.1°E)	0.13	0.08	0.06	0.13	0.07	0.05	mid-lat. summer, sunrise[a]
Mar. 19, 1998	Leon (42.6°N,5.7°W)	0.16	0.08	0.08	0.13	0.06	0.05	mid-lat. spring, sunset[a]
Aug. 19, 1998	Kiruna (67.9°N,21.1°E)	0.16	0.08	0.08	0.19	0.09	0.07	high-lat. summer, sunset[a]
Aug. 20, 1998	Kiruna (67.9°N,21.1°E)	0.14	0.08	0.06	0.10	0.06	0.04	high-lat. summer, sunrise[a]
Feb. 10, 1999	Kiruna (67.9°N,21.1°E)	0.14	0.08	0.06	0.19	0.10	0.07	high-lat. winter, sunset[a]
Jun. 25, 1999	Gap (44.0°N,6.1°E)	0.17	-	-	0.23	-	-	mid-lat. summer, sunrise[a]
Feb. 18, 2000	Kiruna (67.9°N,21.1°E)	0.25	0.14	0.10	0.14	0.08	0.06	high-lat. winter, sunset[a]
Aug. 21, 2001	Kiruna (67.9°N,21.1°E)	0.13	0.06	0.06	0.09	0.02	0.05	high-lat. summer, sunset[b]
Aug. 22, 2001	Kiruna (67.9°N,21.1°E)	0.11	0.06	-	0.09	0.05	-	high-lat. summer, sunset[b]
Mar. 23, 2003	Kiruna (67.9°N,21.1°E)	0.08	0.07	0.09	0.17	0.05	0.03	high-lat. winter, sunset[b]
Oct. 09, 2003	Aire (43.8°N,0.3°W)	0.8	-	-	1.4	-	-	mid-lat. fall, ascent[b]
Mar. 24, 2004	Kiruna (67.9°N,21.1°E)	0.09	0.09	0.08	0.17	0.10	0.07	high-lat. winter, sunset[b]
Jun. 17, 2005	Teresina (5.4°S,42.4°W)	0.15	0.18	0.24	0.05	0.02	0.04	low-lat., sunset[b]

[a] Analyzed by H. Bösch, see Bösch et al. (2003).

[b] Analyzed in the course of the presented study.

ing to twice the statistical detection limit is about 0.2 ppt between 15 km and 25 km altitude and larger below and above that altitude range. Upper limits of IO, corresponding to once the statistical detection limit, inferred from balloon ascent measurements are larger than those inferred from solar occultation except for altitudes below 16 km where they are on the order of 0.1 ppt. The relatively low upper limit inferred from balloon ascent measurements can be explained by the fact that measurements at Teresina started right after balloon launch at about 2 km altitude. Since the weighting functions for balloon ascent measurements are not strongly peaked all spectra recorded below a certain altitude level contribute information to the considered level, e. g. all spectra recorded below 15 km contribute to the inferred upper limit at 15 km. Despite the low upper limit of 0.1 ppt at about 15 km, IO cannot be detected in the spectra recorded during balloon ascent although the solar occultation measurements suggest 0.2 ppt IO in that altitude range. The latter finding is a further hint that the IO abundances inferred from solar occultation are actually fake detection. However, it has to be remembered that different air masses are sampled during balloon ascent and solar occultation.

For OIO, the upper limits inferred from solar occultation are consistently lower than those inferred from balloon ascent. Between 10 km and 20 km the OIO upper limit is less than 0.1 ppt attaining its minimum of 0.01 ppt at the tropopause. Above 20 km the OIO upper limit increases to 0.3 ppt at 25 km.

7.4 Implications for stratospheric iodine and ozone

Table 7.2 provides a list of upper limits of IO and OIO volume mixing ratios inferred according to the discussions in the previous sections. The list is supplemented by data which have been analyzed by Bösch et al. (2003) using the same approach as in the presented work. Table 7.2 puts the tightest constraints on

the stratospheric iodine budget to date.
The presented upper limits are inferred from detection limits of the DOAS spectrograph and thus depend on the absorption cross section used for spectral retrieval. As pointed out in section 7.1 the use of recently measured absorption cross sections of IO, which are larger than the one used here, would further diminish the stated IO upper limits. If the spectral retrieval was for example performed with the absorption cross section given by Spietz et al. (2005), IO upper limits would be lower by 20% to 25%.

Implications for total stratospheric iodine

Bösch et al. (2003) used their upper limits of stratospheric IO and OIO to infer upper limits of total gaseous stratospheric iodine, I_y, for high- and mid-latitudes. They implemented the chemical reactions governing stratospheric iodine chemistry (section 1.2.4) in the LABMOS chemistry model and showed that IO and OIO account for more than 90% of I_y in the lower stratosphere during daytime. During night, IO decreases since it is converted to its nighttime reservoirs $IONO_2$ and OIO. Given the upper limits listed in table 7.2 for the years between 1996 and 2000, they concluded on lower stratospheric ($\leq$ 20 km) $[I_y] \leq (0.10 \pm 0.02)$ ppt and $[I_y] \leq (0.07 \pm 0.01)$ ppt when allowing for and omitting OIO photolysis, respectively. It is important to distinguish between scenarios allowing for and omitting OIO photolysis since IO can be recycled from OIO more effectively if photolysis occurs. Hence, the partitioning IO/OIO and thus IO/I_y and OIO/I_y depend on the chosen scenario for OIO photolysis. When allowing for OIO photolysis it was assumed that the quantum yield for the products I + O_2 and IO + O was 15% and 0.7%, respectively, corresponding to the upper limits given by Ingham et al. (2000). The most recent compendiums on rate constants such as JPL-2002 (Sander et al., 2003) and IUPAC (Atkinson et al., 2006) give no recommendation on OIO photolysis.
The LPMA/DOAS observations in the high-latitude stratosphere between 2001 and 2004 largely confirm the findings of Bösch et al. (2003) on upper limits of IO and OIO. Hence, the stated upper limits of I_y inferred from the high- and mid-latitudinal observations between 1996 and 2000 are directly applicable to the updated dataset.

The LABMOS model calculations performed by Bösch et al. (2003) for high- and mid-latitudes are not applicable for low-latitudes. Here, the model of Bösch et al. (2003) is adapted to the geophysical conditions encountered during the Teresina 2005 balloon flight. Besides the standard LABMOS setup, the chemical scheme comprises the iodine species IO, OIO, I, $IONO_2$, HOI and HI which are linked through the photochemical reactions listed in table 2 of Bösch et al. (2003). Species such as INO, INO_2, ICl, IBr and I_2 are neglected since no large built-up is expected in the stratosphere. The photolysis rates of IO, OIO, $IONO_2$, HOI and HI which have been calculated by Bösch et al. (2003) for an albedo of 0.3 are extrapolated to SZAs encountered at low-latitudes. The model is initialized with 0.2 ppt I_y and run stacked for ten days corresponding to the conditions encountered on June 17, 2005, at 5°S, 43°W. Typically, after ten days the modeled abundances of the iodine species are in photochemical equilibrium and essentially independent of the initial partitioning. All other species except for NO_2 and O_3 are initialized with SLIMCAT output for 5°S, 43°W. NO_2 and O_3 are scaled to match the LPMA/DOAS observations in a similar way as described in section 5.3. Model runs are performed omitting and allowing for OIO photolysis as suggested by Bösch et al. (2003). In the latter case OIO photolysis produces I + O_2 and IO + O with a fractional yield of 15% and 0.7%, respectively.

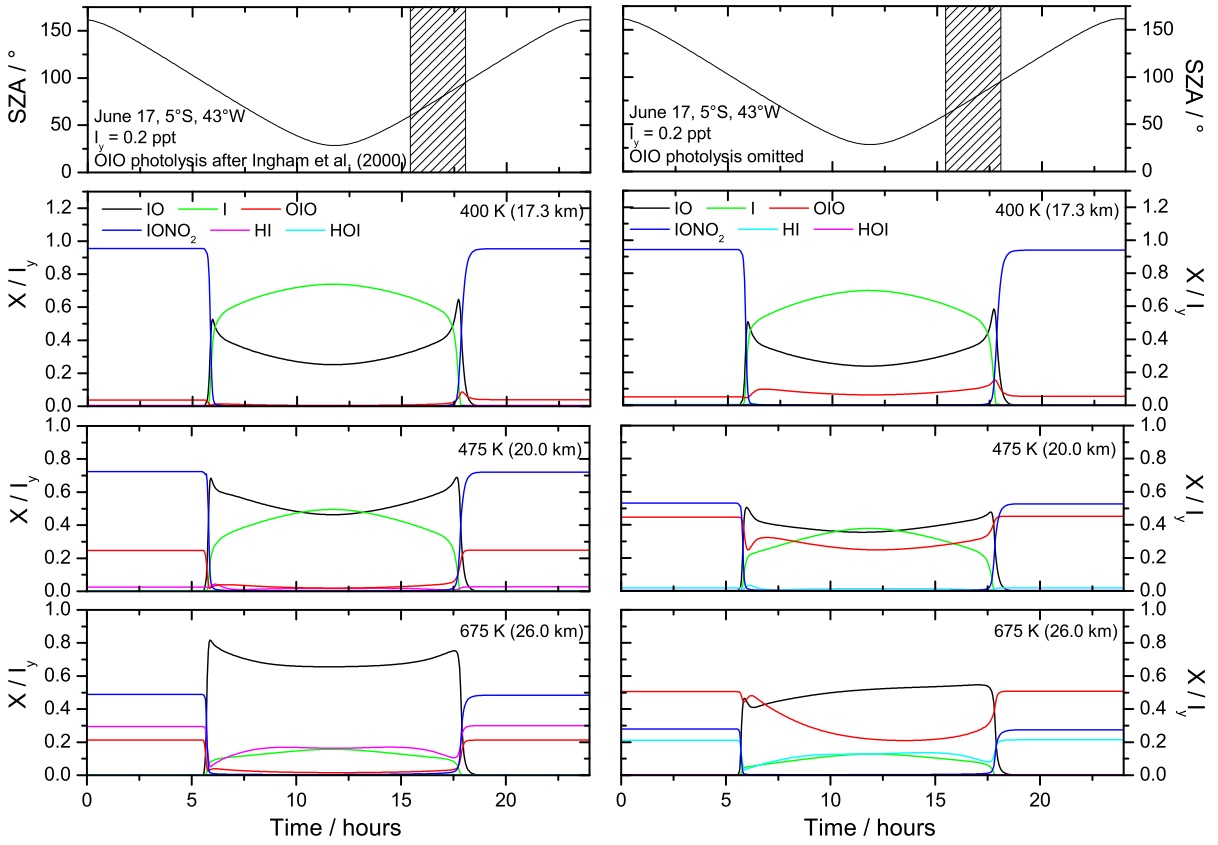

Figure 7.16: Temporal evolution of the most important constituents of stratospheric I_y modeled by LABMOS for June 17 at 5°S, 43°W. Model output is shown on three potential temperature levels as indicated by the legend. The left column of panels corresponds to a model run allowing for OIO photolysis while the right column shows the results when omitting OIO photolysis. The shaded box in the upper row of panels illustrates to the time frame of LPMA/DOAS observations during balloon ascent and sunset.

Figure 7.16 shows the diurnal evolution of the relative partitioning between I_y constituents on the tenth day of the model run for three potential temperature levels. During night the reservoirs $IONO_2$, OIO are the most abundant species while during daytime IO and I dominate iodine partitioning. Close to the tropical tropopause on the 400 K potential temperature level O_3 abundances are very small making conversion of I to IO less effective. Accordingly, I is the most abundant iodine species between 17 km and 20 km altitude for both scenarios of OIO photolysis. IO is an important constituent throughout the stratosphere and becomes the most important species above 20 km. Day-time OIO plays a minor role if the photolysis of OIO is allowed but constitutes up to 30% of I_y in the middle tropical stratosphere if OIO photolysis is omitted. The iodine partitioning during sunset is of particular importance for the LPMA/DOAS observations, since IO and OIO upper limits are inferred from measurements around SZA = 90°. At sunset I is converted to IO which makes the latter the most abundant species at SZA = 90° under all modeled conditions. At slightly larger SZA, IO itself is scavenged by NO_2 or halogen radicals forming the night-time reservoirs $IONO_2$ or OIO.

The LABMOS model runs can be used to calculate modeled IO and OIO SCDs which should have

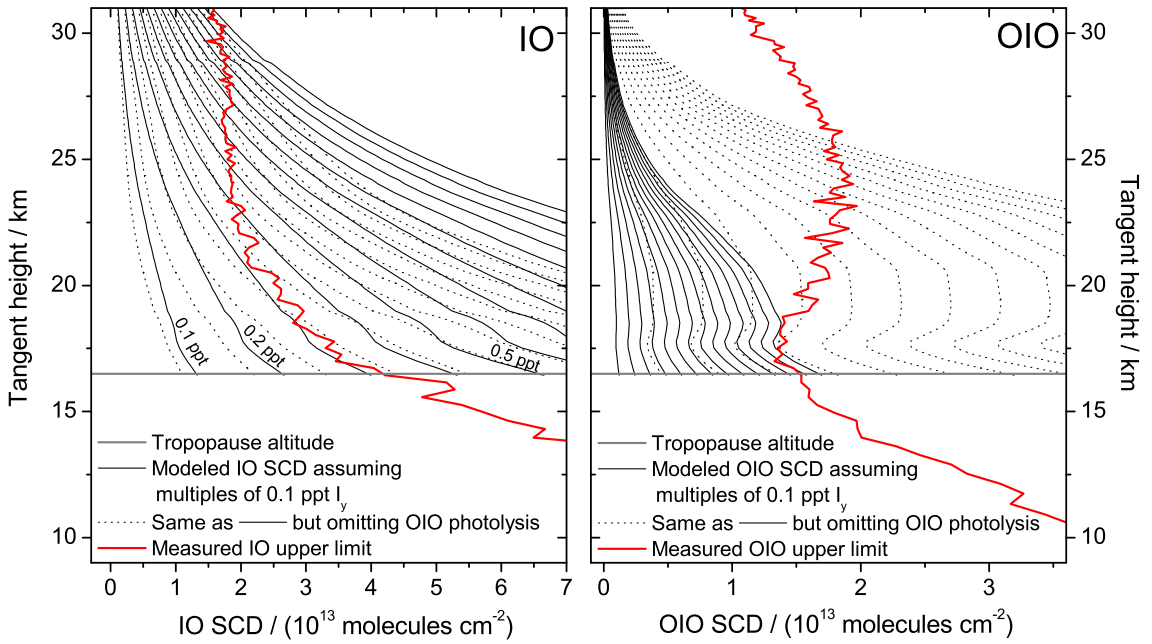

Figure 7.17: Measured upper limits (red lines) of IO (left panel) and OIO (right panel) SCDs as a function of tangent height. Modeled IO and OIO SCDs are shown for scenarios allowing for (black solid lines) and omitting (dotted lines) OIO photolysis. Modeled SCDs are plotted for various stratospheric iodine loadings: 0.1 ppt, 0.2 ppt, 0.3 ppt, ... I_y in steps of 0.1 ppt. Upper limits of I_y can be inferred from the intercepts of the measured IO and OIO upper limits with the modeled IO and OIO SCDs. Model output is cut off below tropopause altitude (gray horizontal line) since LABMOS is not suited for modeling tropospheric chemistry.

been observed by the LPMA/DOAS instruments given the modeled temporal evolution of IO and OIO abundances. Modeled SCDs are obtained by integrating the modeled trace gas concentrations along the LPMA/DOAS lines-of-sight. A similar approach is presented in section 6.4.2 where measured and modeled SCDs of OClO in the winterly polar stratosphere are compared. Figure 7.17 shows modeled SCDs as a function of tangent height. Below the tropopause model results are cut off since the chemical scheme of LABMOS does not include tropospheric processes. The model runs are performed assuming 0.2 ppt I_y throughout the stratosphere. Modeled IO and OIO SCDs corresponding to multiples of 0.1 ppt I_y are calculated by scaling the standard run since IO and OIO should react linearly on variations of I_y given the overall small abundances. As above, model results are shown for two scenarios of OIO photolysis. Upper limits of I_y can be inferred by comparing the measured upper limits of IO and OIO SCDs to the modeled SCDs. At each tangent height the intercept of the measured upper limit with the modeled SCD yields the upper limit of I_y consistent with the observations.

If OIO photolysis is allowed, the measured upper limit of IO SCDs coincides with the modeled SCD for roughly 0.32 ppt I_y between the tropopause and 22 km altitude. At 25 km the measured IO SCDs can be reconciled with the model for 0.50 ppt I_y. The observed upper limits of OIO constrain I_y much less than the upper limits of IO. If OIO photolysis is omitted, I_y upper limits inferred from both, IO and OIO

upper limits, increase from 0.38 ppt at the tropopause to 0.5 ppt at 22 km. Above 22 km, I_y upper limits increase further.

Bösch et al. (2003) discussed errors of the reaction kinetics used for the photochemical modeling of iodine chemistry in great detail. Since the same photochemical scheme is employed here, the error analysis for the tropical upper limit of I_y is performed by sensitivity studies as recommended by Bösch et al. (2003). Model runs are performed where various parameters important for the IO/I_y and OIO/I_y partitioning are varied by their estimated errors. The photolysis rate of IO is varied by $\pm$30% which corresponds to the estimated accuracy of the radiative transfer calculations and the IO absorption cross section. According to (Sander et al., 2003), the rate coefficient for the IO + NO_2 association reaction is uncertain by a factor of 2 at stratospheric temperatures and pressures. The uncertainty of the $IONO_2$ photolysis rate is estimated to 50% from the radiative transfer calculations and the accuracy of the data taken from Mössinger et al. (2002). The reaction rate for I + O_3 is considered uncertain by a factor of 3. The impact of the uncertainty of the interhalogen reactions IO + ClO and IO + BrO is found very small compared to the uncertainty of the I + O_3 reaction which is the "bottleneck" (Bösch et al., 2003) in recycling atomic iodine into IO. For each sensitivity run modeled IO and OIO SCDs are inferred and compared to the model run using standard photochemistry. The differences between each sensitivity run and the standard run yields an estimate of the error of the modeled IO and OIO SCDs and hence, the error of the inferred upper limit of I_y.

Thus, upper limits of total gaseous iodine in the lower tropical stratosphere are given by $[I_y] \leq (0.32 \pm 0.11)$ ppt and $[I_y] \leq (0.38 \pm 0.10)$ ppt if allowing for and omitting OIO photolysis, respectively. The stated upper limits of I_y rely on model calculations and hence depend on rate coefficients and model assumptions while IO and OIO upper limits are directly observed. Further, it has to be pointed out that tropospheric air masses contribute to SCDs for tangent heights below 19 km (figure 7.13) and that upper limits of I_y are inferred from a purely stratospheric chemistry scheme.

The stated upper limits of total gaseous inorganic iodine in the high-, mid-, and low-latitude stratosphere give rise to some thoughts on the fate of organic iodine species emitted at the Earth's surface. Davis et al. (1996) report on 0.1 ppt to 1 ppt of CH_3I in the tropical and subtropical upper troposphere. These findings are in broad agreement with the inferred upper limits of stratospheric I_y and with the inferred upper limits of IO and OIO in the tropical upper troposphere assuming that stratospheric I_y is generated from upward-transported organic source gases (SG), i. e. predominantly CH_3I, or inorganic product gases (PG) of SG decomposition such as IO and OIO. Given the sizeable though highly variable abundances of CH_3I in the marine boundary layer (up to 1830 ppt (Peters et al., 2005)) and its intermediate lifetime ($\tau_{CH_3I} \approx 5$ days), it is surprising that the sum of observed SG and PG concentrations in the upper troposphere and lower stratosphere are as small as the measurements suggest (< 1 ppt). The observations could be misleading in two ways: (1) stratospheric and upper tropospheric iodine is present in other forms than addressed by the measurements, or (2) this and other studies fortuitously missed to probe iodine-rich air masses.

Concerning possibility (1), Bösch et al. (2003) pointed out that the major gas-phase reactions involving iodine bearing species are reasonably well understood under upper tropospheric and lower stratospheric conditions such that the partitioning among the I_y constituents is not a source of major uncertainty. The amount of iodine incorporated in aerosols, however, is not very well known. The formation of higher iodine oxides I_xO_y and iodine clusters, which can be taken up by existing aerosols, is subject of ongoing research (O'Dowd and Hoffmann, 2005). Murphy et al. (1998) and Murphy and Thompson (2000)

indeed detected iodine tied to the upper tropospheric and lower stratospheric aerosol. Clearly, if most of iodine was present in particulate form, the observations presented here could not detect it.
Possibility (2) implies that I_y is very inhomogeneously mixed in the lower and middle stratosphere. Given the 13 LPMA/DOAS balloon flights in high- and mid-latitudes during all seasons (table 7.2) it seems very unlikely that IO and OIO abundances are larger than the inferred upper limits and are not - at least occasionally - detected by our measurements. For tropical latitudes, however, the data set comprises one observation, only, which is carried out at about 5°S in June. At that time of the year the local dry season does not provide ideal conditions for fast convective uplift of tropospheric air masses to the upper troposphere and, possibly, lower stratosphere. Upward convective transport is more effective during the rainy season and, hence, it is well possible that injection of iodine bearing SG and PG into the tropical upper troposphere and lower stratosphere occurs on an event-by-event basis and that our tropical observations missed such events. Schwärzle (2005) observed up to 12 ppt CH_3I and (0.82 ± 0.31) IO in the course of their near-surface measurements during December 2004 and January 2005 at Sao Luis, northern Brazil, which lies about 400 km in the north-west of the launch site of the LPMA/DOAS payload. Surface air masses exhibiting such CH_3I and IO abundances could be transported to the upper troposphere on short timescales by deep convection. Thus, further measurements in tropical upper troposphere and lower stratosphere for different seasons are needed to strengthen the data base.

Implications for stratospheric ozone

Bösch et al. (2003) used model simulations of a 2-D derivative of the 3-D SLIMCAT chemical transport model to show that 0.1 ppt of I_y lead to small changes of the zonal mean ozone distribution under non-ozone hole conditions. $[I_y] = 0.1$ ppt corresponds to the upper limit for high- and mid-latitudes inferred by Bösch et al. (2003) and the presented study. Largest O_3 loss of 1% occurs in fall in the lower mid- and high-latitudinal stratosphere if OIO photolysis yielding I + O_2 and subsequent ozone loss due to I + O_3 is considered. If OIO photolysis is omitted, ozone loss is smaller and amounts to at most 0.6% in high-latitude fall.
Bösch et al. (2003) also discussed IO_x induced ozone loss for low-latitudes. Assuming $[I_y] = 0.1$ ppt, modeled O_3 is decreased by about 0.8% just above the tropical tropopause. However, the upper limit of I_y inferred here for low-latitudes is larger by a factor of 3 to 4 than assumed in the model. Simple scaling results in an upper limit of 2% to 3% IO_x induced ozone loss for the lower tropical stratosphere.

Figure 7.18 shows the modeled fractional contribution of the HO_x, NO_x, ClO_x, BrO_x and IO_x catalytic cycles to odd oxygen loss for spring-time mid-latitudes. The total iodine loading is assumed to be $[I_y] = 0.1$ ppt and two scenarios for the total inorganic bromine burden are discussed. The scenario illustrated in the left panel assumes supply of Br_y from CH_3Br and halons, only, while the scenario shown in the right panel additionally assumes 4 ppt Br_y from very short-lived species as suggested for example by Dorf (2005). Further, two scenarios of IO_x chemistry are considered. "I_y Fast" uses the rate constant for IO + BrO given by Rowley et al. (2001) and assumes that all products of this reaction lead to catalytic loss of ozone implying that photolysis of OIO yields I + O_2. The "I_y Slow" scenario uses JPL-2002 kinetics for IO + BrO and assumes that production of OIO results in no net odd oxygen loss, i. e. OIO photolysis yields IO + O.
The largest contribution to odd oxygen loss from IO_x is observed below 20 km altitude for the "I_y Fast"

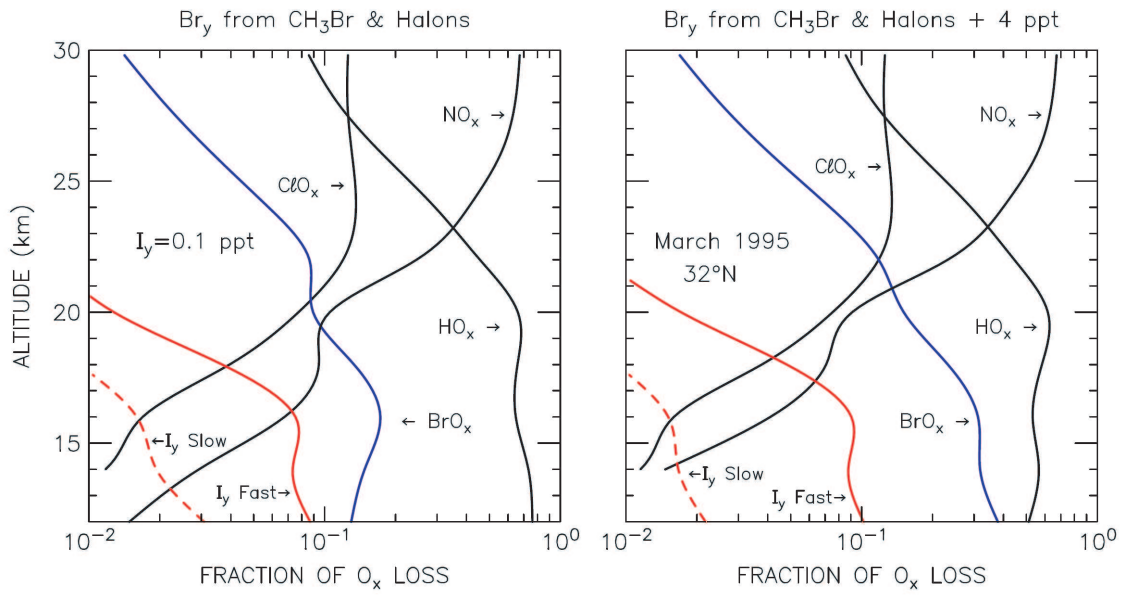

Figure 7.18: Modeled fractional contribution to odd oxygen loss by catalytic cycles involving nitrogen (NO_x), hydrogen (HO_x), chlorine (ClO_x), bromine (BrO_x), and iodine (IO_x) radicals for a mid-latitudinal station at 32°N. Total stratospheric iodine is set to 0.1 ppt. The "I_y Fast" scenario uses the rate constant for IO + BrO given by Rowley et al. (2001) and assumes that all products of this reaction lead to catalytic loss of ozone. In particular, the photolysis of OIO is assumed to yield I + O_2. The "I_y Slow" scenario uses JPL-2002 kinetics for IO + BrO and assumes that production of OIO results in no net odd oxygen loss, i. e. OIO photolysis yields IO + O. For the left hand panel stratospheric Br_y is inferred from the abundances of CH_3Br and halons. For the right hand panel, 4 ppt Br_y from very short-lived bromocarbons is added. Figure by courtesy of R. Salawitch (JPL, Pasadena).

scenario and amounts to at most 10%. As expected, the alternative scenario "I_y Slow" implies less odd oxygen loss and contributes at most 3%. Assuming a contribution of very short-lived bromocarbons to Br_y enhances the importances of the BrO_x involving odd oxygen loss cycles and also slightly increases the relative contribution from IO_x if the IO + BrO reaction rate is assumed to be fast. If IO + BrO occurs according to JPL-2002 kinetics increasing Br_y results in decreased importance of IO_x. The model calculations are strictly valid only for mid-latitudes. However, assuming that the fractional contributions of the various catalysts to odd oxygen loss are similar in the low-latitude stratosphere, the upper limit of fractional IO_x contribution to tropical odd oxygen loss could easily exceed 10% given the upper limit of tropical $[I_y] \leq (0.32 \pm 0.11)$ ppt or $[I_y] \leq (0.38 \pm 0.10)$ ppt for altitudes just above the tropopause.

The implications for ozone inferred from the upper limits of IO, OIO and I_y indicate that the upper limit of IO_x induced ozone loss close to the tropopause at high- and mid-latitudes is barely relevant. The current level of agreement between measured and modeled O_x loss at high- and mid-latitudes is worse than the possible impact of iodine involving chemistry (see for example figure 1.4).
Since for low-latitudes inferred upper limits of IO_x induced O_3 and O_x loss are by a factor of 3 to 4 larger than for mid- and high-latitudes, IO_x could play a role in the tropical lower stratosphere. Hence, further measurements are necessary to minimize upper limits of stratospheric I_y at low-latitudes.

7.5 Conclusions on upper tropospheric and stratospheric iodine

Upper limits of IO and OIO in the high-, mid- and low-latitude stratosphere are reported. The findings for high- and mid-latitudes extend the database presented by Bösch et al. (2003) and confirm that upper limits between 10 km and 20 km altitude range between 0.05 ppt and 0.11 ppt for IO and between 0.01 ppt and 0.11 ppt for OIO. Photochemical modeling by Bösch et al. (2003) constrains total gaseous stratospheric iodine to $[I_y] \leq (0.10 \pm 0.02)$ ppt and $[I_y] \leq (0.07 \pm 0.01)$ ppt allowing for and omitting OIO photolysis, respectively.

The retrieval of IO from spectra recorded at low-latitudes yields IO SCDs twice as large as the detection limit during solar occultation. The retrieved SCDs, however, cannot be considered trustworthy since the spectral retrieval is complicated by systematic residual structures which originate from several instrumental deficiencies and possibly an aerosol layer in the lower tropical stratosphere. Hence, upper limits of IO are estimated in a way consistent with the LPMA/DOAS observations even if IO is truly detected. In the upper tropical troposphere and lower stratosphere the inferred upper limits range between 0.15 ppt and 0.24 ppt for IO and between 0.01 ppt and 0.1 ppt for OIO. Adapting the photochemical model of Bösch et al. (2003) to low-latitudes, constrains I_y in the lower tropical stratosphere to $[I_y] \leq (0.32 \pm 0.11)$ ppt and $[I_y] \leq (0.38 \pm 0.10)$ ppt allowing for and omitting OIO photolysis, respectively. Given the upper limits for I_y, IO and OIO in the tropical lower stratosphere and upper troposphere and the rather large emissions of iodine source gases at the surface, one can wonder if significant amounts of iodine enter the stratosphere in particulate form or if troposphere-to-stratosphere transport of source and product gases occurs occasionally through convective events which are missed by our measurements.

Upper limits of I_y for the high- and mid-latitudinal stratosphere imply that IO_x induced ozone loss does not play a significant role in the respective latitudes. For low-latitudes the stated upper limits of I_y, however, allow for IO_x being a minor contributor to lower stratospheric photochemistry. Hence, further measurements in the tropical upper troposphere and lower stratosphere are necessary either to reduce I_y upper limits or to unambiguously quantify I_y abundances. Future measurements based on the approach presented here should be carried out under different geophysical conditions and focus on minimizing systematic residual structures impacting the IO spectral retrieval.

Conclusion

The present synthesis of balloon borne spectroscopic observations of stratospheric trace gases and model studies aims at providing new insights into stratospheric nitrogen, chlorine and iodine driven ozone-related photochemistry.

Solar absorption spectra in the UV/visible and IR spectral ranges recorded by the LPMA and the DOAS instruments during several stratospheric balloon flights between 1996 and 2005 are analyzed for trace gas abundances. Four of the more recent balloon flights were conducted within the scope of this study including a tropical balloon flight in northern Brazil where the newly implemented DOAS electronics was successfully deployed for the first time. Since instrumentation and retrieval algorithms for DOAS and LPMA are inherently different while the observation geometry is essentially the same, comparison of simultaneously retrieved parameters directly yields an estimate of systematic errors due to instrumental, retrieval-related or spectroscopic effects. The LPMA/DOAS agreement found between inferred abundances of O_3 and NO_2 amounts to $\pm$10% and $\pm$20%, respectively. In comparison to previous studies this finding represents a major improvement which is mainly due to implementation of the multi-fit algorithm in the LPMA retrieval by Dufour (2005) and due to a new temperature correction scheme for the DOAS NO_2 retrieval. An in-depth analysis of the profile retrieval from both datasets reveals that the DOAS setup exhibits better altitude resolution and larger sensitivity to the lower stratosphere than LPMA.

When comparing the LPMA/DOAS measurements with observations by other sensors such as the satellite borne SCIAMACHY instrument, the probed air masses do not coincide in time and space. In this work, an air mass trajectory model is used to model air mass history and to identify measurements most suitable for comparison. For photochemical short-lived species such as NO_2 the photochemical evolution is modeled along these air mass trajectories using a stratospheric chemistry model. Scaling factors are calculated which adjust the LPMA/DOAS observations to the photochemical conditions of the satellite measurements. Employing the combined meteorological and photochemical modeling approach, O_3 and NO_2 vertical profiles in high- and mid-latitudes inferred from SCIAMACHY skylight limb spectra and LPMA/DOAS measurements agree within 20% for both gases in the target altitude range between 20 km and 30 km. Below 20 km agreement is worse mainly due to the low sensitivity of the satellite retrieval and large uncertainties of the meteorological and photochemical models. For the tropical observations SCIAMACHY NO_2 underestimates the balloon borne measurements in the entire altitude range. The validation study shows that the SCIAMACHY instrument allows for a reasonable retrieval of O_3 and NO_2 vertical profiles in the middle stratosphere in high- and mid-latitudes. In the tropics discrepancies between the balloon borne and satellite borne datasets remain. In the lower

stratosphere, the quality of the satellite data is questionable.

The nitrogen budget in the Arctic stratosphere is addressed by simultaneous observations of NO_2, NO, HNO_3 and $ClONO_2$ in summer 2001 and winter 1998/1999. For both seasons HNO_3 is the most abundant nitrogen compound below about 30 km altitude. NO_x is the dominant NO_y constituent above 30 km and makes up more than 10% of NO_y in the lower summer stratosphere. For the winter scenario, strong denoxification is found in the lower stratosphere but no signs of denitrification are inferred from the NO_y-N_2O correlation in accordance with the temperature record. The general findings are corroborated by measurements of NO_2 and HNO_3 in mid-latitudinal fall 1996 and Arctic winter 1996/1997.
Comparison of the observations with model simulations by the SLIMCAT chemical transport model shows that the model is able to reproduce the NO_y budget and partitioning qualitatively well. Even the denoxified layer observed in the Arctic winter 1998/1999 is modeled by SLIMCAT. However, the ratio NO_2/HNO_3 is overestimated by the model for all considered cases independent of season and latitude. Sensitivity studies based on photochemical steady state estimates show that the employed climatological aerosol surface area densities, which are low compared to recent measurements, could be responsible for the observed model-measurement discrepancies in the lower stratosphere. In the middle stratosphere, loss of HNO_3 through photolysis and production of HNO_3 through reaction of NO_2 with OH are the factors controlling NO_2/HNO_3. Errors in the kinetics of the respective reactions or in the calculation of the HNO_3 photolysis rate could combine to produce the observed high-bias of modeled NO_2/HNO_3.

Based on measurements of $ClONO_2$ and HCl and inferred Cl_y^*, case studies of the Cl_y budget and partitioning in the Arctic summer 2001 and winter 1998/1999 show that most of Cl_y resides in HCl and $ClONO_2$ for both seasons. In February 1999, a layer of high ClO_x and low HCl is observed in the lower stratosphere. The layer coincides with the altitude range of denoxification and indicates heterogeneous chlorine activation.
The stratospheric chemistry model LABMOS is constrained by simultaneous observations of all relevant nitrogen (NO_2, NO, HNO_3), chlorine ($ClONO_2$, HCl, Cl_y^*) and bromine (BrO) species and is used to compare modeled and measured OClO at twilight and to infer instantaneous ozone loss rates. Using the standard JPL-2002 recommendations results in very good model-measurement agreement for OClO and a 24-hour ozone loss of about 20 ppb around 20 km altitude. Recent recommendations by Stimpfle et al. (2004), Plenge et al. (2005), Canty et al. (2005) and von Hobe et al. (2005) on the reaction kinetics of the ClO-ClO and ClO-BrO ozone loss cycles produce modeled OClO within the errors of the measurements. A model run with the combined updates also yields very good agreement for OClO but indicates significantly enhanced ozone loss which is as large as 25 ppb over 24 hours. The formation of unstable isomers of $ClONO_2$ and $BrONO_2$ as recommended by Rivière et al. (2004) cannot be reconciled with the LPMA/DOAS observations.

Measurements of IO and OIO in the high- and mid-latitudinal stratosphere corroborate findings of Bösch et al. (2003) that upper limits range between 0.05 ppt and 0.11 ppt for IO an 0.01 ppt and 0.11 ppt for OIO in the lower stratosphere. For the first time ever, upper limits of the iodine budget in the tropical lower stratosphere and upper troposphere are inferred from observations which indicate $[IO] \leq 0.15$ ppt to 0.24 ppt and $[OIO] \leq 0.01$ ppt to 0.1 ppt. The corresponding upper limits of total gaseous iodine in the lower tropical stratosphere inferred from photochemical modeling suggest

$[I_y] \leq (0.32 \pm 0.11)$ ppt and $[I_y] \leq (0.38 \pm 0.10)$ ppt depending on whether OIO photolysis is considered or omitted. The low upper limits of I_y, IO and OIO in the lower stratosphere and tropical upper troposphere are contrasted by rather large emissions of iodine source gases at the surface. One can wonder if significant amounts of iodine enter the stratosphere in particulate form or if tropical troposphere-to-stratosphere transport of source gases and product gases occurs occasionally through convective events which are missed by our measurements. While at high- and mid-latitudes the estimated upper limits constrain stratospheric iodine chemistry to a minor agent for ozone loss, upper limits inferred for tropical latitudes are not yet low enough to discard a significant contribution of iodine compounds to upper tropospheric and lower stratospheric photochemistry.

Outlook

Given the current level of understanding, future investigations of stratospheric photochemistry based on balloon borne observations by the LPMA/DOAS payload must focus on dedicated scenarios under unambiguous geophysical conditions where a comprehensive set of trace gases is measured simultaneously. When discussing the budget and partitioning of trace gas families, it is of major importance to perform observations such that conclusions are not weakened by probing air masses of different dynamic origin. Observations of ozone loss due to the ClO-ClO and ClO-BrO cycles in the Arctic polar vortex for example require measurements well inside a vortex where substantial chlorine activation occurred. Instrumental configurations (e. g. filters, beamsplitters) must be chosen in a way that the retrieval of all relevant species such as HNO_3 and $ClONO_2$ is possible. For sure, the ability to perform lunar observations at night would extend the scope of the LPMA/DOAS experiment and improve its excellence in investigating stratospheric photochemistry, although major instrumental upgrades would be required.
When it comes to detecting minor abundant species such as IO and OIO by the DOAS spectrographs, future work should focus on improving the instrumental performance for example by replacing degraded optical components and measuring a new set of absorption cross sections of O_3, NO_2, BrO and if feasible IO and OIO in the lab-owned absorption cell. Given an improved instrument performance, future observations will be able to further lower the upper limits for inorganic iodine bearing species or to unambiguously detect IO and/or OIO in the tropical upper troposphere and lower stratosphere.
So far, the retrieval of aerosol abundances from DOAS spectra in the UV/visible spectral range received only minor attention because of instrumental shortcomings which, however, were removed in the course of recent studies and as a result of the presented work. Future studies could investigate if and how the center-to-limb darkening effect, which was presented as an effect disturbing trace gas retrievals, can contribute to infer information on aerosol layers in particular in the tropical lower stratosphere.
The LPMA/DOAS instruments are restricted to observations of direct sunlight and, hence, can only provide trace gas profiles for balloon ascent, sunset and sunrise observations. This principle constrained can be overcome by instrumentation which observes scattered skylight such as the versatile instrument developed by Weidner et al. (2005). Time dependent observations of trace gas profiles can be used to validate satellite borne instruments through direct coincidences without requiring meteorological and photochemical modeling. Time dependent photochemical processes such as the diurnal variation of NO_2 or ozone loss by the BrO and ClO involving catalytic cycles during the day could then be directly investigated.

Appendix

List of Fraunhofer offsets for O_3 and NO_2 SCDs inferred from DOAS observations

Table 8.1: O_3 SCDs contained in the pseudo TOA spectra (Fraunhofer offset). The names of the spectra follow the internal numbering of the DOAS balloon group.

Mesasurement site and date	Local pseudo TOA spectrum	Langley TOA spectrum	O_3 molec. cm^{-2}	O_3 error molec. cm^{-2}
Leon, Nov. 23, 1996	V0126901	V0133273	1.91 10^{19}	1.86 10^{17}
Kiruna, Feb. 14, 1997	V0129955	V0133273	3.45 10^{19}	1.95 10^{17}
Gap, June 19, 1997	V0133273	V0133273	1.46 10^{18}	1.67 10^{17}
Leon, March 19, 1998	V0150898	V0133273	5.82 10^{18}	1.68 10^{17}
Kiruna, Aug. 19, 1998	V0182016	V0133273	5.22 10^{18}	1.67 10^{17}
Kiruna, Aug. 20, 1998	V0183436	V0133273	2.13 10^{19}	1.72 10^{17}
Kiruna, Feb. 10, 1999	V0196501	V0133273	1.21 10^{19}	1.68 10^{17}
Gap, June 25, 1999	V0203349	V0133273	5.16 10^{18}	1.68 10^{17}
Kiruna, Feb. 18, 2000	V0212534	V0133273	2.99 10^{19}	2.75 10^{17}
Kiruna, Aug. 21, 2001	V0246866	V0133273	8.41 10^{18}	1.74 10^{17}
Kiruna, March 23, 2003	V0285253	V0328298	2.60 10^{19}	3.54 10^{17}
Aire s. l'A., Oct. 9, 2003	V0328298	V0328298	6.65 10^{18}	3.40 10^{17}
Kiruna, March 24, 2004	V0346180	V0328298	9.84 10^{18}	3.47 10^{17}
Teresina, June 17, 2005	V0428324	V0328298	9.33 10^{18}	4.87 10^{17}

Table 8.2: NO_2 SCDs contained in the pseudo-TOA spectra (Fraunhofer offset). The names of the spectra follow the internal numbering of the DOAS balloon group.

Mesasurement site and date	NO_2(T=217 K) molec. cm^{-2}	NO_2(T=217 K) error molec. cm^{-2}	NO_2(T=230 K) molec. cm^{-2}	NO_2(T=230 K) error molec. cm^{-2}
Leon, Nov. 23, 1996	$1.33\ 10^{16}$	$5.32\ 10^{13}$	$1.48\ 10^{16}$	$5.85\ 10^{13}$
Kiruna, Feb. 14, 1997	$1.59\ 10^{16}$	$3.66\ 10^{13}$	$1.77\ 10^{16}$	$4.05\ 10^{13}$
Gap, June 19, 1997	$7.04\ 10^{14}$	$4.06\ 10^{13}$	$7.86\ 10^{14}$	$4.50\ 10^{13}$
Leon, March 19, 1998	$2.09\ 10^{15}$	$4.09\ 10^{13}$	$2.33\ 10^{15}$	$4.52\ 10^{13}$
Kiruna, Aug. 19, 1998	$2.21\ 10^{15}$	$4.06\ 10^{13}$	$2.43\ 10^{15}$	$4.52\ 10^{13}$
Kiruna, Aug. 20, 1998	$1.42\ 10^{16}$	$1.22\ 10^{14}$	$1.57\ 10^{16}$	$1.76\ 10^{14}$
Kiruna, Feb. 10, 1999	$3.77\ 10^{15}$	$4.44\ 10^{13}$	$4.22\ 10^{15}$	$4.53\ 10^{13}$
Gap, June 25, 1999	$8.97\ 10^{14}$	$4.06\ 10^{13}$	$1.05\ 10^{15}$	$4.50\ 10^{13}$
Kiruna, Feb. 18, 2000	$1.53\ 10^{16}$	$4.52\ 10^{13}$	$1.70\ 10^{16}$	$7.50\ 10^{13}$
Kiruna, Aug. 21, 2001	$3.19\ 10^{15}$	$4.06\ 10^{13}$	$3.54\ 10^{15}$	$4.66\ 10^{13}$
Kiruna, March 23, 2003	$1.60\ 10^{16}$	$3.31\ 10^{14}$	$1.77\ 10^{16}$	$3.63\ 10^{14}$
Aire s. l'A., Oct. 9, 2003	$4.80\ 10^{15}$	$3.30\ 10^{14}$	$5.32\ 10^{15}$	$3.60\ 10^{14}$
Kiruna, March 24, 2004	$4.89\ 10^{15}$	$3.30\ 10^{14}$	$5.42\ 10^{15}$	$3.60\ 10^{14}$
Teresina, June 17, 2005	$6.98\ 10^{15}$	$4.15\ 10^{14}$	$7.79\ 10^{15}$	$4.62\ 10^{14}$

Mesasurement site and date	NO_2(T=238 K) molec. cm^{-2}	NO_2(T=238 K) error molec. cm^{-2}	NO_2(T=294 K) molec. cm^{-2}	NO_2(T=294 K) error molec. cm^{-2}
Leon, Nov. 23, 1996	$1.58\ 10^{16}$	$6.23\ 10^{13}$	$1.72\ 10^{16}$	$6.85\ 10^{13}$
Kiruna, Feb. 14, 1997	$1.89\ 10^{16}$	$4.66\ 10^{13}$	$2.04\ 10^{16}$	$4.99\ 10^{13}$
Gap, June 19, 1997	$8.42\ 10^{14}$	$4.83\ 10^{13}$	$9.14\ 10^{14}$	$5.24\ 10^{13}$
Leon, March 19, 1998	$2.50\ 10^{15}$	$4.85\ 10^{13}$	$2.69\ 10^{15}$	$5.26\ 10^{13}$
Kiruna, Aug. 19, 1998	$2.61\ 10^{15}$	$4.85\ 10^{13}$	$2.80\ 10^{15}$	$5.26\ 10^{13}$
Kiruna, Aug. 20, 1998	$1.69\ 10^{16}$	$2.02\ 10^{14}$	$1.83\ 10^{16}$	$2.08\ 10^{14}$
Kiruna, Feb. 10, 1999	$4.53\ 10^{15}$	$4.88\ 10^{13}$	$4.93\ 10^{15}$	$5.30\ 10^{13}$
Gap, June 25, 1999	$1.16\ 10^{15}$	$4.83\ 10^{13}$	$1.28\ 10^{15}$	$5.24\ 10^{13}$
Kiruna, Feb. 18, 2000	$1.82\ 10^{16}$	$6.27\ 10^{13}$	$1.97\ 10^{16}$	$6.59\ 10^{13}$
Kiruna, Aug. 21, 2001	$3.77\ 10^{15}$	$5.03\ 10^{13}$	$4.04\ 10^{15}$	$5.45\ 10^{13}$
Kiruna, March 23, 2003	$1.89\ 10^{16}$	$3.85\ 10^{14}$	$2.05\ 10^{16}$	$4.28\ 10^{14}$
Aire s. l'A., Oct. 9, 2003	$5.67\ 10^{15}$	$3.80\ 10^{14}$	$6.16\ 10^{15}$	$4.20\ 10^{14}$
Kiruna, March 24, 2004	$5.78\ 10^{15}$	$3.80\ 10^{14}$	$6.28\ 10^{15}$	$4.20\ 10^{14}$
Teresina, June 17, 2005	$8.30\ 10^{15}$	$4.92\ 10^{14}$	$9.02\ 10^{15}$	$5.35\ 10^{14}$

A schematic representation of stratospheric photochemistry

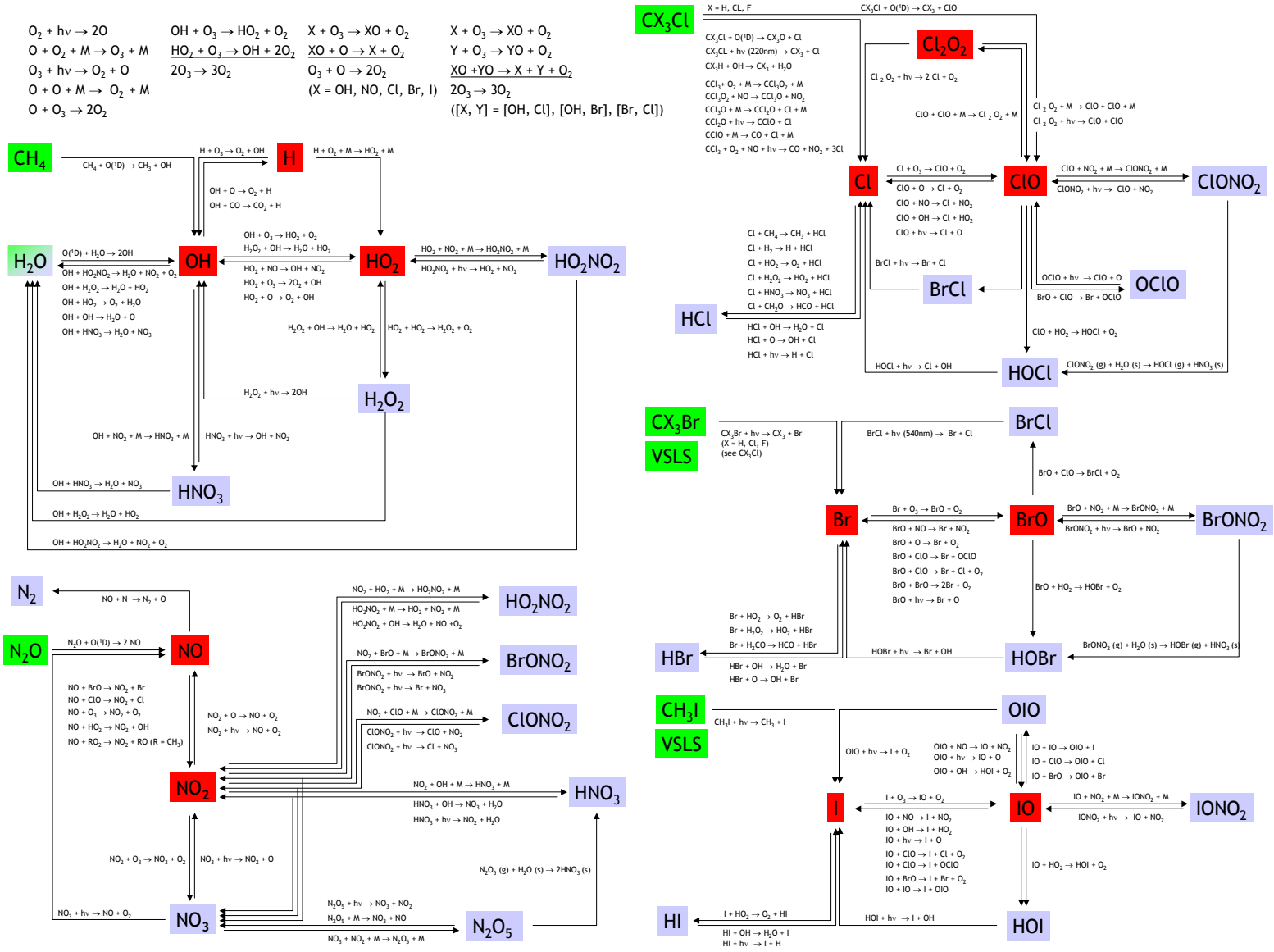

Figure 8.1: Schematic representation of stratospheric photochemistry involving the most important oxygen, hydrogen, nitrogen, chlorine, bromine and iodine bearing compounds. The scheme is compiled from Brasseur and Solomon (1986), Zellner (1999) and Sander et al. (2003) and is not meant to be complete. Green shaded species represent source gases, while blue shaded species tentatively correspond to reservoirs although lifetimes among the blue shaded species vary considerably. Red shading indicates short-lived radicals which are commonly attributed to the HO_x, NO_x, ClO_x, BrO_x and IO_x composites. Reaction rates can be looked up in Sander et al. (2003).

Bibliography

Allan, B., Plane, J. C., and McFiggans, G.: Observations of OIO in the remote marine boundary layer, Geophys. Res. Lett., 28, 1945–1948, 2001.

Anderson, S. and Mauersberger, K.: Laser measurements of ozone absorption cross sections in the Chappuis band, Geophys. Res. Lett., 19, 933–936, 1992.

Arnold, F., Buehrke, T., and Qiu, S.: Evidence for stratospheric ozone-depleting heterogeneous chemistry on volcanic aerosols from El Chichon, Nature, 348, 49, 1990.

Arnold, F., Burger, V., Gollinger, K., Roncossek, M., Schneider, J., and Spreng, S.: Observations of nitric acid perturbations in the winter Arctic stratosphere: Evidence for PSC sedimentation, J. Atmos. Chem., 30, 49–59, 1998.

Atkinson, R., Baulch, D. L., Cox, R. A., Crowley, J., F., H. R., Hynes, R., Jenkin, M., Kerr, J. A., Rossi, M. J., and Troe, J.: Summary of evaluated kinetic and photochemical data for atmospheric chemistry: Web Version February 2006, http://www.iupac-kinetic.ch.cam.ac.uk, 2006.

Bacmeister, J. T., Kuell, V., Offermann, D., Riese, M., and Elkins, J. W.: Intercomparison of satellite and aircraft observations of ozone, CFC-11, and NO(y) using trajectory mapping, J. Geophys. Res., 104(D13), 16 379–16 390, 1999.

Bass, A. M. and Paur, R. J.: The Ultraviolet Cross Section of Ozone, I. The Measurements, in Proc. of the Quadrennial Ozone Symposium, edited by Z. C. and A. Ghazy, 606–616, Chalkidiki, Greece, 1985.

Bates, D. R. and Nicolet, M.: Atmospheric hydrogen, Publ. Astron. Soc. Pac., 62, 106–110, 1950.

Bauer, N.: Charakterisierung des DOAS-Ballon-Spektrographen zur Bestimmung stratosphärischer Spurenstoffe, Diploma thesis, Institut für Umweltphysik, Universität Heidelberg, 1997.

Beirle, S.: Estimating source strengths and lifetime of Nitrogen Oxides from satellite data, Ph.D. thesis, Institut für Umweltphysik, University of Heidelberg, 2005.

Berthet, G., Renard, J.-B., Brogniez, C., Robert, C., Chartier, M., and Pirre, M.: Analysis of OBrO, IO, and OIO absorption signature, in UV-Visible spectra measured at night and sunrise by stratospheric balloon-borne instruments, J. Geophys. Res., 108, 4161, 2003.

Berthet, G., Ricaud, P., Lefèvre, F., Le Flochmoën, E., Urban, J., Barret, B., Lautié, N., Dupuy, E., De la Noë, J., and Murtagh, D.: Nighttime chlorine monoxide observations by the Odin satellite and implications for the ClO/Cl_2O_2 equilibrium, Geophys. Res. Lett., 32, 10.1029/2005GL022649, 2005.

Bevington, P.: Data Reduction and Error Analysis for the Physical Sciences, McGraw-Hill, New York, 1969.

Bloss, W. J., Rowley, D. M., Cox, R. A., and Jones, R. L.: Kinetics and Products of the IO Self-Reaction, J. Phys. Chem. A, 105, 7840–7854, 2001.

Bobrowski, N., Höninger, G., Galle, B., and Platt, U.: Detection of bromine monoxide in a volcanic plume, Nature, 423, 273–276, 2003.

Bonne, G. P., Stimpfle, R. M., Cohen, R. C., Voss, P. B., Perkins, K. K., Anderson, J. G., Salawitch, R. J., Elkins, J. W., Dutton, G. S., Jucks, K. W., and Toon, G. C.: An examination of the inorganic chlorine budget in the lower stratosphere, J. Geophys. Res., 105, 1957–1971, 2000.

Bösch, H.: Studies of Stratospheric Nitrogen and Iodine Chemistry by Balloon Borne DOAS Measurements and Model calculations, Ph.D. thesis, Institut für Umweltphysik, Universität Heidelberg, 2002.

Bösch, H., Camy-Peyret, C., Chipperfield, M., Fitzenberger, R., Harder, H., Schiller, C., Schneider, M., Trautmann, T., and Pfeilsticker, K.: Inter-comparison of measured and modeled stratospheric UV/vis actinic fluxes at large solar zenith angles, Geophys. Res. Lett., 28, 1179–1182, 2001.

Bösch, H., Camy-Peyret, C., Chipperfield, M. P., Fitzenberger, R., Harder, H., Platt, U., and Pfeilsticker, K.: Upper limits of stratospheric IO and OIO inferred from center-to-limb-darkening-corrected balloon-borne solar occultation visible spectra: Implications for total gaseous iodine and stratospheric ozone, J. Geophys. Res., 108, 4455, 2003.

Bovensmann, H.: SCIAMACHY: Mission Objectives and Measurement Modes, J. Atmos. Sci., 56, 127–150, 1999.

Bracher, A., Sinnhuber, M., Rozanov, A., and Burrows, J. P.: Using a photochemical model for the validation of NO_2 satellite measurements at different solar zenith angles, Atmos. Chem. Phys., 5, 393–408, 2005.

Bransden, B. H. and Joachain, C. J.: Physics of atoms and molecules, Prentice Hall, 2003.

Brasseur, G. and Solomon, S.: Aeronomy of the middle atmosphere, D. Reidel Publ., Dordrecht, Boston, Lancaster, Tokyo, 1986.

Brault, J. and Neckel, H.: Solar spectra. Provided by Hamburger Sternwarte distributed through http://www.hs.uni-hamburg.de/DE/Oef/Inf/Einbl/Sospec/sonnspec.html., 1987.

Brinksma, E. J., Bracher, A., Lolkema, D. E., Segers, A. J., Boyd, J. S., Bramstedt, K., Claude, H., Godin-Beekmann, S., Hansen, G., Kopp, G., Leblanc, T., McDermid, I. S., Meijer, Y. J., Nakane, H., Parrish, A., von Savigny, C., Strebel, K., Swart, D. P. J., Taha, G., and Piters, A. J. M.: Geophysical validation of SCIAMACHY Limb Ozone Profiles, Atmos. Chem. Phys., 6, 197–209, 2006.

Brion, J., Chakir, A., Charbonnier, J., Daumont, D., Parisse, C., and Malicet, J.: Absorption spectra measurements for the ozone molecule in the 350–830 nm region, J. Atmos. Chem., 30, 291–299, 1998.

Brown, S. S., Talukdar, R. K., and Ravishankara, A. R.: Rate constants for the reaction OH + NO_2 + M $\longrightarrow$ HNO_3 + M under atmospheric conditions, Chem. Phys. Lett., 229, 227–284, 1999a.

Brown, S. S., Talukdar, R. K., and Ravishankara, A. R.: Reconsideration of the rate constant for the reaction of hydroxyl radicals with nitric acid, J. Phys. Chem. A, 103, 3031–3037, 1999b.

Burkholder, J. and Talukdar, R.: Temperature dependence of the ozone absorption cross section over the wavelength range 410 to 760 nm, Geophys. Res. Lett., 21, 581–584, 1994.

Burkholder, J. B., Orlando, J. J., and Howard, C. J.: Ultraviolet absorption cross section of Cl_2O_2 between 210 nm and 410 nm, J. Phys. Chem., 94, 687–695, 1990.

Burrows, J., Hölzle, E., Goede, A., Visser, H., and Fricke, W.: SCIAMACHY - Scanning Imaging Absorption Spectrometer for Atmospheric Chartography, Acta Astronautica, 35, 445, 1995.

Burrows, J. P., Dehn, A., Deters, B., Himmelmann, S., Richter, A., Voigt, S., and Orphal, J.: Atmospheric remote-sensing reference data from GOME: 1. Temperature-dependent absorption cross sections of NO_2 in the 231-794 nm range, J. Quant. Spec. and Rad. Transf., 60, 1025–1031, 1998.

Burrows, J. P., Dehn, A., Deters, B., Himmelmann, S., Richter, A., Voigt, S., and Orphal, J.: Atmospheric remote-sensing reference data from GOME: 2. temperature-dependent absorption cross sections of O_3 in the 231-794 nm range, J. Quant. Spec. and Rad. Transf., 61, 509–517, 1999.

Bussemer, M.: Der Ring-Effekt: Ursachen und Einfluß auf die spektroskopische Messung stratosphärischer Spurenstoffe, Diploma thesis, Institut für Umweltphysik, Universität Heidelberg, 1993.

Butz, A., Bösch, H., Camy-Peyret, C., Chipperfield, M., Dorf, M., Dufour, G., Grunow, K., Jeseck, P., Kühl, S., Payan, S., Pepin, I., Pukite, J., Rozanov, A., von Savigny, C., Sioris, C., Wagner, T., Weidner, F., and Pfeilsticker, K.: Inter-comparison of stratospheric O_3 and NO_2 abundances retrieved from balloon borne direct sun observations and Envisat/SCIAMACHY limb measurements, Atmos. Chem. Phys., 6, 1293–1314, 2006.

Camy-Peyret, C. and Vigasin, A., A.: Weakly Interacting Molecular Pairs: Unconventional Absorbers of Radiation in the Atmosphere, Proceedings of the NATO Advanced Research Workshop held in Abbaye de Fontevraud, France, from 25 to 28 March 2002, Kluwer Academic Publishers, 2003.

Camy-Peyret, C., Jeseck, P., Hawat, T., Durry, G., Payan, S., Berube, G., Rochette, L., and Huguenin, D.: The LPMA Balloon-Borne FTIR Spectrometer: Remote Sensing of Atmospheric Constituents, Proceedings of the 12th ESA Symposium on Rocket and Balloon Programmes and Related Research, Lillehammer, Norway, 323–328, 1995.

Canty, T., Rivière, E., Salawitch, R., Berthet, G., Renard, J.-B., Pfeilsticker, K., Dorf, M., Butz, A., Bösch, H., Stimpfle, R., Wilmouth, D., Richard, E., Fahey, D., Popp, P., Schoeberl, M., Lait, L., and Bui, T.: Nighttime OClO in the winter Arctic vortex, J. Geophys. Res., 110, D01 301, 2005.

Chance, K. and Spurr, R.: Ring effect studies; Rayleigh scattering, including molecular parameters for rotational Raman scattering and the Fraunhofer spectrum, Appl. Opt., 36, 5224–5230, 1997.

Chandrasekhar, S.: Radiative Transfer, Dover Publications, New York, 1960.

Chapman, S.: On ozone and atomic oxygen in the upper atmosphere, Philos. Mag., 10, 369–383, 1930.

Chipperfield, M.: Un modèle à trois dimensions de la chimie de la stratosphère, Note de Centre GMGEC 13, Meteo France, 1992.

Chipperfield, M.: Multiannual simulations with a three-dimensional chemical transport model, J. Geophys. Res., 104, 1781–1805, 1999.

Connor, B. J., Siskind, D. E., Tsou, J. J.and Parrish, A., and Remsberg, E. E.: Ground-based microwave observations of ozone in the upper stratosphere and mesosphere, J. Geophys. Res., 99 (D8), 16 757–16 770, 1994.

Cox, R., Bloss, W., and Jones, R.: OIO and the atmospheric cycle of iodine, Geophys. Res. Lett., 26, 1857–1860, 1999.

Cox, R. A. and Hayman, G. D.: The stability and photochemistry of dimers of the ClO radical and implications for Antarctic ozone depletion, Nature, 332, 796–800, 1988.

Coy, L., Nash, E. R., and Newman, P. A.: Meteorology of the polar vortex: Spring 1997, Geophys. Res. Lett., 24, 2693–2696, 1997.

Crutzen, P. and Arnold, F.: Nitric acid cloud formation in the cold Antarctic stratosphere: a major cause for the springtime ozone hole, Nature, 324, 651–655, 1986.

Crutzen, P. J.: The influence of nitrogen oxide on the atmospheric ozone content, Q. J. R. Meteorol. Soc., 96, 320–327, 1970.

Damoah, R., Spichtinger, N., Servranckx, R., Fromm, M., Eloranta, E. W., Razenkov, I. A., James, P., Shulski, M., Forster, C., and Stohl, A.: A case study of pyro-convection using transport model and remote sensing data, Atmos. Chem. Phys., 6, 173–185, 2006.

Danilin, M. Y., Koike, M., Yue, G. K., Jones, N. B., and Johnston, P. V.: Nitrogen species in the post-Pinatubo stratosphere: Model analysis utilizing UARS measurements, J. Geophys. Res., 104, 8247–8262, 1999.

Danilin, M. Y., Ko, M. K. W., Bevilacqua, R. M., Lyjak, L. V., Froidevaux, L., Santee, M. L., Zawodny, J. M., Hoppel, K. W., Richard, E. C., Spackman, J. R., Weinstock, E. M., Herman, R. L., McKinney, K. A., Wennberg, P. O., Eisele, F. L., Stimpfle, R. M., Scott, C. J., Elkins, J. W., and Bui, T. V.: Comparison of ER-2 aircraft and POAM III, MLS, and SAGE II satellite measurements during SOLVE using traditional correlative analysis and trajectory hunting technique, J. Geophys. Res., 107, 8315, 2002a.

Danilin, M. Y., Ko, M. K. W., Froidevaux, L., Santee, M. L., Lyjak, L. V., Bevilacqua, R. M., Zawodny, J. M., Sasano, Y., Irie, H., Kondo, Y., Russell, J. M., Scott, C. J., and Read, W. G.: Trajectory hunting as an effective technique to validate multiplatform measurements: Analysis of the MLS, HALOE, SAGE-II, ILAS, and POAM-II data in October-November 1996, J. Geophy. Res., 107(D20), 4420, 2002b.

Davidson, J., Cantrell, C., McDaniel, A., Shetter, R., Madronich, S., and Calvert, J.: Visible-ultraviolet absorption cross section for NO_2 as a function of temperature dependence, J. Geophys. Res., 93, 7105–7112, 1988.

Davies, S., Mann, G. W., Carslaw, K. S., Chipperfield, M. P., Kettleborough, J. A., Santee, M. L., Oelhaf, H., Wetzel, G., Sasano, Y., and Sugita, T.: 3-D microphysical model studies of Arctic denitrification: comparison with observations, Atmos. Chem. Phys., 5, 3093–3109, 2005.

Davis, D., Crawford, J., Liu, S., McKeen, S., Bandy, A., Thornton, D., Rowland, F., and Blake, D.: Potential impact of iodine on tropospheric levels of ozone and other critical oxidants, J. Geophys. Res., 101, 2135–2147, 1996.

de Zafra, R. L., Jaramillo, M., Parrish, A., Solomon, P., Connor, B., and Barnett, J.: High concentrations of chlorine monoxide at low altitudes in the Antarctic spring stratosphere: Diurnal variation, Nature, 328, 408–411, 1987.

DeMore, W. B., Sander, S. P., Howard, C. J., Ravishankara, A. R., Golden, D. M., Kolb, C. E., Hampson, R. F., Kurylo, M. J., and Molina, M. J.: Chemical Kinetics and Photochemical Data for Use in Stratospheric Modeling No. 12, Jet Propulsion Laboratory, Pasadena, Publication 97-4, 1997.

Deshler, T., Hervig, M., Hofmann, D., Rosen, J., and Liley, J.: Thirty years of in-situ stratospheric aerosol size distribution measurements from Laramie, Wyoming (41^oN), using balloon-borne instruments, J. Geophys. Res., 4167–4179, 2003.

Dessler, A. E.: The effect of deep, tropical convection on the tropical tropopause layer, J. Geophys. Res., 107, 10.1029/2001JD000511, 2002.

Dicke, R., H.: The effect of collisions upon the Doppler Width of Spectral Lines, Physical Review, 89, 472–473, 1953.

Dillon, T. J., Tucceri, M. E., Hölscher, D., and Crowley, J. N.: Absorption cross-section of IO at 427.2 nm and 298 K, J. Photochem. Photobio. A: Chemistry, 176, 3–14, 2005.

Dorf, M.: Investigation of Inorganic Stratospheric Bromine using Balloon-Borne DOAS Measurements and Model Simulations, Ph.D. thesis, Institut für Umweltphysik, University of Heidelberg, 2005.

Dorf, M., Bösch, H., Bovensmann, H., Burrows, J., Butz, A., Camy-Peyret, C., Chipperfield, M., Grunow, K., Goutail, F., Hendrick, F., Hrechanyy, S., Naujokat, B., Pommerau, J.-P., van Roozendael, M., Rozanov, A., Sioris, C., Stroh, F., Weidner, F., and Pfeilsticker, K.: Balloon-borne stratospheric BrO measurements: Intercomparison with ENVISAT/SCIAMACHY BrO limb profiles, Atmos. Chem. Phys. Discuss., 13 011–13 052, 2005.

D'Ottone, L., Campuzano-Jost, P., Bauer, D., and Hynes, A. J.: A Pulsed Laser Photolysis-Pulsed Laser Induced Fluorescence Study of the Kinetics of the Gas-Phase Reaction of OH with NO_2, J. Phys. Chem. A, 105, 10 538–10 543, 2001.

Dransfield, T. J., Perkins, K. K., Donahue, N. M., Anderson, J. G., Sprengnether, M. M., and Demerjian, K. L.: Temperature and pressure dependent kinetics of the gas-phase reaction of the hydroxyl radical with nitrogen dioxide, Geophys. Res. Lett., 26, 687–690, 1999.

Drdla, K., Pueschel, R. F., Strawa, A. W., Cohen, R. C., and Hanisco, T. F.: Microphysics and chemistry of sulphate aerosols at warm stratospheric temperatures, J. Geophys. Res., 104, 26 737–26 752, 1999.

Dufour, G.: Spectroscopie moléculaire atmosphérique: mesure diode laser au laboratoire, inversion des spectres enregistrés sous ballon, modélisation photochimique et contribution à la validation satellitaire, Ph.D. thesis, Université Pierre et Marie Curie, Paris VI, 2005.

Dufour, G., Payan, S., Lefevre, F., Berthet, G., Eremenko, M., Butz, A., Jeseck, P., Te, Y., Pfeilsticker, K., and Camy-Peyret, C.: 4D comparison method to study NO_y partitioning in summer polar stratosphere. Influence of aerosol burden., Atmos. Chem. Phys., 5, 919–926, 2005.

Dufour, G., Nassar, R., Bonne, C. D., Skelton, R., Walker, K. A., Bernath, P. F., Rinsland, C. P., Semeniuk, K., Jin, J. J., McConnell, J. C., and Manney, G. L.: Partitioning between the inorganic chlorine reservoirs HCl and $ClONO_2$ during the Arctic winter 2005 from the ACE-FTS, Atmos. Chem. Phys. Discuss., 6, 1249–1273, 2006.

Engel, A., Schmidt, U., and Stachnik, R. A.: Partitioning between chlorine reservoir species deduced from observations in the Arctic winter stratosphere, J. Atmos. Chem., 27, 107–126, 1997.

Engel, A., Strunk, M., Müller, M., Haase, H.-P., Poss, C., Levin, I., and Schmidt, U.: Temporal development of total chlorine in the high-latitude stratosphere based on reference distributions of mean age derived from CO_2 and SF_6, J. Geophys. Res., 107, 10.1029/2001JD000 584, 2002.

Engel, A., Möbius, T., Haase, H.-P., Bönisch, H., Wetter, T., Schmidt, U., Levin, I., Reddmann, T., Oelhaf, H., Wetzel, G., Grunow, K., Huret, N., and Pirre, M.: Observation of mesospheric air inside the arctic stratospheric polar vortex in early 2003, Atmos. Chem. Phys., 6, 267–282, 2006.

EORCU: The European Ozone Research Coordinating Unit - The Northern Hemisphere Stratosphere in the Winter of 1998/1999, Report in the framework of THESEO, 1999.

Eparvier, F. G., Rusch, D. W., Clancy, R. T., and Thomas, G. E.: Solar Mesosphere Explorer satellite measurements of El Chichon stratospheric aerosols 2: Aerosol mass and size parameters, J. Geophys. Res., 99, 20 533–20 544, 1994.

Evans, J. T., Chipperfield, M. P., Oelhaf, H., Stowasser, M., and Wetzel, G.: Effect of near-IR photolysis of HO_2NO_2 on stratospheric chemistry, Geophys. Res. Lett., 30, 10.1029/2002GL016 470, 2003.

Fahey, D. W., Kelly, K. K., Kawa, S. R., Tuck, A. F., Loewenstein, M., Chan, K. R., and Heidt, L. E.: Observations of denitrification and dehydration in the winter polar stratospheres, Nature, 344, 321–324, 1990.

Farman, J., Gardiner, B., and Shanklin, J.: Large losses of total ozone in Antarctica reveal seasonal ClO_x/NO_x interaction, Nature, 315, 207–210, 1985.

Fayt, C. and van Roozendael, M.: WinDOAS 2.1. Software User Manual, technical report, see http://www.oma.be/BIRA-IASB/Molecules/BrO/WinDOAS-SUM-210b.pdf, 2001.

Ferlemann, F.: Ballongestützte Messung stratosphärischer Spurengase mit differentieller optischer Absorptionsspektroskopie, Ph.D. thesis, Institut für Umweltphysik, University of Heidelberg, 1998.

Ferlemann, F., Camy-Peyret, C., Fitzenberger, R., Harder, H., Hawat, T., Osterkamp, H., Schneider, M., Perner, D., Platt, U., Vradelis, P., and Pfeilsticker, K.: Stratospheric BrO profiles measured at different latitudes and seasons: Instrument description, spectral analysis and profile retrieval, Geophys. Res. Lett., 25, 3847–3850, 1998.

Ferlemann, F., Bauer, N., Harder, H., Osterkamp, H., Perner, D., Platt, U., Schneider, M., Vradelis, P., and Pfeilsticker, K.: A new DOAS-instrument for stratospheric balloon-borne trace gas studies, Appl. Opt., 39, 2377–2386, 2000.

Fitzenberger, R., Bösch, H., Camy-Peyret, C., Chipperfield, M., Harder, H., Platt, U., Sinnhuber, B.-M., Wagner, T., and Pfeilsticker, K.: First profile measurement of tropospheric BrO, Geophys. Res. Lett., 27, 2921–2924, 2000.

Frieler, K., Rex, M., Salawitch, R. J., Canty, T., Streibel, M., von der Gathen, P., Stimpfle, R., Anderson, J. G., and Pfeilsticker, K.: Towards a better quantitative understanding of polar stratospheric ozone loss, Geophys. Res. Lett., submitted, 2006.

Frieß, U., Wagner, T., Pundt, I., Pfeilsticker, K., and Platt, U.: Spectroscopic Measurements of Tropospheric Iodine Oxide at Neumeyer Station, Antarctica, Geophys. Res. Lett., 28, 1941–1944, 2001.

Funk, O.: Photon Pathlength Distributions for Cloudy Skies: Oxygen A-Band Measurements and Radiative Transfer Model Calculations, Ph.D. thesis, Institut für Umweltphysik, Universität Heidelberg, 2000.

Gao, R. S., Fahey, D. W., Del Negro, L. A., Donnelly, S. G., Keim, E. R., Neuman, J. A., Teverovskaia, E., Wennberg, P. O., Hanisco, T. F., Lanzendorf, E. J., Proffitt, M. H., Margitan, J. J., Wilson, J. C., Elkins, J. W., Stimpfle, R. M., Cohen, R. C., McElroy, C. T., Bui, T. P., Salawitch, R. J., Brown, S. S., Ravishankara, A. R., Portmann, R. W., Ko, M. K. W., Weisenstein, D. K., and Newman, P. A.: A comparison of observations and model simulations of NO_x/NO_y in the lower stratosphere, Geophys. Res. Lett., 26, 1153–1156, 1999.

Golden, D. M. and Smith, G. P.: Reaction of OH + NO_2 + M: A new view, J. Phys. Chem. A, 104, 3991–3997, 2000.

Gomez Martin, J. C., Spietz, P., and Burrows, J. P.: Spectroscopic studies of the I_2/O_3 photochemistry Part 1: Determination of the absolute absorption cross sections of iodine oxides of atmospheric relevance, J. Photochem. Photobio. A: Chemistry, 176, 15–38, 2005.

Goody, R. M. and Yung, Y. L.: Atmospheric Radiation: Theoretical Basis, Oxford University Press, 1989.

Grainger, J. and Ring, J.: Anomalous Fraunhofer line profiles, Nature, 193, 762, 1962.

Griffiths, P. R. and de Haseth, J. A.: Fourier Transform Infrared Spectrometry, in Chemical Analysis, Vol. 83, New York, 1986.

Gurlit, W., Bösch, H., Bovensmann, H., Burrows, J., Butz, A., Camy-Peyret, C., Dorf, M., Gerilowski, K., Lindner, A., Noel, S., Platt, U., Weidner, F., and Pfeilsticker, K.: The UV-A and visible solar irradiance spectrum: Intercomparison of absolutely calibrated, spectrally medium resolved solar irradiance spectra from balloon- and satellite-borne measurements, Atmos. Chem. Phys., 5, 1879–1890, 2005.

Hansen, D. and Mauersberger, K.: The vapor pressure of HNO_3-H_2O solutions, J. Phys. Chem., 92, 6167–6170, 1988.

Harder, H.: Messung und Modellierung stratosphärischer Spurenstoffprofile zur Abschätzung des anorganischen Gesamt-Brom-Budgets, Ph.D. thesis, Institut für Umweltphysik, University of Heidelberg, 1999.

Harder, H., Camy-Peyret, C., Ferlemann, F., Fitzenberger, R., Hawat, T., Osterkamp, H., Schneider, M., Perner, D., Platt, U., Vradelis, P., and Pfeilsticker, K.: Stratospheric BrO profiles measured at different latitudes and seasons: Atmospheric observations, Geophys. Res. Lett., 25, 3843–3846, 1998.

Harder, H., Bösch, H., Camy-Peyret, C., Chipperfield, M., Fitzenberger, R., Payan, S., Perner, D., Platt, U., Sinnhuber, B.-M., and Pfeilsticker, K.: Comparison of measured and modeled stratospheric BrO: Implications for the total amount of stratospheric bromine, Geophys. Res. Lett., 27, 3695–3698, 2000.

Harder, J., Brault, J., Johnston, P., and Mount, G.: Temperature dependent NO_2 Cross Section at high Spectral Resolution, J. Geophys. Res., 102, 3861–3879, 1997.

Harwood, M. and Jones, R.: Temperature dependent ultraviolet-visible absorption cross sections of NO_2 and N_2O_4: low temperature measurements of the equilibrium constant for 2 $NO_2 \longleftrightarrow N_2O_4$, J. Geophys. Res., 99, 22 955–22 964, 1994.

Harwood, M., Burkholder, J., Hunter, M., Fox, R., and Ravishankara, A.: Absorption Cross Sections and Self-Reaction Kinetics of the IO Radical, J. Phys. Chem. A, 101, 853–863, 1997.

Haug, H.: Raman-Streuung von Sonnenlicht in der Erdatmosphäre, Diploma thesis, University of Heidelberg, 1996.

Hawat, T., Camy-Peyret, C., and Torguet, R.: Description and performance of a balloon-borne heliostat for solar absorption measurements, Proceedings of the 12th ESA Symposium on Rocket and Balloon Programmes and Related Research, Lillehammer, Norway, 1995.

Hendrick, F., Barret, B., Van Roozendael, M., Bösch, H., Butz, A., De Maziere, M., Goutail, F., Hermans, C., Lambert, J.-C., Pfeilsticker, K., and Pommereau, J.-P.: Retrieval of nitrogen dioxide stratospheric profiles from ground-based zenith-sky UV-visible observations: validation of the technique through correlative comparisons, Atmos. Chem. Phys., 4, SRef-ID: 1680-7324/acp/2004-4-2091, 2091–2106, 2004.

Henyey, L. G. and Greenstein, J. L.: Diffuse radiation in the galaxy, Astrophysical Journal, 93, 70–83, 1941.

Hermans, C., Vandaele, A. C., Carleer, M., Fally, S., Colin, R., Jenouvrier, A., Coquart, B., and Mérienne, M.-F.: Absorption Cross-Sections of Atmospheric Constituents: NO_2, O_2, and H_2O, Environ. Sci. & Pollut. Res., 6, 151–158, 1999.

Herzberg, G.: Molecular Spectra and Molecular Structure, Robert E. Krieger Publishing Company, New York, 2. edn., 1950.

Himmelmann, S., Orphal, J., Bovensmann, H., Richter, A., Ladstätter-Weissenmayer, A., and Burrows, J.: First Observation of the OIO Molecule by Time-Resolved Flash-Photolysis Absorption-Spectroscopy, Chem. Phys. Lett., 251, 330, 1996.

Hirsekorn, M.: Measurements of stratospheric aerosol extinction coefficients by balloon-borne DOAS observations, Diploma thesis, IUP Heidelberg, Heidelberg, 2003.

Hoelscher, D. and Zellner, R.: Absorption cross section of the IO radical and kinetics of the IO + IO and IO + NO reactions, in Proceedings of the fifth European Symposium on Stratospheric Ozone, St. Jean de Luz, France, 2000.

Hoffmann, T., O'Dowd, C., and Seinfeld, J.: IO homogeneous nucleation: An explanation for coastal new particle formation, Geophys. Res. Lett., 28, 1949–1952, 2001.

Holton, J. R., Haynes, P. H., McIntyre, M. E., Douglass, A. R., Rood, R. B., and Pfister, L.: Stratosphere-Troposphere Exchange, Reviews of Geophysics, 33, 403–439, 1995.

Hönninger, G.: Referenzspektren reaktiver Halogenverbindungen für DOAS-Messungen, Diploma thesis, University of Heidelberg, 1999.

Houghton, J., Ding, J., Griggs, D. J., Noguer, M., van der Linden, P. J., Dai, X., Maskell, K., and Johnson, C. A.: Climate Change 2001: The Scientific Basis, Cambridge University Press, 2001.

Huppert, R.: Theoretische und experimentelle Untersuchungen zum solaren I_0 Effekt, Diploma thesis, IUP Heidelberg, 2000.

Ingham, T., Cameron, M., and Crowley, J.: Photodissociation of IO (355 nm) and OIO (532 nm): Quantum Yields for O(^{3}P) and I(^{2}P$_J$) Production, J. Phys. Chem. A, 104, 8001–8010, 2000.

Jeseck, P.: Interférométrie de Fourier, sous ballon stratosphérique, en vue de la mesure à distance par spectroscopie infrarouge en absorption et à haute résolution spectrale, des constituants minoritaires de l'atmosphère terrestre, Ph.D. thesis, Université Pierre et Marie Curie, Paris VII, 1996.

Jimenez, J., Bahreini, R., Cocker, D. R., Zhuang, H., Varutbangkul, V., Flagan, R. C. nd Seinfeld, J., O'Dowd, C. D., and Hoffmann, T.: New particle formation from photooxidation of diiodomethan CH_2I_2, J. Geophys. Res., 108, 2003.

Johnson, B. J., Oltmans, S. J., Vömel, H., Smit, H. G. J., Deshler, T., and Kröger, C.: Electrochemical concentration cell (ECC) ozonesonde pump efficiency measurements and tests on the sensitivity to ozone of buffered and unbuffered ECC sensor cathode solutions, J. Geophys. Res., 107, D19, 4393, 2002.

Johnston, H. S.: Reduction of stratospheric ozone by nitrogen oxide catalysts from supersonic transport exhaust, Science, 173, 517–522, 1971.

Johnston, P.: Making UV/Vis cross sections, reference Fraunhofer and synthetic spectra, unpublished manuscript, 1996.

Joseph, D. M., Ashworth, S. H., and Plane, J. M. C.: The absorption cross-section and photochemistry of OIO, J. Photochem. Photobio. A: Chemistry, 176, 68–77, 2005.

Kerr, J., Evans, W., and McConnell, J.: The effect of NO_2 changes at twilight on tangent ray NO_2 measurements, Geophys. Res. Lett., 4, 577–579, 1977.

Kondo, Y., Koike, M., Engel, A., Schmidt, U., Mueller, M., Sugita, T., Kanzawa, H., Nakazawa, T., Aoki, S., Irie, H., Toriyama, N., Suzuki, T., and Sasano, Y.: NO_y-N_2O correlation observed inside the Arctic vortex in February 1997: Dynamical and chemical effects, J. Geophys. Res., 104, 8215–8224, 1999.

Kromminga, H., Orphal, J., Spietz, P., Voigt, S., and Burrows, J. P.: New measurements of OClO absorption cross sections in the 325-435 nm and their temperature dependence between 213-293 K, J. Photochem. Photobiol. A.: Chemistry, 157, 149–160, 2003.

Kurucz, R., Furenhild, I., Brault, J., and Testermann, L.: Solar flux atlas from 296 to 1300 nm, National Solar Observatory Atlas No. 1, 1984.

Langematz, U., Labitzke, K., and Reimer, E.: Synoptic analysis and trajectories during the MAP/GLOBUS campaign 1983, Planetary and Space Science, 35, 525–538, 1987.

Langley, S. P.: On a Possible Variation of the Solar Radiation and its Probable Effect on Terrestrial Temperatures, Astrophysical Journal, 19, 305–321, 1904.

Lary, D. and Pyle, J.: Diffuse radiation, twilight and photochemistry, J. Atmos. Chem, 373–392, 1991.

Laszlo, B., Kurylo, J., and Huie, R., E.: Absorption cross sections, kinetics of formation and self-reaction of the IO radical produced via the laser photolysis of $N_2O/I_2/N_2$ mixtures, J. Phys. Chem., 99, 11 701–11 707, 1995.

Lefèvre, F., Brasseur, G., Folkins, I., Smith, A., and Simon, P.: Chemistry of the 1991-1992 stratospheric winter: Three-dimensional model simulations, J. Geophys. Res., 99, 8183–8195, 1994.

Lindner, A.: Ballongestützte Messungen der extraterrestrischen, spektralen solaren Irradianz, Diploma thesis, University of Heidelberg, 2005.

Lu, C.-H., Yue, G. K., Manney, G. L., Jäger, H., and Mohnen, V. A.: Lagrangian approach for Stratospheric Aerosol and Gas Experiment (SAGE) II intercomparisons, J. Geophys. Res., 105(D4), 4563–4572, 2000.

McCormick, M. P., Hamill, P., Pepin, T. J., Chu, W. P., Swissler, T. J., and McMaster, L. R.: Satellite Studies of the Stratospheric Aerosol, Bulletin of the American Meteorological Society, 60, 1038–1047, 1979.

McElroy, M., Salawitch, R., Wofsy, C., and Logan, J.: Reductions of Antarctic ozone due to synergistic interactions of chlorine and bromine, Nature, 321, 759–762, 1986.

Michelsen, H., Manney, G., Gunson, M., and Zander, R.: Correlations of stratospheric abundances of NO_y,O_3, N_2O and CH_4 derived from ATMOS measurements, J. Geophys. Res., 103, 28 347–28 359, 1998a.

Michelsen, H. A., Manney, G. L., Gunson, M. R., Rinsland, C. P., and Zander, R.: Correlations of stratospheric abundances of CH_4 and N_2O derived from ATMOS measurements, Geophys. Res. Lett., 25, 2777–2780, 1998b.

Michelsen, H. A., Webster, C. R., Manney, G. L., Scott, D. C., Margitan, J. J., May, R. D., Irion, F. W., Gunson, M. R., Russell III, J. M., and Spivakovsky, C. M.: Maintenance of high HCl/Cl_y and NO_x/NO_y in the Antarctic vortex: A chemical signature of confinement during spring, J. Geophys. Res., 104, 26 419–26 436, 1999.

Mie, G.: Beiträge zur Optik trüber Medien, speziell kolloidaler Metallösungen, Annalen der Physik, 25, 377–445, 1908.

Molina, L. T. and Molina, M. J.: Production of Cl_2O_2 from the self reaction of the ClO radical, J. Phys. Chem., 91, 433, 1987.

Molina, L. T. and Rowland, F. S.: Stratospheric sink for chlorofluromethanes: chlorine atom catalyzed destruction of ozone, Nature, 249, 820–822, 1974.

Montzka, S., Butler, J., Hall, B., Mondell, D., and Elkins, J.: A decline in tropospheric organic bromine, Geophys. Res. Lett., 30, 1826–1829, 2003.

Morris, G. A., Considine, D. B., Dessler, A. E., Kawa, S. R., Kumer, J., Mergenthaler, J., Roche, A., and Russell, J. M.: Nitrogen partitioning in the middle stratosphere as observed by the Upper Atmosphere Research Satellite, J. Geophys. Res., 102, 8955–8966, 1997.

Mössinger, J. C., Rowley, D. M., and Cox, R. A.: The UV-visible absorption cross-sections of $IONO_2$, Atmos. Chem. Phys., 1, 227–234, 2002.

Murphy, D. and Thompson, D.: Halogen ions and NO^+ in the mass spectra of aerosols in the upper troposphere and lower stratosphere, Geophys. Res. Lett., 27, 3217–3220, 2000.

Murphy, D., Thompson, D., and Middlebrook, A.: Bromine, iodine, and chlorine in single aerosol particles at Cape Grim, Geophys. Res. Lett., 24, 3197–3200, 1997.

Murphy, D., Thompson, D., and Mahoney, M. J.: In situ measurements of organics, meteoritic material, mercury, and other elements in aerosol at 5 to 19 kilometers, Science, 282, 1664–1669, 1998.

Naujokat, B., Petzold, K., Labitzke, K., Lenschow, R., Rajewski, B., Wiesner, M., and Wohlfahrt, R.-C.: The stratospheric winter 1996/1997, Beilage zur Berliner Wetterkarte, 1997.

Naujokat, B., Labitzke, K., Lenschow, R., Rajewski, B., and Wohlfahrt, R.-C.: The stratospheric winter 1998/1999, Beilage zur Berliner Wetterkarte, 1999.

Nizkorodov, S. A., Sander, S. P., and Brown, L. R.: Temperature dependence of high-resolution air-broadened absorption cross sections of NO_2 (415-525 nm), J. Phys. Chem. A, 108, 4864–4872, 2004.

Nizkorodov, S. S. and Wennberg, P. O.: First spectroscopic observations of gas-phase HOONO, J. Phys. Chem. A, 106, 855, 2002.

O'Dowd, C. and Hoffmann, T.: Coastal New Particle Formation: A review of the current state-of-the-art, Environ. Chem., 2, 245–255, 2005.

Orphal, J.: A critical review of the absorption cross-sections of O_3 and NO_2 in the ultraviolet and visible, J. Photochem. Photobio. A: Chemistry, 157, 185–209, 2003.

Osterkamp, H.: Messung von atmosphärischen O_4-Profilen, Diploma thesis, University of Heidelberg, 1997.

Osterman, G. B., Sen, B., Toon, G. C., Salawitch, R. J., Margitan, J. J., Blavier, J.-F., Fahey, D. W., and Gao, R. S.: Partitioning of NO_y species in the summer Arctic stratosphere, Geophys. Res. Lett., 26, 1157–1160, 1999.

Payan, S.: Restitution de profils verticaux de concentration des constituants minoritaires de la stratosphère à partir de spectres infrarouges à haute résolution enregistrés sous ballon, Ph.D. thesis, Université Pierre et Marie Curie, Paris VI, 1996.

Payan, S., Camy-Peyret, C., Lefevre, F., Jeseck, P., Hawat, T., and Durry, G.: First direct simultaneous HCl and $ClONO_2$ profile measurements in the Arctic vortex, Geophys. Res. Lett., 25, 2663–2666, 1998.

Payan, S., Camy-Peyret, C., Jeseck, P., Hawat, T., Pirre, M., Renard, J.-B., Robert, C., Lefevre, F., Kanzawa, H., and Sasano, Y.: Diurnal and nocturnal distribution of stratospheric NO_2 from solar and stellar occultation measurements in the Arctic vortex: Comparison with models and ILAS satellite measurements, J. Geophys. Res., 104, 21 585–21 593, 1999.

Peters, C., Pechtl, S., Stutz, J., Hebestreit, K., Hönninger, G., Heumann, K. G., Schwarz, A., Winterlik, J., and Platt, U.: Reactive and organic halogen species in three different European coastal environments, Atmos. Chem. Phys., 5, 3357–3375, 2005.

Pfeilsticker, K., Erle, F., and Platt, U.: Observation of the stratospheric NO_2 latitudinal distribution in the northern winter hemisphere, J. Atmos. Chem., 32, 101–120, 1999.

Pfeilsticker, K., Sturges, W., Bösch, H., Camy-Peyret, C., Chipperfield, M., Engel, A., Fitzenberger, R., Müller, M., Payan, S., and Sinnhuber, B.-M.: Lower stratospheric organic and inorganic bromine budget for the Arctic winter 1998/99, Geophys. Res. Lett., 28, 4595–4598, 2000.

Pfeilsticker, K., Bösch, H., Camy-Peyret, C., Fitzenberger, R., Harder, H., and Osterkamp, H.: First Atmospheric Profile Measurements of UV/Visible O_4 Absorption Band Intensities: Implications for the Spectroscopy and the Formation Enthalpy of the O_2-O_2 Dimer, Geophys. Res. Lett., 28, 4595–4598, 2001.

Platt, U.: Differential optical absorption spectroscopy (DOAS), in Air Monitoring by Spectroscopic Techniques, edited by W. M. Sigrist, vol. 127, 27–84, John Wiley & Sons, Inc., 1994.

Platt, U. and Stutz, J.: Differential Optical Absorption Spectroscopy (DOAS), Principle and Applications, ISBN 3-340-21193-4, Springer Verlag, Heidelberg, 2005, in press.

Platt, U., Perner, D., and Pätz, H. W.: Simultaneous Measurement of Atmospheric CH_2O, O_3 and NO_2 by Differential Optical Absorption, J. Geophys. Res., 84, 6329–6335, 1979.

Plenge, J., Kühl, S., Vogel, B., Müller, R., Stroh, F., von Hobe, M., Flesch, R., and Rühl, E.: Bond strength of chlorine peroxide, J. Phys. Chem. A, 109, 6730–6734, 2005.

Plumb, R. A.: A "tropical pipe" model of stratospheric transport, J. Geophys. Res., 101, 3957–3972, 1996.

Plumb, R. A. and Ko, M. K. W.: Interrelationships between mixing ratios of long-lived stratospheric constituents, J. Geophys. Res., 97, 10 145–10 156, 1992.

Plumb, R. A., Waugh, D. W., and Chipperfield, M. P.: The effect of mixing on tracer relationsships in the polar vortices, J. Geophys. Res., 105, 10 047–10 062, 2000.

Poole, L. M. and McCormick, M. P.: Polar stratospheric clouds and the Antarctic ozone hole, J. Geophys. Res., 93, 8423–8430, 1988.

Portmann, R., Brown, S., Gierczak, T., Talukdar, R., Burkholder, J., and Ravishankara, A.: Role of nitrogen oxides in the stratosphere: a reevaluation based on laboratory studies, Geophys. Res. Lett., 26, 2875–2878, 1999.

Prasad, S. S.: A modeling study of the stratospheric NO_x/NO_y and NO_x/HNO_3 ratios: Single- versus dual-channeled mode of OH, NO_2 associtation, J. Geophys. Res., 108, 10.1029/2002JD002970, 2003.

Press, W., Flannery, B., Theukolky, S., and Vetterling, W.: Numerical Recipes in C, Cambridge University Press, London, 1988.

Pundt, I., Pommereau, J.-P., Phillips, C., and Latelin, E.: Upper limit of iodine oxide in the lower stratosphere, J. Atmos. Chem., 30, 173–185, 1998.

Randeniya, L. K., Plumb, I. C., and Ryan, K. R.: NO_y and Cl_y partitioning in the middle stratosphere: A box model investigation using HALOE data, J. Geophys. Res., 104, 26 667–26 686, 1999.

Reichl, U.: Ground-based direct Sun UV/vis spectroscopy in Timon/Northeastern Brazil: Comparison of tropospheric air mass pollution in the dry and wet season, Diploma thesis, University of Heidelberg, 2005.

Rex, M., Harris, N. R. P., von der Gathen, P., Lehmann, R., Braathen, G. O., Reimer, E., Beck, A., Chipperfield, M. P., Alfier, R., Allaart, M., O'Connor, F., Dier, H., Dorokhov, V., Fast, H., Gil, M., Kyrö, E., Litynska, Z., Mikkelsen, I. S., Molyneux, M. G., Nakane, H., Notholt, J., Rummukainen, M., Viatte, P., and Wenger, J.: Prolonged stratospheric ozone loss in the 1995/96 Arctic winter, Nature, 389, 835–838, 1997.

Rex, M., Salawitch, R. J., Toon, G. C., Sen, B., Margitan, J. J., Osterman, G. B., Blavier, J.-F., Gao, R. S., Donnelly, S., Keim, E., Neuman, J., Fahey, D. W., Webster, C. R., Scott, D. C., Herman, R. L., May, R. D., Moyer, E. J., Gunson, M. R., Irion, F. W., Chang, A. Y., Rinsland, C. P., and Bui, T. P.: Subsidence, mixing, and denitrification of Arctic polar vortex air measured during POLARIS, J. Geophys. Res., 104, 26 611–26 623, 1998.

Rex, M., Salawitch, R. J., Santee, M. L., Waters, J. W., Hoppel, K., and Bevilacqua, R.: On the unexplained stratospheric ozone losses during cold Arctic Januaries, Geophys. Res. Lett., 30, 10.1029/2002GL016008, 2003.

Rex, M., Salawitch, R. J., von der Gathen, P., Harris, N. R. P., Chipperfield, M. P., and Naujokat, B.: Arctic ozone loss and climate change, Geophys. Res. Lett., 31, 10.1029/2003GL018844, 2004.

Rinsland, C. P., Mahieu, E., Zander, R., Jones, N. B., Chipperfield, M. P., Goldman, A., Anderson, J., Russell III, J. M., Demoulin, P., Notholt, J., Toon, G. C., Blavier, J.-F., Sen, B., Sussmann, R., Wood, S. W., Meier, A., Griffith, D. W. T., Chiou, L. S., Murcray, F. J., Stephen, T. M., Hase, F., Mikuteit, S., Schulz, A., and Blumenstock, T.: Long-term trends of inorganic chlorine from ground-based infrared solar spectra: Past increases and evidence for stabilization, J. Geophys. Res., 108, 10.1029/2002JD003001, 2003.

Rivière, E., M.Pirre, Berthet, G., Renard, J.-B., Taupin, F., Huret, N., Chartier, M., Knudsen, B., and Lefèvre, F.: On the interaction between nitrogen and halogen species in the Arctic polar vortex during THESEO and THESEO2000, J. Geophys. Res., 108, 8311, 2003.

Rivière, E., M.Pirre, Berthet, G., Renard, J.-B., and Lefèvre, F.: Investigating the Halogen Chemistry from High-Latitude Nighttime Stratospheric Measurements of OClO and NO_2, J. Atm. Chem., 48, 261–282, 2004.

Rodgers, C. D.: Retrieval of Atmospheric Temperature and Composition From Remote Measurements of Thermal Radiation, Rev. Geophys., 14, 609–624, 1976.

Rodgers, C. D.: Inverse methods for atmospheric sounding, World Scientific, Singapore, New Jersey, London, Hongkong, 2000.

Rodgers, C. D. and Connor, B. J.: Intercomparison of remote sounding instruments, J. Geophys. Res., 108, 10.1029/2002JD002299, 2003.

Roedel, W.: Physik unserer Umwelt: die Atmosphäre, Springer Verlag, Berlin, 3., überarb. und aktualisierte Aufl., 2000.

Roehl, C. M., Nizkorodov, S. A., Zhang, H., Blake, G. A., and Wennberg, P. O.: Photodissociation of HNO_4 in the near IR, J. Phys. Chem. A., 106, 3766–3772, 2002.

Roscoe, H. K. and Pyle, J. A.: Measurements of solar occultation - The error in a naive retrieval if the constituent's concentration changes, J. Atmos. Chem., 5, 323–341, 1987.

Roscoe, H. K., Fish, D. J., and L., J. R.: Interpolation errors in UV-visible spectroscopy for stratospheric sensing: implications for sensitivity, spectral resolution, and spectral range, App. Opt., 35, 427–432, 1996.

Rothman, L. S., Rinsland, C. P., Goldman, A., Massie, S. T., Edwards, D. P., Flaud, J.-M., Perrin, A., Camy-Peyret, C., Dana, V., Mandin, J.-Y., Schroeder, J., McCann, A., Gamache, R. R., Wattson, R. B., Yoshino, K., Chance, K. V., Jucks, K. W., Brown, L. R., Nemtchinov, and Varanasi, P.: The HITRAN 2000 molecular spectroscopic database: including updates through 2001, J. Quant. Spec. and Rad. Transf., 82, 1–4, 2003.

Rothman, L. S., Jacquemart, D., Barbe, A., Chris Benner, D., Birk, M., Brown, L. R., Carleer, M. R., Chackerian, C., Chance, K., Dana, V., Devi, V. M., Flaud, J.-M., Gamache, R. R., Goldman, A., Hartmann, J.-M., Jucks, K. W., Maki, A. G., Mandin, J.-Y., Massie, S. T., Orphal, J., Perrin, A., Rinsland, C. P., Smith, M. A. H., Tennyson, J., Tolchenov, R. N., Toth, R. A., Vander Auwera, J., Varanasi, P., and Wagner, G.: The HITRAN 2004 Molecular Spectroscopic Database, J. Quant. Spec. and Rad. Transf., 96, 139–204, 2005.

Rowley, D. M., Bloss, W. J., Cox, R. A., and Jones, R. L.: Kinetics and Products of the IO+BrO Reaction, J. Phys. Chem. A, 105, 7855–7864, 2001.

Rozanov, E., Callis, L., Schlesinger, M., Yang, F., Andronova, N., and Zubov, V.: Atmospheric response to NO_y source due to energetic electron precipitation, Geophys. Res. Lett., 32, 10.1029/2005GL023041, 2005.

Russell, P. B. and McCormick, M. P.: SAGE II aerosol data validation and initial data use: an introduction and overview, J. Geophys. Res., 94, 8335, 1989.

Salawitch, R., Weisenstein, D., Kovalenko, L., Sioris, C., Wennberg, P., Chance, K., Ko, M., and Mclinden, C.: Sensitivity of ozone to bromine in the lower stratosphere, Geophys. Res. Lett., 32, L05 811, 2005.

Salawitch, R. J., Wennberg, P. O., Toon, G. C., Sen, B., and Blavier, J.-F.: Near IR photolysis of HO_2NO_2: Implications for HO_x, Geophys. Res. Lett., 29, 10.1029/2002GL015 006, 2002.

Sander, S., Riedl, R., DeMore, W. B., Golden, D., Howard, C., Ravishankara, A., Kolb, C., Hampson, R., Huie, R., Kurylo, M., Molina, M., and Moortgart, G.: Chemical Kinetics and Photochemical Data for Use in Stratospheric Modeling: supplement to evaluation 12: update of key reactions, NASA/JPL Publication 97-4, 2000.

Sander, S., Friedl, R., Ravishankara, A., Golden, D., Kolb, C. E., Kurylo, M., Huie, R., Orkin, V., Molina, M., Moortgat, G., and Finlayson-Pitts, B.: Chemical Kinetics and Photochemical Data for Use in Atmospheric Studies, NASA/JPL-Publication, 2003.

Schulte: DAMF v1.22 - Direct Light Air Mass Factors, *user manual*, iUP Heidelberg, 1996.

Schwärzle, J.: Spektroskopische Messung von Halogenoxiden in der marinen atmosphärischen Grenzschicht in Alcântara/Brasilien, Staatsexamensarbeit, Universität Heidelberg, 2005.

Sen, B., Toon, G. C., Osterman, G. B., Blavier, J.-F., Margitan, J. J., Salawitch, R. J., and Yue, G. K.: Measurements of reactive nitrogen in the stratosphere, J. Geophys. Res., 103, 3571–3586, 1998.

Sen, B., Osterman, G. B., Salawitch, R. J., Toon, G. C., Margitan, J. J., Blavier, J.-F., Chang, A. Y., May, R. D., Webster, C. R., Stimpfle, R. M., Bonne, G. P., Voss, P. B., Perkins, K. K., Anderson, J. G., Cohen, R. C., Elkins, J. W., Dutton, G. S., Hurst, D. F., Romashkin, P. A., Atlas, E. L., Schauffler, S. M., and Loewenstein, M.: The budget and partitioning of stratospheric chlorine during the 1997 Arctic summer, J. Geophys. Res., 104, 26 653–26 665, 1999.

Shangavi, S.: An efficient Mie theory implementation to investigate the influence of aerosols on radiative transfer, Diploma thesis, University of Heidelberg, 2003.

Sioris, C. E., Kurosu, T. P., Martin, R. V., and Chance, K.: Stratospheric and tropospheric NO_2 observed by SCIAMACHY: first results, Adv. Space Res., 34, 780–785, 2004.

Solomon, P., Barret, J., Connor, B., Zoonematkermani, S., Parrish, A., Lee, A., Pyle, J., and Chipperfield, M.: Seasonal observations of chlorine monoxide in the stratosphere over Antarctica during the 1996-1998 ozone holes and comparison with the SLIMCAT three-dimensional model, J. Geophys. Res., 105, 28 979–29 001, 2000.

Solomon, P., Connor, B., Barrett, J., Mooney, T., Lee, A., and Parrish, A.: Measurements of stratospheric ClO over Antarctica in 1996-2000 and implications for ClO dimer chemistry, Geophys. Res. Lett., 29, 10.1029/2002GL015 232, 2002.

Solomon, S.: Stratospheric ozone depletion: a review of concepts and history, Rev. Geophys., 37, 275–316, 1999.

Solomon, S., Garcia, R., and Ravishankara, A.: On the role of iodine in ozone depletion, J. Geophys. Res., 99, 20 491–20 499, 1994.

Solomon, S., Portman, R., Garcia, R., Randel, W., Wu, F., Nagatani, R., Gleason, J., Thomason, L., Poole, L., and McCormick, M.: Ozone depletion at mid-latitudes: coupling of volcanic aerosols and temperature variability to anthropogenic chlorine, Geophys. Res. Lett., 25, 1871–1874, 1998.

Spietz, P., Gomez Martin, J. C., and Burrows, J. P.: Spectroscopic studies of the I_2/O_3 photochemistry Part 2: Improved spectra of iodine oxides and analysis of the IO absorption spectrum, J. Photochem. Photobio. A: Chemistry, 176, 50–67, 2005.

Stimpfle, R. M., Cohen, R. C., Bonne, G. P., Voss, P. B., Perkins, K. K., Koch, L. C., Anderson, J. G., Salawitch, R. J., Lloyd, S. A., Gao, R. S., Del Negro, L. A., Keim, E. R., and Bui, T. P.: The coupling of $ClONO_2$, ClO, and NO_2 in the lower stratosphere from in situ observations using th NASA ER-2 aircraft, J. Geophys. Res., 104, 26 705–26 714, 1999.

Stimpfle, R. M., Wilmouth, D. M., Salawitch, R. J., and Anderson, J. G.: Firts measurements of ClOOCl in the stratosphere: The coupling of ClOOCl and ClO in the Arctic polar vortex, J. Geophys. Res., 109, 10.1029/2003JD003 811, 2004.

Stohl, A., Bonsanoni, P., Cristofanelli, P., Collins, W., Feichter, J., Frank, A., Forster, C., Gerasopoulos, E., Gäggeler, H., James, P., Kentarchos, T., Kromp-Kolb, H., Krüger, B., Land, C., Meloen, J., Papayannis, A., Priller, A., Seibert, P., Sprenger, M., Roelofs, G. J., Scheel, H. E., Schnabel, C., Siegmund, P., Tobler, L., Trickl, T., Wernli, H., Wirth, V., Zanis, P., and Zerefos, C.: Stratosphere-troposphere exchange: A review, and what we have learned from STACCATO, J. Geophys. Res., 108, 10.1029/2002JD002 490, 2003.

Stowasser, M., Oelhaf, H., Ruhnke, R., Wetzel, G., Friedl-Vallon, F., Kleinert, A., Kouker, W., Lengel, A., Maucher, G., Nordmeyer, H., Reddmann, T., Trieschmann, O., von Clarmann, T., and Fischer, H.: A characterization of the warm 1999 Arctic winter by observations and modeling: NO_y partitioning and dynamics, J. Geophys. Res., 107, 10.1029/2001JD001 217, 2002.

Stutz, J.: Messung der Konzentration troposhärischer Spurenstoffe mittels Differentieller-Optischer-Absorptions-Spektroskopie: Eine neue Generation von Geräten und Algorithmen, Ph.D. thesis, Institut für Umweltphysik, Ruprecht-Karls-Universität Heidelberg, d455, 1996.

Stutz, J. and Platt, U.: Numerical Analysis and Estimation of the Statistical Error of Differential Optical Absorption Spectroscopy Measurements with Least-Squares methods, Appl. Opt., 35, 6041–6053, 1996.

Sugita, T., Kondo, Y., Nakaijma, H., Schmidt, U., Engel, A., Oelhaf, H., Wetzel, G., Koike, M., and Newman, P. A.: Denitrification observed inside the Arctic vortex in february 1995, J. Geophys. Res., 103, 16 221–16 233, 1998.

Thomason, L. W., Poole, L. R., and Deshler, T.: A global climatology of stratospheric aerosol surface area density deduced from Stratospheric Aerosol and Gas Experiment II measurements: 1984-1994, J. Geophys. Res., 102, 8967–8976, 1997.

Toon, G. C., Farmer, C. B., Lowes, L. L., Schaper, P. W., Blavier, J. F., and Norton, R. H.: Infrared aircraft measurements of stratospheric composition over Antarctica during September 1987, J. Geophys. Res., 94, 16 571–16 596, 1989.

Toon, O., Hamill, P., Turco, R., and Pinto, J.: Condensation of HNO_3 and HCl in the winter polar stratosphere, Geophys. Res. Lett., 13, 1284–1287, 1986.

Tucceri, M. E., Hölscher, D., Rodriguez, A., Dillon, T. J., and Crowley, J. N.: Absorption cross section and photolysis of OIO, Phys. Chem. Chem. Phys, 8, 834–846, 2006.

Unsöld, A. and Baschek, B.: Der neue Kosmos: Einführung in die Astronomie und Astrophysik, SpringerJohn, Berlin Heidelberg New York, 6. edn., 1999.

Uppala, S., Kallberg, P., Hemandez, A., Saarinen, S., Florino, M., Li, X., Onogi, K., Sokka, N., Andrae, U., and Da Costa, V.: ERA-40 ECMWF 45-year reanalysis of the global atmosphere and surface conditions 1957-2002, ECMWF Newsl., 101, 2–22, 2004.

Van de Hulst, H.: Light scattering by small particles, Dover publication, New York, 1981.

Vandaele, A., C., Hermanns, C., Simon, P., C., Carleer, M., Colin, R., Fally, S., Mérienne, M., F., Jenouvrier, A., and Coquart, B.: Measurements of the NO_2 absorption cross section from 42,000–10,000 cm^{-1} (238–1000 nm) at 220 and 294 K, J. Quant. Spec. and Rad. Transf., 59, 171–184, 1998.

Vandaele, A., C., Hermanns, C., Fally, S., Carleer, M., Mérienne, M., F., Jenouvrier, A., and Colin, R.: Absorption cross-section of NO_2: simulation of temperature and pressure effects, J. Quant. Spec. and Rad. Transf., 76, 373–391, 2003.

Vogel, B., Müller, R., Engel, A., Grooss, J.-U., Toohey, D., Woyke, T., and Stroh, F.: Midlatitude ClO during the maximum atmospheric chlorine burden: in situ balloon measurements and model simulations, Atmos. Chem. Phys., 5, 1623–1638, 2005.

Vogel, B., Feng, W., Streibel, M., and Müller, R.: The potential impact of ClO_x radical complexes on polar stratospheric ozone loss processes, Atmos. Chem. Phys. Discuss., 6, 981–1022, 2006.

Voigt, S., Orphal, J., Bogumil, K., and Burrows, J. P.: The temperature dependence (203-293 K) of the absorption cross-sections of O_3 in the 230 - 850 nm region measured by Fourier-transform spectroscopy, J. of Photochemistry and Photobiology A: Chemistry, 143, 1–9, 2001.

Voigt, S., Orphal, J., and Burrows, J. P.: The temperature and pressure dependence of the absorption cross-sections of NO_2 in the 250 - 800 nm region measured by Fourier-transform spectroscopy, J. of Photochemistry and Photobiology A: Chemistry, 149, 1–7, 2002.

von der Gathen, P., Rex, M., Harris, N. R. P., Lucic, D., Knudsen, B. M., Braathen, G. O., De Backer, H., Fabian, R., Fast, H., Gil, M., Kyrö, E., Mikkelsen, I. S., Rummukainen, M., Stähelin, J., and Varotsos, C.: Observational evidence for chemical ozone depletion over the Arctic in winter 1991–92, Nature, 375, 131–134, 1995.

von Hobe, M., Grooss, J.-U., Müller, R., Hrechanyy, S., Winkler, U., and Stroh., F.: A re-evaluation of the ClO/Cl_2O_2 equilibrium constant based on stratospheric in-situ observations, Atmos. Chem. Phys., 5, 693–702, 2005.

von Savigny, C., Ulasi, E. P., Eichman, K. U., Bovensmann, H., and Burrows, J. P.: Detection and mapping of polar stratospheric clouds using limb scattering observations, Atmos. Chem. Phys., 5, 3071–3079, 2005.

Voss, P. B., Stimpfle, R. M., Cohen, R. C., Hanisco, T. F., Bonne, G. P., Perkins, K. K., Lanzendorff, E. J., Anderson, J. G., Salawitch, R. J., Webster, C. R., Scott, D. C., May, R. D., Wennberg, P. O., Newman, P. A., Lait, L. R., Elkins, J. W., and Bui, T. P.: Inorganic chlorine partitioning in the summer lower stratosphere: Modeled and measured $ClONO_2$/HCl during POLARIS, J. Geophys. Res., 106, 1713–1732, 2001.

Wagner, G. and Birk, A.: New infrared spectroscopic database for chlorine nitrate, J. Quant. Spec. and Rad. Transf., 82, 443–460, 2003.

Wagner, T., Leue, C., Pfeilsticker, K., and Platt, U.: Monitoring of the stratospheric chlorine activation by Global Ozone Monitoring Experiment (GOME) OClO measurements in the austral and boreal winters 1995 to 1999, J. Geophys. Res., 106, 4971–4989, 2001.

Wahner, A., Tyndall, G., and Ravishankara, A.: Absorption cross sections for OClO as a function of temperature in the wavelength range from 240-490 nm, J. Phys. Chem., 91, 2735–2738, 1987.

Waugh, D. W., Plumb, R. A., Elkins, J. W., Fahey, D. W., Boering, K. A., Dutton, G. S., Volk, C. M., Keim, E., Gao, R.-S., Daube, B. C., Wofsy, S. C., Loewenstein, M. and. Podolske, J. R., Chan, K. R., Proffitt, M. H., Kelly, K. K., Newman, P. A., and Lait, L. R.: Mixing of polar vortex air into middle latitudes as revealed by tracer-tracer scatterplots, J. Geophys. Res., 102, 13 119–13 134, 1997.

Webster, C. R., May, R. D., Jaegle, L., Hu, H., Sander, S. P., Gunson, M. R., Toon, G. C., Russell, J. M., Stimpfle, R. M., and Koplow, J. P.: Hydrochloric acid and the chlorine budget of the lower statosphere, Geophys. Res. Lett., 21, 2575–2578, 1994.

Weidner, F., Bösch, H., Bovensmann, H., Burrows, J., Butz, A., Camy-Peyret, C., Dorf, M., Gerilowski, K., Gurlit, W., Platt, U., von Friedeburg, C., Wagner, T., and Pfeilsticker, K.: Balloon-borne limb profiling of UV/vis skylight radiances, ozone and nitrogen dioxide: Technical set-up and validation of the method, Atmos. Chem. Phys., 5, 1409–1422, 2005.

Wennberg, P., Brault, J., Hanisco, T., Salawitch, R., and Mount, G.: The atmospheric column abundance of IO: Implications for stratospheric ozone, J. Geophys. Res., 102, 8887–8898, 1997.

Wetzel, G., Oelhaf, H., Ruhnke, R., Friedl-Vallon, F., Kleinert, A., Kouker, W., Maucher, G., Reddmann, T., Seefeldner, M., Stowasser, M., Trieschmann, O., von Clarmann, T., and Fischer, H.: NO_y partitioning and budget and its correlation with N_2O in the Arctic vortex and in summer midlatitudes in 1997, J. Geophys. Res., 107, 10.1029/2001JD000916, 2002.

Wittrock, F., Müller, R., Richter, A., Bovensmann, H., and Burrows, J.: Measurements of iodine monoxide (IO) above Spitsbergen, Geophys. Res. Lett., 27, 1471–1474, 2000.

WMO: Scientific Assessment of Ozone depletion: 1998, *World Meteorological Organization Global Ozone Research and Monitoring Project, Report 44*, 1998.

WMO: Scientific Assessment of Ozone depletion: 2002, *World Meteorological Organization Global Ozone Research and Monitoring Project, Report 47*, 2003.

Wofsy, S., McElroy, M., and Yung, L.: The chemistry of atmospheric bromine, Geophys. Res. Lett., 2, 215–218, 1975.

Zellner, R.: Global Aspects of Atmospheric Chemistry, Springer, Germany, 1. edn., 1999.

Publications

Parts of this work are published in:

Butz, A., Bösch, H., Camy-Peyret, C., Chipperfield, M., Dorf, M., Dufour, G., Grunow, K., Jeseck, P., Kühl, S., Payan, S., Pepin, I., Pukite, J., Rozanov, A., von Savigny, C., Sioris, C., Wagner, T., Weidner, F., and Pfeilsticker, K.: Inter-comparison of stratospheric O_3 and NO_2 abundances retrieved from balloon borne direct sun observations and Envisat/SCIAMACHY limb measurements, Atmos. Chem. Phys., 6, 1293–1314, 2006.

Canty, T., Rivière, E., Salawitch, R., Berthet, G., Renard, J.-B., Pfeilsticker, K., Dorf, M., Butz, A., Bösch, H., Stimpfle, R., Wilmouth, D., Richard, E., Fahey, D., Popp, P., Schoeberl, M., Lait, L., and Bui, T.: Nighttime OClO in the winter Arctic vortex, J. Geophys. Res., 110, D01 301, 2005.

Dorf, M., Bösch, H., Bovensmann, H., Burrows, J., Butz, A., Camy-Peyret, C., Chipperfield, M., Grunow, K., Goutail, F., Hendrick, F., Hrechanyy, S., Naujokat, B., Pommerau, J.-P., van Roozendael, M., Rozanov, A., Sioris, C., Stroh, F., Weidner, F., and Pfeilsticker, K.: Balloon-borne stratospheric BrO measurements: Intercomparison with ENVISAT/SCIAMACHY BrO limb profiles, Atmos. Chem. Phys. Discuss., 5, 13011–13052, 2005.

Dufour, G., Payan, S., Lefevre, F., Berthet, G., Eremenko, M., Butz, A., Jeseck, P., Te, Y., Pfeilsticker, K., and Camy-Peyret, C.: 4D comparison method to study NO_y partitioning in summer polar stratosphere. Influence of aerosol burden., Atmos. Chem. Phys., 5, 919–926, 2005.

Gurlit, W., Bösch, H., Bovensmann, H., Burrows, J., Butz, A., Camy-Peyret, C., Dorf, M., Gerilowski, K., Lindner, A., Noel, S., Platt, U., Weidner, F., and Pfeilsticker, K.: The UV-A and visible solar irradiance spectrum: Inter-comparison of absolutely calibrated, spectrally medium resolved solar irradiance spectra from balloon- and satellite-borne measurements, Atmos. Chem. Phys., 5, 1879–1890, 2005.

Hendrick, F., Barret, B., Van Roozendael, M., Bösch, H., Butz, A., De Maziere, M., Goutail, F., Hermans, C., Lambert, J.-C., Pfeilsticker, K., and Pommereau, J.-P.: Retrieval of nitrogen dioxide stratospheric profiles from ground-based zenith-sky UV-visible observations: validation of the technique through correlative comparisons, Atmos. Chem. Phys., 4, 2091–2106, 2004.

Weidner, F., Bösch, H., Bovensmann, H., Burrows, J. P., Butz, A., Camy-Peyret, C., Dorf, M., Gerilowski, K., Gurlit, W., Platt, U., von Friedeburg, C., Wagner, T. and Pfeilsticker, K.: Balloon-borne limb profiling of UV/vis skylight radiances, ozone and nitrogen dioxide: Technical set-up and validation of the method, Atmos. Chem. Phys., 5, 1409–1422, 2005.

List of Figures

List of Tables

Acknowledgements

Finally, I would like to thank all friends and colleagues who contributed to the presented work. Thanks to

Prof. Dr. Klaus Pfeilsticker for guiding my research by his scientific expertise and for broadening my mind by his experience of life.

Directeur de Recherche Claude Camy-Peyret and Prof. Dr. Ulrich Platt for giving a warm welcome to me and for providing a fruitful background for my research at the Institut für Umweltphysik (IUP) and the Laboratoire de Physique Moléculaire pour l'Atmosphère et l'Astrophysique (LPMAA).

Prof. Dr. Frank Arnold and Prof. Dr. Michel Pirre for reviewing this work.

My colleagues of the DOAS and LPMA balloon teams, Marcel Dorf, Frank Weidner, Hartmut Bösch, Pascal Jeseck, Sébastien Payan, Isabelle Pepin, Gaëlle Dufour, and Yao Té, who teached me how to operate the instruments and retrieval algorithms, solved numerous minor and major technical and scientific problems, and became valuable friends. Thanks to Lena Kritten, Benjamin Simmes, Ulrike Reichl, Julia Schwärzle, and Aaron Lindner for their support and company. A special thanks to Marcel, Frank, Lena, Benny and Hartmut for proof-reading this manuscript, to Marcel for providing the OClO and BrO data, and to Sébastien and Gaëlle for providing some of the LPMA data. Thanks to Hartwig Harder for his willingness to help building the new DOAS electronics and to assist in instrumental emergencies. Thanks to Christian Rouillé, Daniel Mayèle, Georges Lerille, and Nicole Gasgnier for their technical assistance and company.

Katja Grunow for the meteorological support and her enjoyable company during measurement campaigns.

Konstantin Gerilowski and Wolfgang Gurlit for their efforts to simulate the Sun and for illuminating boring nights.

Christian von Savigny, Alexei Rozanov, Christopher Sioris, Sven Kühl, and Janis Pukite for letting validate their SCIAMACHY O_3 and NO_2 data.

Andreas Engel for providing observations of the balloon borne cryogenic whole air sampler and Hermann Oelhaf, Gerald Wetzel, and Guido Maucher for making MIPAS-B2 measurements available to us.

Martyn Chipperfield for providing SLIMCAT data.

Ross Salawitch for straightforward cooperation.

The balloon teams of CNES for launching, controlling and recovering the LPMA/DOAS payload such that scientific research is possible.

Hoffmann Meßtechnik for building the new DOAS electronics.

My colleagues at IUP and LPMAA for their company and whatsoever help. In particular, thanks to Thomas Scholl, Andreas Lotter, Christoph Kern, Thierry Marbach, Christina Peters, Sebastian Trick, Jutta Zingler, Katja Seitz, Nicole Bobrowski, Roland von Glasow, Susanne Pechtl, Christian Frankenberg, Suniti Shangavi, and Victor Ferreira. Special thanks to Thierry for assisting in French translations.

Christoph Eichhorn, Christian Traeger, and Andrea Boßlet for their friendship and company during the recent years. Christoph's comments on the physics part of this manuscript are especially appreciated.

My parents Lothar and Christa, and my brother Bastian for their unconditional support and for teaching me their way how to get things done.

A very special thanks to Ellen Schwinger for her congeniality and empathy, for sharing her amazing gift of anticipation and enthusiasm and for mastering "la cuisine souabe".